Chapter 4
Less-Common Carbon Nanostructures

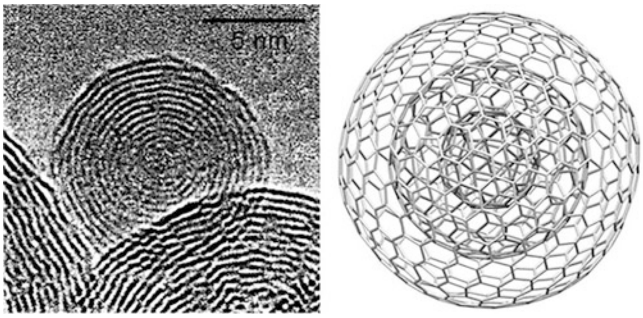

When the area of nanotechnology began to develop intensively as an independent field in the frontiers of physics, chemistry, materials chemistry and physics, medicine, biology, and other disciplines two decades ago, terms such as “nanoparticle,” “nanopowder,” “nanotube,” and “nanoplate,” and other terms related to shape rapidly became very common. At the same time, during the last years, efforts of researchers have led to reports of a large number of the nanostructure types mentioned earlier and the discovery of rarer species, such as “nanodumbbells,” “nanoflowers,” “nanorices,” “nanolines,” “nanotowers,” “nanoshuttles,” “nanobowlings,” “nanowheels,” “nanofans,” “nanopencils,” “nanotrees,” “nanoarrows,” “nanonails,” “nanobottles,” and “nanovolcanoes,” among many others. The naming of a discovered rare nanoform is commonly left to the imagination of researchers. Since any novel nanoform/nanostructure could, theoretically, have useful, unexpected, and unpredictable applications (e.g., famous graphene, discovered not long ago), each new achievement, reproducible or not, is welcome due to the importance of nanotechnology in current and future applications. Without a good understanding of the reasons for shape formation, approaches to the synthesis of nanostructures can be hard to carry out.

According to the available literature, there is no universal generalization of rare and common nanostructures. Several existing classifications are related to dimensionality of the nanostructure itself and its components (for instance, 0D clusters and particles, 1D nanotubes and nanowires, 2D nanoplates and layers, 3D core–shell nanoparticles, or self-assembled massive, intermediate dimensional nanostructures as fractals or dendrimers) or based on the triad symmetry group-shell composition-structural formula of the shell (here nanostructures are divided into branches, classes, and subclasses determined by the symmetry group of a shell and the sets of the quantum numbers of a structure). In our book on less-common nanostructures [1] of 2012, we presented a nonformal classification, which is not directly related to dimensionality and chemical composition of nanostructure-forming compounds or composites and is based mainly on the less-common nanostructures. In this classification, in addition to classic carbon-based and non-carbon nanostructures (carbon nanotubes, fullerenes, nanodiamonds, graphene, and graphane, simple and core–shell nanoparticles, non-carbon nanotubes, nano-metals, nanowires, nanorings, nanobelts, nanopowders, nanocrystals, nanoclusters, nanofibers, and nanodots/quantum dots), a series of relatively rare nanostructures have been described:

Reproduced with permission of the Elsevier Science (*Inorganica Chimica Acta*, **2017**, *468*, 67–76).

B. I. Kharisov, O. V. Kharissova, *Carbon Allotropes: Metal-Complex Chemistry, Properties and Applications*,
https://doi.org/10.1007/978-3-030-03505-1_4

Simple linear 1D, 2D, and 3D nanostructures
Nanolines, nanopencils, nanodumbbells, nanopins, nanoshuttles, nanopeapods, nanochains, nanobelts, nanowicks, nanobars, and nanopillars

Various elongated 3D nanostructures
Nanobricks, nanocones, nanoarrows, nanospears, nanospikes, nanonails, nanobowlings, nanobones, nanobottles, nanotowers, nanoarmors, and nanopins

Circle- and ball-type nanostructures
Nanowheels, nanorings, nanoballs, nanoeggs, nanograins, nanorices, and nanospheres

Nanocage-type structures
Nanocages, nanoboxes, and nanocapsules

"Nanovegetation" world
Nanotrees, nanopines, nanopalms, nanobushes, nanograsses, nanoacorns, nanokelps, nanomushrooms, nanoflowers, nanobouquets, nanoforests, nanocorns, nanoleaves, nanobroccoli, nanomulberry, nanocactus, nanospines, nanosheaves, nanoonions, and nanodewdrops

"Nanoanimal" world
Nano-urchins, nanoworms, nanolarvae, and nanosquamae

"Nanohome" objects
Nanobrushes, nanobrooms, nanocombs, nanocarpets, nanofans, nanowebs, nanospoons, nanoforks, nanobowls, nanotroughs, nanocups, nanospindles, and nanofuns

"Nanotechnical" structures and devices
Nanosaws, nanosprings (nanocoils/nanospirals), nanoairplanes, nanopropellers, nanowindmills, nanoboats, nanobridges, nanocars, nanobatteries, nanotweezers, nanomeshes, nanofoams, nanobalances, nanojunctions, nanopaper, nanorobots, nanothermometers, E-nose, E-tongue, E-eye, and NEMS

Nanostructures classified as polyhedra
Nanotriangles, nanotetrahedra, nanosquares, nanorectangles, nanocubes, nanopyramids, nanooctahedra, nanoicosahedra, nanododecahedra, nanocubes, nanoprisms, and nanocuboctahedra

Other rare nanostructures
Nano–New York, nanopaper, nanovolcanoes, nanosponges, nanostars, nanoglasses, and nanodrugs

A certain part of these rare nanostructures (not all) correspond to carbon-based ones. In this section, we examine carbon less-common nanostructures (i.e., published mainly in the range of $1 \div 100$ reports each one) that correspond to the shapes mentioned earlier. Such structures, as will be shown later, possess unusual shapes and high surface area, which make them very useful for catalytic, medical, electronic, and many other applications.

4.1 Atomic, Dotted, and Chain Molecular Carbon Forms[1]

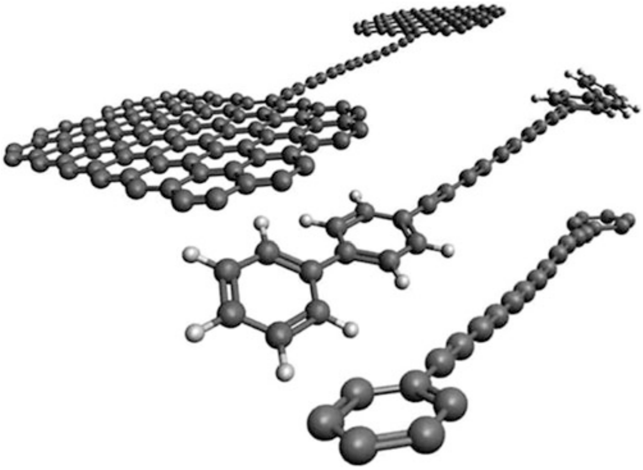

4.1.1 Atomic and Diatomic Carbon[2]

The data on these two carbon allotropes are scarce [2, 3]. Atomic [C] and diatomic [C=C] carbons are unstable molecules existing in gaseous phase only above 3642 °C and forming fullerene or graphite at lower temperatures. They were observed in carbon vapor (electric arcs), blue hydrocarbon flames, comets, stellar atmospheres, and the interstellar medium [4]. Their some features are as follows:

C_1:

- Atomic carbon is created by passing a large current through two adjacent carbon rods, generating an electric arc.
- Atomic carbon is highly reactive; its most reactions are highly exothermic (carried out in the gas phase at 77 K).
- Atomic carbon is generated in the thermolysis of 5-diazotetrazole (CN_6 =:C: + $3N_2$) [5].
- Atomic carbon can also be fabricated by decomposition of tantalum carbide [6].

C_2:

- Bond order of 2 (a double bond between the two carbons in a C_2 molecule should exist).
- Bond length 1.24 Å.
- A quadruple bond could exist in C_2 [7, 8] (Fig. 4.1) and its isoelectronic molecules CN^+, BN, and CB^- (each having eight valence electrons). In contrast, the analogues of C_2 that contain higher-row elements, such as Si_2 and Ge_2, exhibit only double bonding.
- Carbon vapor is around 28% diatomic, but theoretically this depends on the temperature and pressure [9].

---

[1] Reproduced with permission of the *Royal Society of Chemistry* (*Nanoscale*, **2016**, *8*, 4414–4435).

[2] Reproduced with permission of *Nature* (*Nature Chemistry*, **2012**, *4*, 195–200).

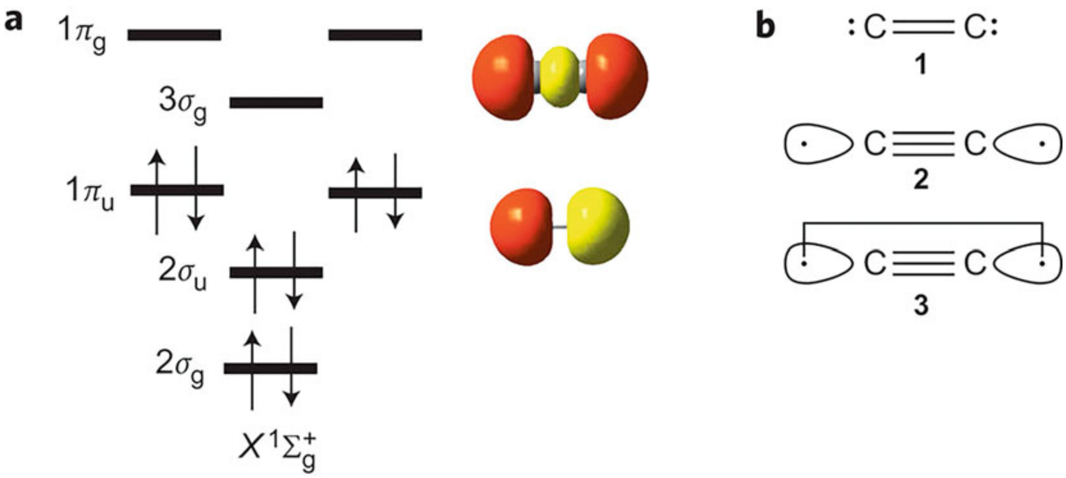

Fig. 4.1 (**a**) Molecular orbital diagram. The shapes of the $2\sigma_u$ and $3\sigma_g$ molecular orbitals, as determined from FCI calculations, are also represented together with their respective energy levels; (**b**) three simplified bonding cartoons. (Reproduced with permission of *Nature*)

4.1.2 Carbon Nanodots[3], [4] and Graphene Quantum Dots

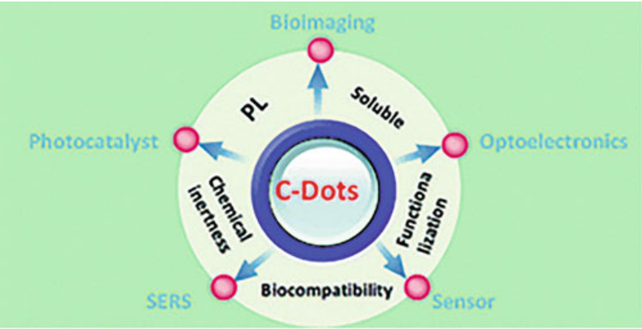

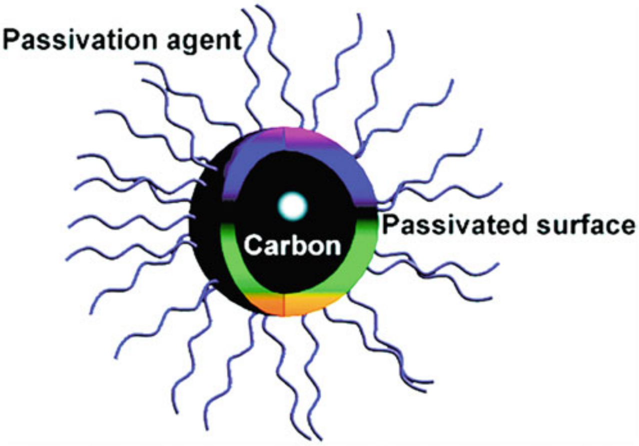

---

[3] Reproduced with permission of the *Royal Society of Chemistry* (*J. Mater. Chem.*, **2012**, *22*, 24230–24253).

[4] Reproduced with permission of the *American Chemical Society* (*J. Phys. Chem. C*, **2010**, *114*, 12062–12068).

Carbon nanodots (CDs), a class of carbon nanomaterials with sizes below 10 nm, were first discovered in 2004 during purification of SWCNTs. Graphene quantum dots (GQDs) consist of a single or a few layers of small graphene fragments. CDs have a much more comprehensive definition compared to GQDs. Carbon nanodots (CDs) (or carbon quantum dots, CQDs), graphene quantum dots (GQDs), doped C-dots/GQDs, carbon nitride dots, and C-dots/GQDs nanocomposites are members of the same family [10]. Main features of CDs and GQDs are as follows:

- CDs are conjugated systems: C atoms are sp^2 hybridized with no saturated sp^3 carbon atoms.
- C-dots hold a discrete and quasispherical structure, usually containing oxygen/nitrogen organic functional groups [11, 12].
- CDs are quasispherical carbon nanoparticles with amorphous to nanocrystalline cores with a diameter of less than 10 nm.
- Due to their strong luminescence, in contrast to macroscopic carbon, CDs are also referred to as nanolights or fluorescent carbon [13, 14].
- The electrochemical, microwave, and hydrothermal methods are common for CD and GQD synthesis, among others.
- CNDs possess high stability, good conductivity, low toxicity, and environmental friendliness.
- CNDs can be synthesized physically, chemically, or electrochemically, by "top-down" (from other carbons) or "bottom-up" (from organic precursors) methods, as well as by "greener" techniques.
- CDs prepared from organic matter such as used tea and ginger possess a great inhibitory effect on the growth of cancer cells [15].
- CNDs can be functionalized and this way dispersed in water and solvents.
- CNDs can be surface-passivated getting new properties.
- Compared to traditional semiconductor quantum dots (QDs), the photoluminescent CDs are superior in terms of high aqueous solubility, robust chemical inertness, easy functionalization, and good biocompatibility.
- CDs with unique properties have great potential applications in bioimaging, biomedicine, optoelectronics, solar cells, supercapacitors, sensors, detection of metal ions, SERS, drug delivery, and photocatalysis, among other uses.

Synthesis A variety of methods for CD synthesis have been offered. In whole, CDs can be prepared (Fig. 4.2) by (1) top-down methods from carbon structures (amorphous carbon (candle soot and carbon black) and regular sp^2 carbon layers (graphite (Fig. 4.3) and carbon nanotubes) by arc discharge, laser ablation, electrochemical oxidation, and nitric acid/sulfuric acid oxidation or (2) bottom-up methods from small molecules (citric acid, glycerol, amino acid, ascorbic acid, carbohydrates, and other molecules with abundant hydroxyl, carboxyl, and amine groups) by dehydration and carbonization/calcination (pyrolysis), in particular by hydrothermal and microwave treatment. Thus, highly luminescent carbon nanodots were fabricated by employing a hydrothermal method with citric acid as the carbon source and ethylenediamine as the nitrogen source, together with adding moderate ammonia water to achieve both appropriate inner structure and excellent N passivation [18]. The photoluminescence quantum yield of the resultant C-dots reached as high as 84.8%, which is of 10.56% higher than that of the C-dots synthesized in the absence of ammonia in the reaction precursors. Hydrothermal method was used also for preparation of the 3D GQDs/*r*GO composites with different ratios of GQDs versus GO (Figs. 4.4 and 4.5) [19]. These GQDs/rGO composites showed improved catalytic activities for the reduction of nitroarene compared with GQDs, 3D *r*GO, and some metal catalysts; the high catalytic activity of the 3D GQDs/rGO was found to be directly related to the GQDs-to-*r*GO ratio.

Natural precursors for CDs are chitosan [20], grape and orange juice, pepper, strawberry, banana juice, watermelon and pomelo peel, soy milk, grass, tea, coffee, and various leaves, among others. For instance, sweet potatoes as carbon source, used for hydrothermal green synthesis, led to fluorescent carbon nanodots ranging from 1 to 3 nm [21]. Such CDs were found to be a very effective fluorescent probe for label-free, sensitive, and selective detection of Hg^{2+} with a detection limit as low as 1 nM. Green microwave-assisted rapid green synthesis of photoluminescent carbon nanodots (C-dots) with diameters in the range of 1–4 nm using flour as the carbon source was decribed in [22]. These C-dots exhibited high sensitivity and selectivity toward Hg^{2+} with detection limit as low as 0.5 nM and a linear range of 0.0005–0.01 M. Also, highly luminescent ultrasmall CDs were prepared by one-step microwave-assisted pyrolysis and functionalized with fluorescein photosensitizer by a diazo-bond [23]. Thus obtained water-soluble yellow-emitting [fluorescein–N=N–CDs]Ru^{2+} showed absorbance maximum the same as CDs but do not contain a mixture of blue- and blue–green-emitting nanoparticles; it was considered as a powerful alternative to cadmium-based toxic quantum dots. A microwave reactor for CDs preparation was also offered [24].

Electrochemical methods are also available for synthesis of CDs (Fig. 4.6) and their study [26]. Among other techniques, fluorescent CDs (5–20 nm in size) were obtained by the laser ablation (laser pulses of 1064, 532, and 355 nm under different irradiation times) of a carbon solid target in liquid environment (acetone) [27]. It was observed that the use of a short-wavelength UV laser source can yield carbon quantum dot-like structure whereas changing the laser ablation to the longer wavelength especially at 1064 nm results in agglomeration. MOFs are rarely used for CDs fabrication. Thus, highly photoluminescent CNDs were synthesized (Fig. 4.7) from metal–organic framework (MOF, ZIF-8) nanoparticles at a mild

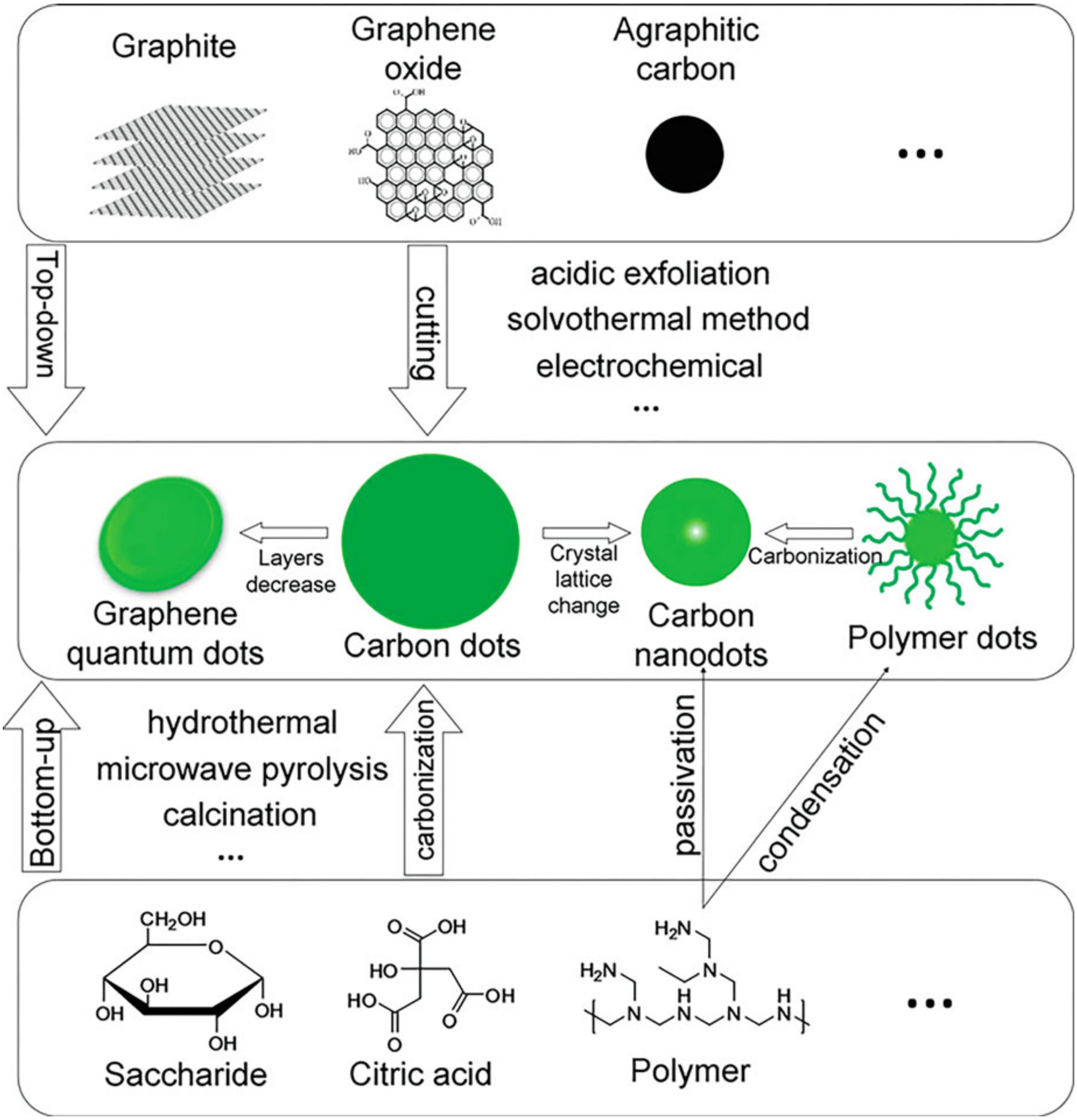

Fig. 4.2 Scheme of CDs of different species [16]. (Reproduced with permission of the *Royal Society of Chemistry*)

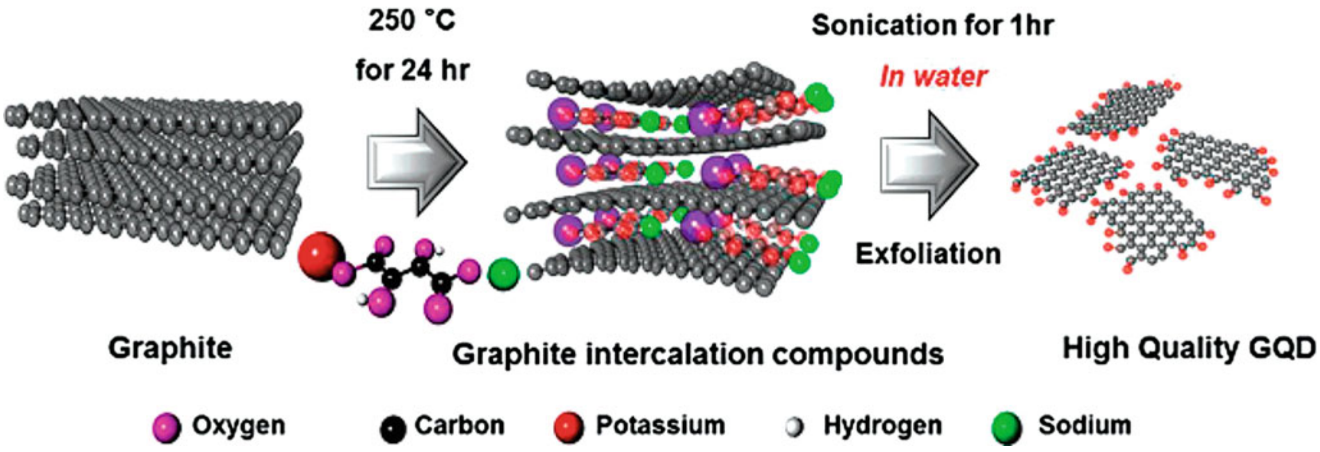

Fig. 4.3 Preparation strategy of CDs by proper intercalation of compounds [17]. (Reproduced with permission of *Wiley*)

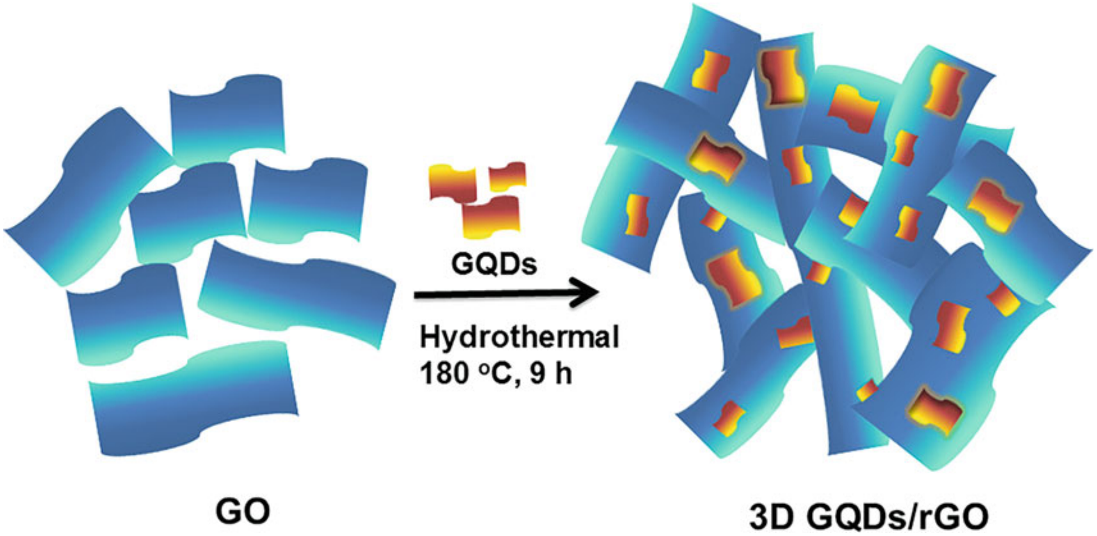

Fig. 4.4 Illustration of the formation process of the 3D GQDs/*r*GO composites. (Reproduced with permission of the *American Chemical Society*)

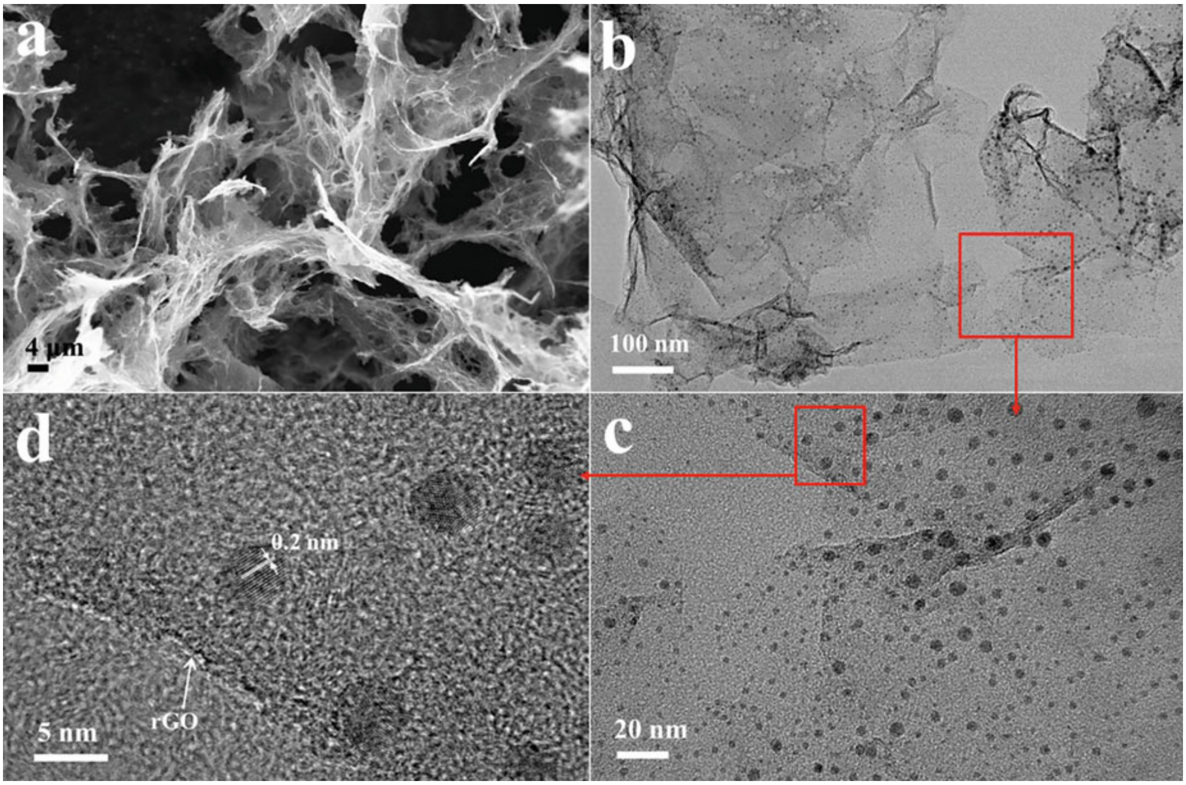

Fig. 4.5 SEM (**a**), TEM (**b**, **c**), and HRTEM (**d**) images of the 3D GQDs/*r*GO composite. (Reproduced with permission of the *American Chemical Society*)

Fig. 4.6 The schematic diagram of electrochemical fabrication of CDs [25]. (Reproduced with permission of the *Royal Society of Chemistry*)

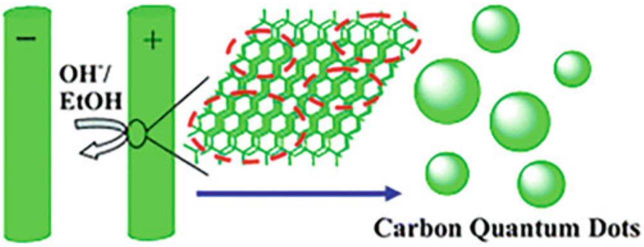

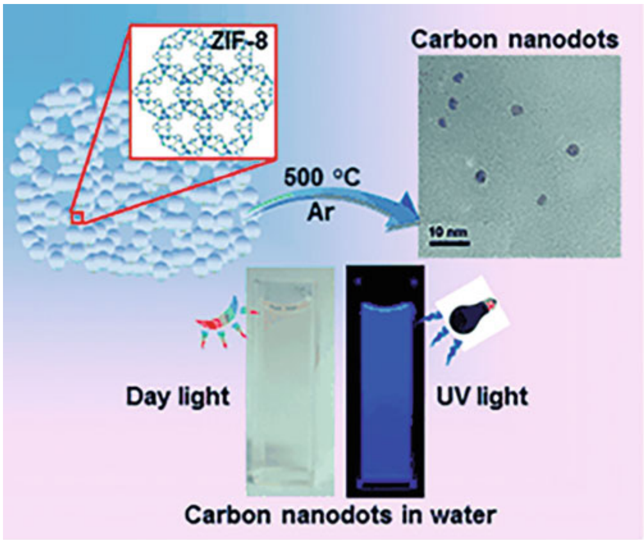

Fig. 4.7 Schematic illustration for the formation of carbon nanodots (CNDs) derived from ZIF-8 NPs and their aqueous dispersion under visible and UV lights. (Reproduced with permission of *Wiley*)

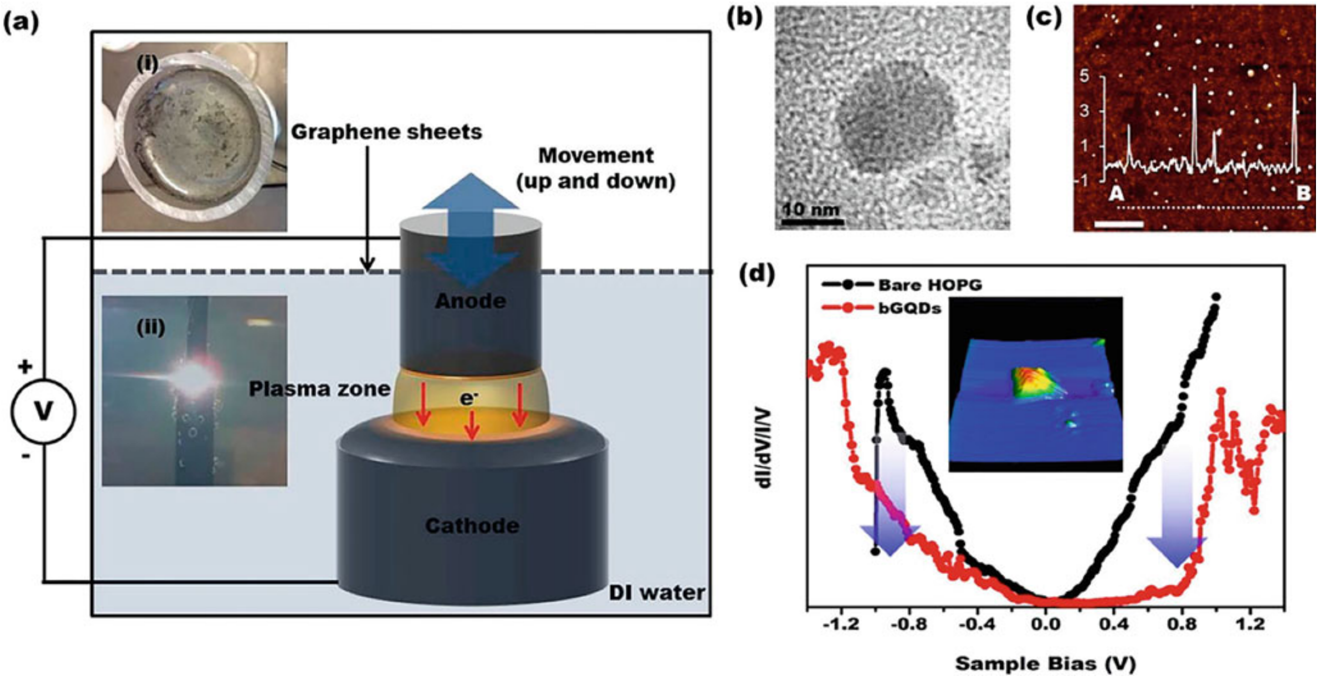

Fig. 4.8 Production of bGQDs through the seamless arc discharge in water. (**a**) Schematic illustration of the seamless arc discharge in water to produce bGQDs shows the vertical movement of the anode, the fixed cathode, and water used as a dielectric medium. (**a**-i) Graphene sheet-based films on the water surface formed by self-assembly of the graphene produced from the exfoliation of graphite electrodes. (**a**-ii) A digital photo image of the plasma zone during the arc-discharge process produced by applying 25 V with either 1 or 4 A. (**b**) A representative TEM image of bGQDs1A after purification by centrifugation at 6000 rpm for 30 min (**c**) An AFM image of bGQDs1A on a silicon wafer for determination of height profiles with the inset of a representative height profile of A–B (scale bar: 500 nm). (**d**) STS results show the presence of a ~ 1.8 eV bandgap (represented by arrows) of bGQDs1A (red) compared to HOPG (0 eV); inset: STM image of bGQDs1A. (Reproduced with permission of the *Elsevier Science*)

temperature (500 °C). Possessing stable fluorescence (maximum emission wavelength is independent on the excitation wavelength in the range of 300–400 nm) and non-toxic characteristics, these carbon nanodots could potentially be used in biosafe color patterning [28].

Aqueous arc-discharge process [29] (Fig. 4.8) was also developed to produce the blue-luminescent graphene quantum dots (bGQDs). The resulting bGQDs were found to be ~15 nm in diameter, and the amount of oxygen-including functional groups can be controlled to 27.4% and 30.8% at 1 and 4 A of a current level, respectively.

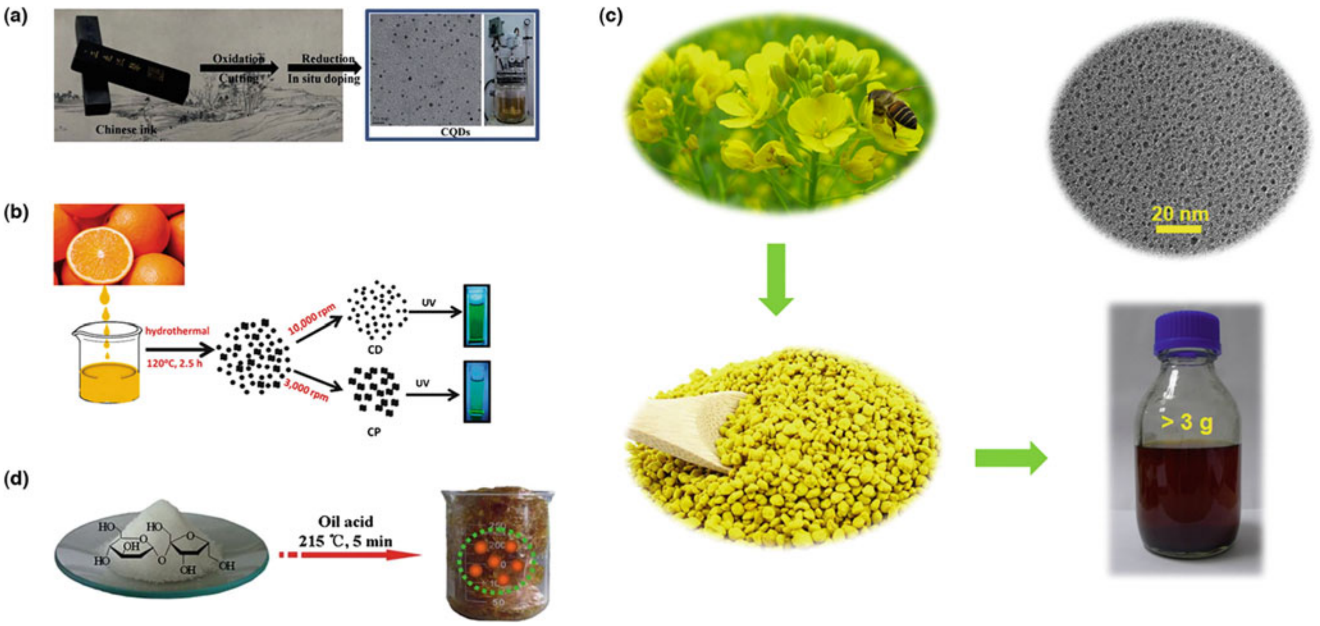

Fig. 4.9 Diagrams for the large-scale synthesis of CDs by adopting (**a**) Chinese ink, (**b**) orange juice, (**c**) bee pollens, and (**d**) sucrose as the carbon source. (Reproduced with permission of the *Elsevier Science*)

The production of CDs can be *scaled-up*; the synthetic methods for CDs in a macroscale manner are described (Fig. 4.9) [30]. As an example, a scalable synthesis of water-dispersible fluorescent carbon nanodots based on the hydrothermal method (180 °C for 6 h) of kitchen wastes (grape peel) is known [31]. The as-prepared nanodots have high selectivity for Fe^{3+} ions based on fluorescence quenching.

Functionalization, Grafting, and Doping As an example of chemical functionalization of CDs, the functionalization of CDs with a *bis*-amino-modified silicone reagent enhanced their fluorescence properties [32]. Further treatment with a poly(ethylene glycol)–phospholipid surfactant increased the water dispersibility and promoted the nanoassembly of the silicone-modified CNDs. The synthesized nanocomposites were found to be biologically compatible and useful for cellular fluorescence imaging. Gd(III)-doped carbon dots (3–4 nm in size) can be used as dual fluorescence-MRI probes for biomedical applications [33]. The derived Gd(III)-doped carbon dots showed uniform particle size (3–4 nm) and gadolinium distribution and form stable dispersions in water. Exhibiting bright fluorescence, strong T1-weighted MRI contrast, and low cytotoxicity, they can be used in biomedical research for multimodal imaging. In addition, CDs, grafted onto the surface of TiO_2 nanotubes, can enhance the photocatalytic properties degrading organic pollutants [34], increasing light absorption, trap and shuttle photo-generated electrons, and enhance the pollutant adsorptivity. Under xenon lamp illumination, irradiation not only induces electrons and holes but also can heat the CDs-TiO_2 at local spots because of the photothermal effect.

Applications CDs have great potential applications mentioned above; we present here some selected examples. For instance, a sensitive and selective detection approach for tetracycline in complex water samples was developed by preparing blue photoluminescent europium-doped carbon quantum dots (Eu-CQDs) through a rapid carbonization method operating at 200 °C for 5 min [35]. The fluorescence of the Eu-CQDs can be quenched efficiently by tetracycline, based on the strong inner filter effect mechanism between Eu-CQDs and tetracycline. Also, CD functional composites with MOFs, combining the advantages of both MOFs and nanoparticles, may exhibit unprecedented properties, for instance, for H_2 storage. Due to the interactions between polar functional groups at the surface of the CDs and H_2 molecules, such systems efficiently enhanced H_2 storage capacity and allowed the sensitive fluorescent sensing for nitroaromatic explosives [36]. In addition, dual-emission CDs can serve as dual-mode nanosensors with both fluorometric and colorimetric output for the selective detection of H_2O_2 [37]. For the case of GQDs, luminescent graphene quantum dots or graphene quantum disks have their future and potential development in bioimaging, in electrochemical biosensors and catalysis, and specifically in photovoltaic devices that can solve increasingly serious energy problems [38, 39].

4.1.3 Carbyne[5], [6], [7]

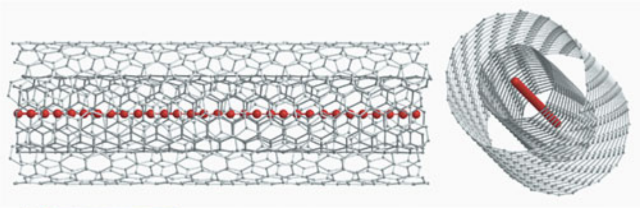

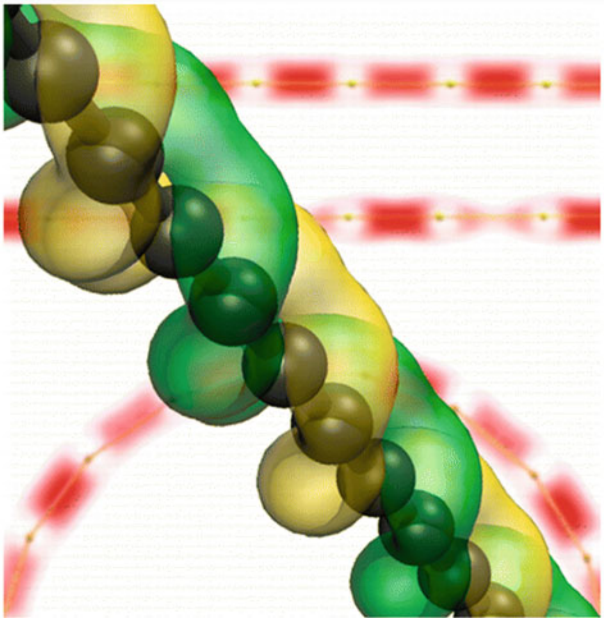

Carbyne [40, 41], an infinite carbon chain with pure sp^1 hybridization, has attracted much interest and significant controversy since the 1960s, after the first claims of detection. It was first proposed in 1885 by Adolf von Baeyer, who described the existence of linear acetylenic carbon. In 1995, the several reports on the preparation of carbyne chains with over 300 carbons or indeterminate length were published, until great success in 2016, when its linear chains of up to 6000 sp-hybridized carbon atoms were prepared (see below). These chains were grown inside DWCNTs and are highly stable protected by their hosts. Main features of carbyne are as follows:

- Carbyne, similar to graphene, is just one atom thick, having an extremely large surface area (a single gram of graphene has a surface area of roughly five tennis courts).
- Carbyne is not a novel substance (carbyne was earlier detected in shock-compressed graphite, interstellar dust, and meteorites).
- The carbyne, made up of a chain of carbon atoms linked by alternate triple and single bonds $(-C \equiv C-)_n$, is actually twice as strong as graphene.
- 1D chain of the cumulene is known to undergo a *Peierls* transition into the polyyne form. This instability shows an energy difference of 2 meV per atom in favor of the polyyne structure over cumulene.
- Carbyne has beat out graphene as the world's strongest material.
- Carbyne Young's modulus is 32.7 TPa – 40 times that of diamond.
- Stretching it by as little as 10% significantly alters its bandgap.

---

[5] Reproduced with permission of *Nature* (upper image: *Nature Mater*., **2016**, *15*, 634–640).

[6] Reproduced with permission of the *American Chemical Society* (image below: *ACS Nano*, **2013**, *7*(11), 10075–10082).

[7] The name *carbyne* has been adopted to indicate an infinite *sp*-carbon wire as a model system; meanwhile *carbynoid structures* have been used to indicate finite systems or moieties comprising *sp*-carbon in amorphous systems.

- A 90-degree end-to-end rotation transforms it into a magnetic semiconductor.
- Chains of carbyne can take on side molecules making energy storage possible.
- Carbyne may be stable at high temperatures (3000 K).
- In several articles, the carbynes are determined as "1D chain-like structures [(-C≡C-)$_n$/(=C=C=)$_n$] with *sp*^{1} carbon-carbon hybridization," but it is accepted nowadays that the $(-C \equiv C-)_n$ formula corresponds to carbyne and the $(=C=C=)_n$ – to cumulene. Formation of π-electron delocalization in carbyne is shown in Fig. 4.10.
- Carbyne exhibited a large nonlinear absorption coefficient β and a refractive index n_2 of 3.53×10^{-13} m W^{-1} and -1.40×10^{-13} esu at 800 nm excitation, respectively [42].

The following report is currently considered as most important in the area of *carbyne synthesis*. Thus, a method for the bulk production of carbyne protected by thin double-walled CNTs by very high temperature and high vacuum (HTHV) was offered, establishing a route for the bulk production of exceptionally long and stable chains composed of more than 6000

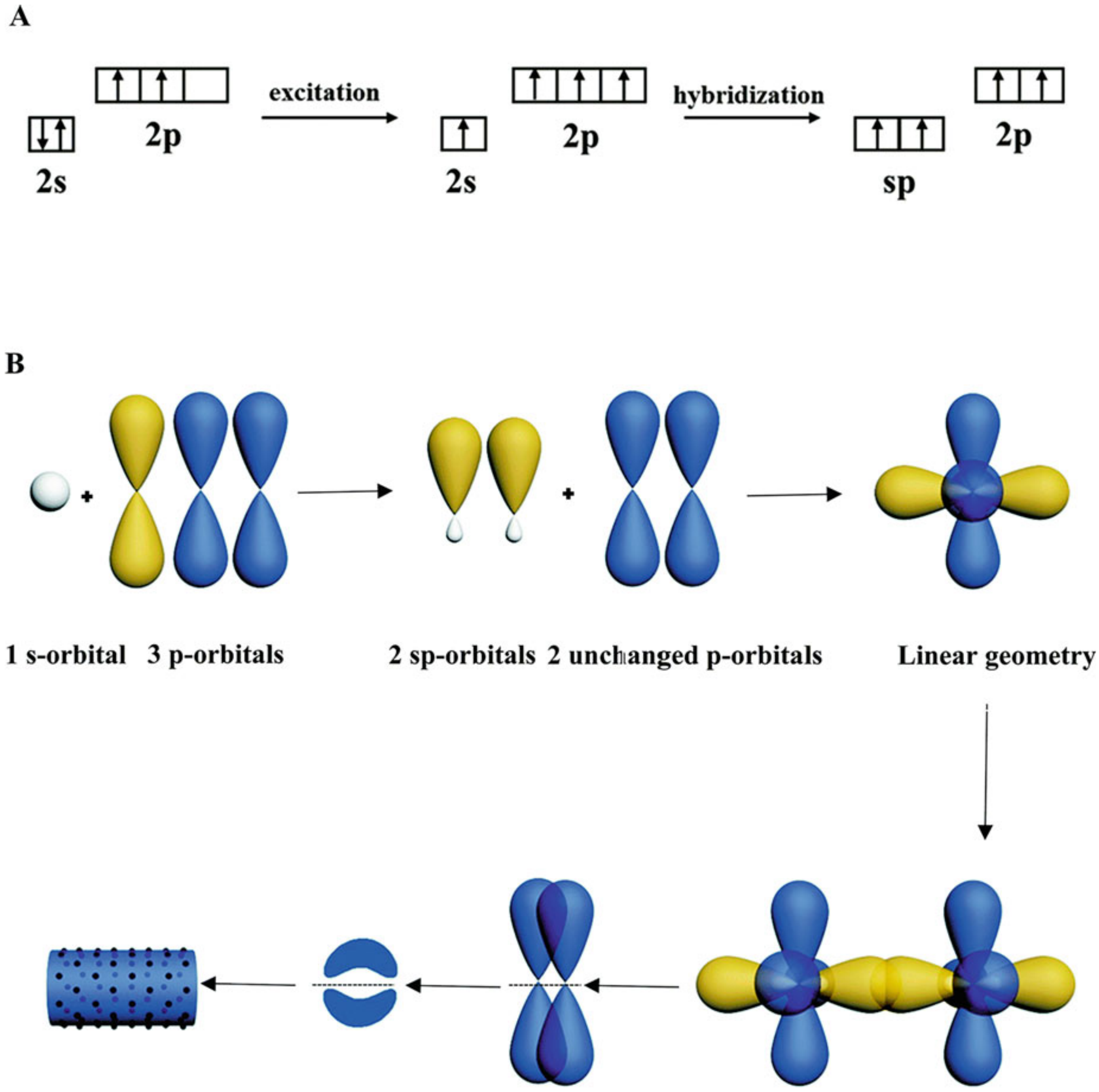

Fig. 4.10 Formation of π-electron delocalization in carbyne. (**a**) Process of atomic orbital *sp* hybridization. (**b**) Existence of extensive π-electron delocalization in carbyne. (Reproduced with permission of the *Royal Society of Chemistry*. *J. Mater. Chem. C*, 2016, *4*, 4692–4698.)

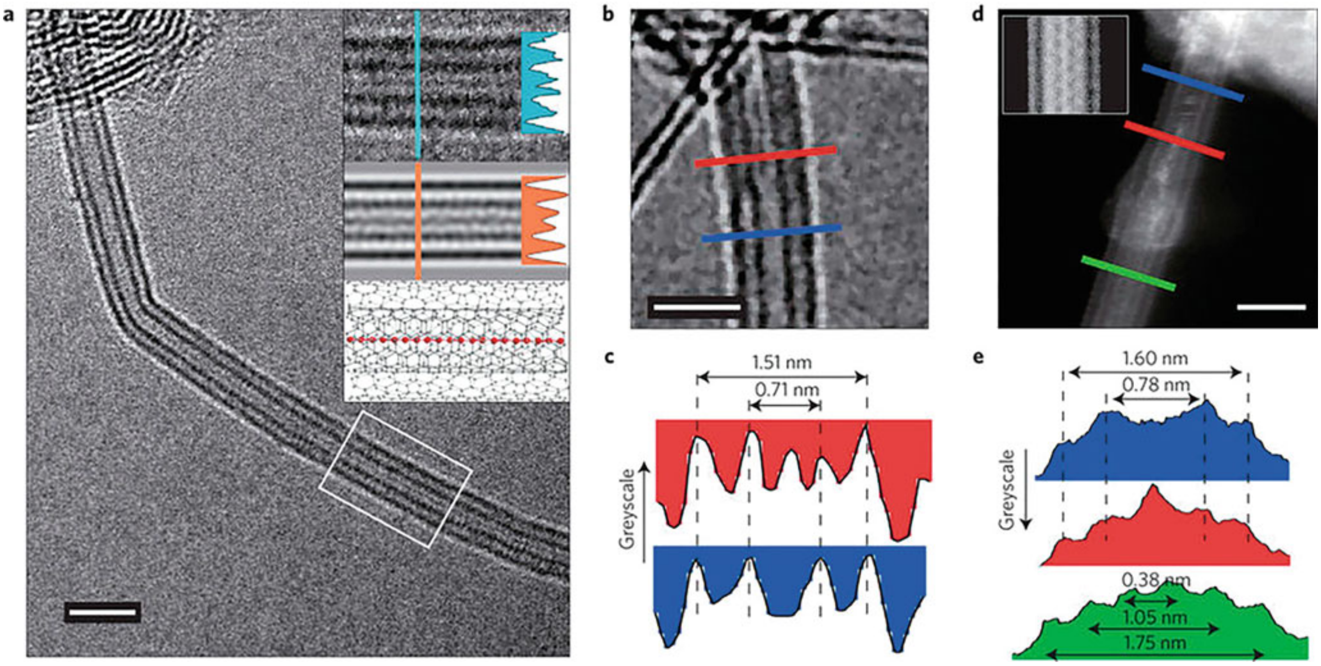

Fig. 4.11 Direct observation of LLCCs@DWCNTs. (**a**) HRTEM image of an LLCC@DWCNT with bending. The LLCC inside a DWCNT is longer than 26 nm, which means that it consists of more than 200 contiguous carbon atoms. Inset: an enlarged part of the HRTEM image (top), a simulated HRTEM of an LLCC@DWCNT (middle), and a molecular model of an LLCC@DWCNT (bottom). The corresponding line profiles of the experimental and a simulated LLCC@DWCNT are shown, respectively. (**b**) A DWCNT with partial LLCC filling. (**c**) The line profiles at positions along the blue and red lines shown in b represent the empty DWCNT and LLCC@DWCNT, respectively. (**d**) STEM image of an LLCC@DWCNT. Inset: a simulated STEM image of an LLCC@DWCNT. (**e**) The line profiles at positions along the blue, red, and green lines shown in d represent an empty DWCNT, an LLCC@DWCNT, and a thin most-inner tube@DWCNT, respectively. Scale bars, 2 nm. (Reproduced with permission of *Nature*)

carbon atoms [43]. Direct observations of the long linear carbon chains (LLCCs) by aberration-corrected HRTEM and STEM are summarized in Fig. 4.11. The HRTEM micrograph in Fig. 4.11a shows a long, bent DWCNT encapsulating a carbon chain.

Other techniques also can lead to carbynes with different lengths and capping groups. Thus, the synthesis of carbyne (Figs. 4.12, 4.13, and 4.14) with finite length, which is clearly composed of alternating single bonds and triple bonds capped by hydrogen, using a process involving laser ablation in liquid, was reported [44]. The combination of gold and alcohol was found to be crucial to carbyne formation. *Structure information and binding energy of formed carbyne is shown in* Table 4.1. *In addition to the hexagonal crystal structure data in this table, we note for comparison that* the crystal structure of a perfect carbyne was also calculated by the molecular mechanics methods showing a difference with the above [45]. It was established that the carbyne crystals should consist of polycumulene chains arranged in hexagonal bundles. The unit cell of the perfect carbyne crystal is here trigonal and contains one carbon atom. The unit cell parameters are as follows: $a = b = c = 0.3580$ nm, $\alpha = \beta = \gamma = 118.5°$, and space group P3$m$1. Another synthesis approach was based on the fact that the removal of Ti atoms from the TiC surface surpasses that of C atoms, leading to enrichment of the TiC surface with carbon [46] (see also the section on carbide-derived carbons for more details). Formed carbon-based films contain carbynes (50–100 nm thick) in the form of nanorod-like clusters (lengths 5–100 nm). Also, metalated carbyne chains were recently synthesized by dehydrogenative coupling of ethyne molecules and copper atoms on a Cu(110) surface under ultrahigh-vacuum conditions (Figs. 4.15 and 4.16) [47]. The length of the fabricated metalated carbyne chains was found to extend to the submicron scale (with the longest ones up to ~120 nm).

The mechanical properties of carbyne were calculated obtained by first-principles-based ReaxFF molecular simulation [48]. The intrinsic thermal transport was determined in two abovementioned carbon sp^1 allotropes, carbyne (polyyne, $(-\mathrm{C} \equiv \mathrm{C}-)_n$, Fig. 4.17a) and cumulene $((=\mathrm{C} = \mathrm{C}=)_n$, Fig. 4.17b), using equilibrium MD simulations and the Green–Kubo approach and knowing that cumulene is less stable than carbyne [49]. Their thermal conductivities at the quantum-corrected room temperature can exceed 54 and 148 kW/m/K, respectively, much higher than that for graphene, being

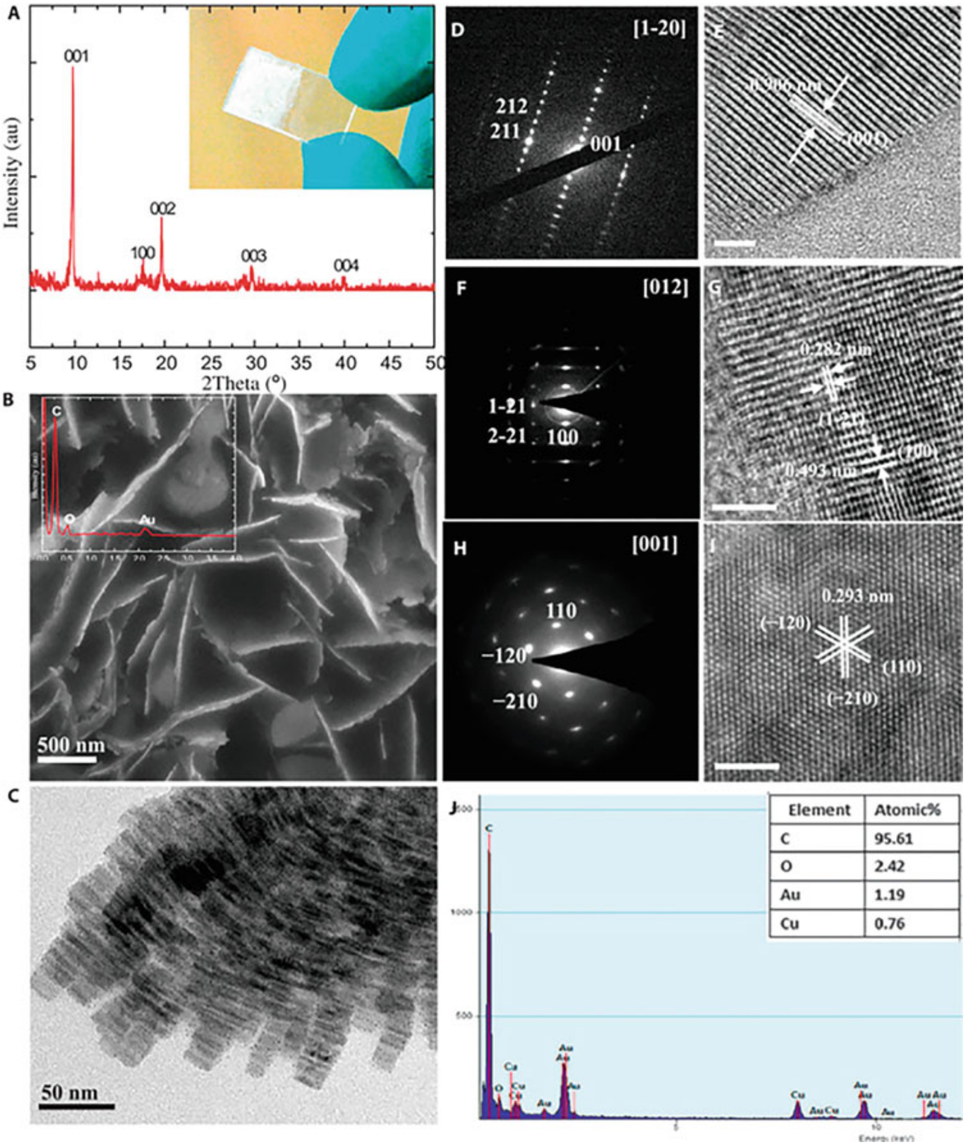

Element	Atomic%
C	95.61
O	2.42
Au	1.19
Cu	0.76

Fig. 4.12 Morphology and structural characterization of carbyne crystals. (**a**) XRD pattern of the sample. The peaks are shaped and strong, showing the good crystallinity of carbyne. There is an obviously preferred orientation along the *c* axis. Inset: white carbyne powder coating on the glass substrate. Rectangular glass substrate with white crystal powder (left) compared with bare glass (right). (**b**) SEM image of carbyne crystals. They are in the shape of flakes stacked together. EDS showing that the sample contains C, O, and Au. O and Au originate from the surface adsorption of oxygen molecules and gold nanocrystals. (**c**) TEM image of carbyne crystals. Carbyne exhibits a rod shape (10–30 nm in width and 50 to >100 nm in length). The tiny spherical particles on the surface of nanorods are gold nanocrystals. (**d**–**i**) SAED patterns and HRTEM images are divided into three categories based on the direction of the incident electron beam ([001, 012, 120], respectively). The former two are rectangular lattices, whereas the last one is a hexagonal lattice. Scale bars, 5 nm (**e**), 3 nm (**g**), and 3 nm (**h**). (**j**) EDS shows that the sample is almost completely composed of carbon and that the Cu signal originated from the Cu grid. (Reproduced with permission of *Science Advances*)

attributed to high phonon energies and group velocities, as well as reduced scattering from non-overlapped acoustic and optical phonon modes. The strength of carbyne equals 251 GPa at $T = 77$ K [50]. This value is close to the strength 7.85 nN (250 GPa) of contact atomic bond between carbyne and graphene sheet, from which the monatomic chain is pulled. Carbyne exhibited a large nonlinear absorption coefficient β and a refractive index n_2 of 3.53×10^{-13} m W^{-1} and -1.40×10^{-13} esu at 800 nm excitation, respectively [42].

Although potential *applications* of carbyne are still under discussion, several uses of carbyne are already clear. Several researchers speculate that the unusual mechanical and electronic properties of carbyne may have great potential for

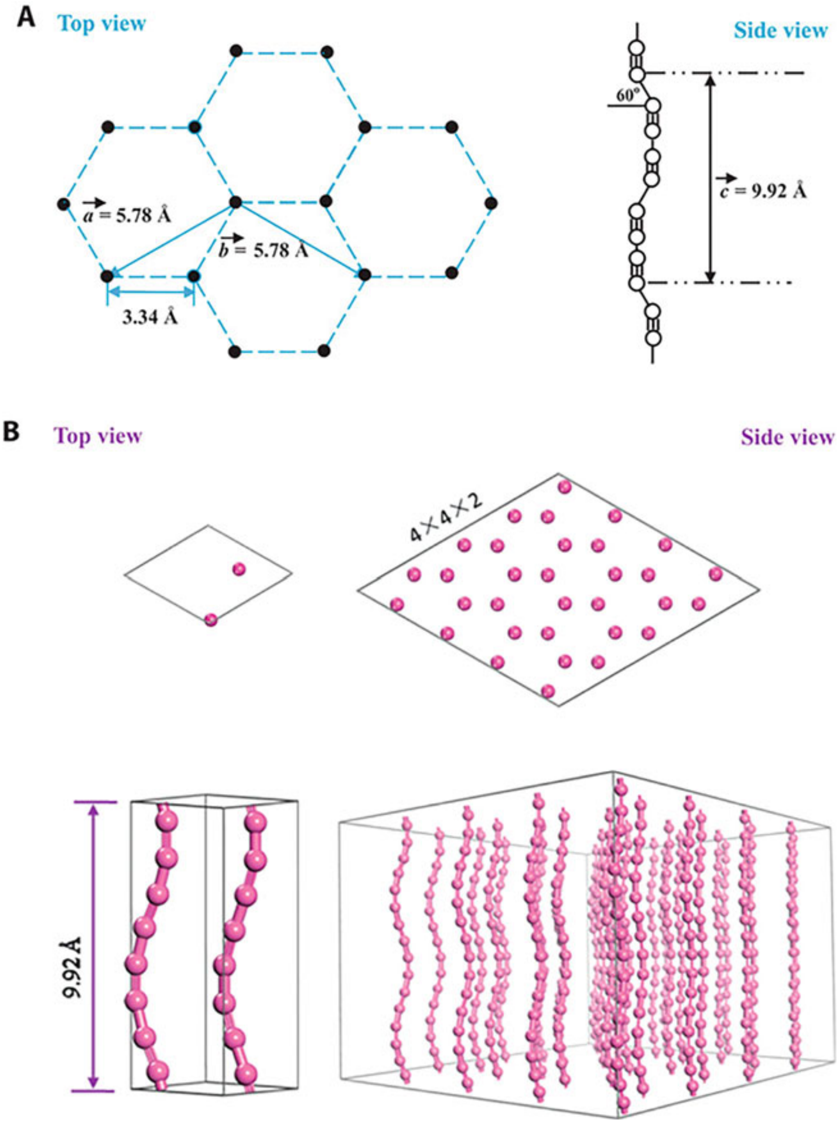

Fig. 4.13 Carbyne crystal structure. (**a**) The proposed hexagonal structure frame ($a = 5.78$ Å, $b = 5.78$ Å, $c = 9.92$ Å, $\alpha = 90°$, $\beta = 90°$, $\gamma = 120°$); the distance between neighboring carbon atoms is 3.34 Å. The corner at the kinks is conjugated by two carbon atoms forming a C–C single bond, and the kinked angle (the angle between the vertical direction and the kinked bond) is 30°. (**b**) The equilibrium configuration of the constructed carbyne crystal based on first-principles calculations. (Left) The unit cell observed from the top (top panel) and side (bottom panel). (Right) The 4 × 4 × 2 supercell observed from the cross-profile perpendicular to the c axis (top panel) and side (bottom panel). (Reproduced with permission of *Science Advances*)

applications in nanomechanics, nanoelectronic/spintronic devices, and MEMS. Decorating a carbyne chain with calcium atoms, which suck up hydrogen molecules, creates a high-density, reversible hydrogen storage device. Carbyne polysulfide (having a sp^2 hybrid carbon skeleton with polysulfide attached on it) was found to serve as a cathode material for rechargeable magnesium batteries [51]. Carbyne can be a precursor of fullerenes; thus, laser ablation of targets of carbonaceous matter containing carbyne nanodomains (the *sp*-hybridized carbon chains) or targets of C_{60} photopolymer produced carbon clusters C_{74}-C_{124} or larger cages with odd number up to C_{162} [52]. Also, carbyne-based nanodevices, consisting of two graphene sheets connected by ten-atom carbyne chain, in the unloaded state has a level of thermal stability, sufficient for application up to the temperatures of order 1200–1400 K [53].

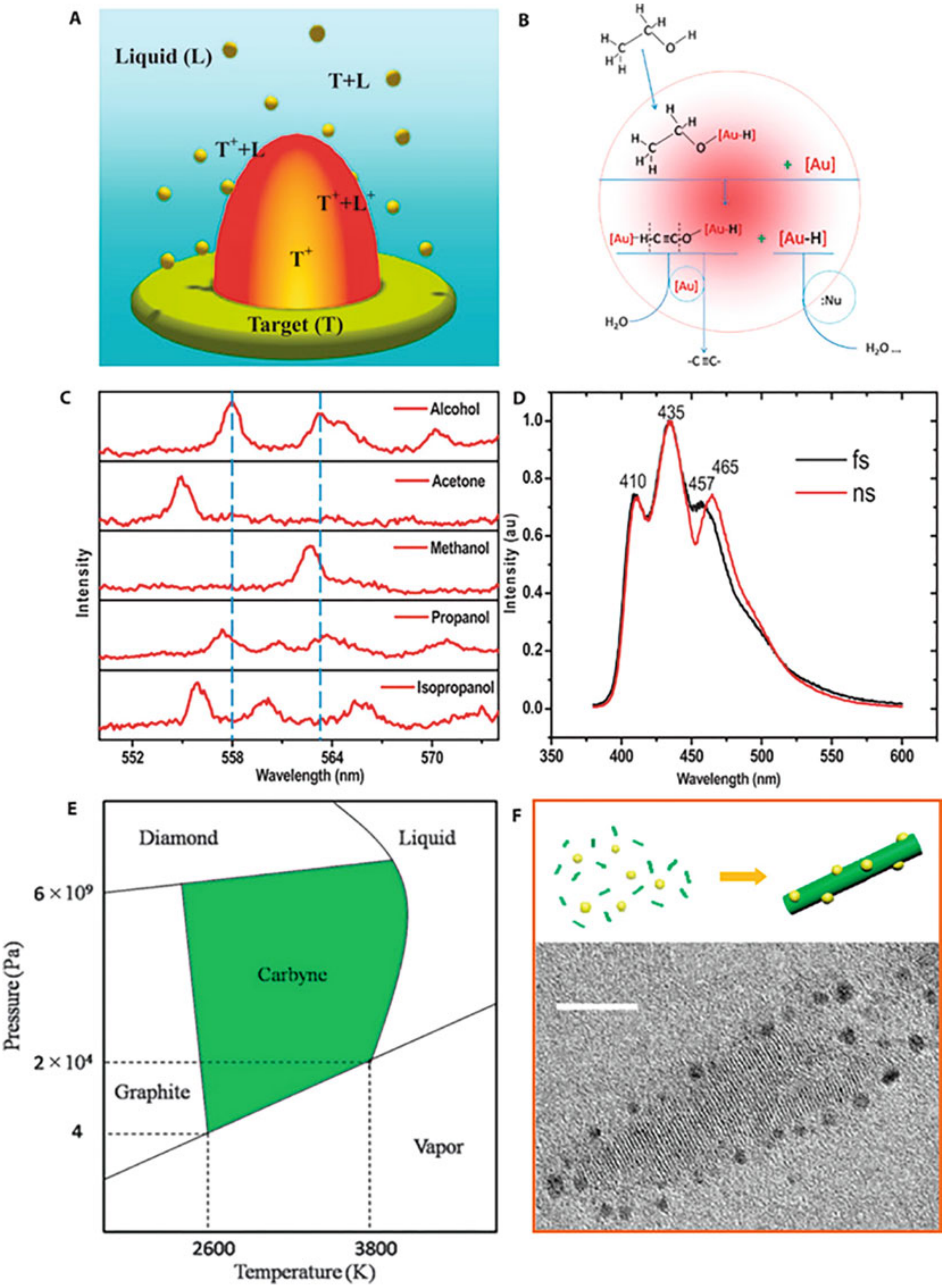

Fig. 4.14 Mechanism of carbyne formation. (**a**) Schematic illustration of four chemical reactions involved in LAL. Carbyne formation is probably involved in the second kind of chemical reaction occurring inside laser-induced plasma (T^+ + L^+) and in the chemical reactions occurring at the interface between the laser-induced plasma and liquid (T^+ + L). T^+, laser-induced target plasma; L^+, excited liquid molecules. (**b**) The pathway from alcohol molecules to the carbon–carbon triple bond, in which alcohol dehydrogenated by Au ions plays a key role. [Au], Au ion; Nu, nucleophile. (**c**) The emission spectra of different solvents during LAL; the peak of alcohol (558.1 and 563.3 nm) in the emission spectrum corresponding to the C_2 swan band for $\Delta v = -1$. The spectra of nonalcohol solvent greatly differ from those of alcohol, and no C_2 signal can be detected. (**d**) Similar fluorescence peaks using nanosecond (ns) and femtosecond (fs) lasers. (**e**) The thermodynamic phase diagram of carbyne. Green region, the preferred thermodynamic region for carbyne formation. (**f**) Individual carbyne nanorod with gold nanocrystals adheres to its surface; the cartoon depicts how this structure forms. Scale bar, 10 nm. (Reproduced with permission of *Science Advances*)

Table 4.1 Structure information and binding energy: carbyne crystal versus graphite and diamond

Structure	Crystal system	Hybridization	Lattice parameters	d_{CC} (Å)	Binding energy (eV/atom)
Carbyne crystal	Hexagonal	*sp*	$a = 5.78$ Å, $b = 5.78$ Å, $c = 9.92$ Å, $\alpha = 90°$, $\beta = 90°$, $\gamma = 120°$	1.30, 1.27	−6.347
Graphite	Hexagonal	sp^2	$a = 2.46$ Å, $b = 2.46$ Å, $c = 6.80$ Å, $\alpha = 90°$, $\beta = 90°$, $\gamma = 120°$	1.42	−7.844 [−7.41]
Diamond	Cubic	sp^3	$a = 3.56$ Å, $b = 3.56$ Å, $c = 3.56$ Å, $\alpha = 90°$, $\beta = 90°$, $\gamma = 90°$	1.54	−7.730 [−7.37]

Reproduced with permission of *Science Advances*
For comparison, the experimental value of binding energy for graphite is given in brackets

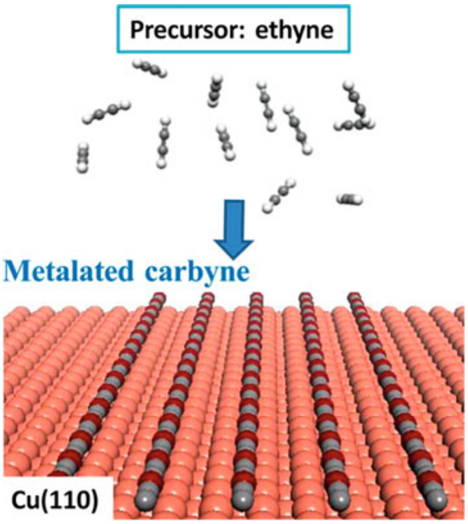

Fig. 4.15 Illustration of the bottom-up synthesis of metalated carbyne on Cu(110) through dehydrogenative coupling of ethyne precursors and copper adatoms on Cu(110) under UHV conditions. Gray, carbon; white, hydrogen; brown, copper substrate atom; red, copper adatom. (Reproduced with permission of the *American Chemical Society*)

4.1.4 Carbon-Atom Wires[8]

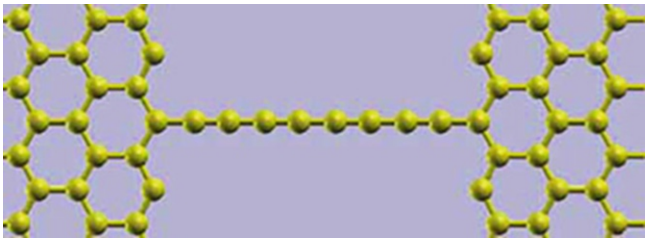

Carbon-atom wires (CAWs) and carbynes are indeed “two sides of the same medal.” Linear strings of *sp*-hybridized carbon atoms are considered as a possible phase of carbon since decades [54]. Nowadays, the occurrence of *sp*-hybridized carbon has been suggested in many carbon-based materials and structures; in carbon–metal moieties, embedded in matrices, after laser irradiation of polymers; in free carbon clusters; in pure sp–sp^2 systems; and in liquids, inside CNTs and connecting graphene sheets. Long, stable, and freestanding linear atomic carbon wires, CAWs, can be considered as extremely narrow graphene nanoribbons or extremely thin carbon nanotubes [55]. Carbon-atom wires can represent a novel nanostructure with tunable functionality. Their peculiarities are as follows:

- The nature of the *sp* bonding along the chain is nontrivial, since in most cases C–C bonds cannot be classified as either purely double or a pure sequence of single–triple bonds.
- Calculations on carbon chains are facilitated by the fact that chains consist of typically ten atoms only and constitute very small systems as compared to 2- or 3D nanomaterials.
- CAWs can be produced in different forms (isolated structures, in liquids, in solid matrices, and in thin films).

---

[8] Reproduced with permission of *Wiley* (*Phys. Status Solidi*, **2010**, *247*(8), 2017–2021).

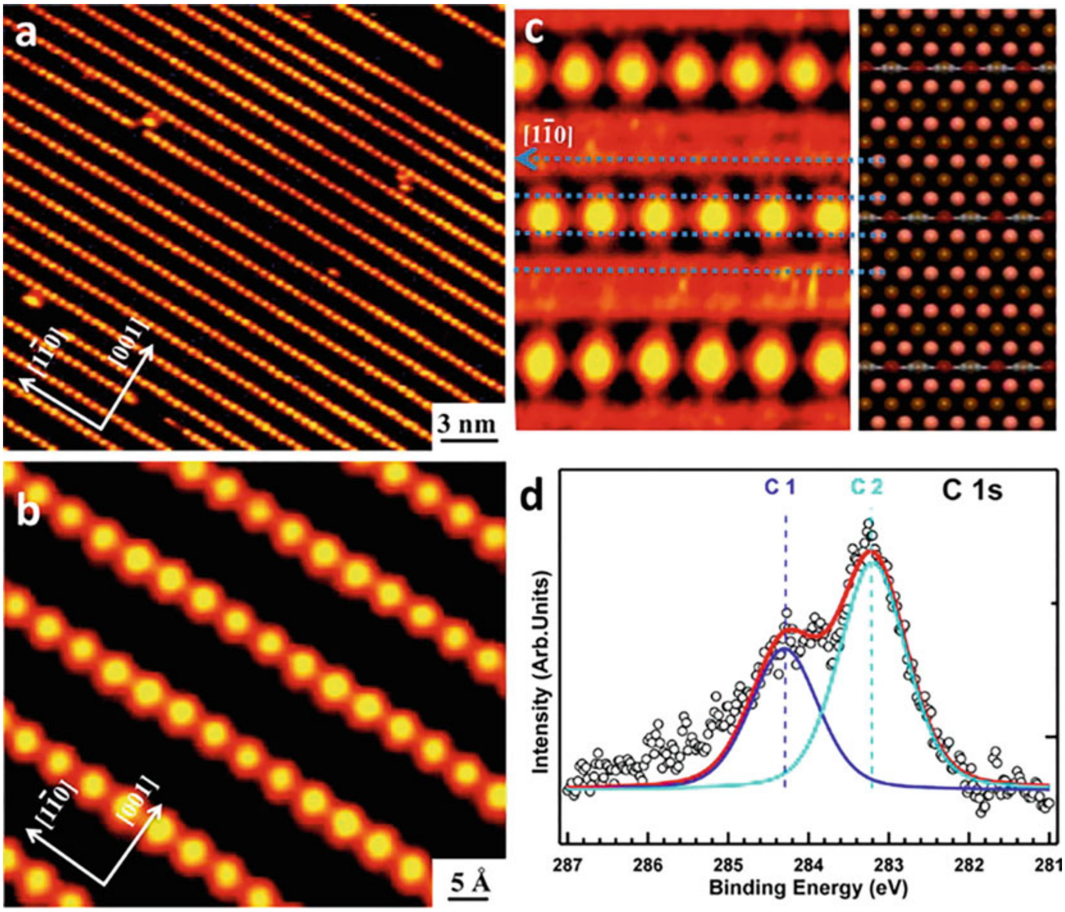

Fig. 4.16 (**a**) Large-scale and (**b**) close-up STM images showing the formation of metalated carbyne chains. (**c**) High-resolution STM image resolving the metalated carbyne and the substrate lattice simultaneously. The underlying copper rows along the [11⌧0] direction are indicated by blue dashed lines. The corresponding DFT-optimized structure model of metalated carbyne is presented aside for comparison. (**d**) C 1s core-level XP spectrum showing the major peak C2 located at a binding energy of 283.2 eV (cyan curve). (Reproduced with permission of the *American Chemical Society*)

- CAWs can be fabricated by a bottom-up approach (production of a carbon vapor followed by a rapid quenching in gas or liquid phase), including the submerged arc discharge or the pulsed laser ablation in liquids, as well as low-energy cluster beam deposition in the gas phase.
- Nanowires with odd number of atoms present a distinct behavior than the ones with even numbers [56].
- The high instability of bulk carbine, due to cross-linking between chains of carbon atoms, makes the availability of this material in bulk quantities and under ambient conditions very unlikely. The research concentrates therefore on isolated chains.
- The nature of the contacts at the ends of the chains is of high importance.

There are essentially two ways to terminate a linear chain on a sp^2 graphitic fragment: [57] either the chain connects perpendicularly to the surface of the fragment (or the surface of a fullerenic cage), by means of an “interface” atom having the sp^3 hybridization, like in the examples shown in Fig. 4.18e–f, or the chain can be attached to an edge, like in Fig. 4.18a–d. In the latter case the “interface” atom is also sp^2. Carbon linear chains, being highly reactive alone, can be substantially stabilized by this way.

Many methods can be applied for the synthesis of *sp*-carbon systems (Fig. 4.19): [58] arc discharge or laser ablation, and quenching can be accomplished by the use of inert gas molecules or liquids, supersonic cluster beam deposition (such as the pulsed microplasma cluster source), laser vaporization methods, and femtosecond laser ablation of graphite. Solid samples in the form of thin films on substrates are normally fabricated, containing sp–sp^2 moieties where *sp* wires are mixed in a mainly sp^2 amorphous carbon matrix (*sp* content up to 40% has been estimated in some cases). Chemical methods are also available, for instance, dehydropolycondensation of acetylene, polycondensation reactions of halides, and dehydrohalogenation of

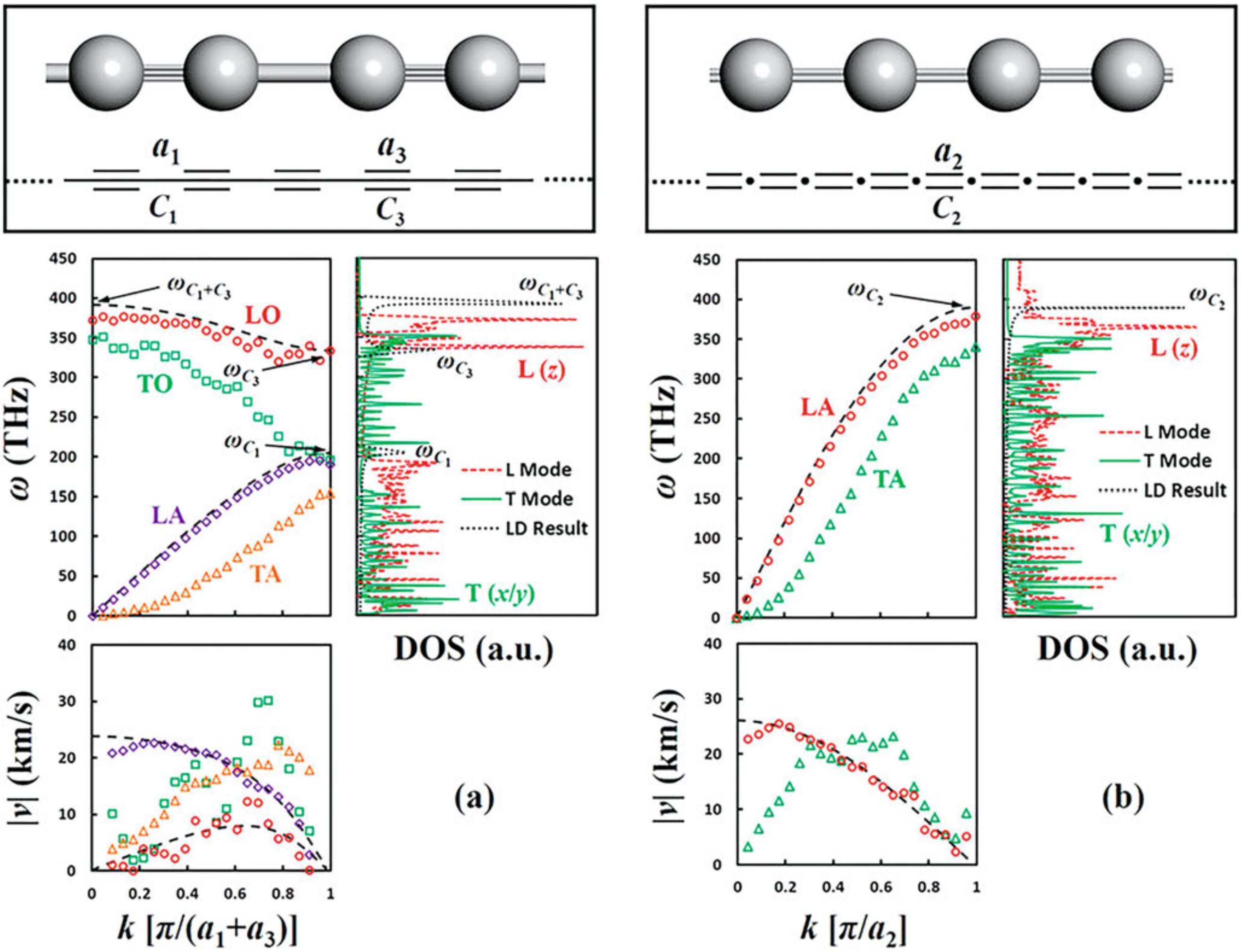

Fig. 4.17 Atomic and chemical structures (top), phonon dispersion (middle left), phonon DOS (middle right), and absolute group velocity (bottom left) of a single (**a**) carbyne chain and (**b**) cumulene chain. (Reproduced with permission of *Nature*)

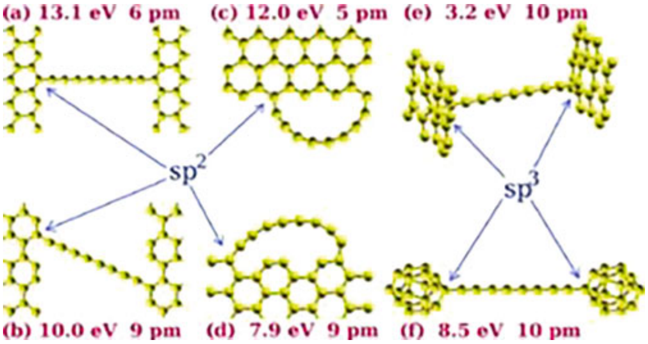

Fig. 4.18 A few representative structures involving an eight-atom sp-bonded carbon chain terminated on *sp*^{2} carbon fragments [(**a**–**e**): NRs; (**f**): C_{20}]. Either edge termination [(**a**–**d**), *sp*^{2}-like] or termination on an internal atom of the fragment [(**e**, **f**), *sp*^{3}-like] is possible. Binding energies (with respect to the uncapped straight chain plus fully relaxed *sp*^{2} fragments) and BLA are reported. (Reproduced with permission of *Wiley*)

polymers, e.g., chemical carbonization of poly(vinylidene halides). Another approach targets molecules with a defined length and endgroup constitution, typically via the dimerization reaction of ethynyl groups. Polyynes are typically easier to produce than cumulenes probably due to higher stability, and nowadays polyynes up to 20 carbon atoms and more can be produced in solution even as size-selected samples.

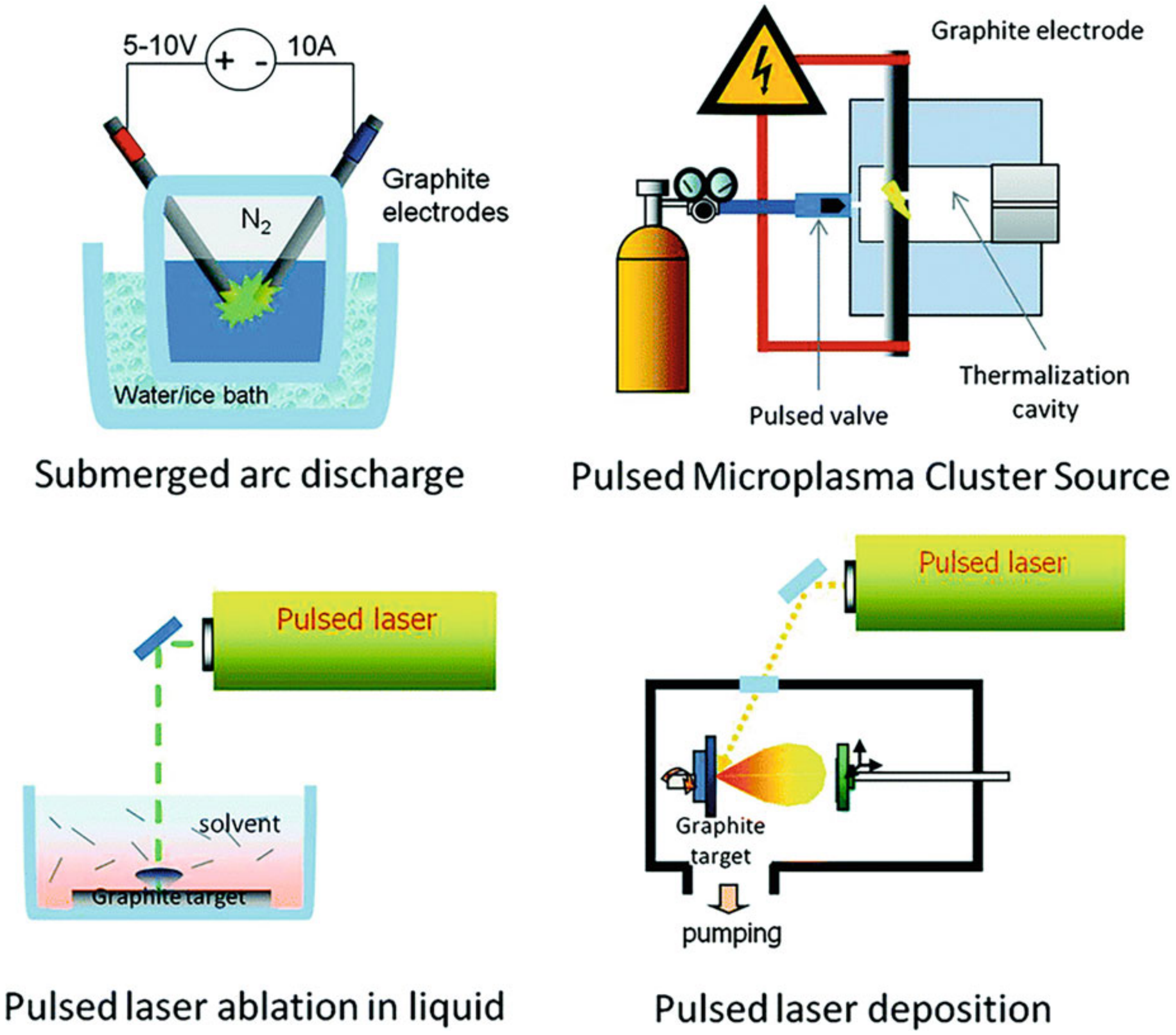

Fig. 4.19 Sketches representing several known physical methods adapted to synthesize linear sp-carbon wires. (Reproduced with permission of the *Royal Society of Chemistry*)

As an example of CAW preparation, the synthesis of CAWs was carried out by nanosecond pulsed laser deposition exploiting the strong out-of-equilibrium conditions occurring when the ablation plasma is confined in a background gas [59]. It was revealed that CAWs are mixed with a mainly sp^2 amorphous carbon in a sp–sp^2 hybrid material, i.e., sp-carbon-atom wires embedded in a mainly sp^2 amorphous network. CAWs form in the gas phase where high-pressure and high-temperature gradients produce strong out-of-equilibrium conditions (i.e., at the plume shock front). Once formed, sp-carbon wires must be deposited on the substrate preventing fragmentation and reorganization. Under optimal conditions the as-produced material is a sp–sp^2 moiety in which CAWs appear to be embedded in an amorphous mainly sp^2 carbon network. CAWs are terminated by sp^2 carbon in many different ways, including both double bond and triple bond terminations which are able to induce both polyyne-like and cumulene-like wires.

The data on conductivity of CAWs are contradictory. Although it is noted in several reports that preliminary experiments do not confirm the predicted electrical conductivity, the electrical-transport measurements of monatomic carbon chains were reported [60] for the chains, obtained by unraveling carbon atoms from graphene ribbons, while an electrical current flowed through the ribbon and, successively, through the chain (Fig. 4.20). It was shown that atomic carbon chains exhibit electrical conductivity, albeit lower than predicted for ideal unstrained chains.

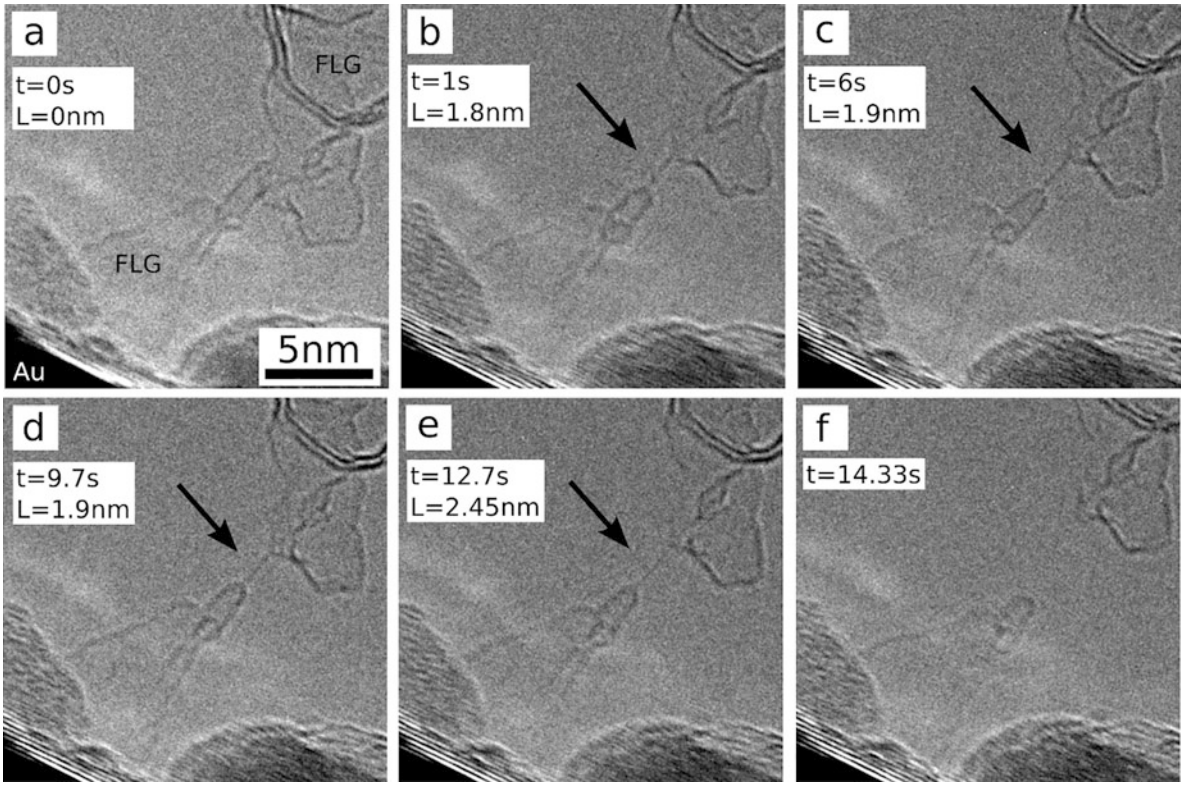

Fig. 4.20 In situ synthesis of a monatomic carbon chain. (**a**) A few-layer graphene (FLG) nanoribbon breaks and forms a carbon chain (arrowed) which is stable for a few seconds (**b–e**). The chain eventually breaks and disconnects the two FLG regions (**f**). The time scale and the measured length of the chain (in the projection onto the image plane) are indicated. (Reproduced with permission of the *American Chemical Society*)

4.2 Elongated Carbon Nanostructures[9]

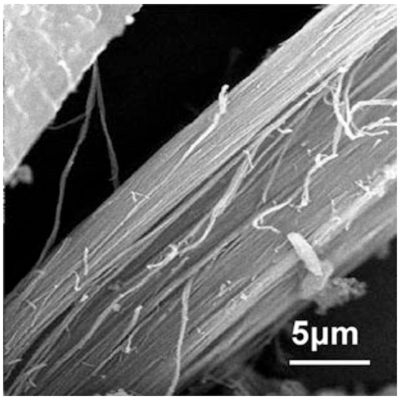

The following closely related nanostructures can be attributed to this type: nanolines, nanopencils, nanodumbbells, nanopins, nanoshuttles, nanopeapods, nanobricks, nanochains, nanowicks, nanobars, and nanopillars. Some of them have not yet been reported for carbon, such as, for instance, nanolines or nanoshuttles.

---

[9] Reproduced with permission of the *American Chemical Society* (*Chem. Mater.*, **2003**, *15*(7), 1470–1473).

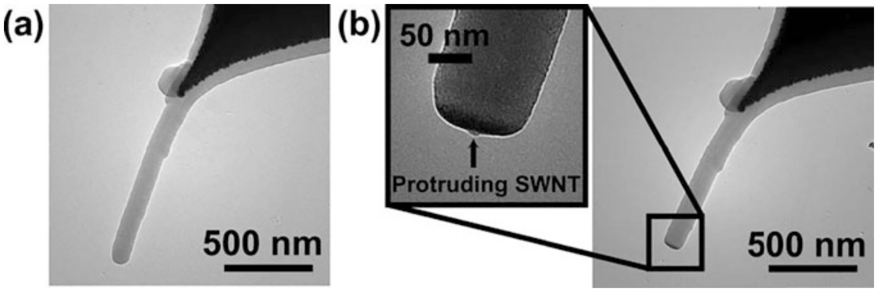

Fig. 4.21 TEM images of the nanopencil. (**a**) Nanopencil before SWCNT electrode exposure initial length: 980 nm. (**b**) Nanopencil after electrode exposure length: 870 nm. The inset shows the clean SWCNT electrode protruding from the SiO_x coating. (Reproduced with permission of the *American Institute of Physics*)

4.2.1 Nanopencils[10]

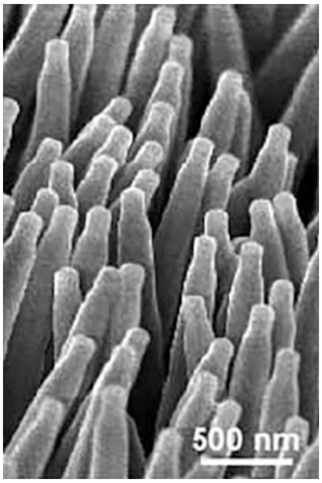

Reports on carbon nanopencils are practically absent. Thus, a nanopencil of silicon oxide on a carbon nanotube (Fig. 4.21) was fabricated [61] by conformal deposition of silicon oxide on a carbon nanotube and subsequent "sharpening" to expose its tip. Its application as a wear-tolerant probe for ultrahigh-density data storage was proposed.

4.2.2 Nanobuds

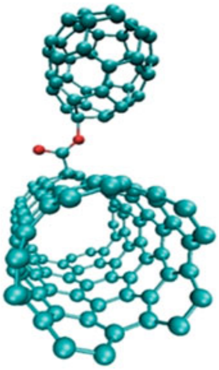

---

[10] The nanopencil image above in the subtitle is reproduced with permission of the *John Wiley and Sons* (*Adv. Funct. Mater*., **2006**, *16*, 410–416).

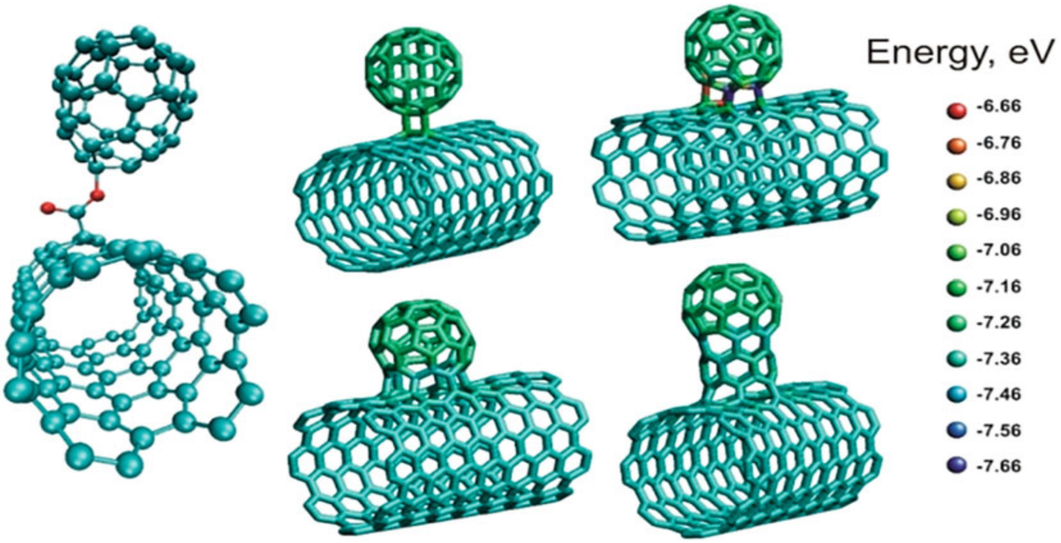

Fig. 4.22 Varieties of nanobuds. (Reproduced with permission from http://www.nanodic.com)

Such carbon allotropes as carbon nanotubes (CNTs) and fullerenes (Fs) are known from the last decades of the twentieth century, but their combinations,[11] called "nanobuds" (NBs) and possessing unique properties superior to CNTs and Fs alone, were discovered relatively recently by *Nasibulin* and *Kauppinen* [62]. This structure seems like fusion of a cylinder with a sphere (Fig. 4.22); there is a covalent bond between outer sidewalls of the nanotube and the fullerene. In this material, fullerenes are covalently bonded to the outer sidewalls of the underlying nanotube [63]. Consequently, NBs exhibit properties of both carbon nanotubes and fullerenes. For example, their electrical conductivity and the mechanical properties are similar to those of CNTs. The attached fullerene molecules possess a higher reactivity, and so they can be functionalized by classic methods of fullerene chemistry [64]. In addition, fullerenes can prevent slipping of CNTs in hybrid materials; resulting mechanical and other properties of final composites could be thus changed.

We could still consider NBs as "less-common nanostructures" [65], despite that almost 10 years have passed after their discovery, due to a relatively low number of reports. In this section, we present main achievements on their synthesis, properties, and applications, with the objective to attract more attention to this unusual combination of carbon allotropes.

Synthesis of Carbon Nanobuds, Their Formation Mechanism, and In Situ Engineering

In the first reports on carbon NBs, the carbon monoxide–ferrocene system, in the presence of H_2O and CO_2 as etching agents, was used for fabrication of a hybrid material (Fig. 4.23) on the basis of single-walled carbon nanotubes (SWCNTs) in the reactor at 885–945 °C [66]. Both NBs precursors (CNTs and fullerenes) appeared as a result of a one-step continuous process of a disproportionation of CO on the surface of iron nanoparticles, formed from ferrocene vapor. For this process, the optimal concentrations of CO_2 and H_2O were found to be between 2000 and 6000 ppm for CO_2 and between 45 and 245 ppm for H_2O. Two main reactions take place: CO disproportionation (4.1)

$$\mathrm{CO(g) + CO(g) \leftrightarrow C(s) + CO_2(g)} \tag{4.1}$$

and CO hydrogenation (4.2)

$$\mathrm{H_2(g) + CO(g) \leftrightarrow C(s) + H_2O(g)} \tag{4.2}$$

Studying the mechanism of carbon nanobud formation [67], the authors assumed that the SWCNTs could appear in the reactor apart of fullerenes. The fullerenes are further deposited on the SWCNT surface. However, due to the detection of a F-SWCNT mixture in all samples, it was tentatively concluded that they are formed at the same time from graphitic carbon on the iron nanoparticle surface (Fig. 4.24). Certain carbon atoms can be attacked by etching molecules, for example, H_2O, releasing H_2 and CO, contributing to the formation of pentagons and hexagons.

---

[11] Other combinations between carbon allotropes are known, for instance, carbon nanodots immobilized on single-walled carbon nanotubes (*Chem. Sci.*, **2015**, *6*, 6878–6885).

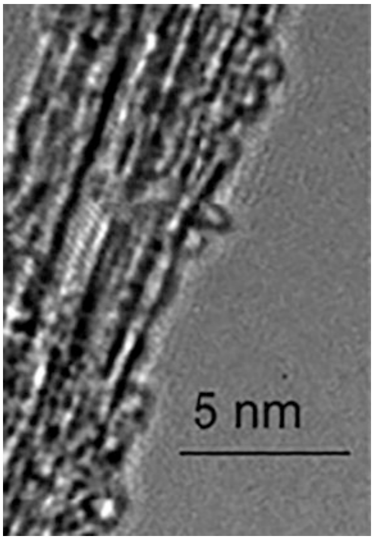

Fig. 4.23 High-resolution TEM images showing fullerenes of different shapes and sizes. (Reproduced with permission of the *Elsevier Science*)

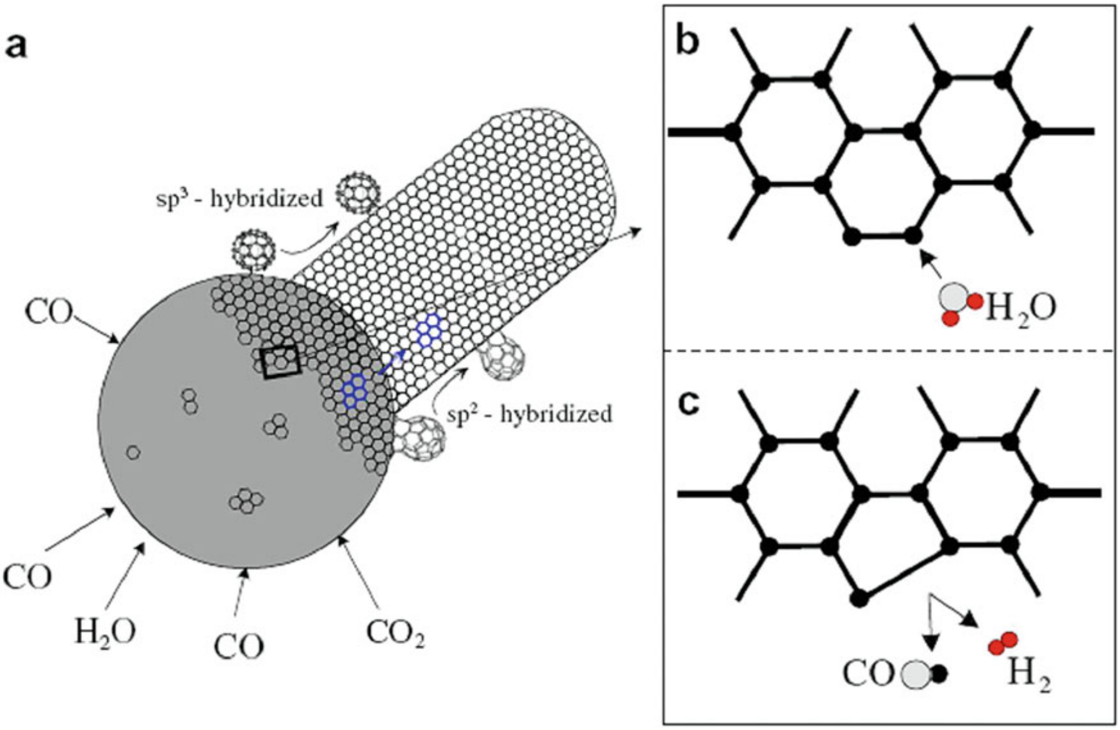

Fig. 4.24 Schematic representations of (**a**) nanobud growth by continuous transportation of a carbon layer from a particle to a SWCNT, (**b**) pentagon formation at the edge of the dynamic layer of a growing SWCNT, and (**c**) the growth mechanism of nanobuds. (Reproduced with permission of the *Elsevier Science*)

As it will be shown below, carbon nanobuds can exist in various types of structures, all being stable. One NB geometry can be transformed to another kind, and this process can be monitored and visualized by transmission electron microscopy (TEM) [68]. The fullerenes can be converted into tubular branches via treatment of the electron-beam irradiation. SWCNT samples with NBs were fabricated by an aerosol-assisted CVD (carbon source, an aerosol of toluene with 5 wt.%; synthesis conditions, 800 °C, 15 min), collected on a substrate, placed at the end of the reactor, dispersed in acetone, sonicated, and transferred onto TEM grids. Resulting products (NBs, Fig. 4.25) contained fullerenes of various sizes on the SWCNTs. The electron beam provides enough energy to allow the fullerene to be transformed into a tube-like structure (Fig. 4.25f) before collapsing entirely (Fig. 4.25h).

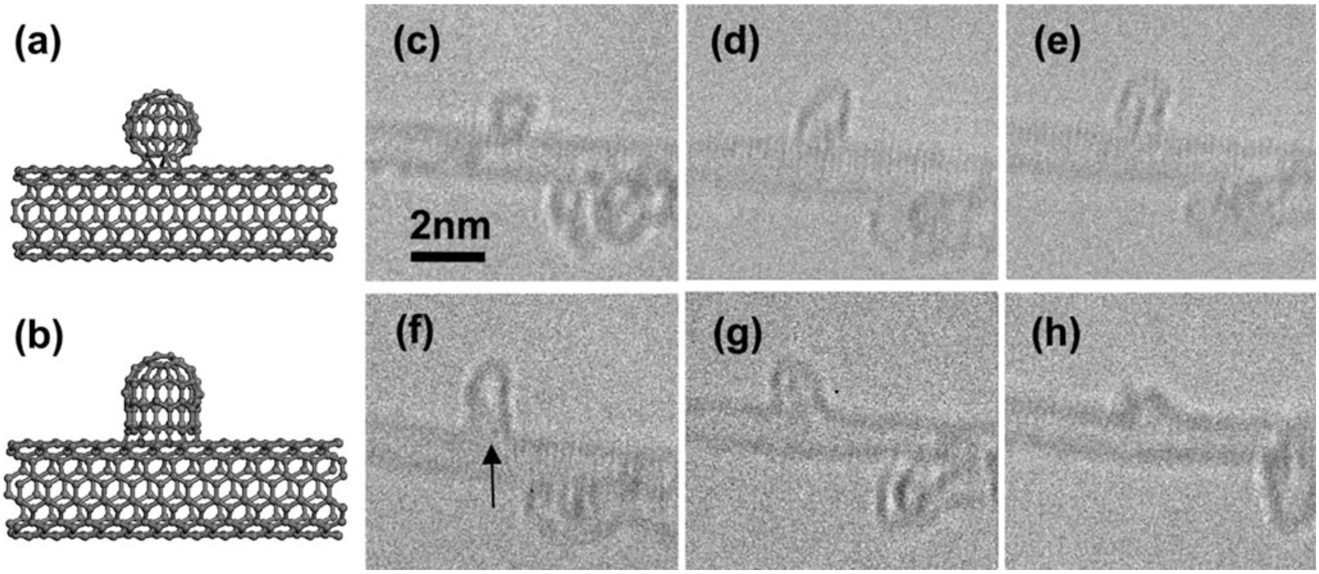

Fig. 4.25 Schematics showing a fullerene attached to a diagram (**a**) and a transient structure of a short, capped nanotube attached to a larger nanotube (**b**). TEM images (**c**–**h**) showing the evolution of a carbon NB under the electron beam. (Reproduced with permission of the *Royal Society of Chemistry*)

DFT and MD Calculations for Carbon NBs

A relatively high number of reports are dedicated to DFT calculations of carbon NBs to investigate their stability, formation mode, and mechanical, electronic, structural, and other properties. Thus, for the fullerene C_{60}, attached on the surface of (10,0) and (6,6) SWCNTs, five types of configurations for the armchair (6,6) and zigzag (10,0) carbon NBs were considered (Fig. 4.26) [69]. All these NBs possess semiconductor properties nondependent on whether the original SWCNT base is semiconducting or metallic (semiconducting or metallic behavior depends on the nanotube size and the combination mode [70]). Young's modulus of the carbon NBs was found to be decreased when attaching a fullerene C_{60} molecule on the surface of zigzag and armchair SWCNTs. In addition, (a) the bandgap can be opened by C_{60} attachment to single-walled CNTs, (b) impurity states can be introduced within the bandgap, and (c) changing the density of attached C_{60}, the bandgap can be modified [71]. Indeed, carbon NBs (i.e., the junction between C_{60} and CNTs) are very stable at room temperature; their relative stabilities depend on the type of carbon–carbon bond dissociated in the cycloaddition reaction. The formation of a C_{60} carbon nanobud on CNT caps is energetically more favorable than that on CNT sidewalls (Figs. 4.27 and 4.28) [72]. The dominant carbon NB formation mode for CNT caps in the conventional CNT sidewall case was found to be the [2 + 2] cycloaddition reaction.

In comparison with "classic" carbon nanobuds above, other different kinds of carbon NBs (in particular, shown in Fig. 4.29) can exist in case of being produced by C_{60} bombardment on the CNTs, according to the molecular dynamic (MD) simulation data [73]. It was emphasized that thus formed fullerene–nanotube hybrid nanostructures generally decrease Young's modulus and the maximum tensile strength of carbon nanotubes. Another intriguing type of carbon NBs is also known. Thus, MD simulations were applied to study the effects and mechanical properties of NBs and heat welded nanobud chains (C_{60} chains embedded or attached on a SWCNT surface) [74]. It was noted that, despite both these hybrid structures lower the ultimate tensile strength of a defect-free SWCNT, heat welded nanobuds chains significantly enhance (by more than 20%) the mean post-peak strength of the CNT (after necking) due to the consolidation of the SWCNT bundles with vacancy defects. While C_{60} chains are being attached, the maximum tensile strength of CNTs bundles with vacancy defects. Figure 4.30a–c illustrates the tensile process of a perfect SWCNT (10,10) containing two C_{60} chains attached on the surface, and Fig. 4.30d–f gives information on the tensile process of a SWCNT (10,10) having a single vacancy defect and two heat welded C_{60} chains connected with the CNT surface. So, the fullerenes definitively take part in the tensile deformation process of carbon nanotube.

In addition to mechanical peculiarities, other carbon NB properties, in particular their magnetism and optical properties, have been predicted by DFT, in particular the robust magnetic state of nanobuds (Fig. 4.31) [75]. Carbon radicals can be

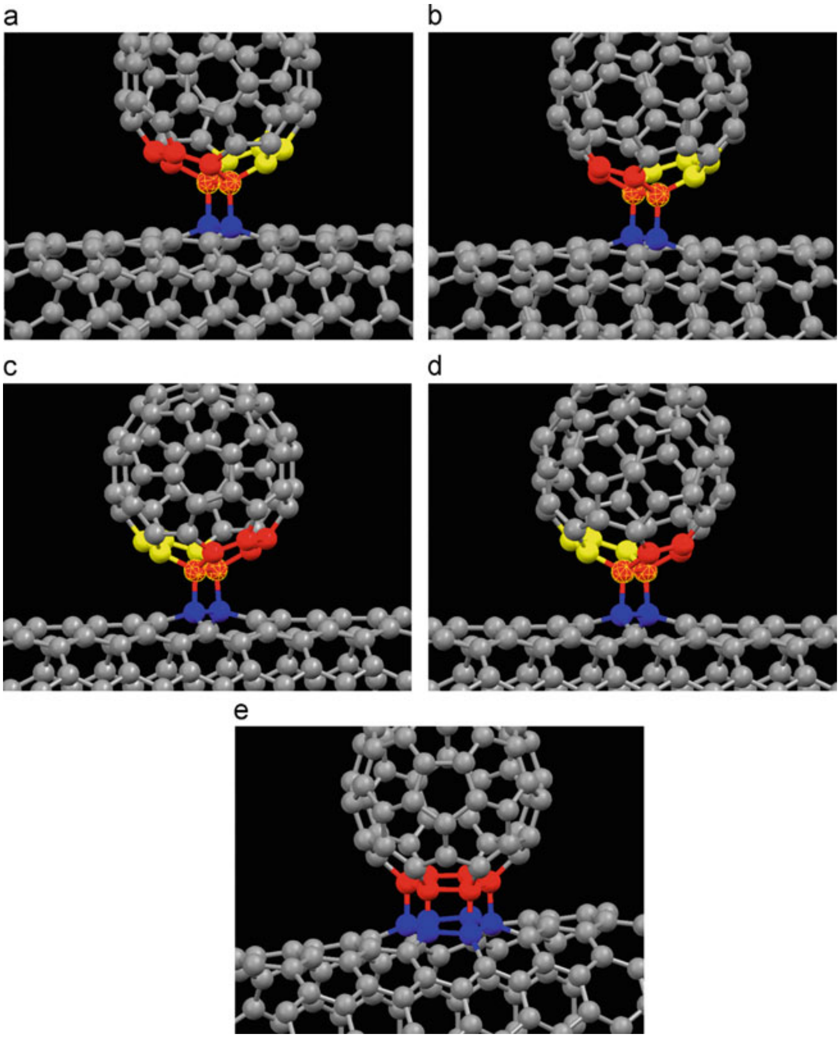

Fig. 4.26 Attachment of fullerene on carbon nanotubes at five different positions: (**a**) first, (**b**) second, (**c**) third, (**d**) fourth, and (**e**) fifth configurations. (Reproduced with permission of the *Elsevier Science*)

generated by substantial emergent amounts of unpaired spins; these radicals are mainly located on the CNT surface within the connecting region with C_{60}. Among other studies [76], optical properties of carbon NBs were studied using by means of optical spectroscopy, electron microscopy, and Raman spectroscopy for validation of results [77–80]. Quantitative information of the bond length, bond energy, mode cohesive energy, binding energy density, Debye temperature, and the compressibility of the C–C bond in carbon NBs and other carbon allotropes is also tabulated [81].

A few reports are devoted to the calculations of properties of carbon NBs, functionalized with inorganic adatoms or organic molecules. Electronic structure, transport, and other properties could be modified this way, so one of these attempts implied the attachment of tetrathiafulvalene molecules, as well as Li and F atoms [82]. Li (electron donor) and F (electron acceptor) adatoms were selected, knowing that they can be easily attached to the CNTs. According to the DFT simulations, these adatoms affect the electronic structure of the carbon NBs. However, the effect works mainly in the fullerene part of the NB and is not expanded to the related nanotube, so the CNT part of a NB is almost the same. In case of Li adsorption (Fig. 4.32) on a graphene–C_{60} nanobud system [83], it was found to be enhanced in comparison with pure graphene and C_{60}, being in the range of 1.784–2.346 eV (adsorption of a single Li atom) and 1.905–2.229 eV (two Li atoms). It was supposed that Li atoms are preferably adsorbed (a) between C_{60} and C_{60}, (b) between graphene and C_{60}, (c) on graphene, or (d) on C_{60}, rather than form Li clusters. An increase of number of metal atoms obviously leads to an enhancement of metallic character of the hybrid; in addition, a charge transfer from graphene to C_{60} was detected.

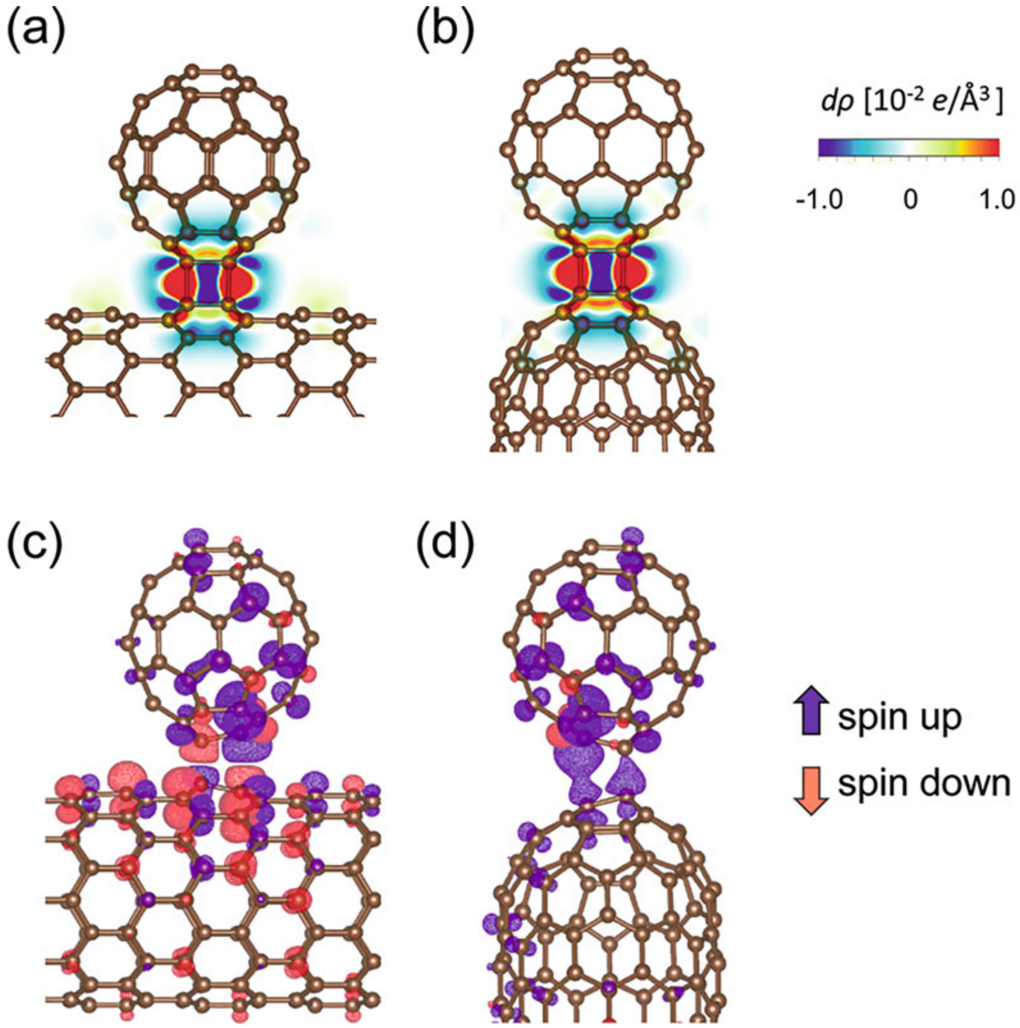

Fig. 4.27 Charge-density difference plots of the CNBs based on the (**a**) sidewall and (**b**) cap (**cap4**) attachment to the (10,0) CNT. Electron accumulation (bond formation) and depletion are shown in red and blue colors, respectively. Spin densities developing at the transition states toward the formation of CNBs in the (10,0) CNT (**c**) sidewall and (**d**) **cap4** attachment cases. In (**c**) and (**d**), the magnitude of isosurface values is 0.0025 e $Å^{-3}$. (Reproduced with permission of the *Royal Society of Chemistry*)

A special case is a carbon nanobud containing *small fullerenes* (<60 carbon atoms). These carbon allotropes were intensively studied by Nobel laureate *Harold Kroto* et al. [84–86] and other researchers [87]. Among these fullerenes, C_{20} (a dodecahedron with 12 pentagons, Fig. 4.33a) is considered to be the smallest. Thermal conduction of carbon NBs with C_{20} was studied by MD simulations [88]. Figure 4.33b shows a schematic diagram of a C_{20} fullerene-chained carbon NB, in which a linear row of closely located fullerenes is connected to a CNT and located close to one another. It was demonstrated that (a) nanobuds conduct thermal energy relatively well, within an order compared to CNTs, and (b) the main conduction path is along the CNTs. The C_{60} nanobud was found to be more conductive than other forms of nanobuds with C_{20}, C_{34}, and C_{42} because the long-wavelength, low-frequency acoustic modes are scattered to a greater degree at the interfaces.

Several reports are devoted to *graphene nanobuds* (e.g., composites $[(C_{60})_6$+(5,5)] [89]), which are closely related analogues of CNT NBs. Their mechanical properties were studied by MD simulations using Large-Scale Atomic/Molecular Massively Parallel Simulator (LAMMPS) code [90], selecting seven configurations with distinct junction lengths and graphene sheet sizes (Fig. 4.34). Resulting failure stress changes were found to be calculated in the range of 100–200 GPa (decreasing with neck's length and temperature increment) and Young's modulus 440–760 GPa. All mechanical properties

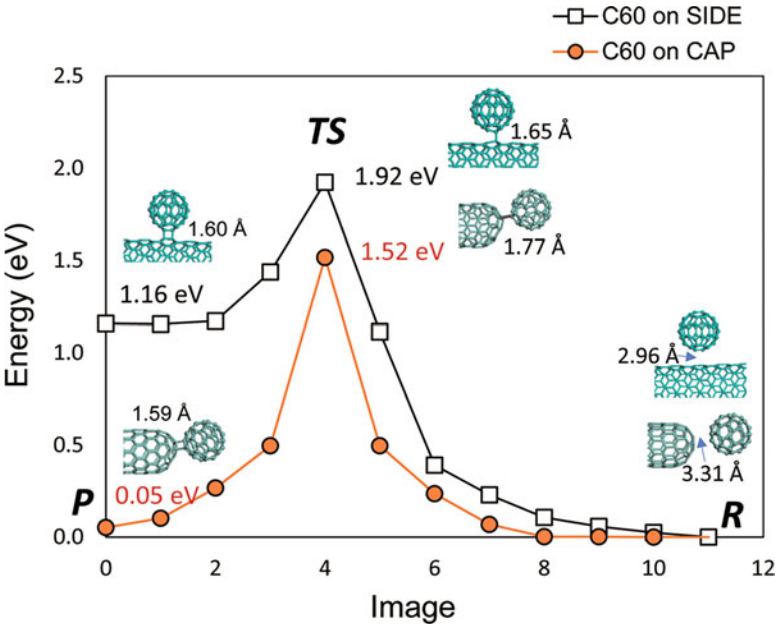

Fig. 4.28 Minimum-energy path for the formation of the C_{60}-**cap4** configuration. The R, TS, and P symbols denote the reactant, transition states, and product, respectively. The energy of the reactant was set to zero. (Reproduced with permission of the *Royal Society of Chemistry*)

above increase with increment of the graphene sheet. We note that this hybrid could be better called as a triple carbon allotrope system "graphene-nanotube-nanobud," since this is a real growth (Fig. 4.34a–d) of a SWCNT between fullerene molecule and graphene surface.

Related Noble Metal Nanobuds Similar to carbon nanobuds above, gold nanobud-like structures are also known [91]. They were grown by CVD thermal decomposition of the two gas-phase precursors, [Au(HMDS)(NHC)] (HMDS = hexamethyldisilazide, NHC = 1,3-diisopropylimidazolidin-2-ylidene) and [Au(HMDS)(PMe_3)], at a variety of temperatures. At longer deposition times, more free sites for nanobudding became available; their formation was attributed by authors to a decline in surface concentration of surfactant. Distinct method (solid-state ionic method) [92] was applied for fabrication of a silver nanobud (AgNB) substrate with superior SERS activity. This product can be used for the analysis of trace biomacromolecules. Finally, a nanoscale neural probing device for in vitro sensing of neural activity, on the basis of single vertical platinum (Pt) nanowires-nanobuds, is known [93]. We note that these nanostructures cannot be strictly called as "nanobuds," since the metallic "fullerene"-like particle on the surface of metal 1D prolonged nanostructure is not hollow, i.e., these hybrids are not similar to their carbon analogues.

Applications of Nanobuds

The carbon nanobuds, consisting of 1 nm diameter CNTs with attached buds, can substitute indium tin oxide (ITO) [94]. These nanobud thin films can bend, flex, and stretch without any adverse effects, instead of being brittle like ITO. The necessity of creation of such material appeared because of chemical neutrality of CNTs, which can be difficult to combine with other materials due to their low coupling and fractures upon compaction. On the contrary, C_{60} is chemically active and creates conditions for good binding. For instance, carbon NBs are easily coupled with plastics, leading to the possibility to collocate sensor surface onto the material with any shape or curvature, enabling the flexible electronics. The stretchability (up to 120%) and bendability (as small as 1 mm) free the designer from flat-surface controllers. In addition, the NB is

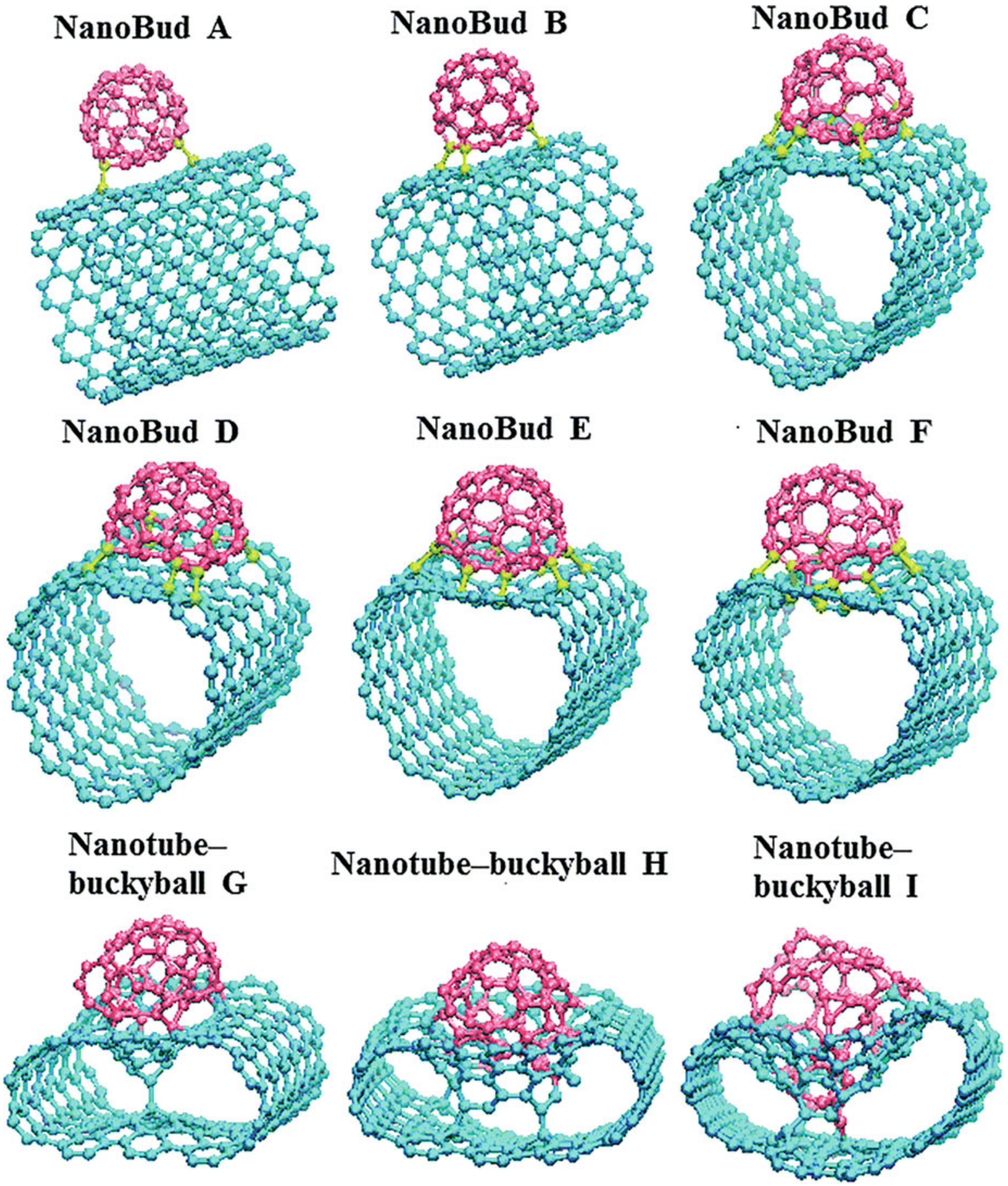

Fig. 4.29 MD simulation data on carbon NBs, formed by C_{60} bombardment on the CNTs. (Reproduced with permission of the *Royal Society of Chemistry*)

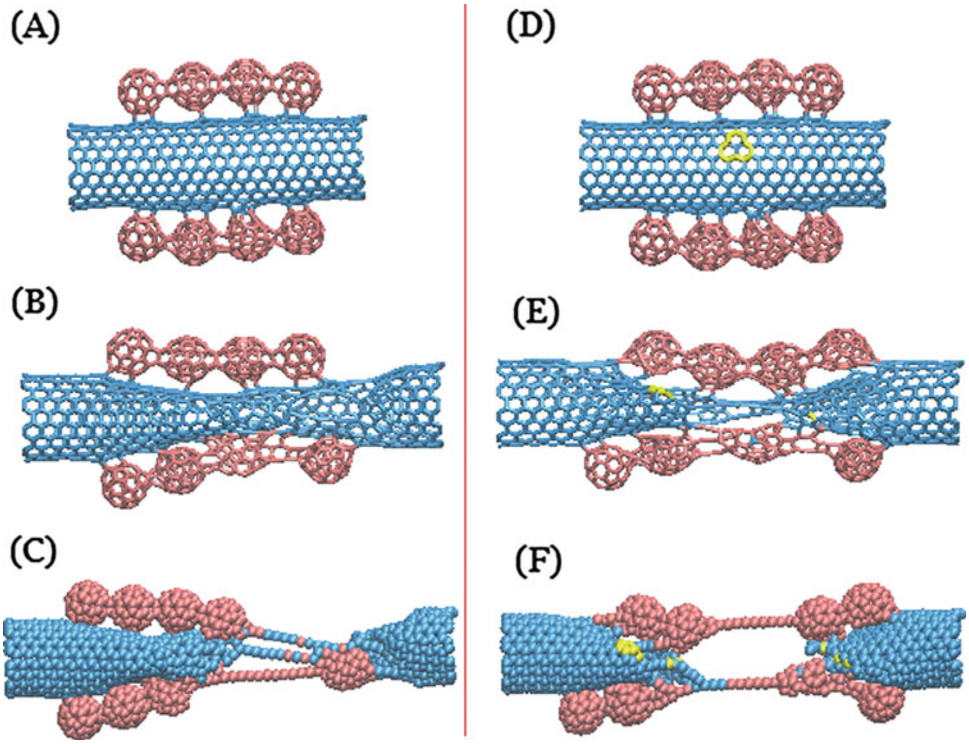

Fig. 4.30 Initial configuration and a typical tensile state of CNT (10,10) with or without a single vacancy defect with two nanobuds chains. (Reproduced with permission of the *Elsevier Science*)

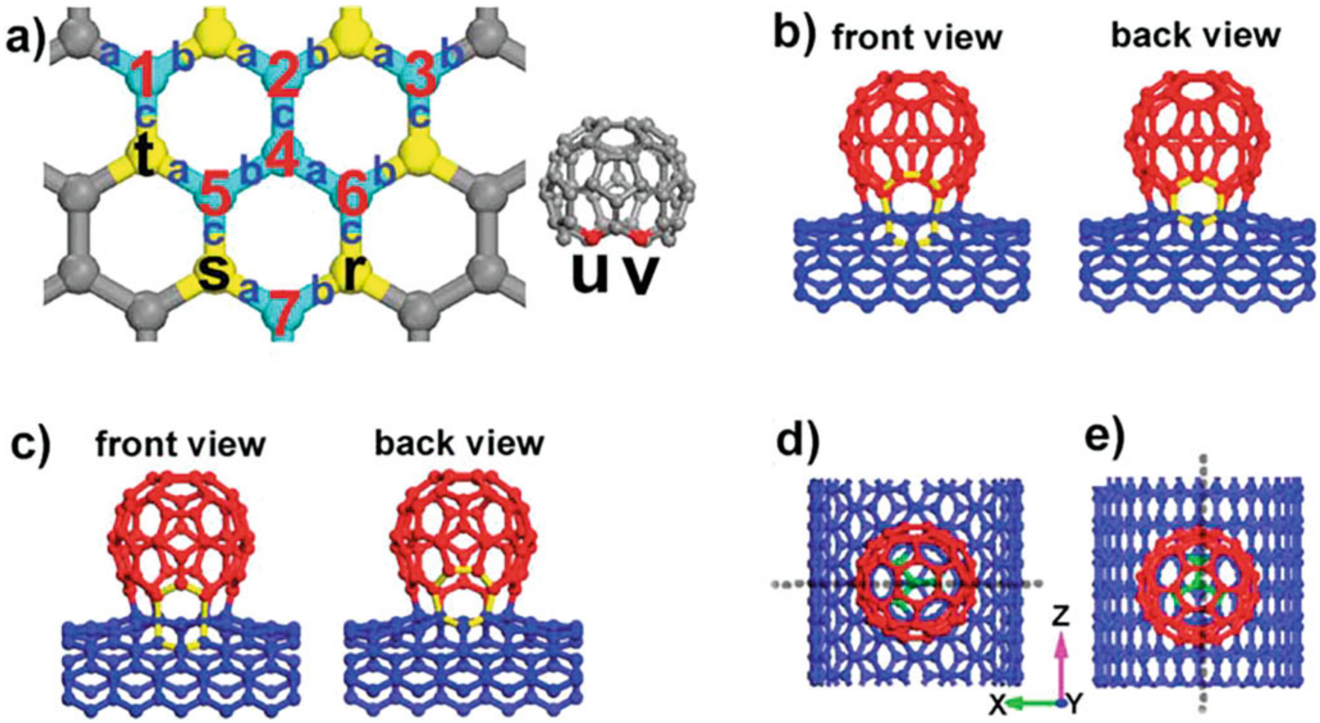

Fig. 4.31 Geometric structures of one class of nanobuds. (**a**) The blue-colored carbon atoms of CNT host major unpaired spins. The yellow-colored carbon atoms of CNT connect the fullerene covalently. The topology is illustrated in detail in the text by atoms labeled as r, s, and t for CNT and u and v for fullerene. Two topological structures of armchair CNT-based nanobuds: the yellow-colored bonds exhibit (**b**) nine- and six-membered rings in 9-6 case and (**c**) eight- and seven-membered rings in 8-7 case. The top views of (**d**) armchair- and (**e**) zigzag-based nanobuds display the locations of the mirror planes, which can be visually observed by different orientations of three green-colored bonds as well. (Reproduced with permission of *APS Physics*)

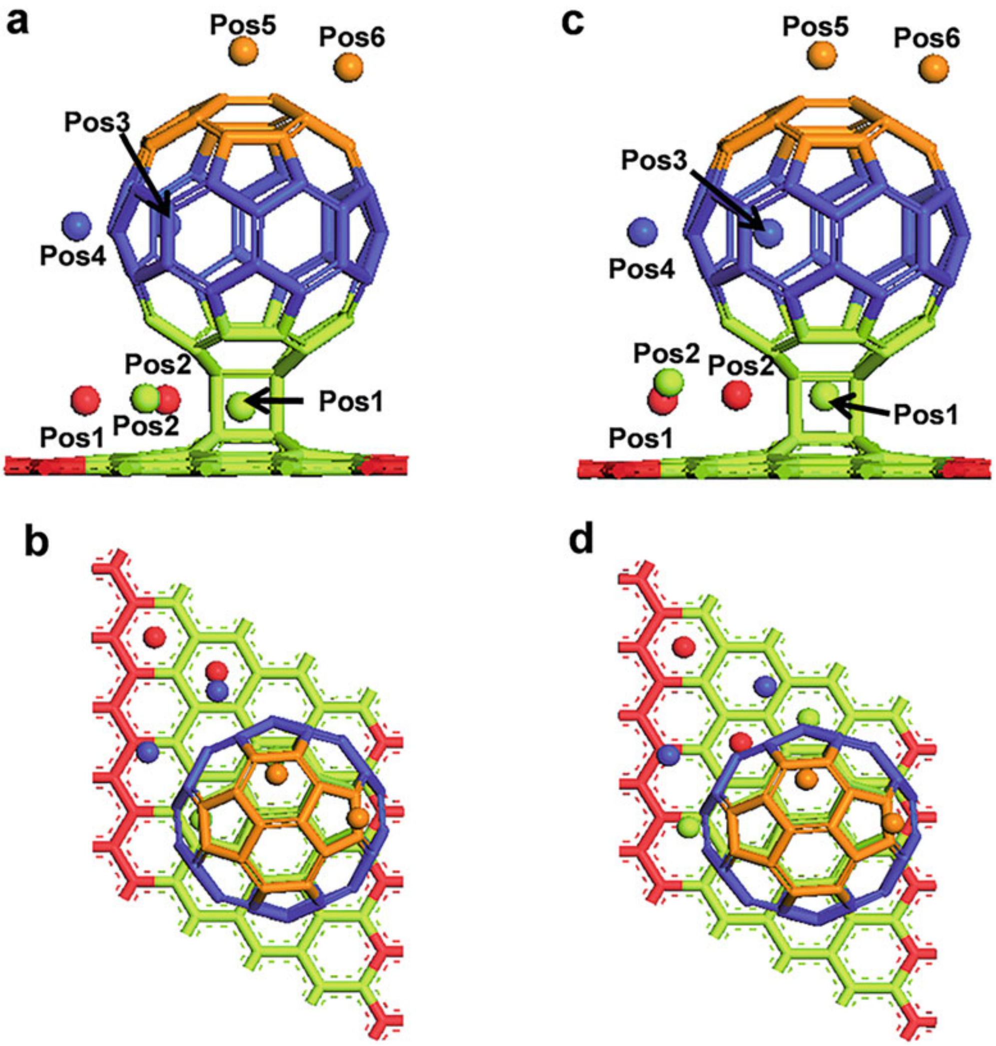

Fig. 4.32 Adsorption of one Li atom at various positions around the graphene–C_{60} nanobud system: (**a**) side and (**b**) top views of initial structure; (**c**) side and (**d**) top views of optimized structure. Region 1, red; region 2, yellow; region 3, blue; and region 4, orange. (Reproduced with permission of the *Royal Society of Chemistry*)

transparent (like ITO), but not fragile. Among other applications, carbon nanobud molecule with attached chromophore molecules is used to saturably absorb electromagnetic radiation [95, 96]. In addition, SWCNTs with and without defects and carbon NBs were tested for ethanol vapor sensing [97]. It was found that the pristine high-quality SWNTs do not exhibit any ethanol sensitivity, while the introduction of defects in the tubes results in the appearance of the ethanol sensitivity.

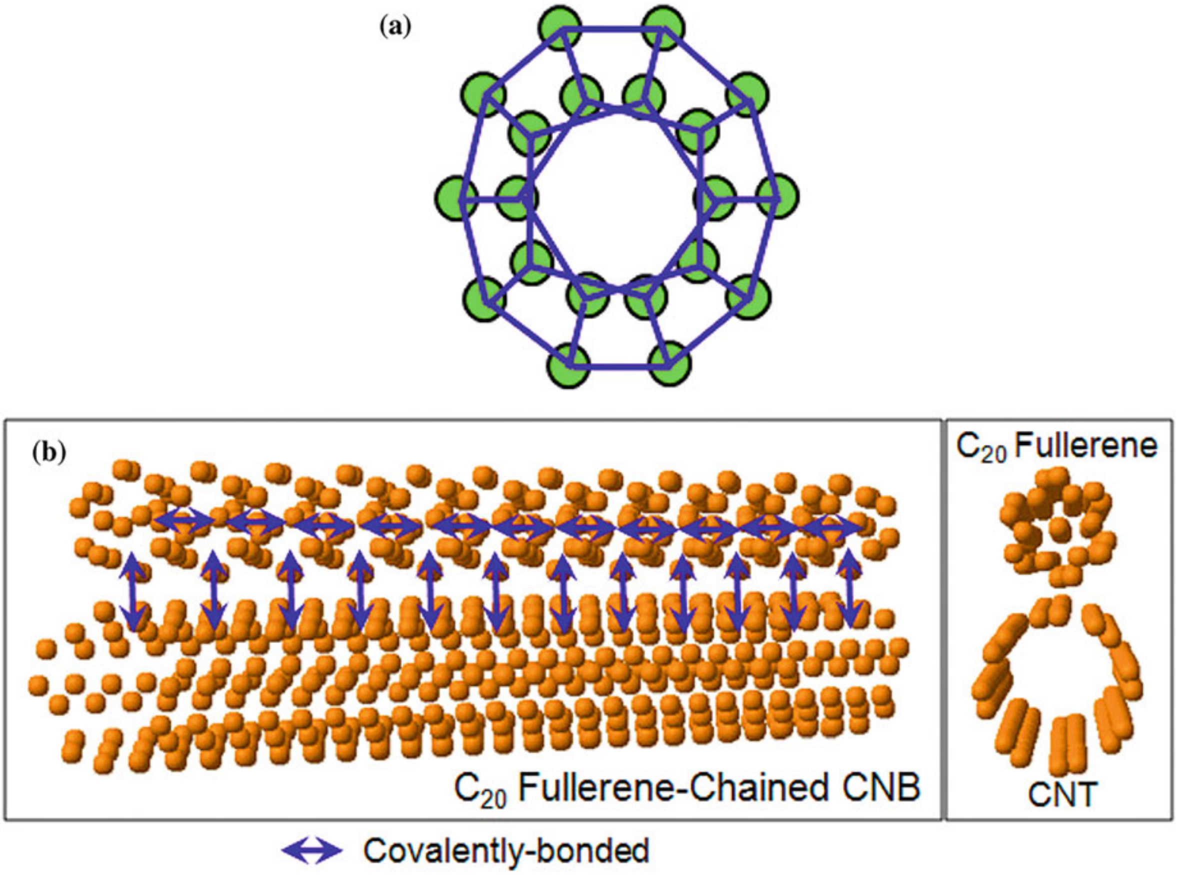

Fig. 4.33 Schematic diagram of (**a**) C_{20} fullerene and (**b**) C_{20} fullerene-chained carbon nanobud: side view and axial view. (Reproduced with permission of the *AIP Publishing*)

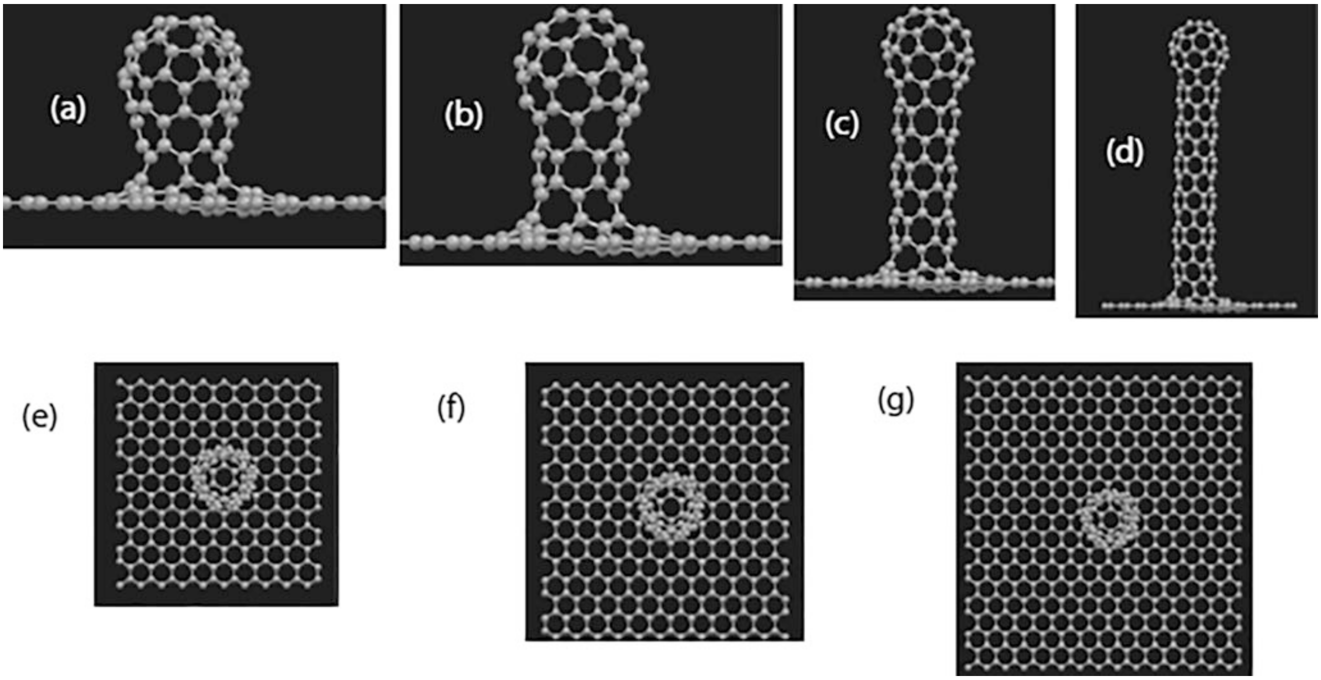

Fig. 4.34 Different neck length and sheet size: (**a**) Neck-0, (**b**) Neck-1, (**c**) Neck-5, (**d**) Neck-10, (**e**) 23 × 23, (**f**) 28 × 28, and (**g**) 36 × 36. (Reproduced with permission of the *Elsevier Science*)

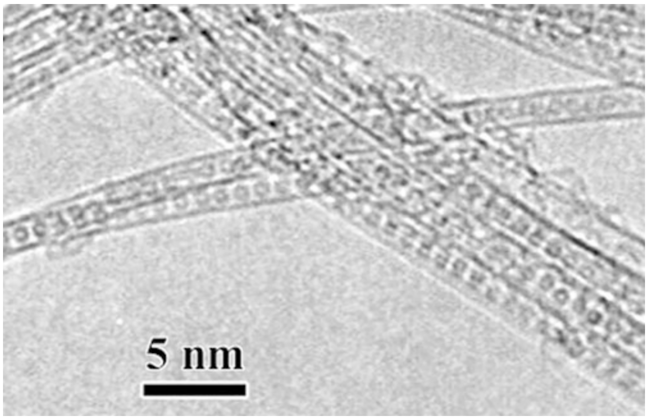

Fig. 4.35 Typical HRTEM image of C_{60} nanopeapods. (Copyright. Reproduced with permission of the *American Chemical Society*)

4.2.3 Nanopeapods

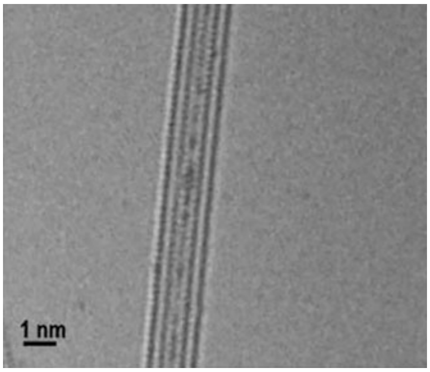

"Peapod"[12] is the descriptive term applied to a supramolecular hybrid assembly in which nanotubes are filled with a 1D chain of molecules [98]. The archetypal peapod is that in which C_{60} molecules [99] are contained within carbon nanotubes (Fig. 4.35) [100]. Nanopeapods are mainly examined for carbon nanotubes and fullerenes (or their endohedral metal complexes), although several examples of other inorganic compounds have been reported. For CNTs and fullerenes incapsulated in them, a comprehensive investigations have been carried out, including, for example, synthesis [101], studies of charge transfer [102], binding fullerene–nanotube [103], atomic structure [104] and electronic properties [105], influence of electromechanical effects [106], fundamental mechanical principles and conventional applied mathematical modeling [107], structural evolutions [108], electrical transport [109], and density-functional study [110], among many others [111]. Thus, the dynamics of C_{60} fullerene molecules inside single-walled carbon nanotubes was studied using inelastic neutron scattering [112]. C_{60} vibrations and their sensitivity to temperature were identified. Additionally, a clear signature of rotational diffusion of the C_{60} was evidenced, which persisted at lower temperature than in 3D bulk C_{60}.

A fascinating structural transformation occurring inside SWCNTs was found to be the fullerene coalescence, which is responsible for forming stable zeppelinlike carbon molecules [113]. Sequences of fullerene coalescence induced by electron irradiation on pristine nanotube peapods were revealed. It was indicated that the merging of fullerenes resulted in stable but corrugated tubules (5–7 Å in diameter) confined within SWCNTs. The process occurred via the polymerization of C_{60} molecules followed by surface reconstruction, which can be triggered either by the formation of vacancies (created under electron irradiation) or by surface-energy minimization activated by thermal annealing. The rotation of fullerene chains in SWCNT peapods was studied using low-voltage high-resolution TEM [114]. Anisotropic fullerene chain structures (i.e., C_{300}) were formed in situ in carbon nanopeapods via electron-beam-induced coalescence of individual fullerenes (i.e., C_{60}). It was established that the large asymmetric C_{300} fullerene structure exhibited translational motion inside the SWCNT and

---

[12] The nanopeapod image above in the subtitle is reproduced with permission of the *Elsevier Science* (*Carbon,* **2015**, 95, 302–308.).

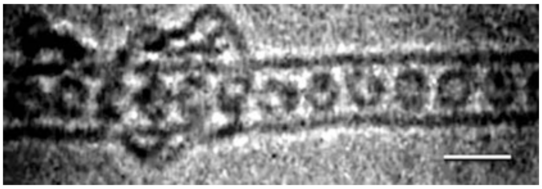

Fig. 4.36 A HRTEM image of (Gd@C_{82})@SWCNT. The scale bar is approximately 2 nm. (Copyright. Reproduced with permission of the *American Physical Society*)

unique corkscrew like rotation motion. The axial stability of single-walled carbon nanopeapods was studied based on an elastic continuum shell model [115]. Dependence of thermal conductivity of carbon nanopeapods on filling ratios of fullerene molecules was recently investigated [116].

In case of metal endofullerenes, after heating nanopeapods of the SWCNTs encapsulating the La_2@C_{80}, the atomic wires of La atoms inside CNTs were obtained [117]. The La atoms formed dimers and linearly arranged inside the CNTs. The valence state of the La in atomic wires was the same as that in the pristine La_2@C_{80} peapods. Also, a direct evidence of the dynamic behavior of the confined atoms in metallofullerenes was given [118] by observing individual atoms using the high-resolution TEM. Rapid movement of Gd atoms in Gd_2@C_{92} peapod was identified. By comparison with simulation, the amplitude of the motion is roughly quantified as 0.2 nm at r.t. and was reduced to almost half at 100 K. In a related work [119], M@C_{82} (M = Gd, Dy) and their composites with SWCNTs (Fig. 4.36) were studied. Cesium-doped C_{60} nanopeapods were prepared from SWCNTs and characterized by electron energy loss spectroscopy [120]. The ordered Cs_2C_{60} structure was observed inside the carbon nanotubes as well as cesium ions on the exterior of the carbon nanotubes. Single-atom migration of Tb, Gd, or Ce metal from cage to cage through an intentionally induced atomic path within a carbon nanopeapod was demonstrated [121]. Additionally, carbon nanotube peapods can be applied to a nano-electro-emitter when encapsulated endofullerenes are electro-emitted from the carbon nanotube under applied external electric fields.

Fullerenes can be encapsulated by not only CNTs but also in other nanotubes. Thus, ab initio simulations of the electronic properties of a chain of C_{60} molecules encapsulated in a boron nitride nanotube [122] – so-called BN nanopeapod – were carried out [123, 124]. It was demonstrated that this structure can be effectively doped by depositing potassium atoms on the external wall of the BN nanotube. The resulting material became a true metallic 1D crystal. Other reported nanopeapods on carbon basis are $AuCl_3$@DWCNT [125].

4.2.4 Nanochains

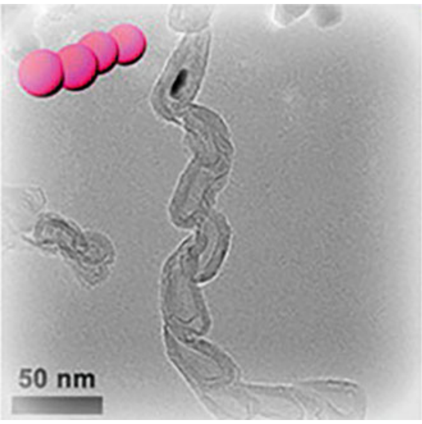

Chain-like nanostructures on carbon basis are quite distinct: connected carbon nanocapsules, carbon nanotubes containing C_{60}, or other species inside like nanoonions.[13] Thus, aligned array of chain-like carbon nanocapsules was prepared by a

---

[13] See sections above on carbynes and carbon-atom wires, which are also carbon chains of lesser size.

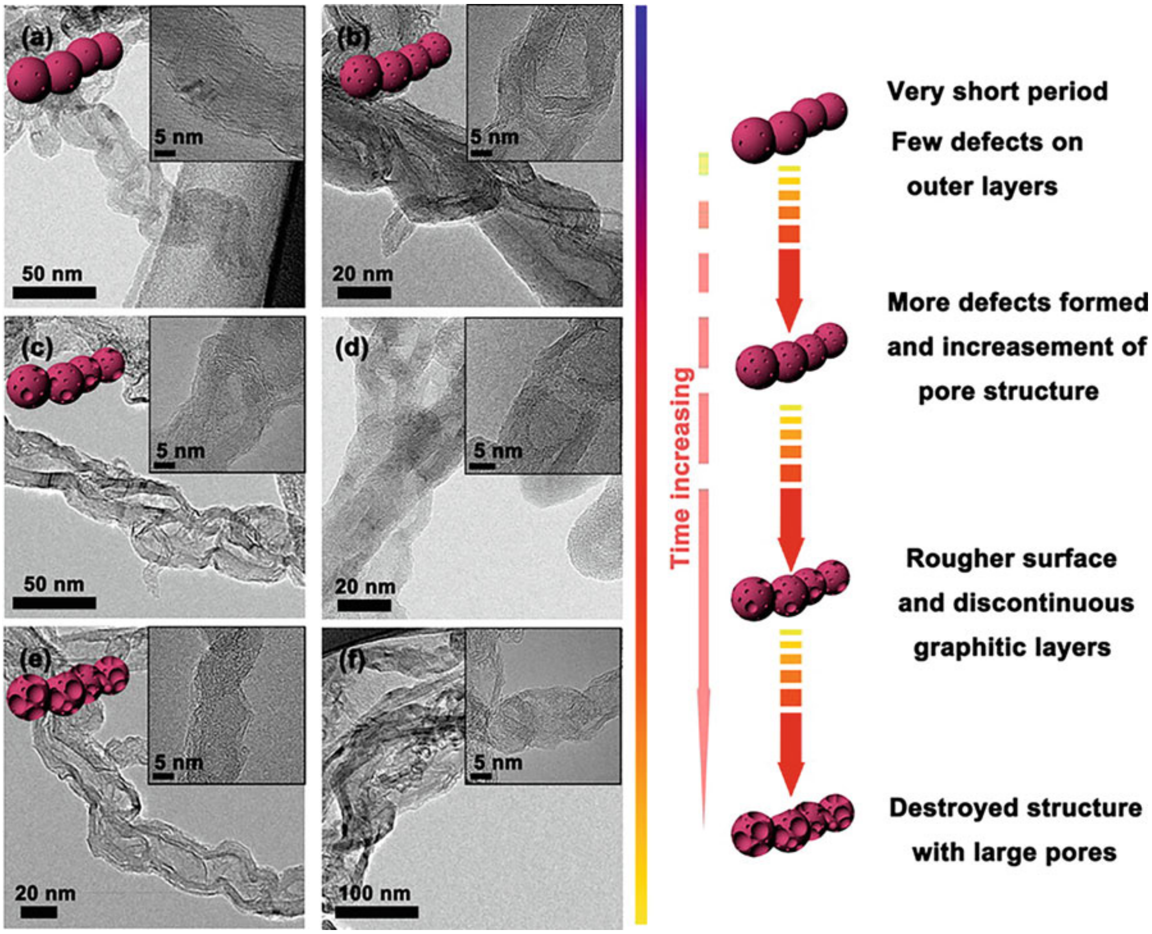

Fig. 4.37 TEM images of activated CNCs (RKOH/CNC = 4) at 900 °C for 5 (**a**), 10 (**b**), 15 (**c**), 20 (**d**), 25 (**e**), and 30 h (**f**). (Reproduced with permission of the *American Chemical Society*)

simple CVD process [126]. It was revealed that the carbon nanochains were filled with Fe_3C particles other than Fe; also, the nanochain was formed by the converging of conjoint multi-nanocapsules. Also, the adsorption of C_{60} on a bilayer film of pentacene on Ag(111) was studied with scanning tunneling microscopy and spectroscopy [127]. At low coverage, C_{60} molecules form extended linear structures due to the templating effect of the pentacene bilayer. The C_{60} molecules in the chains adsorbed at bridge sites between two neighboring pentacene molecules. In addition, carbon nanochains (CNCs), consisting of a 1D chain of interconnected carbon nanoonions (CNOs; see the section above), were produced by CVD method and can be used as supercapacitors (Fig. 4.37) [128]. The CNCs were further chemically activated using KOH (Fig. 4.38) to obtain micro-meso pore structures.

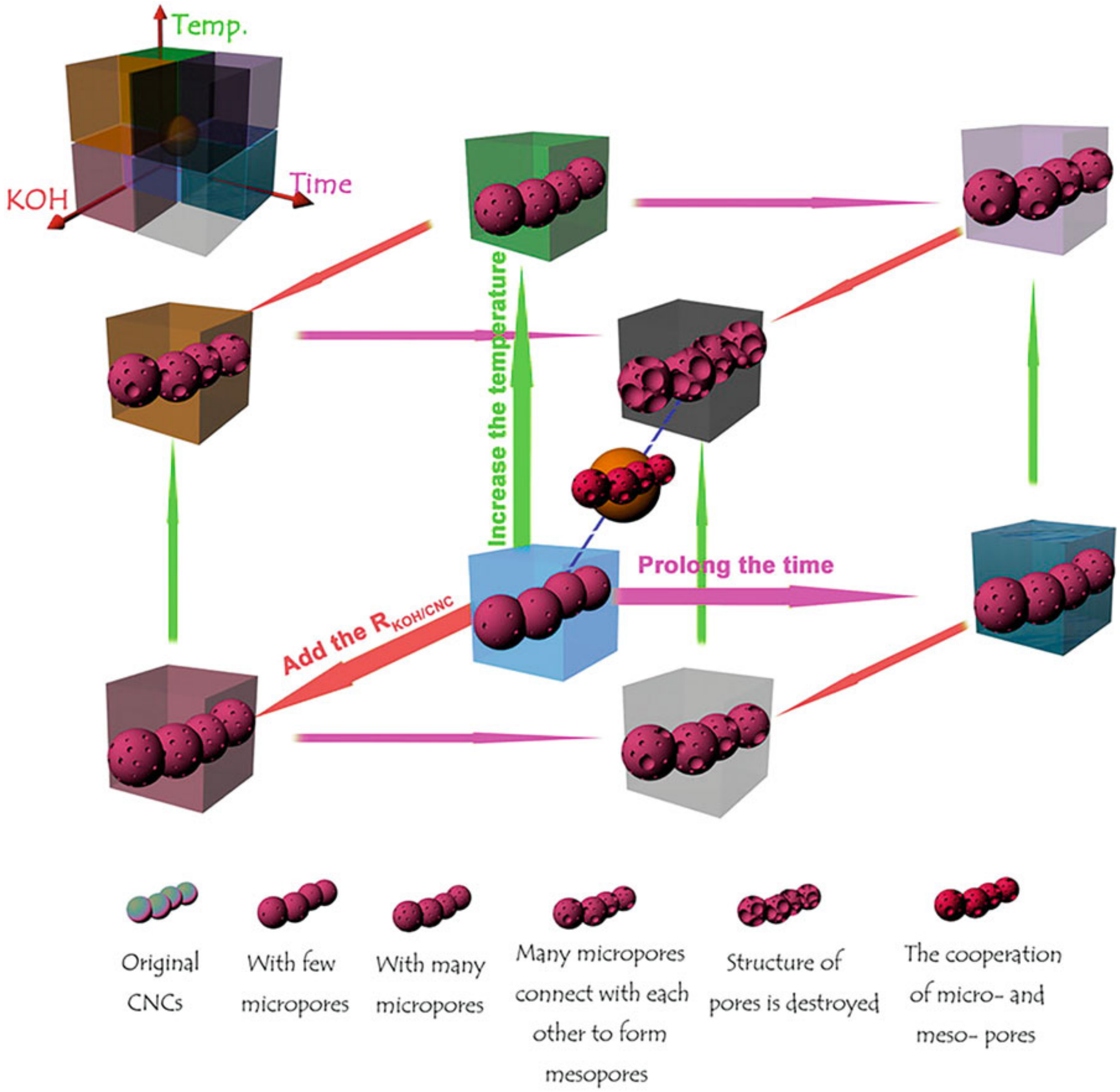

Fig. 4.38 Illustration of KOH activation of CNCs. (Reproduced with permission of the *American Chemical Society*)

4.2.5 Nanobars and Nanobricks

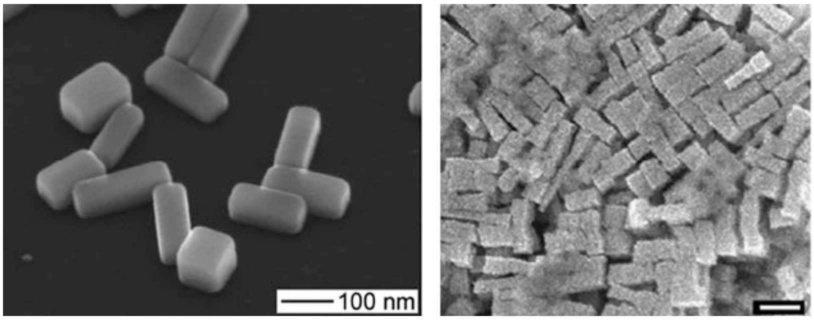

In a difference with metals and their oxides, carbon nanobars are very rare.[14] Thus, the effect of magnetism and perpendicular external electric field strengths on the energy gap of length confined bilayer graphene nanoribbons (or nanobars) was studied [129] as a function of ribbon width and length using a first-principles density-functional electronic structure method and a semi-local exchange-correlation approximation. It was found that the gaps decreased with the applied electric fields due to large intrinsic gap of the nanobar. Magnetism between the layers played a major role in enhancing the gap values resulting from the geometrical confinement, hinting at an interplay of magnetism and geometrical confinement in finite size bilayer graphene. Brick-like objects[15] are relatively rare nanostructures in the nanoworld. These and other nanoforms useful in the nanolandscaping were examined in [130]. Carbon nanocubes and nanobricks were prepared by pyrolyzing rice powder at 600 °C under N_2 atmosphere [131]. Solid-state electronic spectrum showed several bands in the UV and visible region and excitation at 336 and 474 nm generated photoluminescence response in the UV and visible region.

4.2.6 Nanobelts[16]

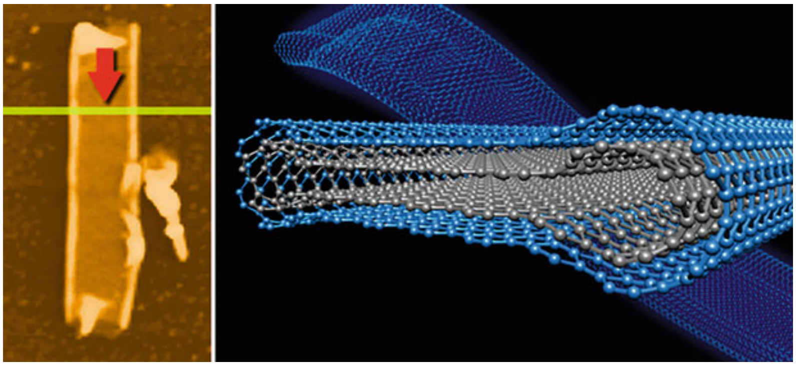

Carbon nanobelts (CNBs) are not widespread for carbon and are usually prepared [132] by pyrolysis/CVD techniques or reduction of carbonous materials (either organic or inorganic) with elemental metals, as well as applying several strategies below (Fig. 4.39). In one of the first reports on carbon nanobelts [134], the method of medial reduction at 500 °C was developed for their synthesis, using Mg as reductant and Na_2CO_3 and CCl_4 as carbon sources (reaction 4.3). It was shown that as-synthesized products were composed of a large number of carbon nanotubes with diameters of 60–200 nm and carbon nanobelts (Fig. 4.40) as coexistent material in the as-prepared products. CNBs were also synthesized on a large scale via pyrolysis of a 1,8-diaminonaphthalene (DAN)–$NiCl_2 \cdot 6H_2O$ mixture in Ar followed by acid leaching (Fig. 4.41) [135]. The product can be used as an effective fluorescent sensing platform for DNA with a detection limit of 5 nM.

$$6Mg + 2Na_2CO_3 + CCl_4 = 4NaCl + 6MgO + 3C \tag{4.3}$$

CNBs (length, tens of micrometers; width, 470 nm; thickness, 5 nm, i.e., the aspect ratio of nanobelts is extremely high to be 1000:100:1 (length/width/thickness)), having long-term emission efficiency, were synthesized (Fig. 4.42) by APCVD at 550 °C using nanoporous anodic alumina as template and ethanol as precursor [136]. The crystallinity of formed nanobelts can be improved by thermal treatment. The formation mechanism of these nanobelts was offered as a radial deformation of large thin nanotubes. Another elevated-temperature approach, "stripping and cutting" strategy (Fig. 4.43) using biomass, was applied to produce N-doped 1D CNBs from tofu with irregular structures through a molten salt ($ZnCl_2$)-assisted technique [137]. $ZnCl_2$ performed several functional roles, including the intercalation of zinc ions into the lamination of tofu, acting as a hard template to generate mesopores during the carbonization process, and being a dehydration reagent to generate considerable micropores. These eco-friendly biomass-derived carbon materials can be applied for high-performance supercapacitor electrodes.

---

[14] The nanobar image above in the subtitle is reproduced with permission of the *American Chemical Society* (*Nano Lett.*, **2007**, *7*(4), 1032–1036).

[15] The nanobrick image above in the subtitle is reproduced with permission of the *American Chemical Society* (*Abstracts of Papers, 237th ACS National Meeting*, Salt Lake City, UT, United States, March 22–26, **2009**, POLY-333.). Nanobricks are closely related to *nanoblocks* (*Chinese Journal of Catalysis*, **2016**, *37*(8), 1275–1282).

[16] The images of nanobelts are reproduced with permission of the *Elsevier Science* (*Carbon*, **2008**, *46*, 741–746).

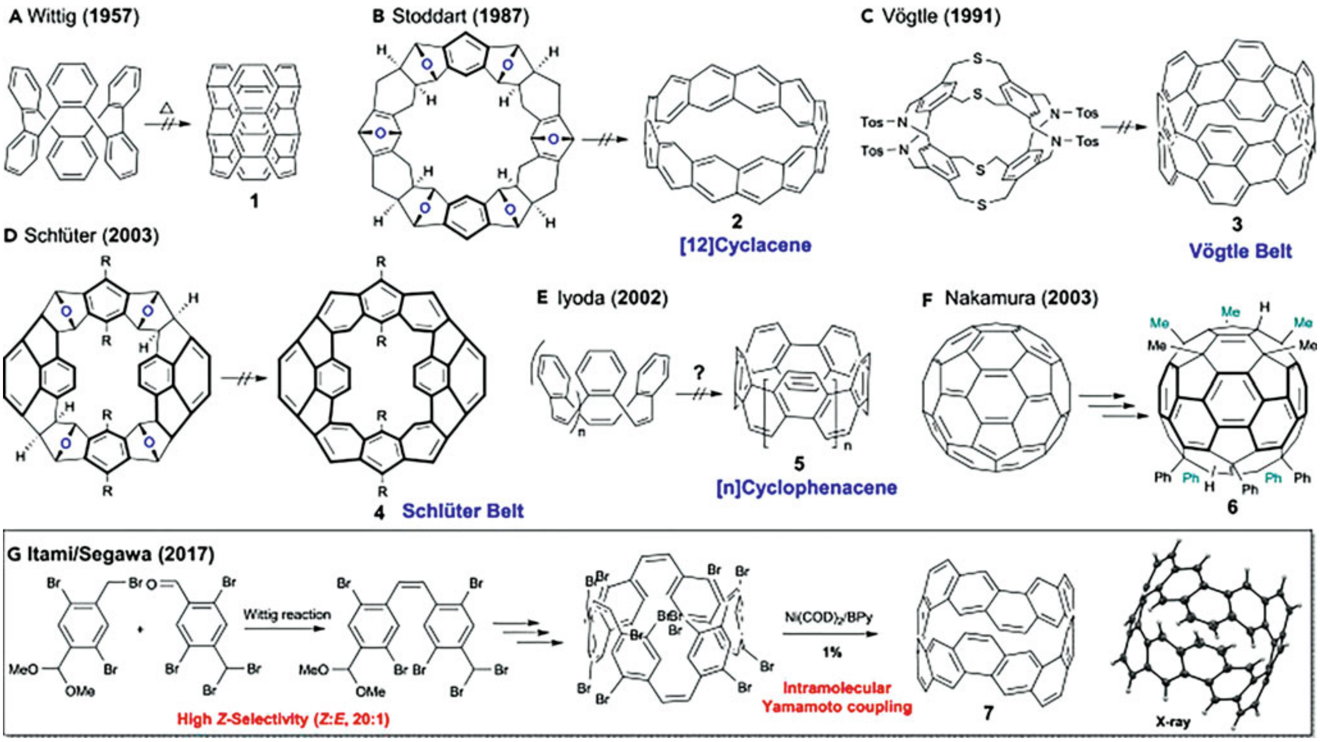

Fig. 4.39 Representative synthetic approaches for carbon nanobelts in the past 60 years [133]. (Reproduced with permission of the *Elsevier Science*)

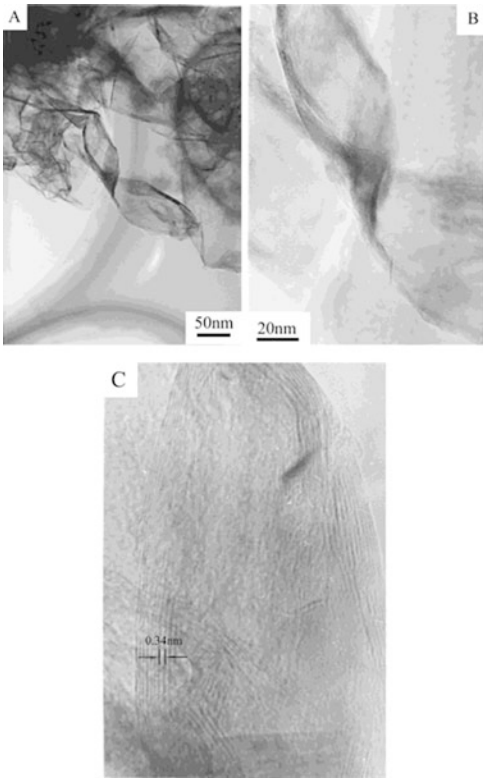

Fig. 4.40 TEM and HRTEM images of carbon nanobelts: (**a**) a representative nanobelt; (**b**) enlarged region of the nanobelt; (**c**) HRTEM image of the nanobelt. (Reproduced with permission of the *American Chemical Society*)

Fig. 4.41 (**a**) SEM image and (**b**) TEM image of the carbonized product after acid leaching. (Reproduced with permission of the *Royal Society of Chemistry*)

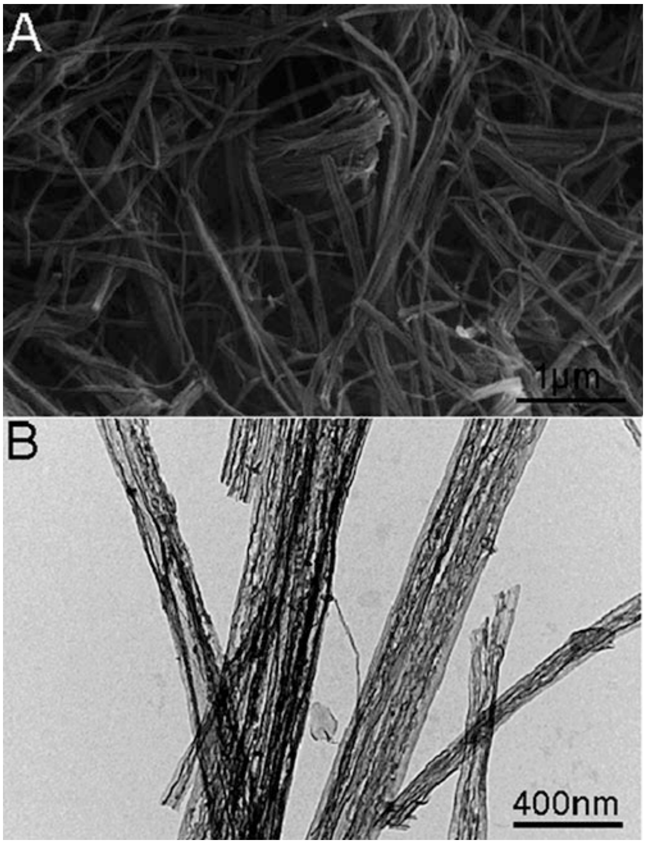

Fig. 4.42 Formation of carbon nanobelts. (Reproduced with permission of the *Elsevier Science*)

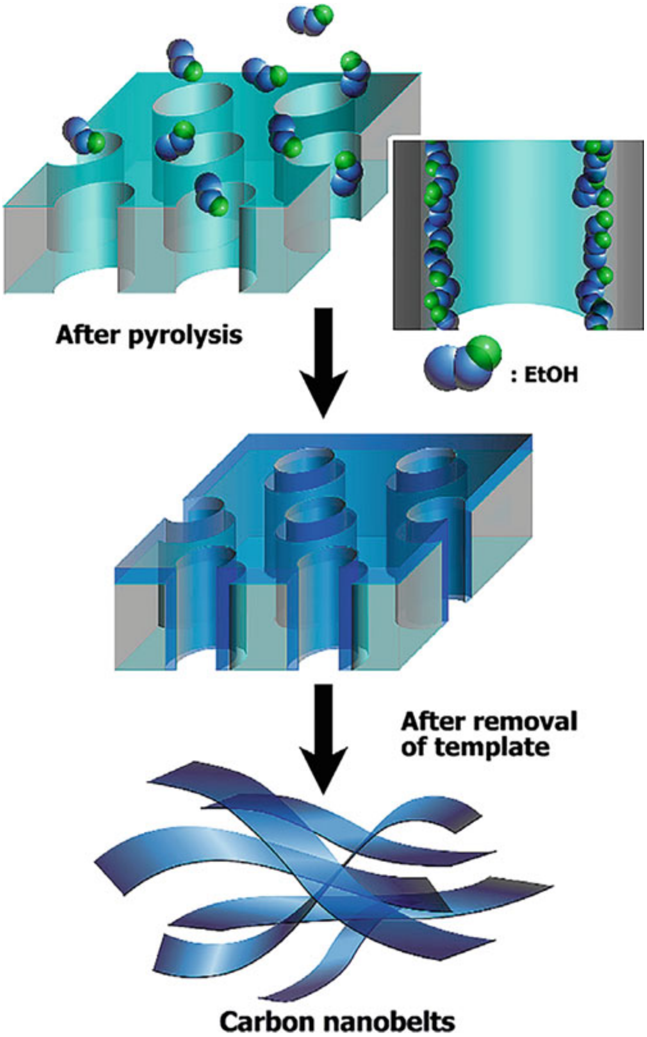

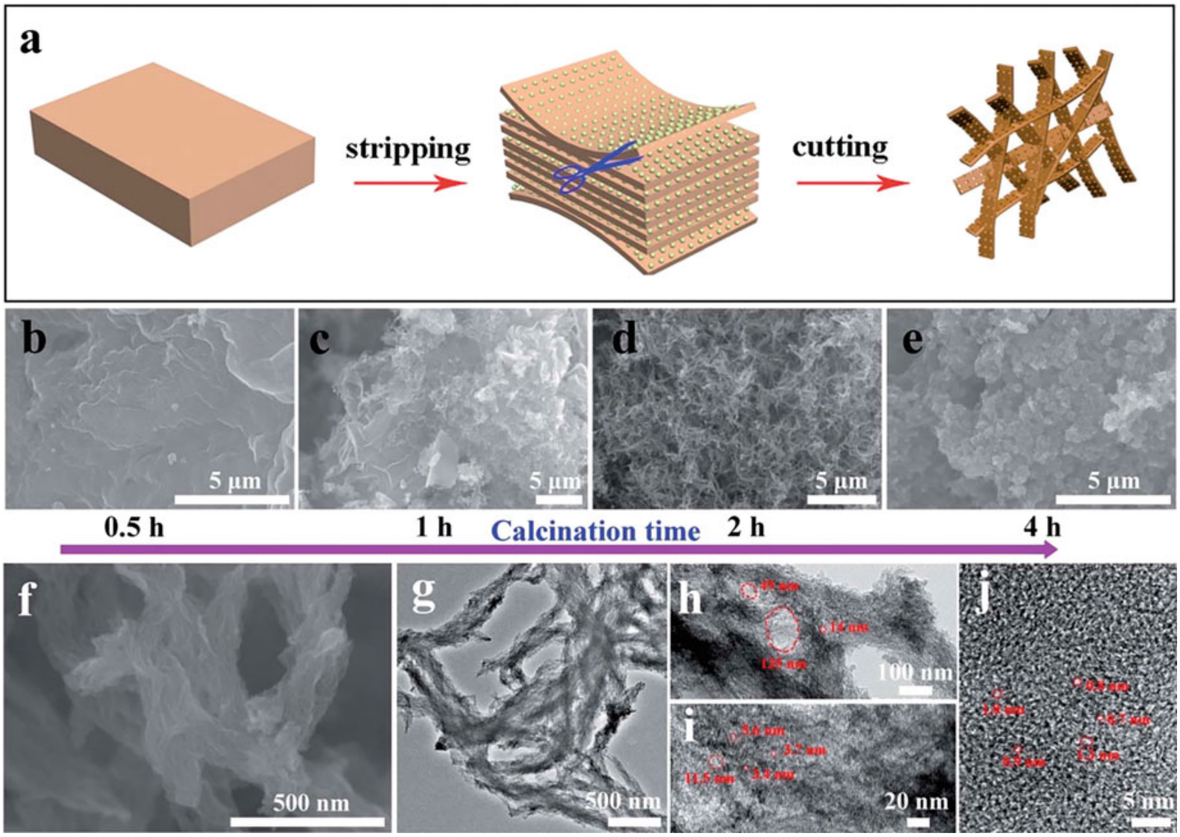

Fig. 4.43 (**a**) A schematic depicting the formation mechanism of the 1D CNB. SEM images of CNB-600-0.5 (**b**), CNB-600-1 (**c**), CNB-600-2 (**d** and **f**), and CNB-600-4 (**e**). TEM (**g**–**i**) and HRTEM (**j**) images of CNB-600-2. (Reproduced with permission of the *Royal Society of Chemistry*)

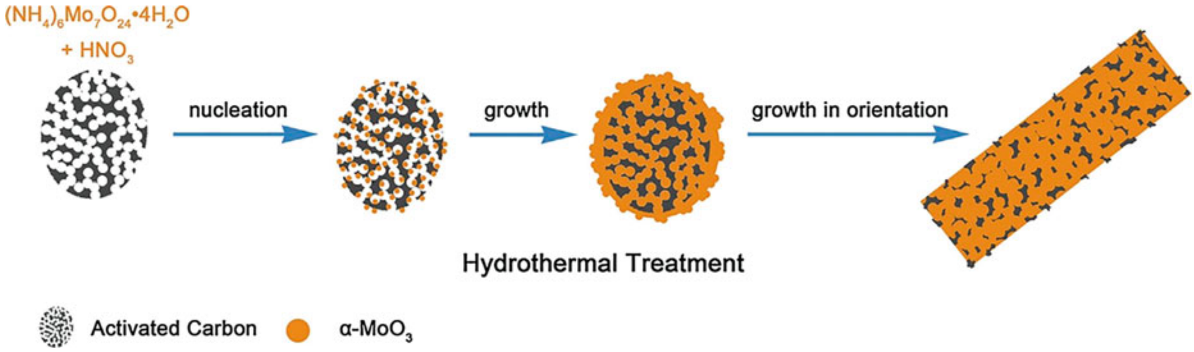

Fig. 4.44 Schematic illustration of the formation process of MoO_3/C nanobelts. (Reproduced with permission of the *Elsevier Science*)

Composite and doped CNBs are rare. As an example, a MoO_3/C nanobelts (Fig. 4.44) anode material for lithium-ion batteries were obtained by a hydrothermal route from $(NH_4)_6Mo_7O_{24}·4H_2O$ and activated carbon as starting materials [138]. The activated carbon possesses a polyporous structure, so molybdenum trioxide is formed in the pores and then grows along the preferential orientation to build nanobelts. These MoO_3/carbon nanobelts with the designed microstructure exhibited a high specific capacity (up to 1000 mAh·g^{-1} after 50 cycles at a current density of 0.1 Ag^{-1}), superior rate capability (retaining a discharge capacity of 675 mAh·g^{-1} at a current density of 5 A·g^{-1}), and long-term cycle stability (to 550 cycles). Also, metastable vanadium dioxide/carbon (VO_2(B)/C) nanobelts (Fig. 4.45, carbon content of 0.96 wt.%, average width of 120–200 nm, thickness of 40–60 nm, and length of 1–3 μm) were synthesized via a facile surfactant-free hydrothermal method using V_2O_5 and sucrose as reactants and showed preferable electrochemical performances [139]. In addition, nitrogen-doped and nitrogen- and oxygen-co-doped carbon nanobelts (CNBs) (denoted as N–CNBs and N–O–

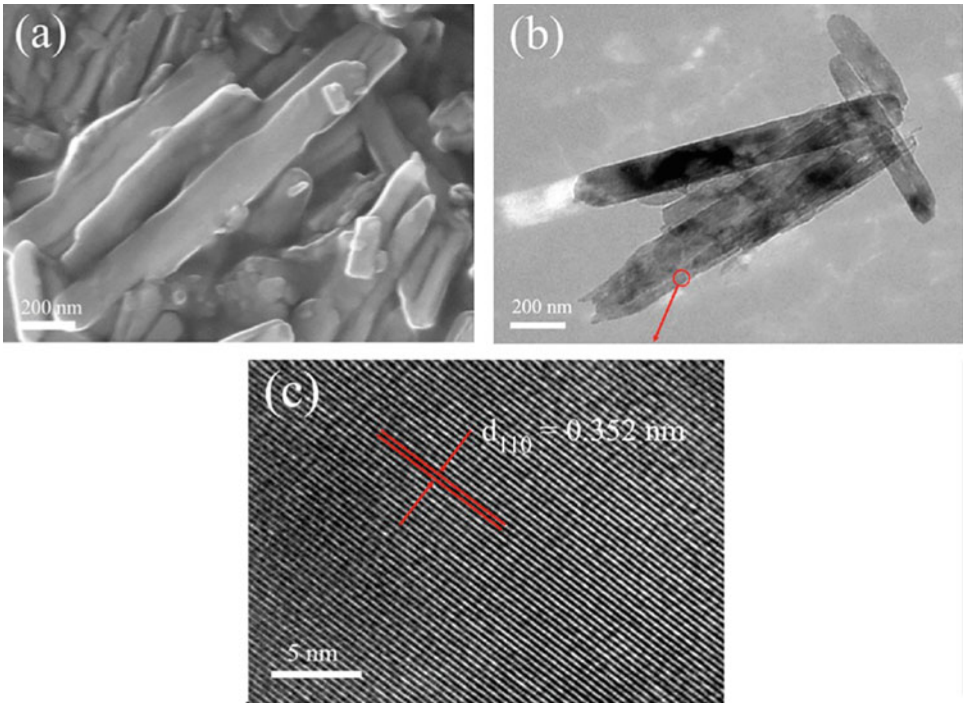

Fig. 4.45 Typical (**a**) SEM, (**b**) TEM, and (**c**) HRTEM images of VO_2(B)/C nanobelts. (Reproduced with permission of the *Elsevier Science*)

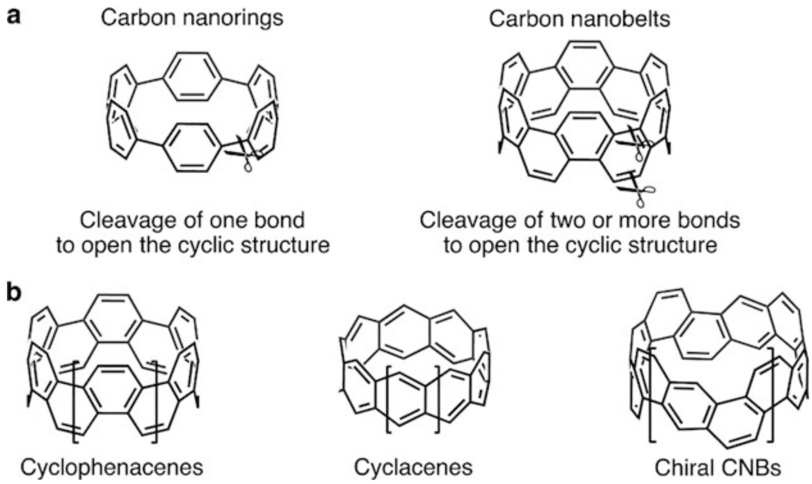

Fig. 4.46 (**a**) Definitions of carbon nanorings (left) and carbon nanobelts (right) used in [143]. (**b**) Representative examples for CNBs. (Reproduced with permission of the *American Chemical Society*)

CNBs, respectively) were, respectively, obtained by pyrolyzing the self-aligned polypyrrole (PPy) NBs and Se@poly (2-methoxy-5-nitroaniline) core@shell nanowires [140]. Among other useful properties, the N–CNBs obtained at the pyrolysis temperature of 800 °C in symmetric electrochemical cells delivered a specific capacitance of 458 $F \cdot g^{-1}$ and ultrahigh volumetric capacitance of 645 $F \cdot cm^{-3}$ in aqueous solution, which the authors consider among the best performance ever reported for carbon-based supercapacitive materials.

Similar to nanorings, the carbon nanobelts [141, 142], as the term, were also used for hydrocarbon aromatic molecules (Fig. 4.46), which are out of the scope of this book.

4.2.7 Nanobottles

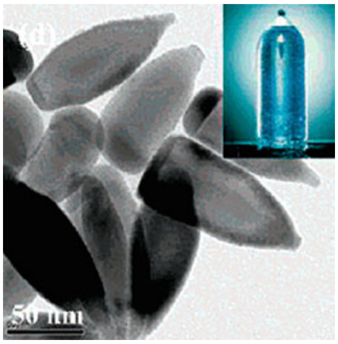

A few examples of elemental nanobottles,[17] having very useful possible applications, have been discovered. Thus, carbon nanobottle with guest molecules and C_{60} was fabricated [144]. It was revealed that C_{60} filled at the extremities of CNTs can act as caps to seal them. Releasing the incorporated molecules, CNT nanobottles could be applied in compound synthesis, in drug delivery, and even in material storage. In addition, a nanocapsule, which combines the advantages of a high-pressure vessel and adsorbents, was developed for storage of a large methane mass content and safekeeping [145]. It was a system of combined nanotubes forming bottle-like pores, the entrance to which was closed by a positively charged endohedral complex ($K@C_{60}$) with the help of an electric field. In r.t., the nanocapsule can retain the amount of methane adsorbed under charging conditions. These nanocapsules can retain ~17.5 wt.% of methane at an internal pressure of 10 MPa and a temperature of 300 K. In a related report [146], the mechanics for methane storage in a nanobottle was studied, comprising a metallofullerene located inside a carbon nanobottle (constructed from a half-fullerene as the base and two nanotubes joined by a nanocone). For methane storage, the metallofullerene serves the dual purposes of opening and closing the nanobottle, as well as an attractor for the methane gas. In addition, the concept of "gold-carbon nanobottles" (Fig. 4.47) was proposed [147] to develop CNTs as smart material for controlled release of cargo molecules. After encapsulating cis-diammineplatinum(II) dichloride (cisplatin) in CNTs, gold nanoparticles were covalently attached at the open-tips of CNTs via different cleavable linkages, namely, hydrazine, ester, and disulfide-containing linkages (Fig. 4.48), to be used as treating agent for human colon adenocarcinoma cells HCT116.

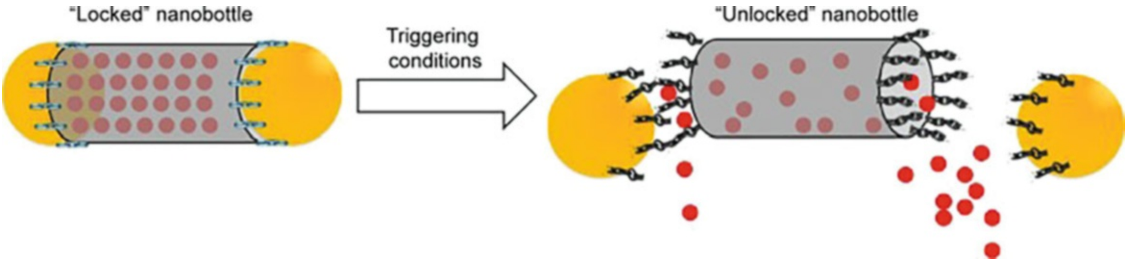

Fig. 4.47 Design of AuNP-capped carbon nanobottle through cleavable linkers. Release of encapsulated content is regulated by the cleavage of the linkers upon specific environmental trigger. Yellow particles are AuNPs (gold nanoparticles). Red particles are the encapsulated CDDP (cisplatin) drug. (Reproduced with permission of *Dove Press*)

---

[17] The nanobottle image above in the subtitle is reproduced with permission of the *American Chemical Society* (*J. Am. Chem. Soc.*, **2006**, *128*, 2520–2521).

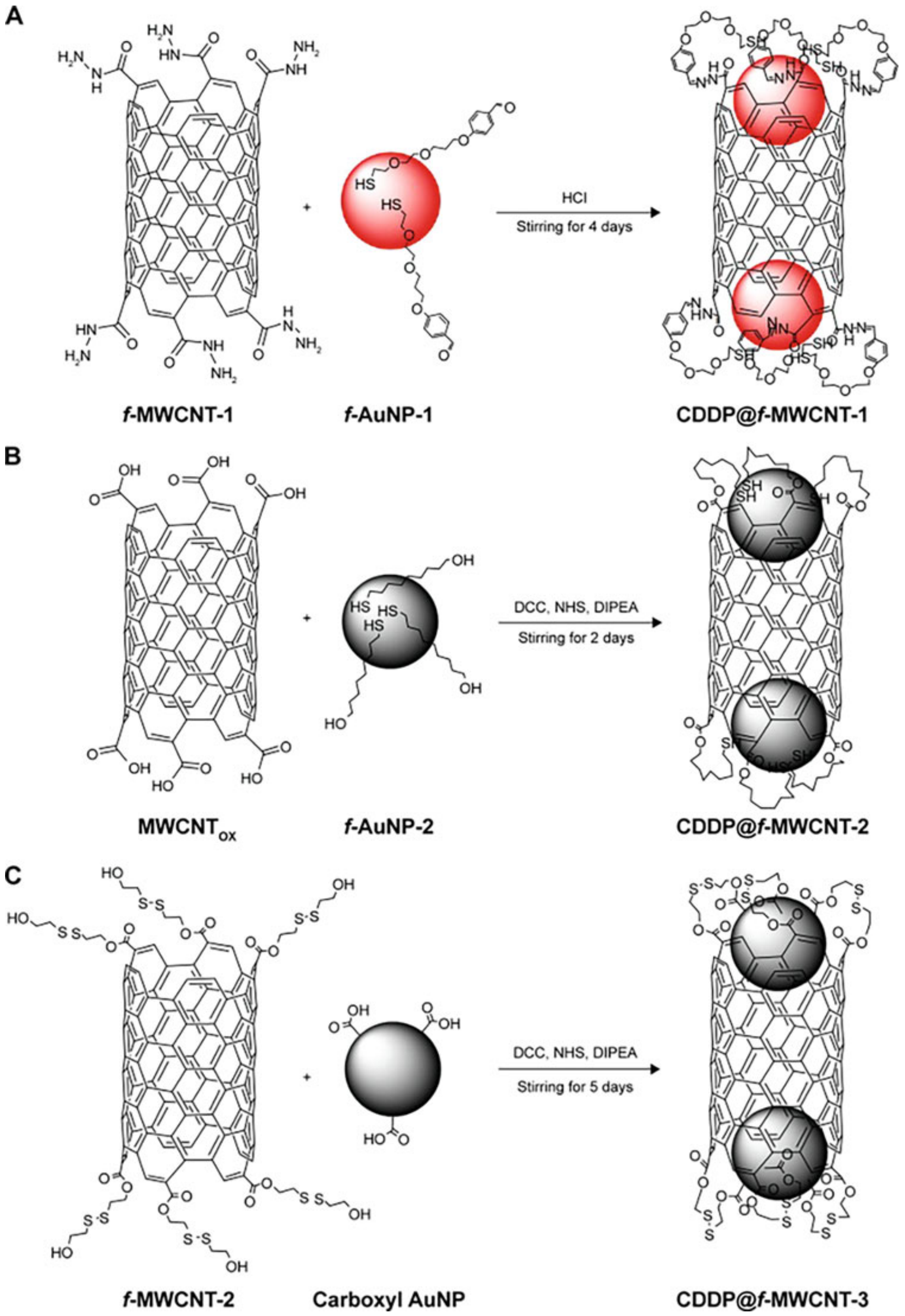

Fig. 4.48 Preparation of AuNP-capped CDDP@MWCNT nanobottles. (**a**) CDDP@f-MWCNT-1 containing hydrazone linkage; (**b**) CDDP@f-MWCNT-2 containing ester linkage; and (**c**) CDDP@f-MWCNT-3 containing disulfide linkage. Abbreviations: AuNPs, gold nanoparticles; CDDP, *cis*-diammineplatinum(II) dichloride; DCC, N, N′-dicyclohexylcarbodiimide; DIPEA, N,N-diisopropylethylamine; MWCNT, multiwalled carbon nanotube; NHS, N-hydroxysuccinimide. (Reproduced with permission of *Dove Press*)

4.2.8 Nanocones[18], [19]

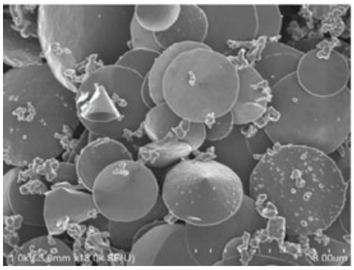

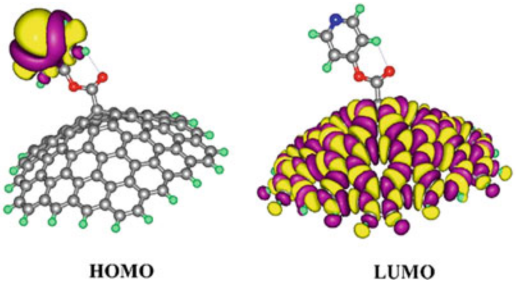

Nowadays, cone-like species on carbon basis are relatively not rare nanostructures, although 10 years ago they indeed belonged to less-common nanostructures. Some of their representative recent examples are discussed in this section. Carbon conical structures are made predominantly from carbon and which have at least one dimension of the order one micrometer or smaller and are promising practical phononic devices. Nanocones have height and base diameter of the same order of magnitude; this distinguishes them from tipped nanowires which are much longer than their diameter. Carbon nanocone (CNC) has a high asymmetric geometry and is characterized by the cone angle [148] {the largest cone angle observed experimentally and theoretically was 113° (Fig. 4.49)}. Also, the pentagonal carbon nanocones were found to be constructed from a graphene sheet by removing a 60° wedge, and joining the edges produces a cone with a single pentagonal defect at the apex [149]. In case of double-walled carbon nanocones, according to DFT calculations, the most favorable double-walled nanocone was found to be that of angles of 60°60°, with rotation angle of 36° and distance between apexes of 4.22 Å [150].

The *growth* of carbon nanocone arrays on metal catalyst particles by deposition from a low-temperature plasma was studied by multiscale Monte Carlo/surface diffusion numerical simulation [151]. It was revealed that the variation in the degree of ionization of the carbon flux provides an effective control of the growth kinetics of the carbon nanocones. The *vibrational behavior* of single-walled carbon nanocones was studied using molecular structural method and molecular dynamics simulations [152]. It was found that decreasing apex angle and the length of carbon nanocone results in an increase in the natural frequency and the effect of end condition on the natural frequency is more prominent for nanocones with smaller apex angles. Similar investigations were carried out with double-walled carbon nanocones [153].

A certain attention has been paid to the grade of *sharpeness* in nanocones and methods of its control. Thus, an approach to sharpen the CNC tip structure to make the material more appropriate for AFM applications was offered [154]. Such tapered nanocone tips can be obtained by heating oxidization in air under optimized conditions, without generation of defects or

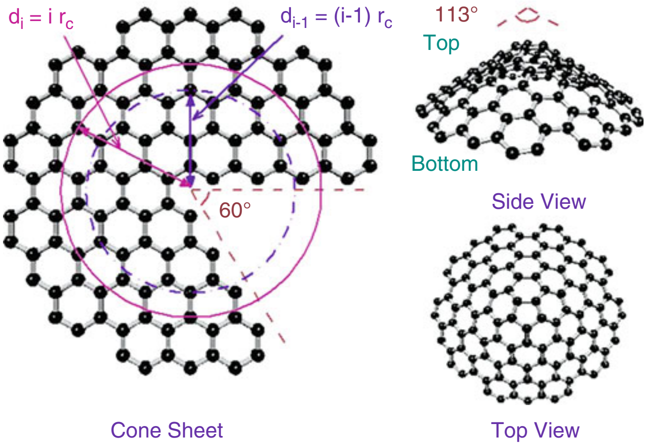

Fig. 4.49 Schematic picture of the carbon nanocone. *d* is the distance from the atom to the center point in cone sheet. (Copyright. Reproduced with permission of the *American Institute of Physics*)

---

[18] Sometimes referred as nanohorns.

[19] The nanocone images above in the subtitle are reproduced with permission of the *Elsevier Science* (*Vacuum*, **2016**, *134*, 40–47.) (right) and from the Web site https://www.forskningsradet.no (left).

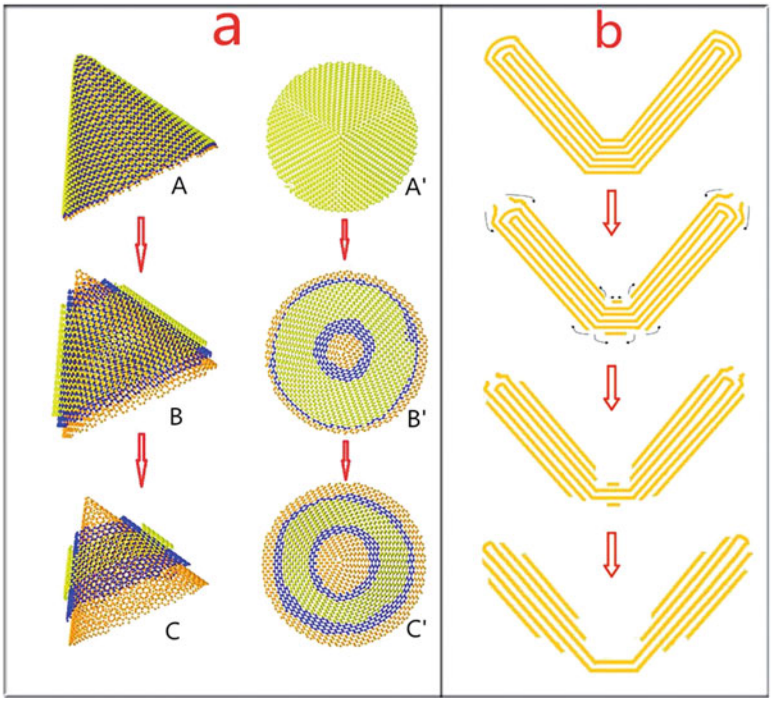

Fig. 4.50 (**a**) 3D models and (**b**) graphic illustration for structural transformation of one CNC during dynamically oxidation processing. (A), (B), and (C) in (**a**) are the side view and (A´), (B´), and (C´) for top view. (Reproduced with permission of the *Royal Society of Chemistry*)

amorphous carbon impurities during the oxidation process. It was proposed that the oxidization initially occurs at the apex of CNCs and proceeds along the sidewall step by step and layer by layer (Fig. 4.50). In addition, a sharp carbon nanocone probe that possesses desirable thermal stability and mechanical toughness was fabricated using resist-free patterning of catalyst nanodots and electric field-guided CVD growth [155]. The catalyst particle on the nanocone tip can be completely eliminated, thus leading to an extremely sharp tip, which can be used for deep profile analysis and AFM imaging.

Large-scale production of conical carbon nanostructures is possible through pyrolysis of hydrocarbons in a plasma torch process [156]. The resulting carbon cones occurred in five distinctly different forms, and disk-shaped particles are produced as well. The carbon nanocones were found to exhibit several interesting structural features; instead of having a uniform cross section, the walls consist of a relatively thin inner graphite-like layer with a noncrystalline envelope, where the amount of the latter can be modified significantly by annealing. In addition to applications of carbon nanocone phononic devices, mentioned above, the carbon nanomaterial (BET surface area of 15–40 m^2/g), containing 70 wt.% nanodisks and 30 wt.% nanocones, was used as a filter material for a gas mixture containing NO_2 and ozone which was permeable to NO_2 and impermeable to ozone [157]. Carbon nanocones can also be potentially applied for adsorption of ternary mixture of noble gases [158], gas storage (on the example of a hydrogen (see also additional data on hydrogen [159] and deuterium [160]) or methane molecule, or neon atom) [161], as nanosensors and nanoscale composites (due to more excellent mechanical properties than the equivalent CNTs) [162], electronic sensor for HCl gas [163] and ammonia [164].

4.2.9 Nanospikes

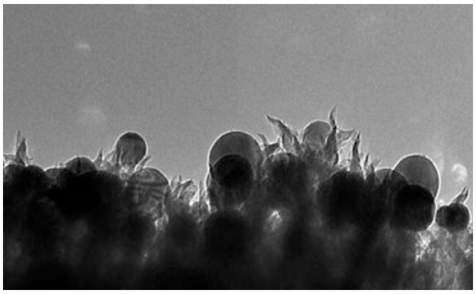

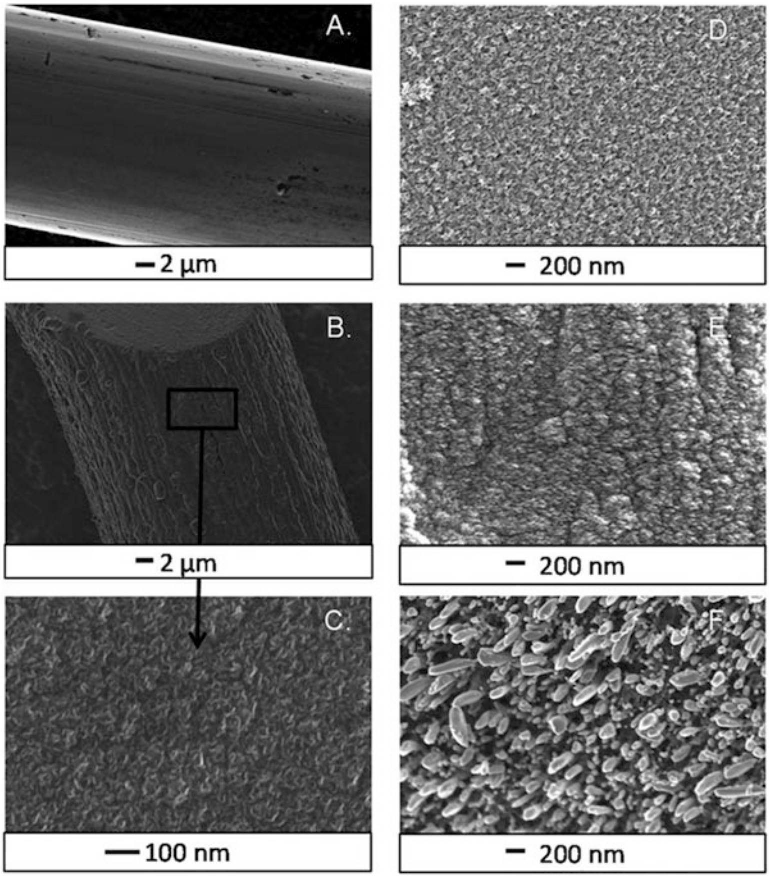

Fig. 4.51 Carbon nanospike (CNS) surfaces (7.5 min growth time). (**a**) SEM of a bare tantalum wire shows distinct grooves and ridges of rough metal surface. (**b**) CNS-coated Ta wire (CNS-Ta) shows no noticeable increase in diameter. (**c**) High magnification of carbon nanospikes grown on Ta wire. There is uniform coverage of aligned carbon spikes over the entire metal wire. (**d**) High magnification of CNSs on Pd wire shows similar features. (**e**) Nb wire also has aligned growth of small carbon spikes. (**f**) Carbon grown on Ni wire has much larger surface features than the other metals. The ends of these features are rounded. (Reproduced with permission of the *Royal Society of Chemistry*)

Carbon-based nanospikes[20] are very rare [165]. Thus, plasma-enhanced chemical vapor deposition (PECVD) was used to directly grow a thin layer of carbon nanospikes (CNS, Fig. 4.51) on cylindrical metal (Ta, Nb, Pd, Ni wires) substrates with no catalyst required [166]. The formation of these growing carbon nanospikes on metal wires was found to be a promising method to produce uniformly coated, carbon nanostructured cylindrical microelectrodes for sensitive dopamine detection. In addition, CNS-Ta microelectrodes exhibited promising selectivity to dopamine, uric acid, and ascorbic acid. Electrochemical sensing applications of several carbon nanostructures, including nanospikes, are reviewed [167]. Also, the catalyst, comprised of Cu nanoparticles on a highly textured, N-doped carbon nanospike film, was offered for the purpose of direct electrochemical conversion of CO_2 to ethanol [168].

In addition to the elongated carbon nanostructures above, the following related shapes are known.

Nanowicks Nanowick can be defined as a strip full of dense arrays of nanotubes for liquid delivery [169]. In case of carbon nanotubes, a miniature wicking element is capable for liquid delivery and potential microfluidic chemical analysis devices. The delivery function of nanowicks enables novel fluid transport devices to run without any power input, moving parts or external pump. The intrinsically nanofibrous structure of nanowicks provides a sieving matrix for molecular separations and a high surface-to-volume ratio porous bed to carry catalysts or reactive agents.

---

[20] The nanospike image above in the subtitle is reproduced with permission of the *Wiley* (*ChemistrySelect*, **2016**, *1*, 6055–6061).

Nanopillars The study of tubulization process of amorphous carbon nanopillars, observed in situ by TEM, revealed that amorphous carbon nanopillars were transformed into graphitic tubules by annealing at 650–900 °C in the presence of iron nanoparticles [170].

4.3 Circle and Ball-Type Nanostructures

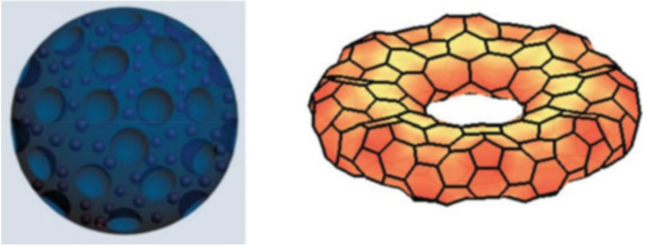

4.3.1 Nanorings[21]

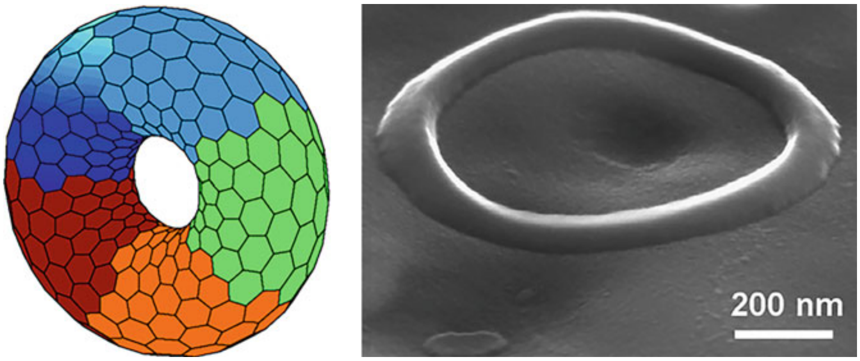

In a difference with nanosize rings of other compounds, the carbon nanorings are scarce. They can be classic (see image above) and of *Möbius* type (one-turn; see below). The nanorings are mainly studied by MD simulations and are rarely obtained in real experimental conditions. Thus, amorphous carbon micro- and nanorings (diameters between 2 and 10 μm and a rim thickness of ~50 nm, Fig. 4.52) were synthesized from carbon nanostructures derived from the carbonization of Pluronic P123 polymer inside mesoporous SBA-15 rods grown in a porous alumina membrane [171]. The presence of the alumina and the silica walls was found to efficiently restrict the diffusion of oxygen during calcination and to facilitate the carbonization process. The resulting carbonized nanostructures self-assembled around the water droplets in the presence of CCl_4 and formed ring structures (Fig. 4.53).

The structure of nanorings at equilibrium was computed by minimizing the total ring Brenner–Tersoff potential using a robust minimization method, resulting a beautiful family of untwisted nanorings with zigzag, armchair, and other chiralities (Fig. 4.54) [172]. Rings with large diameters have nearly circular cross-sectional shapes, whereas rings with small diameters have elliptical, wedding-band, and dog-bone cross-sectional shapes. The electronic structures of nanorings of C_{10} to C_{22}, among other carbon nanostructures, were investigated based on time-of-flight (TOF) mass spectroscopy, laser spectroscopy, and first-principles ab initio calculations [173]. The ring structure with bond length alternation (Peierls' dimerization) was found to be unstable at size up to C_{22} ring.

The axial sliding of carbon-based normal nanorings (NCNs, Fig. 4.55a, b) and one-turn *Möbius* nanorings (MCNs, Fig. 4.55c) along inner coaxial carbon nanotubes with hydrogen-terminated edges was investigated [174] by classical MD simulations. Among other results, the NCN:CNT system exhibited an oscillatory movement with an initial frequency of about

---

[21] The nanoring image is reproduced with permission of the *Elsevier Science* (left: *Computational Materials Science*, **2008**, *43*, 943–950; right: *Chemical Physics Letters*, **2007**, *433*, 327–330).

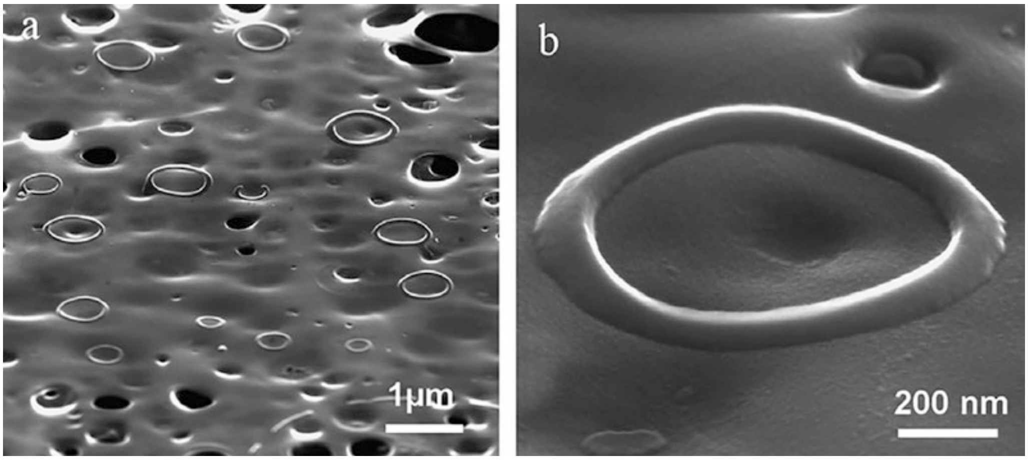

Fig. 4.52 (**a**) FESEM image of carbon nanorings obtained after 2 h HCl treatment. (**b**) High-magnification image of a single carbon nanoring tilted at 60° showing 3D ring structure. (Reproduced with permission of the *Elsevier Science*)

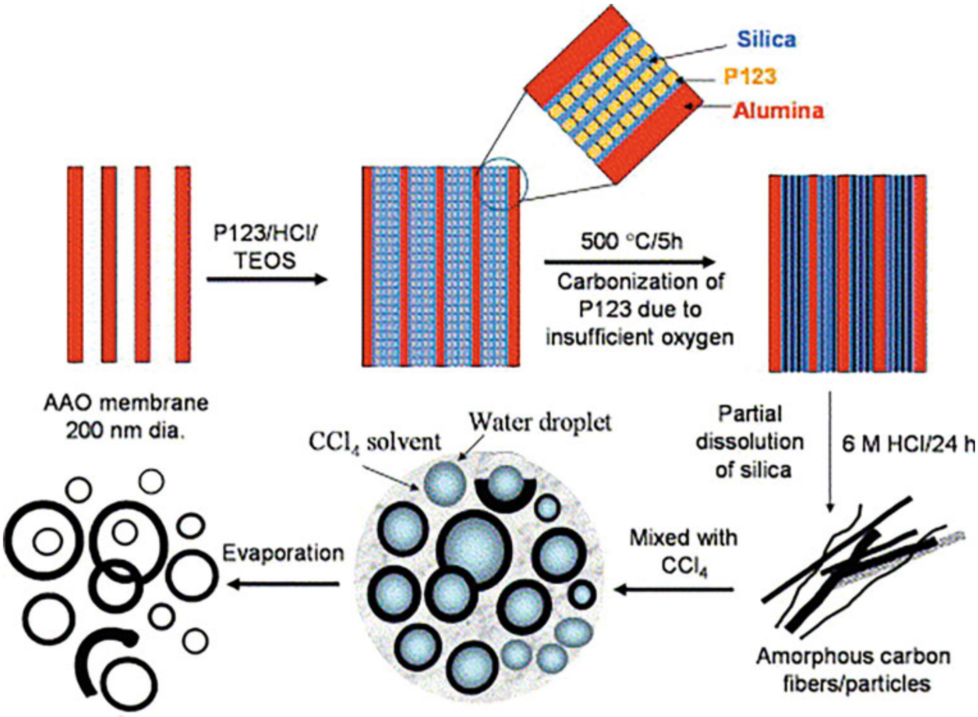

Fig. 4.53 Schematic of carbon nanoring formation. (Reproduced with permission of the *Elsevier Science*)

10 gigahertz decaying slowly with time as the vibrational energy is transferred to radial and torsional modes of the nanoring. It was concluded that the sliding of carbon nanorings and *Möbius* carbon nanorings along a set of armchair nanotubes is strongly dependent on the nanoring topology. The response of a quasi-1D ballistic carbon ring to the field of an electromagnetic wave propagating along the normal to the ring plane was evaluated in the presence of a constant electric field collinear to the field of the wave [175]. In these conditions, the carbon nanoring may serve as a source of terahertz radiation. In addition, by varying the parameters of radiation incident on the ring, one can effectively control the dynamics of the electron in the ring. Also, thermal transport across a hybrid structure formed by two graphene nanoribbons and carbon nanorings (CNRs, Fig. 4.56) was investigated by MD simulations [176]. It was found that the thermal conductivity of overlapped graphene sheets increases significantly with two covalent-bonded CNRs and tops at 68.8 $\mathrm{Wm^{-1}\ K^{-1}}$, 28% of that of single-layer graphene sheet and

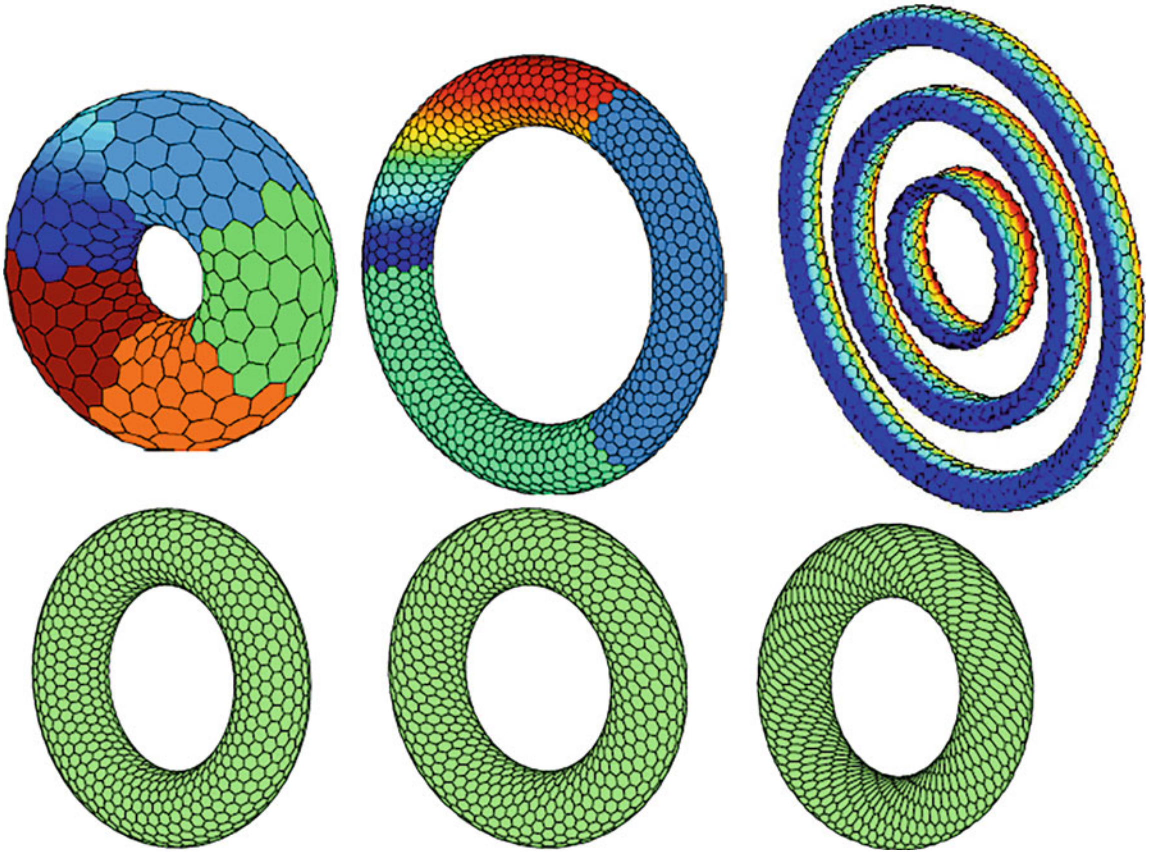

Fig. 4.54 Selected examples of predicted types of nanorings. (Reproduced with permission of the *Elsevier Science*)

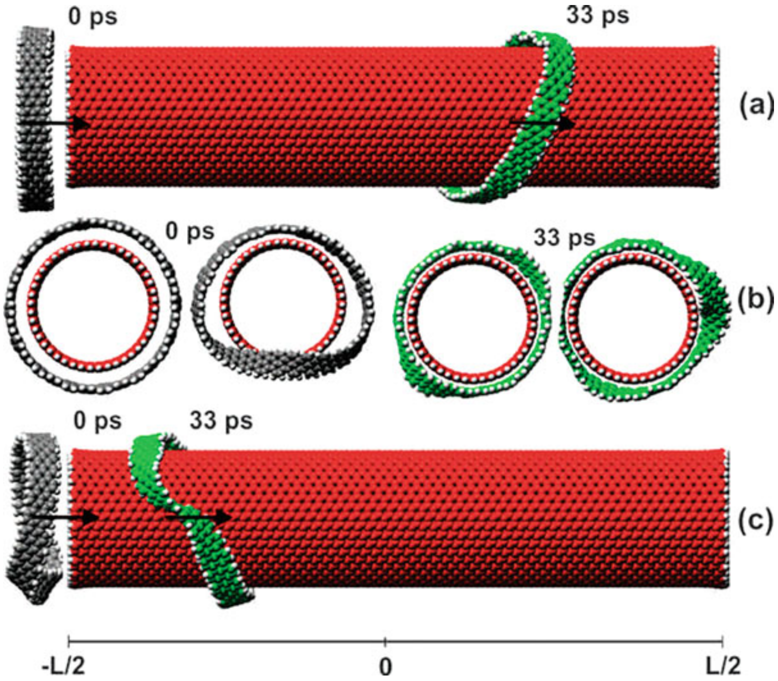

Fig. 4.55 Lateral view of a (**a**) NCN and (**c**) one-turn MCN sliding outside (20, 20) carbon nanotubes at $t = 0$ ps and $t = 33$ ps; (**b**) front views at $t = 0$ ps and $t = 33$ ps of the NCN (left) and MCN (right) sliding coaxially along the inner carbon nanotube. Initial geometries of the NCN and MCN structures (gray color) and $t = 33$ ps geometries (green color) are shown. (Reproduced with permission of the *American Institute of Physics*)

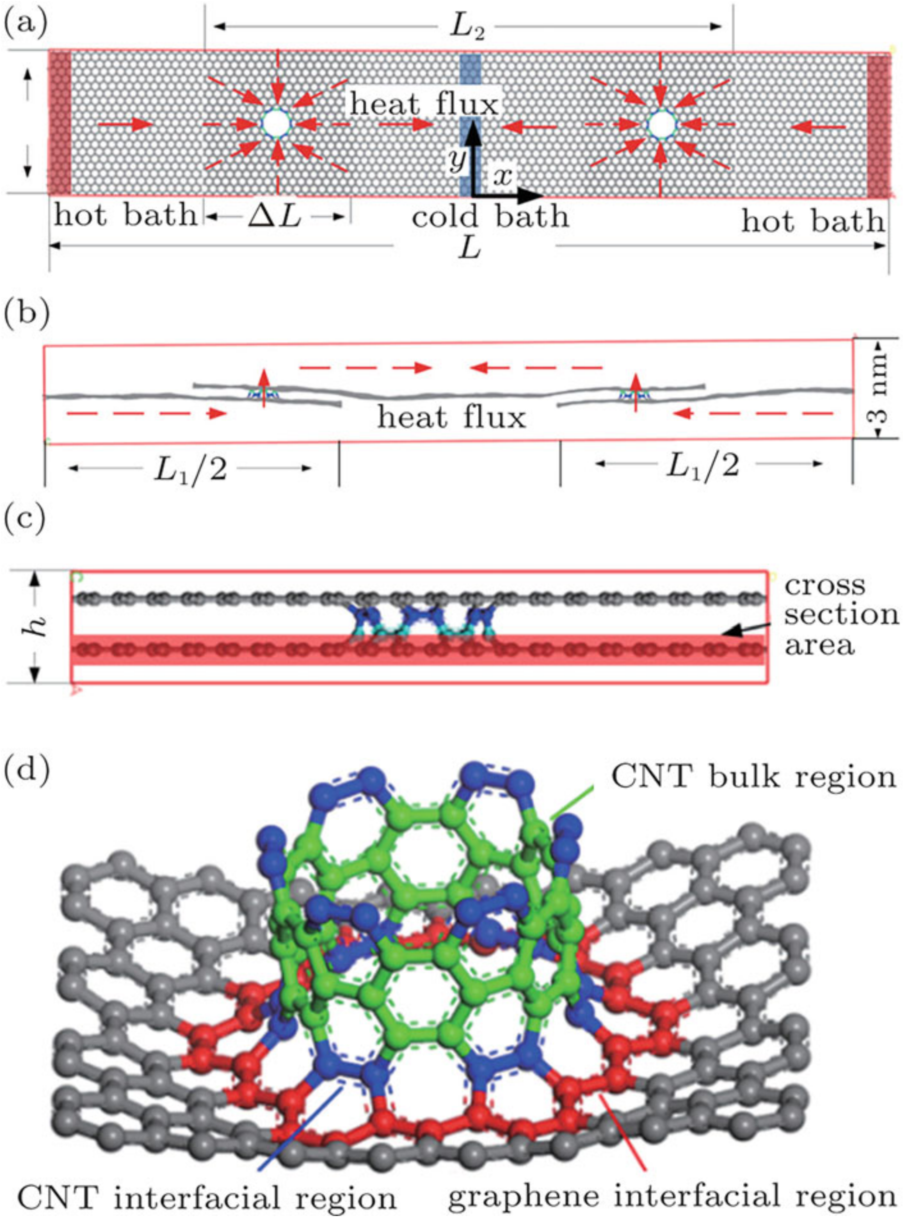

Fig. 4.56 Schematic diagram of a CNR–graphene hybrid structure. (**a**) Top view; (**b**) front view; (**c**) side view; (**d**) schematic diagram of a CNR junction. (Reproduced with permission of the *IOP Science*)

11 times higher than that of overlapped graphene sheets without CNRs. The diameter of CNR and density of CNR are found to be the two most important parameters which govern the thermal transport in the CNR–graphene hybrid structures.

In addition to pure carbon nanorings, we note well-studied hydrocarbon nanorings of sp^2 carbon made of *syn*-tetrabenzoheptafulvalene [177], related cycloparaphenylenes (Fig. 4.57) [179, 180], and their adducts with fullerenes [181–183].

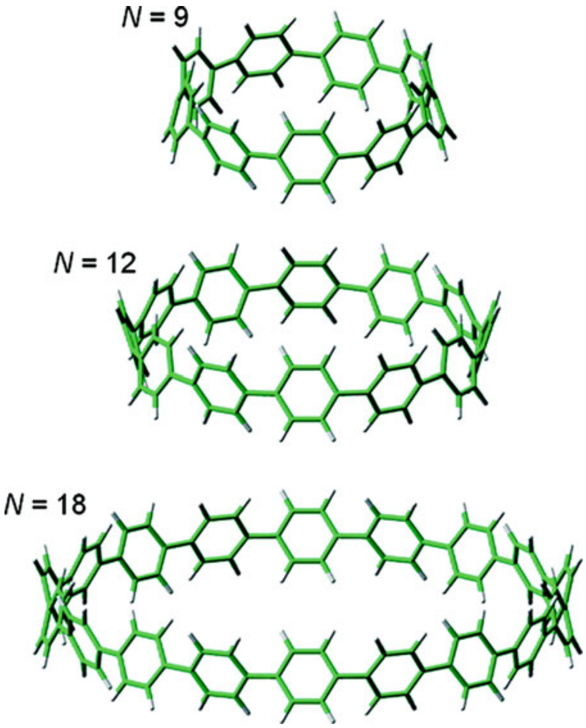

Fig. 4.57 [N]-cycloparaphenylenes with $N = 9$, 12, and 18. Each cycloparaphenylene is composed solely of phenyl rings sequentially connected in the para position to form a single nanoring [178]. (Reproduced with permission of the *American Chemical Society*)

4.3.2 Nanotori[22]

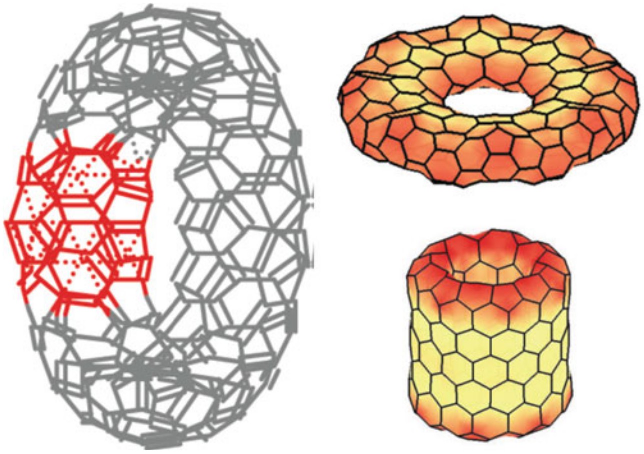

The nanotori are practically the same structural form as nanorings ("two sides of the same medal"), are closely related to graphene, edges in graphene, nanocones, nanochains, and nanotubes, and can be constructed from nanotubes [184] (V-phenylenic nanotori are also known [185, 186]). Theoretically, such rings, stable under large tensile deformation, could be used to fabricate networks that are extremely flexible and offer a high strength-to-density ratio. Nanotori, just like graphene, have no boundary and no defects, i.e., no rings of any sizes other than six, so that such nanotori can be viewed as elemental benzenoids (in having no H atoms) or as graphene with cyclic boundary conditions (in two dimensions) [187]. It was found [188] that SWCNTs with a diameter ≈1.4 nm can be induced to coil and form tori (nanotube rings or "crop circles"; single continuous toroidal nanotubes with no beginning or end, effectively a SWCNT closed around onto itself so that the two

---

[22] The nanotorus image is reproduced with permission of the *American Chemical Society* (left: *J. Phys. Chem. C*, **2009,** *113,* 19123–19133) and *APS Physics* (right: *Phys. Rev. B*, **2015**, *91*, 165433.).

open ends fuse together, stabilized by van der Waals forces alone, to form a perfect “nanotorus” (toroidal SWCNT) [189] with much larger overall diameters of 600–800 nm on treatment with acids plus hydrogen peroxide under sonication.

On the basis of ab initio DFT calculations combined with a continuum elasticity theory approach, CNT-formed nanotori were classified in accordance with their length, height, and rotational symmetry (Fig. 4.58) [190]. Thus, nanotori with changing side length L are shown in Fig. 4.59. The contribution to the excess energy from the elbow joints is negligible in the $L \to \infty$ limit. The elastic energy is accounted for simply by the summation of the energy of the six constituent CNTs in this limit. Figure 4.60 shows the series of polygonal nanotori resembling a segment of height H of a DWCNT. The inner and outer tubes are connected at the top and the bottom by lip–lip interactions consisting of hexagonal and nonhexagonal rings. In the $H \to \infty$ limit, the elastic energy contribution from the two ends is a constant. Figure 4.61 describes polygonal nanotori with changing rotational symmetry number n, being focused on two families of nanotori, where the relative positions of the nonhexagonal rings remain the same, while the rotational symmetry number n changes from $n = 4$ to 13. The dependence of the strain energy on n is very different for the two families of nanotori.

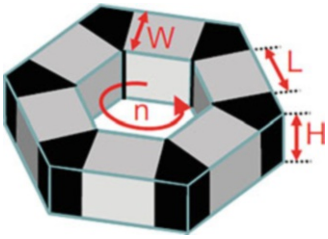

Fig. 4.58 A schematic model of a polygonal nanotorus with n-fold symmetry ($n = 6$ is shown here), consisting of n nanotube segments that are connected by n nanotube elbow joints. The nanotube segments are characterized by the width W, length L, and height H. (Reproduced with permission of *APS Physics*.)

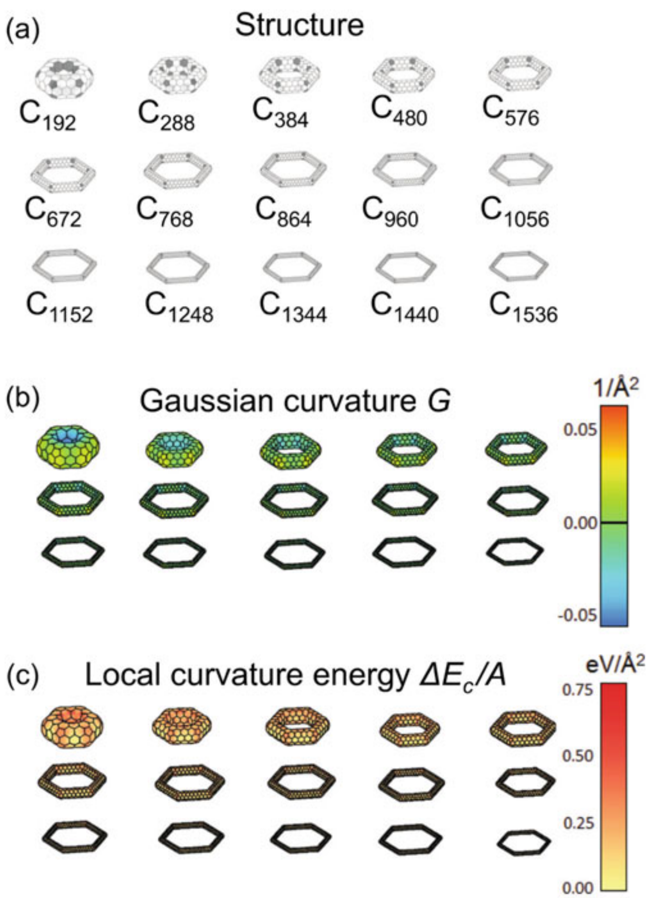

Fig. 4.59 (**a**) Structural models, (**b**) local Gaussian curvature G, and (**c**) local curvature energy E_c/A across the surface of torus isomers with different lengths of the nanotube segments L. The nonhexagonal rings in (**a**) are shaded. The values of G and E_c/A have been interpolated from their values at the atomic sites. (Reproduced with permission of *APS Physics*)

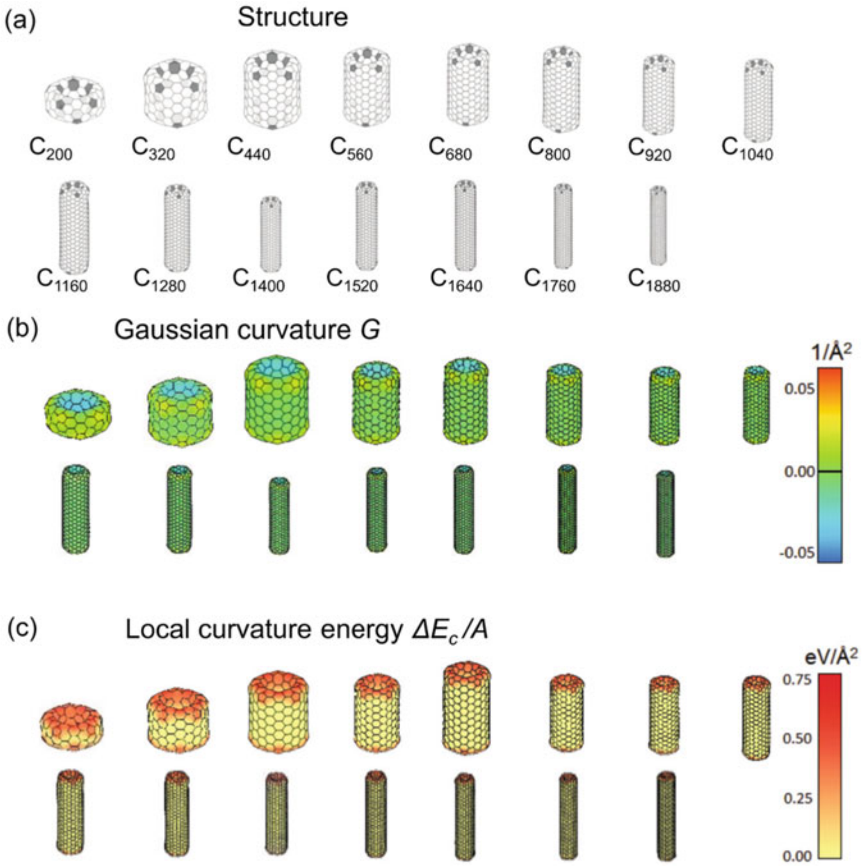

Fig. 4.60 (**a**) Structural models, (**b**) local Gaussian curvature G, and (**c**) local curvature energy E_c/A across the surface of torus isomers with different heights *H*. The nonhexagonal rings in (**a**) are shaded. The values of G and E_c/A have been interpolated from their values at the atomic sites. (Reproduced with permission of *APS Physics*)

In addition, it is possible to construct a large number of toroidal caged carbon molecules, constructed from *elbows* (Figs. 4.62 and 4.63) formed from armchair and zigzag nanotubes connected through a pentagonal and heptagonal defect at each bend site [191]. For elbows constructed from two nanotubes, it was assumed that the atoms remain in their preferred position on the nanotube sections and join them in such a way that the bond lengths between adjacent atoms on the two sections are as close as possible to the carbon–carbon bond length in a least-squares sense. The geometric parameters of 20 possible nanotori were determined. These parameters are useful in incorporating such nanotori in nanomechanical systems (NEMS).

The properties of nanotori, as an example of exotic carbon nanomatter [192], were substantially investigated mainly 10–15 years ago by DFT calculations and other methods [193]. In particular, studying their *electronic structure* (the roles of curvature, hybridization, and disorder) in terms of rotational symmetry [194], it was shown that the curvature-induced σ^*–π^* hybridization effects play an important role in determining their electronic structure. The energy gap exhibits different oscillatory characteristics depending on their structure. With increasing torus size, the electronic structures evolve from one characteristic of the 0D system to that of the quasi-1D system, and a semiconductor–metal phase transition is observed. Among other relevant studies, the *Zeeman effect* on electronic structure of carbon nanotori in the presence of magnetic field perpendicular to the tori's plane was investigated [195]. It was shown that the Zeeman effect has distinct influence on electronic structure of carbon nanotori, e.g., the Zeeman effect may lead to the destruction of periodical AB oscillation. When magnetic flux varies, the armchair tori could change from narrow-gap semiconductors into gapless metals, or vice versa, while the non-armchair (including types of zigzag and chiral) tori show the semiconducting behavior. Also, a series of calculations, using the Landauer–Büttiker formula, on the *electric conductance* of carbon nanotori contacted by SWCNTs, led to the conclusion that the conductance of the contacted carbon nanotorus is very sensitive to the transparency (chemistry) of the contacts [196].

Studies of *magnetism* in corrugated carbon nanotori revealed the existence of ferromagnetic nanocarbons and showed the importance of symmetry, defects, and negative curvature [197]. In particular, the carbon nanotori constructed by either

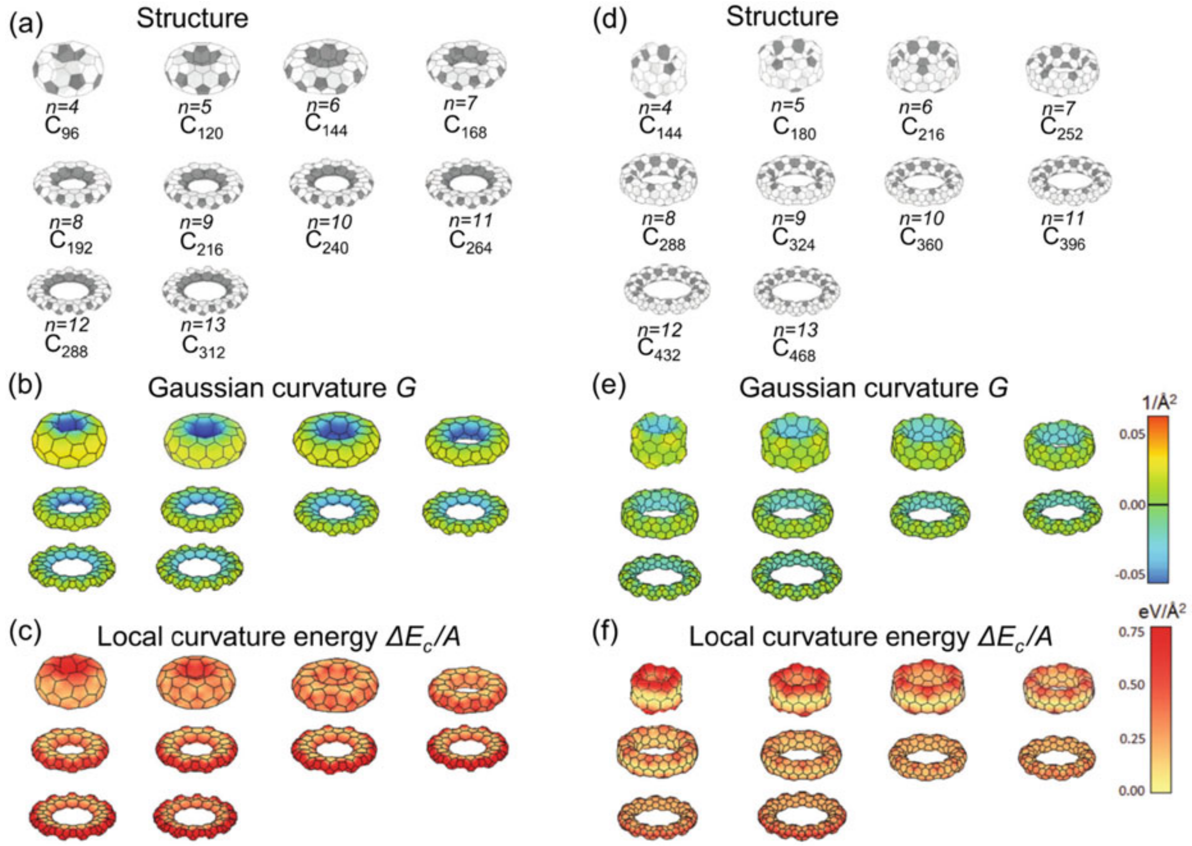

Fig. 4.61 [(**a**) and (**d**)] Structural models, [(**b**) and (**e**)] local Gaussian curvature G, and [(**c**) and (**f**)] local curvature energy E_c/A across the surface of torus isomers with different rotational symmetry numbers *n*. Structures in [(**a**) and (**c**)] and [(**d**) and (**f**)] represent two distinct torus families. The nonhexagonal rings in (**a**) and (**d**) are shaded. The values of G and E_c/A have been interpolated from their values at the atomic sites. (Reproduced with permission of *APS Physics*.)

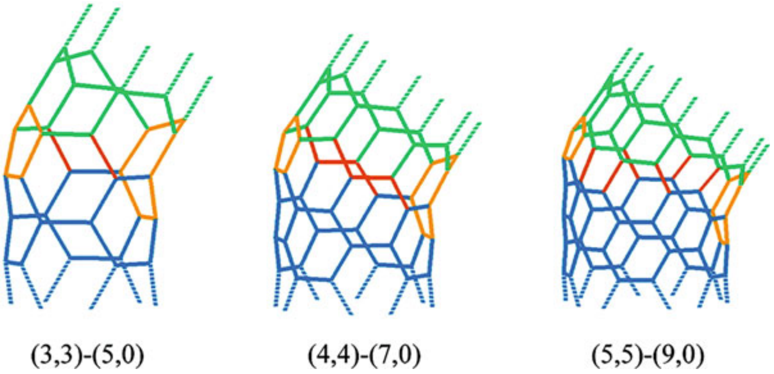

Fig. 4.62 Elbows formed from two nanotube sections. (Reproduced with permission of the *American Chemical Society*)

coalescing C_{60} molecules along the fivefold axis (incorporating pentagons and octagons) or by joining the ends of Haeckelite tubes (containing heptagons, hexagons, and pentagons) exhibit large magnetic moments when an external magnetic field is applied. It was found that the combination of negative and the positive Gaussian curvature (caused by the presence of pentagonal, heptagonal, or octagonal carbon rings) plays a crucial role in their magnetic behavior. Figure 4.64 shows three tori generated by coalescing C_{60} molecules along the two-, three-, and fivefold symmetry axes, respectively. A paramagnetic response of corrugated nanotori containing hexagons, heptagons, pentagons, and octagons which could be obtained for perfect arrangements of nonmagnetic atoms such as carbon can be possible at low temperatures, if the structure does not contain defects. However, ferromagnetism and paramagnetism in carbon nanostructures are very sensitive to the introduction of

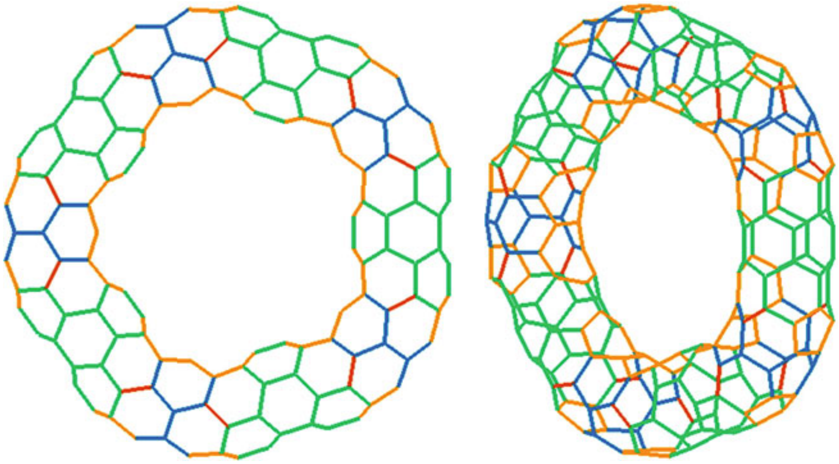

Fig. 4.63 C_{240} molecule with structure $5(3,3)_{185}(5,0)30$. (Reproduced with permission of the *American Chemical Society*)

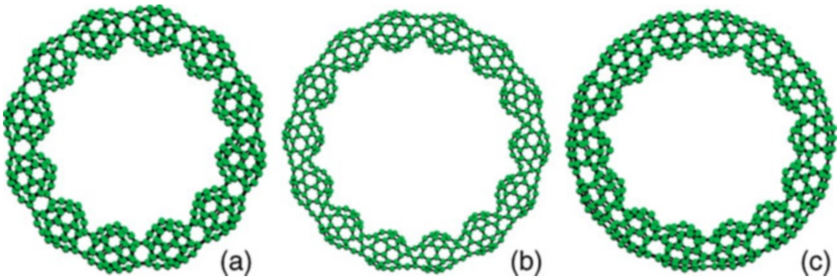

Fig. 4.64 Models of corrugated carbon nanotori constructed by coalescing, covalently, C_{60} molecules along the different axes of symmetry: (**a**) twofold, (**b**) threefold, and (**c**) fivefold. In (**b**) the necks possess heptagonal rings, whereas the structures shown in (**a**) and (**c**) contain octagonal rings within the necks. (Reproduced with permission of the *American Chemical Society*)

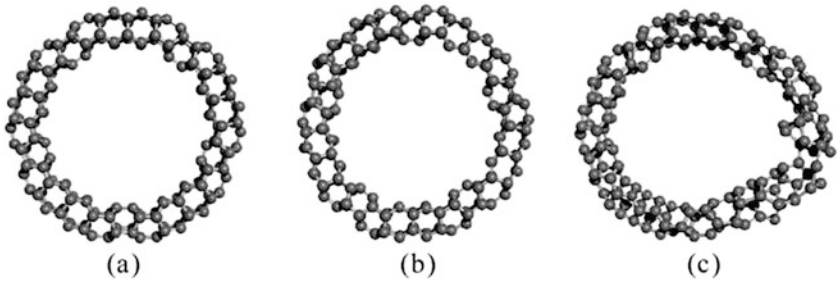

Fig. 4.65 C_{170}: (**a**) Relaxed structure at 1 K, (**b**) at 3600 K, (**c**) 3700 K where the structure considered deforms. (Reproduced with permission of *Taylor and Francis Group*)

defects and the rupture of symmetry. Carbon nanotori with unusually large (giant) paramagnetic moments were also theoretically discovered [198]. In them, the large paramagnetic moment is due to the interplay between the toroidal geometry and the ballistic motion of the π electrons in the metallic nanotube.

The *structural stability* of carbon nanotori (C_{170} (Fig. 4.65), C_{250}, C_{360}, C_{520}, and C_{750} tori) under heat treatment, investigated by performing molecular dynamics simulations [199], revealed their stability at high temperatures: C_{170} nanotorus (almost circular appearance, deformed significantly at about 3700 K), C_{250} (pentagon-like geometry, not distorted much up to deformation temperature at about 3000 K, deformed again at a knee region), C_{360} (also pentagon-like geometry, but more rounded compared to C_{250}, the strongest: it persists up to 4500 K), C_{520} (circular geometry, deformed at about 4200 K, nanotorus also deformed at a knee region), and C_{750} (biggest in that work, pentagon-like inner geometry, deformed at about 4100 K at a knee region). The thermal stability of these nanotori was found to have a complex dependence on geometrical parameters; their deformation temperatures are comparable with carbon nanotubes and nanorods of similar cross-sectional radius.

4.3.3 Nanoballs

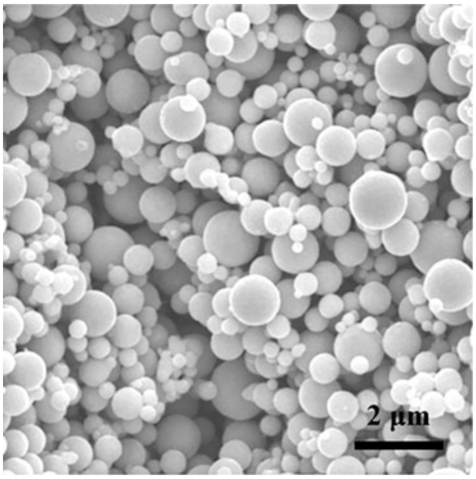

Nanoballs are closely related to nanospheres, but this first term is considerably lesser used in comparison with the last. Elemental nanoballs are represented by carbon (and metals too) [200]. Thus, a swirled fluidized bed chemical vapor deposition (SFCVD) reactor was manufactured and optimized to produce carbon nanostructures (in the absence of a catalyst at temperatures higher than 1000 °C) on a continuous basis using in situ formation of floating catalyst particles by thermal decomposition of ferrocene [201]. The fabrication of graphene-encapsulated nanoballs with copper nanoparticle cores (size range from 40 nm to 1 µm, Figs. 4.66 and 4.67) was reported using a solid carbon source of poly(methyl methacrylate) (PMMA) [202]. The PMMA was first converted to amorphous carbon layers through a pyrolysis process at 400 °C, which prevented the Cu nanoparticles from agglomeration, and they were converted to few-layer graphene at higher temperatures (800–900 °C). Graphene nanoballs were also produced [203] via flame synthesis method. Their studies revealed the crystalline nature and phase purity of the graphene. The samples annealed at higher temperature were shown to have more defects in comparison to unannealed samples. 3D graphene nanoballs were also prepared by flame combustion of edible sunflower oil using cotton wick coated with iron acetylacetonate [204]. Carbon nanoballs can also be synthesized from coal [205].

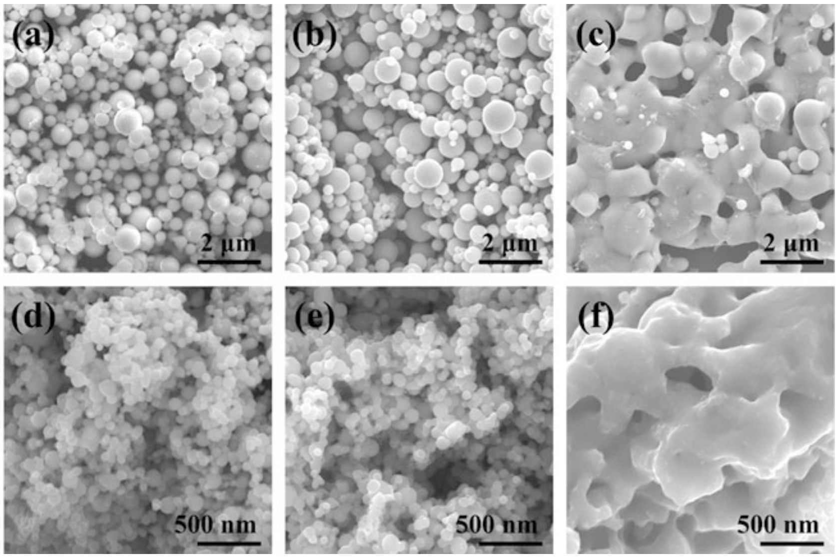

Fig. 4.66 SEM images of samples Cu500 and Cu70 for (**a**, **d**) as-prepared NPs on SiO_2 substrates, (**b**, **e**) after graphene growth using solid carbon source, and (**c**, **f**) after same growth conditions using CH_4. (Reproduced with permission of the *American Chemical Society*)

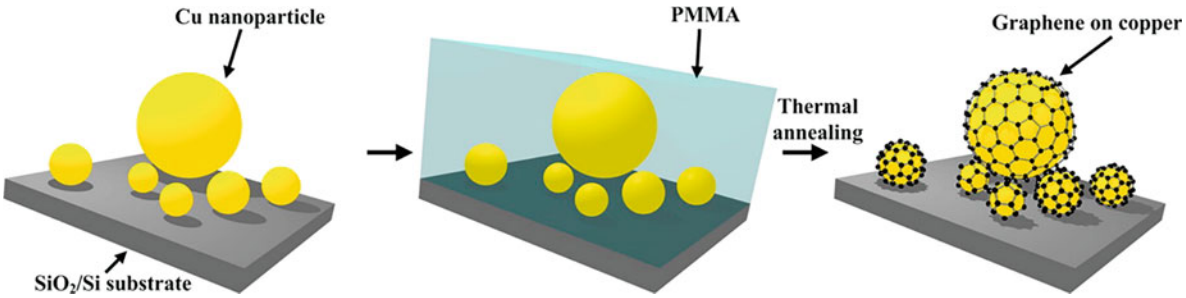

Fig. 4.67 Fabrication process of graphene nanoballs using a solid carbon source (PMMA). (Reproduced with permission of the *American Chemical Society*)

4.3.4 Nanospheres

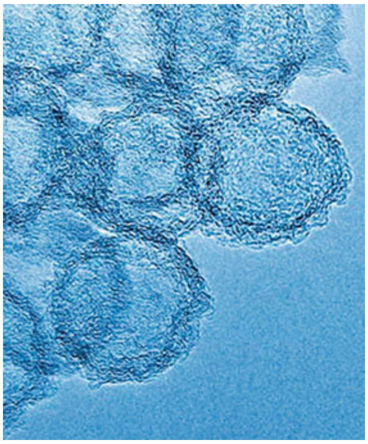

The "nanosphere" term is closely related to nanoball, and it is not really rare; about 10,000 reports on nanotechnology using sphere-like nanoparticles are known, including organic, bioorganic, and polymeric nanospheres having a series of various applications, from drug delivery to hydrogen storage; here we will present only the most recent and representative examples for carbon. In case of carbon, its nanospheres were synthesized with 4% yield through the chemical reactions of calcium carbide and oxalic acid at 65–250 °C without using catalysts [206]. In a series of reports, the pyrolysis was shown to be the principal method. Thus, similar to nanoballs above, carbon nanospheres (diameter of 35–65 nm) with a high BET specific surface area (612.8 m^2/g) were fabricated via the pyrolysis of polyacrylonitrile–poly(methyl methacrylate) (PAN–PMMA) core–shell nanoparticles [207]. These carbon nanospheres exhibited a large adsorption capacity of 190.0 mg/g for methylene blue, thus making them excellent adsorbents for the removal of organic pollutants from water. A general synthetic methodology, based on colloidal amphiphile-templated oxidative self-polymerization of dopamine (Fig. 4.68), was reported to grow ultrafine cobalt-based nanoparticles (2–7 nm in size, Fig. 4.69) *within* high-surface-area mesoporous carbon frameworks [208]. Polydopamine nanospheres containing Co^{2+} ions can be converted into hierarchical porous carbon frameworks containing ultrafine metallic Co nanoparticles using high-temperature pyrolysis. These porous Co-based hybrids were used as electrode materials for supercapacitors, which exhibit excellent supercapacitive performance with outstanding long-term cycling stability. Similarly, Ni/NiO encapsulated in carbon nanospheres was CVD-prepared using $Ni(NO_2)_2{\cdot}6H_2O$ and acetylene (C_2H_2) as the catalyst source and carbon source, respectively [209].

On the contrary, Pd nanoparticles (3 nm) supported and uniformly dispersed *onto* N-doped carbon nanospheres (Fig. 4.70) were prepared by the direct pyrolysis of the metal precursor impregnated on polybenzoxazine-based polymer nanospheres at 500 °C [210]. This hybrid composite was evaluated as catalyst for aerobic benzyl alcohol oxidation under mild conditions without using a base additive, showing good recyclability, and it can be easily regenerated by calcination at 200 °C. We note

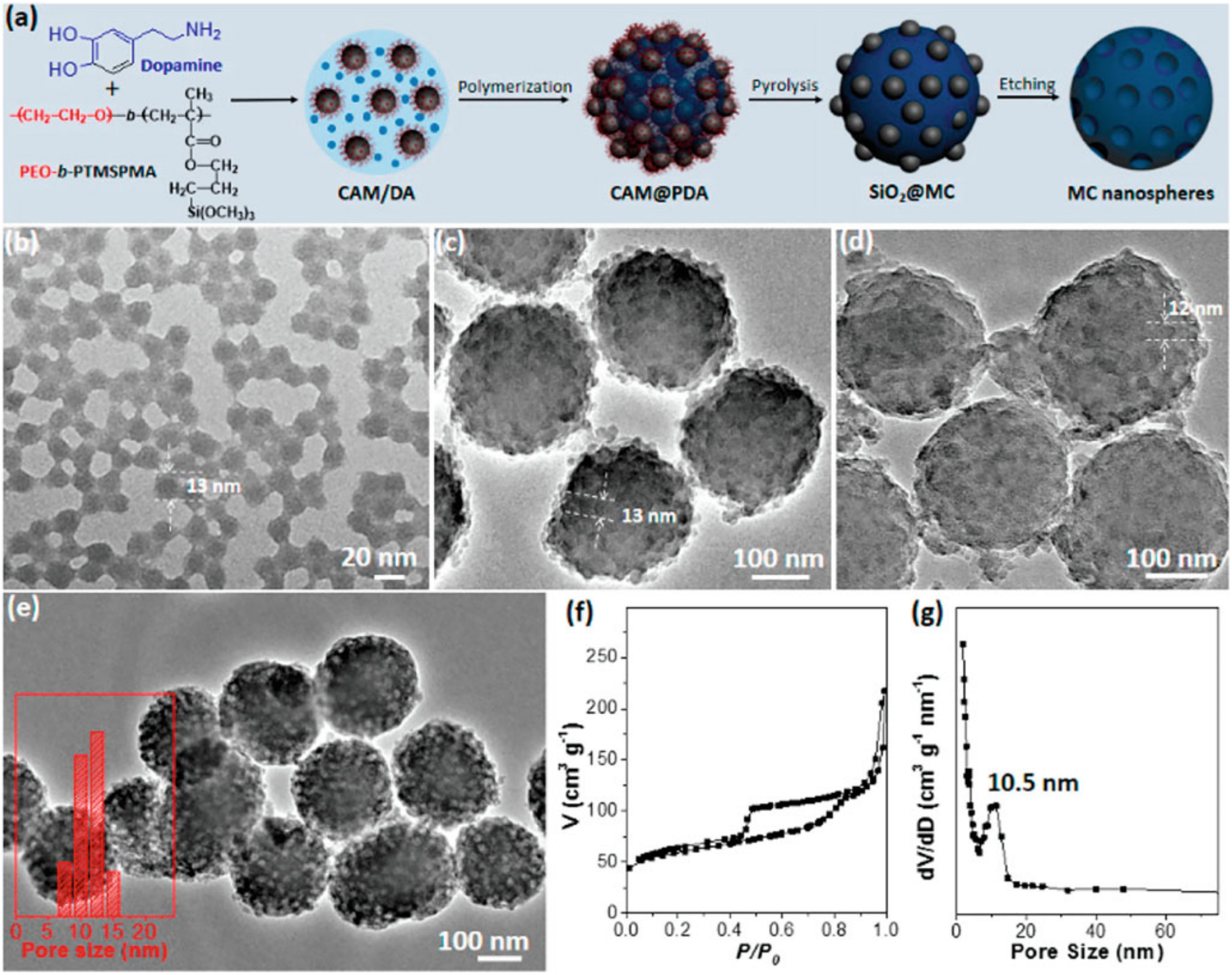

Fig. 4.68 Synthesis and characterizations of MC nanospheres. (**a**) Schematic illustration for the CAM (colloidal amphiphile)-templated synthetic route of MC (mesoporous carbon) nanospheres. TEM images of (**b**) CAM templates, (**c**) as-made CAM@PDA (polydopamine), (**d**) calcined SiO_2@MC, and (**e**) MC nanospheres after the removal of silica residuals. The inset in e is the mesopore size distribution of MC nanospheres measured from TEM images. (**f**) Nitrogen sorption isotherms and (**g**) corresponding pore size distribution of MC nanospheres. (Reproduced with permission of the *American Chemical Society*)

that N-doped hollow carbon nanospheres can be used as an anode material for sodium-ion batteries, since N-doping can form a disordered carbon structure and induce a large number of topological defects on carbon outer wall [211]. Silver-decorated carbon nanospheres (obtained by microwave deposition of Ag onto amorphous carbon templates) serve as effective visible light photocatalyst [212] suitable for the removal of methylene blue molecules from aqueous solutions. Core–shell carbon–TiO_2 composites (as well as hollow TiO_2 nanospheres) were prepared using carbon nanospheres as hard templates, coating them with TiO_2 using atomic layer deposition, and subsequent burning out of the carbon cores [213]. Both types of nanospheres can have great potential in the field of photocatalysis using solar energy. Other examples include graphene/carbon nanospheres/graphene sandwich supported Pt_3Ni nanoparticles possessing enhanced electrocatalytic activity in methanol oxidation [214].

Carbon nanospheres can be also prepared hydrothermally [215]. Their precursors are not only polymers but also various carbon-containing natural materials as hydrocarbon soot [216], deoil asphalt [217], and cooking palm oil [218], among others. In addition to applications above, we note other selected uses of carbon nanospheres. Thus, highly uniform flower-like hierarchical carbon nanospheres (FCNS, 200 nm, Figs. 4.71 and 4.72; see also the section on nanoflowers below) and their

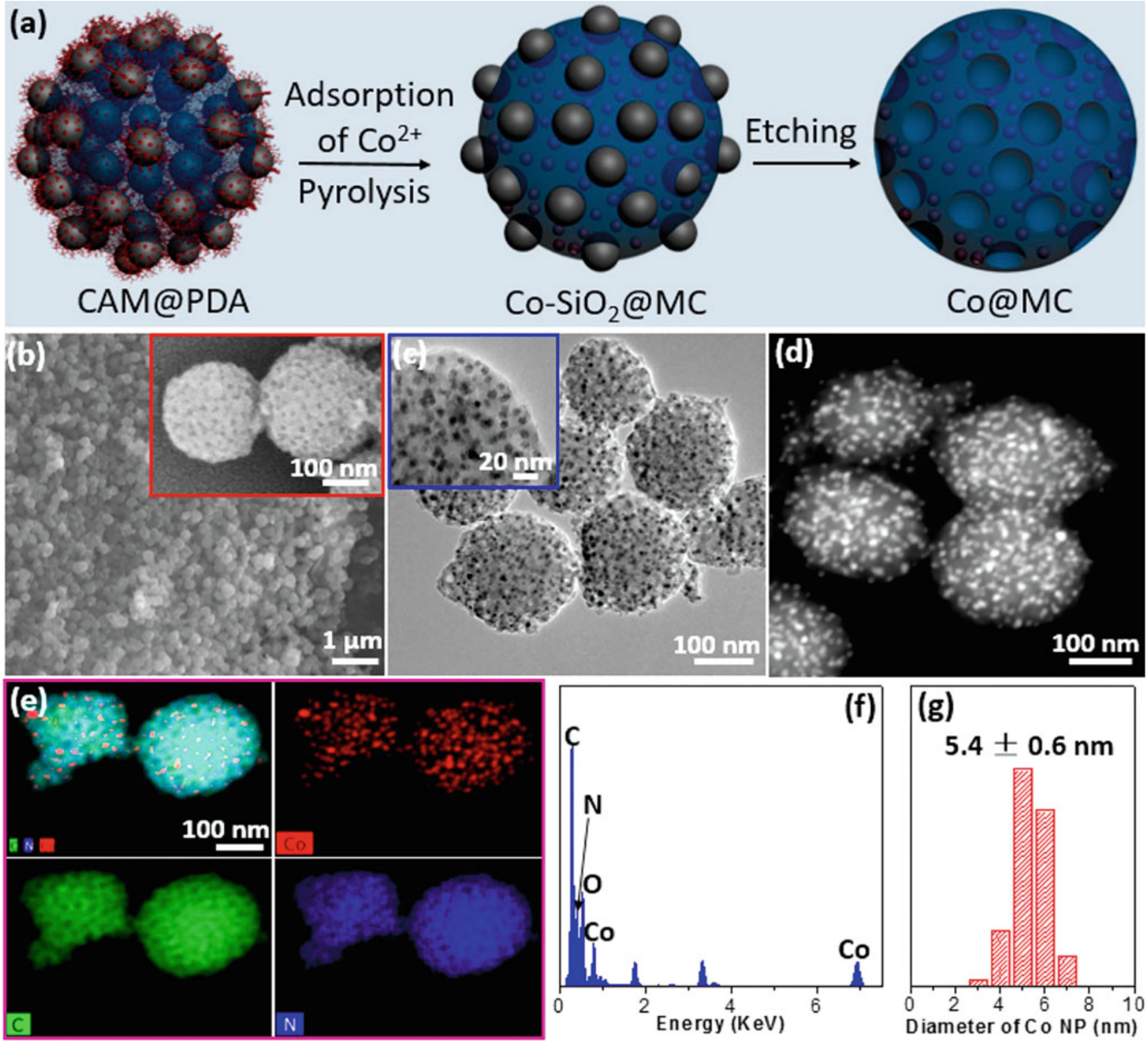

Fig. 4.69 Synthesis and characterizations of Co@MC nanospheres. (**a**) Schematic illustration for the synthetic route of Co@MC nanospheres. (**b**) SEM, (**c**) TEM, (**d**) HAADF-STEM images, (**e**) STEM mappings, and (**f**) corresponding STEM-EDX spectra of Co@MC nanospheres. The sample for SEM in (**b**) was coated by Au. (**g**) Size distribution of Co NPs within Co@MC nanospheres measured from TEM images. (Reproduced with permission of the *American Chemical Society*)

N-doped analogues (NFCNS) are suitable for sulfur accommodation for lithium/sulfur battery cathodes [219]. Medical applications include targeted delivery of chemotherapeutics in breast cancer therapy [220]. Antimicrobial quaternized carbon nanospheres (QCNSs, 110 nm), with superior antibacterial activity, were prepared via a one-pot hydrothermal treatment of chitosan and hexadecylbetaine [221]. These QCNSs could effectively kill (Fig. 4.73) Gram-positive bacteria with a minimum inhibitory concentration (MIC) of 2.0–5.0 µg mL^{-1}, at the same time being cytocompatible with normal human liver and lung cells and good hemocompatibility toward red blood cells. Carbon nanospheres (50–300 nm),

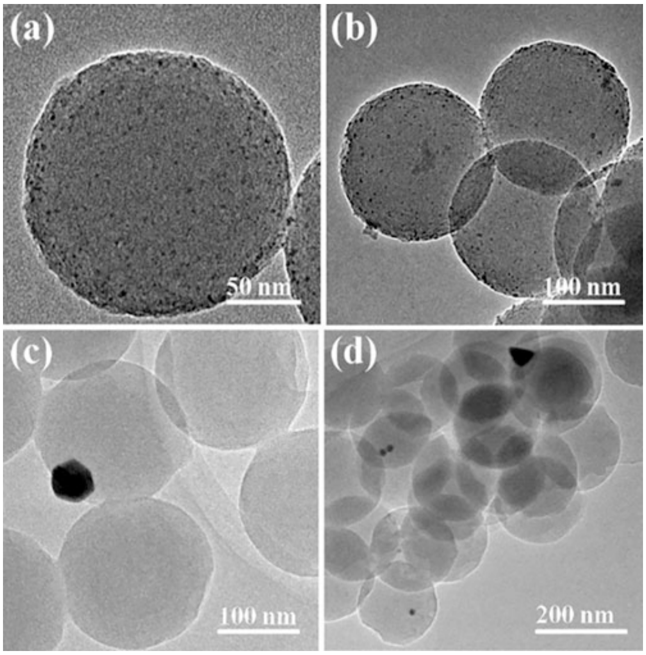

Fig. 4.70 TEM images of the catalysts. (**a**, **b**) Pd@PBFS-500; (**c**, **d**) Pd@CBFS-500. (Reproduced with permission of *Elsevier*)

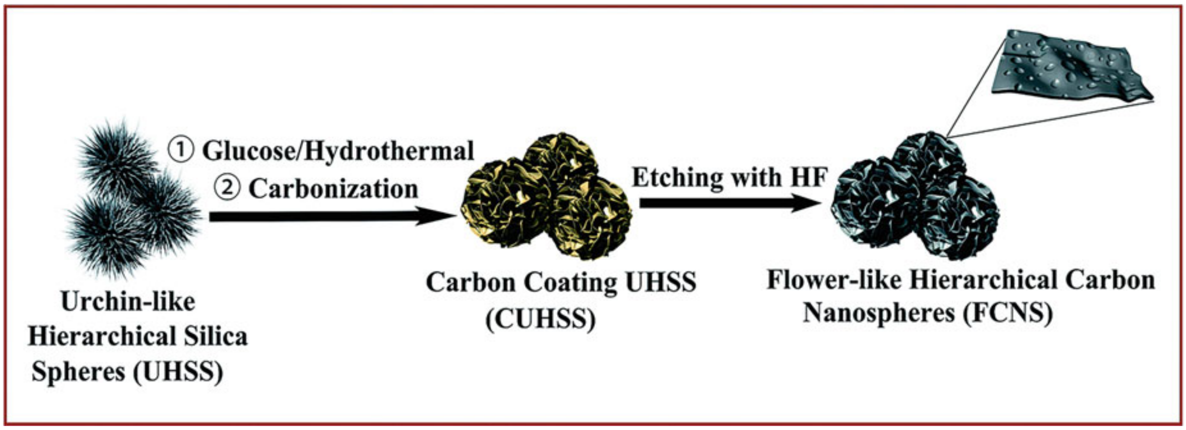

Fig. 4.71 Schematic illustration of the procedure for preparing FCNS. (Reproduced with permission of the *Royal Society of Chemistry*)

synthesized by the pyrolysis of resorcinol formaldehyde copolymer, were applied for the development of inkjet-printed resistive layers and sensors [222].

We also note apart the possibility to carry out a scalable synthesis of sub-100 nm hollow carbon nanospheres for energy storage applications. Thus, hollow carbon nanospheres of unprecedentedly small sizes (~ 32.5–62.5 nm) and thickness of ~ 3.9 nm were produced on a large scale (Figs. 4.74 and 4.75) by a templating process [223].

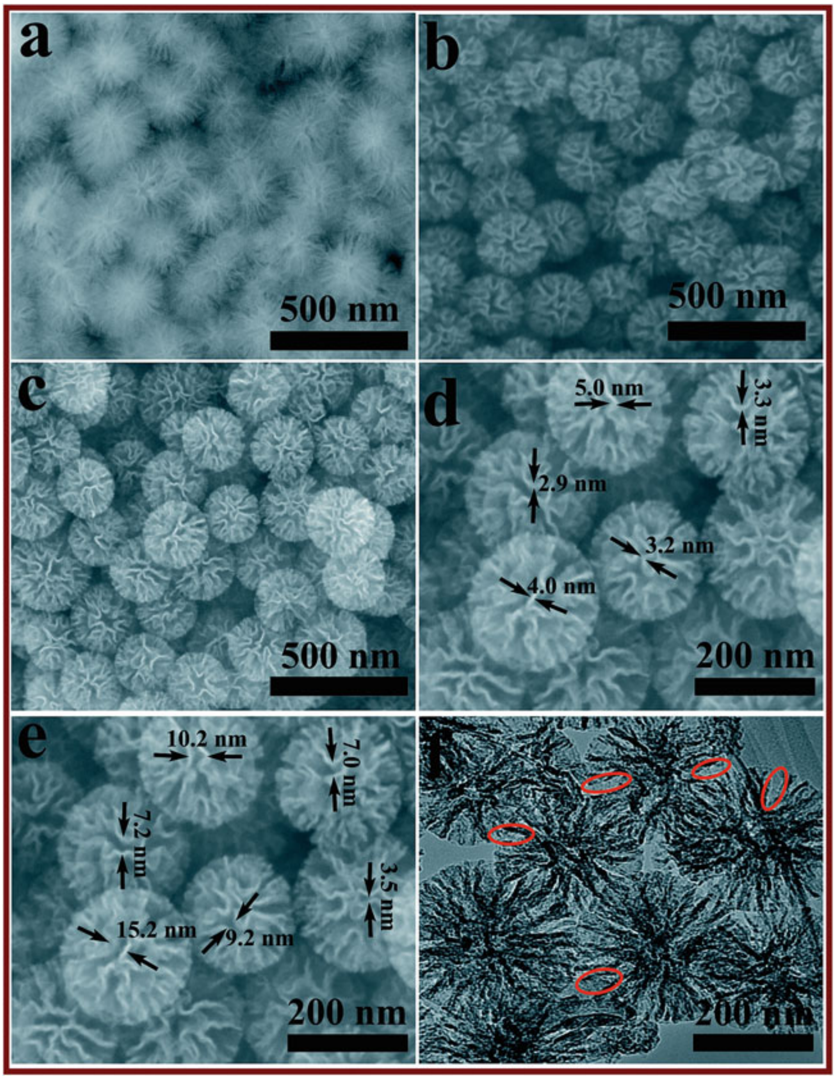

Fig. 4.72 SEM images of flower-like nanospheres. (Reproduced with permission of the *Royal Society of Chemistry*)

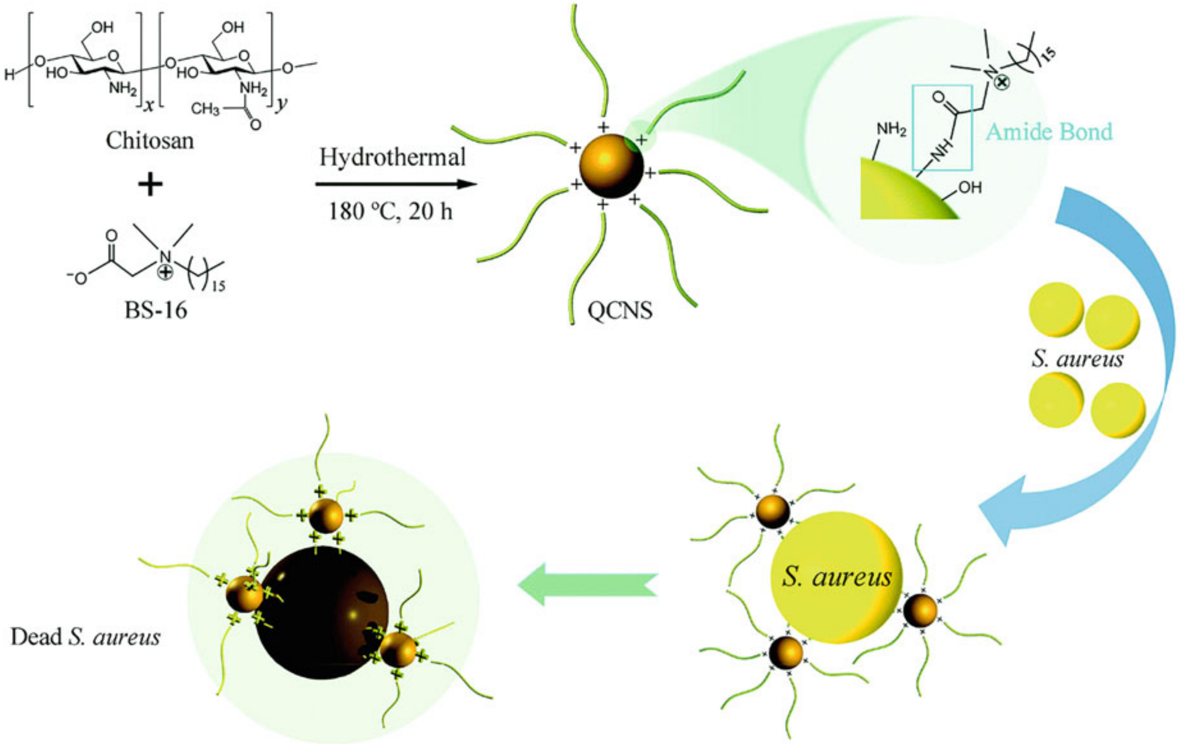

Fig. 4.73 Schematic illustration of the one-step preparation of quaternized carbon nanospheres (QCNSs) and their antibacterial activity toward *Staphylococcus aureus* (*S. aureus*). (Reproduced with permission of the *Royal Society of Chemistry*)

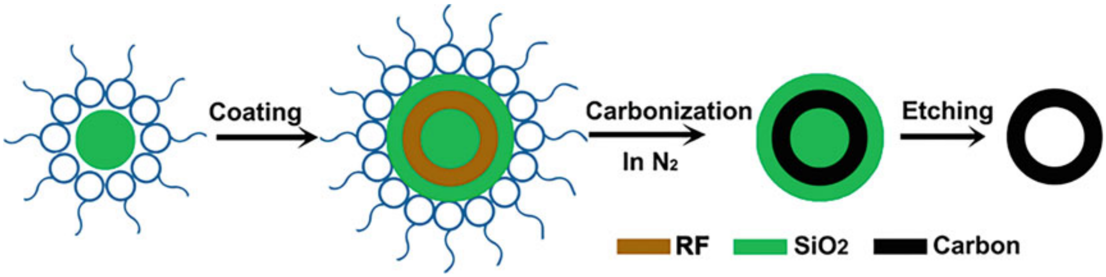

Fig. 4.74 The synthesis route to the hollow carbon nanospheres. (Reproduced with permission of *Springer*)

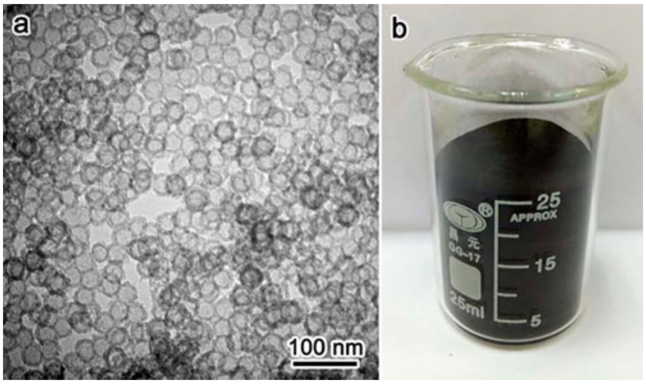

Fig. 4.75 A large-scale synthesis of the hollow carbon nanospheres (carbonized at 600 °C), which yields ~ 5 g of the final product from one pot. (**a**) Typical TEM image of the hollow carbon nanospheres obtained from the large-scale synthesis. (**b**) Digital photograph of the product in a form of powder. (Reproduced with permission of *Springer*.)

4.3.5 Nanoonions

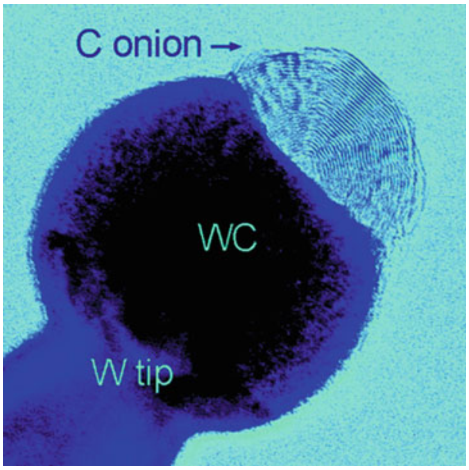

Carbon nanoonions (CNOs,[23] multilayer fullerenes, with the distance between the shells close to 0.34 nm) represent important carbon nanomaterials, which are not yet well-studied. They possess a unique 0D structure, small (<10 nm) diameter, high electrical conductivity, and relatively easy dispersion. The recent reviews [224, 225] describe its complete discovery history, starting from first pioneering experiments of *S. Iijima* in 1980, *Ugarte* in 1992, followed by *L. Echegoyen* [226–233] and *Yu. Gogotsi* [234–236] in this century and other developers. As it will be seen below, CNOs can be fabricated using electron-beam irradiation, vacuum annealing of nanodiamond (large-scale production in gram quantities, 1994), arc discharge between two graphite electrodes in water, laser ablation, plasma method, and chemical vapor deposition (CVD), among other techniques. The nanoonions contain concentric graphene shells, which are rarely ideal spherical; nanoonion structure could be different depending on the synthesis method, including appearance of hollow structures. As it will be seen below, nanoonions can be activated, decorated, and functionalized with a variety of organic molecules, in particular with biomolecules, so, having minimal toxicological effects, they represent a high potential interest for biomedicine. In this section, we will mainly discuss recent achievements in nanoonion area.

Synthesis of Carbon Nanoonions Frequently used classic methods for obtaining carbon nanoonions are as follows, among others (Fig. 4.76):

- *Chemical vapor deposition* (CVD) allows decomposing hydrocarbon gas and getting large quantities of the products. Particles of transition metals, as well as bimetallic alloys (Fe/Co, Fe/Ni, M/Cu, etc.), are used as catalysts.
- Use of *high-energy laser* in the transformation of "hydrocarbon–carbon onion."
- Catalytic decomposition of CH_4 (850 °C, Ni/Fe catalyst).
- *Arc-discharge evaporation* of carbon and metal, resulting encapsulated metal inside graphitic layers, and its further exposition to the *electron beam* in TEM, when the metal particle leaves its initial position and migrates away, yielding *hollow carbon onions*.

Apart we mention traditional (and most important) methods for *massive synthesis* of CNOs:

- Arc discharge in water
- Chemical vapor deposition (CVD)
- ND annealing in a vacuum or in inert gases

Additional methods for fabricating CNOs in a large quantity:

- Synthesis of CNOs using counterflow diffusion flames
- Thermolysis route using a sodium azide (NaN_3)–divinyl acetylene (C_6Cl_6) mixture as a precursor for fabricating gram-scale CNOs (30–100 nm in diameter) [237]
- The reaction between calcium carbide (CaC_2) and copper(II) chloride dehydrate ($CuCl_2 \cdot 2H_2O$) at 600 °C

---

[23] Image above is reproduced with permission of the *American Chemical Society* (*ACS Nano*, **2010**, *4*(8), 4396–4402).

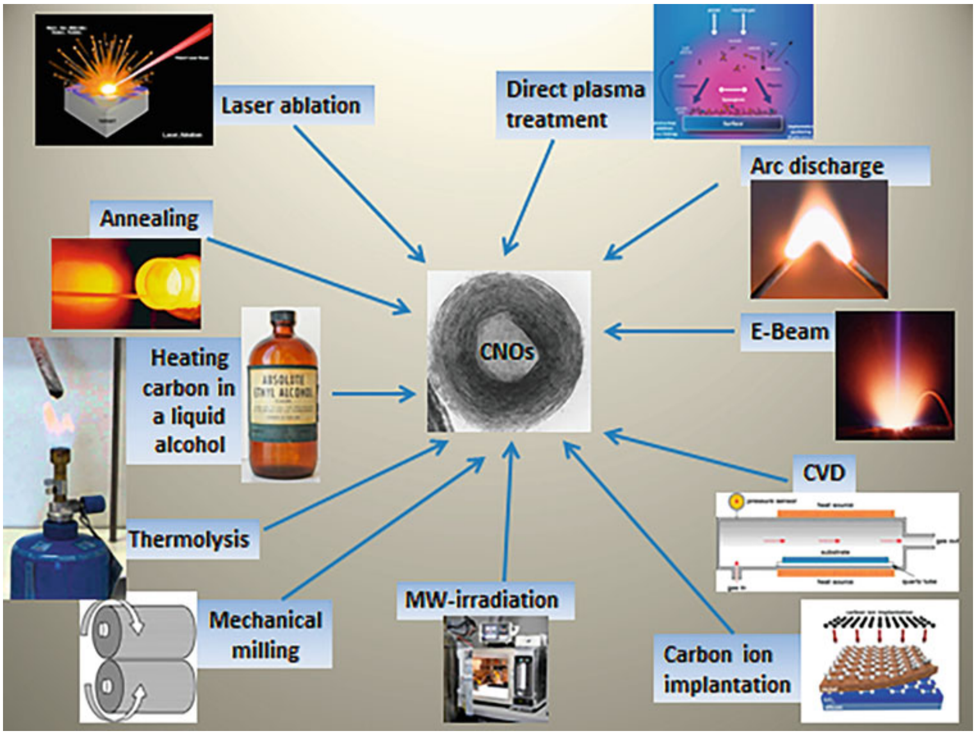

Fig. 4.76 Main synthesis methods for CNOs

- Combustion of naphthalene leading to 50 nm CNOs
- Burning common carbon-rich sources such as camphor and polystyrene foam (5–20 nm CNOs)

Figure 4.77 shows HRTEM images of CNOs synthesized by these methods [238].

In the last decade, these and other methods have been developed and optimized. Thus, the carbon onion can be obtained by *pyrolysis of propane* (propane/oxygen flame) [239], yielding two different types of CNOs with diameters in the ranges of 18–25 and 9–12 nm. Some carbon onions were found to be almost spherical and have slight faceting profiles, and other CNOs have a polyhedral structure. This technique produces multi-shell fullerenes in large quantities and carbon tubular structures on the metal surface. The authors assumed that the substrate nature is a determinant factor in the carbon onion formation. In a related work [240], CNOs (diameters of 70–100 nm) were produced by CVD method at 800 °C starting from methane as carbon source and isolated from the substrate by HNO_3 refluxing, calcination in air at 500 °C, and magnetic separation for removal of catalyst particles and amorphous carbon.

As it was mentioned above, the CNOs (Fig. 4.78) were prepared in a stainless steel autoclave at 600 °C by a simple reaction between $CuCl_2{\cdot}2H_2O$ and CaC_2[24] according to the reactions 4.4–4.9 [241]. It was shown that the crystal water in $CuCl_2{\cdot}2H_2O$ plays an important role in the formation of CNOs. The product can be used as anode materials for lithium-ion batteries, which can deliver a reversible capacity of 391 $mA{\cdot}g^{-1}$ up to 60 cycles. Also, the Fe–Ni alloy nanosheet serves as a catalyst for growing metal-encapsulated CNOs and as a support for anchoring these preformed nanoparticles, resulting in monodispersed catalyst nanoparticles (Figs. 4.79 and 4.80) [242]. As an application, the ferromagnetic $Fe_{0.64}Ni_{0.36}$@CNOs particles demonstrate their application in both water purification and magnetic storage.

$$CuCl_2 + CaC_2 = Cu + 2C + CaCl_2 \tag{4.4}$$

$$CuCl_2 \cdot 2H_2O = CuCl_2 + 2H_2O \tag{4.5}$$

$$CaC_2 + 2H_2O = Ca(OH)_2 + C_2H_2 \tag{4.6}$$

---

[24] More detailed information on the *carbide-derived carbons* see in the chapter below.

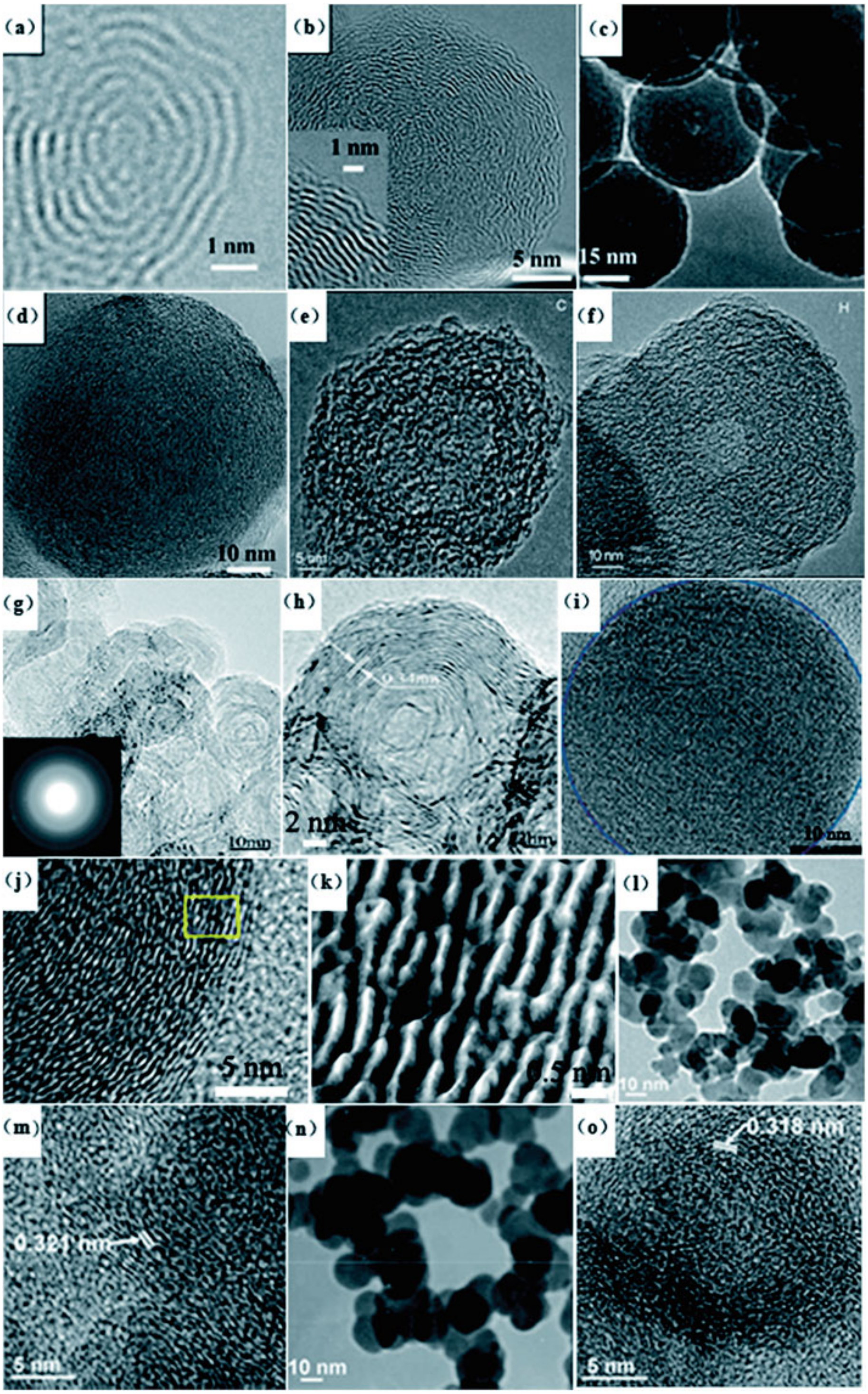

Fig. 4.77 HRTEM images of CNOs synthesized using some new methods. (**a**–**d**) CNOs fabricated by counterflow diffusion flames with methane (CH_4) concentrations of 15%, 25%, 35%, and 45%, respectively. (**e** and **f**) CNOs prepared by thermolysis using a NaN_3–C_6Cl_6 mixture as precursor. (**g** and **h**) CNOs obtained from the reaction between CaC_2 and $CuCl_2{\cdot}2H_2O$. (**i**–**k**) HRTEM images of CNOs prepared using the combustion of naphthalene. (**l** and **m**) CNOs synthesized by burning polystyrene foam. (**n** and **o**) CNOs synthesized by burning camphor. (Reproduced with permission of the *Royal Society of Chemistry*)

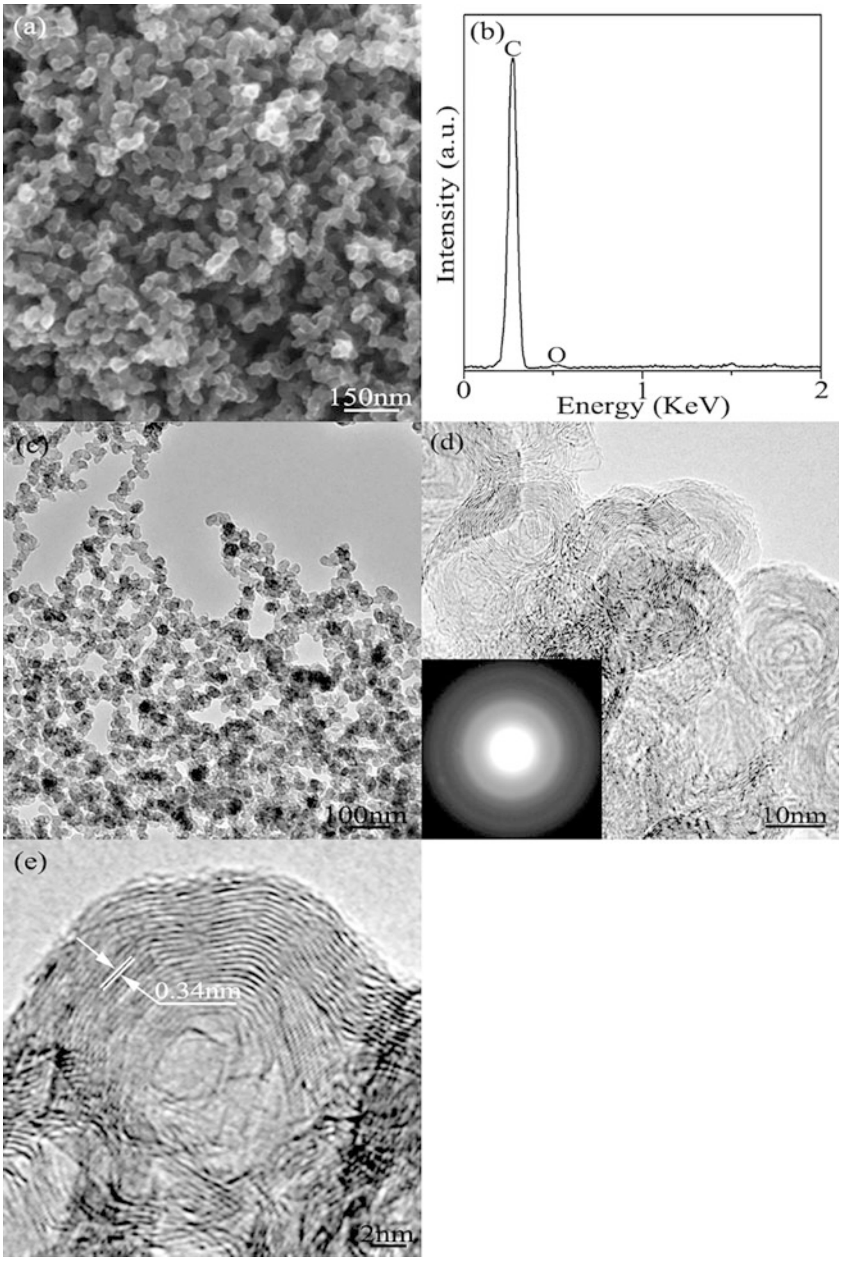

Fig. 4.78 FESEM image (**a**), EDX spectrum (**b**), and HRTEM images (**c**–**e**) of the as-obtained CNOs. The insert in (**d**) is the corresponding SAED pattern. (Reproduced with permission of the *American Chemical Society*)

$$\mathrm{CuCl_2 + C_2H_2 = Cu + 2C + 2HCl} \tag{4.7}$$

$$\mathrm{Ca(OH)_2 + 2HCl = CaCl_2 + 2H_2O} \tag{4.8}$$

$$\text{Overall reaction } \mathrm{CuCl_2 \cdot 2H_2O + CaC_2 = CaCl_2 + Cu + 2C + 2H_2O} \tag{4.9}$$

Arc-discharge fabrication (Fig. 4.81) of high-quality nanoparticles in the form of floating powder on the water surface including spherical CNOs and elongated fullerene-like nanoparticles similar to nanotubes in large quantities without the use of vacuum equipment was reported [243]. Their large specific surface area (984.3 m^2/g, promising for gas storage) was attributed to the "surface roughness" induced by the defective nature of the carbon onion shells. A model of arc discharge in water with two quenching zones was proposed (Fig. 4.82). This arc discharge in water represents an alternative to conventional vacuum processes to produce carbon nanoonions in large quantities.

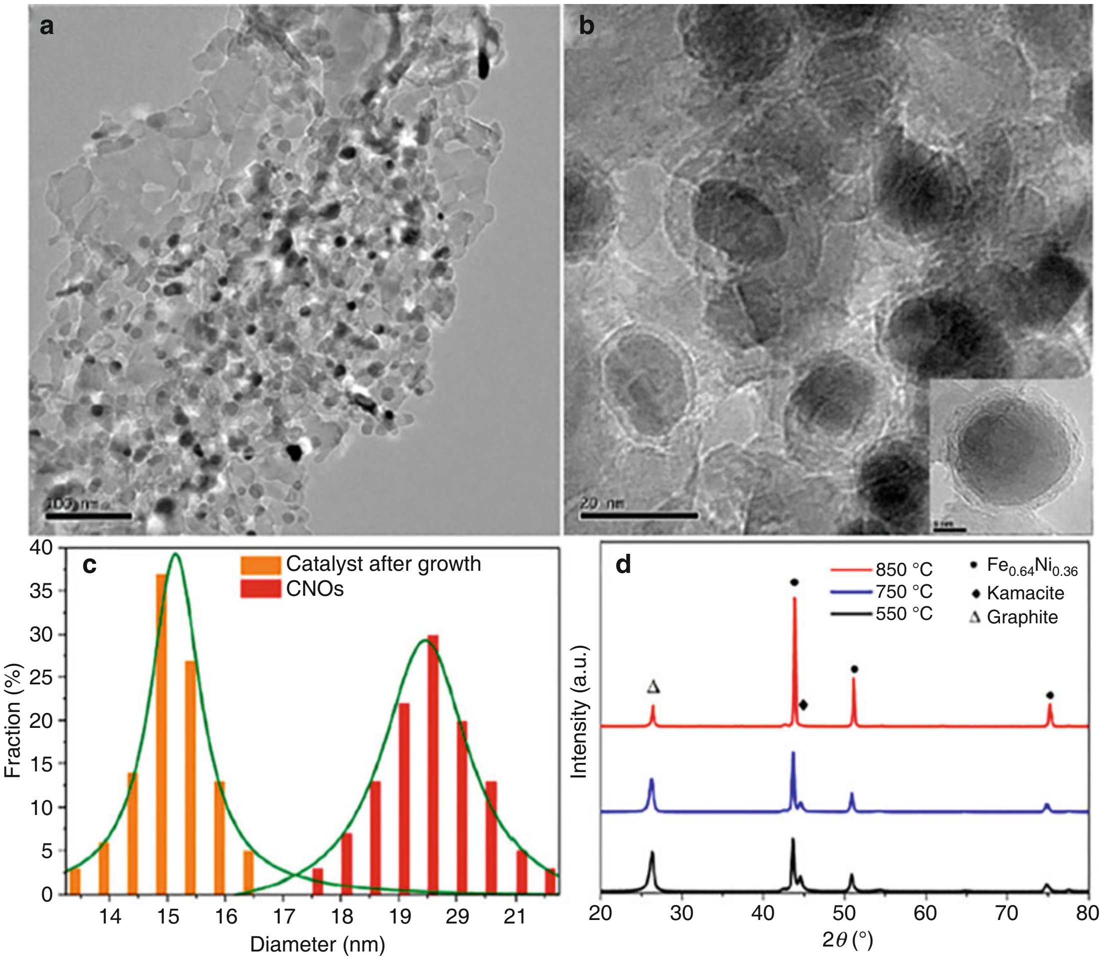

Fig. 4.79 (**a**, **b**) TEM images of CNOs grown by CVD over the self-anchored catalysts on the alloy nanosheet; inset in (**b**) is an HRTEM image of an individual CNO particle. (**c**) Particle size distribution statistics with the corresponding fitting curves for the self-anchored catalysts and CNOs after CVD growth. (**d**) XRD patterns of CNOs grown at different temperatures. (Reproduced with permission of *Springer*.)

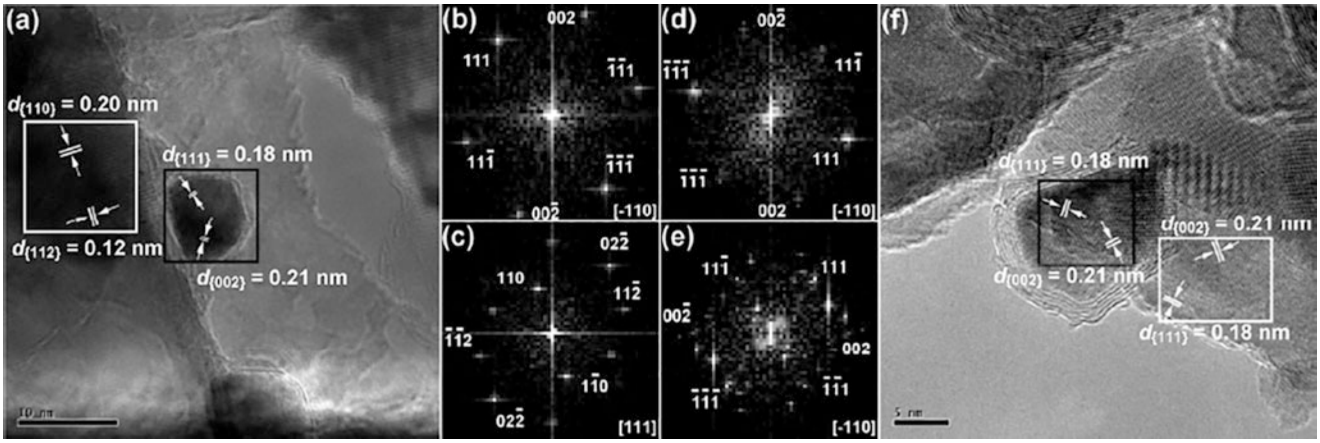

Fig. 4.80 FFT analysis of CNOs grown at (**a**) low (550 °C) and (**f**) high temperatures (850 °C). (**b**, **c**) The diffraction patterns of the areas outlined in black and white from (**a**), respectively. (**d**, **e**) The diffraction patterns of the areas outlined in black and white from (**f**). (Reproduced with permission of *Springer*)

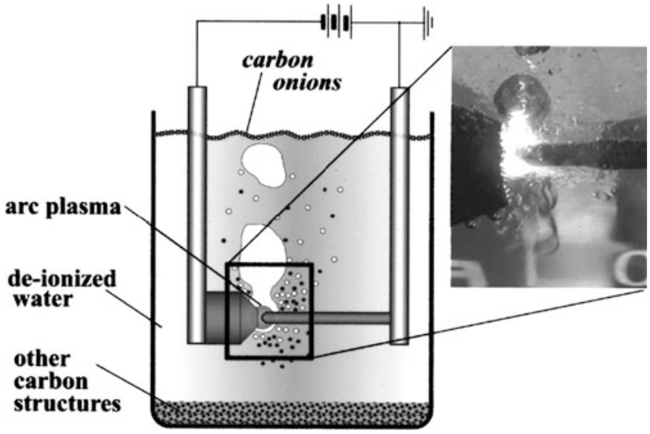

Fig. 4.81 Schematic of the apparatus used for arc discharge in water with a digital image of the discharge. (Reproduced with permission of *AIP Publishing*)

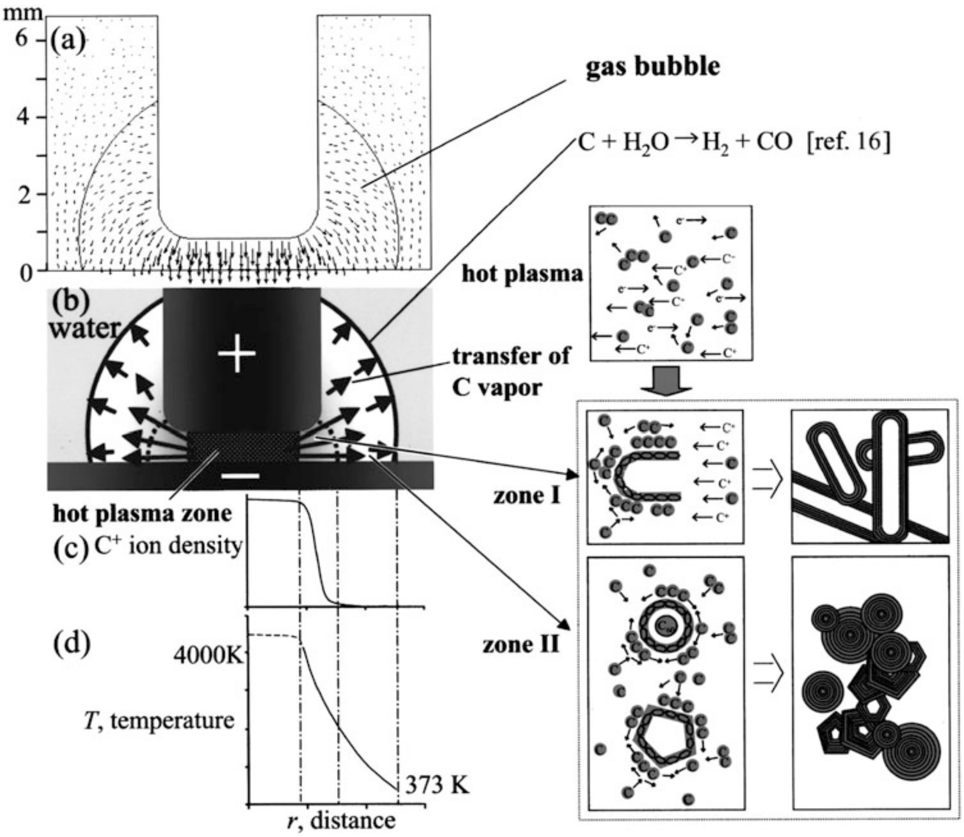

Fig. 4.82 Formation mechanism of CNOs prepared by arc discharge in water. (**a**) Relative electric field strength, shown by arrows, between a rod anode (17 V) and a flat cathode (ground) in a gas bubble surrounded by water. (**b**) Direction of thermal expansion from plasma to the water interface. (**c**) Qualitative ion density distribution. (**d**) Temperature gradient – the formation of elongated nanoparticles in zone (I) and onions in zone (II) is also shown schematically. (Reproduced with permission of *AIP Publishing*)

An unexpected formation of CNO-like honeycomb nanostructures (Figs. 4.83 and 4.84), among other products, was observed as a result of dispersion and unfolding of MWCNTs using a water-soluble cobalt octacarboxyphthalocyanine derivative “theraphthal” in ultrasonic treatment conditions [244]. Commercially fabricated theraphthal (TP) [245, 246] **4.3.5.1** is a water-soluble cobalt phthalocyanine salt and sonosensitizer, used in ultrasound therapy of cancers [247–251] due to insolubility of its calcium salt making a labile solid phase in a tumor [252], as well as a series of metal 2,3,9,10,16,17,23,24-octacarboxyphthalocyanines, their water-soluble sodium salts, and their functional derivatives can generate reactive oxygen species (ROS). Unfolding of MWCNTs in the conditions of TP addition was explained by the in situ formation of reactive

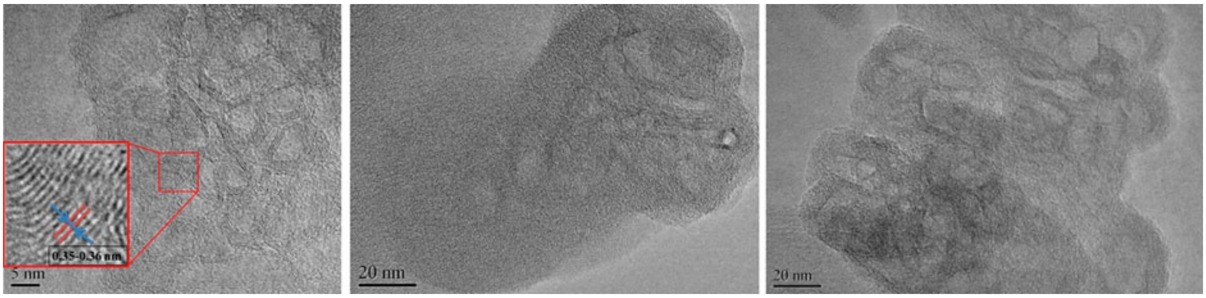

Fig. 4.83 HRTEM images of (**a**, **b**) honeycomb structures of the products formed in diluted TP-MWCNTs dispersions and (**c**) covering of partially destroyed CNTs with TP aggregates. (Reproduced with permission of the *Royal Society of Chemistry*)

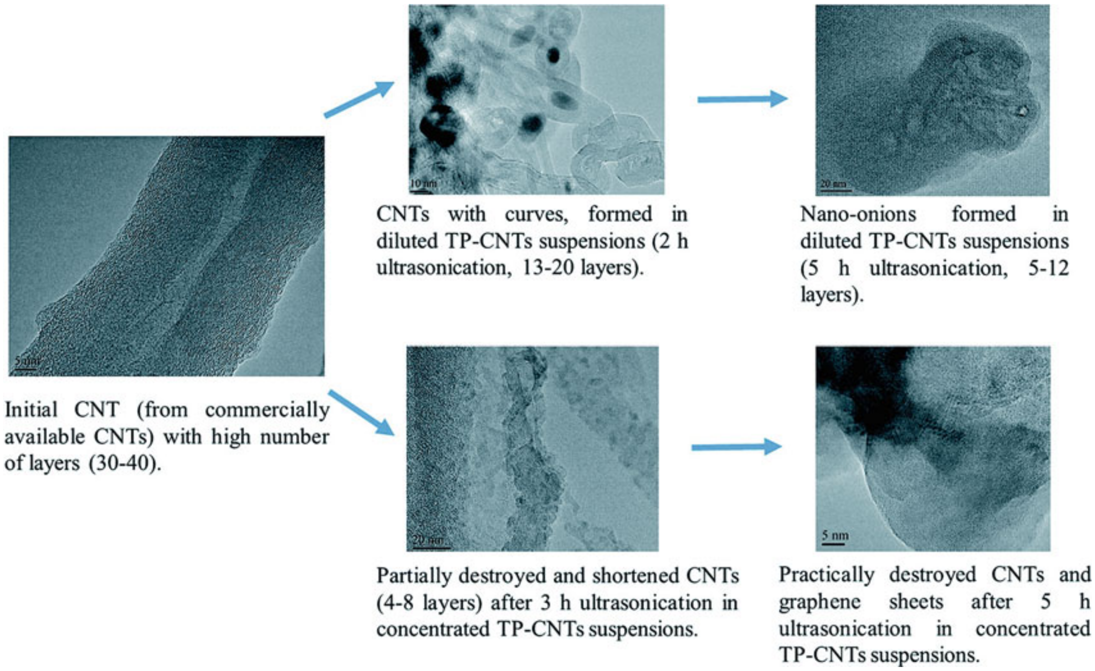

CNTs with curves, formed in diluted TP-CNTs suspensions (2 h ultrasonication, 13-20 layers).

Nano-onions formed in diluted TP-CNTs suspensions (5 h ultrasonication, 5-12 layers).

Initial CNT (from commercially available CNTs) with high number of layers (30-40).

Partially destroyed and shortened CNTs (4-8 layers) after 3 h ultrasonication in concentrated TP-CNTs suspensions.

Practically destroyed CNTs and graphene sheets after 5 h ultrasonication in concentrated TP-CNTs suspensions.

Fig. 4.84 HRTEM images of the evolution process in diluted (top) and concentrated (bottom) TP–CNT dispersions. (Reproduced with permission of the *Royal Society of Chemistry*)

oxygen species in TP solutions under ultrasonic treatment and their further attack on MWCNTs surface. It is well-known that cavitation triggers free radical processes, shock waves, cumulative streams, and a number of other phenomena in a system that are localized at collapsing cavitation bubbles. In these conditions, even at low-intensity ultrasound in cleaners (20–40 kHz), partial destruction of TP slowly takes place, and it is known to be accompanied by the formation of ROS. As a phthalocyanine derivative, TP can be coordinated to CNT surface via π–π-stacking through aromatic supramolecular ring or covalently through COO^- group(s) both those of the TP molecule and in the functionalized CNTs-COOH. Highly water-soluble TP, as ionic salt, transfers MWCNTs to solution and, due to action of appearing free radicals in ultrasound conditions, destroys and unfolds them forming graphene sheets. These sheets can then form co-grown single-walled carbon nanotubes (SWCNTs, diameter 1.7 nm). In some cases (in dilute dispersions), at lower TP concentrations, incomplete unfolding of MWCNTs takes place leading to the appearance of circular nanostructures (nanoonions), which are united to honeycomb nanostructures due to defects in MWCNTs caused by action of free radicals. Graphite is subject to similar transformations [253].

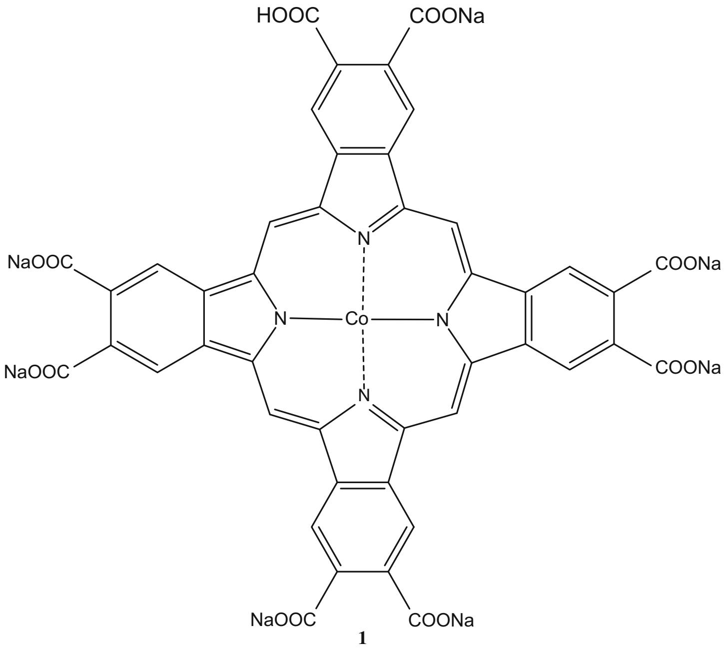

1

Compound 4.3.5.1 (theraphthal)

Main features of CNOs are as follows:

- CNOs are composed of multilayered concentric graphitic shells.
- Size of CNOs is in the range of 3–100 nm, depending on the synthesis method.
- CNOs are of two types: hollow CNOs and core–shell-structured CNOs.
- Hollow CNOs are spherical or polyhedral in shape.
- The innermost layer of the spherical hollow CNO is a C_{60} cage.
- The inner space of the polyhedral CNO is usually much larger than a C_{60} cage in volume.
- Onion-like fullerenes (OLFs) are known; they can be generated by arc discharge in water between pure graphite electrodes [254]. It was revealed that the OLFs with diameter about 25 nm were of high degree graphitization. The structural stability of carbon nanoonion $C_{20}@C_{60}@C_{240}$ was investigated by performing molecular dynamics computer simulations [255].
- A core–shell structured CNO (with transition metals and their oxides, alloy nanoparticles, or nanodiamonds) is usually quasispherical in shape.
- Large specific surface area.
- High electrical conductivity.
- Typically, two broad Raman bands can be readily observed in the area between 1300 and 1600 cm^{-1}.
- Analogous to carbon nanotubes, CNOs display poor solubility in both aqueous and organic solvents because of aggregation, promoted by strong intermolecular interactions such as van der Waals forces. Similar to CNTs, this solubility can be considerably improved by ozonolysis [256] or other types of functionalization.

Chemical Activation of CNOs The CNOs, being a promising candidate for high-power supercapacitors due to the nonporous outer shell, easily accessible to electrolyte ions, suffer a difficulty, since the nonporous ion-accessible outer shells also limit the energy density of the CNOs, requiring large specific surface area. So, their electrochemical performance needs an improvement, which can be reached by chemical activation, for instance, using KOH, introducing porosity on the outer shells of CNOs [257]. This treatment (Fig. 4.85) dispersion of CNOs in KOH solutions under ultrasonication induced changes in structure, specific surface area (SSA), and pore size distribution of CNOs. In particular, the pristine CNOs (5–50 nm, concentric structures containing long-range ordered graphitic striations on each shell) changed to the CNOs with defects in the outer shell, creation of micropores and mesoporoses, and destruction of concentric structures. This porosity allowed improving the energy density and preserving the power density in CNO high-rate supercapacitor electrodes.

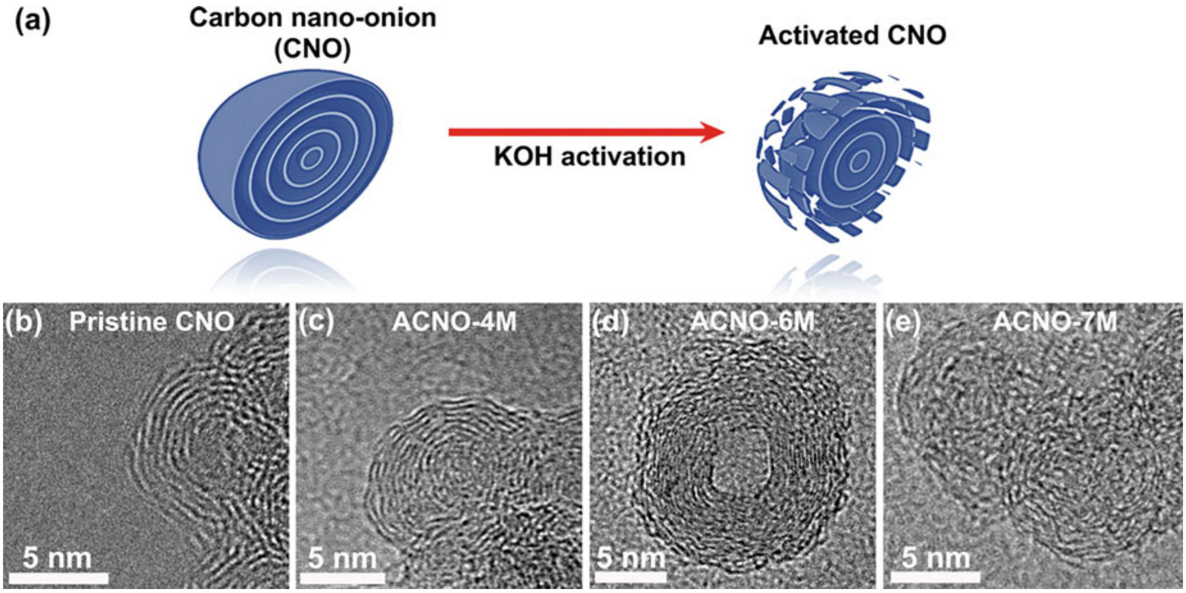

Fig. 4.85 (**a**) A schematic showing the chemical activation of CNOs in KOH. TEM images of pristine CNO (**b**), ACNO-4M (**c**), ACNO-6M (**d**), and ACNO-7M (**e**). "ACNO-*n*M" denotes the activated CNO prepared using *n* mol/L KOH solution. (Reproduced with permission of *Elsevier Science*)

Fig. 4.86 Schematic illustration of the PtNP decoration on CNOs in the vortex fluidic device (VFD). (Reproduced with permission of the *Royal Society of Chemistry*)

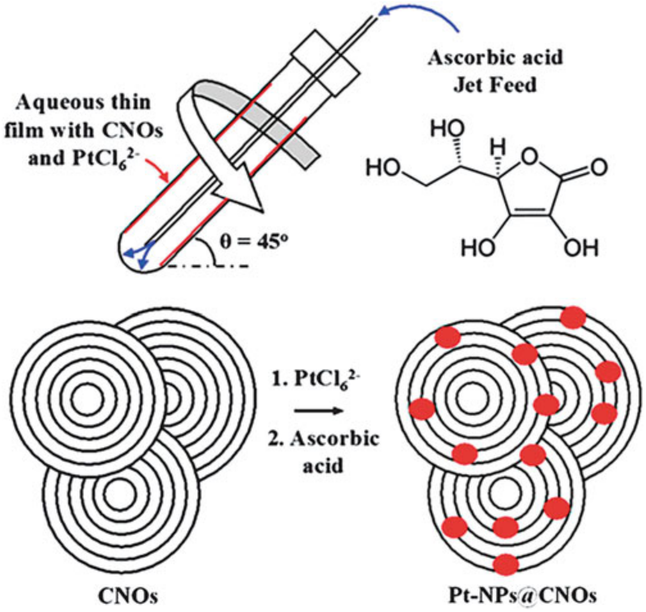

Decoration, Dopation, and Functionalization of CNOs *Decoration* of CNOs with platinum nanoparticles was carried out using ascorbic acid as the reducing agent within a vortex fluidic device (VFD),[25] leading to PtNP@CNO nanocomposites (Fig. 4.86) [258]. Pristine- or plasma-modified CNOs were dispersed in Milli-Q water, mixed with H_2PtCl_6 solution, and placed in the VFD for subsequent reduction with ascorbic acid solution. Resulting agglomerations of Pt nanoparticles on CNOs are shown in Fig. 4.87, revealing promising electrocatalytic activity of the Pt@CNOs, which may be applicable to other forms of carbon for a wide range of applications.

---

[25] The VFD is a microfluidic device that has been used for disassembling self-organized systems, exfoliation of graphite and hexagonal boron nitride, wrapping multilayer graphene sheets around algal cells, and controlling the particle size and distribution of decorated metal nanoparticles on various carbon nanomaterials.

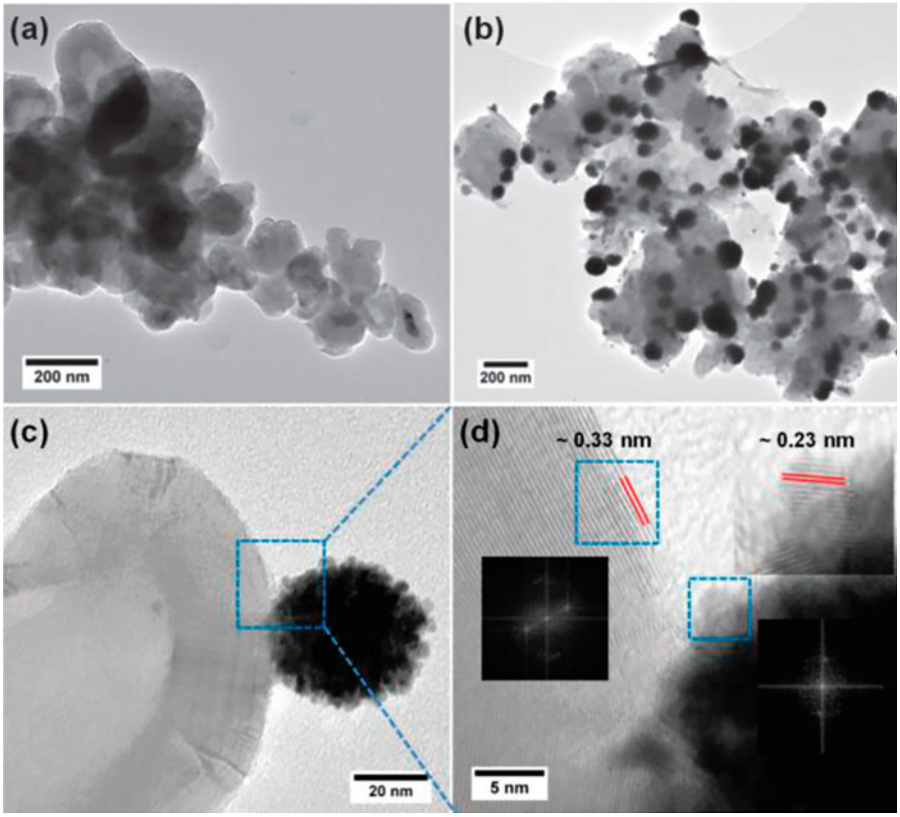

Fig. 4.87 TEM images of (**a**) pristine CNOs and (**b**) decorated CNOs with platinum clusters in batch reaction. (**c**) A zoomed-in image of a platinum cluster on a CNO. (**d**) HRTEM image of the area indicated in (**c**), showing the lattice distances and fast Fourier transform analysis of the areas indicated on CNO and a single Pt-NP. (Reproduced with permission of the *Royal Society of Chemistry*)

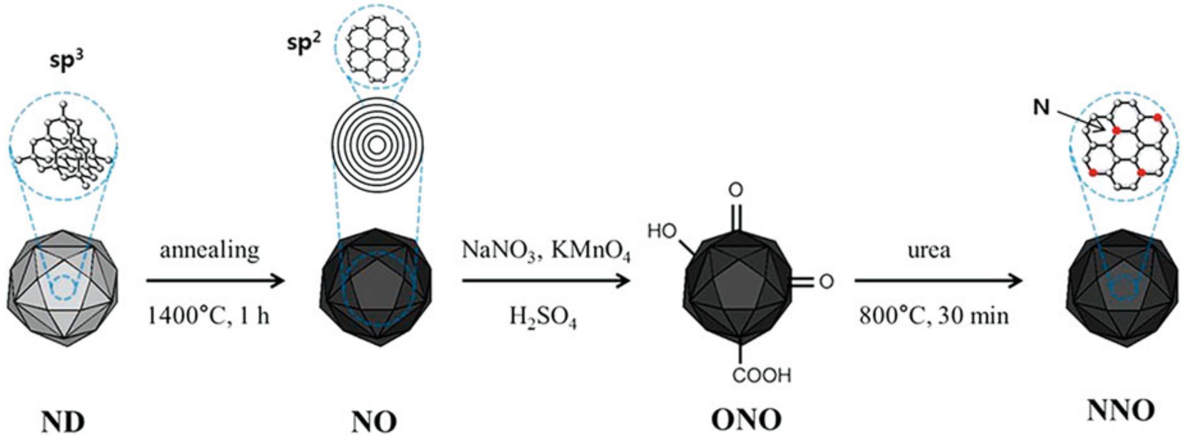

Fig. 4.88 Schematic routes for the fabrication of NO, ONO, and NNO. (Reproduced with permission of *Nature*)

Dopation of CNOs CNOs doped with boron (B-CNOs; 0.76–3.21 at.% of boron substitution) were prepared by annealing commercial nanodiamond particles (NDs) at 1650 °C under an inert He atmosphere in the presence of boron [259]. It was revealed that the increased amount of boron doping resulted in decreased interlayer spacing and polygonization of the structures, leading to enhanced properties as electrodes for electrochemical capacitors. Authors noted that these active sites could also play a vital role in enhancing the catalytic activity of oxygen reduction. Nitrogen-doped nanoonions (NNOs) were prepared [260] from CNOs (in turn, obtained from NDs with size of 4–6 nm) by a modified *Hummers*' method, using urea in the last step (Fig. 4.88). Nitrogen content and molar ratio of nitrogen-containing groups in the NNOs were varied by controlling the oxygen content of ONO (oxygen-doped nanoonions). Studying ORR activities of the NNOs using a rotating disk electrode, the NNOs showed a higher onset potential than that of CNOs, and the ORR activity of the NNO could be improved by increasing the number of active sites (N-containing groups) in the NNO.

Functionalization of CNOs The reactions of CNOs (50–100 nm in diameter) with fluorine in the presence of H_2 in a Monel reactor at three different temperatures, 350, 410, and 480 °C, yield fluorinated nanoonions (F-CNOs, Fig. 4.89) of approximately $C_{10.1}F$, $C_{3.3}F$, and $C_{2.3}F$ stoichiometry, respectively [261]. The purpose of using hydrogen in the process was in situ generation of HF, which is known to catalyze the fluorination of the other sp^2-bonded carbon materials (e.g., graphite and CNTs). It was shown that even after breaking of the graphene layers in CNOs by F_2 action, the F-CNO products maintained the spherical morphology. The F-CNOs were found to be soluble in DMF and alcohols. Even after 1 year the suspension solutions of the most fluorinated F-NO-410 and F-NO-480 samples do not show any visible precipitation (Fig. 4.90). Due to this enhanced solubility, they could be useful for biomedical applications, paints, lubricating composites, etc. Further defluorination of F-CNOs using hydrazine resulted in remarkable “healing” of broken graphene layers which rejoin within the sphere to substantially restore the CNO microstructure. CNOs can also be functionalized with biomolecules. Thus, soluble small non-cytotoxic CNOs (with 6–8 shells) were prepared with high yield and functionalized with carboxylic groups and biomolecules biotin–avidin interactions on a gold surface by layer-by-layer assembly (Fig. 4.91) [262]. The film

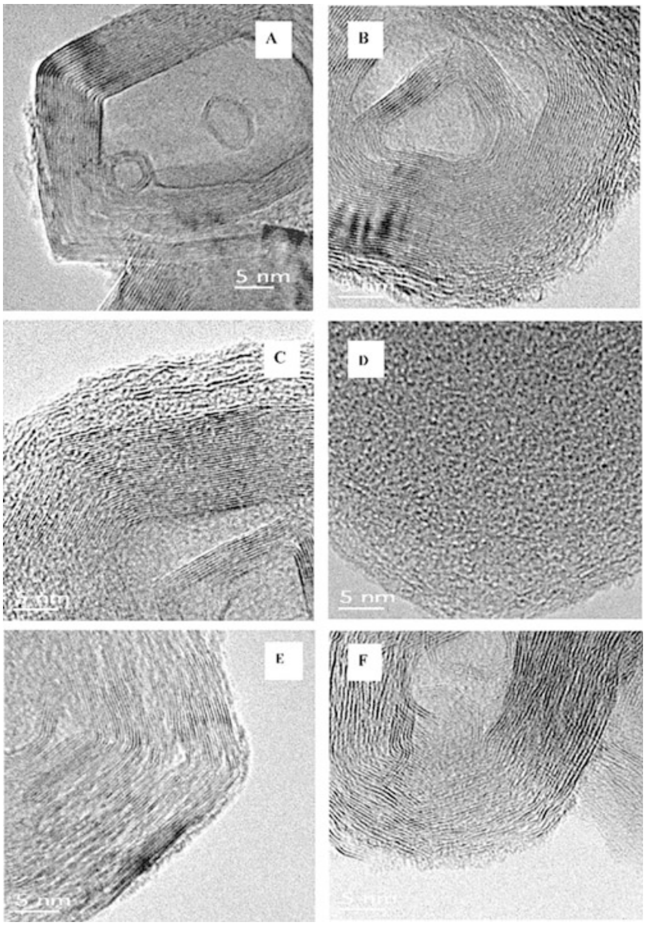

Fig. 4.89 TEM images of carbon nanoonion specimens: (**a**) pristine CNO, (**b**) F-NO-350, (**c**) F-NO-410, and (**d**) F-NO-480; hydrazine-treated F-NO-410 (**e**) and F-NO-480 (**f**). (Reproduced with permission of the *American Chemical Society*)

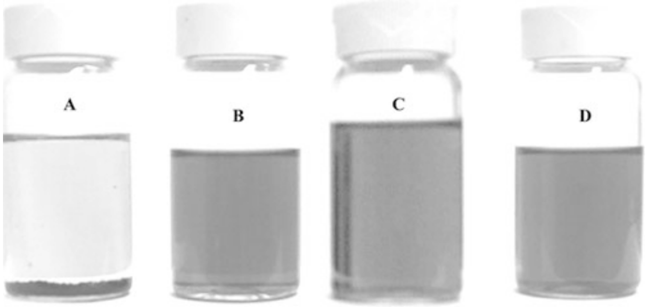

Fig. 4.90 Photographs of the CNO materials dispersed in ethanol: (**a**) pristine CNOs, (**b**) F-CNO-350, (**c**) F-CNO-410, and (**d**) F-CNO-480. (Reproduced with permission of the *American Chemical Society*)

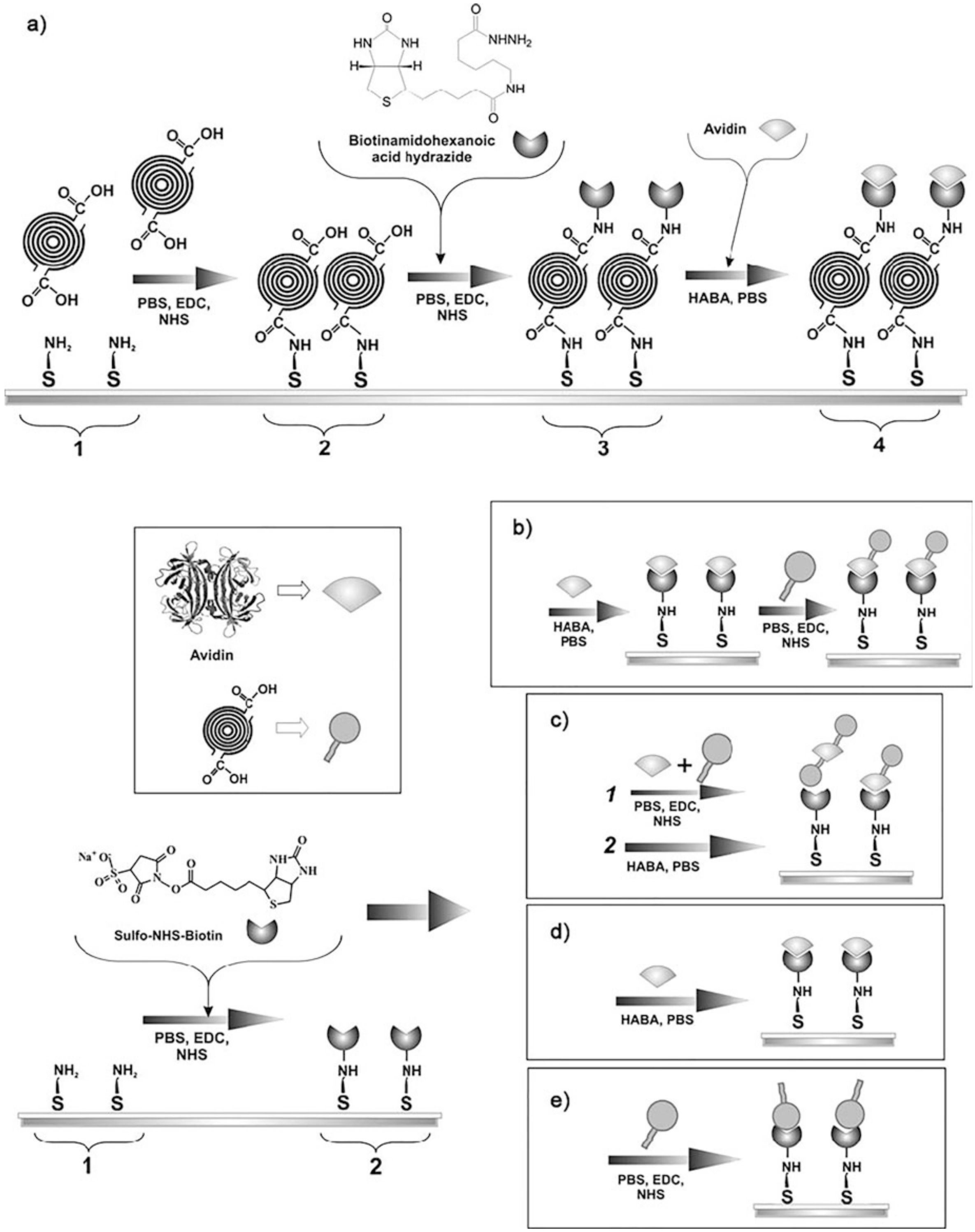

Fig. 4.91 Schematic illustration of the preparation of (**a**) Au/thiol/ox-CNOs/biotin/avidin (avidin PDB ID: 2avi), (**b**) Au/thiol/biotin/avidin/ox-CNO, (**c**) Au/thiol/biotin/avidin+ox-CNOs, (**d**) Au/thiol/biotin/avidin, and (**e**) Au/thiol/biotin/ox-CNOs layers (PBS, phosphate-buffered saline; EDC, 1-(3-dimethylaminopropyl)-3-ethylcarbodiimide hydrochloride; NHS, N-hydroxysuccinimide; HABA, 4′-hydroxyazobenzene-2-carboxylic acid). (Reproduced with permission of *Wiley*)

structure of formed self-assembled monolayers on the gold surface was found to be depended on the sequence of film component deposition. Biomolecules attached to the CNOs retained their biological activity.

Some Properties of CNOs *Diamagnetism* of carbon onions was probed by NMR of adsorbed water. Thus, the ^{1}H chemical shift of water molecules adsorbed on defect sites of CNOs was compared with the shifts of bulk water and water adsorbed by chemically derived graphene (G), graphene oxide (GO), and nanodiamond (ND) [263, 264]. Authors revealed that the positions of ^{1}H resonances for insulator ND and GO are close to that of bulk water, while water molecules adsorbed by G and CNOs possessed a significant deviation in chemical shift from that of bulk water, attributing this to the diamagnetic screening effect of the conducting graphene layers. Highly *fluorescent* CNOs (2.5 nm height and size distribution from 10 to 65 nm, average 40 nm; 0.34 nm interlayer distance) were produced by thermal annealing at 400 °C of perylenetetracarboxylic anhydride in low molecular mass PEG (Fig. 4.92) [265]. These CNOs can be purified by silica gel chromatography to obtain fractions with a very homogeneous particle size of about 35 nm. These CNOs are highly biocompatible with Hep3B cells and can cross the cell membrane.

It is known that CNOs have a hydrophobic character, nonporous texture, moderate specific surface area (200–600 $m^{2} \cdot g^{-1}$), high electrical conductivity, short time charging, and high power density. Taking into account the purpose to be used in supercapacitors, CNOs were chosen as *model material* in order to understand the influence of the surface chemistry (nature and amount of oxygen groups) and structural defects (active surface area, ASA) on the capacitance [266]. The CNOs were prepared from high pure nanodiamonds at 1300 and 1700 °C and further modifications (Fig. 4.93). As a result, a predominant influence of the carbon defects on the capacitance in organic and aqueous electrolytes which counterbalance the functional group effect was highlighted.

Molecular Dynamics Simulations CNOs provide exceptional friction and wear reduction through a rolling and sliding mechanism of the CNOs at the interface, so, the mechanisms of these processes were studied by performing atomistic MD simulations of their sliding between diamond-like carbon substrates (Fig. 4.94) [267]. It was revealed that the ability of the CNOs to roll is inhibited both by increased contact pressure and the presence of a diamond core within the nanoparticles that

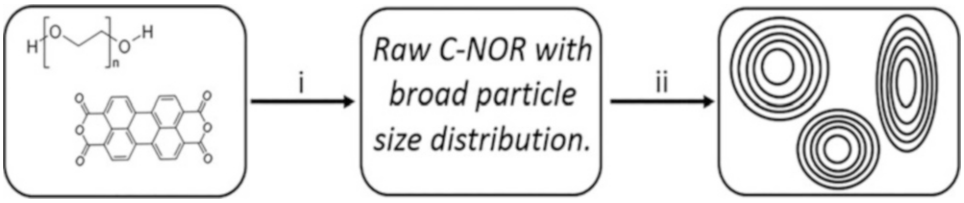

Fig. 4.92 Preparation procedure for C-NOR. (i) Treatment in an oven preheated at 400 °C and slow cool down to room temperature by exposure to the air (20 h) and (ii) purification of the black viscous mixture by silica gel chromatography. (Reproduced with permission of the *Royal Society of Chemistry*)

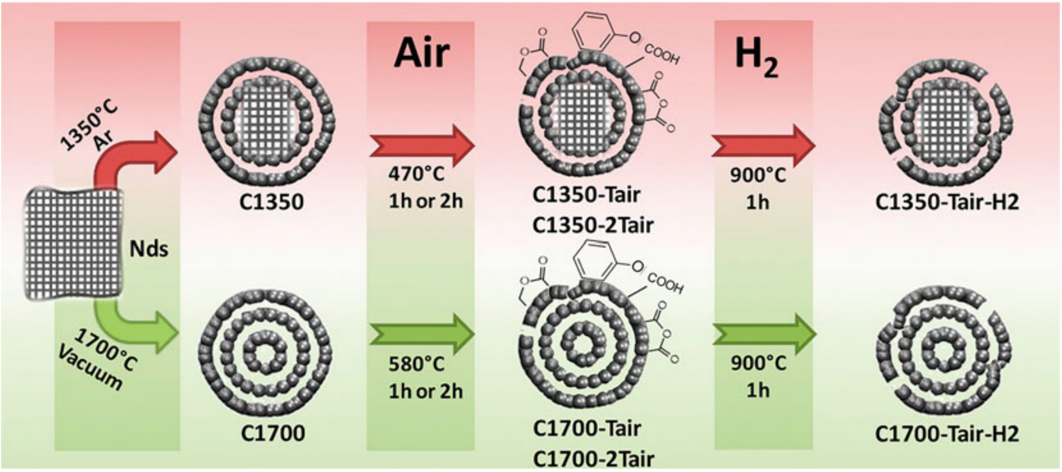

Fig. 4.93 Flowchart that regroups the different synthesis of CNOs under different thermal treatments. (Reproduced with permission of *Elsevier Science*)

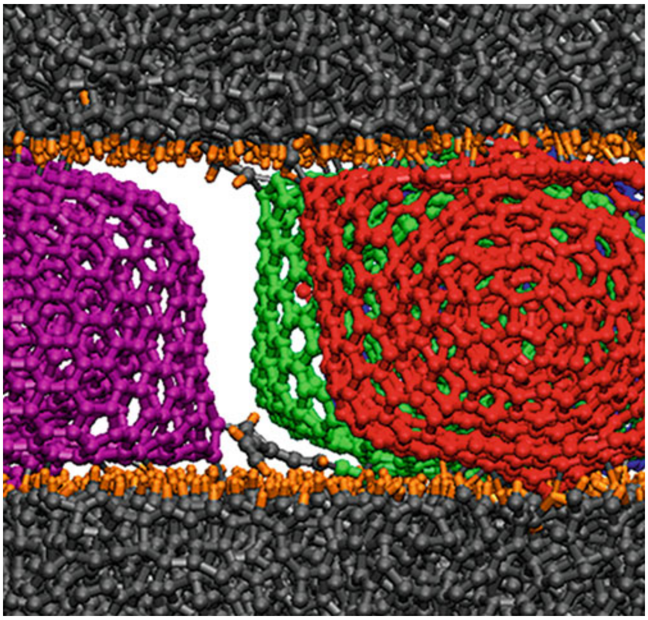

Fig. 4.94 Image of CO simulation with four nanoonions indicating strong interfacial bonding during sliding at 5 GPa contact pressure. (Reproduced with permission of the *Elsevier Science*)

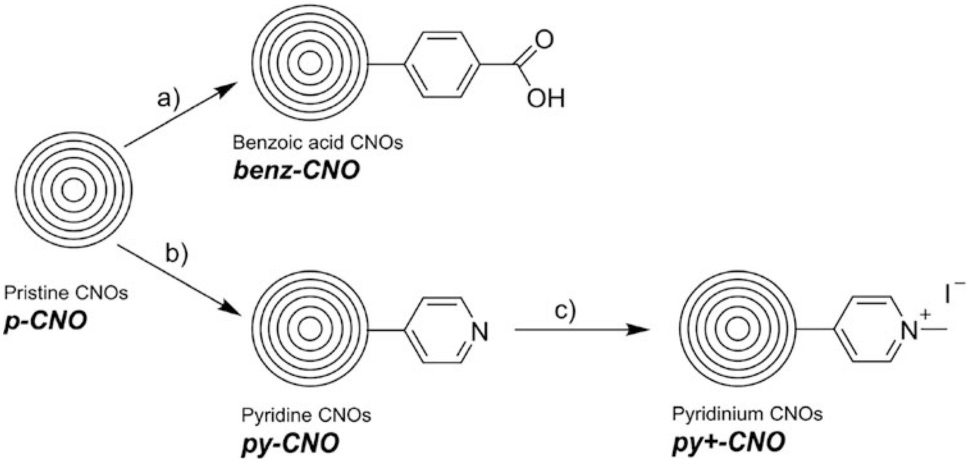

Fig. 4.95 Scheme of synthetic procedures for the surface functionalization of pristine CNOs. (**a**) 4-Aminobenzoic acid, $NaNO_2$, HCl, dimethylformamide/water; (**b**) 4-Aminopyridine, $NaNO_2$, 4N HCl/dimethylformamide. (**c**) Iodomethane, acetonitrile. All CNOs contain multiple functionalities on the surface; this scheme is simplified. (Reproduced with permission of *MDPI*)

enhances the formation of interfacial bonds during friction. The transition from rolling to sliding behavior was accompanied by an order of magnitude increase in the coefficient of friction, from $\mu = 0.024$ to 0.151, respectively.

The *toxicological effects* of pristine and CNOs, chemically modified with benzoicacid, pyridine, and pyridinium moieties (Fig. 4.95), on the development of the freshwater polyp *Hydra vulgaris* were studied in order to elucidate the ecotoxicological effects of CNOs [268]. *Hydra* specimens were exposed to the functionalized CNOs by prolonged incubation within their medium. On the basis of biodistribution of CNO nanoparticles in *Hydra* (Fig. 4.96), it was revealed the absence of adverse effects of CNOs (in the range 0.05–0.1 mg/L) in vivo at the whole animal level, testifying about their biosafety and suitability as materials for biomedical applications. There are indeed no much data on CNO toxicity; in case of closely related fullerenes, several toxic effects have been observed, depending on their properties (size, surface chemistry, solubility, aggregation/ agglomeration, experimental setups such as exposure time, biological models, etc.). So, any data on toxicity of carbon allotropes are useful as a part of complex issue for prediction of potential harmful effects in the designing of new nanoparticle-based products.

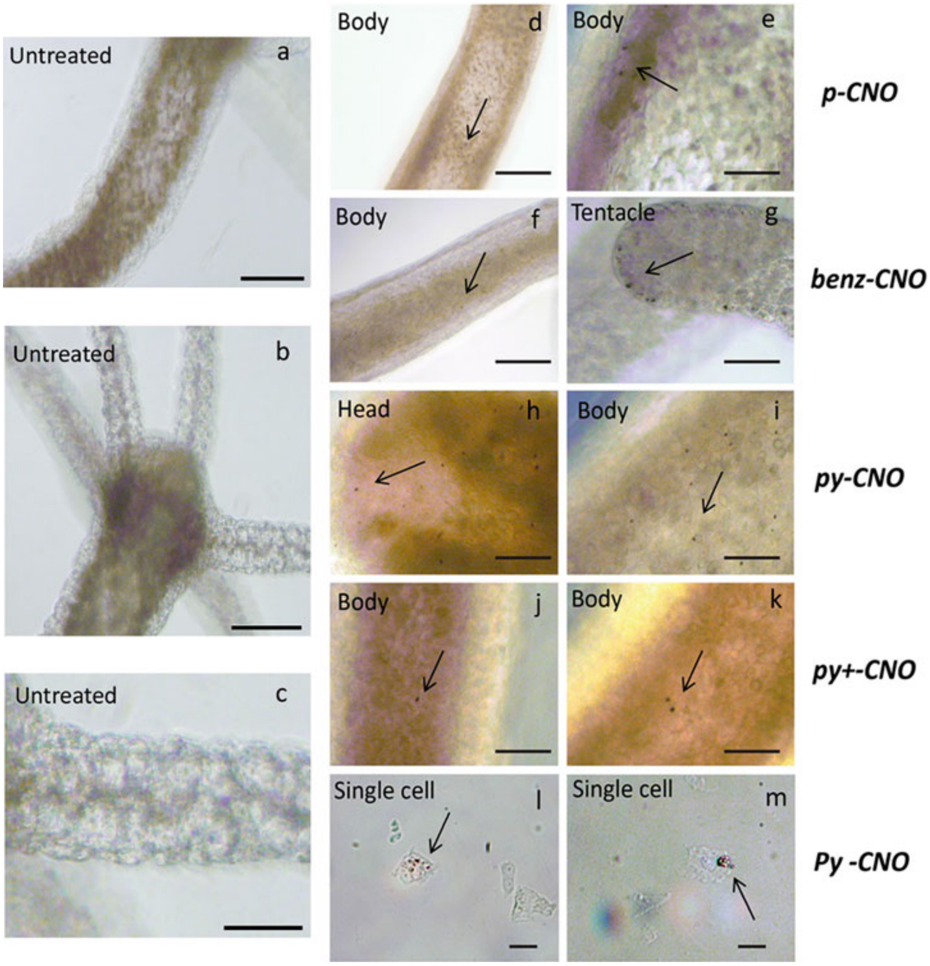

Fig. 4.96 In vivo uptake and biodistribution of CNO nanoparticles in *Hydra*. (**a**–**c**) Bright field images of a living untreated polyp. Scale bar: 200 µm. (**d**–**m**) All different types of CNOs were internalized into *Hydra* tissues, and images show small differences in the uptake efficiency. Internalized CNOs appear as black granular structures and are present in the tentacles, heads, and body columns. Scale bars: 500 µm in (**f**); 50 µm in (**g**); 200 µm in (**e**, **h**–**k**). Single-cell suspensions obtained from treated animals show a granular structure within the cytoplasm of epithelial cells, suggesting a macropinocitosis mechanism mediating the entrance of large amounts of CNOs into the cells. Representative single cells obtained by animals treated with *py-CNO* are shown. Scale bar: 20 µm in (**l**, **m**). (Reproduced with permission of *MDPI*)

Applications of CNOs Current applications of carbon nanoonions are in/as:

- Biosensors (for CNOs functionalized with biomolecules)
- Environmental remediation, in particular for sorption of heavy metal ions
- Lithium-ion batteries (anodes on the basis of highly graphitized and doped hollow CNOs with porous structure)
- Electrode materials in supercapacitors
- Fuel cells (CNOs as catalysts)
- Catalysis (i.e., oxidative dehydrogenation of ethyl benzene to styrene)
- Lubricants
- Optical industry
- Terahertz-based communication systems
- Drug delivery, infection therapy, and neurodegenerative diseases

Potential applications of CNOs include also magnetic storage materials, single-electron devices, point source field emitters, biological marking, encapsulation of foreign materials, etc. These current and potential applications above of CNOs are related with the facts that/due to:

- Their capacity to pass through cell membranes, carrying drugs, genes, biomolecules, and vaccines.
- Biocompatibility.
- Possibility to create collagen CNO materials as scaffolds in tissue generation and artificial implants, as well as smart drugs.
- CNOs resist biodegradation.
- CNOs are powerful engineering candidate over other existing materials used to repair defective organs.
- CNOs are excellent implements for the therapeutic monitoring and the diagnosis of diseases.
- CNOs are suitable for the analysis of drugs in different areas.
- CNOs are applicable in a lot of electronic products, i.e., nanotransistors, nanocapacitors, supercapacitors, quantum computers, etc.
- CNOs can be effectively used in the energy sector (energy-producing, energy-absorbing, and energy storage products), i.e., in batteries or fuel cells.
- CNOs are frequently more durable, stronger, and lighter compared with non-nanotechnologically created materials.
- Physical/chemical activation could increase the SSA of CNOs, improve the degree of graphitization, and introduce a porous structure, which would contribute to an enhanced electrochemical performance of the CNO anodes.

Limits for CNO uses are as follows, among others:

- Relatively high cost compared with traditional technologies
- Toxicity problems
- Possible disappearance of certain markets and loss of jobs, if alternative energy sources on their bases will be developed

Among recent reports on CNO applications, we selected some representative and intriguing reports having good expectative and future progress. Thus, a fluorescent probe based on surface carboxyl-functionalized ND-derived CNOs (Fig. 4.97) for *biological imaging* was developed [269]. These water-soluble low-cytotoxic CNOs with high emission

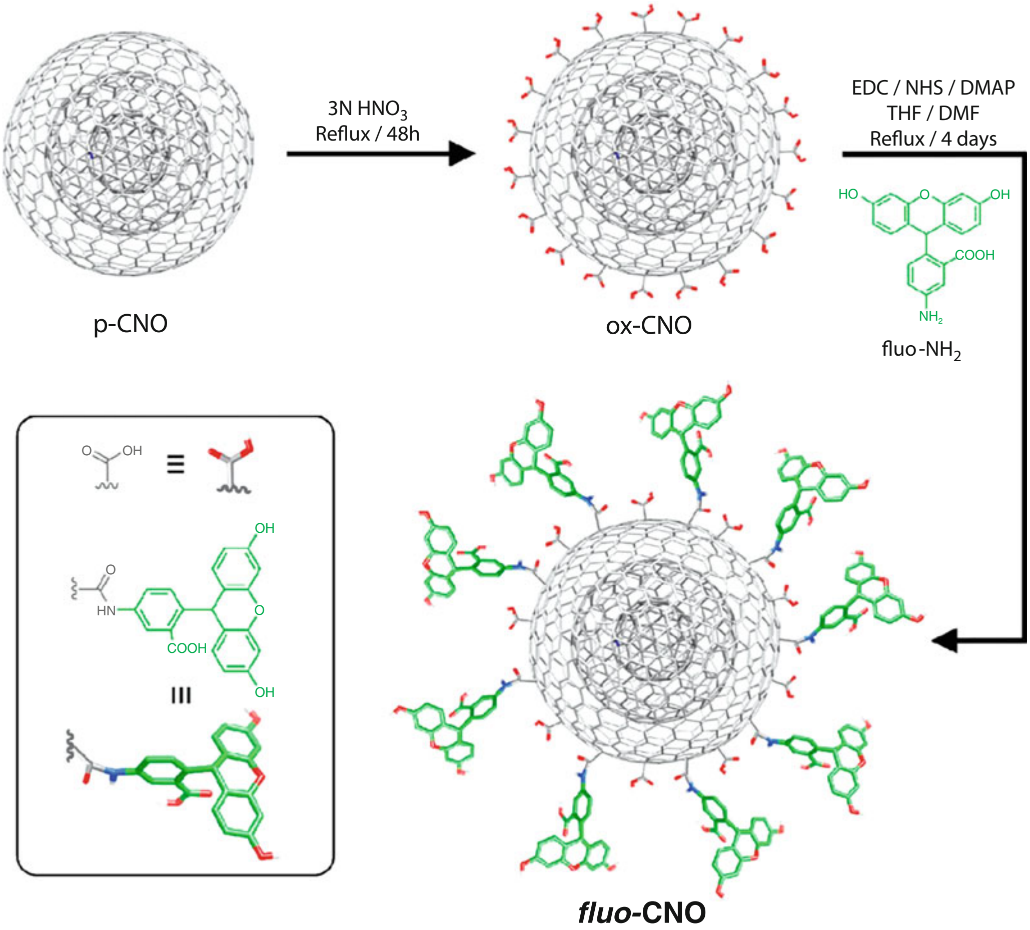

Fig. 4.97 Procedure for the preparation of carboxy-functionalized *ox*-CNO and fluorescently labeled *fluo*-CNO. (Reproduced with permission of the *IOP Publishing*)

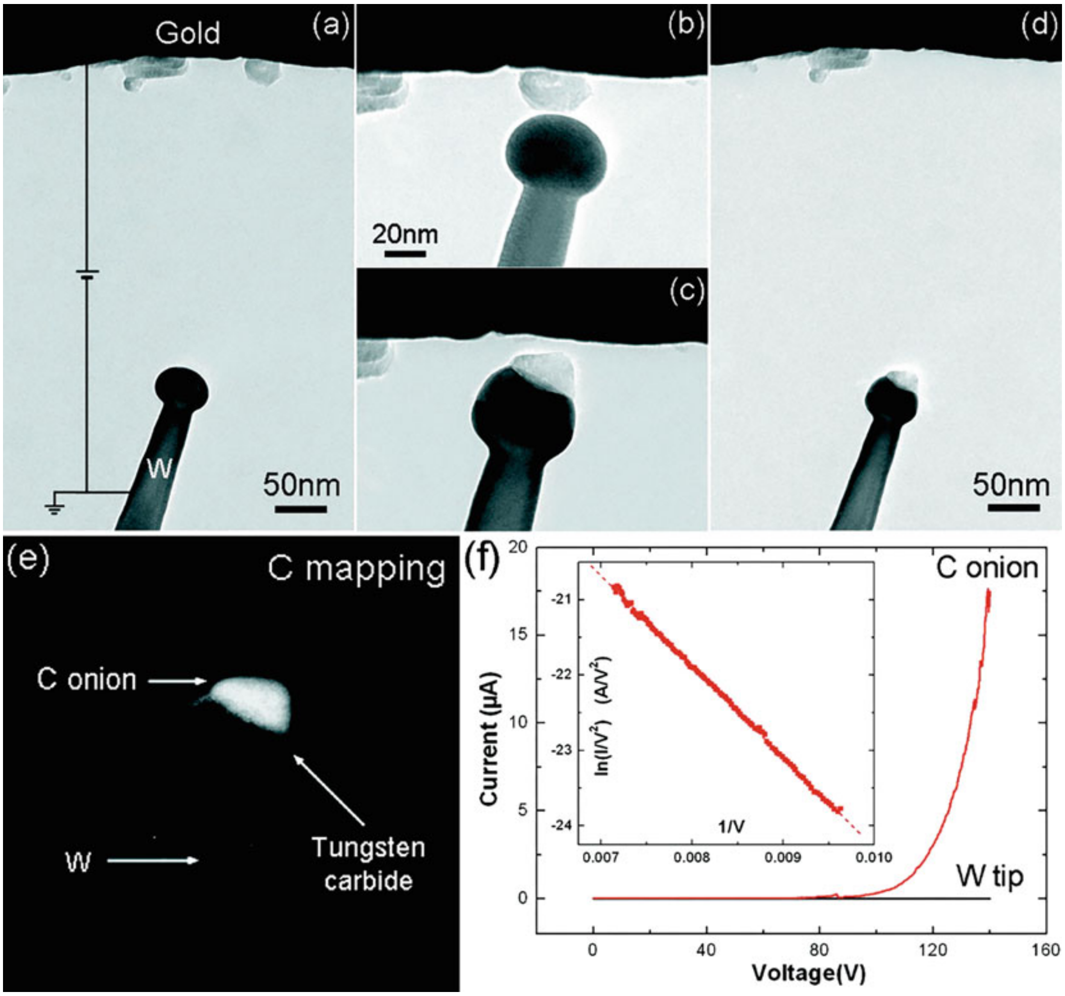

Fig. 4.98 (**a**) TEM image showing the field emission measurement on a standard W tip. This tip was then moved to contact a C onion attached to the counter gold wire (**b**); the tip and onion were then fused together at a high current (**c**). (**d**) The newly formed C-onion/W-tip structure was retracted to the original position as in image a for a comparative FE measurement. (**e**) EELS C map showing the spatially resolved carbon distribution within the emitter end in image d. (**f**) The measured FE I−V curves and F−N plot corresponding to the I−V curve recorded from the C-onion emitter (inset). (Reproduced with permission of the *American Chemical Society*)

properties were prepared by a reaction involving the amide bond formation between fluoresceinamine and the carboxylic acids groups on their surface. Thus obtained CNOs were tested as probe for in vitro imaging of HeLa cells, showing their potential as multifunctional nanomaterial for theranostic applications. More details on CNOs as promising *theranostic agents* are shown in the recent article [270].

Also, a single carbon onion was welded (Fig. 4.98) onto the end of a tungsten tip through an intermediate carbide layer inside a HRTEM, representing a novel type of an *electron field emitter* [271]. Such individual C-onion emitters, similar to CNTs, can sustain large emission currents (>100 μA) and exhibited good long-term emission stability. Authors proposed that these CNO-based emitters can effectively be used as the point electron sources in, for example, high-resolution electron-beam-driven apparatuses in the future.

4.3.6 Nanorice

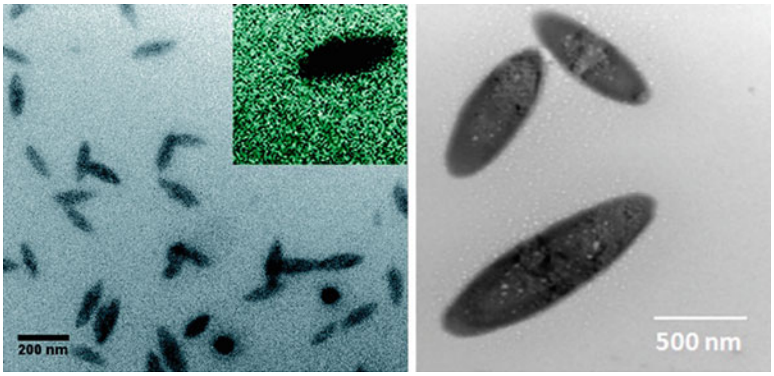

A few reports have been dedicated to a low-temperature hydrothermal synthesis of carbon nanorice. Thus, anisotropic fluorescent carbon nanorice (Fig. 4.99) was hydrothermally prepared, without using any template, from a commercially available beef extract bio-precursor (broth constituent) at a temperature of 150 °C [272]. Authors proposed that these nanorice structures are formed due to the coalescence of initially formed small spherical carbon nanocrystals during hydrothermal treatment. Potential future applications correspond to photonic devices. Carbon nanorice (a diameter in the range of 100 nm and a length of approximately 500 nm) was also prepared by the hydrothermal carbonization of heparin in a Nafion solution at a mild temperature of approximately 100 °C [273]. The mechanism of formation (Fig. 4.100) for this nanoscale rice-like structure was suggested to be a self-assembling process, in which the charring of the heparin caused desulfation followed by

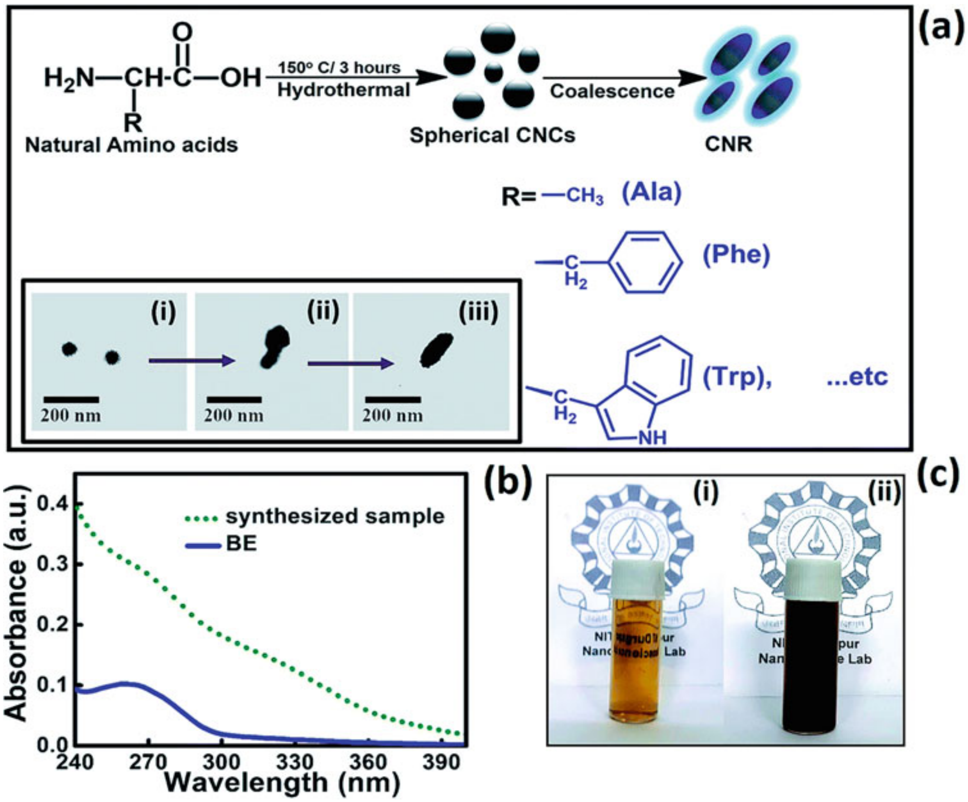

Fig. 4.99 (**a**) Growth model of hydrothermally synthesized CNR structures from commercially available BE precursor. TEM images presented in its inset shows the formation of spherical carbon nanocrystals (i), and via coalescence mechanism (ii), the CNR structures (iii) are formed. (**b**) UV–vis absorption spectra of BE precursor used for the synthesis (solid line) and the as-synthesized CNR sample (dotted line). (**c**) The digital image indicates the color of the BE precursor (i) and as-synthesized CNR sample (ii). (Reproduced with permission of the *Royal Society of Chemistry*)

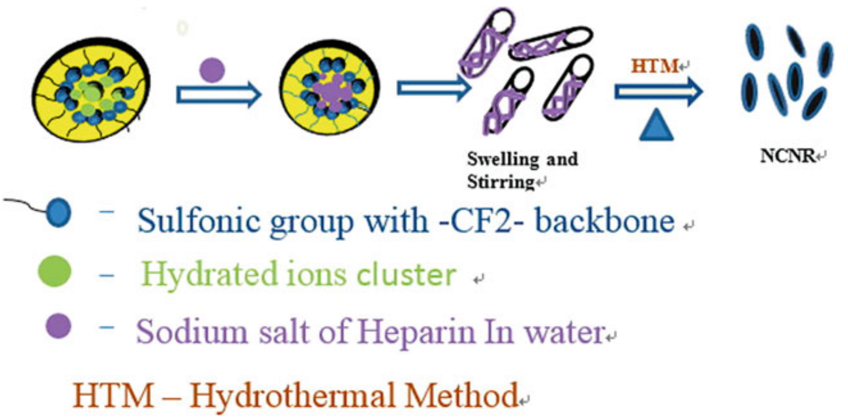

Fig. 4.100 The formation of NCNR by the hydrothermal method from heparin using Nafion membrane as a template. (Reproduced with permission of the *Elsevier Science*)

carbonization, ultimately forming 5-hydroxylmethyl furfural in the presence of a Nafion membrane. Carbon nanorice exhibited fluorescence and so can be useful for biomedical or optoelectronic applications.

4.4 Nanocage-Type Structures

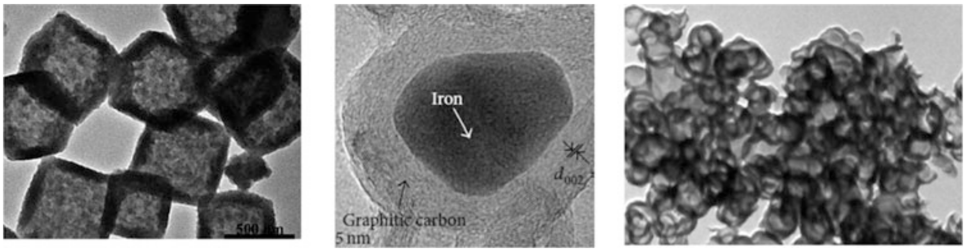

4.4.1 Nanocages[26]

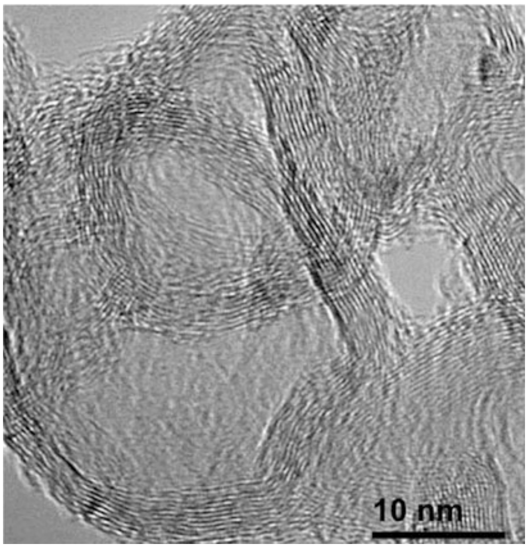

---

[26] The nanocage image is reproduced with permission of *Nature* (*Sci. Rep.*, **2014**, *4*, 4437).

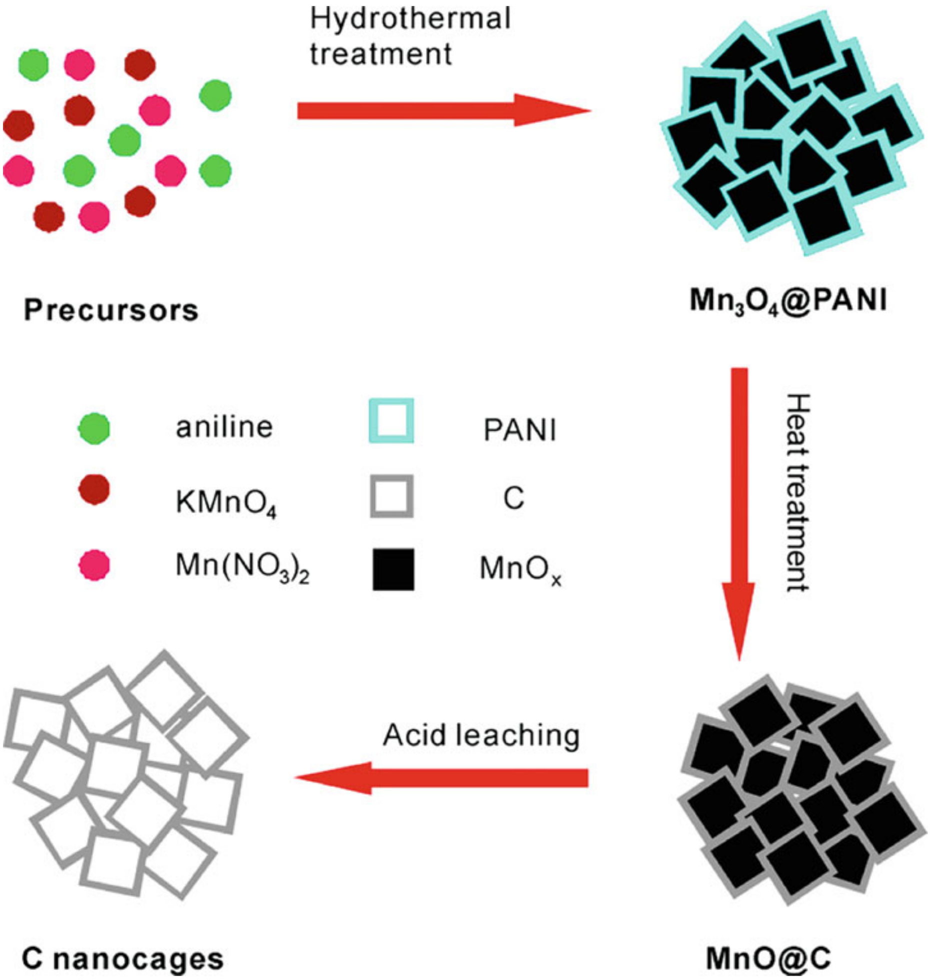

Fig. 4.101 Illustration of the synthetic procedures of carbon nanocages. (Reproduced with permission of the *American Chemical Society*)

Nanocage-type structures include closely related nanocages [274], nanocubes,[27] nanoboxes, and nanocapsules. Carbon cages/boxes have been intensively developed in last 15 years and have various applications (carbon nanocages consisting solely of benzene rings ("all-benzene carbon nanocages") [275] do not fit to the theme of our book). They can be produced by a variety of methods from distinct precursors. Thus, a simple approach for spontaneous, catalyst-free formation of highly graphitic nitrogen-containing carbon nanocages (well-ordered graphitic shells with more compact graphite layer structure than that of conventional bulk graphite) was demonstrated by using commercial available graphite rods as the initial materials [276]. The incorporation of nitrogen into the graphitic backbone of carbon nanocages opens the potential for metal-free catalysis of oxygen reduction reaction in fuel cells. Template synthesis of ultrathin nitrogen-doped graphitic carbon nanocages (CNCs) derived from polyaniline (PANI) and their excellent capacitive properties involved one-pot hydrothermal synthesis of Mn_3O_4@PANI core–shell nanoparticles, carbonization at 800 °C to produce carbon-coated MnO nanoparticles, and then removal of the MnO cores by acidic treatment (Fig. 4.101) [277]. The product showed a great application potential in supercapacitors.

Several methods involve metal addition and/or elimination in reaction steps. Thus, hollow carbon spheres (nanocage sizes of 7.1, 14, and 20 nm in diameter) were prepared [278] using the core–shell (i.e., Cu@C) nanoparticles (obtained by carbonization of the Cu^{2+}–cyclodextrin complexes) at 573 K for 2 h, etching them with HCl (Fig. 4.102). The presence of micropores with an opening of 0.45 nm allowed small molecules to diffuse in and out through the carbon shell, so these nanocages can be filled and used as nanoreactors for catalytic decomposition of methanol. Au nanoparticles were deposited on CNTs, and the nanocages were grown on these gold particles by electrical Joule heating of the CNTs, with further evaporation of metal, leaving the cages intact (Figs. 4.103 and 4.104) [279]. The CNTs were used as a carbon source, and the growth was

---

[27] Nanocubes will be discussed in the section below, dedicated to polyhedral-like carbon nanostructures.

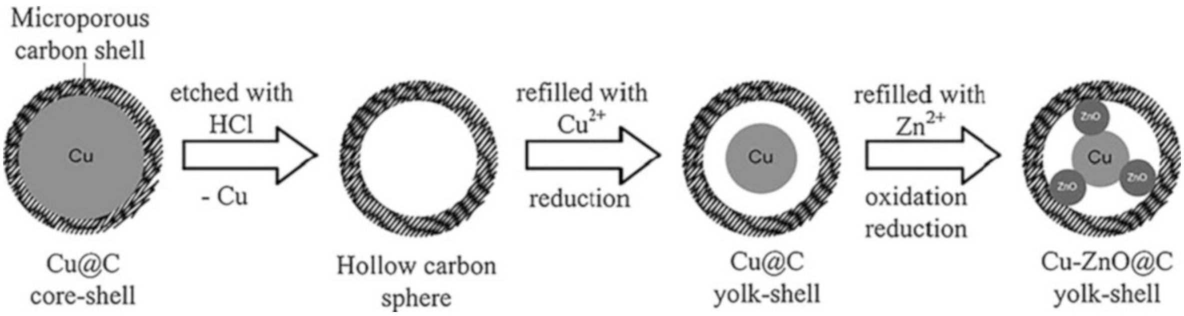

Fig. 4.102 Etching and refilling processes for the preparation of Cu–ZnO@C yolk–shell nanoparticles. (Reproduced with permission of *Springer*)

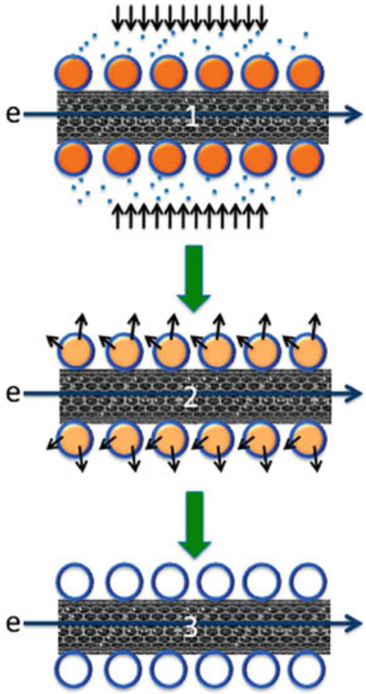

Fig. 4.103 Schematic drawing of the growth process of carbon cages. The arrows labeled with an “e” indicate current passing through the carbon nanotube. (1) A composite of carbon nanotube and gold nanoparticle was contacted by two gold electrodes. An electrical current heated the composite to a temperature when the gold nanoparticles template the deposition of carbon atoms, (2) increasing the current and thus the temperature, lead to the evaporation of the gold nanoparticles, and (3) leaving the empty carbon cages intact. (Reproduced with permission of *Elsevier Science*)

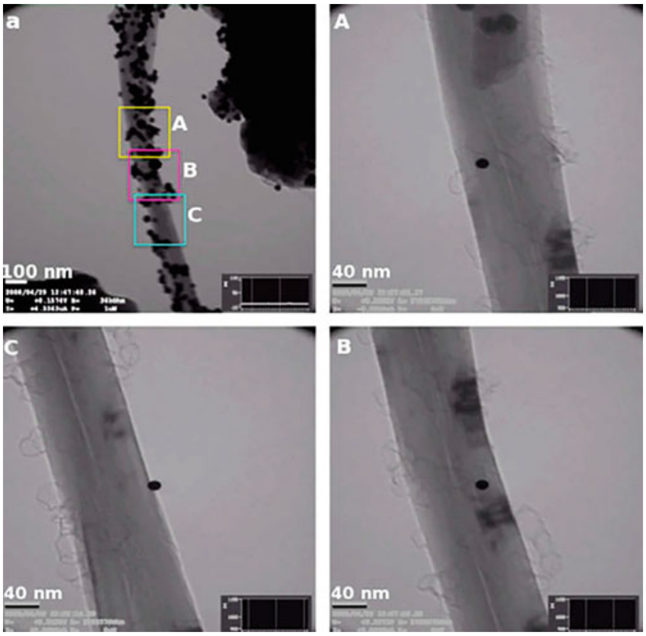

Fig. 4.104 TEM images of the composites of carbon nanotube and gold nanoparticles before (**a**) and after (A, B, and C) gold melting. A, B, and C indicated the three parts on the carbon nanotube in (**a**) where carbon cages were grown. (Reproduced with permission of *Elsevier Science*)

templated by the gold particles, so this gold template technique could provide a general way for fabricating carbon nanostructures of predetermined shape.

Dodecahedral carbon nanocages (NCs, Fig. 4.105) modified with homogenously distributed Fe_3O_4 nanoparticles (Fe_3O_4/C NCs) and possessing a large surface area and inner cavity were obtained (Fig. 4.106) by utilizing a zeolitic imidazolate framework (ZIF-8) as the template and polydopamine (PDA) as the carbon source [280]. Their recommended use is as anode materials in lithium-ion batteries: they display stable capacity retention and cycling performance even at high rates of 3000 mA·g^{-1} in comparison with C NCs.

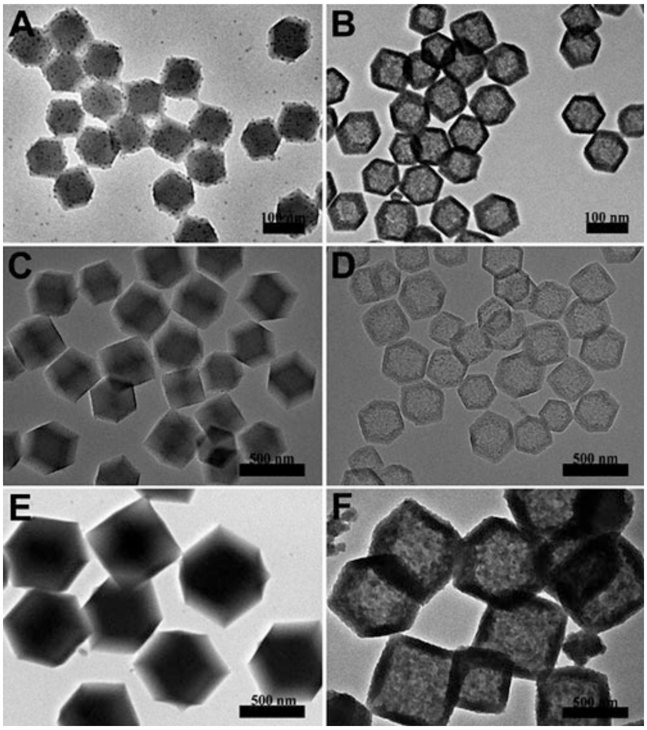

Fig. 4.105 TEM images of Fe_3O_4/ZIF-8 nanostructure with different sizes (97 nm **a**, 350 nm **c**, and 574 nm **e**) and the corresponding Fe_3O_4/C NCs (90 nm **b**, 332 nm **d**, and 561 nm **f**). (Reproduced with permission of the *Royal Society of Chemistry*)

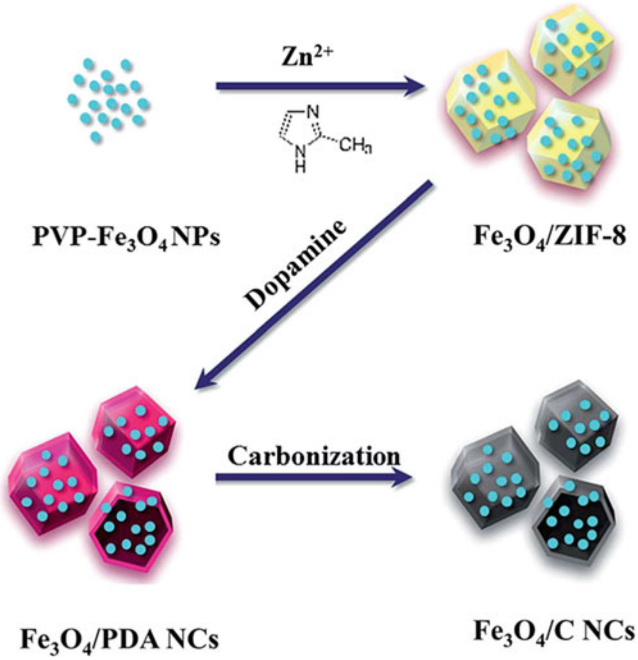

Fig. 4.106 Schematic illustration of the synthesis of Fe_3O_4/C NCs. (Reproduced with permission of the *Royal Society of Chemistry*)

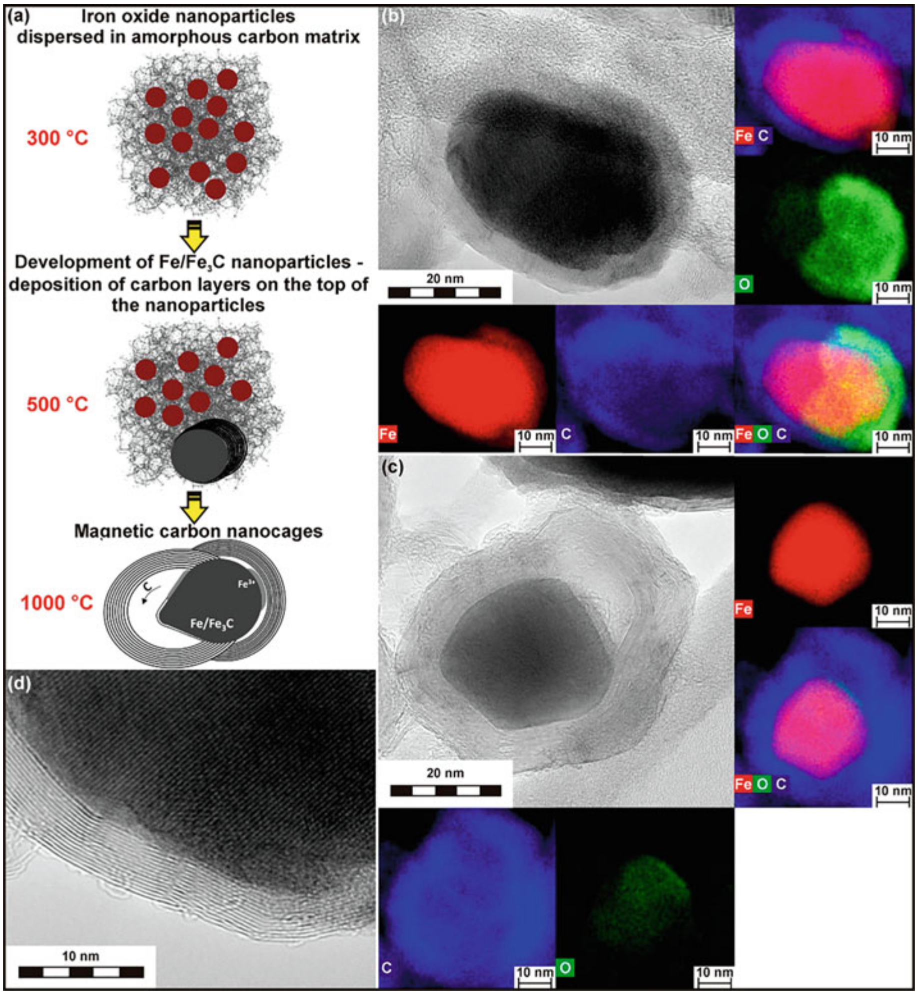

Fig. 4.107 (**a**) Proposed model of formation of magnetic carbon nanocages (Mag@CNCs). (**b–d**) Representative HRTEM images of the Mag@CNCs sample with energy-dispersive X-ray spectroscopy (EDS) elemental mapping (panels **b** and **c**) of selected areas showing Fe, O, and C. (Reproduced with permission of the *American Chemical Society*)

In addition to Fe_3O_4-containing carbon nanocages above, other magnetic iron-containing carbon nanocages with significant surface area (177 $m^2 \cdot g^{-1}$), microporosity, and mesoporosity (Fig. 4.107) were synthesized via a green one-step carbonization process in inert atmosphere using pine resin and iron nitrate salt as a carbon and iron source, respectively [281]. A homogeneous distribution of core–shell-type magnetic nanoparticles within the carbon matrix, formed by iron carbide (Fe_3C) and metallic iron (α-Fe), with sizes of 20–100 nm, surrounded by a few graphitic layers-walls, was observed. The material can be effectively used for As(III) removal from aqueous solutions. Other magnetic carbon nanocages with multiform pore structure (Fig. 4.108), synthesized [282] by a low-temperature carbonization process from biorenewable lignin, possessed a high degree of graphitization crystallinity and can be used as efficient and recycled adsorbents in the removal of dye staff from textile wastewater. Nanocages can be functionalized, as many other nanocarbons such as grapheme or CNTs. Thus, functionalization of ordered cage-type mesoporous carbons through oxidation using ammonium perchlorate led to carboxy carbon nanocage [283]. The degree of functionalization can be easily controlled by the adjustment of the oxidation parameters such as oxidation time, AP concentration, and oxidation temperature.

In addition to applications above, carbon nanocages are frequently used as electrocatalysts for *oxygen reduction and evolution*. Thus, double-shelled hybrid nanocages with outer shells of Co–N-doped graphitic carbon (Co-NGC) and inner shells of N-doped microporous carbon (NC) were elaborated (Fig. 4.109) by templating against core–shell metal–organic frameworks [284] exhibiting superior electrocatalytic properties to Pt and RuO_2 as a bifunctional electrocatalyst for ORR and OER. First-principles calculations revealed that the high catalytic activities of Co-NGC shells are due to the synergistic electron transfer and redistribution between the Co nanoparticles, the graphitic carbon, and the doped N species. The high ORR activity of the defective carbon nanocages (better than that of the B-doped carbon nanotubes and comparable to that of

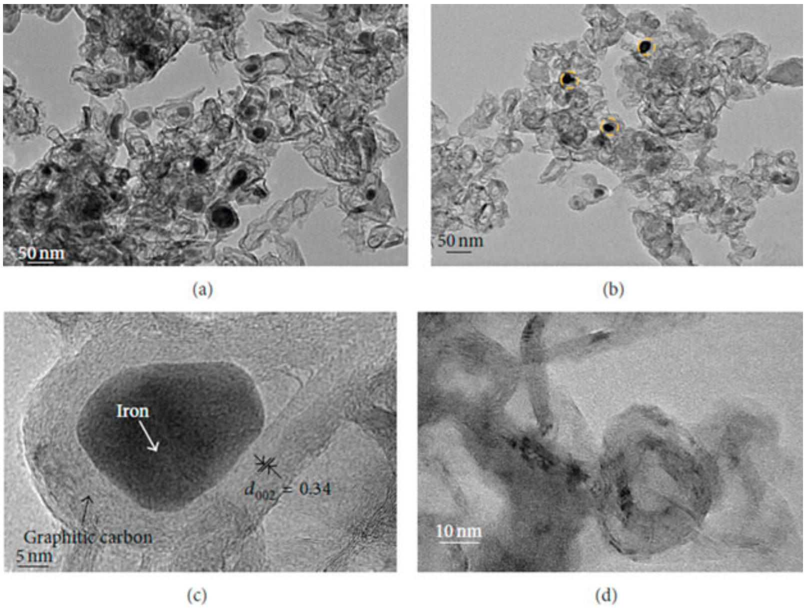

Fig. 4.108 (**a**) TEM and (**c**) HRTEM image of magnetic carbon nanocages before acid treatment; (**b**) TEM and (**d**) HRTEM image of magnetic carbon nanocages after acid treatment. (Reproduced with permission of *Hindawi*)

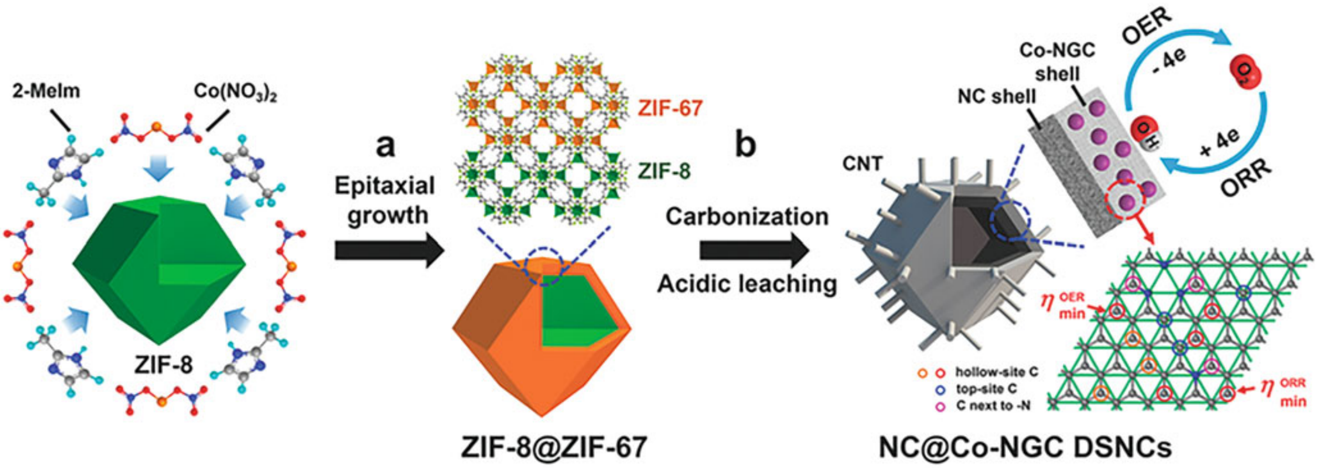

Fig. 4.109 Schematic illustration of the synthesis of NC@Co-NGC DSNCs. (**a**) The growth of core–shell-structured ZIF-8@ZIF-67 crystals by epitaxial growth of ZIF-67 on preformed ZIF-8 polyhedral nanoparticles. (**b**) The formation of NC@Co-NGC DSNCs by annealing the core–shell ZIF-8@ZIF-67 crystals in flowing N_2 at 800 °C, followed by acid washing. (Reproduced with permission of the *Wiley*)

the N-doped carbon nanostructures) was attributed, using DFT calculations, to pentagon and zigzag edge defects (Fig. 4.110) [285]. The carbon nanocages prepared at 700 °C presented a quite good ORR performance with a high onset potential of ~0.11 V versus the normal hydrogen electrode in a 0.1 mol/L KOH solution. Significant contribution of the intrinsic carbon defects to ORR activity was demonstrated.

Other uses are related with such properties of nanocages as adsorbents, sensors, and materials for supercapacitors. Thus, the hierarchical carbon nanocages (hCNC) were proposed as high-rate anodes for Li- and Na-ion batteries [286]. For the same purpose (Li-ion batteries), carbon nanocage-supported synthesis of V_2O_5 nanorods and V_2O_5/TiO_2 nanocomposites was carried out by a carbon nanocage (CNC)-assisted growth process, using vanadium triisopropoxide oxide and titanium isopropoxide precursors in air at 500 °C [287].

Large-pore cage-type mesoporous carbon nanocages, abbreviated by authors as CKT (carbon from KIT-5) using 3D large cage-type face-centered cubic *Fm3m* mesoporous silica materials (KIT-5) as inorganic templates prepared at different temperature [288], showed high adsorption capacity for amino acid (histidine), flavonoid (catechin), vitamin (vitamin E,

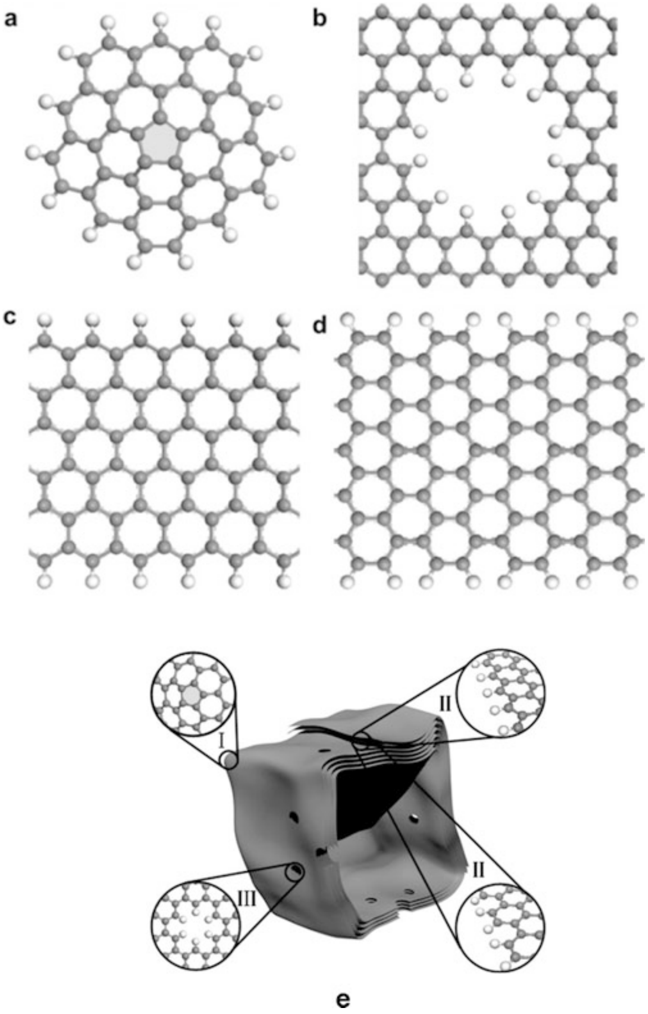

Fig. 4.110 Defect models used for theoretical calculations. (**a**) Pentagon (highlight). (**b**) Hole. (**c**) Zigzag edge. (**d**) Armchair edge. The gray and white spheres represent C and H atoms, respectively. (**e**) Schematic structural characters of the carbon nanocages. (Reproduced with permission of the *American Chemical Society*)

α-tocopherol), endocrine disrupter (nonylphenol), and enzyme (lysozyme) and other biomolecules (Fig. 4.111). Carbon nanocage can also be useful for entrapment of harmful aromatic molecules [289]. Also, a thin-walled graphitic nanocage material with well-developed graphitic structure, large specific surface area, and pronounced mesoporosity was synthesized and used to construct a sensing interface for an amperometric glucose biosensor, showing a high and reproducible sensitivity [290].

4.4.2 *Nanoboxes*

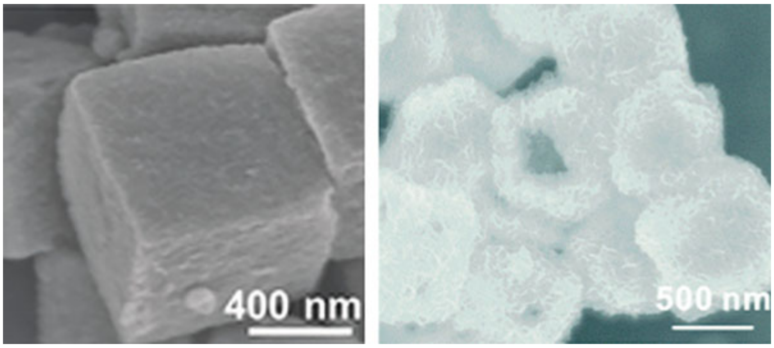

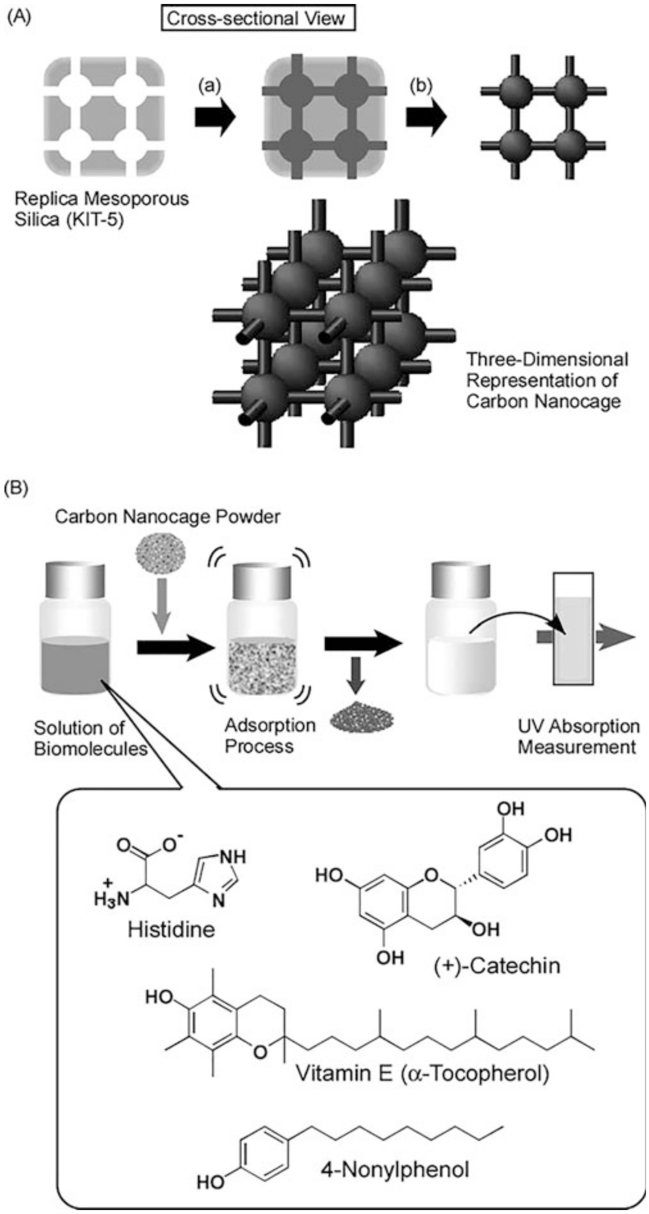

Fig. 4.111 (**a**) Schematic illustration of preparation of the carbon nanocage and (**b**) schematic illustration of adsorption experiment. (Reproduced with permission of *Springer*)

Among several other carbon nanostructures, the nanoboxes were recently reviewed [291]. Main applications correspond to the catalytic and electrochemical areas too, as well as for other nanocage-like structures above. They are normally prepared from organic carbon-rich compounds and metal-containing frameworks, although a direct conversion of carbon dioxide can also lead to shape-controlled formation of nanocarbons [292]. As an example, N-doped porous and highly graphitic carbon nanobox-supported Fe-based nanoparticles (Fe–N-CNBs) were prepared from fructose, NH_3, and $FeCl_3$ by a self-propagating high-temperature synthesis process (Fig. 4.112) followed by a heat treatment process and used as ORR catalysts, showing to have a similar efficiency than expensive Pt/C catalyst in Zn–air batteries [293].

Multicomponent $MoS_2/Co_9S_8/C$ hollow nanocubes, solvothermally produced (Fig. 4.113) and subjected to a subsequent calcination process [294], showed high capacity, rate capability as the anode of sodium-ion batteries, and further potential usage for energy storage devices. Hybrid core–shell nanoboxes CoSe@CNBs (CoSe-enriched inner shell is located within a

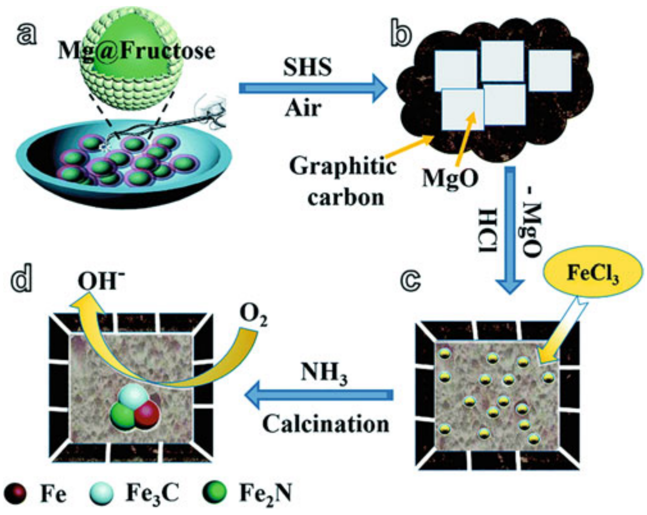

Fig. 4.112 The synthesis process of the Fe–N-CNBs electrocatalysts. (Reproduced with permission of the *Royal Society of Chemistry*)

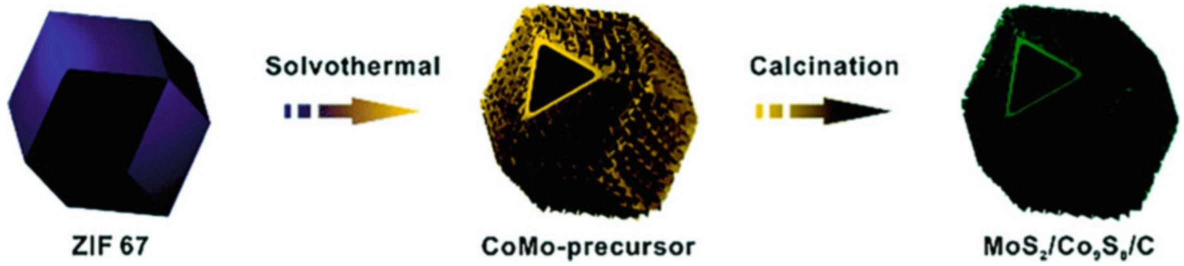

Fig. 4.113 Illustration of the formation of the $MoS_2/Co_9S_8/C$ nanobox by a solvothermal method and a subsequent calcination process. (Reproduced with permission of the *Royal Society of Chemistry*)

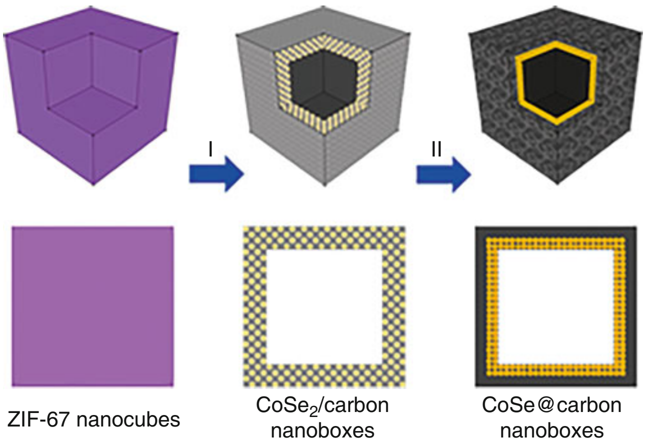

Fig. 4.114 Schematic illustration of the formation process of CoSe@carbon nanoboxes: (I) formation of $CoSe_2$/carbon nanoboxes by annealing ZIF-67 nanocubes and Se powder at 350 °C for 2 h in a nitrogen atmosphere and (II) the growth of CoSe@carbon nanoboxes by further annealing $CoSe_2$/carbon nanoboxes at 600 °C for another 2 h in a nitrogen atmosphere. (Reproduced with permission of *Wiley*)

carbon-enriched outer shell) were synthesized through manipulation of the template-engaged reaction between Co-based zeolitic imidazolate framework (ZIF-67) nanocubes and Se powder at 350 °C (Fig. 4.114) [295]. These nanoboxes showed excellent lithium-storage performance in terms of high specific capacity, excellent cycling stability, exceptional rate capability, and high initial Coulombic efficiency.

4.4.3 Nanocapsules

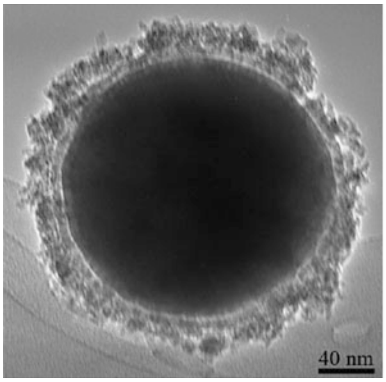

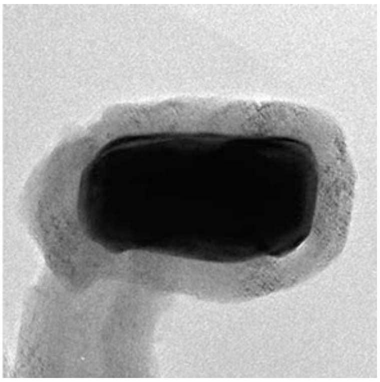

Capsule-like nanostructures[28] for carbon have become widespread during last decade. They can be hollow or metal-filled (main attention is paid nowadays to the last type), possessing simple or core–shell structures. Despite their similarity with nanocubes and nanoboxes, there are several differences in their synthesis, for example, more frequent use of arc-discharge methods. However, classic thermal methods as pyrolysis are also common. Thus, controlled synthesis of uniformly shaped carbon hollow structures was carried out by an ethanol-assisted thermolysis of zinc acetate [296]. It was revealed that the generated zinc oxide nanostructures acted as in situ templates to form (reactions 4.10–4.12) the carbon hollow structures {nanospheres, nanocapsules (Figs. 4.115, 4.116, and 4.117), nanorods, and microtubes}. These as-synthesized carbon hollow

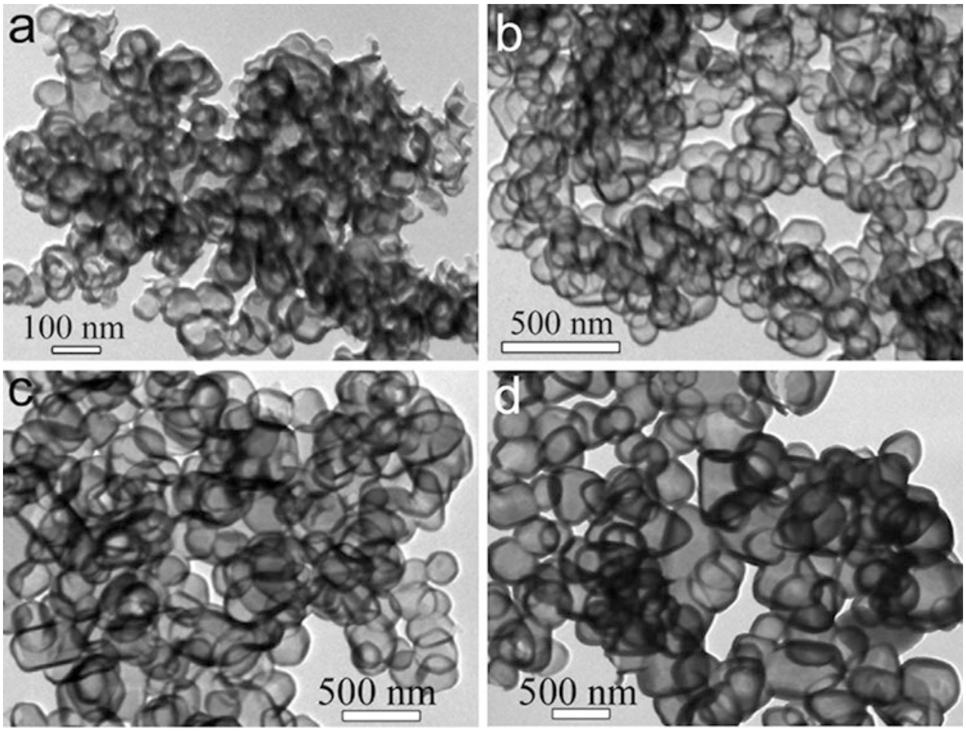

Fig. 4.115 TEM images of carbon nanocapsules prepared by ethanol-assisted thermolysis of $Zn(Ac)_2$ at 600 °C for different times: (**a**) 3 h, (**b**) 6 h, (**c**) 24 h, and (**d**) 48 h. (Reproduced with permission of the *American Chemical Society*)

---

[28] The nanocapsule images above are reproduced with permission of *Elsevier Science* (left, *Materials Chemistry and Physics*, **2010**, *122*, 164–168) and *Hindawi* (right, *Journal of Nanotechnology*, **Volume 2012**, Article ID 613746, 6 pp.).

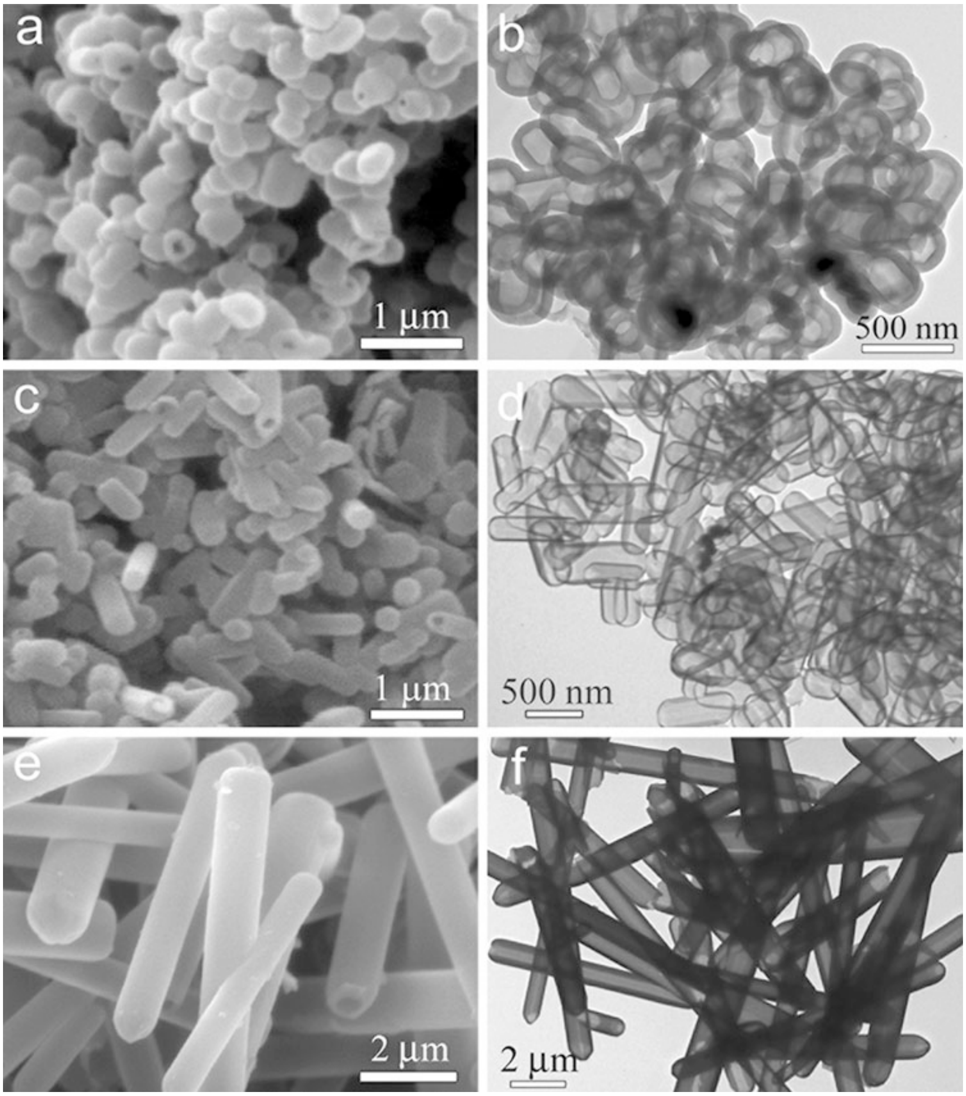

Fig. 4.116 SEM and TEM images of the samples obtained by ethanol-assisted thermolysis of $Zn(Ac)_2$, which was first heated at 400 °C for different times and then heated to 600 °C for 12 h. (**a**, **b**) 1 h, (**c**, **d**) 3 h, and (**e**, **f**) 6 h. (Reproduced with permission of the *American Chemical Society*)

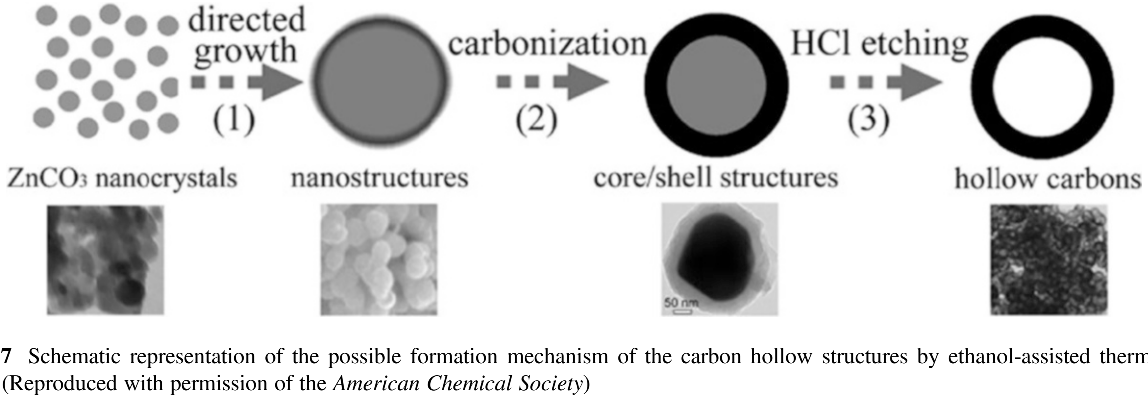

Fig. 4.117 Schematic representation of the possible formation mechanism of the carbon hollow structures by ethanol-assisted thermolysis of $Zn(Ac)_2$. (Reproduced with permission of the *American Chemical Society*)

structures exhibited excellent thermal and structural stability to temperatures as high as 1200 °C. Another example of hollow capsules is monodisperse hollow core–shell carbon nanocapsules (<200 nm) with mesoporous shells, prepared by coating their outer shells with silica to prevent aggregation during their high-temperature annealing [297] (starting material, monodispersed silica nanoparticles; carbon source, octadecyltrimethoxysilane). The drug-loading and drug-release properties of these hollow carbon nanocapsules were also investigated.

$$CH_3COOZnOOCCH_3 \rightarrow ZnCO_3 + CH_3COCH_3 \qquad (4.10)$$

$$ZnCO_3 \rightarrow ZnO + CO_2 \qquad (4.11)$$

$$\textit{In presence of ZnO}: mCH_3COCH_3 + nCH_3CH_2OH \rightarrow ZnO@C \text{ structures} + (2m+n)H_2 + (m-n)H_2O \qquad (4.12)$$

Magnetic metals, their oxides, and carbides are the center of attention in developing core–shell carbon nanocapsules, due to many catalytic and electrochemical applications. Thus, decomposition of hydrocarbons (methane, ethane, and ethylene) on the nickel catalyst led to the formation of many disordered carbon structures and Ni nanocapsules coated with a graphite layer [298]. Electromagnetic wave absorption properties of FeNiMo/C nanocapsules with FeNiMo nanoparticles as cores and carbon as shells were studied [299]. These nanocapsules, synthesized by arc-discharging $Fe_{11}Ni_{79}Mo_{10}$ (at.%) alloy in ethanol, exhibited outstanding reflection loss ($RL < -20$ dB) in the range of 13–17.8 GHz with an absorber thickness of 1.7 mm, and an optimal RL of −64.0 dB was obtained at 13.2 GHz with an absorber thickness of 1.9 mm. The excellent electromagnetic properties were ascribed to the good match between high permeability from the core of FeNiMo nanoparticles and low permittivity from the special core–shell microstructure in the FeNiMo/C nanocapsules.

Fe-filled core–shell carbon nanocapsules (<40 nm; shells, deformed graphite layers; core, α-Fe and γ-Fe in the form of single crystals, Fe_3C) with a narrow size distribution and high magnetization were synthesized by a discharge in ethanol [300]. A MgO-filled rectangular carbon nanocapsules (40–60 nm) were fabricated by pyrolyzing acetonitrile with the assistance of MgO and a small quantity of Fe^{3+} [301]. A small quantity of Fe catalysts plays an important role in their growth. Carbon-encapsulated Fe_3O_4, γ-Fe_2O_3, and Fe nanostructures were prepared using FeOOH as a precursor and carbon nanocapsules as nanoreactors via controllable thermal transformation processes [302]. The magnetic property investigation revealed that all these nanostructures exhibited ferromagnetic behavior with quite high saturation magnetizations. Nanoparticles of iron carbides wrapped in multilayered graphitic sheets (carbon nanocapsules, 100–200 nm) were made by electric plasma discharge in an ultrasonic cavitation field in liquid ethanol, purified by selective oxidation and magnetic separation, and covered with PEG [303]. Also, Fe_3C-encapsulated carbon nanocapsules and carbon nanotubes were synthesized from C_{60}-saturated toluene solution and a solution of 2-propanol containing ferric nitrate nonahydrate ($Fe(NO_3)_3 \cdot 9H_2O$) yielding iron-(Fe-)doped C_{60} nanowhiskers, which were converted to the final product by heating at 1173 K [304]. In addition, core–shell-structured nanocapsules consisting of a nickel ferrite ($NiFe_2O_4$) nanoparticle core encapsulated in an onion-like carbon (C) shell were prepared by a modified arc-discharge method followed by an air annealing process and used in lithium-ion batteries retaining the $NiFe_2O_4$/onion-like C morphology after 500 cycles [305].

For the case of nonferrous metals, carbon-coated Cu nanocapsules were synthesized by an arc-discharge method, and the paraffin-Cu/C nanocapsule composite showed excellent electromagnetic absorption properties [306]. Starting with graphitic carbon nitride g-C_3N_4 and $Co(CH_3COO)_2 \cdot 4H_2O$ as precursors and as the only reactants (Fig. 4.118), Co nanoparticle-encapsulated N-doped carbon nanocapsules with a tetragonal microstructure (Fig. 4.119) were prepared without any template

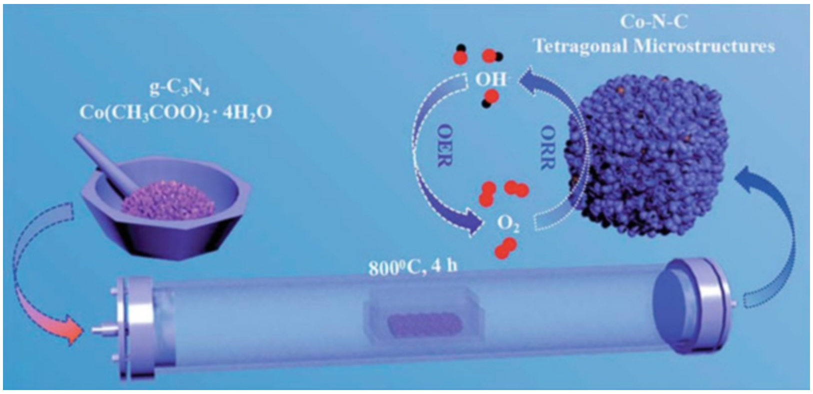

Fig. 4.118 Schematic illustration of the preparation of Co–N–C tetragonal microstructures. (Reproduced with permission of the *Royal Society of Chemistry*)

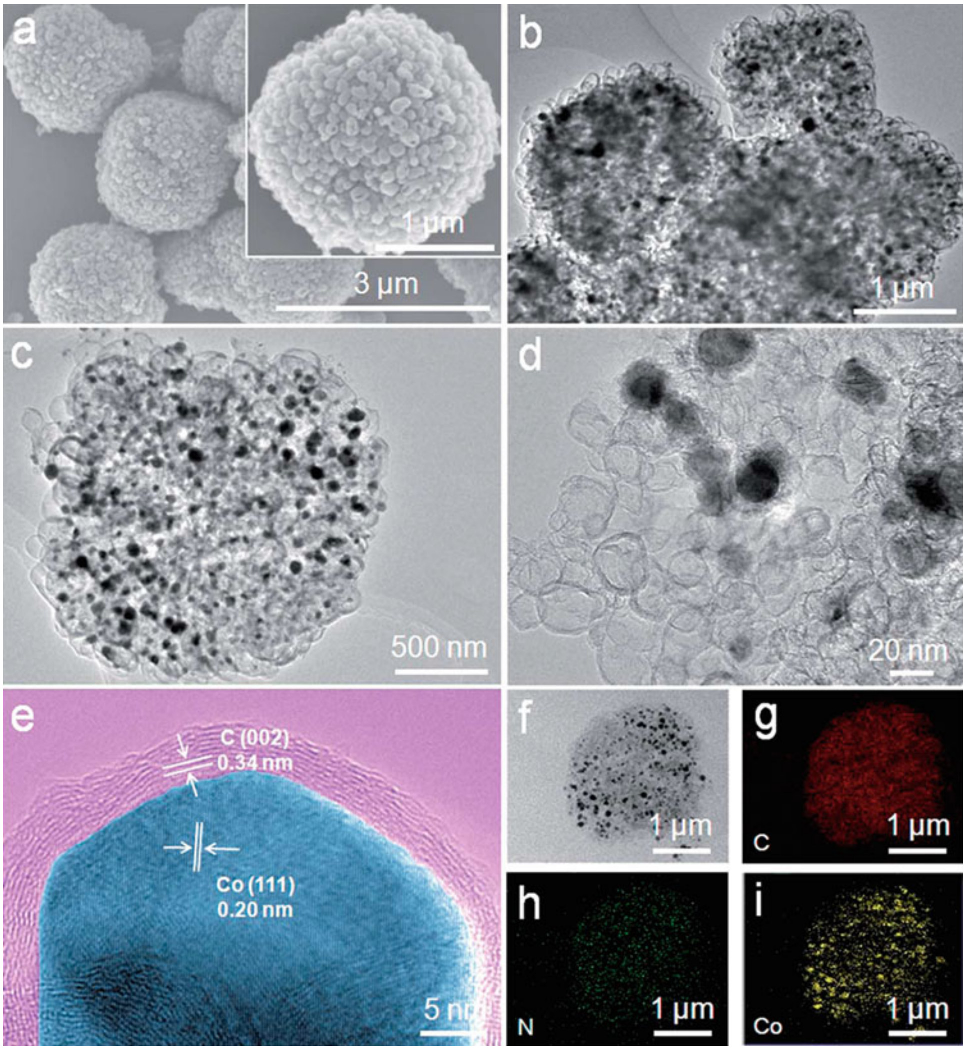

Fig. 4.119 (**a**) SEM image of the as-prepared sample Co–N–C-0.4. The inset in (**a**) shows a single tetragonal microstructure. (**b–d**) TEM images, (**e**) HRTEM image, and (**f**) STEM image of the sample Co–N–C-0.4. (**g–i**) Elemental mapping images of carbon, nitrogen, and cobalt, respectively. (Reproduced with permission of the *Royal Society of Chemistry*)

[307]. This stable catalyst showed excellent catalytic performance for both the ORR and OER. We also note that in situ oxidation of similar carbon-encapsulated cobalt nanocapsules (prepared from metallic cobalt and ethanol by modified arc-discharge technique) allowed to create highly active cobalt oxide catalysts (Fig. 4.120) for hydrocarbon combustion [308].

Possibility of solubilization and dispersion of nanocarbons, together with their toxicity [309], is an important aspect related with biomedical applications, among others. In case of nanocapsules, the solubility of nanospherical carbon nanocapsules was improved (Fig. 4.121) by using platelet-like clays (fluorinated mica, sodium montmorillonite, and synthetic smectite) [310]. We note that the second effective dispersing agent was also used for solubilization of CNTs [311]. This is a representative example on how 2D nanomaterials revealed powerful ability to redistribute or block the aggregated 0D or 1D nanomaterials improving their "solubility." Water-dispersible carbon nanocapsules were also produced from a glycine solution by generating a pulsed arc discharge on the surface of the glycine solution under pressurized argon (Fig. 4.122) [312].

In addition to the applications above, carbon nanocapsules are used for chemotherapeutic delivery (cisplatin@US-tube carbon nanocapsules) [313], for imaging (radiometal-filled nanocapsules (^{64}Cu)) [314], for multifunctional superhydrophobic coatings (on the basis of mesoporous carbon nanocapsules with polyvinylidene fluoride) [315], and even for such nontraditional purposes (for the case of nanocarbons) as production of poly(D,L-lactic acid) nonwoven nanofiber mat [316].

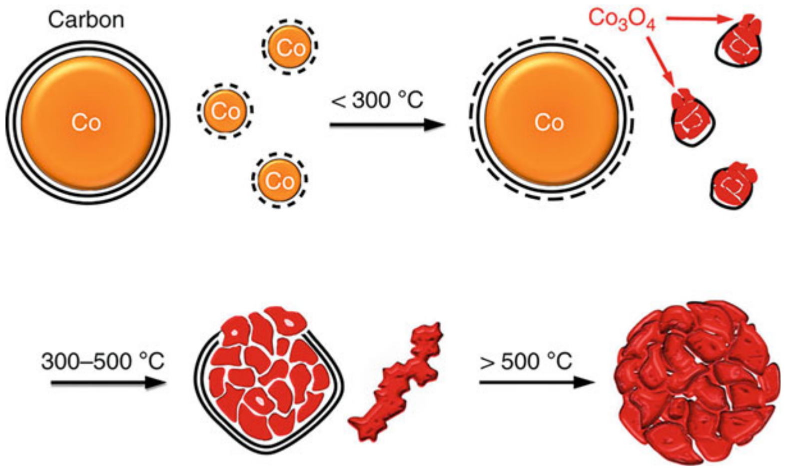

Fig. 4.120 Scheme for the transformation process of the Co_3O_4 catalyst. (Reproduced with permission of the *Nature*)

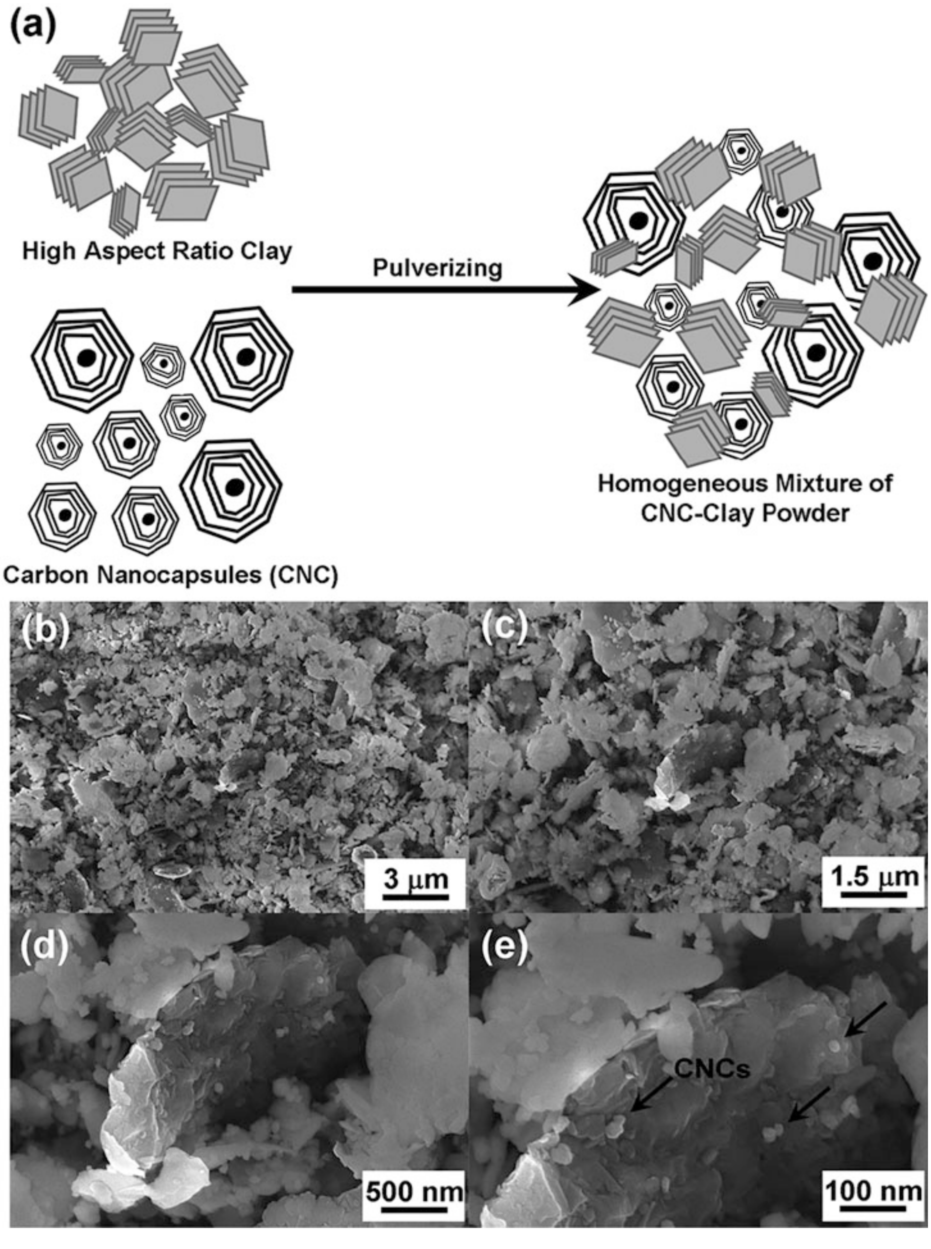

Fig. 4.121 (**a**) Conceptual diagram of dispersing carbon nanocapsules by nanoshaped exclusion. (**b**–**e**) FESEM of CNC-Mica mixture after pulverized. (Reproduced with permission of the *American Institute of Physics*)

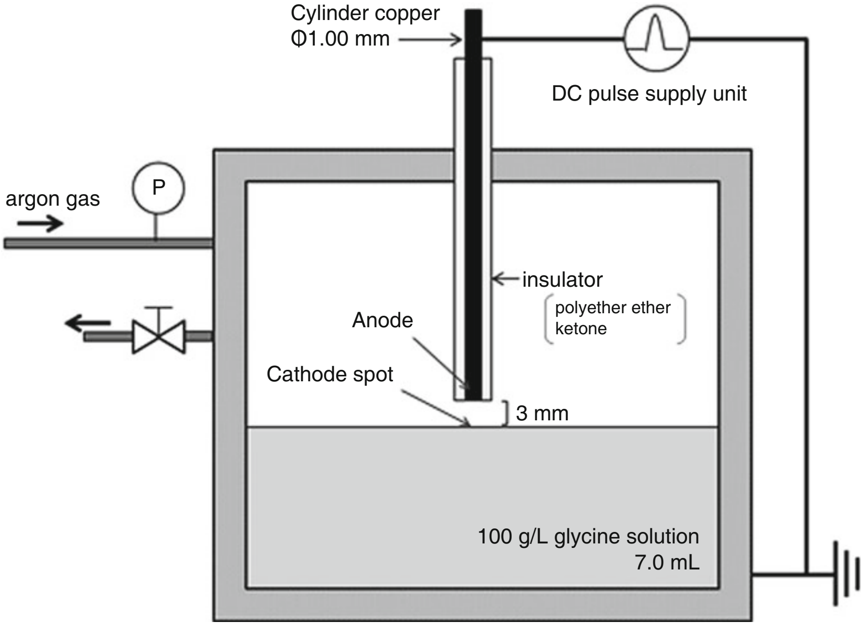

Fig. 4.122 Schematic of experimental apparatus to obtain water-dispersible carbon nanocapsules. (Reproduced with permission of *Springer*)

4.5 "Nanovegetation" World

4.5.1 Nanotrees in General

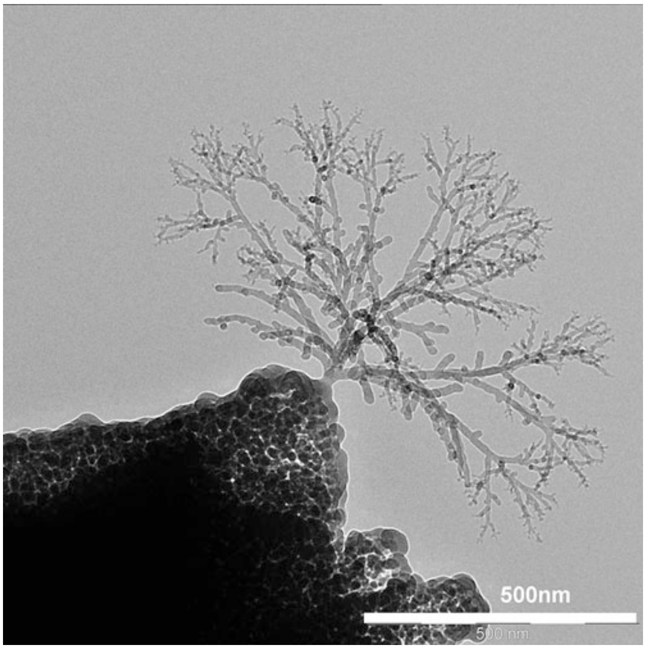

Fig. 4.123 Carbon tree-like nanostructures, obtained in porous silicon sample [318]. (Reproduced with permission of the *Elsevier Science*. Borrowed from *Micron*, **2009**, *40*, 80–84.)

Tree-like is a relatively frequent nano- and microstructural type, obtained for a series of inorganic compounds, mostly for silicon, silica, and carbon. Generally, nanotrees[29] are closely related to nanowires, which are modified with branches, sometimes they are produced from them [317], and can appear together with other nanostructures. Beautiful porous carbon tree-like nanostructures (Fig. 4.123) were obtained [319] (as well as SiC above) by electron-beam-induced deposition method using a TEM in poor vacuum conditions where hydrocarbons (being attracted to the substrates by the local electric fields) were present in the chamber. The authors found that the adequate ion dose to create well-defined sawtooth nano-patterns was between 8 and 10 nC/mm^2. A high concentration of sp^2 sites in nanostructures was revealed suggesting that they were made of graphite-like hydrogenated amorphous carbon. Y-junction hollow carbon nanotrees (with close-ended branches but open-ended roots, length ~5 μm, an average external trunk diameter of ~500 nm, branch diameters ranging from 70 to 100 nm, and wall thickness ranging from 24 to 30 nm) were obtained in a 90% yield by the reaction of ferrocene with 1,2-dichlorobenzene at 180 °C [320]. A simple and effective method based on Coulomb effect for separating SWCNTs from their bundles was developed [321]. The separated SWCNTs were radially distributed at the end of the original bundle and finally formed a nanotree (Fig. 4.124). The formation mechanism was proposed to be Coulomb explosion. As an important application of carbon nanotrees, the fuel cell, equipped with an anode and/or a cathode containing carbon–metal nanotree catalysts consisting of CNT trunks having a plurality of highly oriented carbon nanotube branches, where a metal is attached on inner and/or outer surfaces of the tubes [322], provided high-power generation efficiency by accelerating catalytic functions.

Y- (two-branched carbon nanofibers are connected to a short graphite nanorod supporting them) and comb-type (a second generation of carbon nanofibers nucleate on the inclined carbon nanorods to form a comb-like nanotree, where several parallel carbon nanofibers are lined up) crystallized carbon nanotrees (Fig. 4.125) with continuous connections of the branches were formed from branched carbon nanofibers grown by plasma-enhanced CVD [323]. It was revealed that the splitting of large catalyst particles is required for both kinds of nanotrees, whatever the involved growth mechanism. Stepwise formation of branched carbon nanotrees is shown in Fig. 4.126.

---

[29] The nanotree image above is reproduced with permission of the *American Chemical Society* (*Nano Lett.*, **2009**, *9*(1), 239–244).

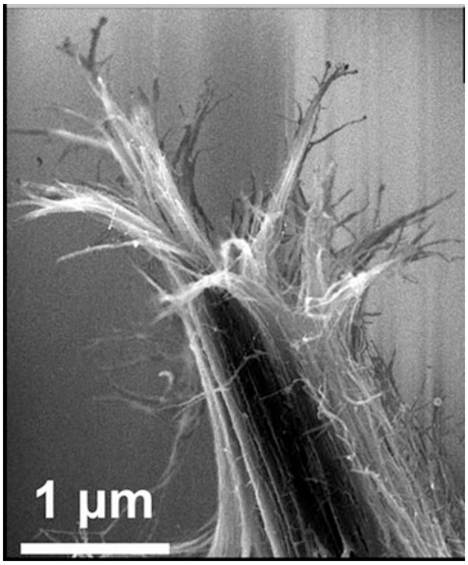

Fig. 4.124 Typical nanotree image of SWCNTs formed at the breaking points of SWCNTs bundle. (Reproduced with permission of the *American Chemical Society*)

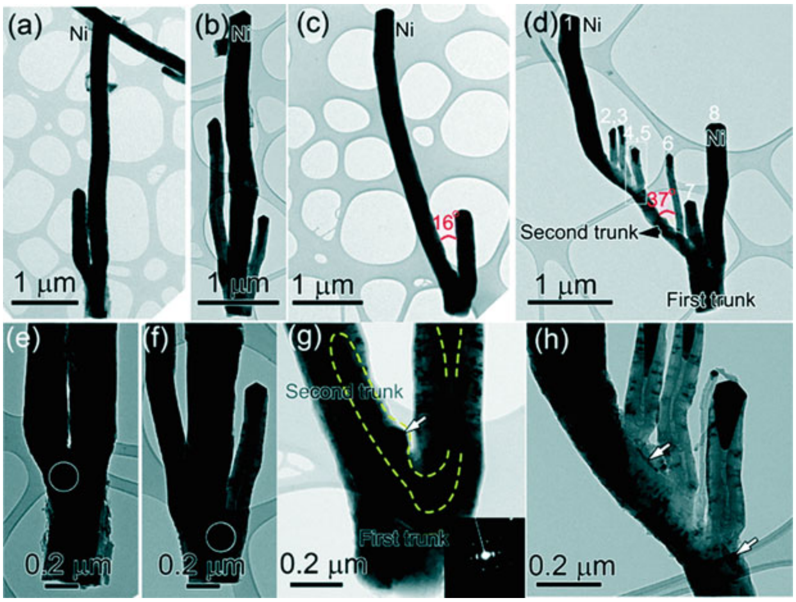

Fig. 4.125 First row: bright field TEM images of branched carbon nanotrees taken at low magnifications. (**a**) A Y-type nanotree with parallel CNF branches; (**b**) a carbon nanotree with three branches; (**c**) a Y-type nanotree with one inclined CNF branch; (**d**) a comb-type nanotree with eight parallel CNF branches. Second row (**e**–**h**): enlarged TEM images of the branching regions of the carbon nanotrees from the first row. The triangle particle at the lower part in (**g**) is tilted to the $[110]_{\mathrm{Ni}}$ direction, as seen in the inserted EDP. (Reproduced with permission of the *Royal Society of Chemistry*)

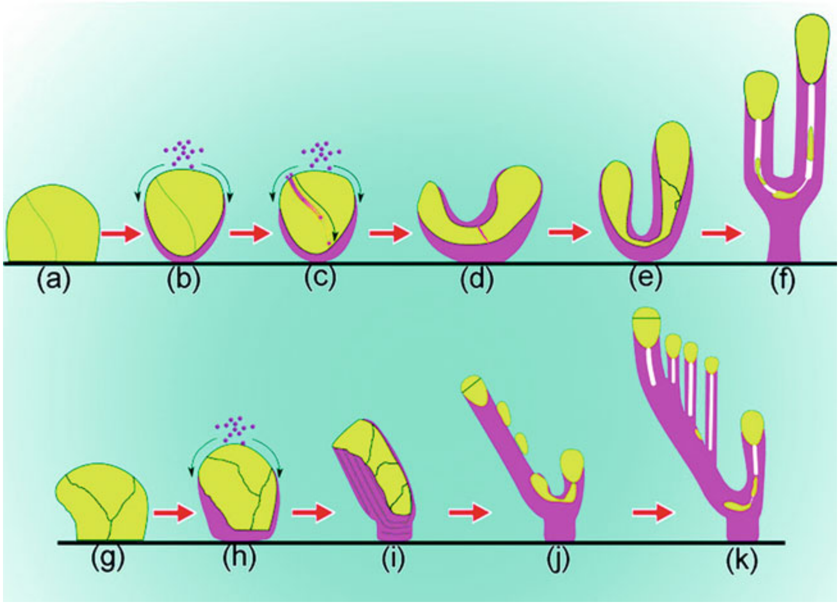

Fig. 4.126 A schematic diagram of the process of generating branched carbon nanotrees. First row (**a–f**): the different steps of the formation of a Y-type connection with parallel CNF branches. Second row (**g–k**): the different steps of the formation of a comb-type connection. The splitting of the large particles is found to be the primary reason for the formation of branched CNFs. (Reproduced with permission of the *Royal Society of Chemistry*)

4.5.2 Nanopalms

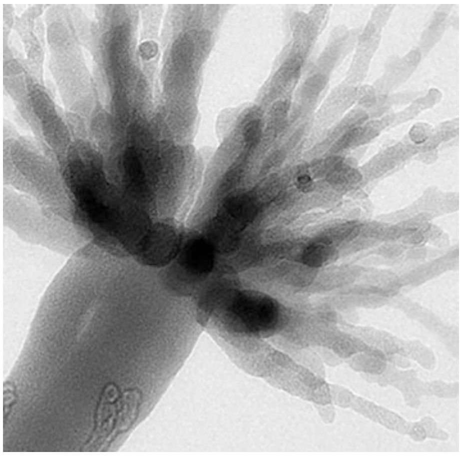

Nanopalm-like carbon-containing trees are practically unknown. Silica nanowires (diameters in the range of 15–49 nm and lengths up to 500 nm), obtained by electron-beam irradiation on porous silicon films, were exposed to poor vacuum conditions in which carbon aggregation from the surrounding gas was promoted by the local electric fields enhanced at the tip of the silica wires, leading to heterostructures showing a nanopalm-like shape (see figure above) [324, 325].

4.5.3 Nanoleaves

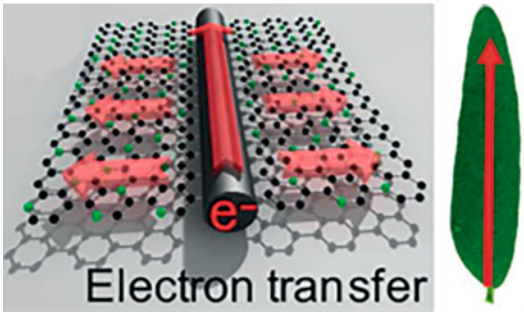

Leaf-like nanostructures are known mainly for metal oxides, although some metals, intermetallic compounds, and metal salts have been also reported, as well as carbon. On the basis of the facts that "…nature always gives us inspiration.… It is well known that a 'leaf' can be simply considered as a hierarchical structure of leaf-blades and leaf-veins coupled with many branches. This exquisite structure ensures that moisture and nutrients are very quickly and adequately delivered to the whole blade through the veins" [326], *L. Chen et al.* asked the question of whether CNTs can be simulated into leaf-like structures with structural controllability through simple processing. As a result, carbon nanoleaf framework, possessing low density, large surface area, and good conductivity, was fabricated (Fig. 4.127) using MWCNTs as a single precursor useful for ORR catalysis. The carbon nanoleaves consisted of two building blocks (Fig. 4.128) in which 1D CNTs were bridged with 1D graphene nanoribbons (GNRs). Various applications, such as supercapacitors, batteries, and oxygen sensors, were offered for these nanostructures.

Highly integrated carbon nanofiber@nitrogen-doped graphene (CNF@NG) "vein-leaf" 3D complexes connected by carbon–carbon bonds were prepared [327] (Fig. 4.129) from biomass (urea and bacterial cellulose) by thermal condensation (calcination) and applied in the ORR exhibiting high activity, excellent tolerance to methanol, and superior stability in alkaline solutions. Carbon nanofibers played the role of the skeleton and nitrogen-doped graphene as the leaf (Fig. 4.130). The conductivity of the monolith of CNF@NG was a little bit higher than that of the bare CNF monolith, demonstrating the advantage of such a "leaf vein" structure for electron transfer by following the principle of water transfer inside real leaves

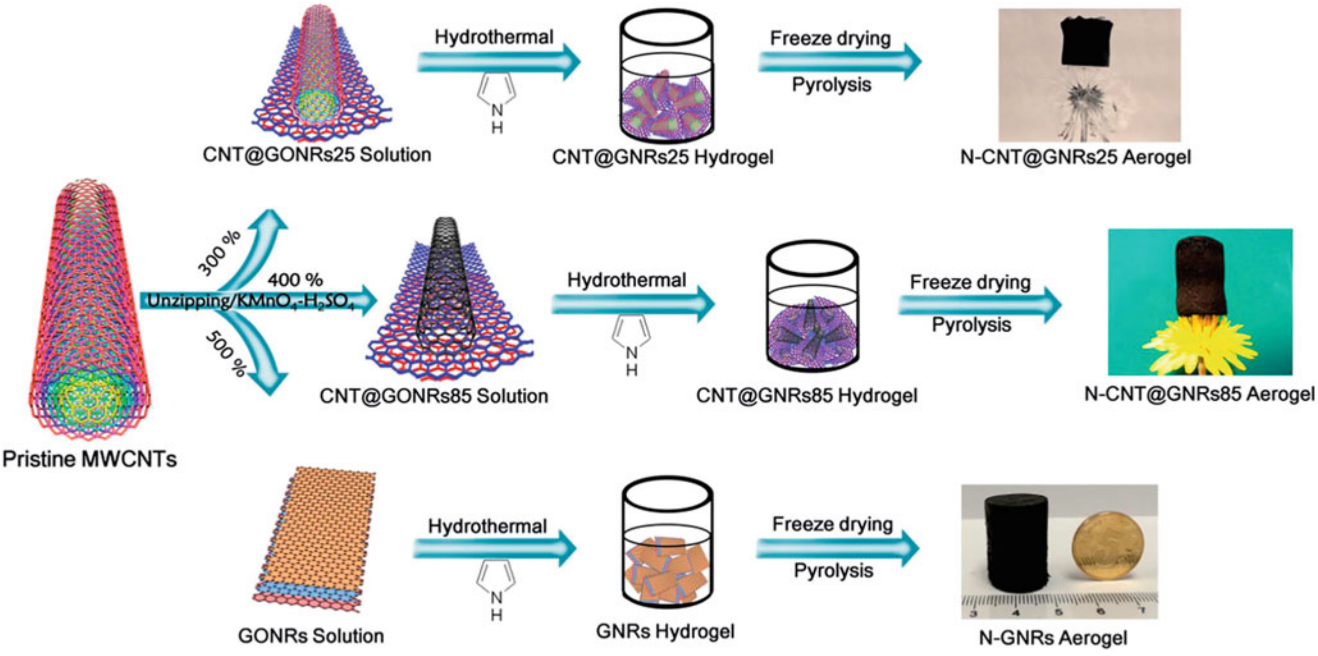

Fig. 4.127 Illustration of the synthetic route for two kinds of carbon nanoleaf aerogels (N-CNT@GNRs25-A and N-CNT@GNRs85-A) and the reference sample (N-GNRs-A). The last image in each row shows the corresponding aerogel. (Reproduced with permission of the *Royal Society of Chemistry*)

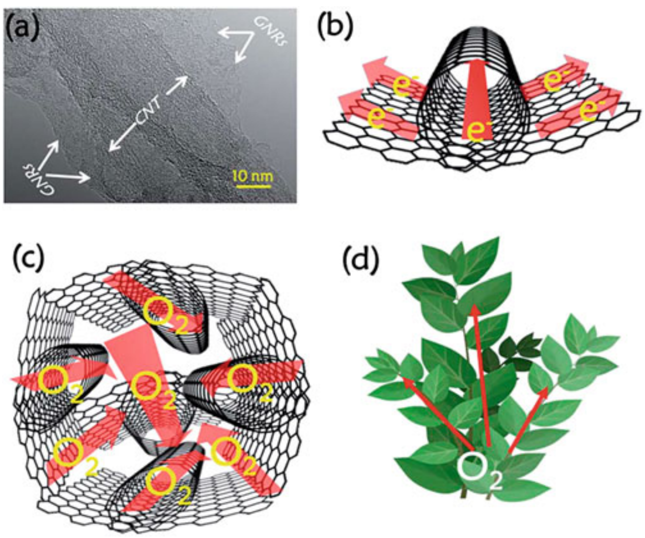

Fig. 4.128 (**a**) HRTEM image of as-prepared carbon nanoleaf aerogels, in which GNRs (graphene nanoribbons) and CNT are labeled. Scheme of (**b**) the carbon nanoleaf bridged structure (CNT@GNRs) for enhancing electron transfer and of (**c**) the interpenetrated 3D porous network for facilitating mass transfer (here exemplified with molecular oxygen). (**d**) Natural pattern for facilitating mass transfer in an actual cluster of leaves. (Reproduced with permission of the *Royal Society of Chemistry*)

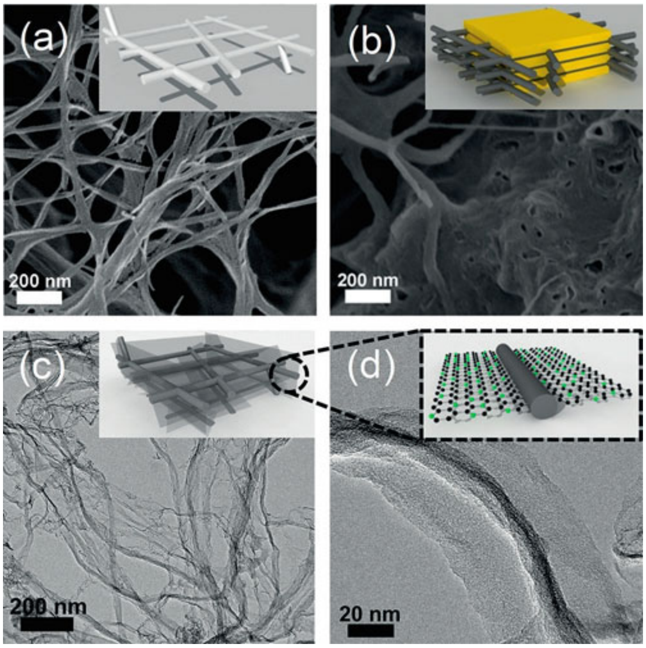

Fig. 4.129 The synthesis of CNF@NG 3D complexes. (**a**) The freeze-dried bacterial cellulose (BC) monolith (white rods) with an interpenetrating 3D network structure. (**b**) The carbonized BC (CNF, black rods) wrapped by the g-C_3N_4 sacrifice template (yellow) after thermal condensation of the mixture of BC and urea at 600 °C resulting in the CNF@g-C_3N_4 hybrid. (**c**) The CNF@NG was released after removal of g-C_3N_4 by heating at 900 °C. (**d**) The amplified view of CNF@NG. Carbon atoms are black or gray, and nitrogen atoms are green. (Reproduced with permission of *Wiley*)

(Fig. 4.130c). In addition, carbon 2D and 3D nanoflowers, prepared on silicon (111) substrates by plasma-enhanced CVD, using CH_4, H_2 and Ar as reactive gases in the presence of Fe catalyst, were formed by various nanoleaves (2D, related closely to the flux ratio of gas and the reaction pressure) or hundreds of nanofibers (3D, depended mainly on the growth temperature) [328].

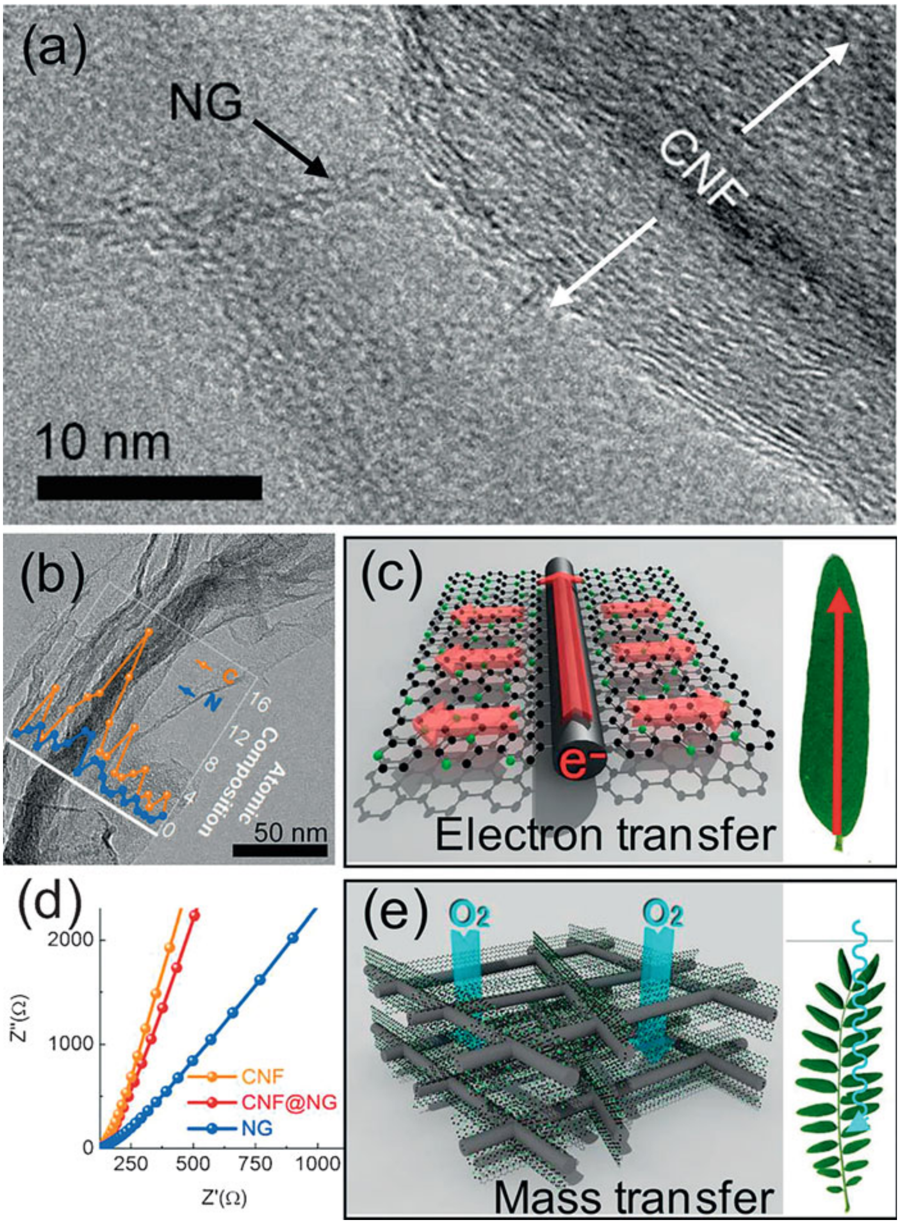

Fig. 4.130 Structural and morphological characterization of the catalyst. (**a**) HRTEM images of CNF@NG, CNF, and NG are labeled. (**b**) Compositional line profile across the CNF@NG. (**c**) Scheme of CNF@NG “vein-leaf” complex structure for enhancing the electron transfer. (Carbon atoms are black or gray, and nitrogen atoms are green.) (**d**) EIS spectra of CNF@NG, NG, and CNF in O_2-saturated KOH solution (0.1 mol L^{-1}). At a low frequency, the steeper slope indicated favorable transport. (**e**) Scheme of the complex interpenetrated 3D network structure of CNF@NG, which facilitates the mass transfer (here exemplified with molecular oxygen). (Reproduced with permission of *Wiley*)

4.5.4 Nanoforests

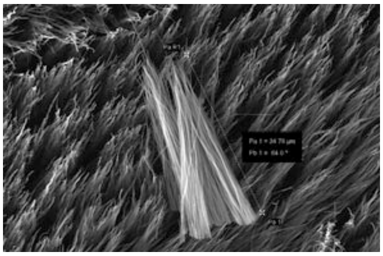

The nanoforests on the basis of carbon nanotubes belong indubitably to the most studied forest-like structures among other compounds, whose number is certainly limited, and have got useful applications. The CNTFs’ peculiarity, in comparison with other carbon and non-carbon species, is that the forests of carbon nanotubes are currently known as the darkest artificially produced materials [329], being able to adsorb the entire visible range of electromagnetic wave much more efficiently than any other black material. They exhibit near-perfect optical absorption (reflectance~0.045%) due to low reflectance and nanoscale surface roughness. At the same time, carbon nanotubes are able to reflect light like a mirror when the CNTs in the forests are mechanically bent and flattened with proper control [330]. Under a controlled mechanical processing of the CNTs, the mirror-like reflection from the processed area with 10%–15% reflectivity was observed, having possible applications for fabrication of monolithically integrated reflector-absorber arrays.

Carbon nanotube forests may include “regular” [331], bamboo-like [332], helical [333], and branched structures, as well as a CNT forest-on-forest, where the number of layers in such a system can vary from 1 [334] to 2 [335], 4 [336], 8 [337], and even 40 [338], and second- and third-order CNT forest structures [339, 340]. Integrated simulation of active carbon nanotube forest growth, the diverse CNT forest morphologies, and mechanical compression is discussed in a recent report [341]. In particular, CNT forest morphologies may be generally aligned to the growth axis or highly tortuous, with persistently wavy CNTs intermixed with aligned and straight carbon nanotubes. This depends on the height of CNT forest, the CNT diameter, surface density, and growth conditions. The length of some CNTs may exceed the height of the carbon nanotube forest; different CNTs in the same nanotube forest can be different in tortuosity and length. Comprehensive information on CNT forests is present in a highly recommended excellent comprehensive recent review [342], citing 679 references. This shows an increasing interest to this type of nanostructure having a variety of applications, from catalysis to biosensors.

Synthesis In general, CNT forests can be synthesized by catalytic pyrolysis on supported catalysts as described below, using various versions of the CVD method [343–345], by the template method with Al_2O_3 membranes, by graphite sputtering (this technique is used much more rarely), by electrophoresis or dielectrophoresis of CNTs from dispersions [346, 347], and by chemical grafting of CNTs onto substrates [348]. Particular aspects of methods for the synthesis of CNTFs are mentioned in several reviews [349, 350]. Among them, we note a wide use of mono- and polymetallic catalysts and supports for their preparation, mainly at high temperatures and using acetylene (reactions 4.13–4.17) as carbon source {although ethylene mixtures with H_2 [351] (the equipment is shown in Fig. 4.131) or $C_2H_4/H_2/H_2O/Ar$ [352] were used}. Thus, the growth of dense CNT forests on some metallic layers (Mo, Ta, W, and Ir) by thermal decomposition of C_2H_2 diluted in NH_3 was studied [353]. The growth process and resulting structure of CNT forests were shown to depend on metal substrates, process duration, temperature, and thickness of the stabilizer (Al). In a related report [354], dense CNT forests (height of ~300 nm and a mass density of 1.2 g·cm^{-3}) were prepared on copper support at 450 °C, using Co/Al/Mo multilayer catalyst. The nanotubes exhibited very narrow inner spacing. Main characteristics of the formed material are high thermal effusivity and a thermal conductivity, suitable for possible uses in heat dissipation devices.

Another classic example consists of vertically aligned SWCNT forest, grown using FePt alloy particles on a MgO substrate [355]. Sometimes, metal-based catalyst should be additionally activated prior to use. Thus, an oxidative pretreatment of Fe,

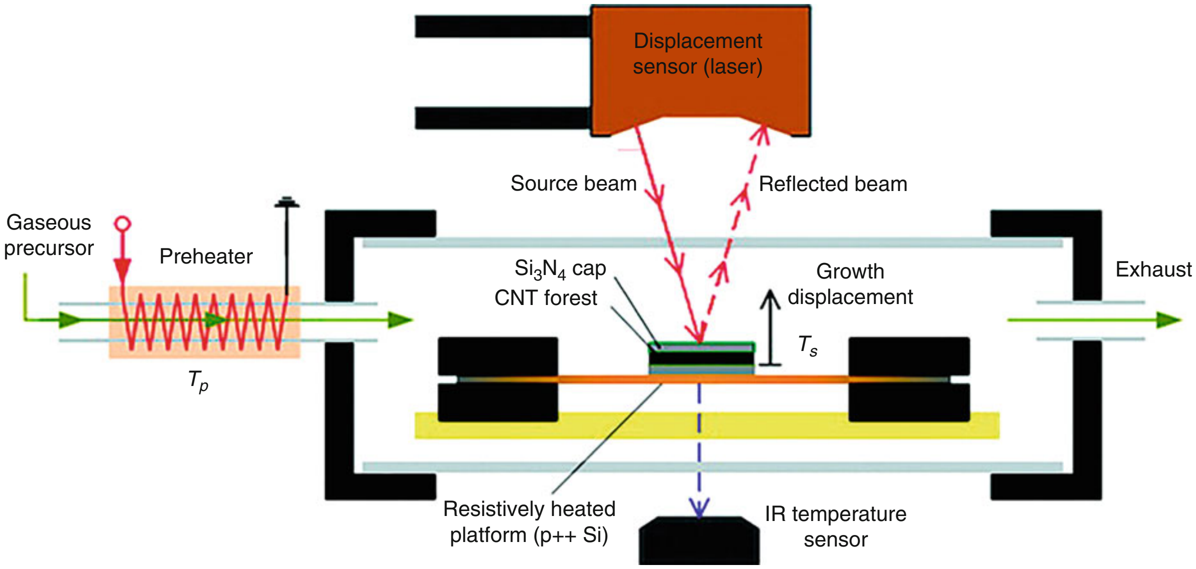

Fig. 4.131 Obtaining CNT forest by CVD method. (Reproduced with permission of the *American Chemical Society*)

Co, or Ni growth catalyst on SiO_2 support can be used to switch the growth mode of CNTs from tip growth to root growth [356]. Dense vertically aligned nanotube forests can be grown this way. The oxidative treatment effect was explained by appeared strong interaction "catalyst-support (SiO_2)," limiting the surface diffusion, sinterization of catalyst NPs, and their binding to the surface of SiO_2. In addition, vertically aligned small diameter (single- and few-walled) carbon nanotube forests were also grown by thermal CVD over the temperature range 560–800 °C and 10^{-5} to 14 mbar partial pressure range, using acetylene as the feedstock and Al_2O_3-supported Fe nanoparticles as the catalyst [357]. The following mechanism of their formation (Fig. 4.132) is described by reactions (4.13–4.17); alternative mechanism is shown in Fig. 4.133 [358]. Curiously

Fig. 4.132 Schematic of CNT growth process. (Copyright. Reproduced with permission of the *American Chemical Society*)

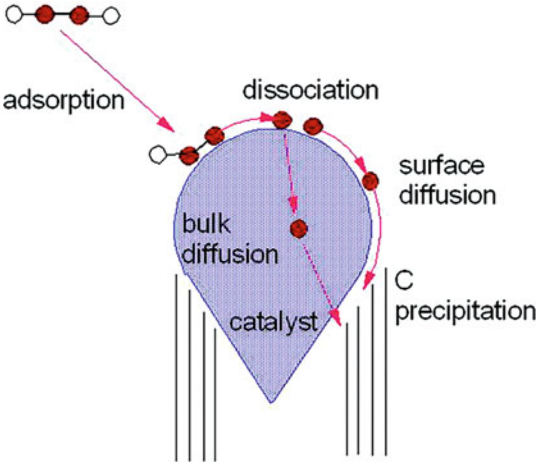

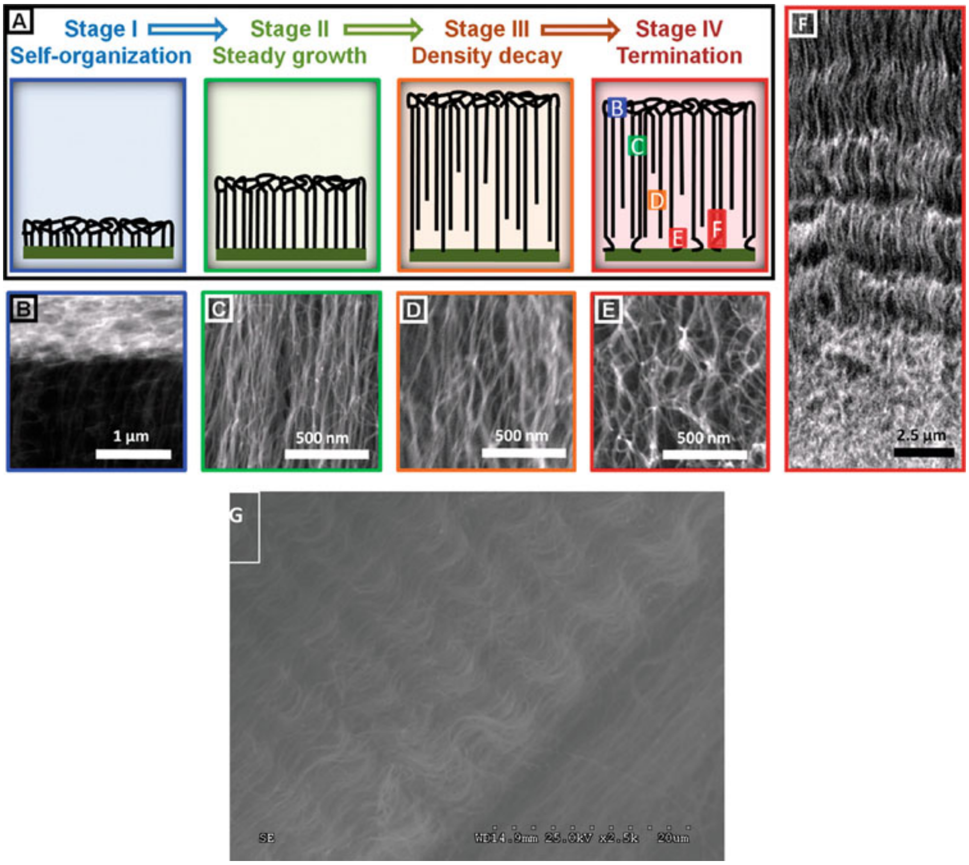

Fig. 4.133 Collective growth mechanism of a CNT forest: (**a**) growth stages and SEM images of (**b**) tangled crust at the top of forest, (**c**) aligned and dense morphology near the top of a self-terminated forest, (**d**) less aligned and less dense morphology in the lower region of a self-terminated forest, and (**e**, **f**) randomly oriented morphology at the bottom, induced by the loss of the self-supporting forest structure. (Reproduced with permission of the *American Chemical Society*) (**g**) View of a coexistence of sinuous-like and almost straight carbon nanotubes in the same image. (Authors' own data.)

(Fig. 4.133g), nanoforest zones consisting of sinuous (Fig. 4.133g, left section, up) and almost straight (Fig. 4.133g, right section, down) carbon nanotubes can be sometimes formed at the same bulk growth conditions.

$$C_2H_{2\ \mathrm{gas}} \leftrightarrow C_2H_{2\ \mathrm{ads}} \tag{4.13}$$

$$C_2H_{2\ \mathrm{ads}} \leftrightarrow 2CH_{\mathrm{ads}} \tag{4.14}$$

$$CH_{\mathrm{ads}} \leftrightarrow C_{\mathrm{ads}} + H_{\mathrm{ads}} \tag{4.15}$$

$$2H_{\mathrm{ads}} \rightarrow H_{2\mathrm{gas}} \tag{4.16}$$

$$C_{\mathrm{ads}} \rightarrow C_{\mathrm{CNT}} \tag{4.17}$$

In addition to metals above as supports, CVD-assisted formation of a dense CNTs (length 13–14 mm and diameter of 10–100 nm) forest is known using spin-coated iron oxide (Fe_2O_3) thin film on Si substrate starting from a mixture of acetylene, hydrogen, and nitrogen for 45 min at 700 °C [359]. Also, vertically aligned ohmic-conductive carbon nanotube forests were grown on TiSiN refractory conductive films and reached area densities of $(5.1 \pm 0.1) \times 10$ [12] tubes cm^{-2} and mass densities of approximately 0.3 $\mathrm{g{\cdot}cm}^{-3}$ [360]. The above support had a function as a diffusion barrier; the resulting nanoforest grew according to the root growth mechanism. An additional discontinuous AlO_x layer, inhibiting catalyst nanoparticle sintering, allowed maximizing the CNT area density. Highly porous and conductive ZnO/C core–shell hexagonal nanosheets (HNS) nanoforests (Fig. 4.134) were fabricated through the direct decomposition of zinc acetate dihydrate in a sealed thermolysis stainless steel vessel at 400 °C without using a catalyst, solvent, or template [361] according to the reactions 4.18–4.21 at heating conditions. The final ZnO/C core–shell structure was then formed by the deposition of carbon onto the ZnO surfaces. The formed nanomaterial could possess practical utility of the materials in dye-sensitized solar cells, nanocrystal photovoltaic devices, white light emitters, and white light photocatalyst applications.

$$\mathrm{Zn(CH_3COO)_2 \cdot 2H_2O \rightarrow Zn(CH_3COO)_2 + 2H_2O} \tag{4.18}$$

$$\mathrm{4\ Zn(CH_3COO)_2 + 2H_2O \rightarrow Zn_4O(CH_3COO)_6 + 2CH_3COOH} \tag{4.19}$$

$$\mathrm{Zn_4O(CH_3COO)_6 + 3H_2O \rightarrow 4ZnO + 6CH_3COOH} \tag{4.20}$$

$$\mathrm{Zn_4O(CH_3COO)_6 \rightarrow 4ZnO + 3CH_3OCH_3 + 3CO_2} \tag{4.21}$$

To optimize high-temperature growth of CNTFs, several studies have been carried out, since an important obstacle of CNT fabrication in industrial mass production is the growth efficiency. Thus, for the case of C_2H_2 as precursor in water-assisted CVD, it was established [362] that, for 10 min. optimum growth conditions, SWCNT forests with ~350 μm/min initial growth rates, ~2500 μm height, and extended catalyst lifetimes could be reached by increasing the dwell time to ~5 s. It demonstrated the generality of dwell time control to highly reactive gases. In another research, in order to tune the CVD growth of CNT forests (DWCNTs or SWCNTs) on wafers, introduction of CO_2 is a simple and controlled way [363]. When its concentration grows, the CNT forests are transformed as follows: CNT forests → radial blocks → bowl-shaped forests. It is possible to control the diameter distribution and wall number of the CNTs this way. At 36.8 mol% of CO_2, the content of SWCNTs in the forest was found to be 70%. Also, under increased CO_2 concentration, a smaller diameter and decreased wall number for CNTs were revealed. It was suggested that CO_2 could be as a weak oxidant and generates water. Among other synthesis methods [364] for CNTFs, we note high-voltage electrophoretic deposition (HVEPD), used to obtain forests of aligned MWCNTs on long strips of conductive substrates [365].

Special Studies of CNTF Internal Structure and Other Properties XPS analysis of a CVD-grown forest of MWCNTs using monochromatic Al Kα radiation showed essentially only carbon presence (1 s peak at 284.5 eV) [366]. In order to evaluate properties of the "internal content" of CNTFs, the precise and continuous control method for the average diameter of SWCNTs in a forest ranging from 1.3 to 3.0 nm with 1 Å resolution was offered [367]. This control was reached through tuning of the catalyst state (composition, size, and density) applying arc plasma deposition of nanoparticles. These results showed a direct relationship between the achievable height and the diameter of SWCNTs. On their basis, the fundamental difficulty in fabrication of tall and small diameter SWCNT forests was suggested. In addition, the internal nanostructure of the CNT forest, consisting of mostly empty space between the nanotubes, allows to capture photons effectively yet allows electrons to escape easily (Fig. 4.135) [368]. This makes possible to use CNT forests in ranging from photocathodes to solar cells.

Vertically aligned CNTs possess a peculiarity of *waviness*, regardless of the control of their fabrication process. Study of this phenomena showed [369] that the inherent waviness is the main mechanism by which the effective modulus of CNTs is

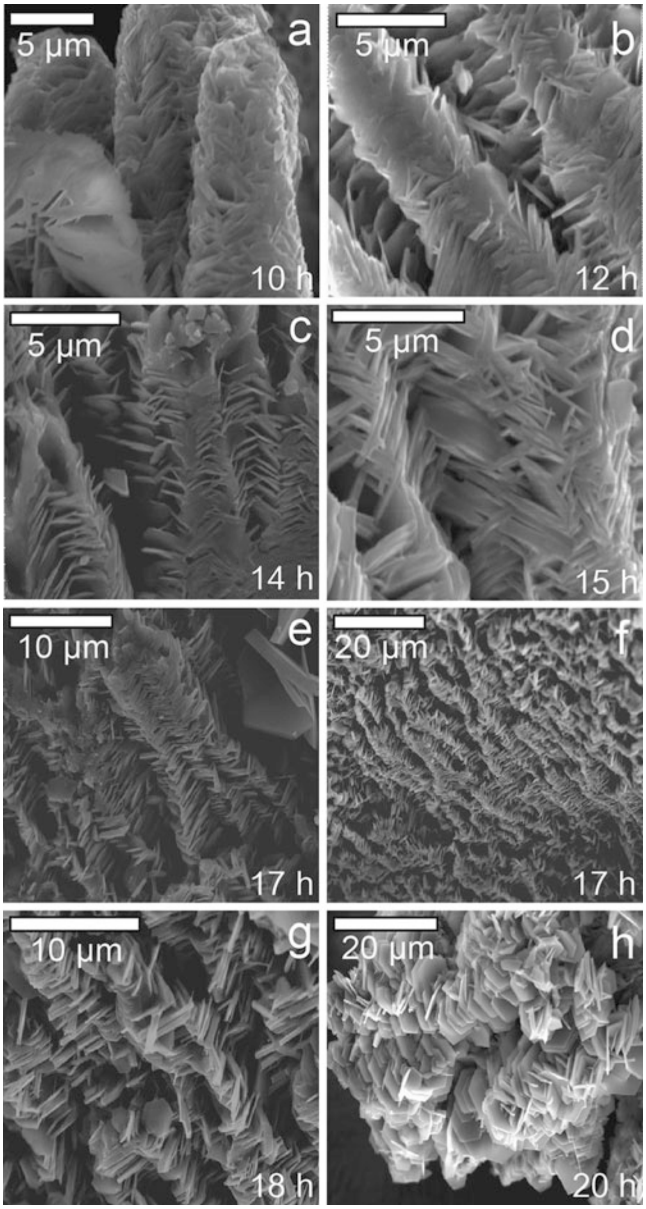

Fig. 4.134 SEM images obtained during the growth of the ZnO/C core–shell HNS nanoforests at 400 °C as a function of time. (**a**) Tower-like rods formed upon heating over 10 h. (**b**) Sheets grew from the rod-like towers over 12 h. (**c**) The number of sheets that formed increased after 14 h. (**d**) The rods split into nanosheets at 15 h. (**e**, **f**) Nanosheets that resembled a forest formed after 17 h. (**e**) shows a magnified image obtained from f. (**g**) The sizes and shapes of the nanosheets developed further up to 18 h. (**h**) Complete growth of the HNS nanoforest was achieved after 20 h. (Reproduced with permission of *Springer*)

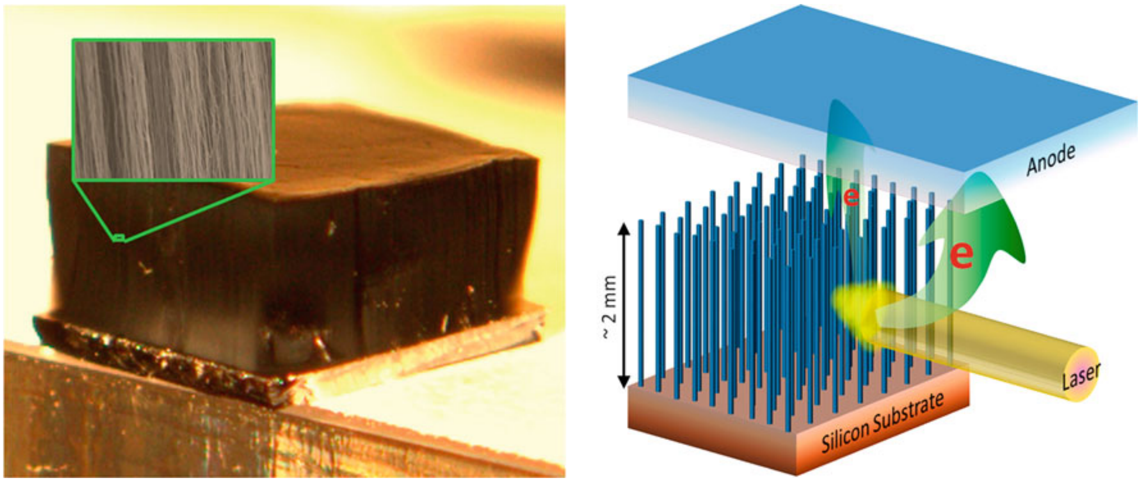

Fig. 4.135 (Left) A photo of a carbon nanotube forest over 2 mm tall and 5 mm on each side (note the silicon substrate with a thickness of 0.5 mm), effectively forming a macroscopic object. Inset is a scanning electron micrograph of the sidewall of the forest, showing the overall alignment of the nanotubes and the significant internanotube distance. (Right) A schematic of the experiment, showing the electrons exiting from the sidewall of the forest, as well as those emerging from the top surface of the forest. (Reproduced with permission of the *American Chemical Society*)

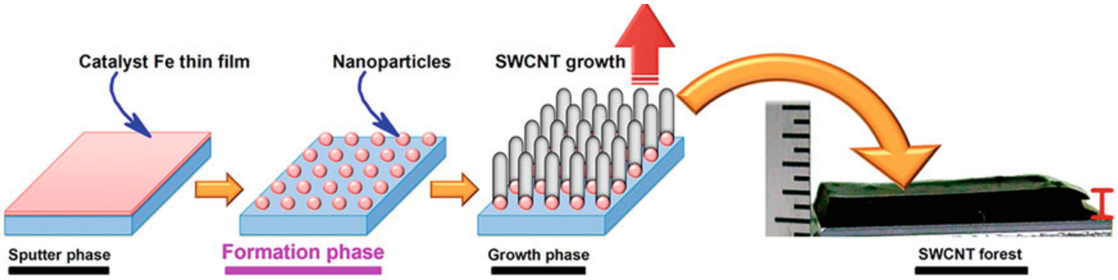

Fig. 4.136 Schematic of synthesizing SWCNT forests by tailoring Fe thin film thickness and formation temperature. (Reproduced with permission of the *American Chemical Society*)

reduced by several orders of magnitude. The high compliance of forests of carbon nanotubes was found to be because of the inherent waviness of individual CNTs and not necessarily due to bending and buckling of CNTs. The *mechanical compression effect* on the thermal conductivity of the closely aligned parallel SWCNT forest was investigated by molecular dynamics simulations [370]. Among other findings, the thermal conductivity was shown to be linearly enhanced by increasing compression before the buckling of SWCNT forests. At the same time, the thermal conductivity decreases quickly with further increasing compression after the forest is buckled. The intertube van der Waals interaction is strengthened by the compression, and the smoothness of the intertube interface is maintained during compression. In addition, *buckling-driven delamination* of CNT forests from their growth substrates when subjected to compression was revealed [371]. It was postulated that the post-buckling tensile stresses, being developed at the base of the CNT forests, serve as the driving force for delamination. Also, the fundamental dependence *electrical conductance* and *thermal diffusivity* on the diameter and defect level for aligned SWCNT forests (fabrication scheme see Fig. 4.136) was evaluated [372]. It was definitively concluded that high thermal diffusivity and electrical conductance would be extremely difficult to simultaneously reach by a single SWCNT forest structure using CVD technique.

Liquid flow slippage over superhydrophobic surfaces made of CNT forests, incorporated in microchannels, was also studied [373]. We need to note that CNTF composites with highly hydrophobic properties can be created by special methods. Thus, a stable superhydrophobic surface was created using the nanoscale roughness inherent in a vertically aligned CNT forest [374]. This became possible due to the use of a thin conformal hydrophobic polytetrafluoroethylene (PTFE), which coated the surface of the CNTs. In this material, essentially spherical, micrometer-sized water droplets can be suspended on top of the CNT forest. This effect could be explained on the basis that that the appearing difluorocarbene radicals may attach covalently to the nanotube surface and subsequently polymerize from these sites. The product could get several applications, in particular as fillers for nanocomposites and single-strand conductors in molecular electronics. Among other important studies, we mention the linearized Gouy–Chapman–Stern theory of an electric double layer, generalized for morphologically complex and disordered electrodes [375]; in particular its significance was illustrated for a forest of nanopillars. The theory allows analyzing the effect of compact layer thickness, concentration, shapes, and their fluctuations, developing a general understanding of capacitance in complex interfacial systems.

Applications of CNTFs and their composites belong to a variety of areas, from academic to technical and medicinal. Thus, CNT nanoforests, each with a thin conformal coating of dielectric, can provide an economic fabrication of sensitive and uniform SERS templates [376]. CNTFs are also considered as particularly promising templates for the formation of porous metal oxides (Al_2O_3, TiO_2, V_2O_5, and ZnO) [377]. A bilayer Au–carbon nanotube composite (a vertically aligned MWCNT forest, sputtered with an Au layer) was fabricated as a potential low-force electrical contact surface for possible applications in MEM switching devices [378]. The penetration of Au atoms into the forest directly influences the electrical characteristics of the composite, depending on loading conditions (the effective resistivities are in the range from 303 nΩ m down to 54 nΩ m).

Sensing uses are also common. Thus, a unique combination process of a sharp Si microneedle array and MWCNT forest was developed and applied as a reference electrode for a nonenzymatic glucose sensing [379]. The registered sensitivity was found to be 17.73 ± 3 μA/mM-cm^2. This electrode can be used for painless diabetes testing applications. Also, carbon nanofiber forests (CNFFs) grown on glass microballoons are able to detect directly *Plasmodium falciparum* histidine-rich protein-2 (PfHRP-2) antigen as low as 0.025 ng/mL concentration in phosphate-buffered saline [380]. This effect can be applied for early diagnosis of malaria and other infectious diseases. Among technical applications, CNT forests have been revealed to reduce the access of abrasive particles to compressible sealing elements of joints [381]. In addition, a spray-based coating technique was applied for deposition of nanoscale coatings of polystyrene and poly-3-hexylthiophene onto carbon nanotube forests, being as a bonding medium that produces thermal resistance by expanding the area available for heat transfer at CNT contacts [382].

Diamond-based nanoforests are known, in addition to CNTFs and CNFFs above. Thus, an electrode with 3D structure on the basis of boron-doped diamond nanorod forest (BDDNF) was fabricated by hot-filament CVD method (HFCVD) method (Fig. 4.137) [383]. In its preparation, the electroless metal deposition (EMD) method and HFCVD technique were combined

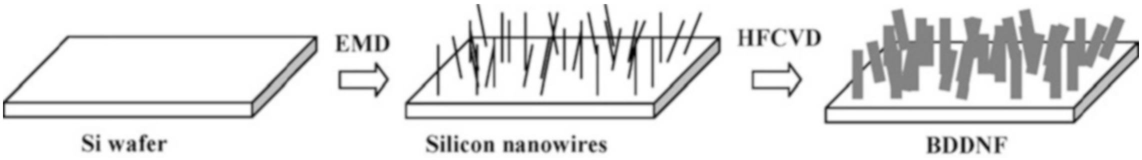

Fig. 4.137 Plots of fabrication of the BDDNF. (Reproduced with permission of the *American Chemical Society*)

for growing the BDDNF on Si nanowires; as a result, a 2D B-doped diamond electrode was transformed to 3D analogue. This electrode was found to exhibit a better selectivity and sensitivity for biomolecule detection (e.g., for glucose oxidation in basic conditions) in comparison with conventional planar B-doped diamond electrodes.

4.5.5 Nanobushes

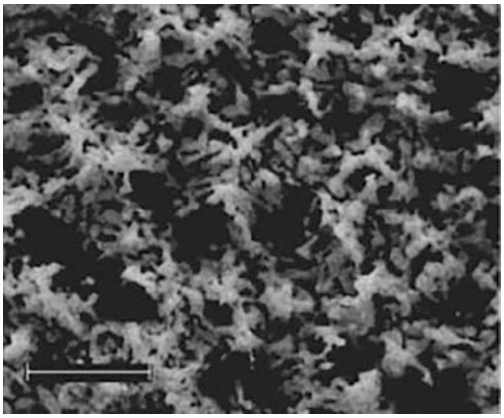

Nanobush[30] structures are still rare for carbon. The CNTs were grown with bush-like nanostructures covered around the micron-fibers or web-like nanostructures crossing between the fibers at different synthetic conditions [384, 385]. The developed CNT-metal-filter had higher filtration efficiency without significant difference in pressure drop compared with the conventional metal filter, which is because the CNTs function as the trap of pollutant nanoparticles.

4.5.6 Nanomushrooms

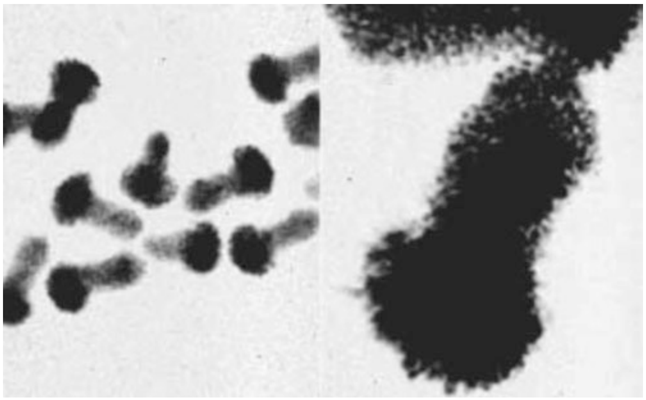

---

[30] The nanobush image above was reproduced with permission of the *American Institute of Physics* (*Appl. Phys. Lett.*, **2006**, 89, 223102).

Mushroom-like nanostructures are known for a series of elemental substances, their oxides, nitrides, salts, polymers, as well as their combinations. Carbon, traditionally obtained in a grand variety of nanostructures, can sometimes exist also as nanomushrooms.[31] Thus, two types of nanocarbons with a mushroom shape (of a conical tip, made from helically stacked graphitic cones, and pyramidal tip, made from graphitic cups stacking to each other), having ~2 μm length and 0.5 ~μm diameter, were found in common glassy carbon powder [386]. It was established that their diamagnetic behavior strongly depends on both the temperature and the magnetic field. A facile thermal CVD method for fabricating dense and vertically well-aligned bamboo-like CNT arrays on a Cu substrate from acetone was developed [387] resulting mushroom-like carbon nanostructures, formed at 800 °C, and well-aligned CNTs, produced at 850 °C.

4.5.7 Nanoflowers

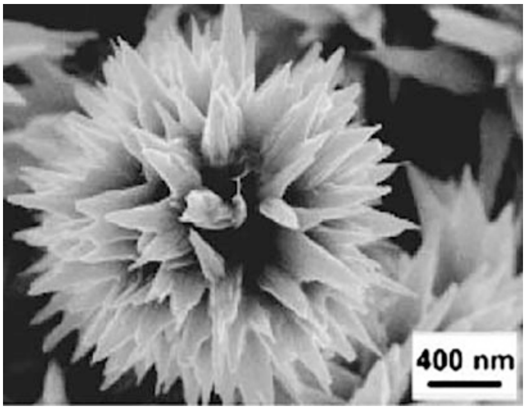

Nanoflowers[32] (flower-like nanoparticles) [388, 389] are not currently reported so frequently, as, for example, nanowires [390] or one of the hottest nanotechnology area – well-known carbon nanotubes. However, last decade the number of related literature is being increased. Last years, a series of various nanoflower and nanoflower-like structures have been obtained, frequently together or in equilibrium with other nanoforms, depending on reaction conditions. Nanoflower structure may consist of such simpler nanostructures, as nanorods, nanowalls, or nanowires. Current and possible applications of nanoflowers as optoelectronics devices or sensors, in catalysis, and solar cells caused a definite interest to them. Nanoflowers obviously are at the initial stage of their research, and it is expected further intensive development of this area.

In respect of carbon itself, in addition to thousands of patents, books, and experimental and review articles, dedicated to intensively studied carbon nanotubes and fullerenes, this element was obtained also in the nanoflower form. Thus, carbon nanoflowers with graphitic feature were prepared at 650 °C with high yields using a reduction–pyrolysis–catalysis route using glycerin as carbon source and magnesium and ferrocene as reductants and catalysts [391]. The obtained nanoflowers with a hollow core had diameters ranging from 200 to 600 nm. In another report [392], iron was used as a catalyst for CNTs flowers formation from a gas mixture of Ar and C_2H_2 at a temperature range of 700–900 K for 300 s (5 min). Iron wire was sparked for 1, 2, 10, and 100 times to form iron dots/islands on the glass slides, where CNTs, composed of carbon with hexagonal structure, were further grown. Also, carbon nanoflowers, among other nanostructures (fullerene, carbon nanopowders, nanofibers, and nanotubes), were produced by carrying out a gas membrane microarc discharge on a cathode in an aqueous solution (basic electrolyte, 0.01–2 mol/L solutions of mineral acids, bases, or chlorides) [393].

Flower-like carbon dots/manganese dioxide (CQDs/MnO_2) nanocomposites with specific surface area of 168.8 $m^2\ g^{-1}$ were investigated as electrode materials for supercapacitors [394]. CQDs were found to be uniformly distributed on the transparent petal of δ-MnO_2. In addition, nitrogen-doped mesoporous hollow 3D carbon nanoflowers (N-HCNF, Fig. 4.138) with high specific surface area (507.5 $m^2\ g^{-1}$) were prepared (Fig. 4.139) by a facile hard-template route via a hydrothermal process, subsequent carbonization, and etching [395] and recommended to be used as a potential anode material for lithium-ion batteries. Their outstanding electrochemical performances were attributed to the N-doped carbon shell, large BET surface

---

[31] The nanomushroom image above was reproduced with permission of the *Royal Society of Chemistry* (*Chem. Commun*., **2009**, (24), 3615–3617.).

[32] The nanoflower image above was reproduced with permission of the *American Chemical Society* (*J. Phys. Chem. B*, **2005**, 109, 10779–10785).

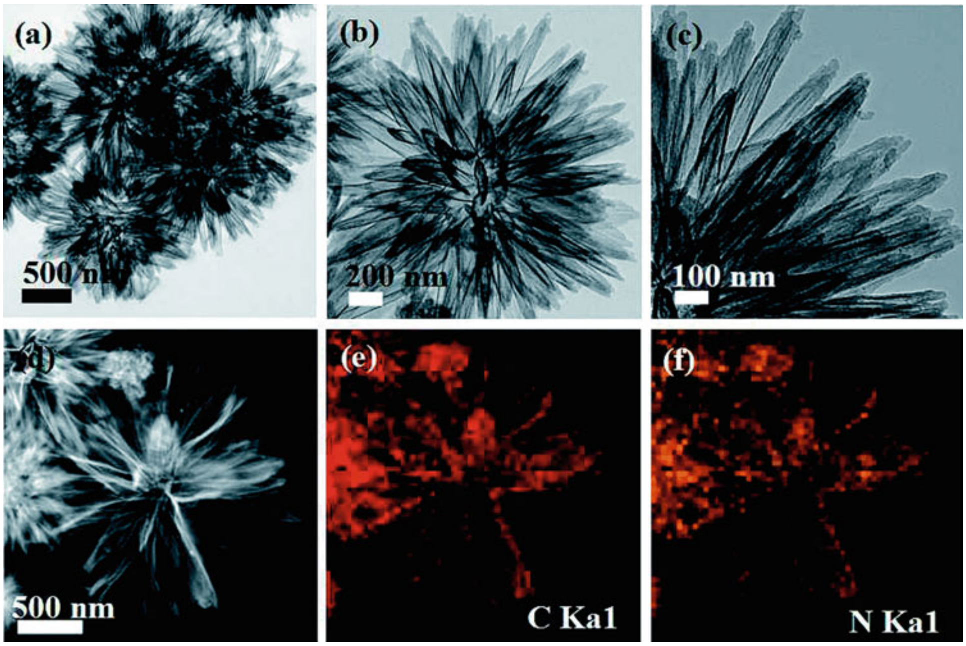

Fig. 4.138 TEM images of (**a**–**c**) nitrogen-doped hollow carbon nanoflowers (N-HCNF). (**d**) HAADF-STEM image of N-HCNF and element mappings of (**e**) C Ka1, (**f**) N Ka1. (Reproduced with permission of the *Royal Society of Chemistry*)

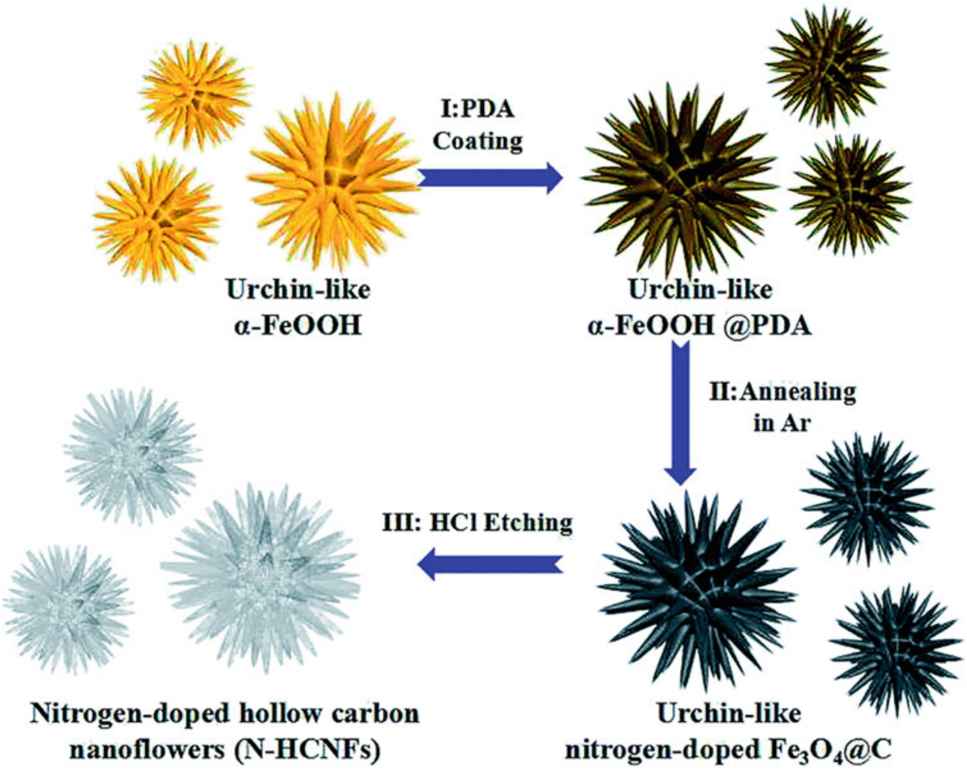

Fig. 4.139 Schematic illustration of the synthesis process of nitrogen-doped hollow carbon nanoflowers (N-HCNF). (Reproduced with permission of the *Royal Society of Chemistry*)

area, and unique hollow flower-like nanostructure. For similar uses, Na-ion battery anodes and flower-like MoS_2/C nanospheres were fabricated [396].

4.5.8 Nanobouquets

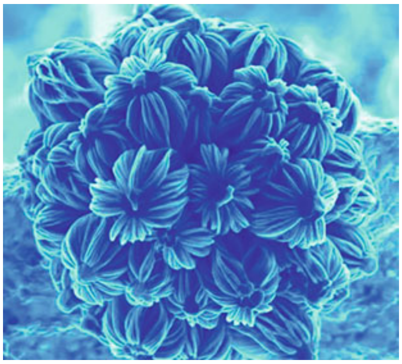

The term “nanobouquets”[33] is a blurred (diffuse) one: corresponding nanostructures may be called quite differently. Nanobouquets, which may be formed together with other nanostructures in varying synthesis conditions, can consist usually not only of nanoflowers but also of nanowires, nanorods, nanotrees, and nanoplates. Carbon-based nanobouquets are little known up to date. Thus, the nitrogen-doped carbon nanotube bouquets (Fig. 4.140) were synthesized by the pyrolysis of nitrogen-containing ion-exchange resin [397]. The material shows excellent ORR performance after being supported by the Pt nanoparticles, confirming the hypothesis that carbon supports doped with nitrogen improve catalyst support interactions by improving dispersion, electrical conductivity, durability, and catalytic activity of the overlying Pt nanoparticles.

4.5.9 Broccoli-Like Architectures

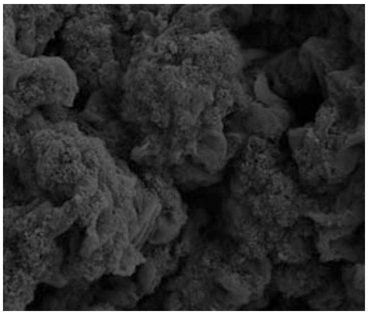

A few reports have been dedicated to clearly expressed broccoli-like nano- and microparticles on carbon basis. Thus, superhydrophobic polyvinylidene fluoride (PVDF/DMF/candle soot particle and PVDF/DMF/camphor soot particle composite) porous materials were fabricated by combustion of precursors (Fig. 4.141) [398], yielding, in particular, broccoli-like particles (Fig. 4.142c, d). Such hierarchical architecture combined with micro- and nano-scaled roughness of both formation of nanocauliflower and nanobroccoli structure is schematically illustrated in Fig. 4.143. As-measured wettability property of the obtained PVDF-based composite coatings revealed superhydrophobicity with water contact angle nearly touches 170°; thus it was considered by authors as water-repellent materials.

---

[33] The nanobouquet image above was reproduced with permission of the http://radio-weblogs.com/0105910/2004/06/22.html

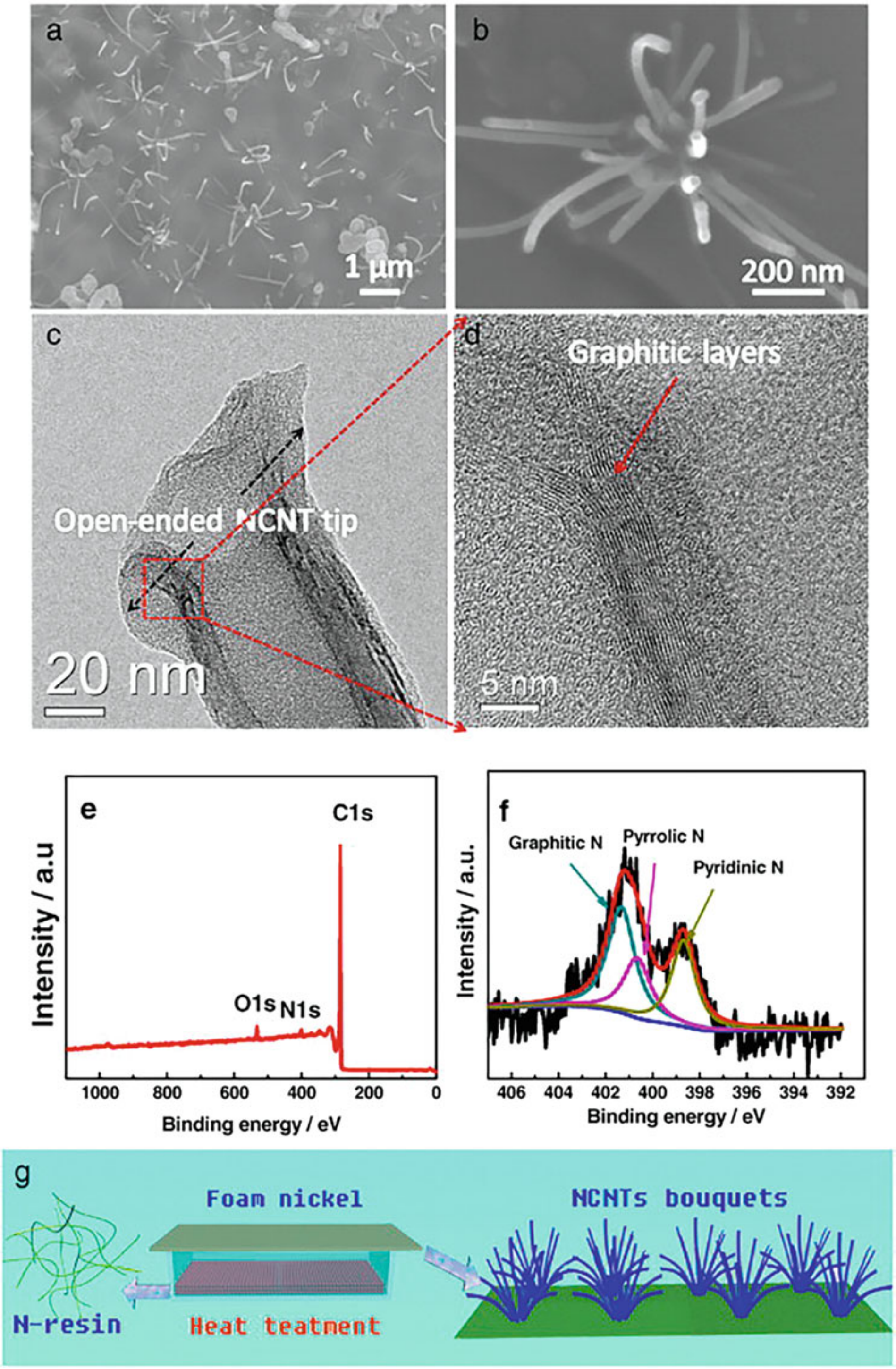

Fig. 4.140 (**a**) A typical SEM image NCNT bouquets, (**b**) high-magnification SEM image of an individual NCNT bouquet in (**a**), (**c**) TEM image of NCNTs with open-end tip, (**d**) a close-up TEM image of the red square in c, (**e**) XPS spectrum, (**f**) high-resolution N1s XPS spectrum, and (**g**) the schematic view of the approach for the synthesis of NCNT bouquets. (Reproduced with permission of the *Elsevier Science*)

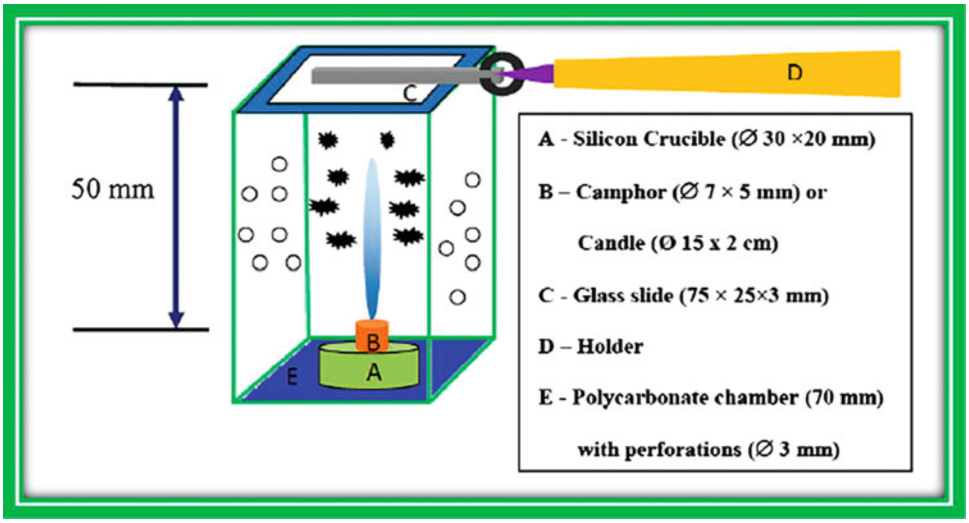

Fig. 4.141 Schematics for collection of soot particles of combustion of camphor and candle. (Reproduced with permission of the *Elsevier Science*)

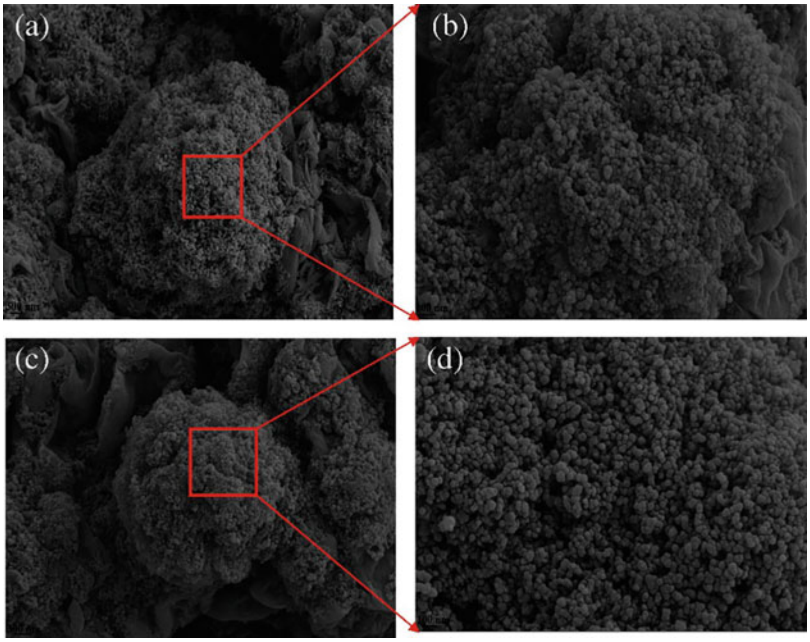

Fig. 4.142 FESEM images of (**a**) nanocauliflower-like structure of PVDF/candle soot particles and (**c**) FESEM images of nanobroccoli-like structure of PVDF/DMF/camphor soot particle composite coating, (**b** and **d**) magnified surface morphology of nanocauliflower- and nanobroccoli-like structure obtained from PVDF/candle soot and PVDF/camphor soot particles, respectively. (Reproduced with permission of the *Elsevier Science*)

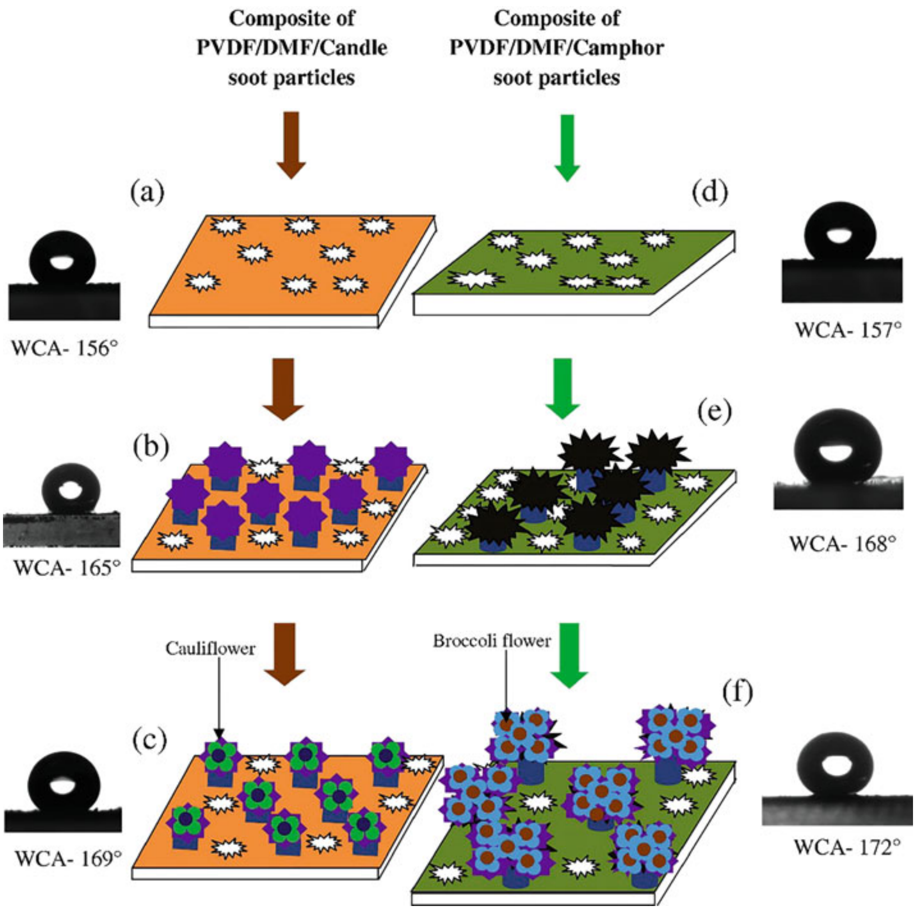

Fig. 4.143 Schematic for the formation of (I) cauliflower-like hierarchical microstructure of PVDF/DMF/candle soot particle composite for different quenching time (**a**) 48, (**b**) 96, and (**c**) 144 h, (II) broccoli-like hierarchical microstructure of PVDF/DMF/candle soot particle composite for different quenching time (**d**) 48, (**e**) 96, and (**f**) 144 h. (Reproduced with permission of the *Elsevier Science*)

4.5.10 Nanograsses

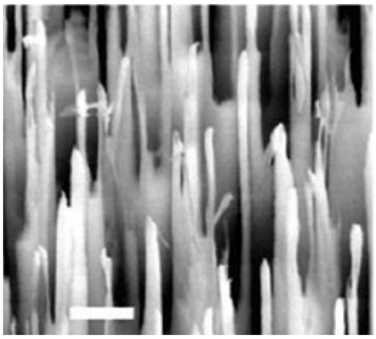

Nanograss[34] (as well as *nanofur*) is an example of dynamically tunable nanostructured surfaces, whose behavior can be reversibly switched between superhydrophobic and hydrophilic states either actively, by the application of electric voltage, or passively, in response to the change in environmental conditions such as humidity [399]. Such "superlyophobic" surfaces that repel virtually any liquid even if the surface material by itself is highly wettable have potential applications in an exceptionally

---

[34] The nanograss image above was reproduced with permission of the *American Chemical Society* (*J. Phys. Chem.C*, **2010**, *114*(7), 2936–2940.).

broad range, including areas as diverse as self-cleaning coatings, controllable permeability membranes for portable power generation, substrates for directed biological cell migration and differentiation, and hydrodynamic drag reduction surfaces.

Carbon nanoforms in nanograss forms are little known. Thus, boron-doped diamond (BDD) nanograss array was prepared [400] simply on a heavily doped BDD film by reactive ion etching for use as an electrochemical sensor, which improved the reactive site, promoted the electrocatalytic activity, accelerated the electron transfer, and enhanced the selectivity. In particular, detection of catechol was performed on the as-grown BDD electrodes and the nanograss array BDD [401]. The nanograss array BDD showed higher electrocatalytic activity toward the catechol detection than did the as-grown BDD. Good linearity was observed for a concentration range from 5 to 100 μM with a sensitivity of 719.71 mAM^{-1} cm^{-2} and a detection limit of 1.3 μM on the nanograss array BDD. Various morphologies of CNTs such as individuals, random networks parallel to the surface of the substrate (“grasses”), and vertically aligned forests of single- and multiwalled carbon nanotubes were CVD-grown by varying the nominal thickness of cobalt catalyst under the same reaction condition [402]. Longer growth time increased the CNT length, which caused further change in CNT morphologies from individuals to grasses and grasses to forests. Additionally, CNT nanograss is applied as gamma detector [403].

4.6 “Nanoanimal” World

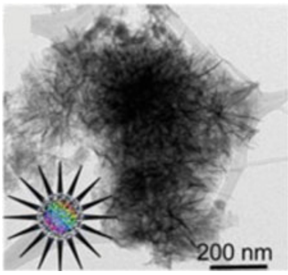

4.6.1 *Nanoworms*

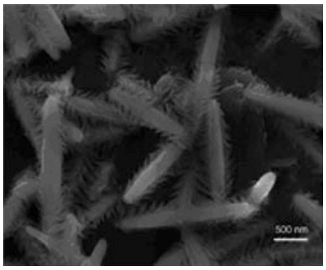

Several carbon nanostructures are known in worm-like[35] forms, which are frequently formed together with various other structures at the same time depending on reaction conditions. Thus, high-purity (99.21 wt.%) helical carbon nanotubes (HCNTs) were prepared in large quantity over Fe nanoparticles (fabricated using a coprecipitation/H_2 reduction method) by acetylene decomposition at 450 °C, together with worm-like carbon nanotubes (CNTs) as well as carbon nanocoils (CNCs, produced in large quantities), if H_2 was present throughout acetylene decomposition [404]. Since the HCNTs and worm-like CNTs were attached to Fe nanoparticles, the nanomaterials were found to be high in magnetization. Pyrolysis of ruthenocene carried out in an atmosphere of argon or hydrogen was found to give rise to spherical carbon nanostructures, in particular worm-like carbon structures (Fig. 4.144) [405]. Worm-like expanded structures (graphite flakes) (Fig. 4.145) are commonly observed in expanded graphite intercalated compounds. Also, properties of graphene wormholes in which a short nanotube acts as a bridge between two graphene sheets, where the honeycomb carbon lattice is curved from the presence of 12 heptagonal defects, were studied [407].

---

[35] The nanoworm image above was reproduced with permission of the *American Chemical Society* (*J. Phys. Chem. C*, **2008**, *112*(1), 106–111).

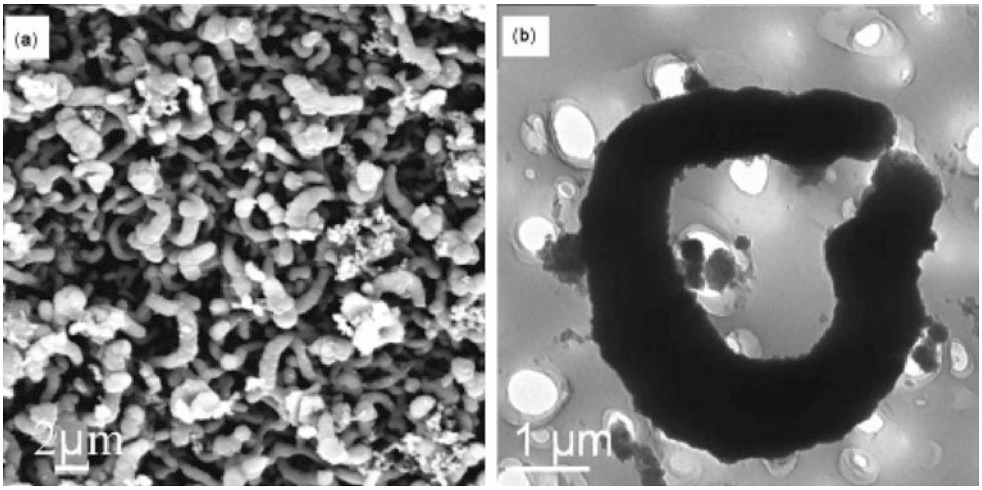

Fig. 4.144 (**a**) SEM image of carbon structures prepared by pyrolysis of ruthenocene with a mixture of argon (150 sccm) and ethylene (50 sccm) bubbled through thiophene at 950 °C and (**b**) shows the TEM image of these structures. (Reproduced with permission of *Springer*)

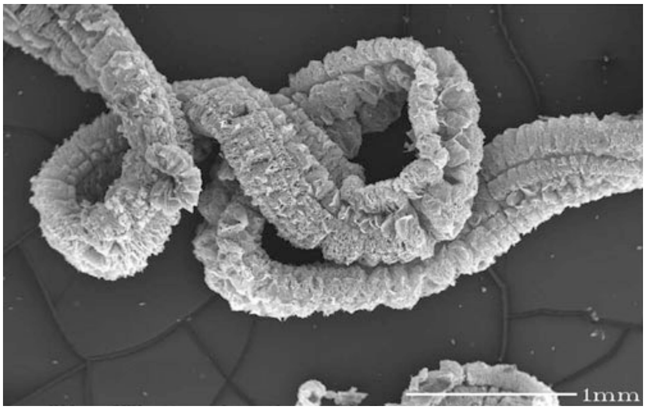

Fig. 4.145 Worm-like expanded structures (graphite flakes) commonly observed in expanded graphite intercalated compounds [406]. (Reproduced with permission of *Taylor & Francis*)

An interesting worm-like nanostructure was reported for cubic Pd crystals inside giant carbon clusters, forming worm-like carbon nanoworms [408]. The head of the worm, typically 20–50 nm, consisted of Pd encapsulated in carbon, and the body of the worm, several hundred nanometers in length, consisted of many sections of carbon tubes with cone-shaped voids. Graphite was found to be a superior support for Pd (worm-like small Pd nanostructures) catalyst for the direct synthesis of H_2O_2 from H_2 and O_2 [409]. Worm-like nanostructures have been used in other catalytic processes; in particular, the catalytic carbon "nanoworm" model (Fig. 4.146) was used to understand the role of the phases prevailing in the catalyst particles and the causes of the synergistic effects observed in gasification rates of activated carbon by CO_2, NO, and N_2O [410, 411].

4.6.2 *Nano-urchins*[36]

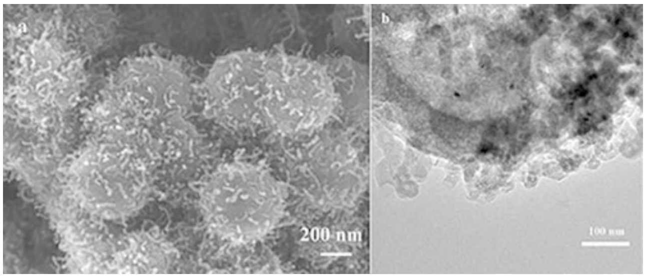

---

[36] Image reproduced with permission of the *Royal Society of Chemistry* (*J. Mater. Chem.*, **2006**, *16*(29), 2984–2989).

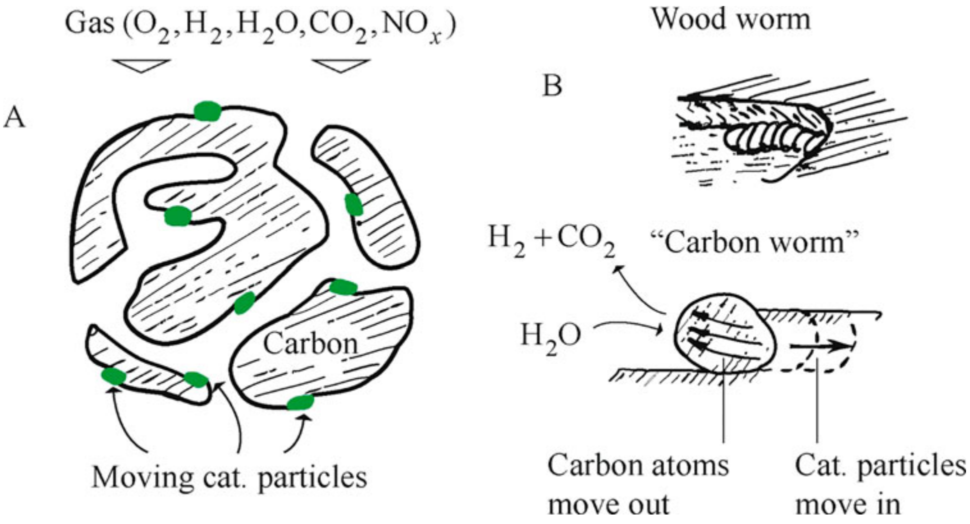

Fig. 4.146 Catalyst nanoparticles. (**a**) Porous carbon cut showing catalyst nanoparticles (moving under reaction conditions); (**b**) analogy with a woodworm and detail of a single "carbon-worm" particle. It shows the diffusion of carbon atoms through the particle in one direction and the particle itself moving in the opposite direction and keeping tight contact with carbon (into a step, corresponding to a crystallographic a direction). (Reproduced with permission of *Elsevier Science*)

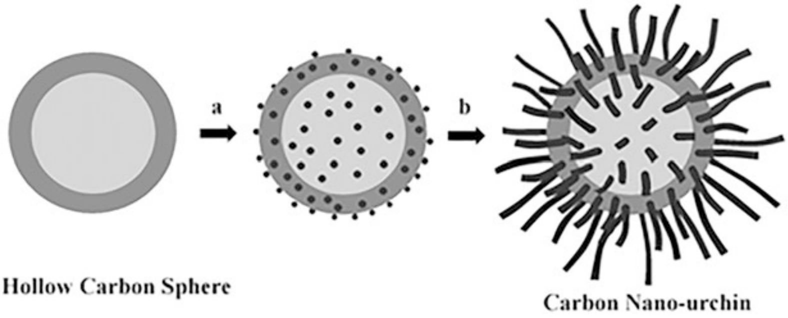

Fig. 4.147 Schematic diagram of the procedure for preparing carbon nano-urchins: (**a**) adsorption of iron oxide nanoparticles onto hollow carbon spheres, (**b**) growth of carbon nanotubes on hollow carbon spheres by CVD. (Reproduced with permission of the *Royal Society of Chemistry*)

Nano-urchins which belong to a similar structural type as nanoflowers (indeed, nano-urchins are frequently confused with flower-like nanostructures) are known for a variety of inorganic compounds and a few organics and have a lot of applications, first of all in catalysis due to high surface area of this nanostructures. In case of carbon, sea urchin-shaped nanostructured hollow carbon microspheres (e.g., hollow carbon microspheres containing carbon nanotubes extending outward from the central microsphere) were fabricated by formation of the carbon microsphere followed by incorporation of iron nanospheres (as growth catalysts) and then CVD of carbon (as nanotubes) from ethylene as the carbon source (Fig. 4.147) [412]. After incorporation of platinum on such carbon support, the formed nanocomposite could be used for methanol electrochemical oxidation in fuel cells. Hollow, urchin-like ferromagnetic carbon spheres with electromagnetic function and high conductivity at room temperature could be used as a reversible dye adsorbent. These nanostructures were prepared from template-free-synthesized, urchin-like, hollow spheres of polyaniline (PANI) containing $FeCl_3$ as the precursors by a carbonization process at 1200 °C under an argon atmosphere [413]. The high conductivity at room temperature resulted from the graphite-like structure, whereas α-Fe or γ-Fe_2O_3 nanoparticles produced by $FeCl_3$ during the carbonization were attributed to the ferromagnetic properties.

An urchin-structured multiwalled carbon nanotubes-hard carbon spherule (MWNTs/HCS) composite, where HCS was thoroughly coated by intercrossed MWNTs, was synthesized through acetylene pyrolysis [414] and showed an outstanding lithium uptake/release property: reversible charge capacity of 445 $mAh \cdot g^{-1}$ can be delivered by this composite after 40 cycles. The hybrid sphere/CNT nanostructures were grown in the aerosol phase by an on-the-fly process by spray pyrolysis, followed by CNT catalytic growth (Fig. 4.148) at the surface of the spherical nanoparticles yielding urchin-like nanostructures consisting of numerous CNTs attached to an alumina/iron oxide sphere [415]. These hybrid nanoparticles were dispersed

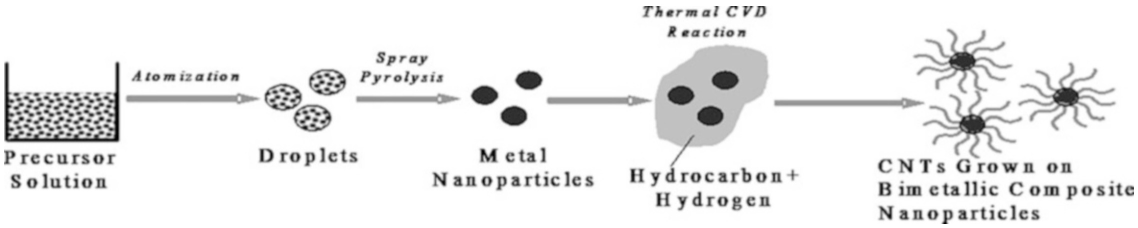

Fig. 4.148 Schematic of gas phase growth pathways of CNTs grown on metal oxide nanoparticles. The precursor solution was prepared with 3 wt.% $Fe(NO)_3$ + $Al(NO_3)_3$ solution with the $Fe(NO)_3$:$Al(NO_3)_3$ ratio of = 1:1 for hybrid sphere/CNT particles. (Reproduced with permission of *IOP Science*)

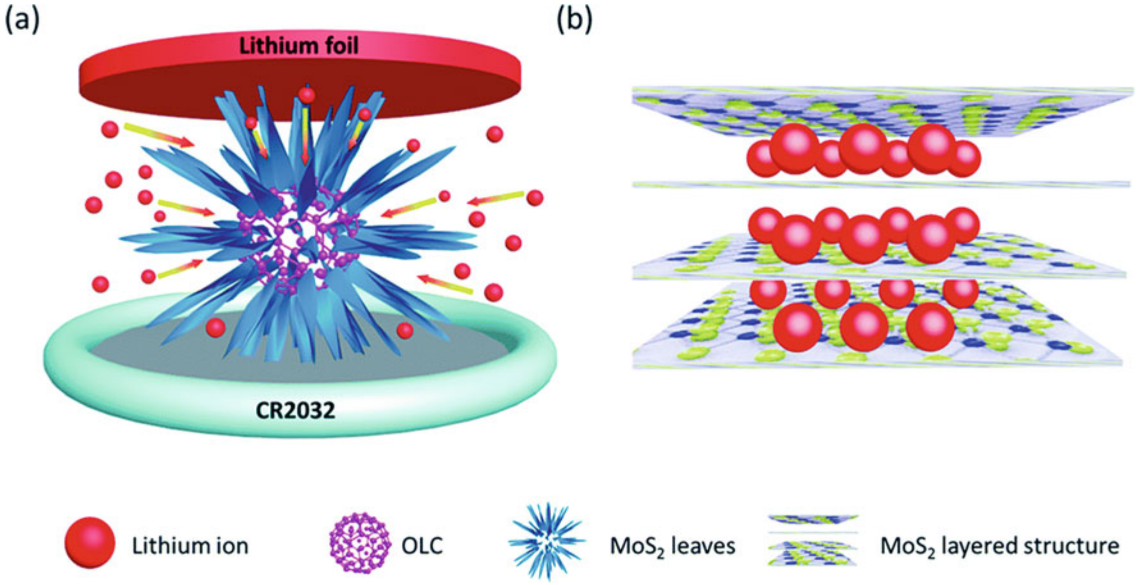

Fig. 4.149 Schematic diagrams of (**a**) pre-lithiation process and device configuration and (**b**) MoS_2 layered structure with the intercalated lithium ions during the pre-lithiation process. (Reproduced with permission of the *Royal Society of Chemistry*)

to poly-alpha-olefin with sonication and a small amount of surfactants to form stable nanofluids, whose effective thermal conductivity of the fluids was increased by about 21% at room temperature for particle volume fractions of 0.2%. The role of sulfur in the synthesis of novel carbon morphologies was studied [416]. For the materials, obtained by sulfur-assisted CVD, it was demonstrated that S not only acted on the catalyst, but also can be detected in the carbon lattice of the nanostructures. Sulfur is responsible for inducing curvature and therefore influencing the final carbon nanostructure morphology, in particular sea urchin-like nanostructures. Carbon nano-urchins are reviewed, among other nanostructures, as nanostructured materials for batteries [417].

Among most recent reports, we note that hydro-/solvothermal techniques are predominant for preparation of nano-urchin hybrid composites. Thus, hybrid urchin-like nanostructures composed of a spherical onion-like carbon (OLC) core and MoS_2 nanoleaves were synthesized by a solvothermal method followed by thermal annealing treatment [418] and offered to be used for lithium-ion batteries. A pre-lithiation method (Fig. 4.149) based on placing the nano-urchins in direct contact with the lithium foil was then employed to increase the initial CE to 97.6%. Similarly, a hybrid nano-urchin structure consisting of spherical onion-like carbon and MnO_2 nanosheets (Fig. 4.150) was synthesized by hydrothermal method [419]. Using the formed material for rechargeable lithium batteries, the improved performance arose from the unique nanostructure which facilitated fast ion and electron transport and stabilized the MnO_2 nanoparticles during charge storage.

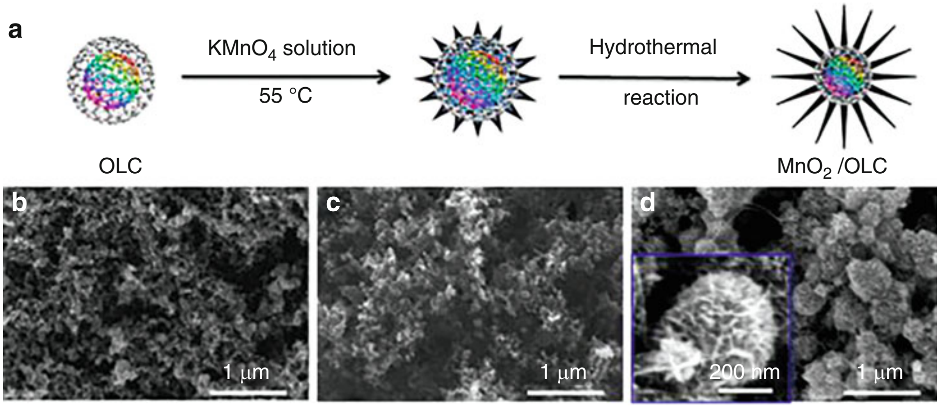

Fig. 4.150 (**a**) Schematic diagram of the synthesis procedure of the core-leaf OLC/MnO$_2$ hybrid nano-urchins. Scanning electron micrographs of (**b**) pure OLC, (**c**) intermediate product, and (**d**) final hybrid nano-urchins. Inset in (**d**) is the magnified image of a single urchin-like nanoarchitecture. (Reproduced with permission of the *Elsevier Science*)

4.7 “Home”-Like Nanostructures

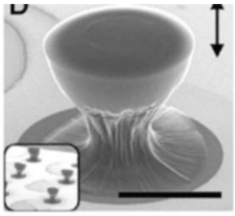

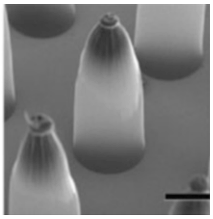

4.7.1 Nanobowls

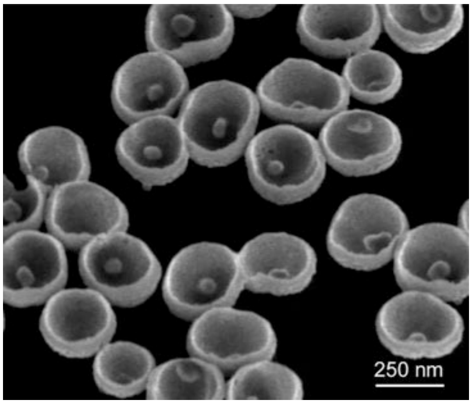

Nanobowl-like structures[37] are rare for carbon. Thus, vertically aligned CNT film was grown on a metal-coated polystyrene (PS) submicron sphere array and then transferred onto a polycarbonate (PC) substrate by microwave heating leading a new architecture of 2D metallic nanobowl array on a thermoplastic substrate [420]. In case of CNT nanobowls theirselves, the introduction of CO$_2$ was found to be a facile way to tune the growth of vertically aligned double- or single-walled carbon

---

[37] The nanobowl image is reproduced with permission of the *American Chemical Society* (*Langmuir*, **2009**, *25*(3), 1822–1827).

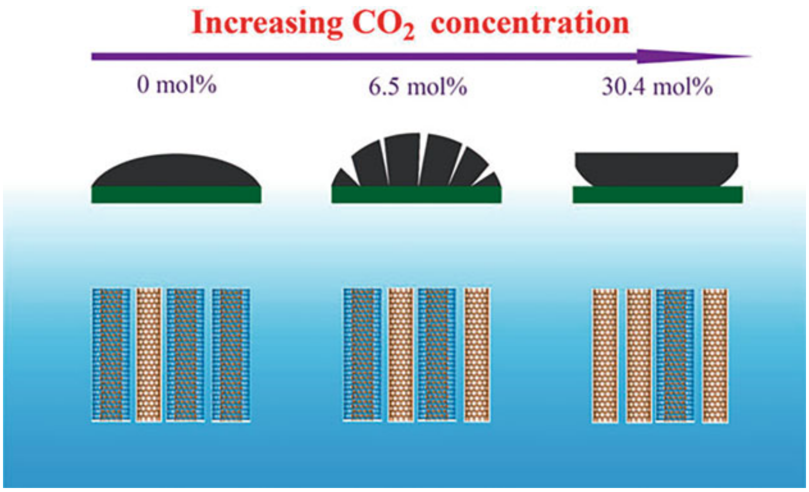

Fig. 4.151 Schematic diagram of the evolution of the forest morphology (middle panel) and the approximate resulting wall number distribution of CNTs in the forest (bottom panel) with increasing CO_2 concentration. (Reproduced with permission of *Springer*)

nanotube forests on wafers in the CVD fabrication of CNTs from ethylene as a precursor [421]. In the absence of CO_2, a double-walled CNT convexity was obtained; meanwhile with increasing concentration of CO_2, the morphologies of the forests transformed first into radial blocks and finally into bowl-shaped forests (Fig. 4.151). The addition of CO_2 was speculated to generate water and serve as a weak oxidant for high-quality CNT growth.

4.7.2 Nanocups

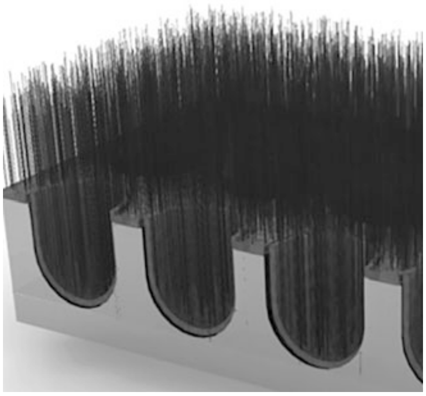

Nanocups are closely related to nanobowls and nanocaps. In case of carbon, the electrochemical activity of stacked N-doped carbon nanotube cups (NCNCs, Fig. 4.152) was explored in comparison to commercial Pt-decorated carbon nanotubes [422], demonstrating for the nanocup catalyst comparable performance to that of Pt catalyst in oxygen reduction reaction. The NCNC electrodes were used for H_2O_2 oxidation and consequently for glucose detection. Also, highly engineered hollow CNT nanocup arrays were fabricated (Fig. 4.153) using precisely controlled short nanopores inside anodic aluminum oxide templates [423]. The nanocups were effectively used to hold and contain metal nanoparticles, leading to the formation of multicomponent hybrid nanostructures with unusual morphologies. Also, cup-shaped nanocarbons generated by the electron-transfer reduction of cup-stacked carbon nanotubes were functionalized with porphyrins (H_2P) as light-capturing chromophores [424]. In addition, high-power electric double-layer capacitors (EDLCs) were fabricated (Fig. 4.154) using carbon-based 3D hybrid nanostructured electrodes, consisting of vertically aligned CNTs on highly porous carbon nanocups (CNCs), by a combination of anodization and CVD techniques [425, 426]. A 3D electrode-based supercapacitor showed enhanced areal capacitance by accommodating more charges in a given footprint area than that of a conventional CNC-based device. The increase in this capacitance was attributed to the larger surface area of the hybrid 3D CNT–CNC structure.

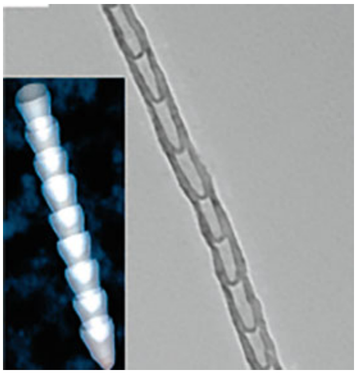

Fig. 4.152 TEM image of stacked nitrogen-doped carbon nanotube cups (NCNCs). Inset: cartoon illustrating orientation of the nanocups in stacked NCNC. (Reproduced with permission of the *American Chemical Society*)

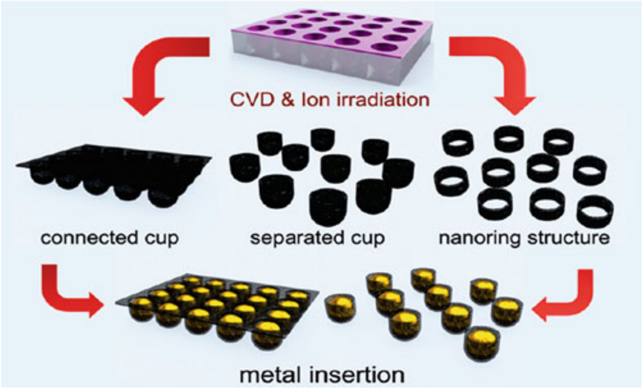

Fig. 4.153 Schematic illustrating the fabrication process and resulting architectures of a connected arrays of CNT nanocup film, individually separated nanocups, nanorings, and metal nanoparticle–nanocup heterostructures. (Reproduced with permission of the *American Chemical Society*)

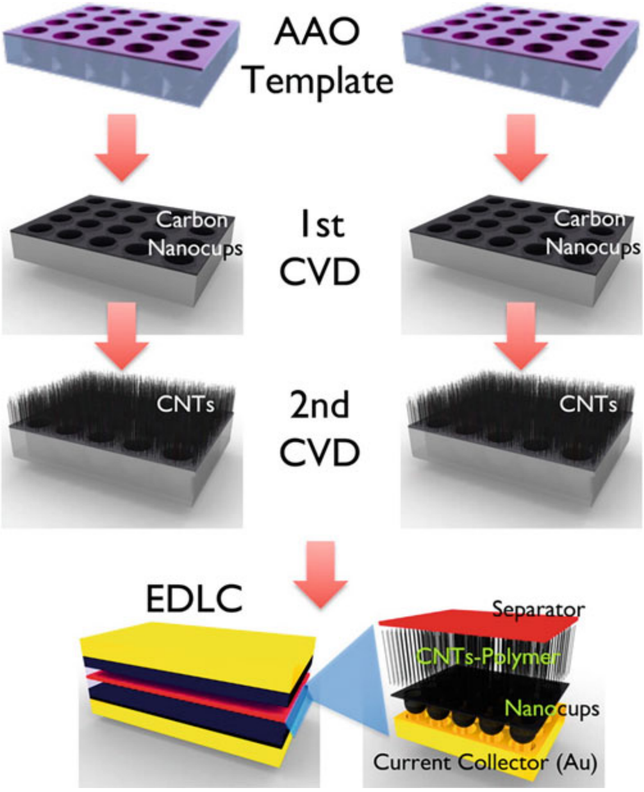

Fig. 4.154 Schematic illustrating the fabrication process. First, the CVD process synthesizes the highly porous carbon nanocups (CNC) structure, and the vertically aligned CNTs are synthesized on CNC by second CVD process. The supercapacitor consisted of two CNT–CNC hybrid structures on Au current collectors. (Reproduced with permission of the *American Chemical Society*)

4.7.3 Nanoplates

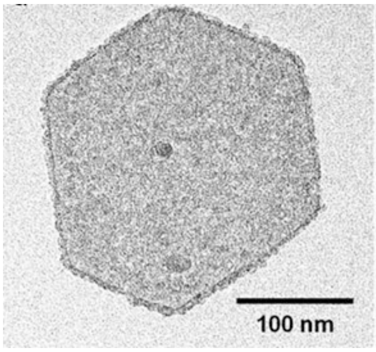

The plate-like[38] nanostructures are relatively widespread and represented practically by inorganic compounds, mainly by noble metals (gold, silver, palladium, rhodium, sometimes as composites with polymers), metal oxides, and oxygen-containing metal salts. In case of carbon, we have observed only a few examples of carbon nanoplates (despite the fact that graphene nanoplates are the thinnest material discovered in the universe [427]), in particular those fabricated starting from natural precursors. Thus, carbon-based microporous nanoplates containing numerous heteroatoms (H-CMNs) were fabricated (Fig. 4.155) from regenerated silk fibroin by the carbonization and activation of KOH,[39] exhibiting superior electrochemical

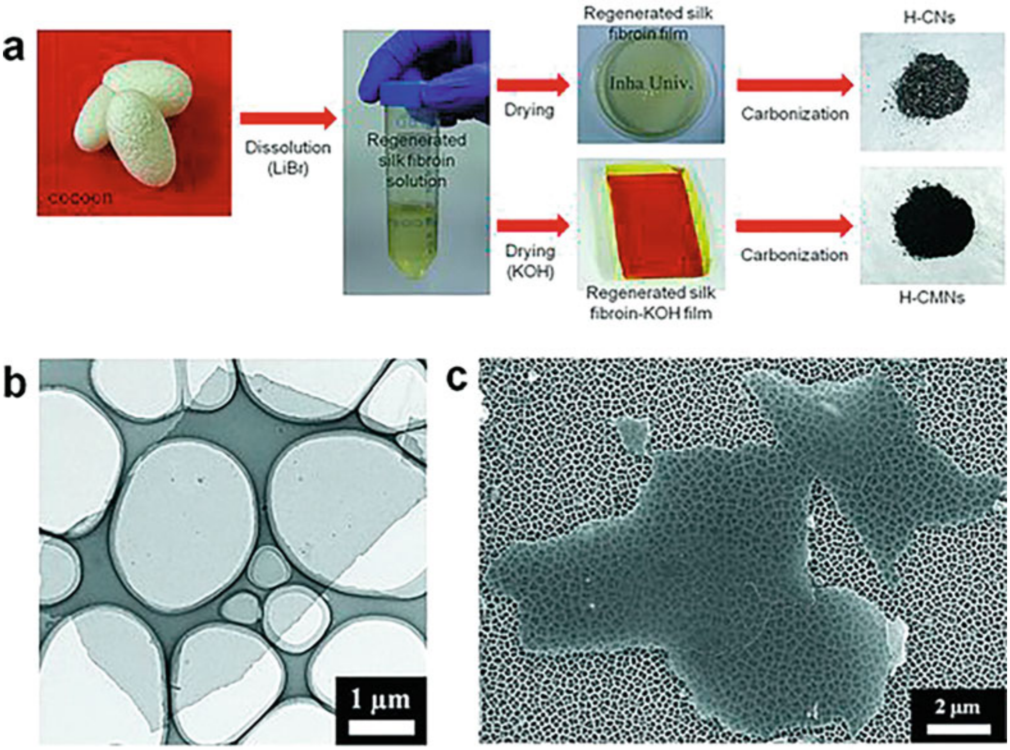

Fig. 4.155 Schematic images and morphologies of the H-CMNs. (**a**) Fabrication process of the H-CMNs. Silk fibroin fibers degummed from natural cocoons were dissolved in LiBr (9.3 M), and then as-casted regenerated silk fibroin film and regenerated silk fibroin-KOH film were carbonized. (**b**) FE-TEM image of the H-CMNs on a holey carbon grid. (**c**) FESEM image of the H-CMNs on alumina template membranes. (Reproduced with permission of *Wiley*)

---

[38] The nanoplate image is reproduced with permission of the *American Chemical Society* (*ACS Appl. Mater. Interfaces*, **2016**, *8*(43), 29628–29636).

[39] We note that KOH activation was also used for other nanocarbons (see previous sections).

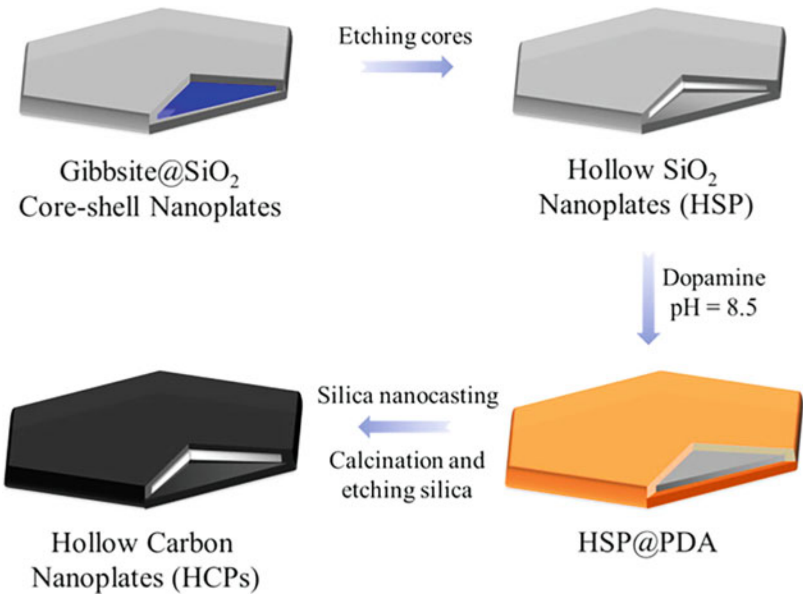

Fig. 4.156 Schematic synthesis route to prepare hollow carbon nanoplates (HCPs). (Reproduced with permission of the *American Chemical Society*)

performance suitable for usage as supercapacitors [428]. Similar conditions (pyrolysis and KOH activation) were also used for obtaining carbon nanoplated from cellulose [429]. Dispersible mesoporous N-doped hollow carbon nanoplates were synthesized by pyrolysis using gibbsite nanoplates as templates and dopamine as carbon precursor (Fig. 4.156) [430]. The product possessed uniform hexagonal morphology with specific surface area of 460 $m^2 \cdot g^{-1}$ and fairly accessible small mesopores (~3.8 nm); excellent colloidal stability in water was applied as electrode materials for symmetric supercapacitors. Some data on the toxicity of graphite nanoplates are also available [431].

4.7.4 Nanobrooms and Nanotepees

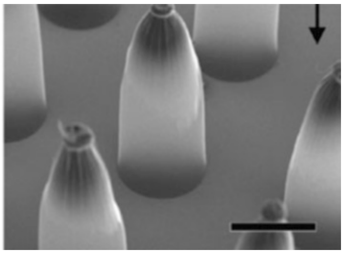

Several reports on relatively rare broomlike nanostructures belonging to distinct types of mainly inorganic compounds are known. Carbon nanotubes were also obtained in the said form. Thus, a dual-porosity CNT material of seamlessly connected highly porous aligned nanotubes and lowly porous closely packed nanotubes was created [432] by using capillary action of liquids. Millimeter-tall SWCNT forests synthesized by water-assisted chemical vapor deposition were used as model system. As a result, diverse structures using toothpicks, broomlike objects (Fig. 4.157b, c), tepees (Fig. 4.157f), as well as liquid thin films, bubbles, vapors, and superink jet printing were obtained.

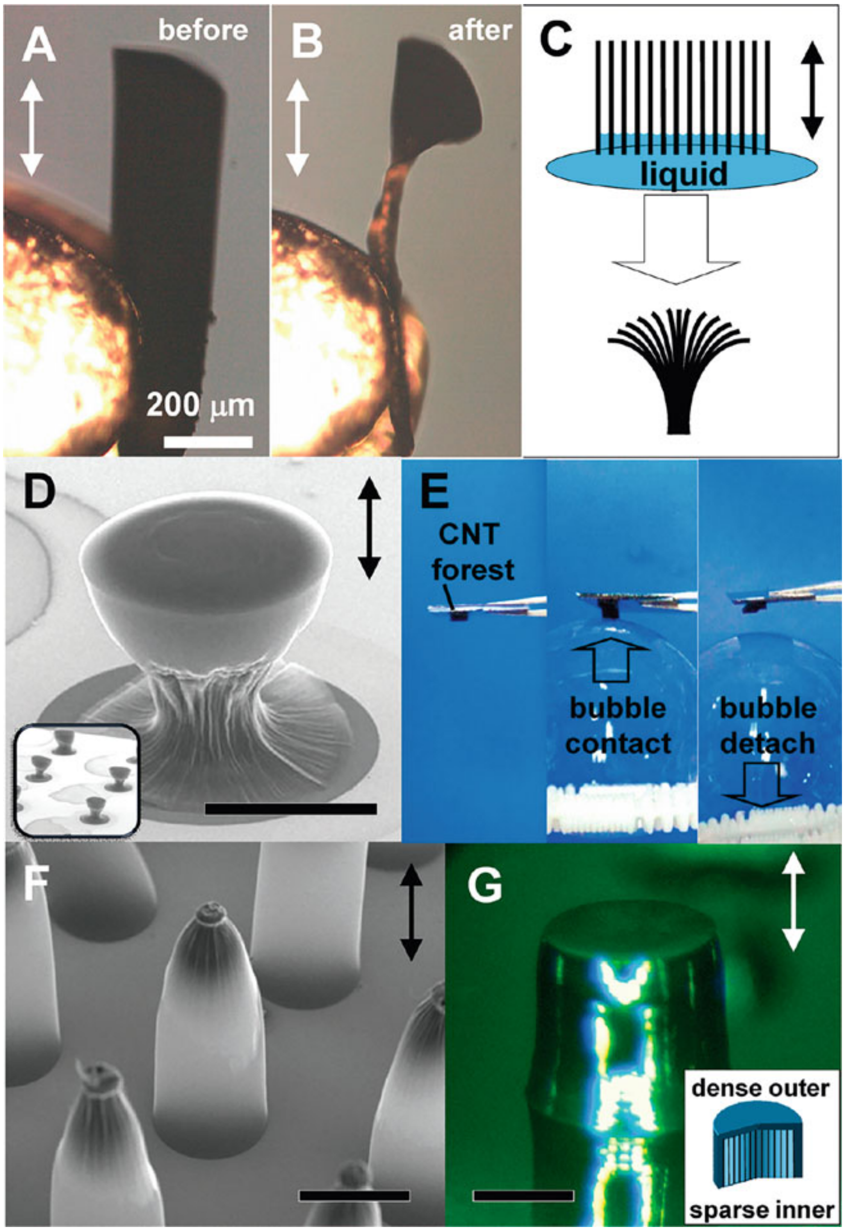

Fig. 4.157 Hybrid dual-porosity SWCNT material. (**a**, **b**) Before and after images of a high porosity SWCNT forest material (**a**) and hybrid dual-porosity material (**b**) made by partial collapse of the forest material. White lines indicate the tube alignment direction. (**c**) Model of the partial collapse process. (**d**) Mushroom brush structure created by bottom contact using thin liquid layer. Scale bar: 250 µm. Inset, array of mushrooms. (**e**) Photograph of bubble process. (**f**) Tepee structures created from top contact using bubble process. Scale bar: 500 µm. (**g**) Hard-coated SWCNT structure created by complete liquid bubble envelopment. Inset, diagram of the hard-coated sparse SWNTs. Scale bar: 250 µm. (Reproduced with permission of the *American Chemical Society*)

4.7.5 *Nanobrushes*

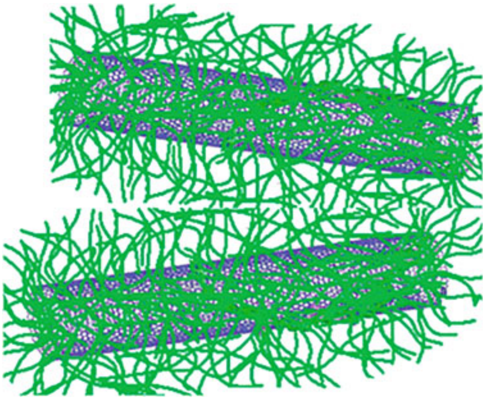

This nanostructural type, as well as some others reported above and below, are mainly represented by zinc oxide, prepared by distinct routes. Carbon-based nanobrushes are generally formed by CNT arrays. Thus, a multifunctional nanobrush[40] (attributed to nanodevices) using carbon nanotubes was described [433]. In a related report, superlong (7 mm) aligned, mainly double-walled, high-density CNTs (Fig. 4.158) were synthesized from ethylene, used as the source gas of carbon, with high reproducibility using CVD technique (typical CVD growth was carried out at 750 °C for 30 min as the standard growth time) [434]. Thin layers of Fe were used as the catalyst, and an Al_2O_3 buffer layer was used between the Si/SiO_2 substrate and the Fe catalyst. The relative levels of ethylene and water, as well as ethylene and H_2 during the CVD, were found to be the most important factor for the growth of such superlong aligned CNTs. Also, amorphous carbon nanotube brushes (Fig. 4.159) were prepared using glucose as the carbon precursor [435]. The functional surfaces of these nanotubes were covered with gallium ions and then calcined to get gallium oxide nanotube brushes, which were further converted to crystalline GaN nanotube brushes by treatment of ammonia at 800 °C.

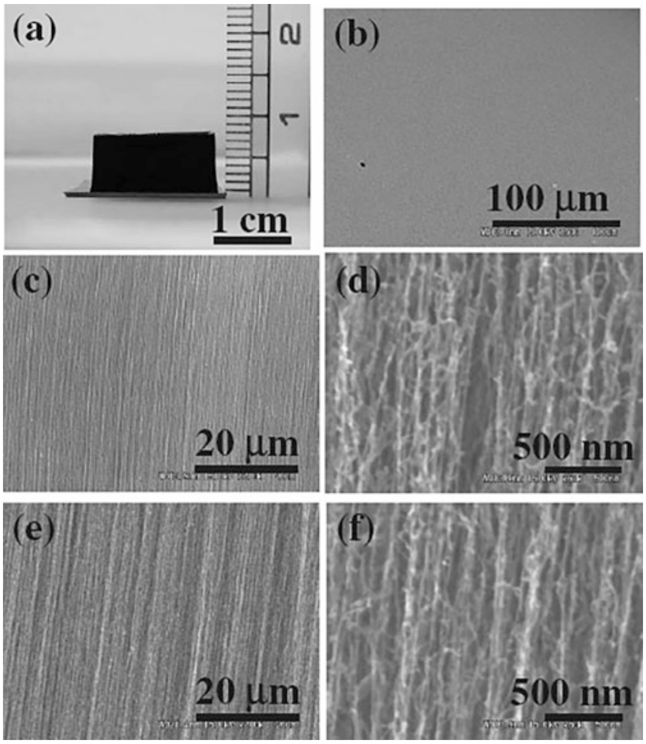

Fig. 4.158 Images of a superlong aligned brush-like CNTs: (**a**) digital photographic image of 7-mm-long aligned CNTs, (**b**) a SEM image of the top surface of the 7-mm-long aligned CNTs, (**c**) a low-magnification SEM image of the upper part of the aligned nanotubes, (**d**) a high-magnification SEM image of the upper part, (**e**) a low-magnification SEM image of the lower part of the aligned nanotubes, and (**f**) a high-magnification SEM image of the nanotubes. (Reproduced with permission of the *Japanese Journal of Applied Physics*)

---

[40] The nanobrush image above is reproduced with permission of *Springer* (*J. Mater. Sci. Mater. Med.* **2015**, *26*(1), 5356).

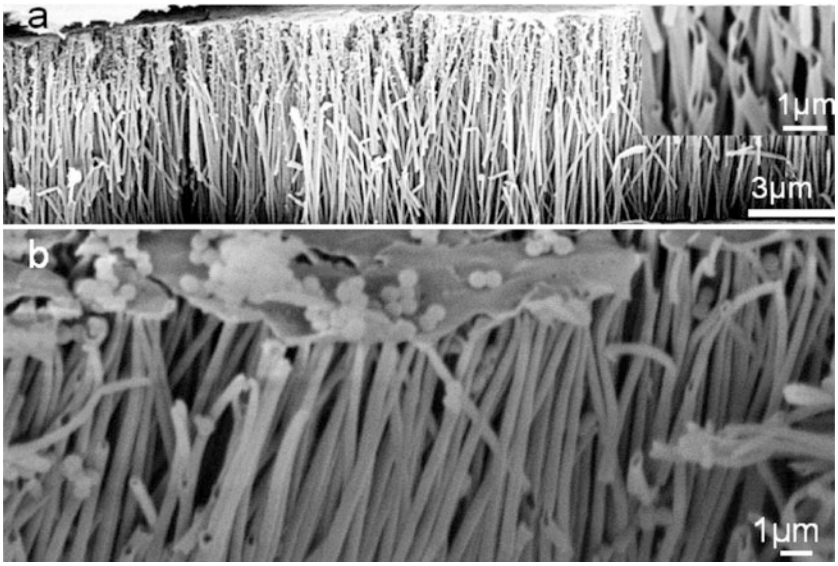

Fig. 4.159 (**a**) SEM image of amorphous carbon nanotube brushes. Inset shows penings of the nanotubes. (**b**) SEM image showing a coverage of the nanotube brushes by a thin carbon film. (Reproduced with permission of the *American Chemical Society*)

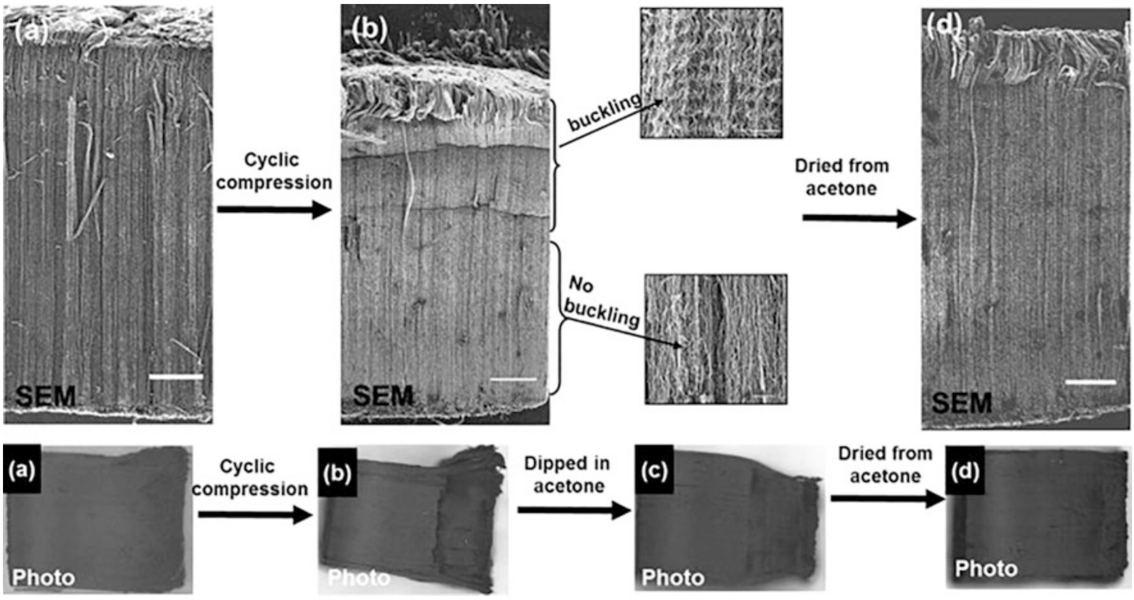

Fig. 4.160 Top portion and bottom portion are the SEM (scale ~0.5 mm) and optical micrograph photo images of the MWTs in different states, respectively. (**a**) Carbon nanotube block, as-prepared (**b**) carbon nanotubes which underwent cyclic compression loading at 35% strain for 105 cycles. The nanotubes are seen exfoliated at the upper portion of the block, where the density of the nanotubes is lower. (**c**) The nanotube block is immersed in the acetone for 10 min and removed. (**d**) Once the nanotube block is dried, it recovers to its nearly original state. (Reproduced with permission of the *Elsevier Science*)

CNT arrays, as nanobrush formers, being used in switches and other devices, can undergo to damage, exfoliation, and deformations at high strains [436]. These damages (Fig. 4.160) can be nearly recovered by capillary evaporation of solvents from the freestanding aligned nanotube brushes.

Nanobrushes on carbon basis have found a few applications. Thus, the composites of carbon nanobrushes embedded in a biocompatible poloxamer gel have relevance for tissue and cellular engineering and tissue regeneration in clinical medicine [437, 438]. Another example is a bioactive microelectrode for glucose biosensing, suitable especially for potential use in implantable devices, which was designed on the basis of CNT fiber directly spun from an aerogel, showing a unique, well-aligned nanostructure (nano-pore and nanobrush, Fig. 4.161) [439].

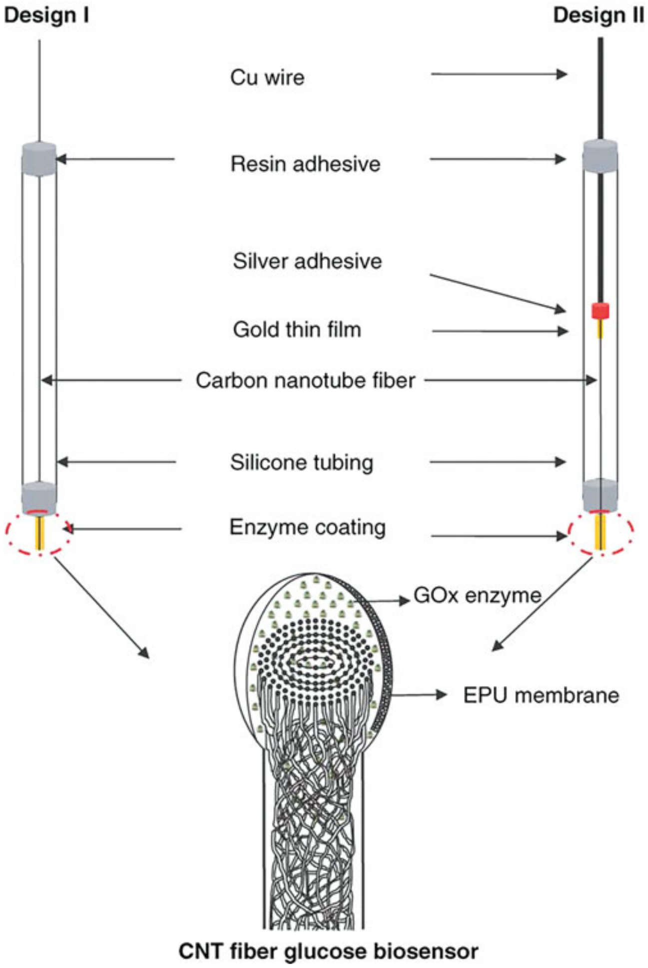

Fig. 4.161 Schematic diagram of CNT fiber microelectrode assembly with two designs. Design I, the CNT fiber was insulated in a silastic tubing to fit in the test unit. Design II, Cu wire and a gold coating were introduced to improve the connection. The sensor working parts in both designs are demonstrated here: a GOx enzyme is immobilized at the brush-like end of the CNT fiber, and the enzyme layer is encapsulated by the epoxy-polyurethane (EPU) semi-permeable membrane. (Reproduced with permission of *Wiley*)

4.7.6 Nanocarpets

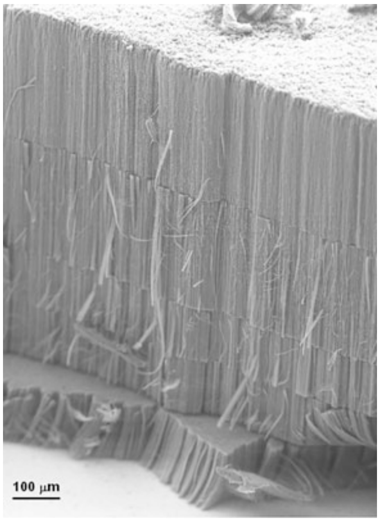

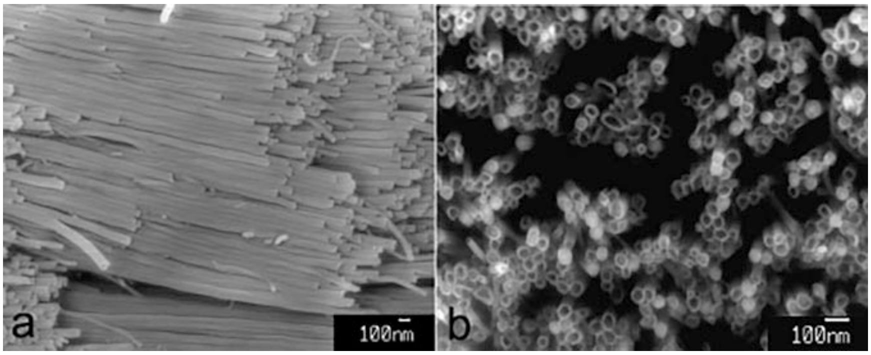

Fig. 4.162 MWCNT carpet: (**a**) side view and (**b**) view looking down on the top of the carpet. (Reproduced with permission of *Wiley-VCH*)

Fig. 4.163 Carpet-like CNT films. (Reproduced with permission of *IOP Publishing*)

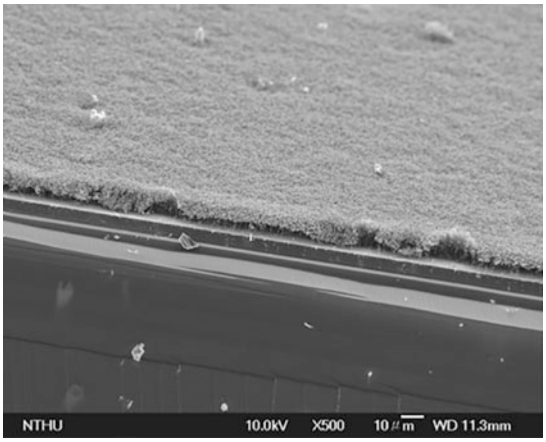

Relatively rare carpet-like nanostructures,[41] related to nanobrushes, are formed mainly by nanotubes, nanowires, or nanorods, belong to different type of compounds, and possess especial properties (in particular, superhigh hydrophobicity) in comparison with major part of other less-common nanostructures. For slender nanostructures, the nanostructure may change after coming into contact with liquid (this phenomenon is known as the "nanocarpet effect" [440–442]). The newly formed nanostructures may have a great impact on the hydrophobicity of a surface. The nanocarpet effect is a simple and effective way to apply to a variety of nanowire, nanotube, or nanorod structures to generate a hierarchical structure with both microscale domains and nanoscale feature (nanorod tips) for superhydrophobicity and other surface property studies.

Carbon nanotube carpet-like nanostructures have been obtained mainly by CVD. Thus, massive carpets of well-packed, vertically aligned, and very long MWCNTs were synthesized by this classic technique [443]. Ferrocene was frequently used as a precursor in such syntheses, for instance, in a CVD-assisted growth of MWCNTs (Fig. 4.162) in 60:40 toluene/1,2-diazine at 760 °C in argon [444] or in the pyrolysis of aerosols obtained from C_6H_6/$NiCp_2$/$FeCp_2$ mixtures generating aligned Invar (Fe–Ni alloy, $Fe_{65}Ni_{35}$)-filled carbon nanotube carpet-like samples of high purity [445]. Radio-frequency hot-filament CVD (RFHFCVD), where the reactant gases (methane and hydrogen gas used as the carbon source and diluted gas, respectively) were first dissociated by the MW field before entering the chamber, thus, ensuring that there was a dense growth of CNTs from a large Ni catalyst particle, was proposed for CNT films and carpet-like nanostructure (Fig. 4.163) fabrication [446]. The growth mechanisms were found to be either "tip growth" or "base growth" depending on the size of the catalyst metal particles involved. It was concluded that the oxide iron group alloys like Ni/NiO_x, CuNi/$CuNiO_x$, and AgNi/$AgNiO_x$ were essential to yield successful growth of CNTs.

In similar reports, CVD method was used for anchoring densely packed, vertically aligned arrays of CNTs (Fig. 4.164) into silicone layers using spin-coating, CNT insertion, curing, and growth substrate removal [447]. CNT arrays of 51 and 120 μm in height were anchored into silicone layers of thickness 26 and 36 μm, respectively. Alternatively to CVD techniques, the pulse electrodeposition technique was utilized to deposit nanosized (≤10 nm) Ni catalysts on carbon fabric (CF) [448]

---

[41] The nanocarpet image above is reproduced with permission of the *American Chemical Society* (*Nano Lett.*, **2005**, *5*(12), 2394–2398).

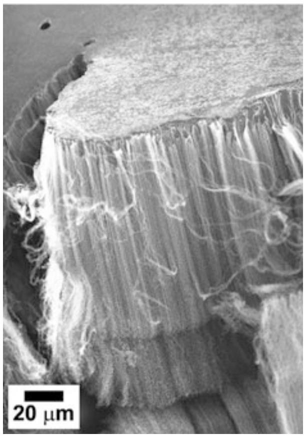

Fig. 4.164 Double-anchored CNTs nanocarpet. (Reproduced with permission of *IOP Publishing*)

allowing the growth of carbon nanofibers (CNFs) on CF. The preparation of CNF-coated CF (carpet-like CF) was carried out in a thermal CVD system with an optimum loading of Ni catalysts deposited in the PED pulse range from 20 to 320 cycles. CNFs that grew at 813 K had a hydrophobic surface, like lotus leaves. Among other potential applications for carbon-based nanocarpets, an effective technique for large-scale integration of oriented CNTs inside functional devices, based on capillary assembly and buried dielectrophoresis electrodes allowing aligning and assembling with high accuracy dense CNT carpets, was offered [449].

4.7.7 Nanospindles

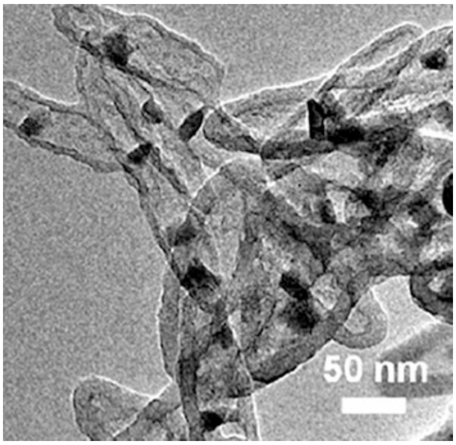

Spindle-like nanostructures have been found for a series of elements and inorganic compounds; we note that a certain number of reports are devoted to oxides and salts of rare-earth elements. Frequently, this nanostructural type was formed together with a variety of other structures, such as, for example, nanorods or nanoflowers. For carbon, nanospindles are almost unknown. Thus, the pyrolysis strategy was applied for obtaining robust yolk–shell nanospindles with very sufficient internal void space for high-rate and long-term lithium-ion batteries, in which an Fe_3O_4@Fe_3C core@shell nanoparticle is well confined in the compartment of a hollow carbon nanospindle (Fig. 4.165) [450]. These nanospindles were fabricated in situ thermally annealing the as-made Fe_2O_3@RF core@shell nanospindles at 550 °C. In this structure, a heterogeneous Fe_3O_4@Fe_3C core@shell nanoparticle (15–25 nm) was found to be sandwiched in the compartment of a hollow carbon nanospindle (30 nm in width and 100 nm in length).

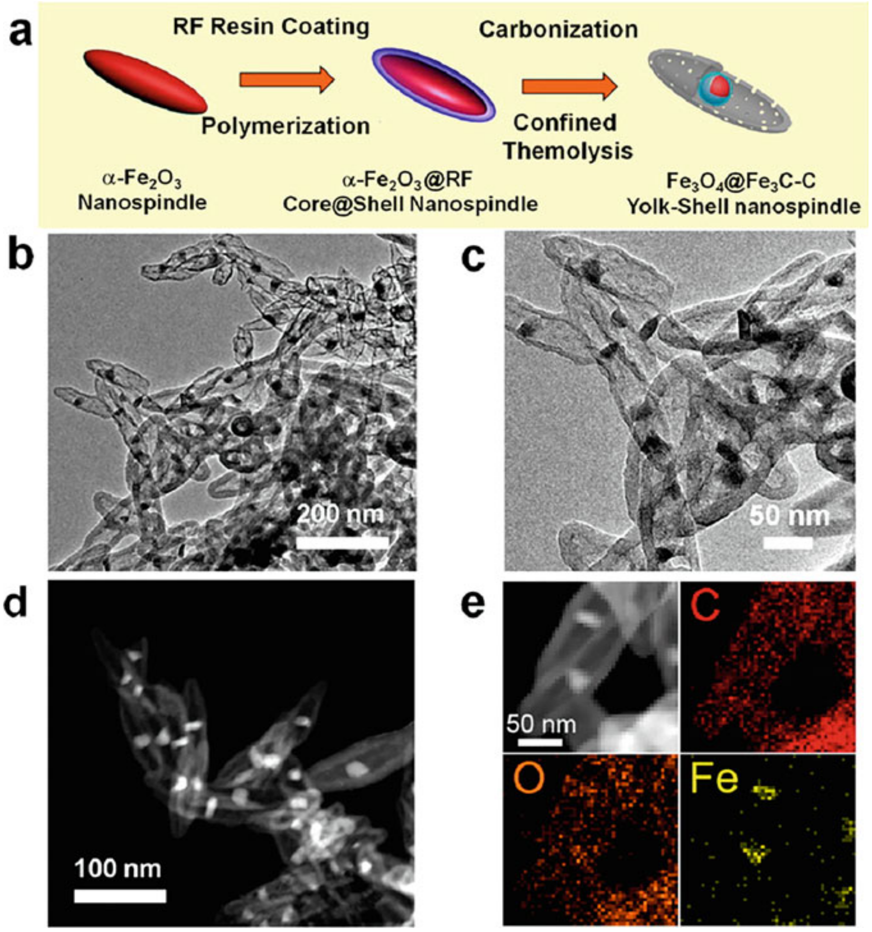

Fig. 4.165 (**a**) Schematic illustration of the synthesis of the Fe_3O_4@Fe_3C–C yolk–shell nanospindles. (**b**, **c**) TEM image, (**d**) STEM image, and (**e**) TEM-EDS mapping. (Reproduced with permission of the *American Chemical Society*)

4.7.8 Nanowebs

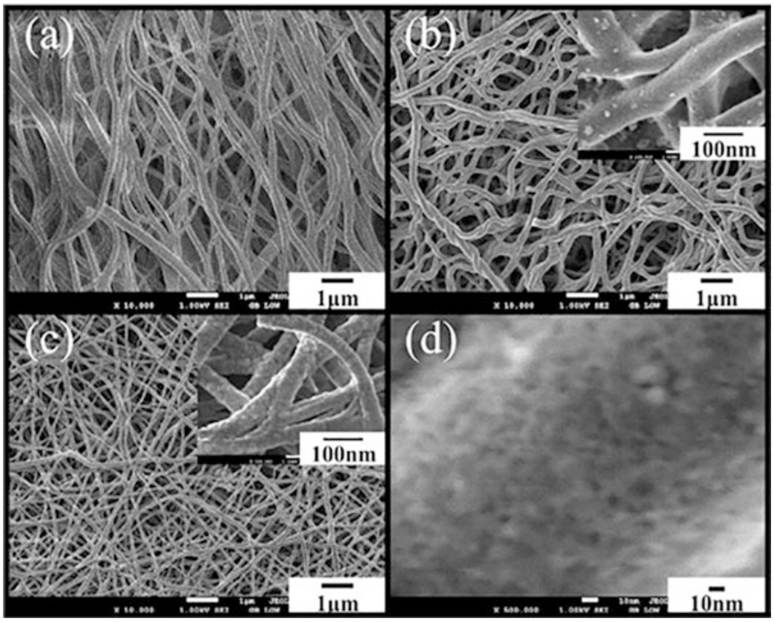

Nanowebs [451] [42] are of great technological interest since they contain nanowire densities on the order of 10^9/cm^2. Nanowebs are beautiful objects, reported for some nonrelative to each other compounds. First of all, we note that a series of porous polymers [452], frequently obtained by electrospinning technique, have been reported in web-like nanoform; here we note only some of them. Nanoweb porous structures are currently applied in filters [453–455], fibers [456], and composites [457, 458], in particular those containing carbon nanotubes, for example, MWCNT/poly(ethylene terephthalate) (PET) nanowebs, obtained by electrospinning [459]. It was established that tensile strength, tensile modulus, thermal stability, and the degree of crystallinity increased with increasing MWCNT concentration. Another example of CNTs–polymer composite nanowebs is polyurethane (PU) and PU/MWCNT nanocomposite nanofibers and nanowebs, both with diameters of 350 nm, which were prepared by an electrospinning process from PU DMF solutions [460]. Multifunctional nanowebs were prepared using cyclodextrin-based inclusion complex (CD-IC) to disperse MWCNTs within electrospun polyvinylidene fluoride nanofibrous membranes (PVdF-NFM) [461]. Subsequently, MWCNT(CD-IC)/PVdF-NFM was loaded with gold particles. The Au/MWCNT(CD-IC)/PVdF-NFM was found to be electroactive and showed excellent electrocatalytic activity toward oxidation of ascorbic acid. As an example of non-CNT-containing web-like polymers, we note the octaphenyl-POSS (polyhedral oligomeric silsesquioxane OPPOSS), which was blended with PMMA to prepare inorganic–organic hybrid nanofibers/nanowebs using electrospinning method [462].

Web-like carbon nanotubes (Fig. 4.166) were formed by laser ablation (Nd:YAG laser with 532 nm wavelength, 10.54 W power, 30 min) using a graphite target containing Ni and Co catalysts, each with weight percentage of 10% [463]. It was shown that the diameter of the carbon nanotubes formed using Ni and Co catalysts was between 50 and 150 nm in size. Carbon nanostructures may be precursors of other nanoweb structures. Thus, when carbon nanofilms were deposited on the Si (100) wafers at substrate temperatures from r.t. to 700 °C by ultrahigh-vacuum ion-beam sputtering [464], a nanoweb-like morphology of the crystalline SiC formation was also observed on the surface of film. The much enhanced hardness and Young's modulus at 700 °C were attributed to the SiC formation as well as nanoweb-like morphology. Additionally, web-like SWCNT structures on the surface of zeolite template (Fig. 4.167) were reported. Carbon-based nanowebs are also readily

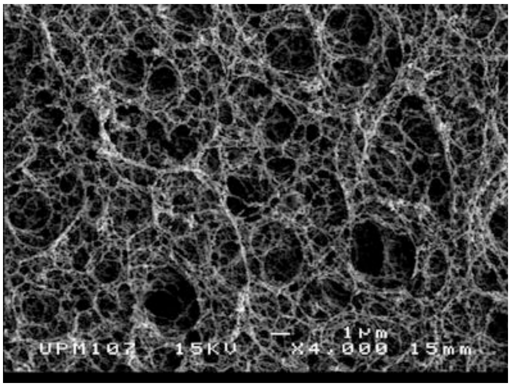

Fig. 4.166 SEM image of CNTs collected from the PLAD process by using graphite-Ni pellet. (Reproduced with permission of *Solid State Science and Technology*)

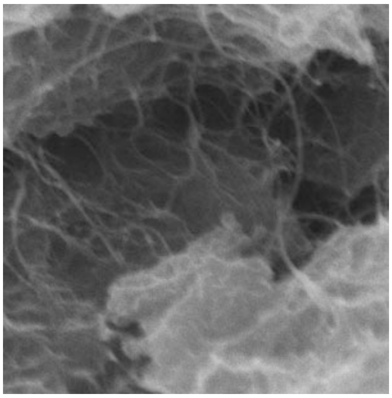

Fig. 4.167 Web-like SWCNT structures on the surface of zeolite template [465]. (Reproduced with permission of *The Royal Society of Chemistry*)

---

[42] The nanoweb image above is reproduced with permission of the *Elsevier Science* (*Energy*, **2013**, *55*, 925–932).

prepared from natural precursors. Thus, cellulose nanowhisker (CNW), prepared by acid hydrolysis of microcrystalline cellulose, was carbonized at different temperatures in the range of at 800–1200 °C, yielding carbon nanoweb [466]. The better carbon structure was observed when the carbonization temperature was higher.

A considerable part of carbon nanoweb applications is related with their uses in supercapacitors and lithium batteries. Thus, air-electrode architecture based on 3D open macroporous carbon nanowebs was found to be particularly advantageous for Li-O_2 batteries utilizing the redox mediators in the electrolyte by facilitating the efficient transport [467]. Oxygen- and nitrogen-doped carbon nanowebs were applied as an efficient, metal-free ORR catalyst for hybrid Li-air batteries [468]. The oxygen- and nitrogen-doping led to highly active pyridone species on the carbon nanoweb surface for ORR. Also, uniform $Li_4Ti_5O_{12}$/carbon composite nanowebs with high surface area and porosity consisting of ultrasmall crystals in carbon core–shell architecture were prepared by thermal pyrolysis and oxidation of a composite of electrospun lithium–titanium/polyacrylonitrile nanowebs in argon atmosphere [469]. This composite was found to be a promising anode candidate for lithium-ion batteries. In addition, high-performance wearable supercapacitor (area capacitance of 2.5 mA cm^{-2}) fabrics based on flexible metallic fabrics (Ni–cotton), on which nanofiber webs containing MWCNTs are directly electrospun without the need for any post-treatment, was fabricated (Fig. 4.168) [470]. Such supercapacitor fabrics can be integrated into commercial textiles with any desirable forms.

Catalytic applications are also common. Thus, studying Co_3O_4/CNW bifunctional catalysts (Fig. 4.169), individual functionality of Co_3O_4 and the N-doped carbon nanoweb (CNW) in ORR and OER was investigated [471] by rotating disk electrode measurements. It was found that Co_3O_4 alone exhibited poor ORR catalytic activity, but, in the presence of CNW, it assisted the selective four-electron oxygen reduction over the two-electron pathway. CNW underwent serious degradation at the high potential of the OER, but its stability improved greatly upon the deposition of Co_3O_4.

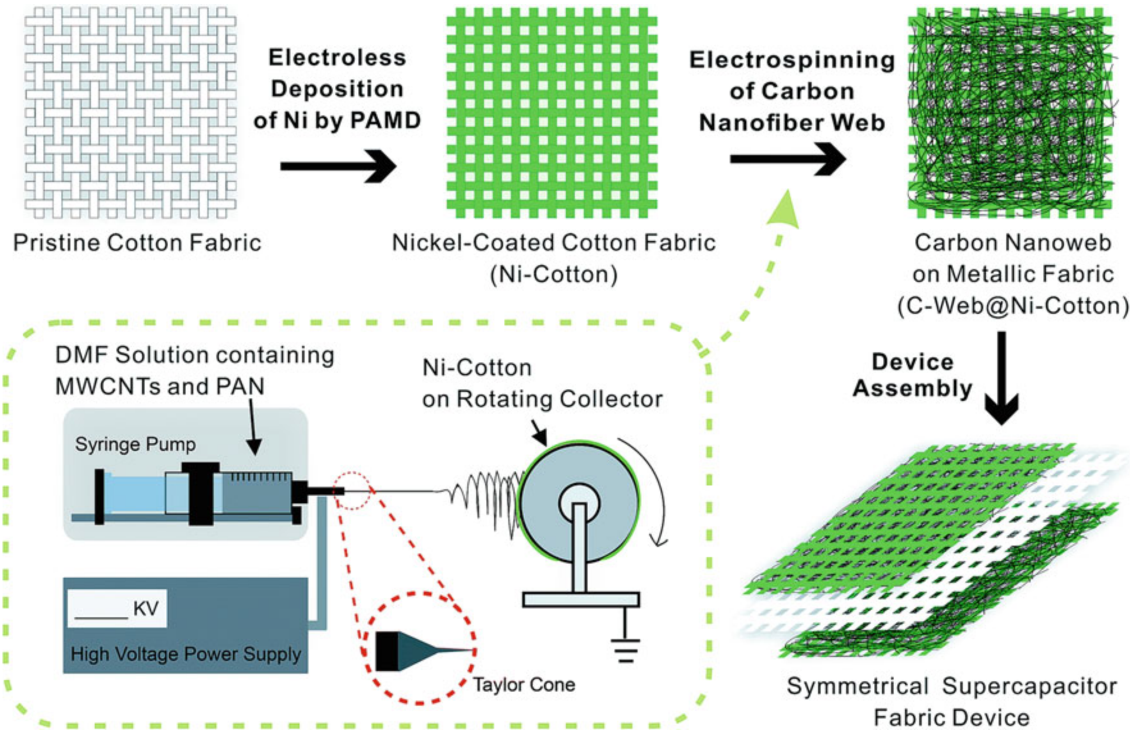

Fig. 4.168 Schematic illustration of the fabrication procedures of supercapacitor fabrics. The inset shows the details of the one-step electrospinning setup. (Reproduced with permission of the *Royal Society of Chemistry*)

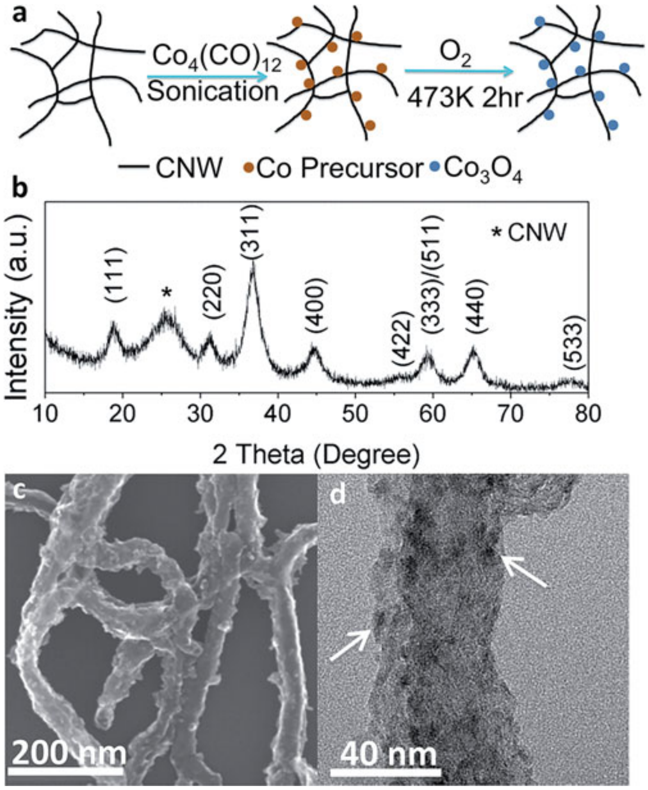

Fig. 4.169 (**a**) Schematic pathway for the ultrasonic synthesis of Co_3O_4/CNW. (**b**) X-ray diffraction pattern of Co_3O_4/CNW-C. (**c**) SEM image of Co_3O_4/CNW-C. (**d**) HRTEM image of Co_3O_4/CNW-C. (Reproduced with permission of the *Royal Society of Chemistry*)

4.7.9 Nanosponges[43]

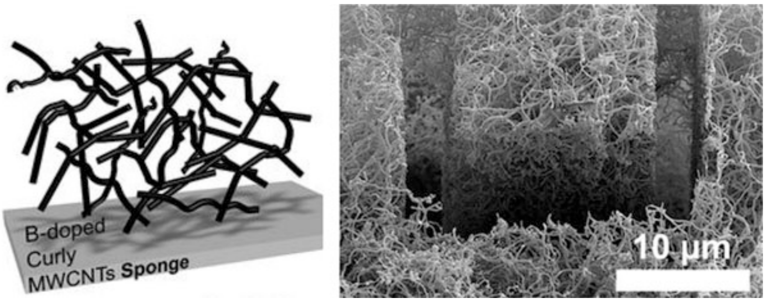

Carbon-based nanosponges are normally prepared by CVD, although they can be also obtained by laser ablation (see below) or by a pulsed microplasma cluster source [472] in the presence of a metal–organic catalyst (Fig. 4.170), and are of the permanent interest for the purposes of oil adsorption. Thus, carbon nanostructures (nanotubes, nanofibers, and nanosponges, identified as a mixture of sp^2 and sp^3 hybridizations) were synthesized onto Si (001) substrates using a microwave-assisted plasma-enhanced CVD (PECVD) from C_2H_2–Ar mixtures at low substrate temperatures (120 °C) [473]. For the higher C_2H_2 partial pressures, dense sponge-like (nanosponge) structures, consisting of a large number of bundles, were formed, in a difference with less C_2H_2 partial pressures, when other nanostructures were observed. Boron-infused carbon nanosponge can

---

[43] The nanosponge images above are reproduced with permission of *Nature* (*Sci. Rep.*, **2012**, *2*, Article number: 363).

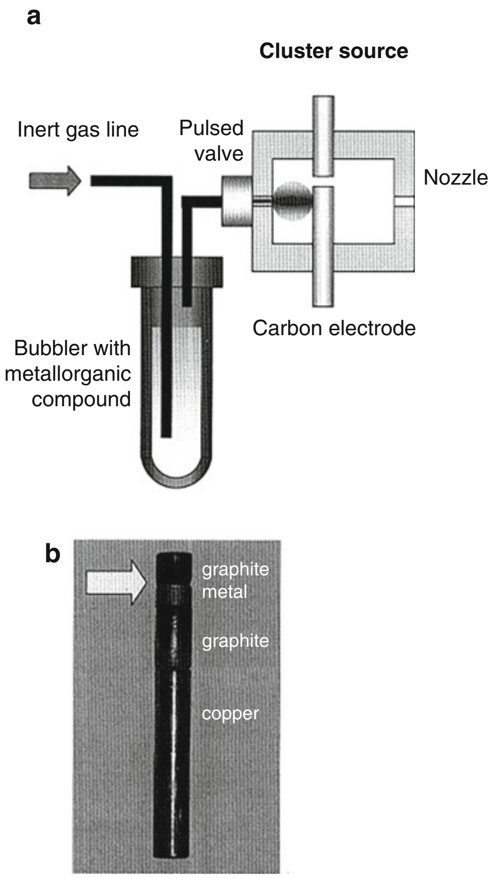

Fig. 4.170 Schematic representation of a PMCS source with the two methods for metal cluster doping. (**a**) A bubbler is inserted in the gas line prior to the source in order to entrain metal–organic species in the gas flux. (**b**) Photograph of a composite carbon–metal rod. A metal disk is inserted in the ablation region in order to provide metallic atoms and clusters during the erosion and condensation process. (Reproduced with permission of the *Elsevier Science*)

be applied for oil absorption,[44] reaching nearly 100% of the oil [474]. It was revealed that sponges with higher amounts of boron infused into them are able to achieve the special properties of boron that helped increased the surface area and the extremely oleophilic nature of the sponge.

Similar ultra-lightweight 3D architectures consisting of boron-doped MWCNTs (CB_XMWNTs, macroscale (cm^3 in size), entirely made up of randomly orientated and entangled CNTs with little to no amorphous carbon, Fig. 4.171), were grown directly onto the walls of a quartz tube furnace via an aerosol-assisted catalytic CVD method using triethylborane as the boron source [475]. Boron was found to be responsible for the creation of “elbow-like” junctions and covalent nanojunctions. CB_XMWNTs can be used as sorbent materials (in particular, for oil), hydrogen storage, and flexible conductive scaffolds as porous 3D electrodes. Also, CVD synthesis of carbon nanotubes and nanofibers on the surface of expanded vermiculite was used to produce a highly hydrophobic floatable absorbent to remove oil spilled on water [476]. It was shown that the carbon nanotubes and nanofibers grew on FeMo catalyst impregnated on the vermiculite surface to form a “sponge structure.” As a result of these carbonaceous nanosponges, the absorption of different oils remarkably increased ca. 600% with a concomitant strong decrease of the undesirable water absorption.

SWCNT bundles dispersed in a highly polar fluid were found to agglomerate into a porous structure (Fig. 4.172) being exposed to low levels of laser radiation (514.5 nm) in DMF [477]. An interesting effect was observed: under laser illumination, the bundles agglomerate, leading to a substantial decrease in the measured sound velocity (significantly lower than that of pure DMF, though the SWCNT bundles have a much higher sound speed than the DMF) with increasing SWCNT concentration.

---

[44] Applications of nanomaterials for oil remediation were recently reviewed. (a) *Journal of Petroleum Science and Engineering*, **2014**, *122*, 705–718; (b) Nanomaterial-based methods for cleaning contaminated water in oil spill sites. In: *Nanotechnology for Energy Sustainability*. B. Raj, M. Van de Voorde, Y. Mahajan (Eds.), Wiley-VCH, **2016**, 1139–1160.).

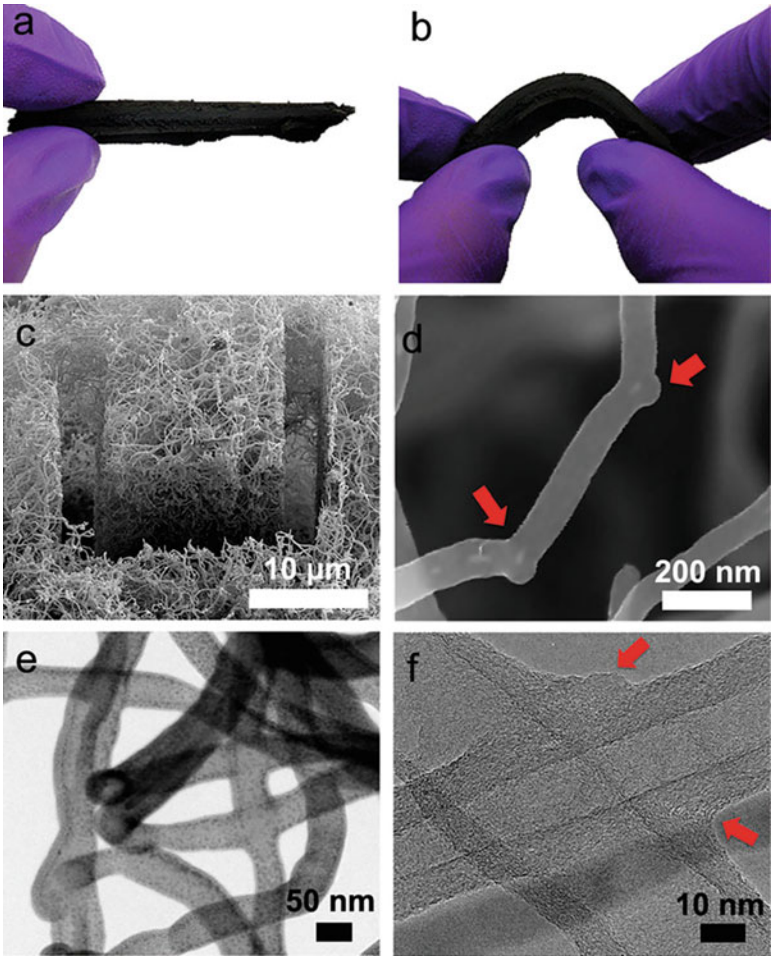

Fig. 4.171 (**a**) Photograph of 3D macroscopic CB_xMWNT solid sponge material as-produced; (**b**) shows photograph of the flexibility and mechanical stability upon bending the sample (**a**) by hand; (**c**) SEM image after ion-beam “slice and view” feature showing the interior porous structure of the entangled nanotube network; (**d**) closer look at the “elbow” defects found in CB_xMWNT solids; (**e**) STEM image showing two, four-way covalent nanojunctions in series; (**f**) TEM image showing two overlapping CB_xMWNTs welded together assisted by boron doping. (Reproduced with permission of *Nature*)

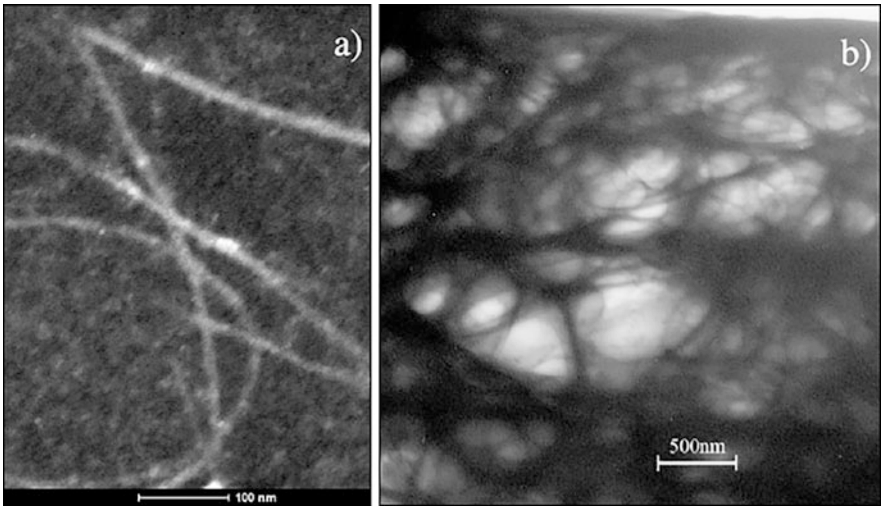

Fig. 4.172 (**a**) TEM image of SWCNTs. The images were from specimens obtained by drying a sonicated DMR-SWCNT bundle suspended on a grid. (**b**) TEM image of light-induced agglomerated bundles. The clear regions are pores, while the dark regions are the SWCNT bundles. (Reproduced with permission of the *American Physical Society*)

4.7.10 Nanofoams

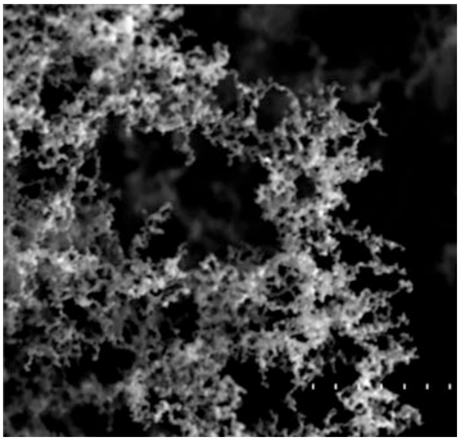

Currently, nanofoams[45] are known for a series of elements and compounds, mainly for carbon [478], and are applied, in particular, as materials for supercapacitors [479–481] and cathode catalysts for Li–O_2 batteries [482, 483]. Fundamental properties of high-quality uniform carbon nanofoams, comprised of predominantly sp^2-type carbon, were recently studied, hydrothermally producing them with different densities by changing the process temperature in the autoclave reactor [484]. The low-density foams were found to consist of micropearls with ≈2–3 μm average diameter, and higher-density foams contained larger-sized micropearls (≈6–9 μm diameter), frequently coalesced to form nonspherical μm-sized units. With higher autoclave temperature, the carbonization process became more effective, leading to an increase in sphere size and a thickening of the internal wall structure. Among other conclusions, the nanofoam materials exhibit physical properties originating from a mixture of carbon atoms with sp^2 and sp^3 hybridization. This was also confirmed by DFT calculations [485]. The foam may accommodate the same type of defects as graphene (Fig. 4.173). In addition, a fundamental theoretical finding of the re-emergence of superconductivity in heavily compressed CaC_6 and formation of carbon nanofoam in these conditions was reported [486].

Laser ablation is one of techniques leading to carbonization and foam formation [487]. The corresponding equipment is shown in Fig. 4.174 [488]. Thus, high-repetition-rate laser ablation and deposition of carbon vapors resulted in the formation of quite different carbonaceous structures depending on the pressure of the ambient Ar gas in the chamber [489]. Diamond-like carbon films formed at a pressure below ~ 0.1 Torr, whereas a diamond-like carbon nanofoam (Fig. 4.175) was created above 0.1 Torr. The bulk density of various foam samples was found to be in the range $(2–10) \times 10^{-3}$ g/cm^3, and the specific surface area was 300–400 m^2/g. Carbon nanofoams (CNFs) were also prepared [490] by air cooling the pyrolysate of high purified acetylene gas. Each particle of the nanofoam was constructed by 2 to 4 mutually nested carbon balls with ~300 nm in diameter. Undoubted room-temperature ferromagnetism with saturation magnetization of 0.11 emu/g at 300 K in CNFs can be

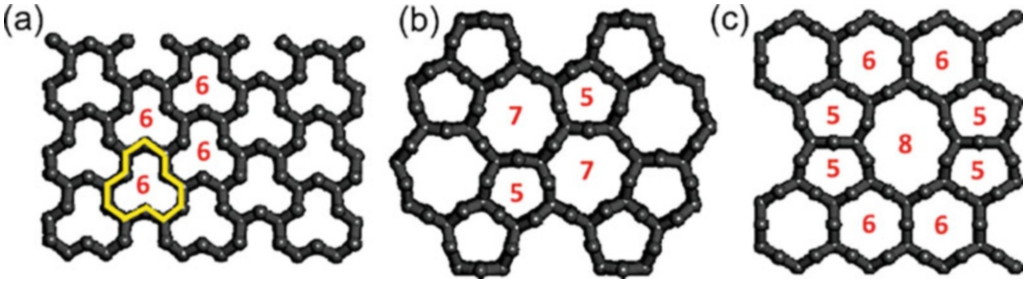

Fig. 4.173 Defects in the foam. (**a**) Folding of the perfect foam, induced by applying hydrostatic pressure or by electron doping. Foam structures containing (**b**) 5775 and (**c**) 558 defects, familiar from defective graphene. (Reproduced with permission of *APS Physics*)

---

[45] The nanofoam image above is reproduced with permission of the *Springer* (*Nanoscale Res. Lett.*, **2013**, *8*, 233).

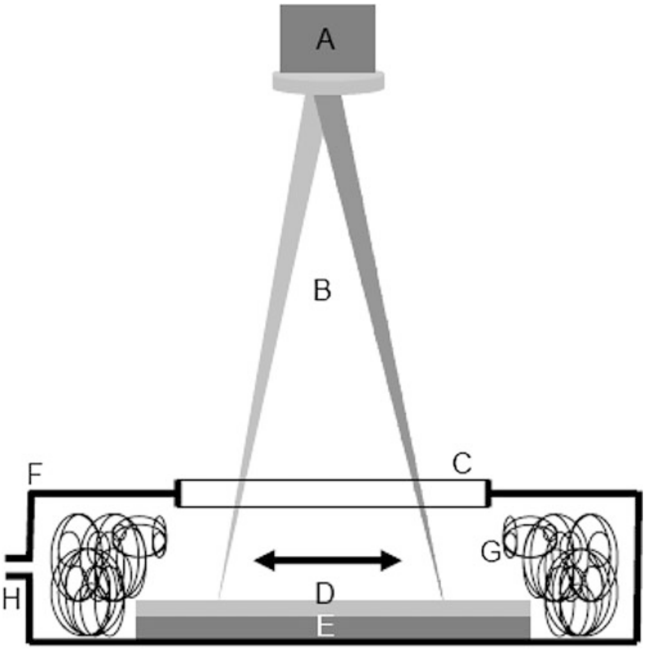

Fig. 4.174 Schematic diagram of the experimental setup used for the laser ablation production of carbon nanofoamss. A galvanometer mirror box (**a**) distributes the laser radiation (**b**) through a flat-field focal lens and a silica window (**c**) onto layers of the employed organometallic compounds (**d**) deposited onto a ceramic tile substrate (**e**) placed inside a portable evaporation chamber (**f**). The synthesized soot is mainly collected on an entangled metal wire system (**g**). The produced vapors are evacuated through a nozzle (**h**). (Reproduced with permission of *Springer*)

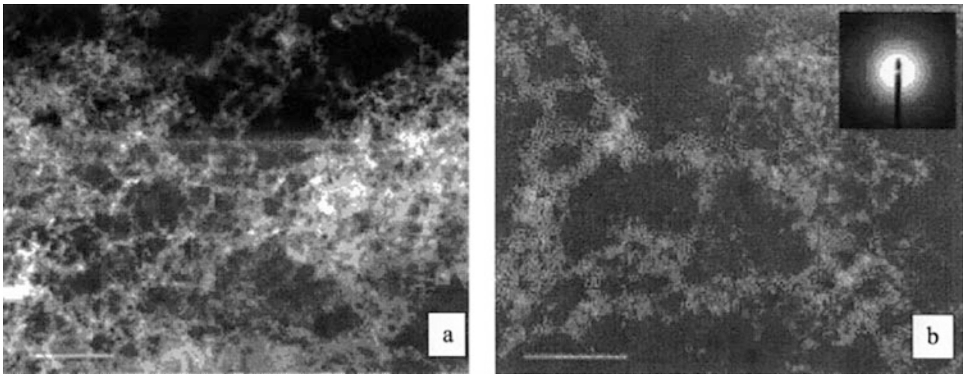

Fig. 4.175 Scanning (**a**) and transmission (**b**) electron microscope images showing the freestanding carbon foam. The bars in the images are 1 mm (Fig. 4.175a) and 100 nm (Fig. 4.175b). (Reproduced with permission of the *Springer*)

attributed to the carbon balls themselves instead of impurities. Additionally, within foam-like carbon, onion concentric fullerene-like structures (see details below) can be formed [491]. It was shown that an optimal annealing temperature of 4000 K is required to form well-ordered onions concentric fullerene-like spheres. The onions formed from the outer layer first, and a model was offered in which the background pressure must be sufficient to allow atoms to cluster, yet low enough to allow annealing into well-ordered onions.

4.7.11 Nanoladders

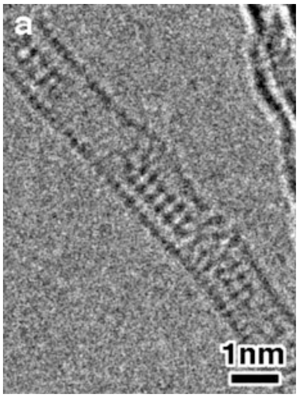

A series of reports are devoted to carbon nanotube ladder-like structures. Thus, various single-walled CNTs (SWCNTs) and double-walled CNTs (DWCNTs) having different diameters were used as containers for cubic octameric $H_8Si_8O_{12}$ molecules (Fig. 4.176) [492]. Depending on the diameter of the CNTs, two types of structures were formed inside the CNTs: in the case of those CNTs having inner diameters ranging from 1.2 to 1.4 nm, an ordered self-assembled structure composed of $H_8Si_{4n}O_{8n\text{-}4}$ molecules was formed through the transformation of $H_8Si_8O_{12}$; in the case of CNTs having inner diameters larger than 1.7 nm, a disordered structure was formed, indicating strong interactions between the CNTs and the encapsulated $H_8Si_{4n}O_{8n-4}$ molecules. Also, multiwalled carbon nanotubes (MWCNTs) were uniformly grown directly on metal-catalyzed carbon fibers by catalytic decomposition of acetylene at ~700 °C using thermal CVD process, accompanying by formation of

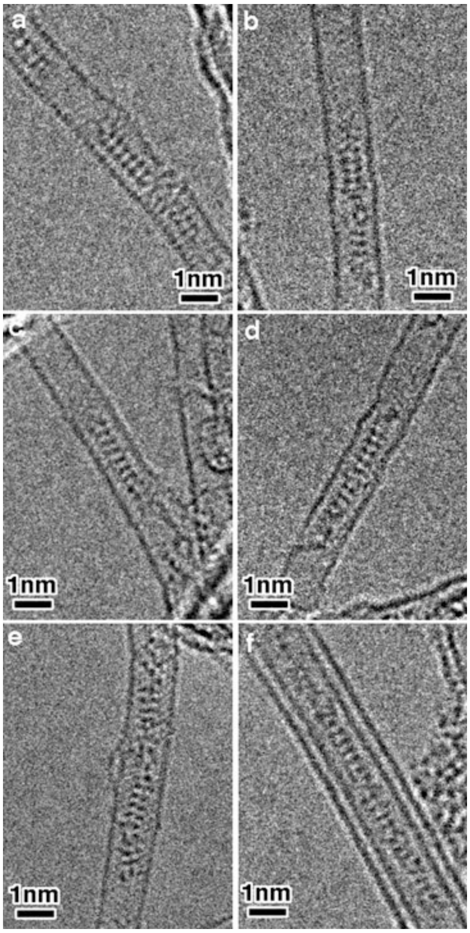

Fig. 4.176 HRTEM images of $H_8Si_8O_{12}$ encapsulated inside the various CNTs. (**a–d**) HRTEM images of $H_8Si_8O_{12}$@HiPCO SWCNTs, (**e**) HRTEM image of $H_8Si_8O_{12}$@FH-P SWCNT, (**f**) HRTEM image of $H_8Si_8O_{12}$@FH-P DWCNT. (Reproduced with permission of the *American Chemical Society*)

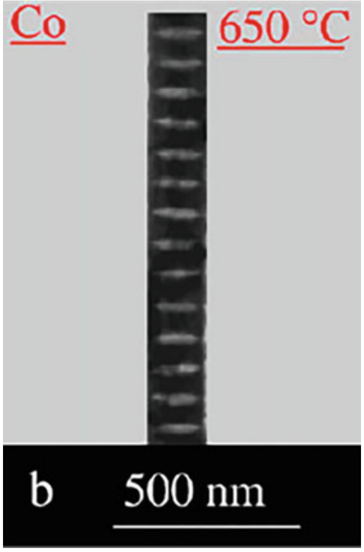

Fig. 4.177 Carbon nanoladder. (Reproduced with permission of the *Elsevier Science*)

various carbon nanostructures such as nanofilaments, nanofibers, nanoladders (Fig. 4.177), nanospirals, nanojunctions, nanocones, nanoonions, etc. accompanying nanotubes [493]. The authors noted that precise control of the process parameters was extremely important to grow a desired morphology; otherwise it could result in a wide variety of undesired carbon nanospecies too.

4.8 “Nanotechnical” Structures and Devices

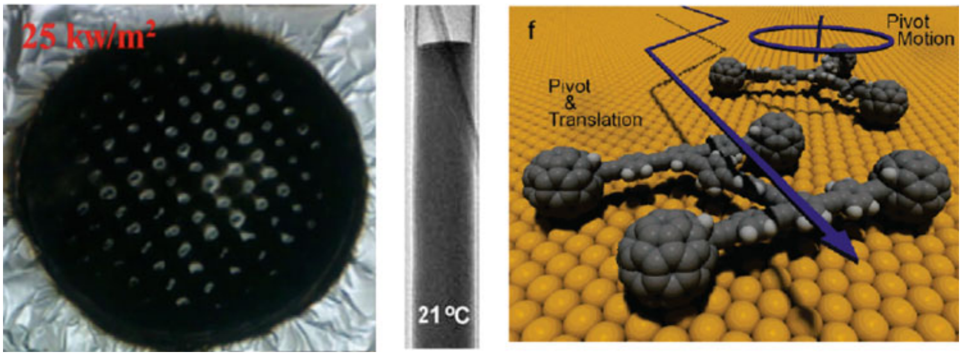

4.8.1 *Nanosprings/Nanocoils/Nanospirals*

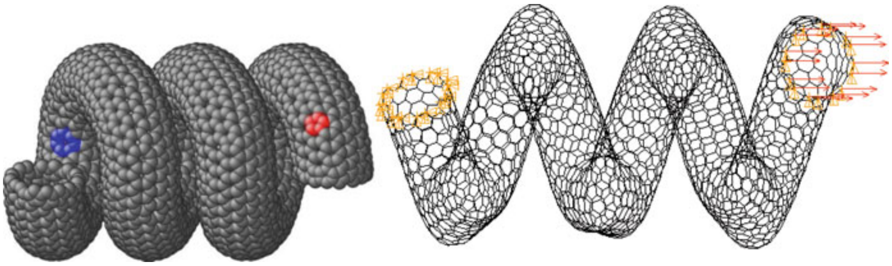

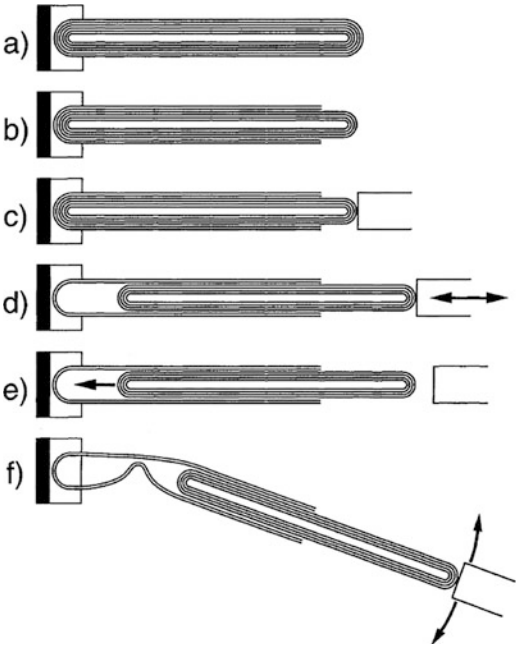

Fig. 4.178 A schematic for MWCNT processing and mechanical manipulations. (Reproduced with permission of the *American Institute of Physics*)

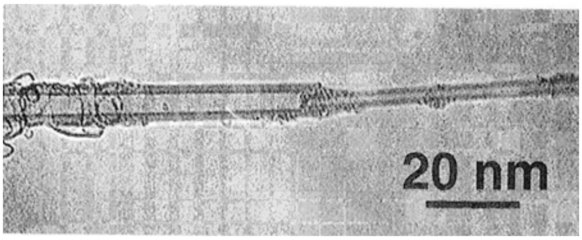

Fig. 4.179 A fully telescoped MWCNT. (Reproduced with permission of the *American Institute of Physics*)

Helix-shaped nanostructures are described in available literature as nanosprings, nanocoils,[46] and nanospirals. These structures are generally reviewed among other related nanoforms (such as nanowires, nanorods, or nanoneedles) [494, 495]. Computational quantum chemistry design of nanospirals was also reported [496]. As well as majority of other related nanostructures, helix nanostructures are represented mainly by inorganic compounds, in particular carbon nanotubes [497, 498] and other carbon nanoforms. Thus, a constant-force nanospring might be formed from a configuration of concentric carbon nanotubes (Fig. 4.178), where the van der Waals force provided the extension-independent restoring force [499]. A telescoped nanotube with only one active (sliding) surface pair was expected to act as a constant-force spring. A fully telescoped MWCNT (Fig. 4.179) originally had nine walls, with an outer diameter of 8 nm and an inner diameter of 1.3 nm.

Carbon microcoils can be prepared by catalytic CVD of acetylene, using Ni as the catalyst and thiophene as the promoter [500]. A catalyst (ball-milled nickel sulfide) was developed on purpose to avoid the introduction of noxious and unpleasant thiophene during the reaction process. Additionally, coil-in-coil [501] carbon nanocoils (CNCs, Fig. 4.180) were similarly synthesized by means of acetylene decomposition using nickel nanoparticles as catalysts. It was revealed that there were often several CNCs self-assembled in one nanospring. The yield of coil-in-coil CNCs was high up to 11 g in each run at the decomposition temperature of 450 °C. Among metal–carbon composite helices, tungsten-containing carbon (WC) nanosprings fabricated by focused-ion-beam CVD (FIB-CVD) using a source gas mixture of phenanthrene and W $(CO)_6$ showed unique characteristics they could expand and contract as flexibly as macroscale springs [502]. It was found that the spring constants of the springs rose as the tungsten content increased.

Diamond-like carbon (DLC) nanowires were used to compose nanosprings fabricated by focused-ion-beam CVD (FIB-CVD) [503]. The DLC nanowires of the as-grown nanosprings had elastic double structures, in which a 50-nm-diameter core containing 3-at.% gallium in addition to carbon was enclosed in an outer 25-nm-wide DLC shell. It was revealed that the

---

[46] The nanocoil images above are reproduced with permission of *AIP Publishing Co.* (up, *AIP Adv.*, **2015**, *5*, 117114.) and *Elsevier Science* (down, *Comput. Mater. Sci.*, **2012**, *55*, 344–349).

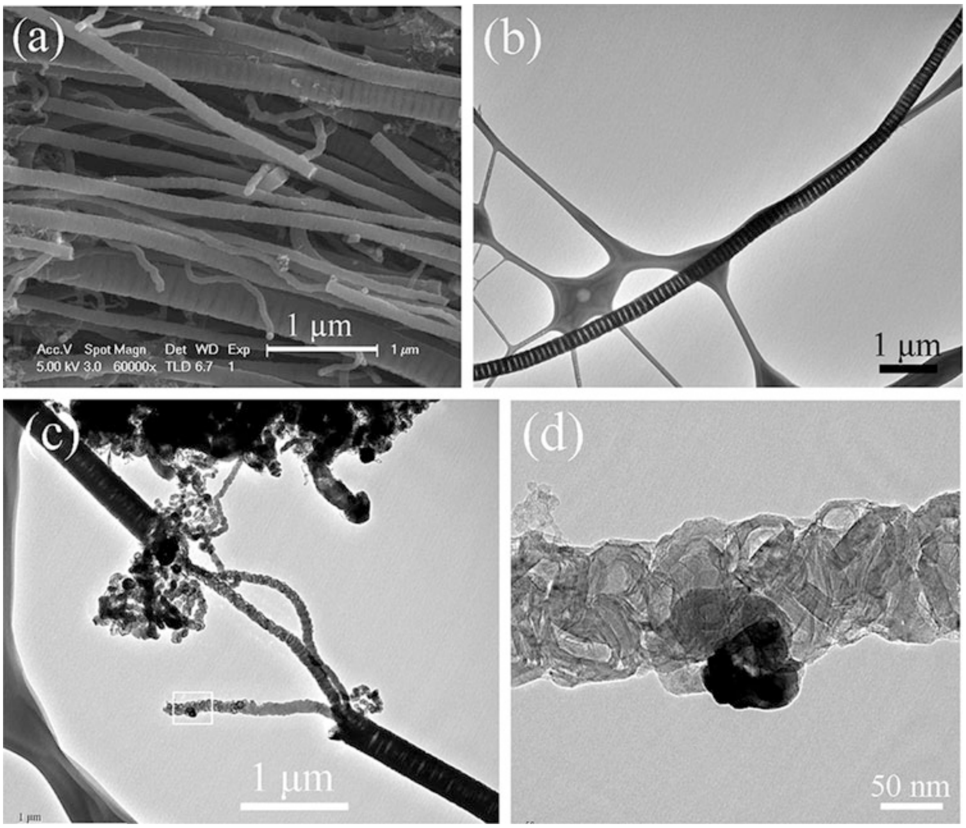

Fig. 4.180 Microstructure of the CNCs. (**a**) FESEM image. (**b–d**) TEM images: (**c**) CNC which was ruptured after being agitated in an ultrasonic bath; (**d**) magnified image of the corresponding position marked in panel **c**. (Copyright. Reproduced with permission of the *American Chemical Society*)

carbon densities of the core and the shell were similar, indicating that the density of the core was higher than that of the shell owing to the incorporation of Ga into the core. However, the core density was approximately halved by 800 °C annealing. This was attributed to the vaporization of Ga and the movement of C from the core to the shell.

An individual carbon nanocoil was clamped between two AFM cantilevers and loaded in tension to a maximum relative elongation of ~42% [504]. The nanocoil behad like an elastic spring with a spring constant K of 0.12 N/m in the low strain region. No plastic deformation was detected. In several reports, nanocoil-like structures have been investigated by MD simulations, for instance, their elastic behavior [505]. Also, the instability of a freestanding one-sided hydrogenated/fluorinated graphene nanoribbon, i.e., graphone/fluorographene, was studied using ab initio, semiempirical, and large-scale MD simulations (Fig. 4.181) [506]. Freestanding semi-infinite armchair-like hydrogenated/fluorinated graphene (AC-GH/AC-GF) and boatlike hydrogenated/fluorinated graphene (B-GH/B-GF) (nanoribbons which are periodic along the zigzag direction) are unstable and spontaneously transform into spiral structures. The spiral structures exhibited strong mechanical rigidity that prevents them from unrolling. Possible applications of carbon nanosprings and related structures can be related with adjustment of the viscoelasticity and reduction of the resulting hysteresis loss of elastomeric polymer materials [507].

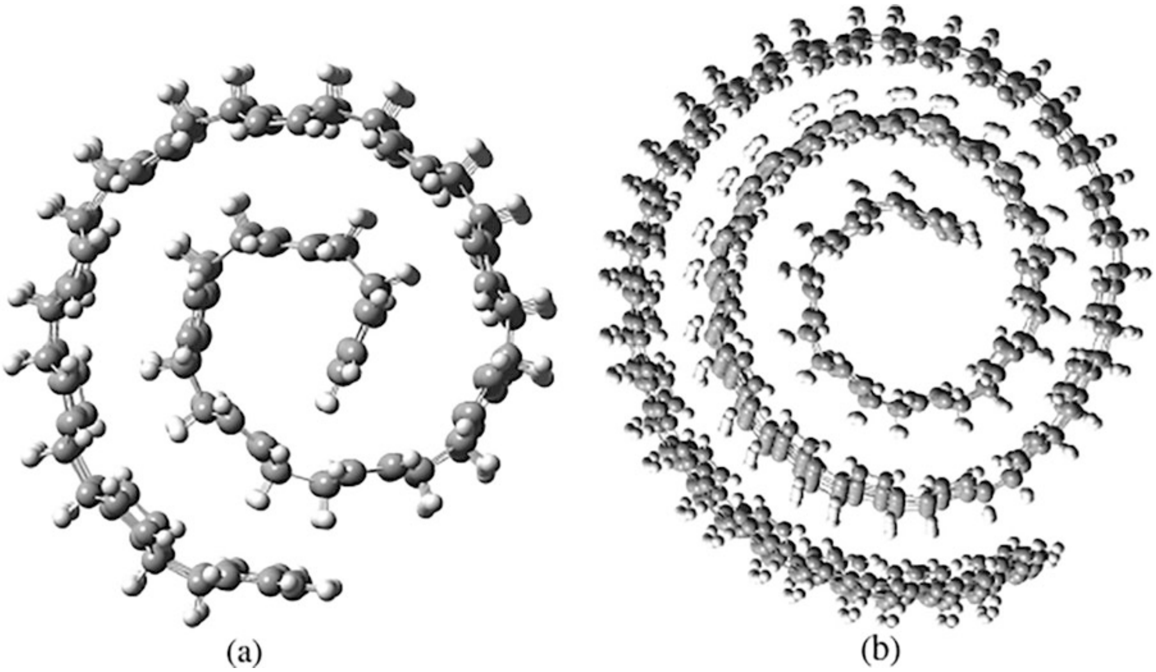

Fig. 4.181 (**a**) The spiral B-GH using DFT calculations for 504 atoms. (**b**) The spiral B-GH using semiempirical calculations (PM6) for 1320 atoms. (Reproduced with permission of the *American Physical Society*)

4.8.2 Nanothermometers

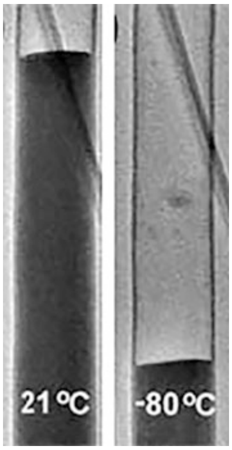

Several reviews on nanothermometers have been published [508, 509], in particular those describing nanothermometers using liquid metals and nanotubes of oxides (e.g., In_2O_3, MgO, SiO_2) [510–512]. But the first and the most important example of these nanodevices consisted on carbon nanotubes. Thus, a nanothermometer on the basis of carbon nanotubes was synthesized in a vertical radio-frequency furnace (which differs from a one-step arc-discharge method) [513]. In a related work [514], an interesting concept was proposed for an electromechanical nanothermometer. The temperature measurements were performed by measuring the conductivity of the nanosystem on the CNT basis (shuttle nanothermometer with a movable outer wall and the telescopic nanothermometer with a movable inner wall, Fig. 4.182), which depends substantially on the temperature due to the relative thermal vibrations of nanoobjects forming the nanosystem. It was shown that this nanothermometer can be used for measuring the temperature in localized regions with sizes of the order of several hundred nanometers. Also, the systems of the shuttle nanothermometer with a movable inner wall and the telescopic nanothermometer with a movable outer wall are also possible. In addition, the mechanics of CNTs constituting two well-known configurations for nanothermometer, namely,

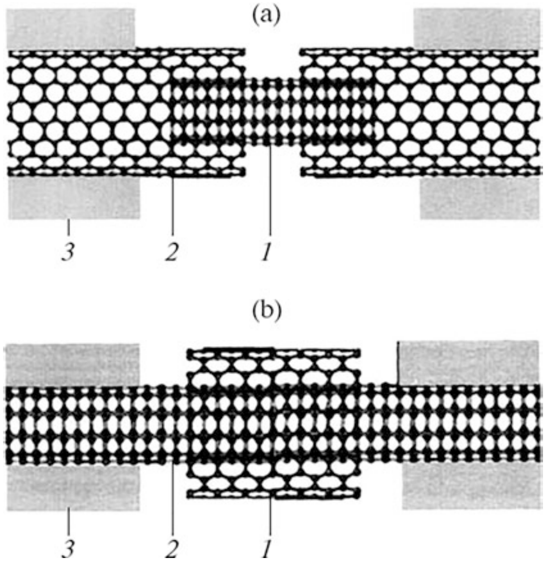

Fig. 4.182 Schematic diagrams of the nanothermometers based on double-walled carbon nanotubes: (**a**) the telescopic nanothermometer with a movable inner wall and (**b**) the nanothermometer with a movable shuttle in the form of an outer wall. Designations: (1) movable wall, (2) fixed wall, and (3) electrodes. (Reproduced with permission of the *Springer*)

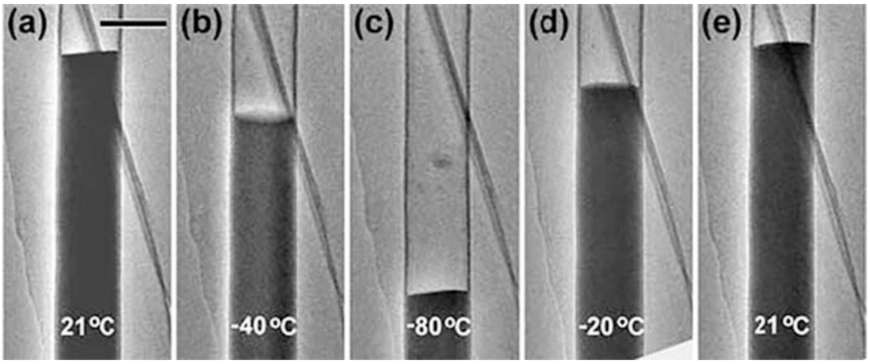

Fig. 4.183 TEM images of a carbon nanotube confined with Ga at different temperatures. (**a**) was taken at room temperature; (**b**) was taken at −40 °C; (**c**) was taken at −80 °C, and the confined Ga was solidified at this temperature; (**d**) was taken −20 °C, and the solid Ga was melted at this temperature; (**f**) was taken at room temperature. Scale bar = 100 nm. (Source: Zongwen Liu, University of Sydney). http://www.atip.org/atip-publications/atip-news/2006/4226-060721an_carbon_nanotubes_as_nano-thermometers.html. (Reproduced with permission of the *ATIP*)

shuttle configuration and *telescope configuration*, were fully investigated [515]. It was found that these geometrical parameters have a considerable effect on the potential energy.

A homogeneous mixture of Ga_2O_3 and pure, amorphous, active carbon (weight ratio, 7.8:1) was reacted in an open carbon crucible under a flow of pure N_2 gas: at 1360 °C, the reaction 4.22 occurred. However, on the inner surface of a pure graphite outlet pipe at the top of the furnace, the temperature was lower (around 800 °C), causing the reaction 4.23 to occur, during which the “nanothermometers” (Fig. 4.183) were created. As an improvement of this technique, the following oxidation-assisted approach was proposed [516]. When a Ga-filled carbon nanotube was heated in air for an appropriate length of time, an oxide marker was formed on the inner wall of the carbon nanotube due to partial oxidation of the gallium. Thus, the temperature to which the nanotube was exposed can be retrieved by progressively heating the carbon nanotube until the liquid gallium reached the oxide marker. Additionally, it was found that Ga-filled carbon nanotubes possess a unique combination of two types of conductivity: low-resistive Ga-filled nanotube segments and relatively high-resistive empty nanotube regions [517]. It was possible to produce gaps in the Ga filling of any required length by AFM indentation, thus affecting the nanotube electrical properties.

$$Ga_2O_3(\text{solid}) + 2C(\text{solid}) \rightarrow Ga_2O(\text{vapor}) + 2CO(\text{vapor}) \tag{4.22}$$

$$Ga_2O(\text{vapor}) + 3CO(\text{vapor}) \rightarrow 2Ga(\text{liquid}) + C(\text{solid}) + 2CO_2(\text{vapor}) \tag{4.23}$$

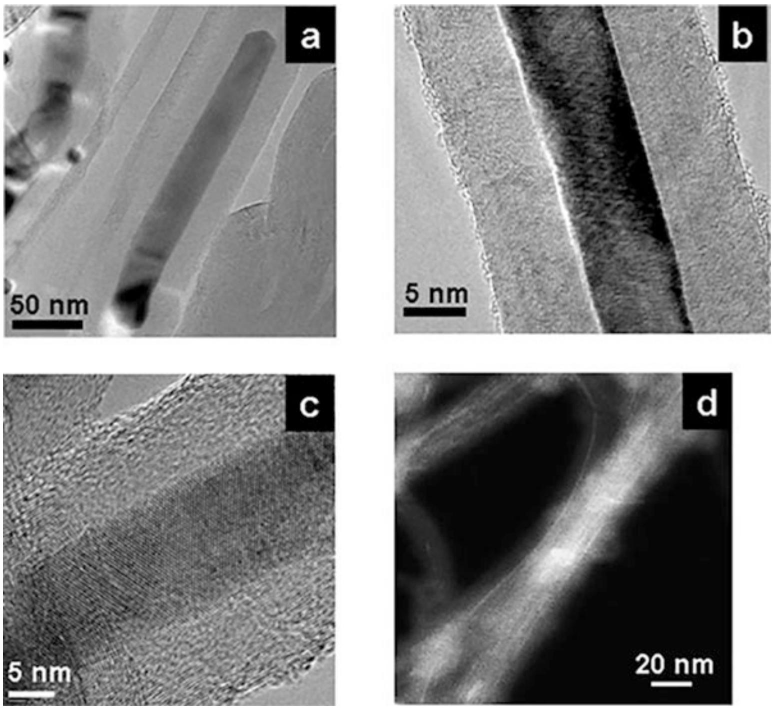

Fig. 4.184 TEM images of (**a**) cobalt-, (**b**) iron-, (**c**) CuI- and (**d**) AgCl-filled CNT. (Reproduced with permission of the *John Wiley and Sons*)

In addition to gallium-filled CNTs, described above, indium-filled carbon nanotubes (diameters of 100–200 nm and length of ~10 μm) were synthesized via a CVD technique [518]. It was shown that the melting and expansion behavior of indium were different from that in a macroscopic state allowing to clarify the problems of indium filling usage in carbon nanotube-based nanothermometer. Fabrication of non-filled CNTs nanothermometers is also possible; thus, an interesting concept was proposed for an electromechanical nanothermometer [519, 520]. In this device, the temperature measurements were performed by measuring the condition of the nanosystem (CNTs), which depends substantially on the temperature due to the relative thermal vibrations of nanoobjects forming the nanosystem. It was shown that this nanothermometer can be used for measuring the temperature in localized regions with sizes of the order of several hundred nanometers.

Nanothermometers, on the basis of CNTs or other inorganics, have been applied also for biological systems. Thus, filled carbon nanotubes (Fig. 4.184) have potential to act as sensors that might provide noninvasive temperature control in biological systems on a cellular level; in this case the temperature can be detected by measuring NMR parameters on the filling materials [521]. The most temperature-sensitive parameter was found to be the [126] spinlattice relaxation rate in CuI-CNT which can provide the temperature detection with an accuracy of 2 K. The beneficial feature of a carbon nanotube was to provide protection of both *(i)* a human body against toxic adverse effects from the filling material and *(ii)* a filling material against chemical and biochemical exposure.

Another approach, without use of CNTs, was applied for creation of another type of nanothermometers on carbon nanodots basis. Thus, temperature measurements in biology and medical diagnostics are of great importance; however, it still faces significant challenges. To develop this area, a "turn-on" carbon-dot-based fluorescent nanothermometry device for spatially resolved temperature measurements in living cells was presented [522]. *p*-Phenylenediamine was carbonized by microwave irradiation in an ethanol/H_2O solution to form CNDs (Fig. 4.185). Red-emitting CNDs can be utilized for "turn-on" fluorescent nanothermometry through the fluorescence quenching and recovery processes, respectively (Fig. 4.186). In a related report [523], the nanothermometer was based on biocompatible fluorescent carbon nanodots (CDs) obtained via one-step microwave-assisted synthesis too and two kinds of polymers, including thermosensitive poly (N-isopropylacrylamide) (PNIPAM) and non-thermosensitive polyethylene glycol (PEG) (Fig. 4.187). When heating up above the lower critical solution temperature (LCST) of PNIPAM, hydrophobic phase transition occurred to PNIPAM, and the nanothermometer evolved into the core–shell–corona structure, with a freshly formed and collapsed PNIPAM shell. The fluorescence response to temperature of the MSCD can be followed through gradual heating up from 20 to 50 °C (Fig. 4.188). In addition to microwave-assisted synthesis, carbon nanodots, to be used as nanothermometers, can be prepared solvothermally [524] or by simple heating of C_3N_4 and ethanediamine at 80 °C for 12 h yielding N-doped carbon dots [525].

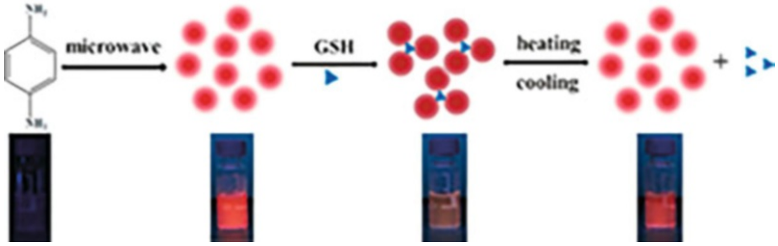

Fig. 4.185 Schematic diagram for preparing red-emitting CNDs for the fluorescence "on–off–on" sensing of GSH and temperature. (Reproduced with permission of *Wiley*)

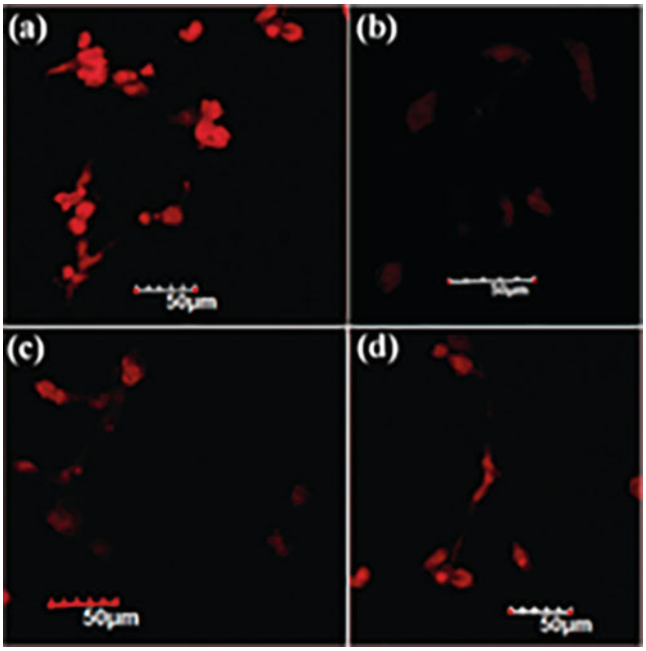

Fig. 4.186 Confocal fluorescence images of MC3T3-E1 cells upon 8 h incubation with red-emitting CNDs in various conditions: (**a**) 20 °C, (**b**) GSH solution (0.1 mm) at 20 °C, (**c**) 30 °C, and (**d**) 40 °C. (Reproduced with permission of *Wiley*)

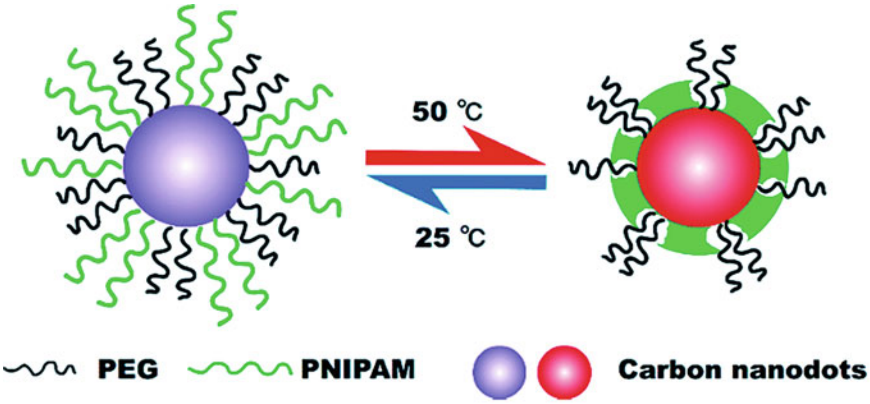

Fig. 4.187 Schematic representation of the structure and the functioning mechanism of the fluorescent nanothermometer based on mixed shell carbon nanodots (MSCDs). (Reproduced with permission of the *Royal Society of Chemistry*)

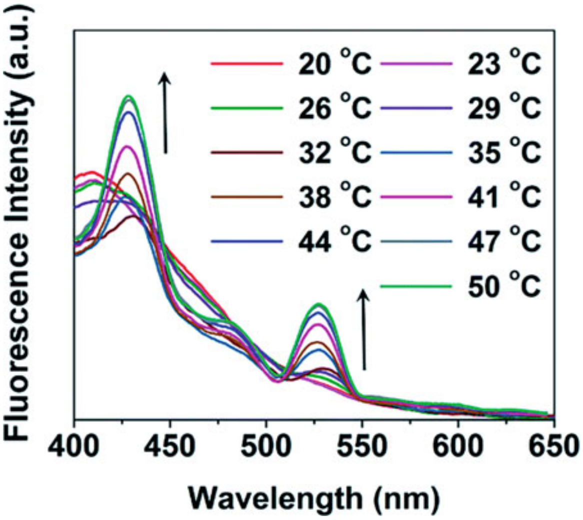

Fig. 4.188 Overlaid fluorescence spectra of the MSCDs at various temperatures (from 20 to 50 °C, $\lambda_{ex} = 320$ nm). Every spectrum was acquired after reaching equilibrium. (Reproduced with permission of the *Royal Society of Chemistry*)

4.8.3 Nanotweezers[47]

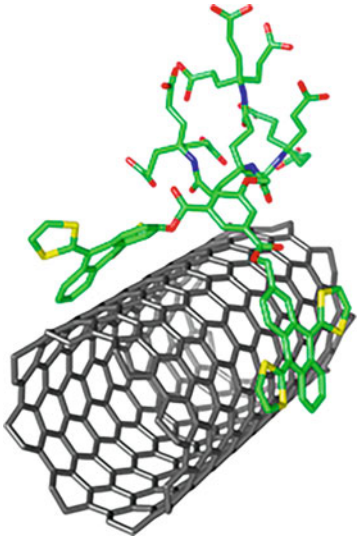

CNT nanotweezers are well-known objects in the nanoworld [526, 527]. Thus, both bent-type and straight-type nanotweezers based on two carbon nanowires by means of localized CVD using a focused ion beam (FIB-CVD) were demonstrated [528]. The location, dimension, and gap between the two nanowires were precisely controlled such that the tweezing motion and the operation voltage can be easily adjusted. Potential applications of these nanotweezers include manipulation of nanoparticles and nanoscale objects. Also, a method to make a nanotweezer composed of two CNT arms was offered [529]. The CNT arm was fabricated by attaching a multiwalled carbon nanotube on a tungsten tip via manual assembly. Since each CNT arm has a macro-actuator, namely, a separated tweezer arm, it was possible to close and open the nanotweezer repeatedly. Electrochemical etching was used to cut the carbon nanotube in the CNT arm, and the cutting resolution was ~ a few hundred nanometers.

---

[47] The nanotweezer image is reproduced with permission of the *American Chemical Society* (*J. Am. Chem. Soc.*, **2012**, *134*, 9183–9192).

In addition to CNTs-based nanotweezers, carbon nanotubes themselves can be objects for manipulations by organic/organometallic spacers on porphyrin and pyrene basis acting as nanotweezers. Thus, host–guest chemistry for separation of CNTs according to diameter, metallicity, and even handedness was developed using host molecules named “nanotweezers” consisting of a rigid core and two receptors and suitable for CNT separation (Figs. 4.189 and 4.190) [530]. These nanotweezers are much deeper and wider cavities to accept CNTs and much more interactions of π–π and C–H–π to make CNT complexes much more stable.

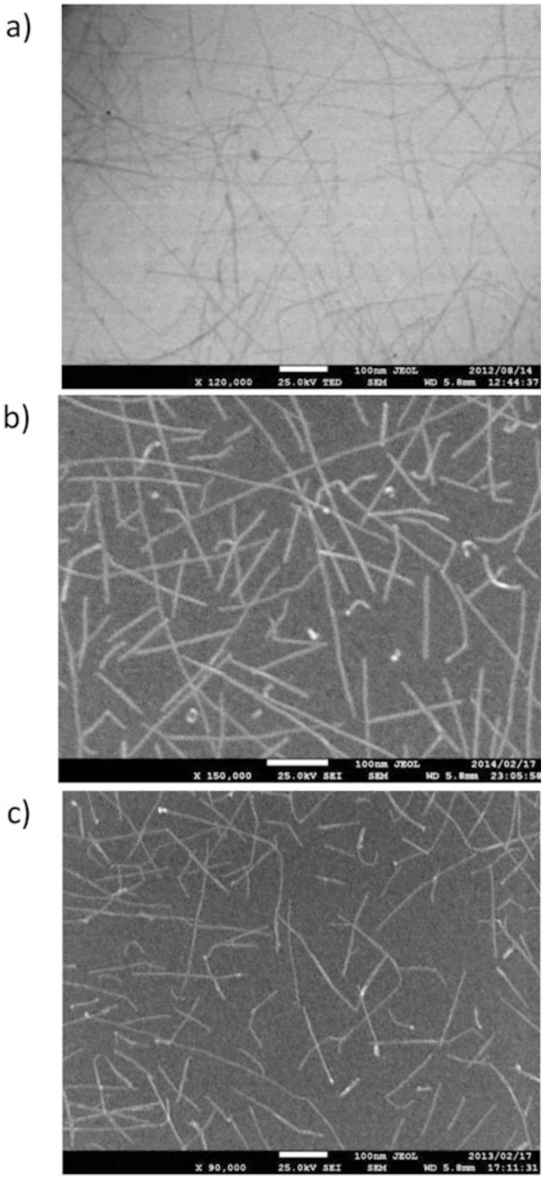

Fig. 4.189 STEM (**a**) and SEM images (**b**, **c**) for SWNTs (**a**, **c**) and DWNTs (**b**) extracted with different nanotweezers. (Reproduced with permission of the *Royal Society of Chemistry*)

Fig. 4.190 Computer-generated molecular modeling of the complex structures of SWCNTs and nanotweezers. (Reproduced with permission of the *Royal Society of Chemistry*)

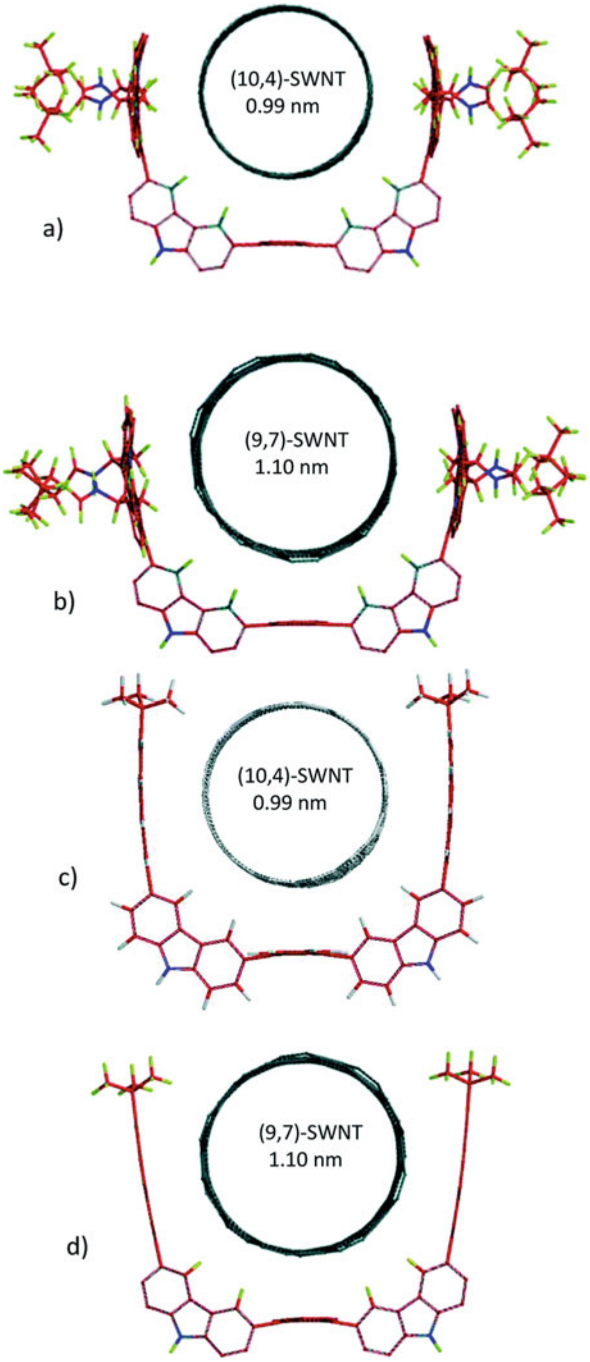

4.8.4 Nanocars and Nanotrucks

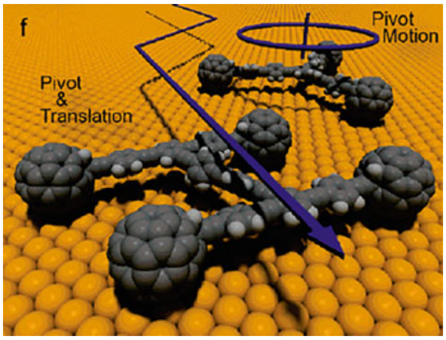

Nanocars, being developed by research group of *James M. Tour* [531–537], are “molecular machines consisting of molecular-scale chassis, axles and wheels that can directionally roll across solid surfaces.” Two complementary approaches can be considered in fabrication of miniaturized devices: [538] (a) the top-down approach, which reduces the size of macroscopic objects to reach an equivalent microscopic entity using photolithography and related techniques and (b) the bottom-up approach, which builds functional microscopic or nanoscopic entities from molecular building blocks. These nanocars are mainly based on carborane and fullerene wheels; additionally, a class of molecular wheels was developed based on a *trans*-alkynyl(dppe)$_2$ruthenium complex [539, 540]. The low rotation barrier around the alkyne bond in this complex allows a free rotation of the wheel, while the bulky phosphine ligands offer good interactions with metallic surfaces.

A motorized nanocar (Fig. 4.191) was synthesized which bears a light-activated unidirectional molecular motor and an oligo(phenylene ethynylene) chassis and axle system with four carboranes to serve as the wheels [541]. His proposed propulsion scheme is shown in Fig. 4.192.

Design, syntheses (Fig. 4.193) by in situ ethynylation of fullerenes, and testing of fullerene-wheeled single molecular nanomachines (Fig. 4.194), namely, nanocars and nanotrucks, composed of three basic components that include spherical fullerene wheels, freely rotating alkynyl axles, and a molecular chassis, were also presented [542, 543]. The use of spherical wheels based on C_{60} and freely rotating axles based on alkynes permitted directed nanoscale rolling of the molecular structure on gold surfaces. The obtained nanocars were stable and stationary on the gold surface at room temperature for a wide range of tunneling parameters. The authors attributed their stability to a relatively strong adhesion force between the fullerene wheels and the underlying gold.

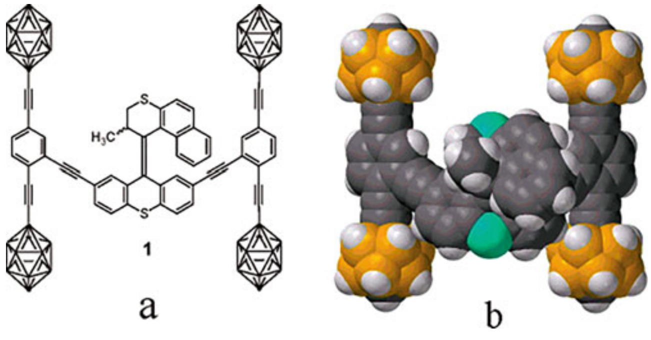

Fig. 4.191 (**a**) Structure of motorized nanocar on *p*-carborane basis. The *p*-carborane wheels have BH at every intersection except at the top and bottom vertexes which represent C and CH positions, ipso and para, respectively, relative to the alkynes. (**b**) The space-filling model of this nanocar. (Reproduced with permission of the *American Chemical Society*)

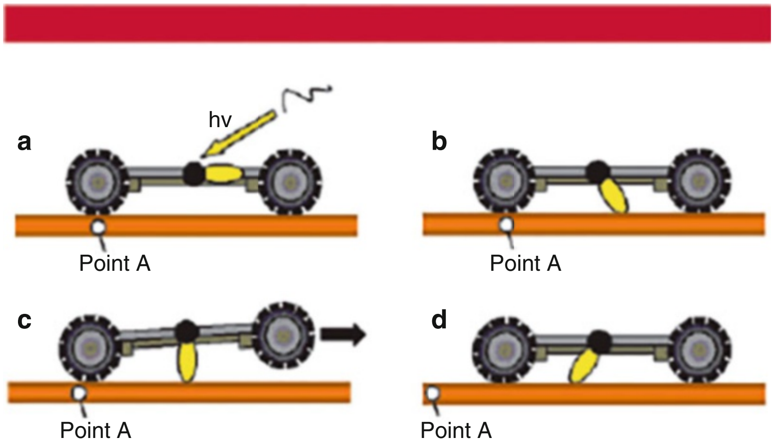

Fig. 4.192 Proposed propulsion scheme for the motorized nanocar where (**a**) 365 nm light would impinge upon the motor which in conjunction with a heated substrate (at least 65 °C) (**b**) affording motor rotation and (**c**) sweeping across the surface to (**d**) propel the nanocar forward. (Reproduced with permission of the *American Chemical Society*)

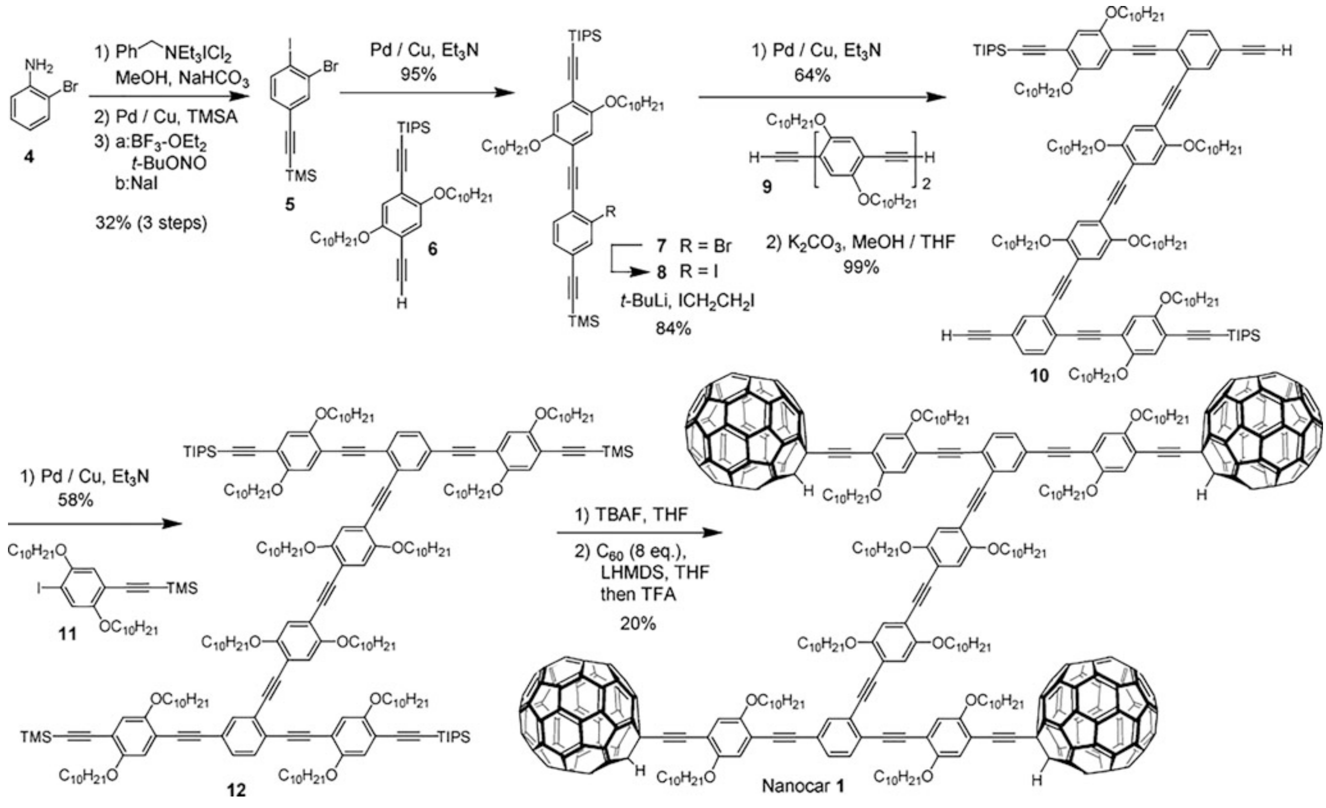

Fig. 4.193 Synthesis of nanocars. (Reproduced with permission of the *American Chemical Society*)

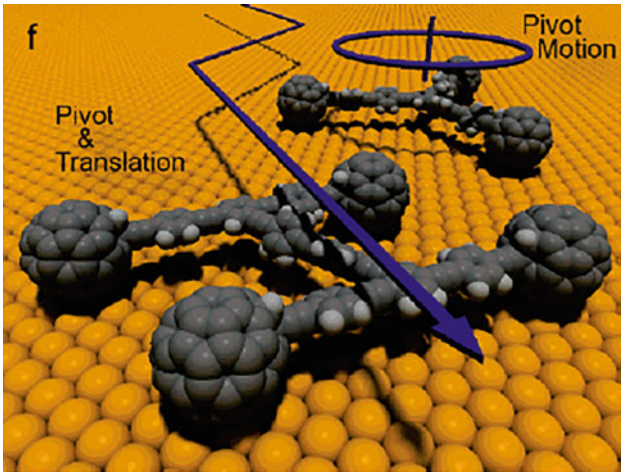

Fig. 4.194 A summary of the two methods of motion for the different nanocar structures. (Reproduced with permission of the *American Chemical Society*)

4.8.5 Nanobalances

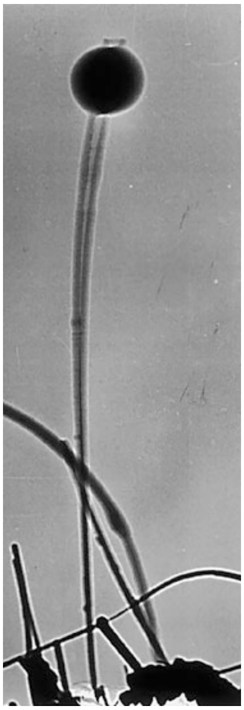

The nanobalance for applying a voltage across the nanotube and its count electrode was constructed on the basis of carbon nanotubes (have diameters of 5–50 nm and lengths of 1–20 μm), produced by an arc-discharge technique and agglomerated into a fiber-like rod [544]. The specimen holder required the translation of the nanotube via either mechanical movement by a micrometer or axial directional piezo. The carbon nanotube can be charged by an externally applied voltage. The induced charge is distributed mostly at the tip of the carbon nanotube and the electrostatic force results in the deflection of the nanotube (Fig. 4.195). The nanotube is a very flexible structure, and it can be bent to 90° and still recovers its original shape. Additionally, the mass of a particle attached at the end of the spring (Fig. 4.196) can be determined if the vibration frequency is measured, provided the spring constant is calibrated. This “nanobalance” (the most sensitive and smallest balance in the world) was shown to be able to measure the mass of a particle as small as 22 ± 6 fg ($1\ \text{f} = 10^{-15}$). Other nanobalances have been described in [545–547].

Fig. 4.195 Electrostatic deflection of a carbon nanotube induced by a constant field across the electrodes. Quantification of the deflection gives the electrical charge on the carbon nanotube and the mechanical strain on the fiber. (Reproduced with permission of the *Elsevier Science*)

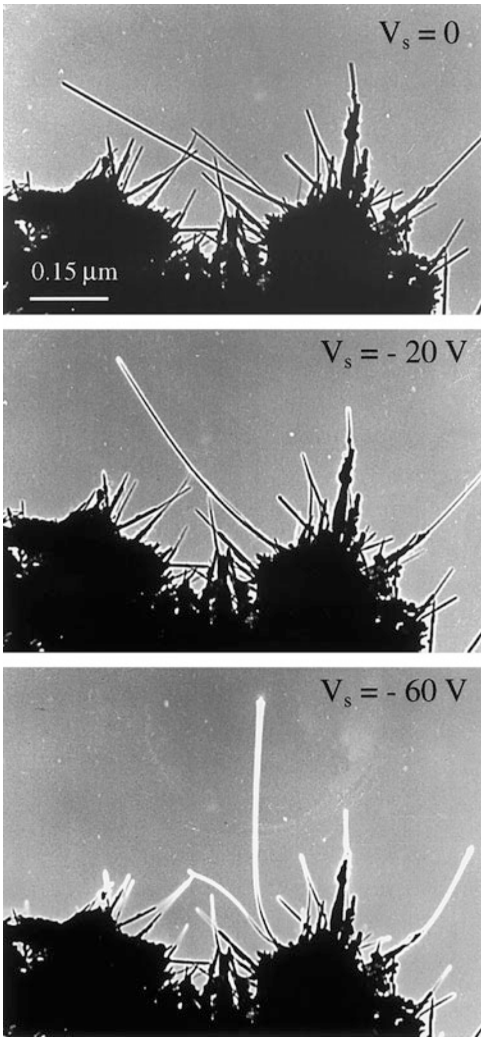

Fig. 4.196 A small particle attached at the end of a carbon nanotube at (**a**) stationary and (**b**) first harmonic resonance ($\upsilon = 0.968$ MHz). The effective mass of the particle was measured to be ~22 fg (1 f = 10^{-15}). (Reproduced with permission of the *Elsevier Science*)

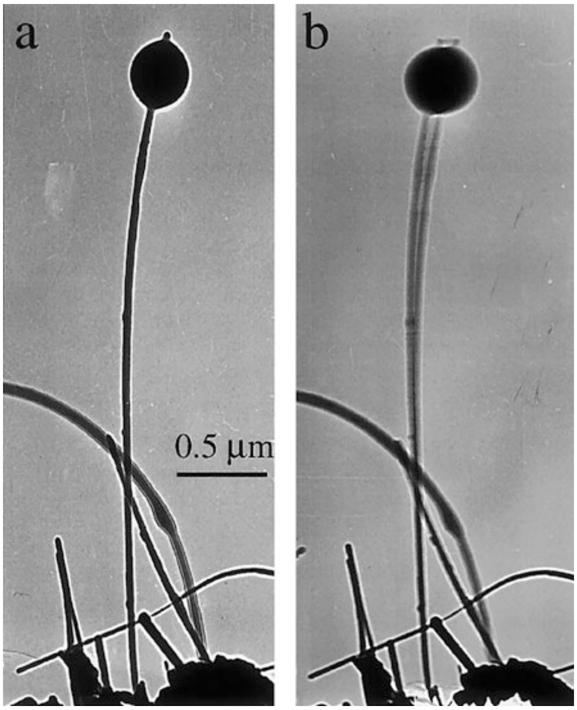

4.8.6 Nanomesh

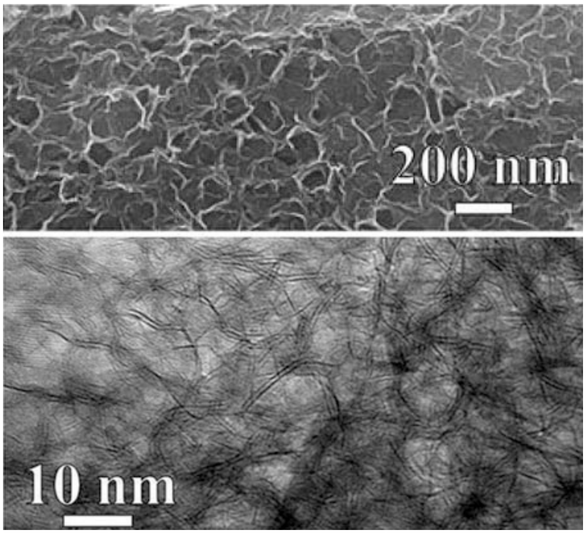

Several carbon-based mesh[48]-like nanostructures are known, in particular those of C_{60} and graphene [548]. A variety of precursors and physical, chemical, and biological methods to create channels have been used. Thus, a new graphene nanostructure, called by authors [549] as a graphene nanomesh, can open up a bandgap in a large sheet of graphene to create a semiconducting thin film. These nanomeshes were prepared using block copolymer lithography and can have variable periodicities and neck widths as low as 5 nm. Graphene nanomesh field-effect transistors can support currents nearly 100 times greater than individual graphene nanoribbon devices, and the on–off ratio, which is comparable with the values achieved in individual nanoribbon devices, can be tuned by varying the neck width. Among other related publications, hexagonal graphene nanomeshes with sub-10 nm ribbon width were fabricated [550].

Local photodegradation of graphene oxide sheets at the tip of ZnO nanorods was used to achieve semiconducting graphene nanomeshes (Fig. 4.197) [551]. These graphene nanomeshes contained smaller O-containing carbonaceous bonds and higher defects as compared to the as-prepared graphene oxide sheets. An extended 2D C_{60} nanomesh was fabricated by controlling the binary molecular phases of C_{60} and pentacene on Ag(111) [552]. The skeleton of the C_{60} nanomesh was found to be stabilized by the strong molecule–metal interfacial interactions [C_{60}-Ag(111) and pentacene-Ag(111)] and was further modified by the pentacene-C_{60} donor–acceptor intermolecular interactions. This C_{60} nanomesh can serve as an effective template to selectively accommodate guest C_{60} molecules at the nanocavities.

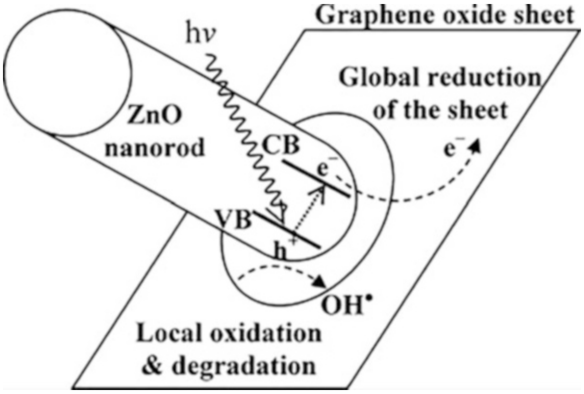

Fig. 4.197 Schematic illustration of the mechanism describing formation of graphene nanomeshes by using the photocatalytic property of the ZnO nanorods. (Copyright. Reproduced with permission of the *American Chemical Society*)

---

[48] The nanomesh images above are reproduced with permission of the *Royal Society of Chemistry* (*J. Mater. Chem. A*, **2017**, *5*, 9709–9716).

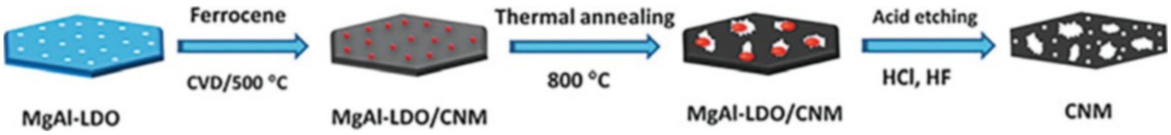

Fig. 4.198 Schematic illustration of the fabrication steps for CNM. (Reproduced with permission of *Wiley*)

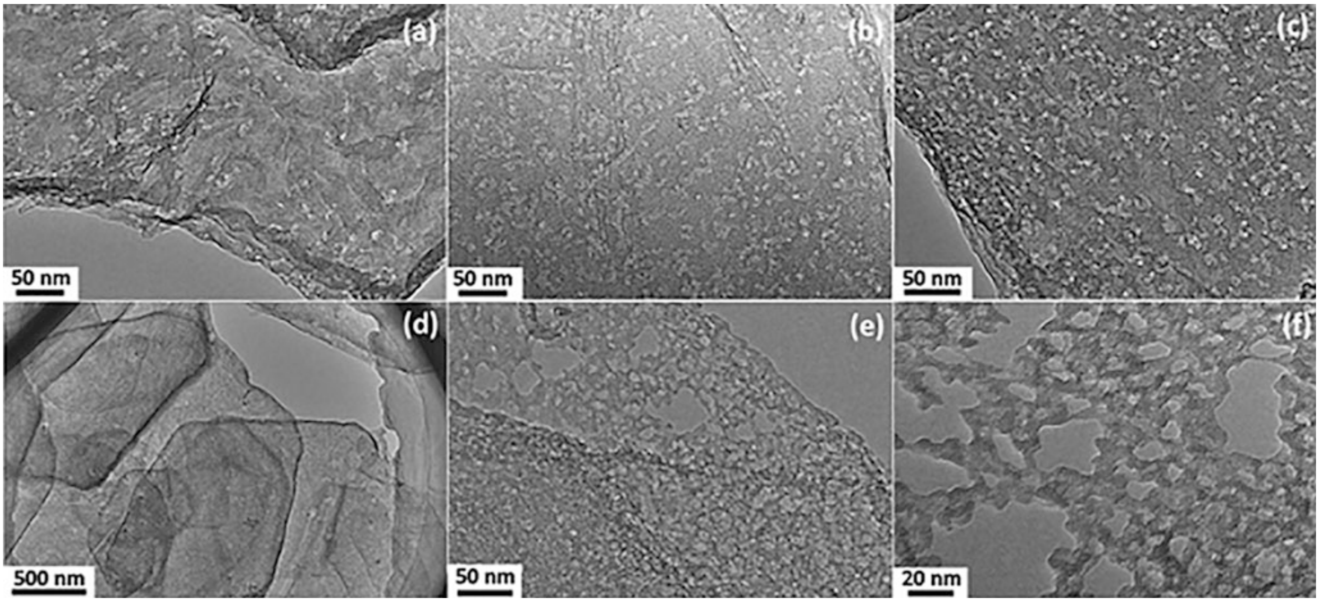

Fig. 4.199 TEM images of CNM. (Reproduced with permission of *Wiley*)

CVD method was applied to prepare carbon nanomesh (CNM, Figs. 4.198 and 4.199) with MgAl-layered double oxides (LDO) as sacrificial template and ferrocene as carbon precursor [553]. This hexagonal thin-sheet CNM featured a hierarchical pore system consisting of micropores and small mesopores with a size range of 1–6 nm and a great number of random large mesopores with a pore size of 10–50 nm and was found to be suitable as supercapacitor electrode. The in-plane large mesopores serve as fast ion channels across the carbon thin sheets, which helps to greatly accelerate the ion kinetic in the interior of the electrode, resulting in an improved capacitive performance. A graphene nanomesh was also prepared through UV-mediated oxidation of a graphene oxide film in air (Fig. 4.200) [554]. It was observed that a nanoporous network structure was progressively produced in the basal plane, which can be attributed to the fact that highly ROS (UV-generated O_3) preferentially attack sp^3 carbon-rich regions of the GO. The field-effect transistors were fabricated using graphene nanomesh as the active channel. Finally, in order to produce nanostructured channels of SWCNTs for localized active devices such as local bottom-gated field-effect transistors (FETs), a biologically templated approach in combination of microfabrication processes was offered, assembling in solution a large-scale nanostructured network, nanomesh, of SWCNTs using an M13 phage [555].

In addition to classic chemicals, carbon-rich natural wastes have been also used as carbon nanomesh precursors, for instance, biowaste-poplar catkins [556]. Their in situ calcination (at 600 °C) etching with $Ni(NO_3)_2{\cdot}6H_2O$ and KOH in N_2 flow combined with an acid dissolution technique led to the formation of hollow activated carbon nanomesh (PCACM) with a hierarchical porous structure (Fig. 4.201, reactions 4.24–4.31). PCACM kept the natural tubular morphology of poplar catkins with a fascinating nanomesh structure on the walls, large specific surface area ($S_{BET} = 1893.0\ m^2\ g^{-1}$), and high pore volume ($V_p = 1.495\ cm^3\ g^{-1}$). The formed nanomesh has potential uses as electrode materials for supercapacitors. Together with applications as transistors [557], this use of nanomesh is typical for various nanocarbons.

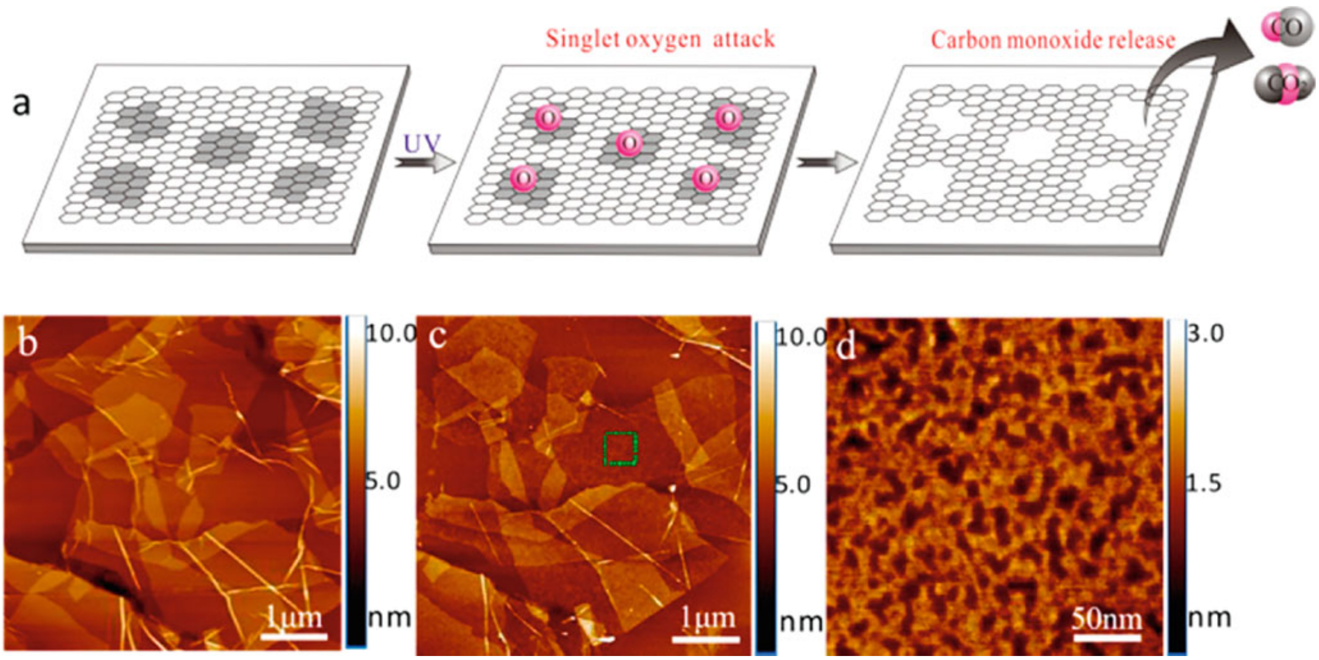

Fig. 4.200 (**a**) Schematic illustration of the UV exposure process of GO to form a perforated GNM. First, GO solution was deposited onto the freshly prepared mica sheet surface (1.0 × 1.0 cm^2) and dried in the vacuum oven. Then, the dried substrates were put into a sealed box with UV irradiation. Note: the dark gray areas represent sp^3 carbon clusters, and the remaining regions are sp^2 carbon domains. (**b**–**d**) AFM images of GO sheets on the mica substrate: (**b**) the starting GO sheets, (**c**) the UV-irradiated GO, and (**d**) zoom-in of a square region; see (**c**) showing the perforated structure of an individual sheet. (Reproduced with permission of *the American Chemical Society*)

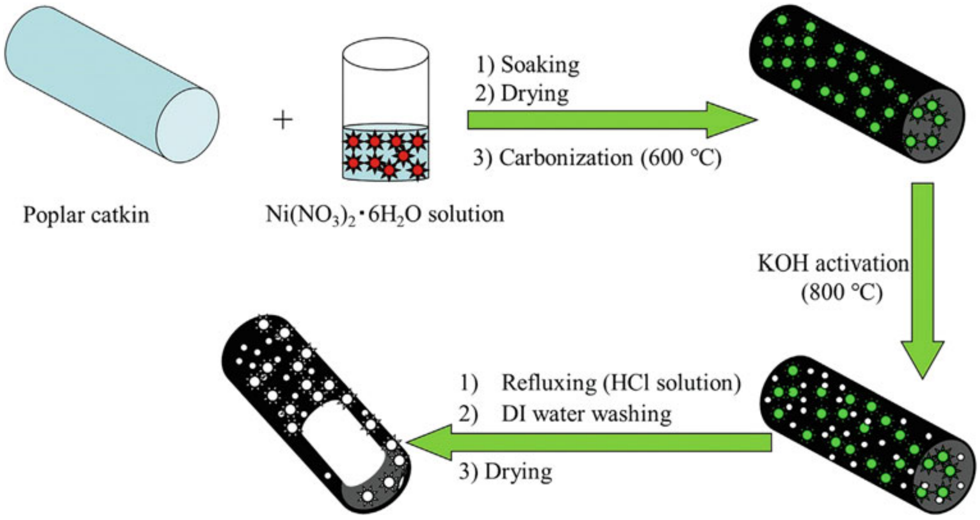

Fig. 4.201 Schematic illustration for the preparation of PCACM. KOH activation has been also used for other nanocarbons above described. (Reproduced with permission of the *Elsevier Science*)

$$2Ni(NO_3)_2 = 2NiO + 2NO_2 \tag{4.24}$$

$$C + 6KOH = 2K_2CO_3 + 2K + 3H_2 \tag{4.25}$$

$$K_2CO_3 = K_2O + CO_2 \tag{4.26}$$

$$K_2CO_3 + 2C = 2K + 3CO \tag{4.27}$$

$$K_2O + C = 2K + 3CO \tag{4.28}$$

$$2\mathrm{K} + 2\mathrm{H_2O} = 2\mathrm{KOH} + \mathrm{H_2} \tag{4.29}$$

$$\mathrm{KOH} + \mathrm{HCl} = \mathrm{KCl} + \mathrm{H_2O} \tag{4.30}$$

$$\mathrm{NiO} + 2\mathrm{HCl} = \mathrm{NiCl_2} + \mathrm{H_2O} \tag{4.31}$$

4.8.7 Nanojunctions[49]

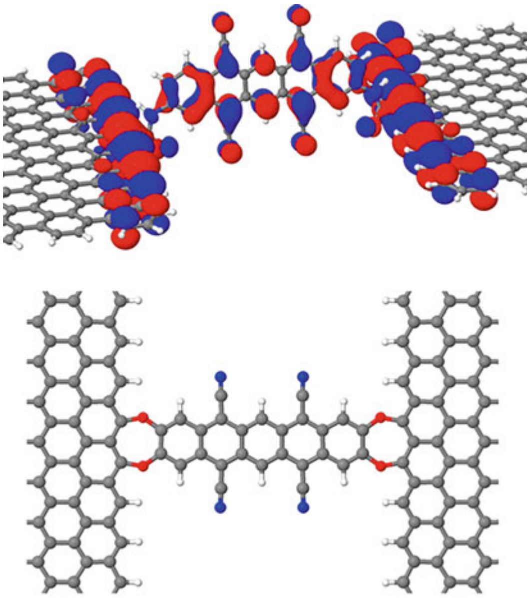

Nanojunctions are known mainly for metals, although some oxides and other compounds have also been reported. For carbon allotropes, the available data are highly limited [558]. Thus, Fe_3W_3C/WC/graphitic carbon (GC) ternary nanojunction hybrids were synthesized through a solid-state pyrolysis process to be used for dye-sensitized solar cells (DSSCs) [559]. Using hybrid counter electrodes on their basis, a photoelectrical conversion efficiency of 7.1% was achieved (for comparison: pure GC – 5.02%, WC/GC hybrids – 6.11%). DFT calculations were used to study electronic properties and doping and structural defects in carbon nanojunctions, for instance, to investigate charge transport in pentacene–graphene nanojunctions employing DFT calculations and the Landauer transport formalism [560]. It was revealed that the unique electronic properties of graphene strongly influence the transport in the nanojunctions. The charge transport was found to be strongly influenced by the edge structure of the graphene electrodes. The behavior of B-doped defects in nanodevice carbon heterojunctions was investigated by DFT for 36 different heterojunction CNTs [561]. Among other discoveries, the highest surface reactivity was found for the B-doped zigzag–armchair heterojunctions, followed by B-doped armchair–armchair heterojunctions, and the smallest surface reactivity is for B-doped zigzag–zigzag heterojunction CNTs. Similarly, quantum conductance of silicon-doped carbon wire nanojunctions was evaluated [562].

---

[49] The nanojunction image above is reproduced with permission of the *American Chemical Society* (*J. Phys. Chem. Lett.*, **2013**, *4*(5), 809–814).

4.8.8 Nanopaper

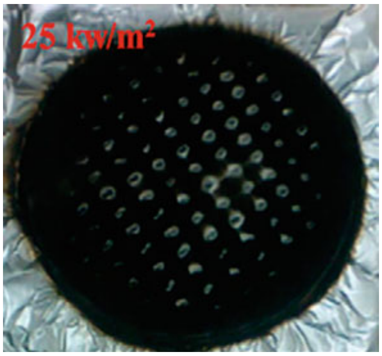

Nanopapers[50] are known, in particular, for various carbon-containing [563] compounds and are being intensively developed during the last decade. An excellent comprehensive review [564] describes nanopapers on the basis of cellulose; carbon (highly recommended state-of-the-art section on carbon nanopapers); inorganic compounds; electrospun nanopaper; water-repellent nanopaper; fire-retardant nanopapers; electrically and thermally conductive nanopapers; magnetic, photocatalytic, and bioactive nanopapers; and their multiple applications. Carbon nanopapers ("on-woven fibrous entangled assemblies of carbon nanomaterials with a 2D paper-like morphology, held together by van der Waals forces between carbon nanomaterial junctions, similar to ordinary paper made from wood pulp fiber") are made of carbon-based nanomaterials (e.g., carbon nanofibers, graphene, and CNTs) [565] and nonionic surfactants (e.g., Triton X-100 and sodium lauryl sulfate), which aid their dispersion into aqueous or organic solvents (Fig. 4.202). Another route to the carbon nanopaper is mechanical pressing/rolling. A representative example of a composite nanopaper (binder-free), made of graphite oxide and Si nanoparticles as an anode material for Li-ion batteries, is shown in Fig. 4.203.

Among various types of carbon nanopapers (e.g., those with flame-retardant efficiency [568]), considerable efforts have been recently made, mainly by the research group of *H. Lu*, in the development of the area of *shape-memory* materials on their basis,

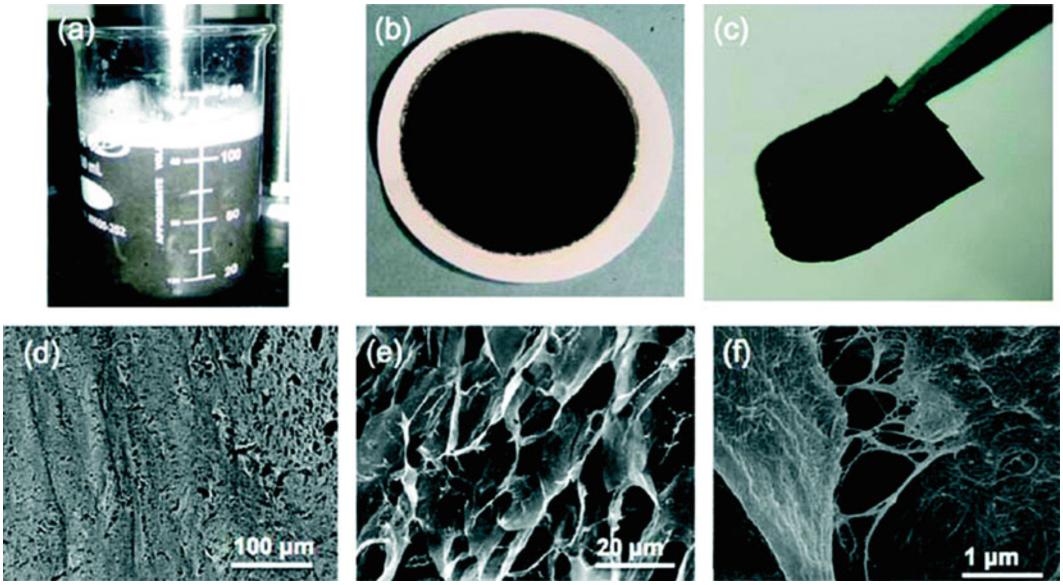

Fig. 4.202 Fabrication of conductive, flexible nanopaper aerogels. (**a**) Aqueous dispersion of CNTs and CNFs. (**b**) A web film made of slurry in (**a**). (**c**) A freeze-dried conductive nanopaper (200 μm thick). (**d–f**) SEM of conductive nanopaper with different magnifications [566]. (Reproduced with permission of *Elsevier Science*)

---

[50] The nanopaper image above is reproduced with permission of the *Elsevier Science* (*Composites: Part B*, **2012**, *43*, 3293–3305).

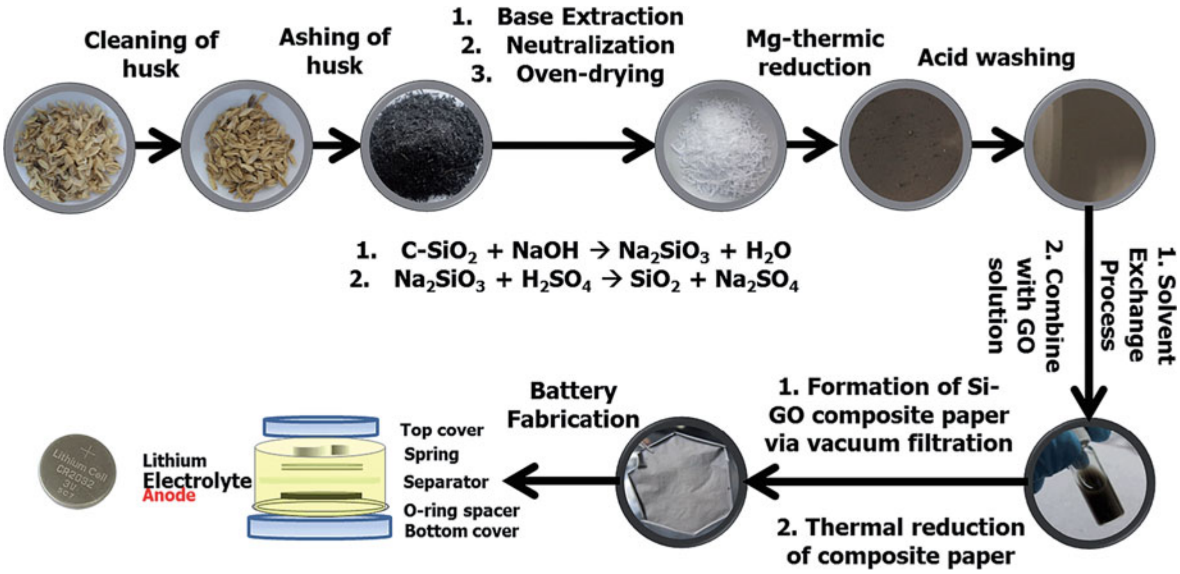

Fig. 4.203 Schematic diagram of the process used to convert rice husk into Si nanoparticles and the subsequent fabrication of the composite paper with GO solution and battery fabrication. Thermal annealing at 700 °C under an argon atmosphere is used to convert the GO into more conductive reduced GO, which improved the conductivity of the composite paper. (Reproduced with permission of the *Royal Society of Chemistry* [567])

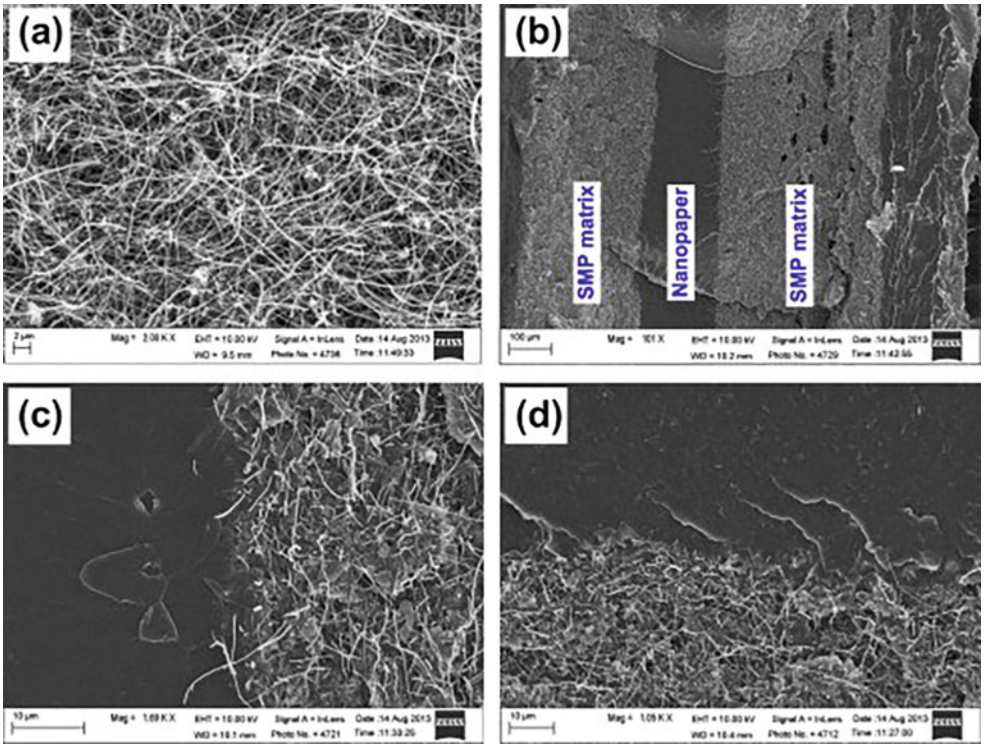

Fig. 4.204 The morphology and structure of multilayered nanopaper and the SMP nanocomposite at an accelerating voltage of 10.00 keV. (**a**) Morphology of multilayered nanopaper. (**b**) Structure of multilayered nanopaper-enabled SMP nanocomposite. (**c**, **d**) Morphology and structure of the interface between the multilayered nanopaper and the SMP matrix. (Reproduced with permission of the *Elsevier Science*)

including their manufacturing, characterization, improvement, and development [569]. Thus, the electrical and shape-memory behavior of self-assembled carbon nanofiber (CNF) nanopaper incorporated with shape-memory polymer (SMP) was studied [570, 571]. The CNF nanopaper could have highly conductive properties. Being aligned into the nanopaper upon a magnetic field, CNTs made significantly lower the electrical resistivity of SMP nanocomposites [572]. CNFs were self-assembled to form multilayered nanopaper (Fig. 4.204) to enhance the bonding and shape recovery behavior of SMP, respectively [573]. It was

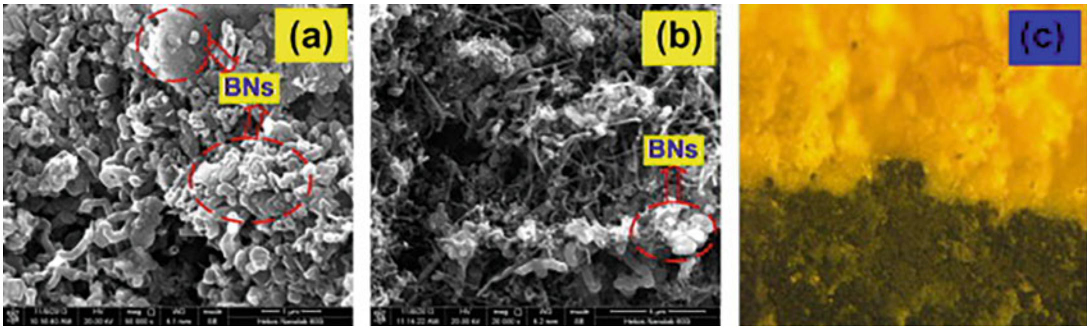

Fig. 4.205 (**a**, **b**) Morphology and network structure of CNF and BN nanopaper revealed by SEM, in which the scare bars are 1 μm and 4 μm, respectively. (**c**) Optical microscope at a magnification of 1000×. (Reproduced with permission of the *Elsevier Science*)

revealed that both glass transition temperature (T_g) and electrical properties of the SMP nanocomposites can be improved by incorporating multilayers of self-assembled nanopapers. In addition, the synergistic effect of self-assembled CNF and boron nitride (BN) nanopaper (Fig. 4.205) on the electrical and thermal properties, and electro-activated shape-memory effect (SME) of polymeric shape-memory nanocomposites, was studied [574]. BN was introduced to improve the thermal conductivity and large dissimilarity of the nanocomposite for enhanced heat transfer and electric-activated shape recovery.

Multifunctional nanocomposites were fabricated using carbon nanopaper sheets [575]. Vapor-grown carbon nanofibers were preformed as carbon nanopaper sheet, resulting in a porous structure with highly entangled carbon nanofibers, which was integrated into the laminates through vacuum-assisted resin transfer molding process. It was revealed that carbon nanopaper sheet was fully integrated to the laminates. Metal-coated carbon nanopapers have been reported too. For instance, after synthesizing a nanopaper (10–20-μm-thick, freestanding sheets of self-assembled SWCNTs), it was decorated with Pt nanoparticles by electroless deposition [576]. Also, the carbon nanopaper sheet, consisting of randomly oriented single-walled nanotubes and vapor-grown carbon nanofibers, was coated with nickel by laser pulse deposition [577].

4.8.9 Nanobatteries[51]

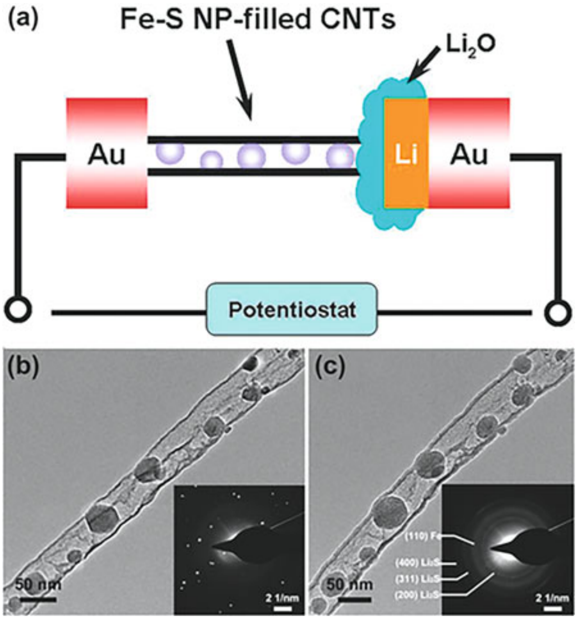

---

[51] The nanobattery image above is reproduced with permission of *Wiley* (*Adv. Sci.*, **2016**, *3*, 1600113).

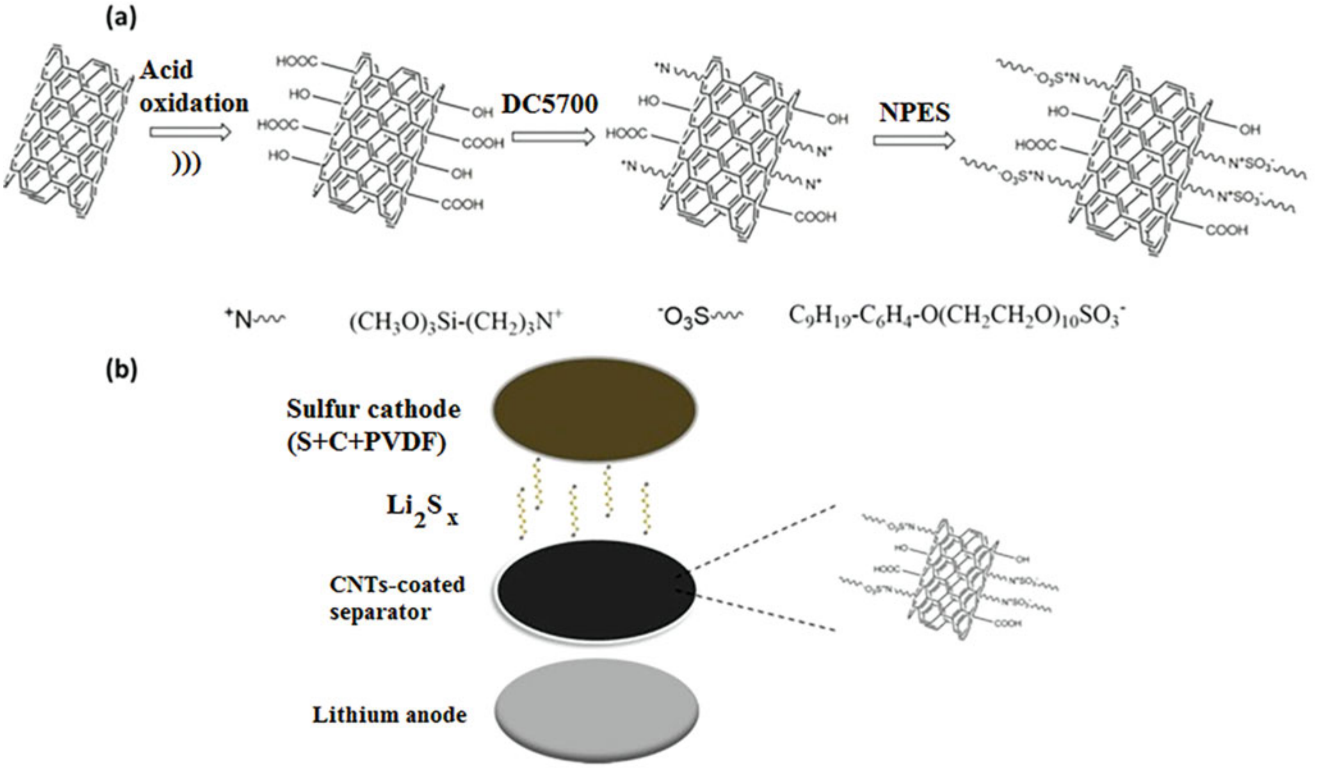

Fig. 4.206 Schematic illustration of (**a**) organic modification process of carbon nanotubes and (**b**) cell configuration of lithium–sulfur (Li–S) batteries. (Reproduced with permission of *MDPI*)

Nanobatteries are fabricated batteries employing nanoscale technology, which can be nano in size or may use nanotechnology in a macroscale battery. In the first case, for example, carbon nanotubes, encapsulating metallic lithium, can potentially act as a miniaturized nanobattery [578]. Such a battery would be potentially useful in the next generation of communication and remote sensing devices, where a pulse of current is required for their operation. Both anode and cathode in nanobatteries can be nanostructured. Talking about carbon materials in Li- and Na-ion batteries, the electrodes can be made or coated with mainly carbon nanotubes, as well as graphite, graphene, and various carbon-based composites to improve their rate capability. High number of reports is observed during the last decade in the field of nanocarbons to be used in batteries [579–582], so here we present only selected representative recent examples on CNTs composites.

An effective method was offered for the modification of separators in lithium–sulfur batteries [583]. Grafted long-chain molecules and tube-like CNTs were shown to enable the formation of micropores in CNTs, which could accommodate polysulfides. The hydrophilic groups (Fig. 4.206) help trapping polysulfides to suppress shuttle effect. Also, the conductive nature of CNTs also contributes to a decrease in internal resistance. In case of CNTs filled with iron sulfide nanoparticles, prepared [584] by inserting sulfur and ferrocene into the hollow core of CNTs followed by heat treatment, it was found that FeS nanoparticles (15 nm in size) are encapsulated in the tubular cavity of the CNTs (Fe-S@CNTs, Fig. 4.207). The CNTs not only play an essential role in accommodating the volume expansion of the Fe–S nanoparticles but also provide a fast transport path for Li ions. Being used as the anode material of lithium-ion batteries, this material exhibited excellent electrochemical lithium-storage performance in terms of high reversible capacity, good cyclic stability, and desirable rate capability. Also, electrodes on the basis of mesoporous Si-coated CNT composite powders, prepared by combining a sol–gel method and the magnesiothermic reduction process, exhibited excellent cycle and rate performances as anodes in Li-ion batteries, which can be attributed to the efficient accommodation of volume change from mesoporous Si structure and the enhanced electrical conductivity from CNT core [585].

Among other nanocarbons, 3D macroporous CNT foam (see also the section above on nanofoams) was tested as a sulfur cathode for lithium sulfur batteries, revealing stable electrochemical performance with high initial capacity and decent cycleability [586]. A seamless graphene–carbon nanotube (GCNT, Fig. 4.208) electrode contributed to reversibly store Li metal with complete dendrite formation suppression [587]. A full battery based on GCNT-Li/sulfurized carbon (SC) showed high-energy density (752 Wh kg^{-1} total electrodes, where total electrodes = GCNT-Li + SC + binder), high areal capacity (2 mAh cm^{-2}), and cyclability (80% retention at >500 cycles), at the same time being free of Li polysulfides and dendrites that would cause severe capacity fade.

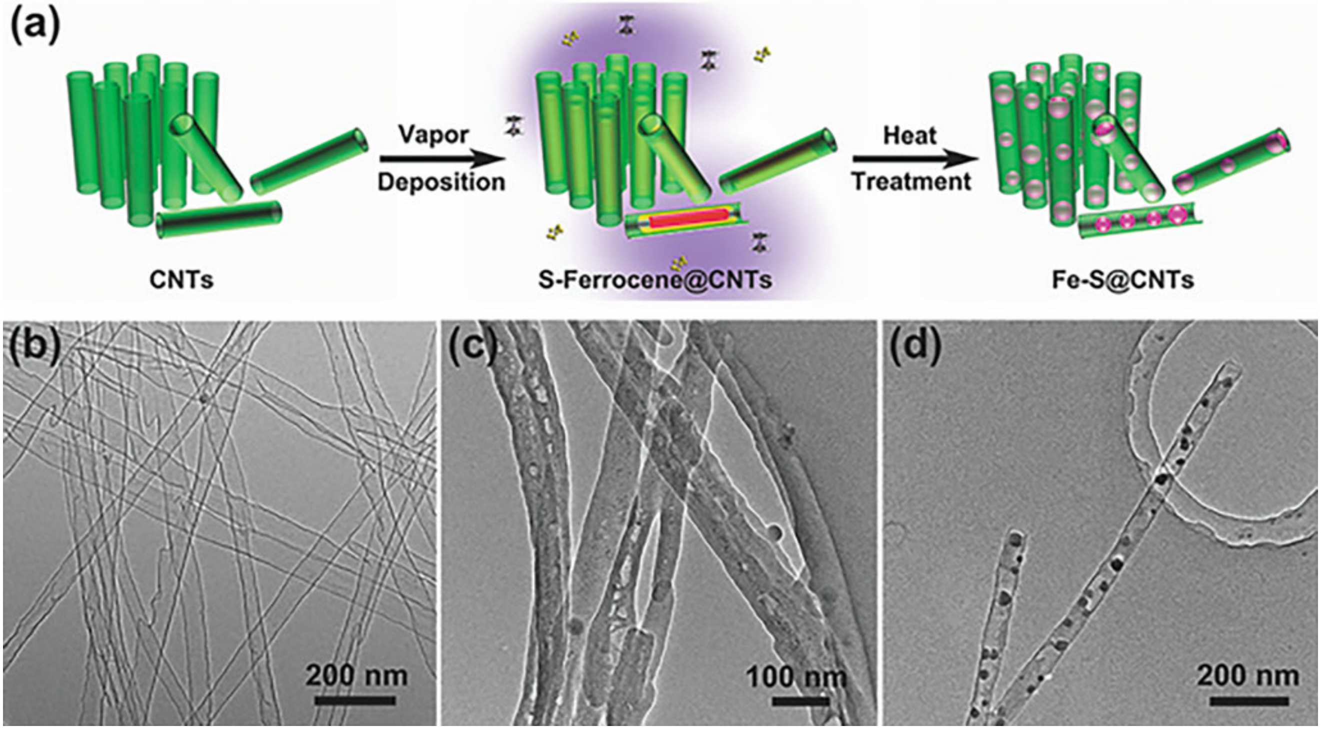

Fig. 4.207 (**a**) Schematic showing the preparation of the Fe-S@CNT material and corresponding TEM images of (**b**) pristine CNTs, (**c**) intermediate sulfur-/ferrocene-filled CNTs, and (**d**) Fe-S@CNTs. (Reproduced with permission of *Wiley*)

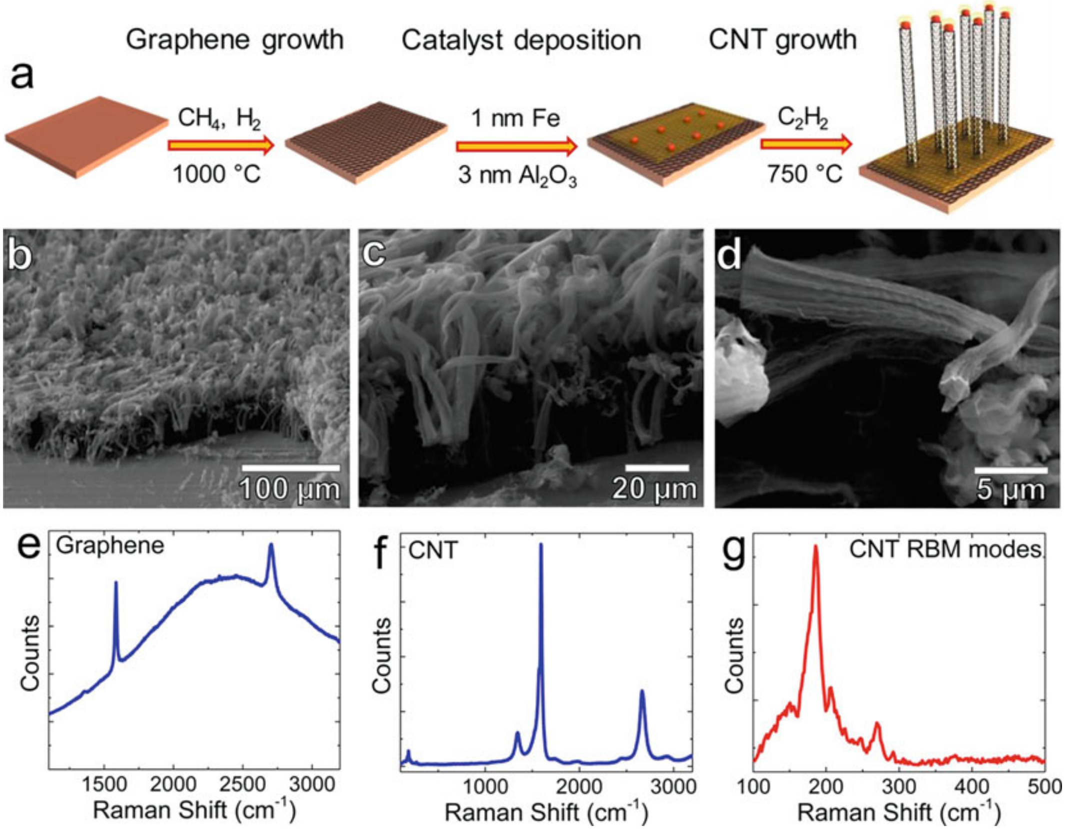

Fig. 4.208 Growth schematic and structural characterization of GCNT. (**a**) Schematic of GCNT growth. E-beam-deposited 1 nm iron nanoparticles are noncontinuous, and they serve as the catalysts for the CNT growth, while a 3 nm layer of aluminum oxide provides the support for a vertical tip growth. (**b–d**) Scanning electron micrograph (SEM) images of GCNT showing a CNT carpet grown vertically from a graphene-covered Cu substrate. (**e**) Raman spectrum of graphene as-grown on Cu. The graphene is conformally connected to its native Cu substrate upon which it is grown. The G band appears at 1589 cm^{-1}, 2D band at 2705 cm^{-1}, IG/I2D ratio > 1, and a trace D band at ~1360 cm^{-1}. The Raman scattering signatures signify a high-quality multilayer graphene. The skewed baseline occurred because the spectrum is obtained atop Cu. (**f**) Raman spectrum of CNTs grown on the Cu-graphene substrate with the G band at 1587 cm^{-1}, 2D band at 2652 cm^{-1}, and D band at 1336 cm^{-1}. (**g**) Raman RBMs of the CNTs in expanded format. (Reproduced with permission of the *American Chemical Society*)

4.8.10 E-Nose[52] and E-Tongue

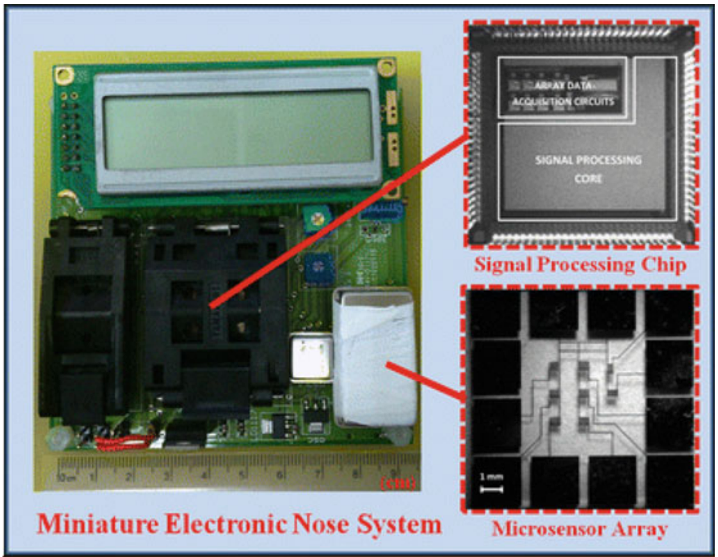

Electronic instruments mimicking the mammalian olfactory system are often referred to as “electronic noses” (E-noses, Fig. 4.209) [589, 590]. The human nose is widely used as an analytical sensing tool to assess the quality of drinks, foodstuffs, perfumes, and many other household products in our daytime activities and of many products in the food, cosmetic, and chemical industries [591]. However, practical use of the human nose is severely limited by the fact that the human senses of smell is subjective, often affected by physical and mental conditions, and tires easily. Consequently, there is considerable need for a device that could mimic the human sense of smell and could provide an objective, quantitative estimation of smell or odor. Thanks to recent nanotechnology breakthroughs the fabrication of mesoscopic and even nanoscopic E-noses is now feasible in the size domain where miniaturization of the microanalytical systems encounters principal limitations. Electronic noses have provided a plethora of benefits to a variety of commercial industries, including the agricultural, biomedical, cosmetics, environmental, food, manufacturing, military, pharmaceutical, regulatory, and various scientific research fields [592]. Advances have improved product attributes, uniformity, and consistency as a result of increases in quality control capabilities afforded by electronic-nose monitoring of all phases of industrial manufacturing processes.

Among a series of reported E-noses and E-tongues on carbon basis, a portable E-nose based on hybrid carbon nanotube-SnO_2 gas sensors were fabricated using electron-beam (E-beam) evaporation by powder mixing [593]. Doping of carbon nanotube (CNT) improved the sensitivity of hybrid gas sensors, while quantity of CNT had a direct effect on the selectivity to volatile organic compounds, i.e., MeOH and EtOH. Based on the proposed methods, this instrument can monitor and classify 1 vol.% of MeOH contamination in whiskeys. Similar SnO_2–glycine-functionalized carbon nanotube-based electronic nose was used for detection of explosive materials [594]. Wearable electronic nose (CNTs/polymer sensor array) can respond to a

---

[52] The E-nose image above is reproduced with permission from *Springer* (*Anal. Bioanal. Chem.*, **2014**, *406*(16), 3985–3994).

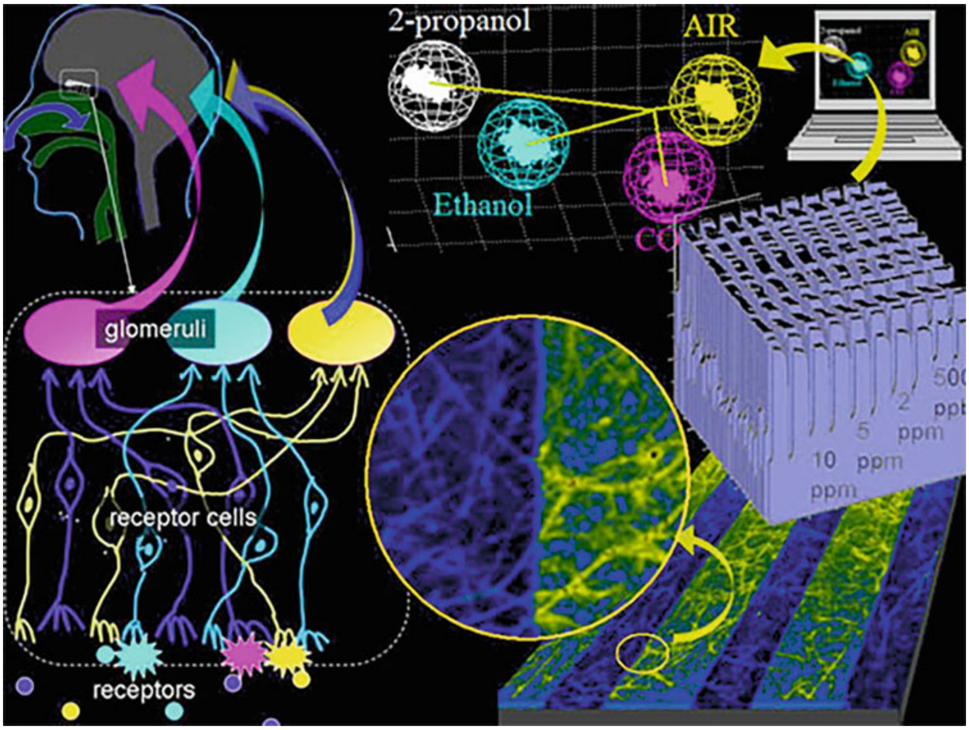

Fig. 4.209 Function of an E-nose [588]. (Reproduced with permission of the http://www.nanowerk.com/)

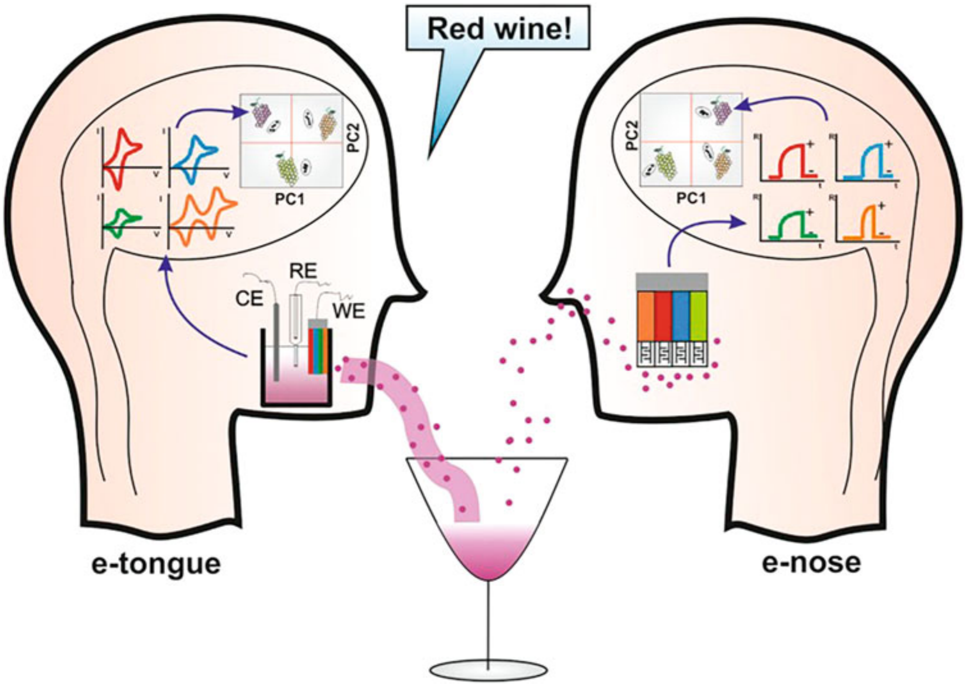

Fig. 4.210 Working principle of E-tongues and E-noses. (Reproduced with permission of *NCBI*)

variety of complex odors [595]. Detection of cotton damaged by *Nezara viridula* is useful in agriculture [596]. Other uses of E-noses and E-tongues include determination of the quality of foods and beverages, consisting of several hundred components in different ranges of concentrations (the working principle is shown in Fig. 4.210) [597].

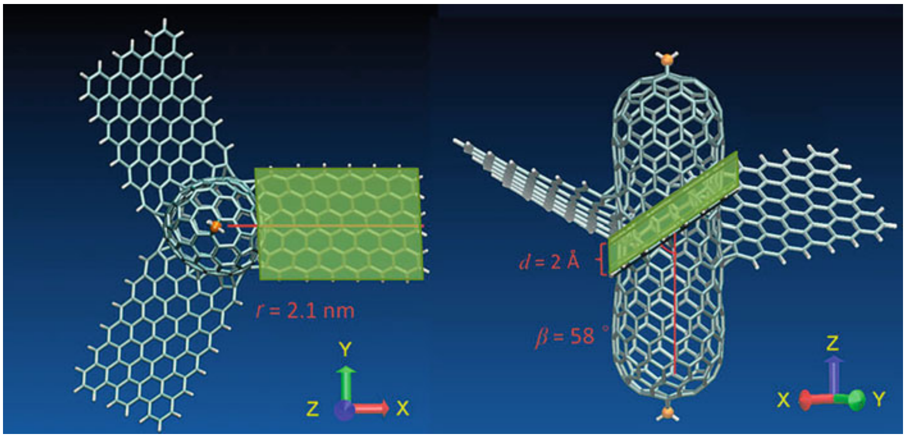

Fig. 4.211 The two fixed pole carbon atoms are shown as the golden balls. The rotation of nano-turbine is driven by the water flow along the z-direction. The 2-Å slab above the turbine blade is shown as the green region. (Reproduced with permission of *Nature*)

Another rapidly developing area, which could be attributed to this "nanotechnical" section, corresponds to *nanoelectromechanical systems* (NEMs). We here only note this field of nanotechnology mentioning three new types of nanoelectromechanical systems based on carbon nanotubes, reported in [598]: an electromechanical *nanothermometer* (see also section above), a *nanorelay*, and a *nanomotor*. The nanorelay was a prototype of a memory cell, and the nanoactuator can be used for transformation of the forward force into the relative rotation of the walls. Relative motion of the walls in these nanosystems was defined by the shape of the interwall interaction energy surface. In addition, such rare "technical" carbon nanostructures are nanoturbins (Fig. 4.211) [599], nanogrids [600], and those based on hybrids of fullerenes and carbon nanotubes A^+@C_n@tubeC_m, called *nano-autoclaves* [601]. This autoclave was used to dimerize C_{20}. It was shown that $(C_{20})_2$ dimer can be really synthesized this way. The advantage of such nano-autoclave is garantized absence of any impurities inside the capsule tube@C_n, so the final dimerization product $(C_{20})_2$ does not contain atoms of other chemical elements.

4.9 Nanostructures Classified as Polyhedral

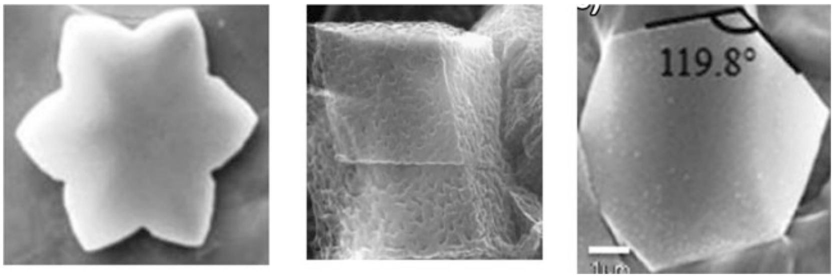

Despite a variety of polyhedron-like nanostructures for other compounds (elemental metals, their oxides or salts), similar data for nanocarbons are relatively rare. In this respect, for geometrical structures with high coordination numbers, important observations on icosahedron and related structures were generalized in a review [602]. The authors emphasized that classical theory of nanoparticle stability predicts that for sizes <1.5–2 nm the icosahedral structure should be the most stable and then between around 2–5 nm, the decahedral shape should be the most stable. Beyond that, face-centered-cubic (FCC) structures will be the predominant phase. However, in the experimental side, icosahedral (I_h) and decahedral (D_h) particles can be observed (Fig. 4.212) much beyond the 5 nm limit. In fact, it is possible to find I_h and D_h particles even in the mesoscopic range. Conversely, it is possible to find FCC particles with a size <1.5 nm. Mechanisms to stabilize fivefold nanoparticles are as follows, among others: internal strain, introduction of planar defects (twins, stacking faults), the introduction of steps, and

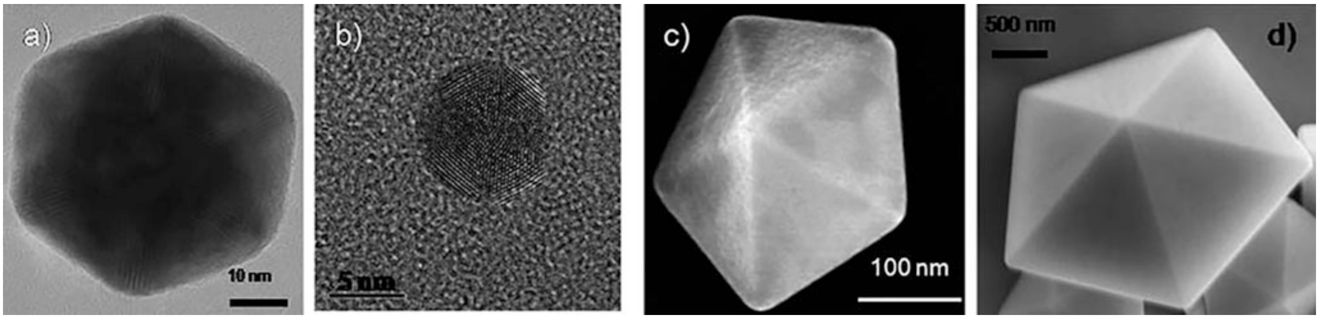

Fig. 4.212 Electron microscopy images of an (**a**) icosahedron of ~80 nm, (**b**) an icosahedron of about 7 nm, (**c**) a decahedron of ~300 nm, and (**d**) a decahedron of few micrometers. (Copyright. Reproduced with permission of the *Royal Society of Chemistry*)

kinks on the surface, external modification of shape by facet truncation, displacement of the five-fold axis which reduces the elastic energy, and splitting of the fivefold axis.

4.9.1 Nanotriangles

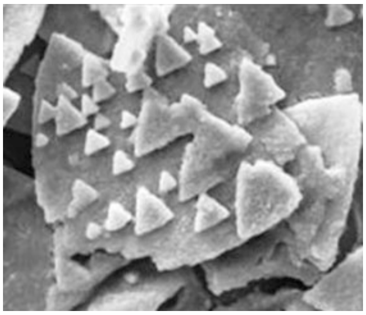

Nanotriangles are very common for gold, but very scarce for nanocarbons [603]. Graphene, nanofiber, nanoonion triangles have been obtained, as well as some their composites. Thus, the electronic shell structure of triangular, hexagonal, and round graphene quantum dots (flakes) near the Fermi level was studied using a tight-binding method [604]. Armchair triangles can be used as building blocks for other types of flakes. The interaction between calf-thymus dsDNA and water-soluble carbon nanoonion (wsCNO) in water followed denaturation of ds (double-stranded) DNA to ss (single-stranded) DNA [605]. The ssDNA concomitantly wrapped the spiky surface of wsCNO to create triangular aggregate (Fig. 4.213) as the building block as observed by time-dependent SEM images. These triangles further aggregate leading to six-petal flower arrangement (Fig. 4.214) via hexagon and finally reach a dead-end network.

Vertically aligned carbon nanofibers were grown by catalytically controlled glow discharge CVD [606] from C_2H_2/NH_3 gas mixture using Ni catalyst, yielding flattened carbon nanostructures (carbon nanotriangles, Fig. 4.215). The morphology and chemical composition of isolated product were found to have a strong dependence upon the growth conditions. In addition, an unusual sp^3 hybridization-assembled metallic 3D conductive carbon allotrope, named *Tri-carbon* (Fig. 4.216), constructed by helical triangle chains and mechanically and dynamically stable at ambient pressure, was computationally reported [607]. High ring strain in the carbon triangle blocks forces the C–C bond in Tri-carbon to be a “bent bond” rather than the common single bond in diamond or the π bond in graphite. The electron density difference for Tri-carbon in comparison with graphite and diamond to gain more insight into the chemical bonding is shown in Fig. 4.217. Tri-carbon is expected to be synthesized by chemical methods, such as the synthesis of cyclopropane derivatives (e.g., triangulane and tetrahedrane).

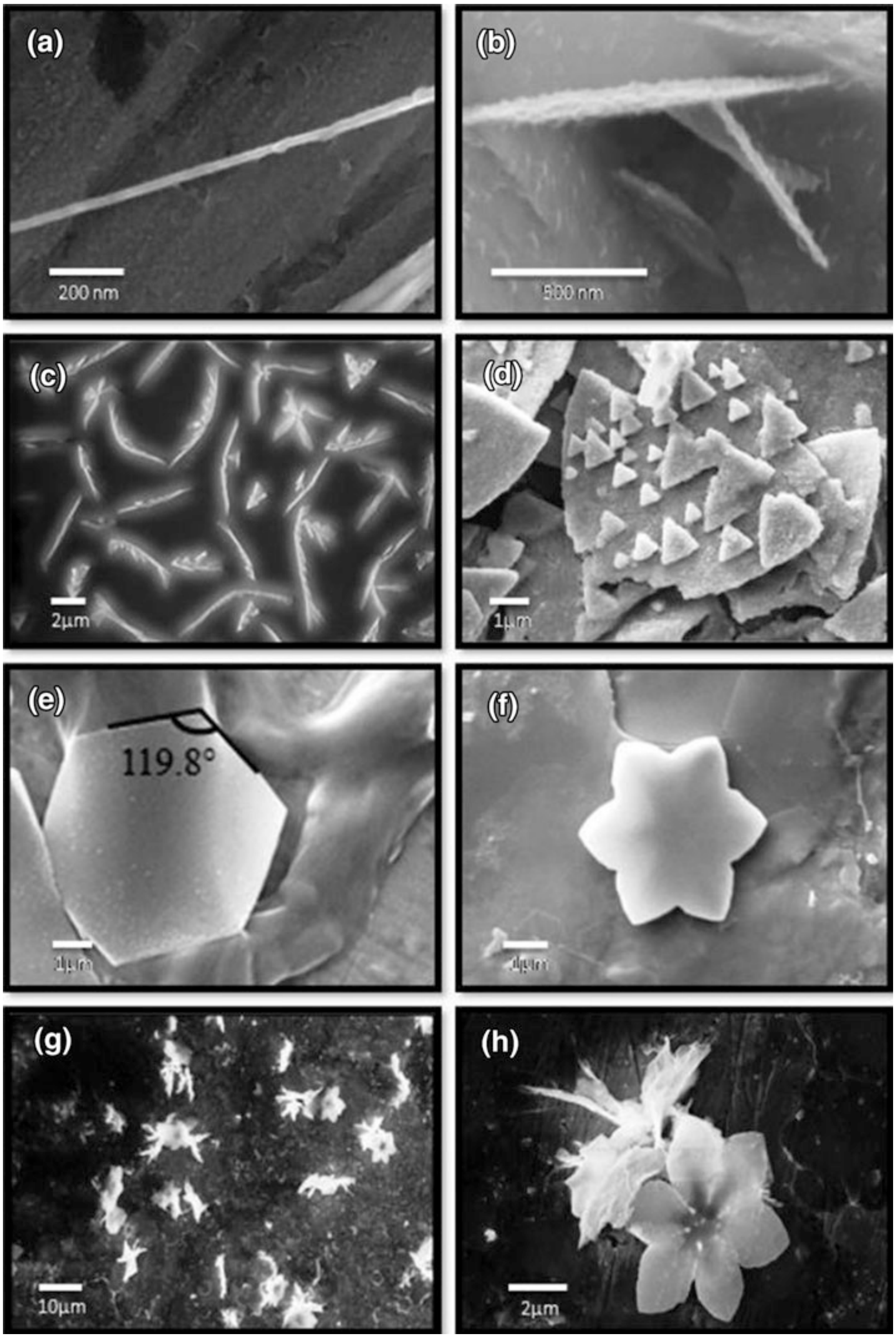

Fig. 4.213 Images of DNA composite: (**a**) 1 h, DNAwsCNO; (**b**) 4 h, growth; (**c**) 8 h, aggregation; (**d**) 16 h, triangle formation; (**e**) hexagon; (**f**) flower; (**g**) assorted flowers; (**h**) selected six-petal flower. (Reproduced with permission of *Springer*)

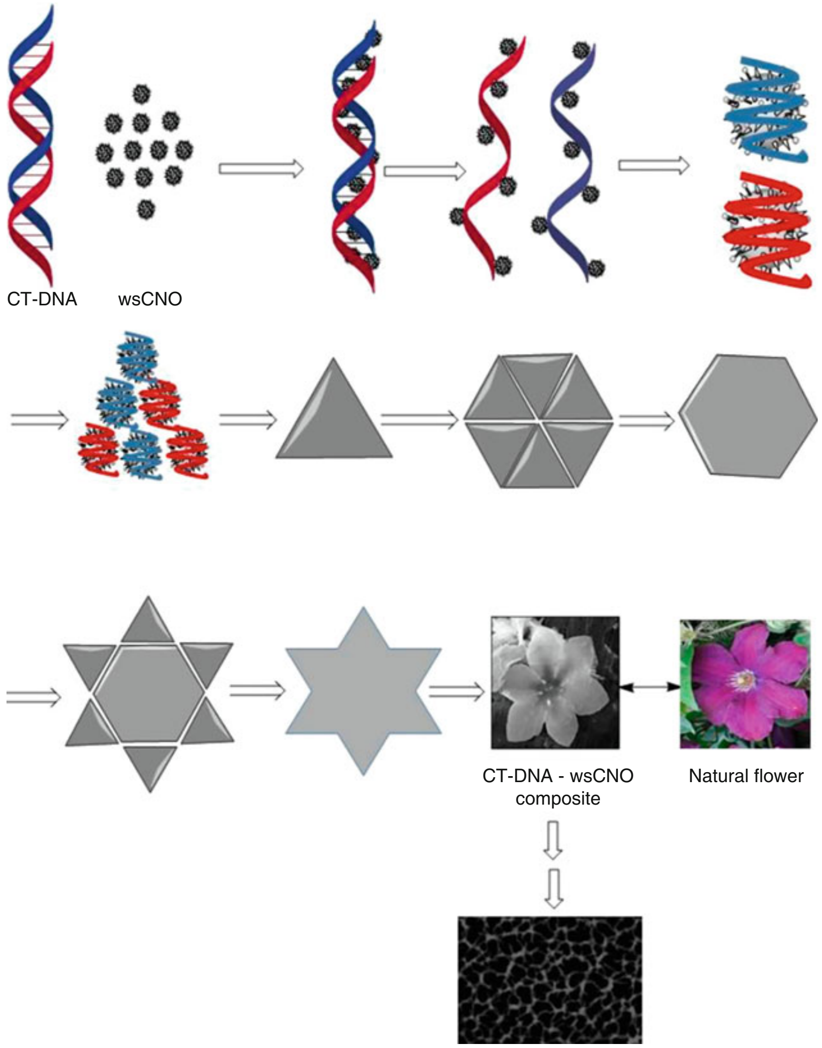

Fig. 4.214 The formation of flower shape composite of wsCNOs and CT-DNA with triangle and hexagon as intermediates finally to dead-end network structure. (Reproduced with permission of *Springer*)

Fig. 4.215 SEM images of carbon nanotriangles taken at (**a**) 45° and (**b**) 30° tilt angle. A schematic representation of nanotriangle formation is shown at (**c**) the beginning and (**d**) near the end of growth. (Reproduced with permission of *AIP*)

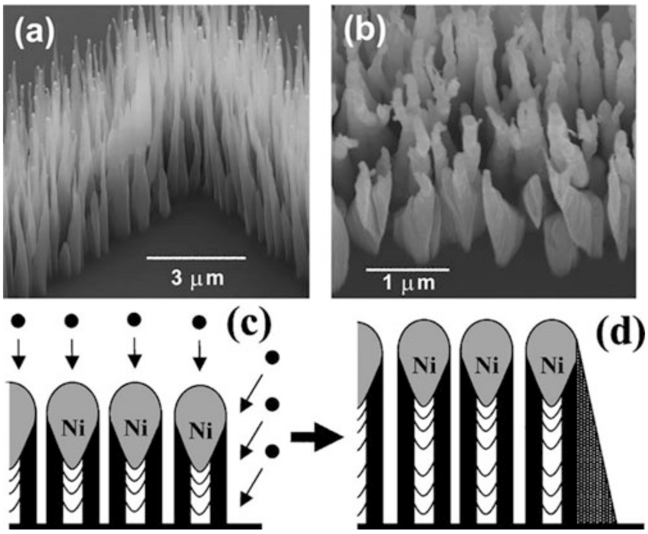

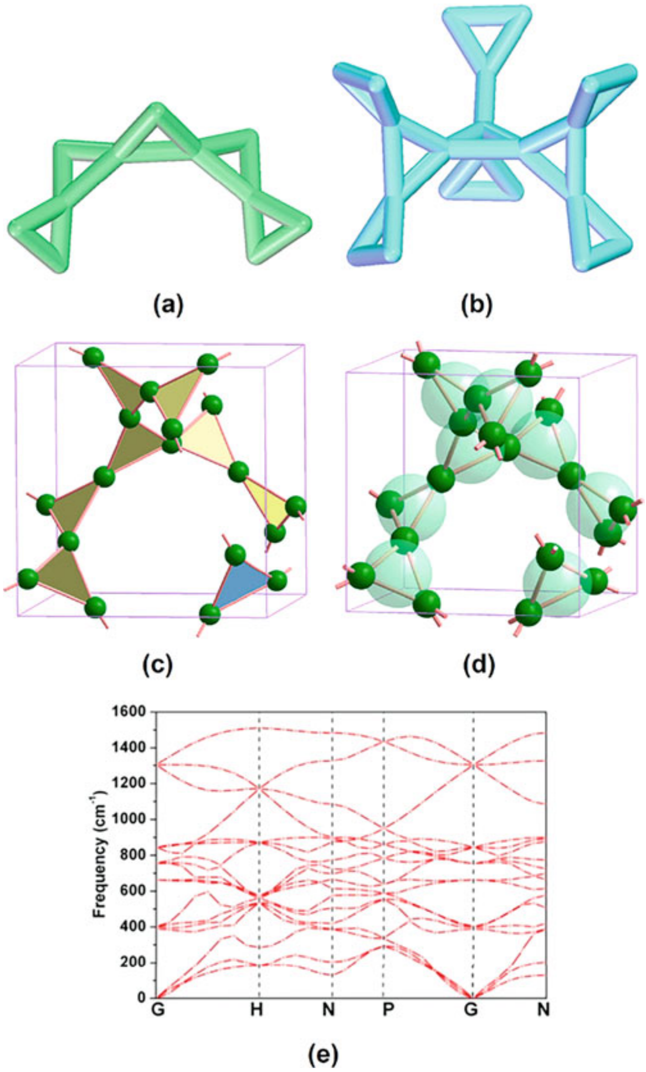

Fig. 4.216 (**a**) A linear triangulane containing five carbon triangle units. (**b**) A branched triangulane containing ten carbon triangle units. (**c**) Tri-carbon described by helical carbon triangle chains, where the yellow and blue triangles represent a branched triangulane and a cyclopropane, respectively. (**d**) Tri-carbon described by K4 carbon model. The light green spheres are the center of the corresponding triangles, which comprise the exact K4 carbon form. (**e**) Phonon dispersion curves of Tri-carbon under ambient pressure. (Reproduced with permission of *IOP Publishing*)

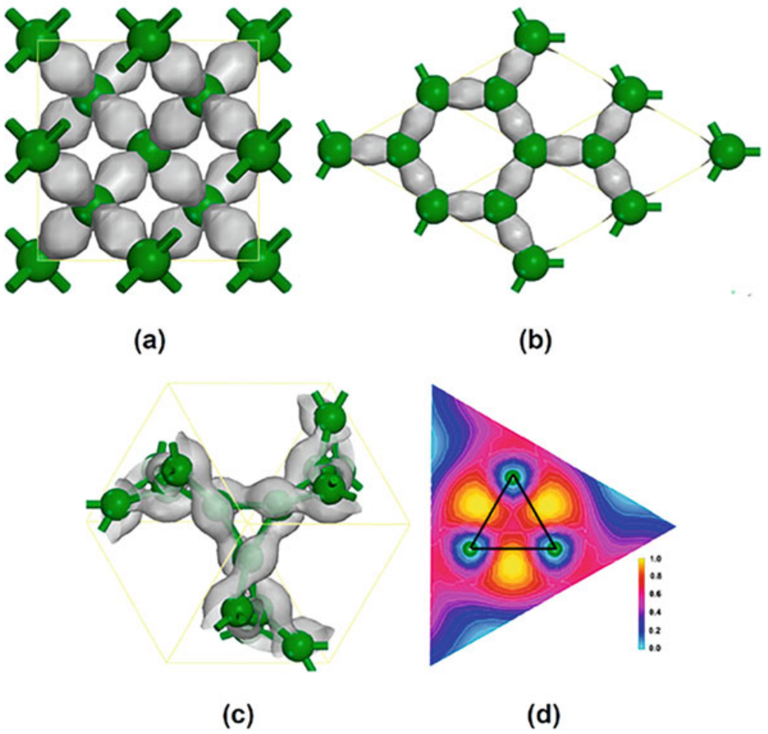

Fig. 4.217 Simulated isosurfaces of electron density difference for (**a**) diamond, (**b**) graphite, and (**c**) Tri-carbon. (**d**) ELF plots in <111> plane crossing the center triangle layer in (**c**). (Reproduced with permission of *IOP Publishing*)

4.9.2 *Nanotetrahedra*

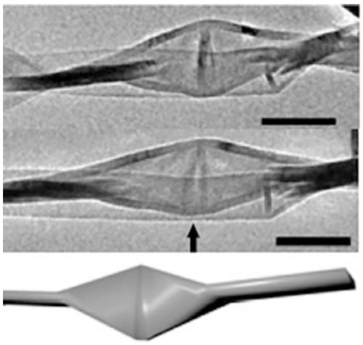

Collapse of a carbon nanotube can result in the formation of a nanoribbon, and a switching of the collapse direction yields a nanotetrahedron in the middle of a nanoribbon (Fig. 4.218) [608, 609]. These nanotetrahedron/nanoribbon structures were found to be thermally stable and did not transform into a tubular form up to a temperature at which they were broken off. Studying these processes in detail, it was revealed that chains of carbon nanotetrahedra/nanoribbons (Fig. 4.219) can be formed via sequential switching of the flattening direction of MWCNTs, in which neighboring two nanotetrahedra are

Fig. 4.218 A series of TEM images of a nanotetrahedron/ribbon structure during the first Joule heating. The position of the nanotetrahedron is indicated by the star. The tip of the W probe was attached to the right of the nanoribbon. The nanoribbon was broken off at the moment between (**d**) and (**e**) at the position indicated by the arrow. (Reproduced with permission of *AIP Publishing*.)

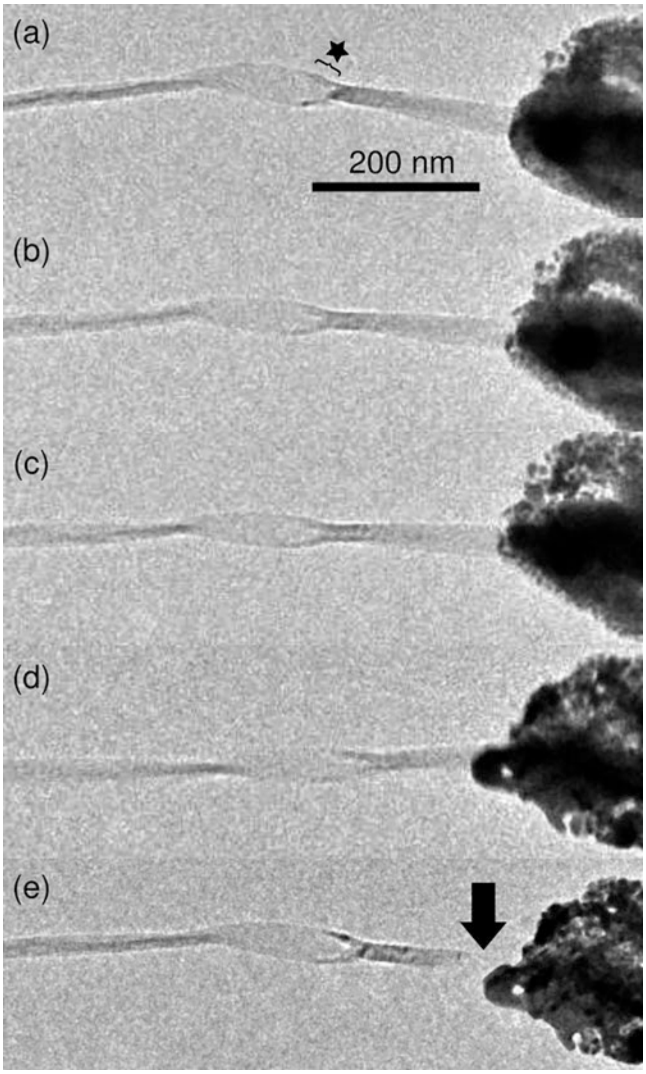

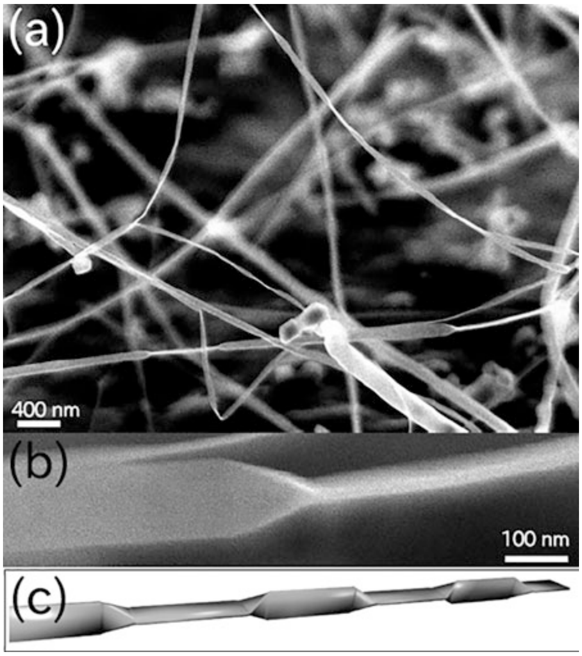

Fig. 4.219 (**a**) SEM image of chains of carbon nanotetrahedra/ nanoribbons. (**b**) Enlarged SEM image of a carbon nanotetrahedron. (**c**) Three-dimensional schematic model of a chain of carbon nanotetrahedra/ nanoribbons. (Reproduced with permission of *Nature*)

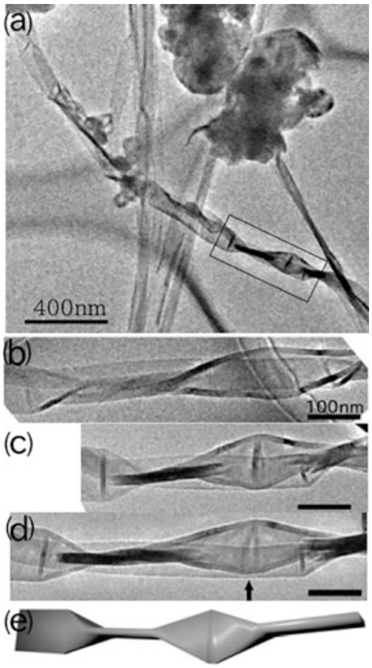

Fig. 4.220 (**a**) TEM image of a nanoribbon with two adjoining nanotetrahedra. (**b–d**) Enlarged images viewed along different directions. (**e**) Schematic 3D model of the nanoribbon with adjoining nanotetrahedra. (Reproduced with permission of *Nature*)

connected by a short nanoribbon [610]. It was proposed that the formation of nanotetrahedra chains is caused by a *quasi*periodic instability of catalyst iron nanoparticles during the CVD growth. In addition, two adjoining carbon nanotetrahedra were found (Fig. 4.220). The splitting-and-joining process involving only one metal catalyst nanoparticle and a self-folding mechanism (called by authors as the *origami* mechanism) was offered to explain the process and the formation of these nanoribbons and nanotetrahedra (Fig. 4.221) [611].

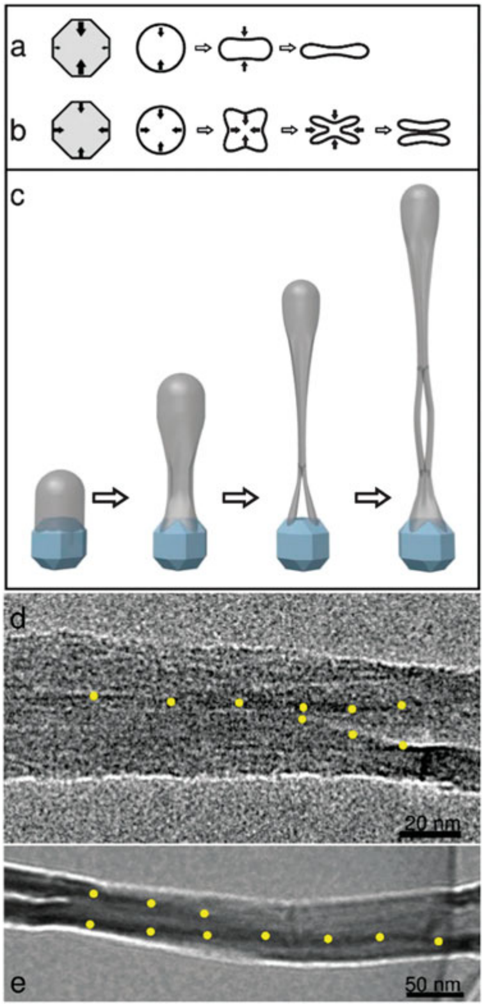

Fig. 4.221 (**a**–**c**) Schematic illustration of the proposed formation mechanism. The gray and white areas represent catalyst metal nanoparticles and the CNTs, respectively. (**a**) One of two flattening directions is superior when a nanotube is expelled from a metal catalyst nanoparticle, which results in the formation of a simple nanoribbon (flattened nanotube). (**b**) Flattening occurs equally in both directions, which results in X-shaped folding and splitting. Viewed along the growth direction in (**a**) and (**b**). (**c**) A nanotube grown from a metal nanoparticle splits into two nanoribbons due to the process shown in (**b**) and then joins together via the reverse process. As a result, an O-shaped carbon nanotube is formed. (**d**, **e**) TEM images of CNTs with X-shaped cross section. (Reproduced with permission of the *Royal Society of Chemistry*)

4.9.3 Nanocubes

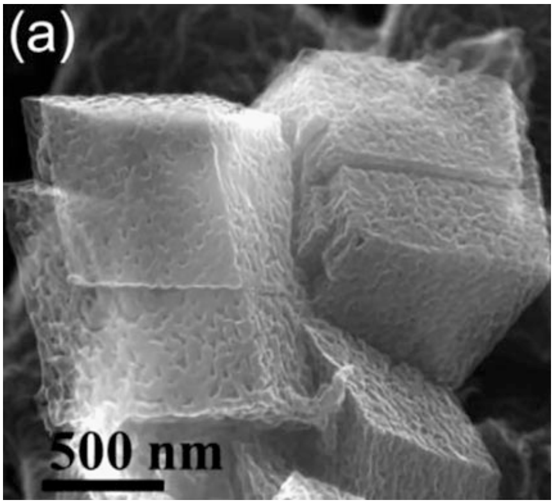

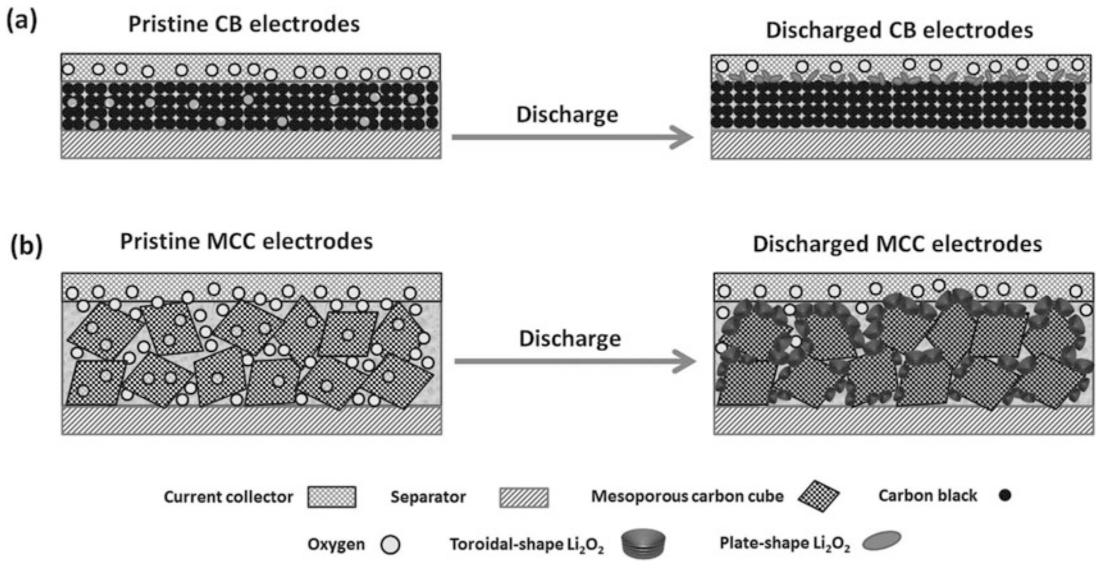

Fig. 4.222 Schematic illustrations of the electrode morphology changes before and after discharge. (**a**) The deposition process of plate-shape Li_2O_2 on the carbon black (CB) electrodes. (**b**) The deposition process of toroidal-shape Li_2O_2 on the mesoporous carbon nanocube (MCC) electrodes. (Reproduced with permission of *Wiley*.)

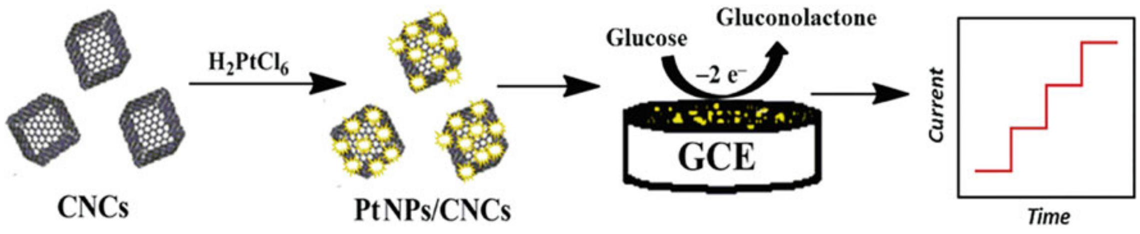

Fig. 4.223 Schematic illustration for the construction of glucose biosensor based on PtNPs/CNCs composites. (Reproduced with permission of the *Elsevier Science*)

Nanocubes[53] on carbon basis are not so frequently reported as nanocages (see one of sections above). They are mainly prepared by pyrolysis (in particular, pyrolysis of such natural products as rice [612]) and generally have electrochemical (batteries) and electrocatalytic applications [613] (in particular, due to certain advantages being compared with carbon black electrodes,[54] Fig. 4.222) (although other uses, as, e.g., bioimaging [614], have been reported). Thus, high-surface nitrogen-doped porous CNCs with a high surface area, prepared by carbonization from Prussian blue (PB) nanocubes coated with poly (furfuryl alcohol), were used as a support for Pt nanoparticles to be applied as an electrocatalyst for the oxidation of methanol [615]. Similarly, nanocomposites of Pt nanoparticles (3–5 nm) anchored on carbon nanocubes (PtNPs/CNCs, Fig. 4.223) efficiently catalyzed the electrochemical oxidation of glucose [616]. The proposed biosensor displayed relatively wider linear range and lower detection limit for glucose detection; the current response of the electrode retained 93.7% of the initial signal after 20 days storage, demonstrating acceptable long-term stability of the system.

Other carbon nanostructures can also take part as supports for nanocubes of the same PB, like in the case of graphene oxide sheets (GOs)–PB nanocomposites, which were fabricated via a spontaneous redox reaction in a aqueous solution containing $FeCl_3$, $K_3[Fe(CN)_6]$, and graphene oxide sheets [617]. The products represented PB nanocubes formed on the surface of GOs retaining their excellent electrochemical activity; moreover, the obtained nanocomposites even showed a higher sensitivity toward the electrocatalytical reduction of H_2O_2 than that of MWCNT/PB nanocomposites. Main applications for these

---

[53] The nanocube image above is reproduced with permission of *Elsevier Science* (*Nano Energy*, **2015**, *16*, 268–280).

[54] "For the CB electrode, the nanopores are formed between CB nanoparticles. During the discharge process, the nanopores are easily to be blocked by the discharge products in the initial discharge process. The MCC electrode consists of carbon nanocubes. Each carbon nanocube contains numerous mesopores, which can facilitate the electrolyte impregnation and oxygen diffusion. Furthermore, large amount of macropores is also formed between carbon nanocubes." (adapted from *Adv. Funct. Mater*. **2015**, *25*, 4436–4444).

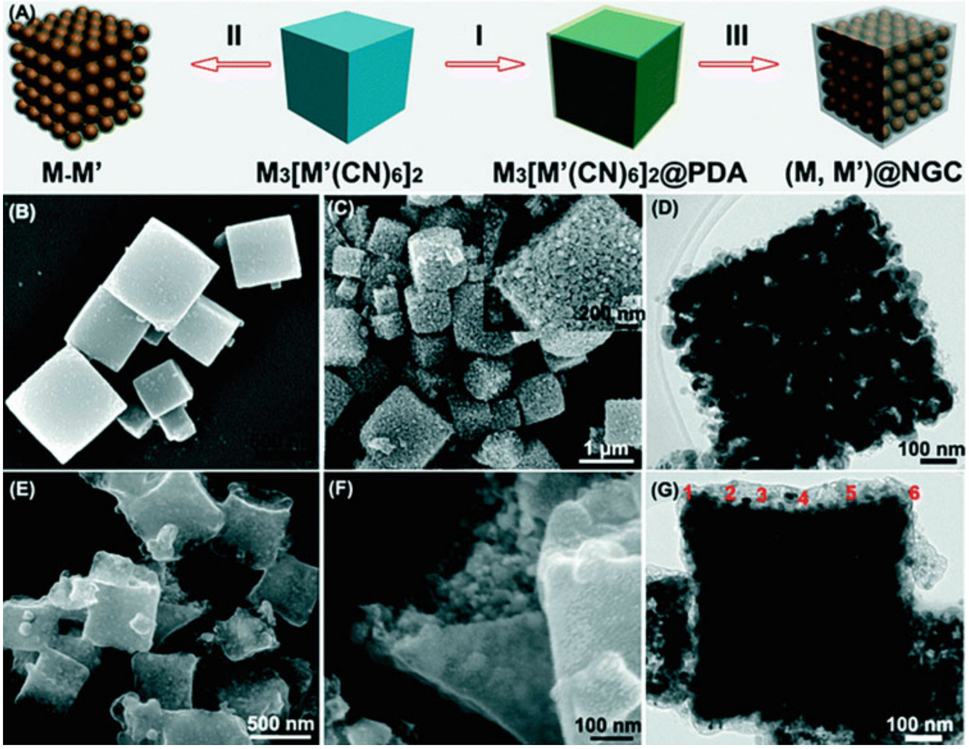

Fig. 4.224 (**a**) Schematic graph of the formation process of the (M, M′)@nitrogen-doped graphitic carbon (NGC) NCs. (**b**) SEM image of the $Fe_3[Co(CN)_6]_2$ NCs. (**c, d**) SEM and TEM images of the (Fe,Co) NCs (inset: high-magnification SEM image). (**e–g**) SEM and TEM images of the (Fe,Co)@NGC NCs. (Reproduced with permission of the *Royal Society of Chemistry*)

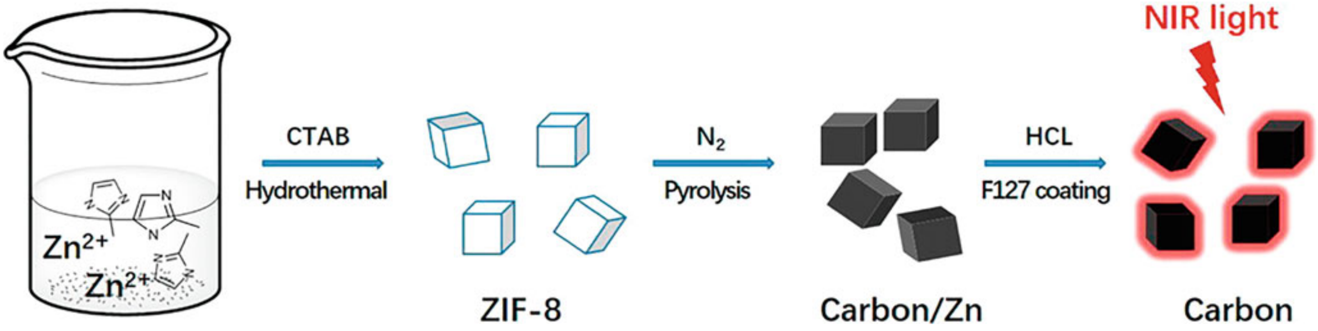

Fig. 4.225 Schematic illustration of the GCNC synthesis. (Reproduced with permission of the *American Chemical Society*)

nanocomposites could be electrochemical sensor and biofuel cell. Also, (Fe,Co)@nitrogen-doped graphitic carbon (NGC) nanocubes (NCs), obtained via the pyrolysis of polydopamine-encapsulated $Fe_3[Co(CN)_6]_2$ NCs at 700 °C (Fig. 4.224), showed comparable catalytic activity for oxygen reduction reaction (ORR) to the Pt/C catalyst [618]. It was recommended as a component of highly efficient nonprecious electrocatalysts in order to replace precious metal catalysts for energy conversion application.

Other nanocubes can serve as templates for CNCs. Thus, graphitic carbon nanocubes (GCNCs), prepared by pyrolysis of ZIF-8 nanocubes (Fig. 4.225) [619], resembled the structure of N-doped graphite and exhibited a high photothermal conversion efficiency of 40.4%. They are highly biocompatible and induced an effective photothermal therapy effect under 808 nm irradiation. As the first work on the simultaneous generation of FeN_x and CoN_x active species from crystalline precursors, hollow FeCo-N-doped porous carbon (Fig. 4.226) was obtained by pyrolysis at 900 °C of metalloporphyrinic MOFs, PCN-224-FeCo, with adjustable molar ratio of Fe^{II}/Co^{II} alternatively residing inside the porphyrin center and was shown to be suitable for efficient electrocatalysis for ORR reactions [620].

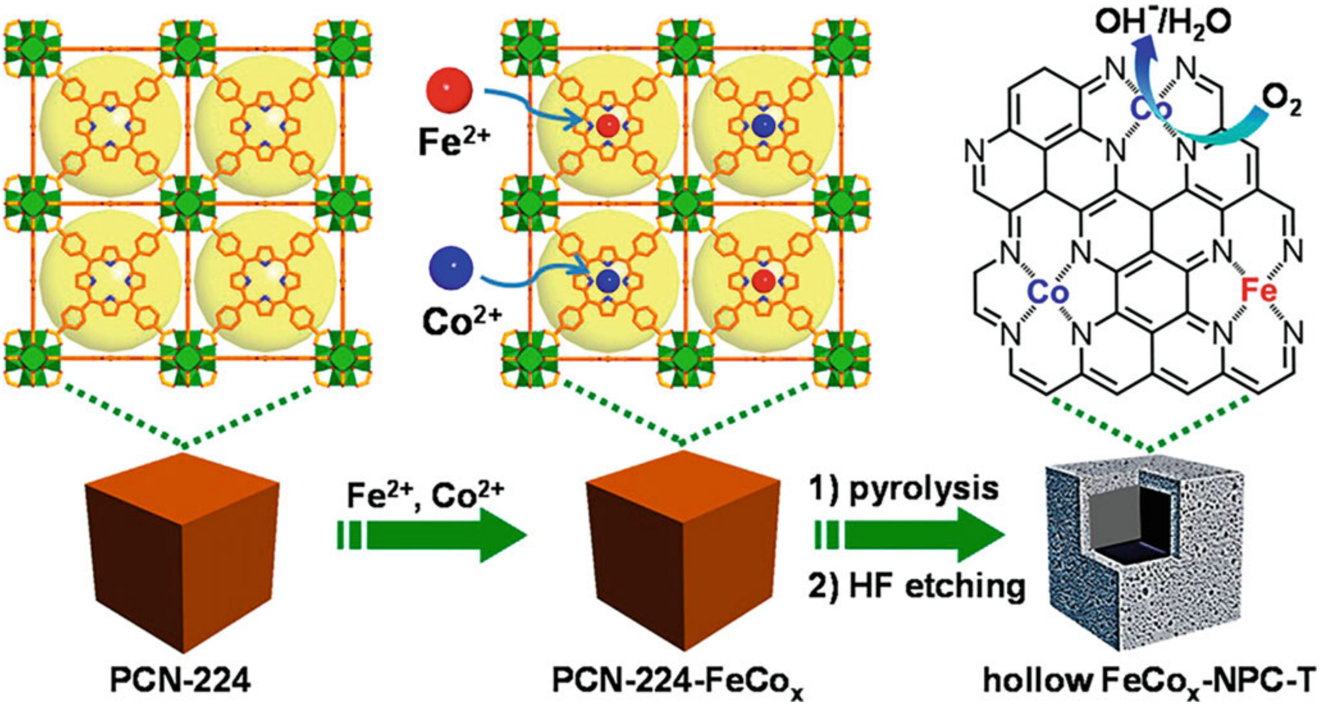

Fig. 4.226 Illustration of the stepwise fabrication of hollow porous FeCo$_x$-NPC-*T* nanocubes with varying Co/Fe molar ratios at different pyrolysis temperatures. (Reproduced with permission of *Wiley*)

An example of carbon nanocube use as containers is homogenous poly(3,4-ethylenedioxythio-phene) (PEDOT)-coated multi-chambered micro-/mesoporous carbon nanocube encapsulated sulfur (P@CNC-S) composites (Fig. 4.227), which can serve as polysulfide reservoirs for lithium–sulfur batteries (Fig. 4.228) [621].

4.9.4 Nanoprisms[55]

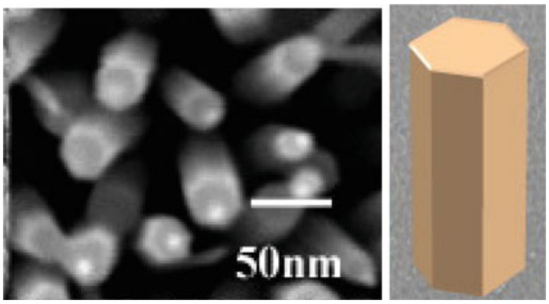

Nanocarbons in nanoprism form are rare. Thus, large-area vertically aligned uniform-shape carbon hexagonal nanoprism (30 nm in diameter, 30° internal angles, Fig. 4.229) arrays were grown (Figs. 4.230 and 4.231) on molybdenum substrates by the catalyst-assisted pulsed laser deposition techniques [622]. The sample of these nanoprism arrays showed better field emission behavior than that with aligned carbon nanorod arrays.

---

[55] The nanoprism image above is reproduced with permission of *Elsevier Science* (*Appl. Surf. Sci.*, **2009**, *255*, 5939–5942).

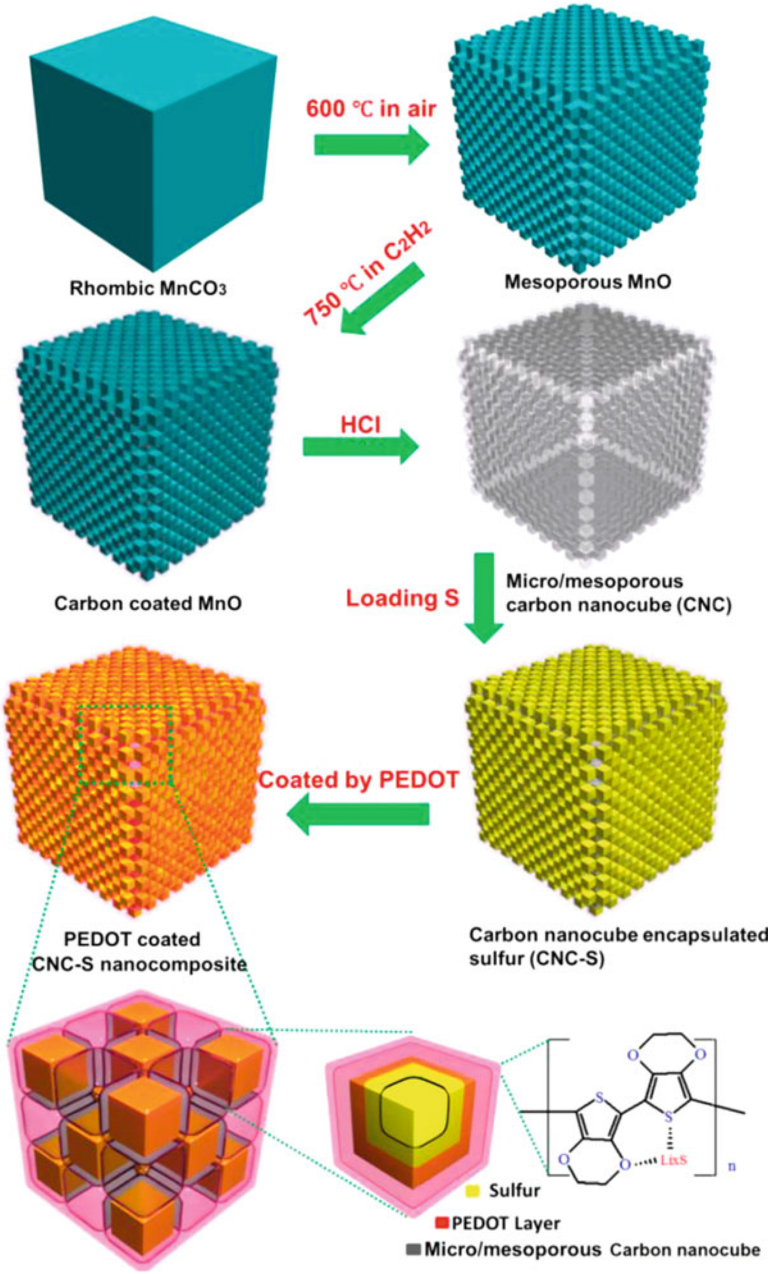

Fig. 4.227 A schematic illustration for preparing PEDOT coated multi-chambered micro-/mesoporous carbon nanocube-sulfur composites. (Reproduced with permission of the *Elsevier Science*)

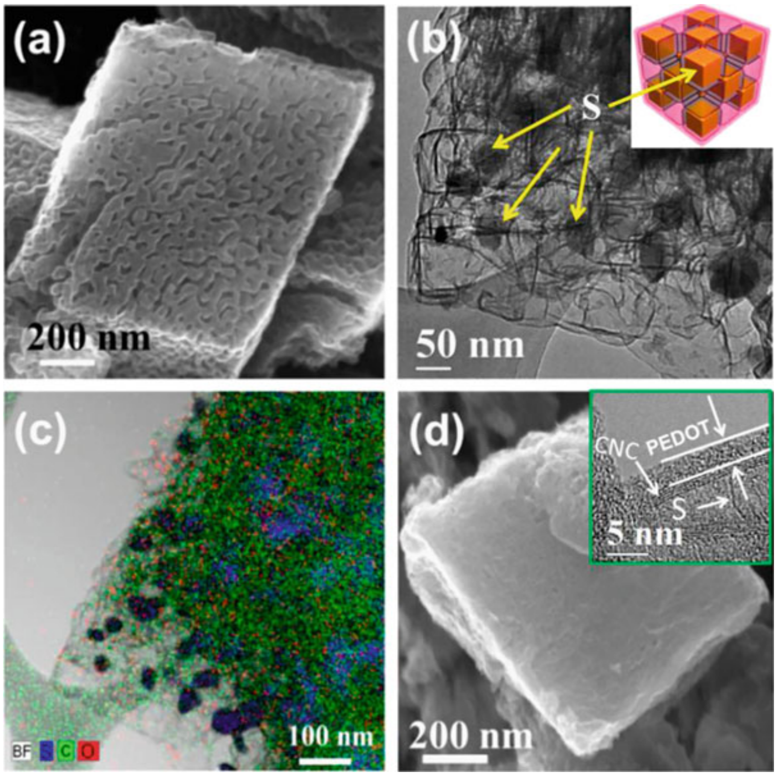

Fig. 4.228 (**a**) SEM images of CNC-S composites. (**b**) TEM image of CNC-S composites. (**c**) Elemental mapping image of CNC-S composites. (**d**) SEM image of P@CNC-S composites within set HRTEM image of the details of P@CNC-S composites. (Reproduced with permission of the *Elsevier Science*)

Fig. 4.229 (**a**) Low-magnification side-view SEM image of the aligned carbon hexagonal nanoprisms at an angle 30°. (**b**) TEM image of the carbon hexagonal nanoprisms. (**c**) Simulated model of the carbon hexagonal nanoprism. The inset in (**a**) shows the high-magnification top-view SEM image of the hexagonally patterned carbon nanoprisms. (Reproduced with permission of the *Elsevier Science*)

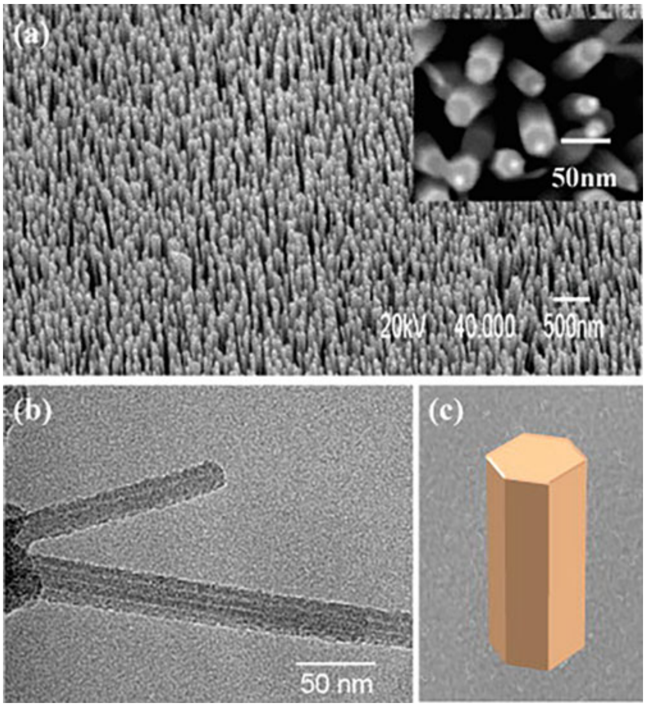

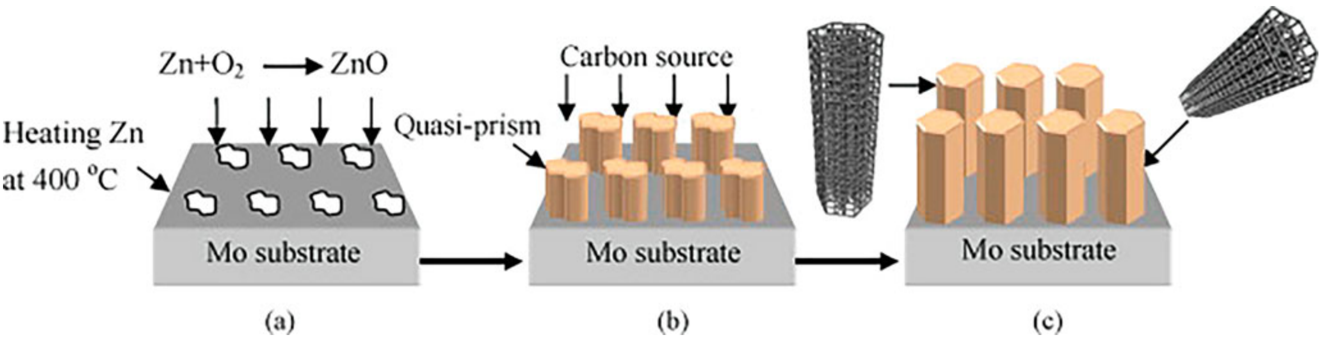

Fig. 4.230 Schematic illustration of the growth mechanism of the carbon hexagonal nanoprisms: (**a**) the formation of ZnO nuclei on the surface Zn nanoparticles deposited on Mo substrate, (**b**) formation of quasi prism-shaped carbon nanostructures on the surface of Zn particles, and (**c**) growth of the carbon hexagonal nanoprisms. (Reproduced with permission of the *Elsevier Science*)

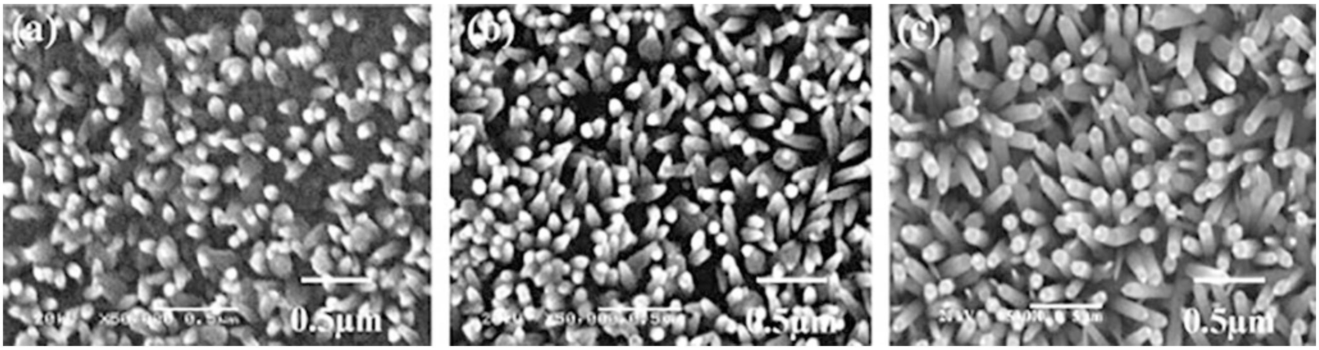

Fig. 4.231 SEM images showing the growth process of carbon hexagonal nanoprisms obtained by the PLD techniques in the presence of catalyst. (**a**) 7 min, (**b**) 15 min, and (**c**) 30 min. (Reproduced with permission of the *Elsevier Science*)

References

1. B.I. Kharisov, O.V. Kharissova, U. Ortiz Mendez, *Handbook on Less-Common Nanostructures* (CRC Press, Boca Raton, 2012)
2. G.G. Parigger, J.O. Hornkohl, A.M. Keszler, L. Nemes, Measurement and analysis of atomic and diatomic carbon spectra from laser ablation of graphite. Appl. Opt. **42**(30), 6192–6198 (2003)
3. C.G. Parigger, A.C. Woods, D.M. Surmick, et al., Computation of diatomic molecular spectra for selected transitions of aluminum monoxide, cyanide, diatomic carbon, and titanium monoxide. Spectrochim. Acta B At. Spectrosc. **107**, 132–138 (2015)
4. R. Hoffmann, Marginalia: C_2 in all its guises. Am. Sci. **83**(4), 309–311 (1995)
5. P.B. Shevlin, Formation of atomic carbon in the decomposition of 5-tetrazolyldiazonium chloride. J. Am. Chem. Soc. **94**(4), 1379–1380 (2002)
6. S.A. Krasnokutski, F.A. Huisken, A simple and clean source of low-energy atomic carbon. Appl. Phys. Lett. **105**(11), 113506 (2014)
7. S. Shaik, D. Danovich, W. Wu, P. Su, H.S. Rzepa, P.C. Hiberty, Quadruple bonding in C_2 and analogous eight-valence electron species. Nat. Chem. **4**, 195–200 (2012)
8. J.M. Matxain, F. Ruipérez, I. Infante, X. Lopez, J.M. Ugalde, G. Merino, M. Piris, Chemical bonding in carbon dimer isovalent series from the natural orbital functional theory perspective. J. Chem. Phys. **138**, 151102 (2013)
9. P.S. Skell, J.H. Plonka, Chemistry of the singlet and triplet C_2 molecules. Mechanism of acetylene formation from reaction with acetone and acetaldehyde. J. Am. Chem. Soc. **92**(19), 5620–5624 (1970)
10. B. Garg, T. Bisht, Carbon nanodots as peroxidase nanozymes for biosensing. Molecules **21**, 1653, 16 pp (2016)
11. J. Wang, H. Soo Choi, Y.-X.J. Wáng, Exponential growth of publications on carbon nanodots by Chinese authors. J. Thorac Dis. **7**(7), E201–E205 (2015)
12. A.M. Ibarra-Ruiz, D.C. Rodríguez Burbano, J.A. Capobianco, Photoluminescent nanoplatforms in biomedical applications. Adv. Phys. **1**(2), 194–225 (2016)
13. Q. Li, T.Y. Ohulchanskyy, R.L. Liu, K. Koynov, D.Q. Wu, A. Best, R. Kumar, A. Bonoiu, P.N. Prasad, Photoluminescent carbon dots as biocompatible nanoprobes for targeting cancer cells *in vitro*. J. Phys. Chem. C **114**, 12062–12068 (2010)
14. J. Zuo, T. Jiang, X. Zhao, X. Xiong, S. Xiao, Z. Zhu, Preparation and application of fluorescent carbon dots. J. Nanomater. **2015**, 787862, 13 pp (2015)
15. P. Roy, P.-C. Chen, A.P. Periasamy, Y.-N. Chen, H.-T. Chang, Photoluminescent carbon nanodots: synthesis, physicochemical properties and analytical applications. Mater. Today **18**(8), 447–458 (2015)
16. Y. Song, S. Zhu, B. Yang, Bioimaging based on fluorescent carbon dots. RSC Adv. **4**, 27184–27200 (2014)

17. S.H. Song, M.-H. Jang, J. Chung, S.H. Jin, B.H. Kim, et al., Highly efficient light-emitting diode of graphene quantum dots fabricated from graphite intercalation compounds. Adv. Opt. Mater. **2**(11), 1016–1023 (2014)
18. X. Han, S. Zhong, W. Pan, W. Shen, A simple strategy for synthesizing highly luminescent carbon nanodots and application as effective down-shifting layers. Nanotechnology **26**, 065402, 11 pp (2015)
19. J. Zhang, F. Zhang, Y. Yang, et al., Composites of graphene quantum dots and reduced graphene oxide as catalysts for nitroarene reduction. ACS Omega **2**, 7293–7298 (2017)
20. Y. Cheng, B. Li, B. Li, B. Li, L. Wang, D. Wei, Y. Feng, D. Jia, Fluorescent zinc doped carbon nanodots derived from chitosan/metal ions complex for cell imaging. Nanomedicine **12**(2), 506–507 (2016)
21. W. Lu, X. Qin, A.M. Asiri, A.O. Al-Youbi, X. Sun, Green synthesis of carbon nanodots as an effective fluorescent probe for sensitive and selective detection of mercury(II) ions. J. Nanopart. Res. **15**, 1344 (2013)
22. X. Qin, W. Lu, A.M. Asiri, A.O. Al-Youbi, X. Sun, Microwave-assisted rapid green synthesis of photoluminescent carbon nanodots from flour and their applications for sensitive and selective detection of mercury(II) ions. Sensors Actuators B **184**, 156–162 (2013)
23. A. Loukanov, R. Sekiya, M. Yoshikawa, N. Kobayashi, Y. Moriyasu, S. Nakabayashi, Photosensitizer-conjugated ultrasmall carbon nanodots as multifunctional fluorescent probes for bioimaging. J. Phys. Chem. C **120**(29), 15867–15874 (2016)
24. V. Strauss, J.T. Margraf, C. Dolle, et al., Carbon nanodots: toward a comprehensive understanding of their photoluminescence. J. Am. Chem. Soc. **136**(49), 17308–17316 (2014)
25. H. Li, Z. Kang, Y. Liu, S.-T. Lee, Carbon nanodots: synthesis, properties and applications. J. Mater. Chem. **22**, 24230–24253 (2012)
26. B.-P. Qi, L. Bao, Z.-L. Zhang, D.-W. Pang, Electrochemical methods to study photoluminescent carbon nanodots: preparation, photoluminescence mechanism and sensing. ACS Appl. Mater. Interfaces **8**(42), 28372–28382 (2016)
27. D. Reyes, M. Camacho, M. Camacho, et al., Laser ablated carbon nanodots for light emission. Nanoscale Res. Lett. **11**, 424, 11 pp (2016)
28. A. Jose Amali, H. Hoshino, C. Wu, M. Ando, Q. Xu, From metal–organic framework to intrinsically fluorescent carbon nanodots. Chem. **20** (27), 8279–8282 (2014)
29. S. Kim, J.K. Seo, J.H. Park, Y. Song, Y.S. Meng, M.J. Heller, White-light emission of blue-luminescent graphene quantum dots by europium (III) complex incorporation. Carbon **124**, 479–485 (2017)
30. J. Zhang, S.-H. Yu, Carbon dots: large-scale synthesis, sensing and bioimaging. Mater. Today **19**(7), 382–393 (2016)
31. J. Xu, T. Lai, Z. Feng, X. Weng, C. Huang, Formation of fluorescent carbon nanodots from kitchen wastes and their application for detection of Fe^{3+}. Luminescence **30**(4), 420–424 (2015)
32. S.A. Chechetka, E. Miyako, Optical regulation of carbon nanodots by chemical functionalization. Chem. Lett. **45**(8), 854–856 (2016)
33. A.B. Bourlinos, A. Bakandritsos, A. Kouloumpis, D. Gournis, M. Krysmann, E.P. Giannelis, K. Polakova, K. Safarova, K. Hola, et al., Gd(III)-doped carbon dots as a dual fluorescent-MRI probe. J. Mater. Chem. **22**, 23327–23330 (2012)
34. J. Zhang, L. Tang, G. Hu, et al., Carbon nanodots-based nanocomposites with enhanced photocatalytic Performance and photothermal effects. Appl. Phys. Lett. **111**, 013904 (2017)
35. M. Li Liu, B. Bin Chen, T. Yang, et al., One-pot carbonization synthesis of europium-doped carbon quantum dots for highly selective detection of tetracycline. Methods Appl. Fluoresc. **5**(1), 015003 (2017)
36. J.-S. Li, Y.-J. Tang, S.-L. Li, et al., Carbon nanodots functional MOFs composites by a stepwise synthetic approach: enhanced H2 storage and fluorescent sensing. CrystEngComm **17**, 1080–1085 (2015)
37. C.-L. Shen, L.-X. Su, J.-H. Zang, et al., Carbon nanodots as dual-mode nanosensors for selective detection of hydrogen peroxide. Nanoscale Res. Lett. **12**, 447, 10 pp (2017)
38. J. Shen, Y. Zhu, X. Yang, C. Li, Graphene quantum dots: emergent nanolights for bioimaging, sensors, catalysis and photovoltaic devices. J. Chem. Soc. Chem. Commun. **48**, 3686–3699 (2012)
39. W. Dai, Y. Lei, M. Xu, et al., Rare-earth free self-activated graphene quantum dots and copper-cysteamine phosphors for enhanced white light-emitting-diodes under single excitation. Sci. Rep. **7**, 12872 (2017)
40. A. Kocsis, S.W. Cranford, Carbyne: a one dimensional carbon allotrope, in *Carbon Nanomaterials Sourcebook. Nanoparticles, Nanocapsules, Nanofibers, Nanoporous Structures, and Nanocomposites*, ed. by K. D. Sattler (Ed), vol. II, (CRC Press, Boca Raton, FL, USA, 2016), pp. 3–25
41. J.M. Alred, N. Gupta, M. Liu, Z. Zhang, B.I. Yakobson, Mechanics of materials creation: nanotubes, graphene, carbyne, borophenes. 2016 IUTAM Symposium on Nanoscale Physical Mechanics. Procedia IUTAM **21**, 17–24 (2017)
42. C.R. Ma, J. Xiao, G.W. Yang, Giant nonlinear optical responses of carbyne. J. Mater. Chem. C **4**, 4692–4698 (2016)
43. L. Shi, P. Rohringer, K. Suenaga, et al., Confined linear carbon chains as a route to bulk carbyne. Nat. Mater. **15**, 634–640 (2016)
44. B. Pan, J. Xiao, J. Li, P. Liu, C. Wang, G. Yang, Carbyne with finite length: the one-dimensional *sp* carbon. Sci. Adv. **1**(9), e1500857 (2015)
45. E.A. Belenkov, V.V. Mavrinsky, Crystal structure of a perfect carbyne. Crystallogr. Rep. **53**(1), 83–87 (2008)
46. G.M. Demyashev, A.L. Taube, E. Siores, Surface modification of titanium carbide with carbyne-containing nanocoatings. J. Nanosci. Nanotechnol. **2**(2), 133–137 (2002)
47. Q. Sun, L. Cai, S. Wang, Bottom-up synthesis of metalated carbyne. J. Am. Chem. Soc. **138**(4), 1106–1109 (2016)
48. A.K. Nair, S.W. Cranford, M.J. Buehler, The minimal nanowire: mechanical properties of carbyne. EPL **95**, 16002, 5 pp (2011)
49. M. Wang, S. Lin, Ballistic thermal transport in carbyne and cumulene with micron-scale spectral acoustic phonon mean free path. Sci. Rep. **5**, 18122 (2015)
50. S. Kotrechko, I. Mikhailovskij, T. Mazilova, E. Sadanov, A. Timoshevskii, N. Stetsenko, Y. Matviychuk, Mechanical properties of carbyne: experiment and simulations. Nanoscale Res. Lett. **10**, 24 (2015)
51. Y. NuLi, Q. Chen, W. Wang, et al., Carbyne polysulfide as a novel cathode material for rechargeable magnesium batteries. Sci. World J. **2014**, 107918, 7 pp (2014)
52. F. Cataldo, Y. Keheyan, Generation of higher fullerenes from laser ablation of carbyne and C_{60} photopolymer astrochemical implications. Fullerenes, Nanotubes, Carbon Nanostruct. **10**, 99–106 (2002)
53. S. Kotrechko, A. Timoshevskii, E. Kolyvoshko, Y. Matviychuk, N. Stetsenko, Thermomechanical stability of carbyne-based nanodevices. Nanoscale Res. Lett. **12**, 327 (2017)
54. F. Banhart, Chains of carbon atoms: a vision or a new nanomaterial? Beilstein J. Nanotechnol. **6**, 559–569 (2015)

55. L. Shen, M. Zeng, S.-W. Yang, C. Zhang, X. Wang, Y. Feng, Electron transport properties of atomic carbon nanowires between graphene electrodes. J. Am. Chem. Soc. **132**(33), 11481–11486 (2010)
56. R.Y. Oeiras, E.Z. da Silva, Bond length and electric current oscillation of long linear carbon chains: density functional theory, MpB model, and quantum spin transport studies. J. Chem. Phys. **140**, 134703 (2014)
57. G. Onida, N. Manini, L. Ravagnan, E. Cinquanta, D. Sangalli, P. Milani, Vibrational properties of sp carbon atomic wires in cluster-assembled carbon films. Phys. Status Solidi **247**(8), 2017–2021 (2010)
58. C.S. Casari, M. Tommasini, R.R. Tykwinski, A. Milani, Carbon-atom wires: 1-D systems with tunable properties. Nanoscale **8**, 4414–4435 (2016)
59. C.S. Casari, C.S. Giannuzzi, V. Russo, Carbon-atom wires produced by nanosecond pulsed laser deposition in a background gas. Carbon **104**, 190–195 (2016)
60. O. Cretu, A.R. Botello-Mendez, I. Janowska, et al., Electrical transport measured in atomic carbon chains. Nano Lett. **13**, 3487–3493 (2013)
61. N. Tayebi, Y. Narui, R.J. Chen, C.P. Collier, K.P. Giapis, Y. Zhang, Nanopencil as a wear-tolerant probe for ultrahigh density data storage. Appl. Phys. Lett. **93**(10), 103112/1–103112/3 (2008)
62. A.G. Nasibulin, P.V. Pikhitsa, H. Jiang, D.P. Brown, A.V. Krasheninnikov, A.S. Anisimov, P. Queipo, A. Moisala, D. Gonzalez, G. Lientschnig, A. Hassanien, S.D. Shandakov, G. Lolli, D.E. Resasco, M. Choi, D. Tománek, E.I. Kauppinen, A novel hybrid carbon material. Nat. Nanotechnol. **2**, 156–161 (2007)
63. Y. Tian, D. Chassaing, A.G. Nasibulin, P. Ayala, H. Jiang, A.S. Anisimov, A. Hassanien, E.I. Kauppinen, The local study of a nanoBud structure. Phys. Status Solidi B **245**(10), 2047–2050 (2008)
64. http://www.nanodic.com/carbon/Carbon_nanobud.htm. Accessed on May 5, 2016
65. B.I. Kharisov, O.V. Kharissova, U. Ortiz-Mendez, *Handbook of Less-Common Nanostructures* (CRC Press, 2012), 862 pp
66. A.G. Nasibulin, A.S. Anisimov, P.V. Pikhitsa, H. Jiang, D.P. Brown, M. Choi, E.I. Kauppinen, Investigations of NanoBud formation. Chem. Phys. Lett. **446**, 109–114 (2007)
67. A. Anisimov, Aerosol synthesis of carbon nanotubes and nanobuds. Ph.D. thesis, Aalto University, Finland, 2010
68. R.J. Nicholls, J. Britton, S. Shayan Meysami, A.A. Koos, N. Grobert, *In situ* engineering of NanoBud geometries. Chem. Commun. **49**, 10956–10958 (2013)
69. M. Ghorbanzadeh Ahangari, M.D. Ganji, F. Montazar, Mechanical and electronic properties of carbon nanobuds: first-principles study. Solid State Commun. **203**, 58–62 (2015)
70. H.Y. He, B.C. Pan, Electronic structures and Raman features of a carbon Nanobud. J. Phys. Chem. C **113**, 20822–20826 (2009)
71. X. Wu, X. Cheng Zeng, First-principles study of a carbon Nanobud. ACS Nano **287**, 1459–1465 (2008)
72. J. Il Choi, H. Seok Kim, H. Seul Kim, G. In Lee, J.K. Kang, Y.-H. Kim, Carbon nanobuds based on carbon nanotube caps: a first-principles study. Nanoscale **8**, 2343–2349 (2016)
73. X. Yang, L. Wang, Y. Huang, Z. Han, A.C. To, Carbon nanotube–fullerene hybrid nanostructures by C_{60} bombardment: formation and mechanical behavior. Phys. Chem. Chem. Phys. **16**(39), 21615–21619 (2014)
74. X. Yang, L. Wang, Y. Huang, A.C. To, B. Cao, Effects of nanobuds and heat welded nanobuds chains on mechanical behavior of carbon nanotubes. Comput. Mater. Sci. **109**, 49–55 (2015)
75. X. Zhu, H. Su, Magnetism in hybrid carbon nanostructures: Nanobuds. Phys. Rev. B **79**, 165401 (2009)
76. J. Yazdani, A. Bahrami, Topological index of carbon Nanobud. Aust. J. Basic Appl. Sci. **4**(8), 3575–3577 (2010)
77. Z. Haseeb, A. Kumari, Study of the optical properties of SWCNT and nanobuds. IJECT **6**(4), 45–48 (2015)
78. S. Gorantla, F. Börrnert, A. Bachmatiuk, M. Dimitrakopoulou, R. Schönfelder, F. Schäffel, J. Thomas, T. Gemming, E. Borowiak-Palen, J.H. Warner, B.I. Yakobson, J. Eckert, B. Büchnera, M.H. Rümmeli, *In situ* observation of fullerene fusion and ejection in carbon nanotubes. Nanoscale **2**, 2077–2079 (2010)
79. Y. Tian. Optical Properties of Single-walled Carbon Nanotubes and Nanobuds. Ph.D. Thesis, Aalto University, 2012
80. Y. Tian, Combined Raman spectroscopy and transmission electron microscopy studies of a NanoBud structure. J. Am. Chem. Soc. **130**, 7188–7189 (2008)
81. X.X. Yang, Z.F. Zhou, Y. Wang, J.W. Li, N.G. Guo, W.T. Zheng, J.Z. Peng, C.Q. Sun, Raman spectroscopic determination of the length, energy, Debye temperature, and compressibility of the C–C bond in carbon allotropes. Chem. Phys. Lett. **575**, 86–90 (2013)
82. P. Havu, A. Sillanpaa, N. Runeberg, J. Tarus, E.T. Seppala, R.M. Nieminen, Effects of chemical functionalization on electronic transport in carbon nanobuds. Phys. Rev. B **85**, 115446 (2012)
83. W. Koh, J. Hye Lee, S. Geol Lee, J. Il Choic, S. Soon Jang, Li adsorption on a graphene–fullerene nanobud system: density functional theory approach. RSC Adv. **5**, 32819–32825 (2015)
84. H.W. Kroto, The stability of the fullerenes C_n, with $n = 24, 28, 32, 36, 50, 60$ and 70. Nature **329**, 529–531 (1987)
85. H.W. Kroto, $C_{60}{}^B$ buckminsterfullerene, other fullerenes and the icospiral shell. Comp. Math. Appl. **17**(1–3), 417–423 (1989)
86. P.W. Dunk, N.K. Kaiser, M. Mulet-Gas, A. Rodríguez-Fortea, J.M. Poblet, H. Shinohara, C.L. Hendrickson, A.G. Marshall, H.W. Kroto, The smallest stable Fullerene, $M@C_{28}$ ($M = Ti, Zr, U$): stabilization and growth from carbon vapor. J. Am. Chem. Soc. **134**(22), 9380–9389 (2012)
87. X. Lu, Z. Chen, Curved Pi-conjugation, aromaticity, and the related chemistry of small fullerenes ($<C_{60}$) and single-walled carbon nanotubes. Chem. Rev. **105**, 3643–3696 (2005)
88. G.C. Loha, D. Baillargeat, Thermal transport in C_{20} fullerene-chained carbon nanobuds. J. Appl. Phys. **113**, 123504 (2013)
89. E.F. Sheka, L.Kh. Shaymardanova, C_{60}-based composites in view of topochemical reactions. III. C_{60} + graphene nanobuds. arXiv:1106.0644 [cond-mat.mtrl-sci], Cornell University Library, 2011
90. A. Fereidoon, M. Khorasani, M. Darvish Ganji, F. Memarian, Atomistic simulation study of mechanical properties of periodic graphene nanobuds. Comput. Mater. Sci. **107**, 163–169 (2015)
91. M.B.E. Griffiths, S.E. Koponen, D.J. Mandia, J.F. McLeod, J.P. Coyle, J.J. Sims, J.B. Giorgi, E.R. Sirianni, G.P.A. Yap, S.T. Barry, Surfactant directed growth of gold metal nanoplates by chemical vapor deposition. Chem. Mater. **27**, 6116–6124 (2015)
92. C. Deng, W. Ma, J.-L. Sun, Fabrication of highly rough Ag nanobud substrates and surface-enhanced raman scattering of λ-DNA molecules. J. Nanomater **2012**, 820739, 5 pp (2012)

93. D.S. Choi, A.O. Fung, H. Moon, G. Villareal, Y. Chen, D. Ho, N. Presser, G. Stupian, M. Leung, Detection of neural signals with vertically grown single platinum nanowire-nanobud. J. Nanosci. Nanotechnol. **9**(11), 6483–6486(4) (2009)
94. R. Colin Johnson, Carbon nanobuds flex, replace indium tin oxide. Unique nanobuds stretch, bend, flex. http://www.eetimes.com/document.asp?doc_id=1324698. Accessed May 5, 2016
95. D.P. Brown, B.J. Aitchison, Uses of a carbon nanobud molecule and devices comprising the same. EP 2308112 A1, 2011; WO 2009156596 A1, 2009
96. D.P. Brown, B.J. Aitchison, Uses of a carbon nanobud molecule and devices comprising the same. Patent US 20110127488, 2011
97. I.V. Anoshkin, A.G. Nasibulin, P.R. Mudimela, M. He, V. Ermolov, E.I. Kauppinen, Single-walled carbon nanotube networks for ethanol vapor sensing applications. Nano Res. **6**(2), 77–86 (2013)
98. D. E. Luzzi. Synthesis, structure, and properties of fullerene and nonfullerene nanopeapods, in *Abstracts of Papers*, 225th ACS National Meeting, New Orleans, 23–27 March 2003, COLL-370
99. T. Okazaki, H. Shinohara, Nano-peapods encapsulating fullerenes, in *Applied Physics of Carbon Nanotubes*, ed. by S. V. Rotkin, S. Subramoney (Eds), (Springer, New York, 2005), pp. 133–150
100. T. Okazaki, S. Okubo, T. Nakanishi, S.-K. Joung, T. Saito, M. Otani, S. Okada, S. Bandow, S. Iijima, Optical band gap modification of single-walled carbon nanotubes by encapsulated fullerenes. J. Am. Chem. Soc. **130**, 4122–4128 (2008)
101. Q. Wang, R. Kitaura, Y. Yamamoto, S. Arai, H. Shinohara, Synthesis and TEM structural characterization of C_{60}-flattened carbon nanotube nanopeapods. Nano Res. **7**(12), 1843–1848 (2014)
102. Y. Cho, S. Han, G. Kim, H. Lee, J. Ihm, Orbital hybridization and charge transfer in carbon nanopeapods. Phys. Rev. Lett. **90**(10), 106402/1–106402/4 (2003)
103. T. Yumura, M. Kertesz, S. Iijima, Local modifications of single-wall carbon nanotubes induced by bond formation with encapsulated fullerenes. J. Phys. Chem. B **111**(5), 1099–1109 (2007)
104. R. Kitaura, H. Shinohara, Carbon-nanotube-based hybrid materials. Nanopeapods. Chem. Asian J. **1**(5), 646–655 (2006)
105. A.N. Enyashin, A.L. Ivanovskii, Atomic structure and electronic properties of nanopeapods: isomers of endohedral dititanofullerenes $Ti_2@C_{80}$ in carbon nanotubes. Zh. Neorg. Khim. **51**(9), 1576–1585 (2006)
106. I.V. Krive, R. Ferone, R.I. Shekhter, M. Jonson, P. Utko, J. Nygaard, The influence of electro-mechanical effects on resonant electron tunneling through small carbon nano-peapods. New J. Phys. **10**(Apr.), 043043 (2008)
107. D. Baowan, N. Thamwattana, J.M. Hill, Encapsulation of C_{60} fullerenes into single-walled carbon nanotubes: Fundamental mechanical principles and conventional applied mathematical modeling. Phys. Rev. B: Condens. Matter Mater. Phys. **76**(15), 155411/1–155411/8 (2007)
108. A. Gloter, K. Suenaga, H. Kataura, R. Fujii, T. Kodama, H. Nishikawa, I. Ikemoto, K. Kikuchi, S. Suzuki, Y. Achiba, S. Iijima, Structural evolutions of carbon nano-peapods under electron microscopic observation. Chem. Phys. Lett. **390**(4–6), 462–466 (2004)
109. R. Pati, L. Senapati, P.M. Ajayan, S.K. Nayak, Theoretical study of electrical transport in a fullerene-doped semiconducting carbon nanotubes. J. Appl. Phys. **95**(2), 694–697 (2004)
110. Y. Liu, R.O. Jones, X. Zhao, Y. Ando, Carbon species confined inside carbon nanotubes: A density functional study. Phys. Rev. B: Condens. Matter Mater. Phys. **68**(12), 125413/1–125413/7 (2003)
111. H. Terrones, Beyond Carbon Nanopeapods. ChemPhysChem **13**(9), 2273–2276 (2012)
112. S. Rols, J. Cambedouzou, M. Chorro, H. Schober, V. Agafonov, P. Launois, V. Davydov, A.V. Rakhmanina, H. Kataura, J.-L. Sauvajol, How confinement affects the dynamics of C_{60} in carbon nanopeapods. Phys. Rev. Lett. **101**(6), 065507/1–065507/4 (2008)
113. E. Hernandez, V. Meunier, B.W. Smith, R. Rurali, H. Terrones, M. Buongiorno Nardelli, M. Terrones, D.E. Luzzi, J.-C. Charlier, Fullerene coalescence in nanopeapods: a path to novel tubular carbon. Nano Lett. **3**(8), 1037–1042 (2003)
114. J.H. Warner, Y. Ito, M. Zaka, L. Ge, T. Akachi, H. Okimoto, K. Porfyrakis, A.A.R. Watt, H. Shinohara, G.A.D. Briggs, Rotating fullerene chains in carbon nanopeapods. Nano Lett. **8**(8), 2328–2335 (2008)
115. A.N. Sohi, R. Naghdabadi, Stability of single-walled carbon nanopeapods under combined axial compressive load and external pressure. Physica E Low Dimens. Syst. Nanostruct. **41**(3), 513–517 (2009)
116. L. Cui, Y. Feng, X. Zhang, Dependence of thermal conductivity of carbon nanopeapods on filling ratios of fullerene molecules. J. Phys. Chem. A **119**(45), 11226–11232 (2015)
117. L. Guan, K. Suenaga, S. Okubo, T. Okazaki, S. Iijima, Metallic wires of lanthanum atoms inside carbon nanotubes. J. Am. Chem. Soc. **130**(7), 2162–2163 (2008)
118. K. Suenaga, R. Taniguchi, T. Shimada, T. Okazaki, H. Shinohara, S. Iijima, Evidence for the intramolecular motion of Gd atoms in a $Gd_2@C_{92}$ nanopeapod. Nano Lett. **3**(10), 1395–1398 (2003)
119. R. Kitaura, H. Okimoto, H. Shinohara, Magnetism of the endohedral metallofullerenes $M@C_{82}$ (M=Gd, Dy) and the corresponding nanoscale peapods: Synchrotron soft x-ray magnetic circular dichroism and density-functional theory calculations. Phys. Rev. B **76**, 172409 (2007)
120. Y. Sato, K. Suenaga, S. Bandow, S. Iijima, Site-dependent migration behavior of individual cesium ions inside and outside C_{60} fullerene nanopeapods. Small **4**(8), 1080–1083 (2008)
121. K. Urita, Y. Sato, K. Suenaga, A. Gloter, A. Hashimoto, M. Ishida, T. Shimada, H. Shinohara, S. Iijima, Defect-induced atomic migration in carbon nanopeapod: tracking the single-atom dynamic behavior. Nano Lett. **4**(12), 2451–2454 (2004)
122. A. Trave, F.J. Ribeiro, S.G. Louie, M.L. Cohen, Energetics and structural characterization of C_{60} polymerization in BN and carbon nanopeapods. Phys. Rev. **70**, 205418 (2004)
123. V. Timoshevskii, M. Cote, Doping of C_{60}-induced electronic states in BN nanopeapods: Ab initio simulations. Phys. Rev. B: Condens. Matter Mater. Phys. **80**(23), 235418/1–235418/5 (2009)
124. X. Li, W. Yang, B. Liu, Fullerene coalescence into metallic heterostructures in boron nitride nanotubes: a molecular dynamics study. Nano Lett. **7**(12), 3709–3715 (2007)
125. S. Tsuruoka, H. Matsumoto, V. Castranov, et al., Differentiation of chemical reaction activity of various carbon nanotubes using redox potential: classification by physical and chemical structures. Carbon **95**, 302–308 (2015)
126. J. Su, Y. Gao, R. Che, Synthesis and microstructure of Fe_3C encapsulated inside chain-like carbon nanocapsules. Mater. Lett. **64**(6), 680–683 (2010)

127. D.B. Dougherty, W. Jin, W.G. Cullen, G. Dutton, J.E. Reutt-Robey, S.W. Robey, Local transport gap in C_{60} nanochains on a pentacene template. Phys. Rev. B: Condens. Matter Mater. Phys. **77**(7), 073414/1–073414/4 (2008)
128. M. Zhang, C. He, E. Liu, et al., Activated carbon nanochains with tailored micro-meso pore structures and their application for supercapacitors. J. Phys. Chem. C **119**(38), 21810–22181 (2015)
129. B. Sahu, H. Min, S.K. Banerjee, Effects of magnetism and electric field on the energy gap of bilayer graphene nanobars. arXiv.org, e-Print Archive, *Condensed Matter*, 2009, 1–6, arXiv:0910.2719v1 [cond-mat.mtrl-sci]. Publisher: Cornell University Library
130. T. Krupenkin, Nanograss, nanobricks, nanonails, and other things useful in your nanolandscaping, in *Abstracts of Papers, 237th ACS National Meeting*, Salt Lake City, 22–26 Mar 2009, POLY-333
131. S.K. Sonkar, M. Saxena, M. Saha, S. Sarkar, Carbon nanocubes and nanobricks from pyrolysis of rice. J. Nanosci. Nanotechnol. **10**(6), 4064–4067 (2010)
132. X. Wang, C.-m. Zhao, T. Deng, et al., From amorphous carbon to carbon nanobelts and vertically oriented graphene nanosheets synthesized by plasma-enhanced chemical vapor deposition. Chem. Res. Chin. Univ. **29**(4), 755–758 (2013)
133. X. Lu, J. Wu, After 60 years of efforts: the chemical synthesis of a carbon nanobelt. Chem **2**(5), 619–620 (2017)
134. J. Liu, M. Shao, Q. Tang, S. Zhang, Y. Qian, Synthesis of carbon nanotubes and nanobelts through a medial-reduction method. J. Phys. Chem. B **107**, 6329–6332 (2003)
135. X. Sun, Z. Xing, R. Ning, A.M. Asiri, A.Y. Obaid, Carbon nanobelts as a novel sensing platform for fluorescence-enhanced DNA detection. Analyst **139**, 2318–2321 (2014)
136. C.-T. Lin, T.-H. Chen, T.-S. Chin, C.-Y. Lee, H.-T. Chiu, et al., Quasi two-dimensional carbon nanobelts synthesized using a template method. Carbon **46**, 741–746 (2008)
137. T. Ouyang, K. Cheng, F. Yang, et al., From biomass with irregular structures to 1D carbon nanobelts: a stripping and cutting strategy to fabricate high performance supercapacitor materials. J. Mater. Chem. A **5**, 14551–14561 (2017)
138. Q. Xia, H. Zhao, Z. Du, et al., Facile synthesis of MoO_3/carbon nanobelts as high-performance anode material for lithium ion batteries. Electrochim. Acta **180**, 947–956 (2015)
139. Q. Zhao, L. Jiao, W. Peng, et al., Facile synthesis of $VO_2(B)$/carbon nanobelts with high capacity and good cyclability. J. Power Sources **199**, 350–354 (2012)
140. C. Su, C. Pei, B. Wu, J. Qian, Y. Tan, Highly doped carbon nanobelts with ultrahigh nitrogen content as high-performance supercapacitor materials. Small **13**, 1700834, 12 pp (2017)
141. G. Povie, Y. Segawa, T. Nishihara, Y. Miyauchi, K. Itami, Synthesis of a carbon nanobelt. Science **356**, 172–175 (2017)
142. K. Matsui, M. Fushimi, Y. Segawa, K. Itami, Synthesis, structure, and reactivity of a cylinder-shaped cyclo[12]orthophenylene[6]ethynylene: toward the synthesis of zigzag carbon nanobelts. Org. Lett. **18**, 5352–5355 (2016)
143. Y. Segawa, A. Yagi, H. Ito, K. Itami, A theoretical study on the strain energy of carbon nanobelts. Org. Lett. **18**, 1430–1433 (2016)
144. Y. Ren, G. Pastorin, Incorporation of hexamethylmelamine inside capped carbon nanotubes. Adv. Mater. **20**(11), 2031–2036 (2008)
145. A.V. Vakhrushev, M.V. Suyetin, Methane storage in bottle-like nanocapsules. Nanotechnology **20**, 125602 (2009)
146. R.K. Lee, J.M. Hill, Design parameters for carbon nanobottles to absorb and store methane. J. Nanosci. Nanotechnol. **11**(8), 6893–6903 (2011)
147. J. Li, S.L. Yoong, W.J. Goh, et al., In vitro controlled release of cisplatin from gold-carbon nanobottles via cleavable linkages. Int. J. Nanomedicine **10**, 7425–7441 (2015)
148. N. Yang, G. Zhang, B. Li, Carbon nanocone: A promising thermal rectifier. Appl. Phys. Lett. **93**, 243111 (2008)
149. M.H. Khalifeh, H. Yousefi-Azari, A.R. Ashrafi, A method for computing the Wiener index of one-pentagonal carbon nanocones. Curr. Nanosci. **6**(2), 155–157 (2010)
150. E. Brito, A. Freitas, T. Silva, T. Guerra, S. Azevedo, Double-walled carbon nanocones: stability and electronic structure. Eur. Phys. J. B. **88**, 153 (2015)
151. I. Levchenko, K. Ostrikov, J. Khachan, S.V. Vladimirov, Growth of carbon nanocone arrays on a metal catalyst: the effect of carbon flux ionization. Phys. Plasmas **15**, 103501 (2008)
152. R. Ansari, A. Momen, S. Rouhi, S. Ajori, On the vibration of single-walled carbon nanocones: molecular mechanics approach versus molecular dynamics simulations. Shock. Vib. **2014**, 410783, 8 pp (2014)
153. S. Rouhi, R. Ansariy, S. Nickabadiz, Modal analysis of double-walled carbon nanocones using the nite element method. Int. J. Mod. Phys. B **31**, 1750262, 18 pp (2017)
154. W. Huang, J. Xu, X. Lu, Tapered carbon nanocone tips obtained by dynamic oxidation in air. RSC Adv. **6**, 25541–25548 (2016)
155. I.-C. Chen, L.-H. Chen, X.-R. Ye, C. Daraio, S. Jin, Extremely sharp carbon nanocone probes for atomic force microscopy imaging. Appl. Phys. Lett. **88**, 153102 (2006)
156. S.N. Naess, A. Elgsaeter, G. Helgesen, K.D. Knudsen, Carbon nanocones: wall structure and morphology. Sci. Technol. Adv. Mater. **10**(6), 065002 (2009)
157. A. Pauly, M. Dubois, K. Guerin, A. Hamwi, J. Brunet, C. Varenne, B. Lauron, Use of carbon nanomaterials as a filtration material impermeable to ozone. WO 2010000956, 2010, 20 pp
158. R. Majidi, Adsorption of ternary mixture of noble gases on carbon nanocone: molecular dynamics simulation. Nanosci. Nanotechnol. Lett. **5** (7), 750–753 (2013)
159. S.A. Aal, A.S. Shalabi, K.A. Soliman, High capacity hydrogen storage in Ni decorated carbon nanocone: a first-principles study. J. Quan. Inf. Sci **5**, 134–149 (2015)
160. S. Moradi, Deuterium adsorption on Multi Carbon Nano-cone (MNC_x, X=2-7) including BN Nano-cone: a model for D_2 storage. Orient. J. Chem. **31**(3), 1355–1364 (2015)
161. O.O. Adisa, B.J. Cox, J.M. Hill, Open carbon nanocones as candidates for gas storage. J. Phys. Chem. C **115**, 24528–24533 (2011)
162. M.-L. Li, F. Lin, Y. Chen, Study on the mechanical properties of carbon nanocones using molecular dynamics simulation. Acta Phys. Sin. **62** (1), 016102 (2013)
163. E. Vessally, F. Behmagham, B. Massoumi, A. Hosseinian, L. Edjlali, Carbon nanocone as an electronic sensor for HCl gas: quantum chemical analysis. Vacuum **134**, 40–47 (2016)

164. M.T. Baei, A. Ahmadi Peyghan, Z. Bagheri, Carbon nanocone as an ammonia sensor: DFT studies. Struct. Chem. **24**, 1099–1103 (2013)
165. L.B. Sheridana, D.K. Hensley, N.V. Lavrik, et al., Growth and electrochemical characterization of carbon nanospike thin film electrodes. J. Electrochem. Soc. **161**(9), H558–H563 (2014)
166. A.G. Zestos, C. Yang, C.B. Jacobs, D. Hensley, B.J. Venton, Carbon nanospikes grown on metal wires as microelectrode sensors for dopamine. Analyst **140**, 7283–7292 (2015)
167. A.S. Shanta, K.A. Al Mamun, S.K. Islam, N. McFarlane, Carbon nanotubes, nanofibers and nanospikes for electrochemical sensing: a review. Int. J. High Speed Electron. Syst. **26**(3), 1740008, 12 pp (2017)
168. Y. Song, R. Peng, D.K. Hensley, et al., High-selectivity electrochemical conversion of CO_2 to ethanol using a copper nanoparticle/N-doped graphene electrode. ChemistrySelect **1**, 6055–6061 (2016)
169. J. Zhou, Nanowicking: multi-scale flow interaction with nanofabric structures, Ph.D. Thesis, California Institute of Technology, 2005, 129 pp
170. T. Ichihashi, J.-i. Fujita, M. Ishida, Y. Ochiai, *In situ* observation of carbon-nanopillar tubulization caused by liquidlike iron particles. Phys. Rev. Lett. **92**(21), 215702, 4 pp (2004)
171. K. Sai Krishna, M. Eswaramoorthy, Novel synthesis of carbon nanorings and their characterization. Chem. Phys. Lett. **433**, 327–330 (2007)
172. C. Pozrikidis, Structure of carbon nanorings. Comput. Mater. Sci. **43**, 943–950 (2008)
173. H. Ding, J.P. Maier, Electronic structures of one-dimension carbon nano wires and rings. J. Phys. Conf. Ser. **61**, 252–256 (2007)
174. S.G. dos Santos, J. Mendes Filho, V.N. Freire, E.W.S. Caetano, E.L. Albuquerque, Carbon-based nanorings sliding along inner coaxial nanotubes: Mobius topology effects in damping gigahertz oscillations. J. Appl. Phys. **116**, 124311, 5 pp (2014)
175. E.G. Fedorov, N.N. Yanyushkina, M.B. Belonenko, Terahertz radiation from carbon nanorings in external collinear constant and varying electric fields. Tech. Phys. **58**(4), 584–588 (2013)
176. G. Shi, J. Zhang, Y. He, S. Ju, D. Jiang, Thermal conductivity of carbon nanoring linked graphene sheets: a molecular dynamics investigation. Chin. Phys. B **26**(10), 106502, 6 pp (2017)
177. K. Yin Cheung, S. Yang, Q. Miao, From tetrabenzoheptafulvalene to sp^2 carbon nano-rings. Org. Chem. Front. **4**, 699–703 (2017)
178. B.M. Wong, Optoelectronic properties of carbon nanorings: excitonic effects from time-dependent density functional theory. J. Phys. Chem. C **113**, 21921–21927 (2009)
179. H. Omachi, Y. Segawa, K. Itami, Synthesis of cycloparaphenylenes and related carbon nanorings: a step toward the controlled synthesis of carbon nanotubes. Acc. Chem. Res. **45**(8), 1378–1389 (2012)
180. R. Franklin-Mergarejo, D. Ondarse Alvarez, S. Tretiak, S. Fernandez-Alberti, Carbon nanorings with inserted acenes: breaking symmetry in excited state dynamics. Sci. Rep. **6**, 31253, 11 pp (2016)
181. T. Kawase, M. Oda, Complexation of carbon nanorings with fullerenes. Pure Appl. Chem. **78**(4), 831–839 (2006)
182. K. Miki, T. Matsushita, Y. Inoue, et al., Electron-rich carbon nanorings as macrocyclic hosts for fullerenes. Chem. Commun. **49**, 9092–9094 (2013)
183. T. Kawase, K. Tanaka, Y. Seirai, N. Shiono, M. Oda, Complexation of carbon nanorings with fullerenes: supramolecular dynamics and structural tuning for a fullerene sensor. Angew. Chem. Int. Ed. **42**, 5597–5600 (2003)
184. N. Chen, M.T. Lusk, A.C.T. van Duin, W.A. Goddard III, Mechanical properties of connected carbon nanorings via molecular dynamics simulation. Phys. Rev. B **72**, 085416 (2005)
185. V. Alamian, A. Bahrami, B. Edalatzade, PI polynomial of V-phenylenic nanotubes and nanotori. Int. J. Mol. Sci. **9**, 229–234 (2008)
186. Y. Chel Kwun, M. Munir, W. Nazeer, S. Rafique, S. Min Kang, M-polynomials and topological indices of V-phenylenic nanotubes and nanotori. Sci. Rep. **7**, 8756, 9 pp (2016)
187. A.T. Balaban, D.J. Klein, Claromatic carbon nanostructures. J. Phys. Chem. C **113**, 19123–19133 (2009)
188. J. Liu, H. Dai, J.H. Hafner, D.T. Colbert, R.E. Smalley, S.J. Tans, C. Dekker, Fullerene ‘crop circles’. Nature **385**, 780–781 (1997)
189. T.A. Hilder, J.M. Hill, Orbiting atoms and C_{60} fullerenes inside carbon nanotori. J. Appl. Phys. **101**, 064319 (2007)
190. P.C. Chuang, J. Guan, D. Witalka, et al., Relative stability and local curvature analysis in carbon nanotori. Phys. Rev. B **91**, 165433 (2015)
191. B.J. Cox, J.M. Hill, New carbon molecules in the form of elbow-connected nanotori. J. Phys. Chem. C **111**, 10855–10860 (2007)
192. F. Koorepazan-Moftakhar, A. RezaAshrafi, O. Ori, M.V. Putz, Geometry and topology of nanotubes and nanotori, in *Exotic Properties of Carbon Nanomatter, Carbon Materials: Chemistry and Physics*, ed. by M. V. Putz, O. Ori (Eds), (Springer, Dordrecht, 2015), pp. 131–152
193. S. Madani, A.R. Ashrafi, The energies of (3,6)-fullerenes and nanotori. Appl. Math. Lett. **25**(12), 2365–2368 (2012)
194. C.P. Liu, J.W. Ding, Electronic structure of carbon nanotori: the roles of curvature, hybridization, and disorder. J. Phys. Condens. Matter **18**, 4077–4084 (2006)
195. C.P. Liu, Zeeman effect on the electronic structure of carbon nanotori in a strong magnetic field. Int. J. Mod. Phys. B **22**(27), 4845–4852 (2008)
196. Y.Y. Chou, G.-Y. Guo, Electrical conductance of carbon nanotori in contact with single-wall carbon nanotubes. J. Appl. Phys. **96**(4), 2249–2253 (2004)
197. J.A. Rodriguez-Manzo, F. Lopez-Urias, M. Terrones, H. Terrones, Magnetism in corrugated carbon nanotori: the importance of symmetry, defects, and negative curvature. Nano Lett. **4**(11), 2179–2183 (2004)
198. L. Liu, G.Y. Guo, C.S. Jayanthi, S.Y. Wu, Colossal paramagnetic moments in metallic carbon nanotori. Phys. Rev. Lett. **88**(12), 217206, 4 pp (2002)
199. E. Taşci, E. Yazgan, O.B. Malcıoğlu, Ş. Erkoç, Stability of carbon nanotori under heat treatment: molecular-dynamics simulations. Fullerenes, Nanotubes, Carbon Nanostruct. **13**, 147–154 (2005)
200. M. Tonigold, J. Hitzbleck, S. Bahnmueller, G. Langstein, D. Volkmer, Copper (II) Nanoballs as monomers for polyurethane coatings: synthesis, urethane derivatization and kinetic stability. Dalton Trans. (8), 1363–1371 (2009)
201. S.E. Iyuke, T.A. Mamvura, K. Liu, V. Sibanda, M. Meyyappan, V.K. Varadan, Process synthesis and optimization for the production of carbon nanostructures. Nanotechnology **20**(37), 375602/1–375602/10 (2009)
202. S. Lee, J. Hong, J.H. Koo, et al., Synthesis of few-layered graphene nanoballs with copper cores using solid carbon source. ACS Appl. Mater. Interfaces **5**(7), 2432–2437 (2013)
203. K.S. Chetna, A. Kapoor. Effect of annealing on structural and optical properties of graphene nanoballs. in: Recent Trends in Materials and Devices, ed by V. Jain, S. Rattan, A. Verma. Springer Proceedings in Physics (Springer, New York, 2017), vol. 178

204. N. Kumar, A. Shukla, J. Singh, M.K. Patra, P. Ghosal, S.R. Vadera, Simple route for synthesis of multilayer graphene nanoballs by flame combustion of edible oil. Graphene **1**(1), 63–67 (2013)
205. T. Das, B.K. Saikia, B.P. Baruah, Formation of carbon nano-balls and carbon nano-tubes from northeast Indian Tertiary coal: Value added products from low grade coal. Gondwana Res. **31**, 295–304 (2016)
206. Y. Xie, Q. Huang, B. Huang, X. Xie, Low temperature synthesis of high quality carbon nanospheres through the chemical reactions between calcium carbide and oxalic acid. Mater. Chem. Phys. **124**(1), 482–487 (2010)
207. D. Wei, Y. Zhang, J. Fu, Fabrication of carbon nanospheres by the pyrolysis of polyacrylonitrile–poly(methyl methacrylate) core–shell composite nanoparticles. Beilstein J. Nanotechnol. **8**, 1897–1908 (2017)
208. B. Liu, L. Jin, H. Zheng, H. Yao, Y. Wu, A. Lopes, J. He, Ultrafine co-based nanoparticle@mesoporous carbon nanospheres toward high-performance supercapacitors. ACS Appl. Mater. Interfaces **9**(2), 1746–1758 (2017)
209. F. Ghaemi, L. Chuah Abdullah, P. Tahir, Core/shell structure of Ni/NiO encapsulated in carbon nanosphere coated with few- and multi-layered graphene: synthesis, mechanism and application. Polymers **8**, 381 (2016)
210. Y. Hao, S. Wang, Q. Sun, L. Shi, A.-H. Lu, Uniformly dispersed Pd nanoparticles on nitrogen-doped carbon nanospheres for aerobic benzyl alcohol oxidation. Chin. J. Catal. **36**, 612–619 (2015)
211. Y. Yang, M. Qiu, L. Liu, D. Su, Y. Pi, G. Yan, Nitrogen-doped hollow carbon nanospheres derived from dopamine as high-performance anode materials for sodium-ion batteries. NANO: Brief Rep. Rev. **11**(11), 1650124, 9 pp (2016)
212. W. Armstrong, B. Sapkota, S.R. Mishra, Silver decorated carbon nanospheres as effective visible light photocatalyst, in *MRS Proceedings*, 2013, Volume 1509, mrsf12-1509-cc09-38
213. L.P. Bakos, N. Justh, K. Hernádi, et al., Core-shell carbon nanosphere-TiO_2 composite and hollow TiO_2 nanospheres prepared by atomic layer deposition. J. Phys. Conf. Ser. **764**, 012005 (2016)
214. W. Niu, L. Li, X. Liu, et al., One-pot synthesis of graphene/carbon nanospheres/graphene sandwich supported Pt_3Ni nanoparticles with enhanced electrocatalytic activity in methanol oxidation. Int. J. Hydrog. Energy **40**, 5106–5114 (2015)
215. P. Karna, M. Ghimire, S. Mishra, S. Karna, Synthesis and characterization of carbon nanospheres. Open Access Library Journal **4**, e3619 (2017)
216. A.N. Mohan, B. Manoj, Synthesis and characterization of carbon nanospheres from hydrocarbon soot. Int. J. Electrochem. Sci. **7**, 9537–9549 (2012)
217. M. Ibrahim Mohammed, R. Ismaeel Ibrahim, L. Hussein Mahmoud, M. Abdulahad Zablouk, N. Manweel, A. Mahmoud, Characteristics of carbon nanospheres prepared from locally deoiled asphalt. Adv. Mater. Sci. Eng. **2013**, 356769, 5 pp (2013)
218. H. Kristianto, C.D. Putra, A.A. Arie, M. Halim, J.K. Lee, Synthesis and characterization of carbon nanospheres using cooking palm oil as natural precursors onto activated carbon support. Procedia Chem. **16**, 328–333 (2015)
219. D. Guo, X. Chen, H. Wei, et al., Controllable synthesis of highly uniform flower-like hierarchical carbon nanospheres and their application in high performance lithium–sulfur batteries. J. Mater. Chem. A **5**, 6245–6256 (2017)
220. L. Zhang, P. Wang, W. Zheng, X. Jiang, Hollow carbon nanospheres for targeted delivery of chemotherapeutics in breast cancer therapy. J. Mater. Chem. B **5**, 6601–6607 (2017)
221. Y.-W. Jiang, G. Gao, X. Zhang, H.-R. Jia, F.-G. Wu, Antimicrobial carbon nanospheres. Nanoscale **9**, 15786–15795 (2017)
222. R. Vié, E. Drahi, O. Baudino, S. Blayac, S. Berthon-Fabry, Synthesis of carbon nanospheres for the development of inkjetprinted resistive layers and sensors. Flex. Print. Electron **1**, 015003 (2016)
223. H. Zhao, F. Zhang, S. Zhang, et al., Scalable synthesis of Sub-100 nm hollow carbon nanospheres for energy storage applications. Nano Res. **11** (4), 1822–1833 (2018)
224. J. Saini, M. Kumar, K. Anshu, S. Singh, S. Singh Kamal, G. Kaur, S.L. Harikumar, Future prospectives of nano onions: a review. Int. J. Curr. Med. Pharma. Res. **2**(3), 222–234 (2016)
225. J. Bartelmess, S. Giordani, Carbon nano-onions (multi-layer fullerenes): chemistry and applications. Beilstein J. Nanotechnol. **5**, 1980–1998 (2014)
226. A.N. Papathanassiou, M.E. Plonska-Brzezinska, O. Mykhailiv, L. Echegoyen, I. Sakellis, Combined high permittivity and high electrical conductivity of carbon nano-onion/polyaniline composites. Synth. Met. **209**, 583–587 (2015)
227. D.M. Bobrowska, K. Brzezinski, L. Echegoyen, M.E. Plonska-Brzezinska, A new perspective on carbon nano-onion/nickel hydroxide/oxide composites: Physicochemical properties and application in hybrid electrochemical systems. Fullerenes, Nanotubes, Carbon Nanostruct. **25**(3), 193–203 (2017)
228. J. Bartelmess, M. Frasconi, P.B. Balakrishnan, A. Signorellia, L. Echegoyen, T. Pellegrino, S. Giordani, Non-covalent functionalization of carbon nano-onions with pyrene-BODIPY dyads for biological imaging. RSC Adv. **5**, 50253–50258 (2015)
229. D.M. Bobrowska, J. Czyrko, K. Brzezinski, L. Echegoyen, M.E. Plonska-Brzezinska, Carbon nano-onion composites: physicochemical characteristics and biological activity. Fullerenes, Nanotubes, Carbon Nanostruct. **25**(3), 185–192 (2017)
230. M.E. Plonska-Brzezinska, A. Molina-Ontori, L. Echegoyen, Post-modification by low-temperature annealing of carbon nano-onions in the presence of carbohydrates. Carbon **67**, 304–317 (2014)
231. L. Zhou, C. Gao, D. Zhu, et al., Facile functionalization of multilayer fullerenes (carbon nano-onions) by nitrene chemistry and “grafting from” strategy. Chem. Eur. J. **15**, 1389–1396 (2009)
232. S. Giordani, J. Bartelmess, M. Frasconi, I. Biondi, S. Cheung, M. Grossi, D. Wu, L. Echegoyen, D.F. O'Shea, NIR fluorescence labelled carbon nano-onions: synthesis, analysis and cellular imaging. J. Mater. Chem. B **2**, 7459–7463 (2014)
233. C.T. Cioffi, A. Palkar, F. Melin, et al., Carbon nano-onion–ferrocene donor–acceptor system:synthesis, characterization and properties. Chem. Eur. J. **15**, 4419–4427 (2009)
234. D. Pech, M. Brunet, H. Durou, P. Huang, V. Mochalin, Y. Gogotsi, P.-L. Taberna, P. Simon, Ultrahigh-power micrometre-sized supercapacitors based on onion-like carbon. Nat. Nanotechnol. **5**, 651–654 (2010)
235. J.K. McDonough, A.I. Frolov, V. Presser, J. Niu, C.H. Miller, T. Ubieto, M.V. Federov, Y. Gogotsi, Influence of the structure of carbon onions on their electrochemical performance in supercapacitor electrodes. Carbon **50**(9), 3298–3309 (2012)
236. J.K. McDonough, Y. Gogotsi, Carbon onions: synthesis and electrochemical applications. Electrochem. Soc. Interface **22**(3), 61–66 (2013)

237. P. Bystrzejewski, M.H. Rummeli, T. Gemming, H. Lange, A. Huczco, Catalyst-free synthesis of onion-like carbon nanoparticles. New Carbon Mater. **25**(1), 1–8 (2010)
238. Y. Zheng, P. Zhu, Carbon nano-onions: large-scale preparation, functionalization and their application as anode material for rechargeable lithium ion batteries. RSC Adv. **6**, 92285–92298 (2016)
239. T. Garcia-Martin, P. Rincon-Arevalo, G. Campos-Martin, Method to obtain carbon nano-onions by pyrolisys of propane. Cent. Eur. J. Phys. **11**(11), 1548–1558 (2013)
240. W.-k. Zhang, J.-j. Fu, J. Chang, M. Zhang, Y.-q. Yang, L.-z. Gao, Fabrication and purification of carbon nano onions. New Carbon Mater. **29**(5), 398–403 (2014)
241. F.-D. Han, B. Yao, Y.-J. Bai, Preparation of carbon nano-onions and their application as anode materials for rechargeable lithium-ion batteries. J. Phys. Chem. C **115**, 8923–8927 (2011)
242. C. Zhang, J. Li, C. Shi, C. He, E. Liu, N. Zhao, Self-anchored catalysts for substrate-free synthesis of metal-encapsulated carbon nano-onions and study of their magnetic properties. Nano Res. **9**(4), 1159–1172 (2016)
243. N. Sano, H. Wang, I. Alexandrou, M. Chhowalla, K.B.K. Teo, G.A.J. Amaratunga, Properties of carbon onions produced by an arc discharge in water. J. Appl. Phys. **92**(5), 2783–2788 (2002)
244. O.V. Kharissova, H.V.R. Dias, B.I. Kharisov, J. Jiang, Preparation of carbon nano-onions by the low-temperature unfolding of MWCNTs via interaction with theraphthal. RSC Adv. **5**, 57764–57770 (2015)
245. O.L. Kaliya, E.A. Luk'yanets, On the article about the component composition of Theraphthal preparation. Pharm. Chem. J. **43**(10), 587–587 (2009)
246. M.S. Goizman, E.V. Degterev, K.F. Turchin, A.P. Arzamastsev, Quality control of theraphthal production. 1. Chemical composition. Pharm. Chem. J. **41**(12), 670–675 (2007)
247. Patent of Russian Federation 2106146 (1995)
248. M.E. Volpin, Agent for suppressing tumor growth, U.S. Patent 6,004,953, 1999
249. Patent of Japan 3672928, 2005
250. Canada application for a patent 2200220, 1996
251. Antitumor composition comprising ascorbic acid and metal complexes of (na)phthalocyanines. EP 0786253 (1997)
252. A.L. Nikolaev, A.V. Gopin, V.E. Bozhevolnov, S.E. Mazina, A.V. Severin, V.N. Rudin, N.V. Andronova, E.M. Treschalina, O.L. Kaliya, L.I. Solovyeva, E.A. Lukyanets, Sonodynamic therapy of cancer. A comprehensive experimental study. Russ. Chem. Bull. **63**(5), 1 (2014)
253. O.V. Kharissova, J. Rodríguez, B.I. Kharisov, Non-standard ROS-generating combination "theraphthal–ascorbic acid" in low-temperature transformations of carbon allotropes. Chem. Pap. (2018). https://doi.org/10.1007/s11696-018-0571-y
254. Y. Yao, X. Wang, J. Guo, X. Yang, B. Xu, Tribological property of onion-like fullerenes as lubricant additive. Mater. Lett. **62**(16), 2524–2527 (2008)
255. S. Erkoc, Stability of carbon nanoonion $C_{20}@C_{60}@C_{240}$: molecular dynamics simulations. Nano Lett. **2**(3), 215–217 (2002)
256. M.E. Plonska-Brzezinska, A. Lapinski, A.Z. Wilczewska, et al., The synthesis and characterization of carbon nano-onions produced by solution ozonolysis. Carbon **49**(15), 5079–5089 (2011)
257. Y. Gao, Y. Shen Zhou, M. Qian, et al., Chemical activation of carbon nano-onions for high-rate supercapacitor electrodes. Carbon **51**, 52–58 (2013)
258. Y.A. Goh, X. Chen, F. Md Yasin, et al., Shear flow assisted decoration of carbon nano-onions with platinum nanoparticles. Chem. Commun. **49**, 5171–5173 (2013)
259. O. Mykhailiv, K. Brzezinski, B. Sulikowski, et al., Boron-doped polygonal carbon nano-onions: synthesis and applications in electrochemical energy storage. Chem. Eur. J. **23**, 7132–7141 (2017)
260. E.Y. Choi, C.K. Kim, Fabrication of nitrogendoped nano-onions and their electrocatalytic activity toward the oxygen reduction reaction. Sci. Rep. **7**, 4178 (2017)
261. Y. Liu, R.L.V. Wal, V.N. Khabashesku, Functionalization of carbon nano-onions by direct fluorination. Chem. Mater. **19**, 778–786 (2007)
262. J. Luszczyn, M.E. Plonska-Brzezinska, A. Palkar, A.T. Dubis, A. Simionescu, D.T. Simionescu, B. Kalska-Szostko, K. Winkler, L. Echegoyen, "Small" noncytotoxic carbon nano-onions: first covalent functionalization with biomolecules. Chem. Eur. J. **16**, 4870–4880 (2010)
263. A.M. Panich, V.Y. Osipov, K. Takai, Diamagnetism of carbon onions probed by NMR of adsorbed water. Carbon **82**, 608–610 (2015)
264. A.M. Panich, V.Y. Osipov, K. Takai, Diamagnetism of carbon onions probed by NMR of adsorbed water. New Carbon Mater. **29**(5), 392–397 (2014)
265. H.G. Baldoví, J.R. Herance, V.M. Víctor, M. Alvaro, H. Garcia, Perylenetetracarboxylic anhydride as a precursor of fluorescent carbon nanoonion rings. Nanoscale **7**, 12484–12491 (2015)
266. G. Moussa, C. Matei Ghimbeu, P.-L. Taberna, P. Simon, C. Vix-Guterl, Relationship between the carbon nano-onions (CNOs) surface chemistry/defects and their capacitance in aqueous and organic electrolytes. Carbon **105**, 628–637 (2016)
267. E.W. Bucholz, S.R. Phillpot, S.B. Sinnott, Molecular dynamics investigation of the lubrication mechanism of carbon nano-onions. Comput. Mater. Sci. **54**, 91–96 (2012)
268. V. Marchesano, A. Ambrosone, J. Bartelmess, F. Strisciante, A. Tino, L. Echegoyen, C. Tortiglione, S. Giordani, Impact of carbon nano-onions on hydra vulgaris as a model organism for nanoecotoxicology. Nano **5**, 1331–1350 (2015)
269. M. Frasconi, V. Maffeis, J. Bartelmess, L. Echegoyen, S. Giordani, Highly surface functionalized carbon nano-onions for bright light bioimaging. Methods Appl. Fluoresc. **3**, 044005 (2015)
270. A. Camisasca, S. Giordani, Carbon nano-onions in biomedical applications: promising theranostic agents. Inorg. Chim. Acta **468**, 67 (2017)
271. M.-S. Wang, D. Golberg, Y. Bando, Carbon "onions" as point electron sources. ACS Nano **4**(8), 4396–4402 (2010)
272. A. Pramanik, S. Biswas, A.K. Kole, C.S. Tiwary, R.N. Krishnarajd, P. Kumbhakar, Template-free hydrothermal synthesis of amphibious fluorescent carbon nanorice towards anti-counterfeiting applications and unleashing its nonlinear optical properties. RSC Adv. **6**, 99060–99071 (2016)

273. P.S. Parasuraman, H.-C. Tsai, T. Imae, In-situ hydrothermal synthesis of carbon nanorice using Nafion as a template. Carbon **77**, 660–666 (2014)
274. Q. Wu, L. Yang, X. Wang, Z. Hu, From carbon-based nanotubes to nanocages for advanced energy conversion and storage. Acc. Chem. Res. **50**(2), 435–444 (2017)
275. K. Matsui, Y. Segawa, K. Itami, All-benzene carbon nanocages: size-selective synthesis, photophysical properties, and crystal structure. J. Am. Chem. Soc. **136**(46), 16452–16458 (2014)
276. Y. Li, C. Zhou, X. Xie, G. Shi, L. Qu, Spontaneous, catalyst-free formation of nitrogen-doped graphitic carbon nanocages. Carbon **48**(14), 4190–4196 (2010)
277. Y. Tan, C. Xu, G. Chen, et al., Synthesis of ultrathin nitrogen-doped graphitic carbon nanocages as advanced electrode materials for supercapacitor. ACS Appl. Mater. Interfaces **5**(6), 2241–2248 (2013)
278. C.-K. Tsai, H.Y. Kang, C.-I. Hong, et al., Preparation of hollow spherical carbon nanocages. J. Nanopart. Res. **14**, 1315 (2012)
279. R. Zhang, M. Hummelgard, H. Olin, Carbon nanocages grown by gold templating. Carbon **48**, 424–430 (2010)
280. S. Xiang, Y. Shi, K. Zhang, et al., Design and synthesis of dodecahedral carbon nanocages incorporated with Fe_3O_4. RSC Adv. **7**, 13257–13262 (2017)
281. E. Petala, Y. Georgiou, V. Kostas, et al., Magnetic carbon nanocages: an advanced architecture with surface- and morphology-enhanced removal capacity for arsenites. ACS Sustain. Chem. Eng. **5**(7), 5782–5792 (2017)
282. H. Qin, Y. Huang, S. Liu, et al., Synthesis and properties of magnetic carbon nanocages particles for dye removal. J. Nanomater. **2015**, 604201, 8 pp (2015)
283. J.T. Li, A mild method prepared carboxy carbon nanocage. Adv. Mater. Res. **560–561**, 742–746 (2012)
284. S. Liu, Z. Wang, S. Zhou, et al., Metal–organic-framework-derived hybrid carbon nanocages as a bifunctional electrocatalyst for oxygen reduction and evolution. Adv. Mater. **29**(31), 1700874 (2017)
285. Y. Jiang, L. Yang, T. Sun, et al., Significant contribution of intrinsic carbon defects to oxygen reduction activity. ACS Catal. **5**, 6707–6712 (2015)
286. Z. Lyu, L. Yang, D. Xu, et al., Hierarchical carbon nanocages as high-rate anodes for Li-and Na-ion batteries. Nano Res **8**(11), 3535–3543 (2015)
287. M.J. Armstrong, D.M. Burke, et al., Carbon nanocage supported synthesis of V_2O_5 nanorods and V_2O_5/TiO_2 nanocomposites for Li-ion batteries. J. Mater. Chem. A **1**, 12568–12578 (2013)
288. A. Vinu, M. Miyahara, T. Mori, K. Ariga, Carbon nanocage: a large-pore cage-type mesoporous carbon material as an adsorbent for biomolecules. J. Porous. Mater. **13**(3–4), 379–383 (2006)
289. K.K.R. Datta, A. Vinu, S. Mandal, et al., Carbon nanocage: super-adsorber of intercalators for DNA protection. J. Nanosci. Nanotechnol. **11**(4), 3084–3090 (2011)
290. C.X. Guo, Z.M. Sheng, Y.Q. Shen, Z.L. Dong, C.M. Li, Thin-walled graphitic nanocages as a unique platform for amperometric glucose biosensor. ACS Appl. Mater. Interfaces **2**(9), 2481–2484 (2010)
291. M. Hui Yap, K. Loon Fow, G. Zheng Chen, Synthesis and applications of MOF-derived porous nanostructures. Green Energy Environ **2**, 218–245 (2017)
292. H. Zhang, X. Zhang, X. Sun, Y. Ma, Shape-controlled synthesis of nanocarbons through direct conversion of carbon dioxide. Sci. Rep. **3**, 3534 (2013)
293. L. Cao, Z.-h. Li, Y. Gu, Rational design of N-doped carbon nanobox-supported $Fe/Fe_2N/Fe_3C$ nanoparticles as efficient oxygen reduction catalysts for Zn–air batteries. J. Mater. Chem. A **5**, 11340–11347 (2017)
294. J. Xiang, T. Song, One-pot synthesis of multicomponent (Mo, Co) metal sulfide/carbon nanoboxes as anode materials for improving Na-ion storage. Chem. Commun. **53**, 10820–10823 (2017)
295. H. Hu, J. Zhang, B. Guan, X.W. (David) Lou, Unusual formation of CoSe@carbon nanoboxes, which have an inhomogeneous shell, for efficient lithium storage. Angew. Chem. **55**(33), 9514–9518 (2016)
296. M. Zheng, Y. Liu, S. Zhao, W. He, Y. Xiao, D. Yuan, Simple shape-controlled synthesis of carbon hollow structures. Inorg. Chem. **49**(19), 8674–8683 (2010)
297. B. Quan, G.-E. Nam, H. Jae Choi, Y. Piao, Synthesis of monodisperse hollow carbon nanocapsules by using protective silica shells. Chem. Asian J. **8**(4), 765–770 (2013)
298. U. Narkiewicz, M. Podsiadly, R. Jedrzejewski, I. Pelech, Catalytic decomposition of hydrocarbons on cobalt, nickel and iron catalysts to obtain carbon nanomaterials. Appl. Catal. A Gen. **384**(1–2), 27–35 (2010)
299. X.G. Liu, Z.Q. Ou, D.Y. Geng, Z. Han, H. Wang, B. Li, E. Brueck, Z.D. Zhang, Enhanced absorption bandwidth in carbon-coated supermalloy FeNiMo nanocapsules for a thin absorb thickness. J. Alloys Compd. **506**(2), 826–830 (2010)
300. H. Kuratani, Y. Fujiwara, K. Maeda, T. Kobayashi, M. Jimbo, Synthesis of carbon nanocapsules containing Fe produced by discharge in ethanol. J. Magn. Soc. Jpn. **37**(3–2), 206–209 (2013)
301. Y. Liu, J. Su, Synthesis and characterization of MgO-filled rectangular carbon nanocapsules. Adv. Mater. Res. **785-786**, 444–448 (2013)
302. P. Wu, N. Du, H. Zhang, J. Yu, D. Yang, Carbon nanocapsules as nanoreactors for controllable synthesis of encapsulated iron and iron oxides: magnetic properties and reversible lithium storage. J. Phys. Chem. C **115**, 3612–3620 (2011)
303. S. Kim, R. Sergiienko, E. Shibata, T. Nakamura, Iron-included carbon nanocapsules coated with biocompatible poly(ethylene glycol) shells. Mater. Chem. Phys. **122**, 164–168 (2010)
304. T. Kizuka, K. Miyazawa, D. Matsuura, Synthesis of carbon nanocapsules and nanotubes using Fe-doped fullerene nanowhiskers. J. Nanotechnol. **613746**, 6 (2012)
305. D. Han, G. Song, B. Liu, H. Yan, Core–shell-structured nickel ferrite/onion-like carbon nanocapsules: an anode material with enhanced electrochemical performance for lithium-ion batteries. RSC Adv. **5**, 42875–42880 (2015)
306. Y. Suna, C. Feng, X. Liu, S. Wing Orc, C. Jin, Synthesis, characterization and microwave absorption of carbon-coated Cu nanocapsules. Mater. Res. **17**(2), 477–482 (2014)

307. E. Hu, J. Ning, B. He, et al., Unusual formation of tetragonal microstructures from nitrogen-doped carbon nanocapsules with cobalt nanocores as a bi-functional oxygen electrocatalyst. J. Mater. Chem. A **5**, 2271–2279 (2017)
308. H. Wang, C. Chen, Y. Zhang, et al., *In situ* oxidation of carbon-encapsulated cobalt nanocapsules creates highly active cobalt oxide catalysts for hydrocarbon combustion. Nat. Commun. **6**, 7181 (2015)
309. A.C.L. Tang, G.-L. Hwang, S.-J. Tsai, et al., Biosafety of non-surface modified carbon nanocapsules as a potential alternative to carbon nanotubes for drug delivery purposes. PLoS One **7**(3), e32893 (2012)
310. Y.-F. Lan, S.-C. Cheng, Dispersion of carbon nanocapsules by using highly aspect-ratio clays. Appl. Phys. Lett. **100**, 153109 (2012)
311. O.V. Kharissova, B.I. Kharisov, *Solubilization and Dispersion of Carbon Nanotubes* (Springer-Nature, New York, 2017), 250 pp
312. Y. Hayashi, N. Takada, W. Diono, H. Kanda, M. Goto, One-step synthesis of water–dispersible carbon nanocapsules by pulsed arc discharge over aqueous solution under pressurized argon. Res. Chem. Intermed. **43**, 4201–4211 (2017)
313. A. Guven, I.A. Rusakova, M.T. Lewis, L.J. Wilson, Cisplatin@US-tube carbon nanocapsules for enhanced chemotherapeutic delivery. Biomaterials **33**(5), 1455–1461 (2012)
314. H. Ge, P.J. Riss, V. Mirabello, et al., Behavior of supramolecular assemblies of radiometal-filled and fluorescent carbon nanocapsules in vitro and in vivo. Chem **3**, 437–460 (2017)
315. N. Mittal, R. Kumar, G. Mishra, D. Deva, A. Sharma, Mesoporous carbon nanocapsules based coatings with multifunctionalities. Adv. Mater. Interfaces **3**(10), 1500708 (2016)
316. H.-S. Chien, C. Wang, Effects of temperature and carbon nanocapsules (CNCs) on the production of Poly(D,L-lactic acid) (PLA) nonwoven nanofibre mat. Fibres Text. East. Eur **97**(1), 72–77 (2013)
317. P. Gentile, T. David, F. Dhalluin, D. Buttard, N. Pauc, M. Den Hertog, P. Ferret, T. Baron, The growth of small diameter silicon nanowires to nanotrees. Nanotechnology **19**(12), 125608/1–125608/5 (2008)
318. http://www.ifn.upr.edu/people/17-luis-fonseca
319. F. Sola, O. Resto, A. Biaggi-Labiosa, L.F. Fonseca, Growth and characterization of branched carbon nanostructures arrays in nano-patterned surfaces from porous silicon substrates. Micron **40**, 80–84 (2009)
320. Z. Yao, X. Zhu, X. Li, Y. Xie, Synthesis of novel Y-junction hollow carbon nanotrees. Carbon **45**(7), 1566–1570 (2007)
321. G. Liu, Y. Zhao, K. Zheng, Z. Liu, W. Ma, Y. Ren, S. Xie, L. Sun, Coulomb explosion: a novel approach to separate single-walled carbon nanotubes from their bundle. Nano Lett. **9**(1), 239–244 (2009)
322. M. Haba, Fuel cell using carbon-metal nanotree electrocatalyst. 2006, JP 2006294493 (11 pp)
323. Z. He, J.-L. Maurice, C. Seok Lee, C.S. Cojocaru, D. Pribat, Growth mechanisms of carbon nanostructures with branched carbon nanofibers synthesized by plasma-enhanced chemical vapour deposition. CrystEngComm **16**, 2990–2995 (2014)
324. F. Sola, O. Resto, A.M. Biaggi-Labiosa, L.F. Fonseca, Electron-beam induced growth of silica nanowires and silica/carbon heterostructures. Mater. Res. Soc. Symp. Proc. (2007), 1017E (Low-Dimensional Materials--Synthesis, Assembly, Property Scaling, and Modeling), Paper #: 1017-DD12-31
325. F. Sola, O. Resto, A. Biaggi-Labiosa, L.F. Fonseca, Electron-beam induced growth of silica nanorods and heterostructures in porous silicon. Nanotechnology **18**, 405308 (2007)
326. L. Chen, C. Xu, R. Du, et al., Rational design of three-dimensional nitrogendoped carbon nanoleaf networks for highperformance oxygen reduction. J. Mater. Chem. A **3**, 5617–5627 (2015)
327. T.-N. Ye, L.-B. Lv, X.-H. Li, M. Xu, J.-S. Chen, Strongly veined carbon nanoleaves as a highly efficient metal-free electrocatalyst. Angew. Chem. **126**, 7025–7029 (2014)
328. X. Ma, B. Yuan, Fabrication of carbon nanoflowers by plasma-enhanced chemical vapor deposition. Appl. Surf. Sci. **255**(18), 7846–7850 (2009)
329. H. Butt, R. Rajesekharan, Q. Dai, S. Sarfraz, R.V. Kumar, G.A.J. Amaratunga, T.D. Wilkinson, Cylindrical Fresnel lenses based on carbon nanotube forests. Appl. Phys. Lett. **101**(24), 243116 (2012)
330. T. Saleh, M. Vahdani Moghaddam, M. Sultan Mohamed Ali, M. Dahmardeh, C. Alden Foell, A. Nojeh, K. Takahata, Transforming carbon nanotube forest from darkest absorber to reflective mirror. Appl. Phys. Lett. **101**, 061913 (2012)
331. H. Chen, A. Roy, J.-B. Baek, L. Zhu, J. Qu, L. Dai, Controlled growth and modification of vertically-aligned carbon nanotubes for multifunctional applications. Mater. Sci. Eng. R. Rep. **70**, 63–91 (2010)
332. N. Hayashi, S.-I. Honda, K. Tsui, K.-Y. Lee, T. Ikuno, K. Fujimoto, S. Ohkura, M. Katayama, K. Oura, T. Hirao, Highly aligned carbon nanotube arrays fabricated by bias sputtering. Appl. Surf. Sci. **212–213**, 393–396 (2003)
333. C. Daraio, V.F. Nesterenko, S. Jin, Impact response by a foamlike forest of coiled carbon nanotubes. J. Appl. Phys. **100**, 064309, 4 pp (2006)
334. Y. Taki, M. Kikuchi, K. Shinohara, A. Tanaka, Selective growth of vertically aligned single-, double-, and triple-walled carbon nanotubes by radiation-heated chemical vapor deposition. Jpn. J. Appl. Phys. **47**, 721–724 (2008)
335. A.M. Cassell, M. Meyyappan, J. Han, Multilayer film assembly of carbon nanotubes. J. Nanopart. Res. **2**(4), 387–389 (2000)
336. Q. Zhang, W. Zhou, W. Qian, R. Xiang, J. Huang, D. Wang, F. Wei, Synchronous growth of vertically aligned carbon nanotubes with pristine stress in the heterogeneous catalysis process. J. Phys. Chem. C **111**, 14638–14643 (2007)
337. X. Li, A. Cao, Y.J. Jung, R. Vajtai, P.M. Ajayan, Bottom-up growth of carbon nanotube multilayers: unprecedented growth. Nano Lett. **5**, 1997–2000 (2005)
338. S. Huang, L. Dai, A.W.H. Mau, Nanotube “crop circles”. J. Mater. Chem. **9**, 1221–1222 (1999)
339. C.K. Tan, K.P. Loh, T.T.L. John, Direct amperometric detection of glucose on a multiple-branching carbon nanotube forest. Analyst **133**, 448–451 (2008)
340. S. Li, H. Li, X. Wang, Y. Song, Y. Liu, L. Jiang, D. Zhu, Super-hydrophobicity of large-area honeycomb-like aligned carbon nanotubes. J. Phys. Chem. B **106**(36), 9274–9276 (2002)
341. M.R. Maschmann, Integrated simulation of active carbon nanotube forest growth and mechanical compression. Carbon **86**, 26–37 (2015)
342. E.G. Rakov, Materials made of carbon nanotubes. The carbon nanotube forest. Russ. Chem. Rev. **82**(6), 538–566 (2013)
343. M. Pinault, V. Pichot, H. Khodja, P. Launois, C. Reynaud, M. Mayne-L'Hermite, Evidence of sequential lift in growth of aligned multiwalled carbon nanotube multilayers. Nano Lett. **5**(12), 2394–2398 (2005)

344. R. Xiang, G. Luo, Z. Yang, Q. Zhang, W. Qian, F. Wei, Temperature effect on the substrate selectivity of carbon nanotube growth in floating chemical vapor deposition. Nanotechnology **18**(41), 415703 (2007)
345. Z. Yang, H. Nie, X. Zhou, Z. Yao, S. Huang, X. Chen, Synthesizing a well-aligned carbon nanotube forest with high quality via the nebulized spray pyrolysis method by optimizing ultrasonic frequency. Nano **6**, 343–348 (2011)
346. C. Du, N. Pan, High power density supercapacitor electrodes of carbon nanotube films by electrophoretic deposition. Nanotechnology **17**(21), 5314–5318 (2006)
347. S. Shekhar, P. Stokes, S. Khondaker, Ultrahigh density alignment of carbon nanotube arrays by dielectrophoresis. ACS Nano **5**(3), 1739–1746 (2011)
348. P. Diao, Z. Li, Vertically aligned single-walled carbon nanotubes by chemical assembly – methodology, properties, and applications. Adv. Mater. **22**, 1430–1449 (2010)
349. C. Soldano, S. Talapatra, S. Kar, Carbon nanotubes and graphene nanoribbons: potentials for nanoscale electrical interconnects. Electronics **2**, 280–314 (2013)
350. J. Prasek, J. Drbohlavova, J. Chomoucka, J. Hubalek, O. Jasek, V. Adam, R. Kizek, Methods for carbon nanotubes synthesis—review. J. Mater. Chem. **21**, 15872–15884 (2011)
351. E.R. Meshot, D.L. Plata, S. Tawfick, Y. Zhang, E.A. Verploegen, A.J. Hart, Engineering vertically aligned carbon nanotube growth by decoupled thermal treatment of precursor and catalyst. ACS Nano **3**(9), 2477–2486 (2009)
352. K. Hasegawa, S. Noda, H. Sugime, K. Kakehi, S. Maruyama, Y. Yamaguchi, Growth window and possible mechanism of millimeter-thick single-walled carbon nanotube forests. J. Nanosci. Nanotechnol. **8**(11), 6123–6128 (2008)
353. J. Olivares, T. Mirea, B. Díaz-Durán, M. Clement, M. De Miguel-Ramos, J. Sangrador, J. De Frutos, E. Iborra, Growth of carbon nanotube forests on metallic thin films. Carbon **90**, 9–15 (2015)
354. H. Sugime, S. Esconjauregui, L. D'Arsié, J. Yang, A.W. Robertson, R.A. Oliver, S. Bhardwaj, C. Cepek, J. Robertson, Low-temperature growth of carbon nanotube forests consisting of tubes with narrow inner spacing using Co/Al/Mo catalyst on conductive supports. ACS Appl. Mater. Interfaces **7**(30), 16819–16827 (2015)
355. T. Ohashi, T. Shima, Synthesis of vertically aligned single-walled carbon nanotubes with metallic chirality through facet control of catalysts. Carbon **87**(1), 453–461 (2016)
356. S. Esconjauregui, M. Fouquet, B.C. Bayer, S. Eslava, S. Khachadorian, S. Hofmann, J. Robertson, Manipulation of the catalyst-support interactions for inducing nanotube forest growth. J. Appl. Phys. **109**, 044303 (2011)
357. C.T. Wirth, C. Zhang, G. Zhong, S. Hofmann, J. Robertson, Diffusion- and reaction-limited growth of carbon nanotube forests. ACS Nano **3** (11), 3560–3566 (2009)
358. M. Bedewy, E.R. Meshot, H. Guo, E.A. Verploegen, W. Lu, A.J. Hart, Collective mechanism for the evolution and self-termination of vertically aligned carbon nanotube growth. J. Phys. Chem. C **113**(48), 20576–20582 (2009)
359. R. Siddheswaran, D. Manikandan, R.E. Avila, C.E. Jeyanthi, R.V. Mangalaraja, Formation of carbon nanotube forest over spin-coated Fe2O 3 reduced thin-film by chemical vapor deposition. Fullerenes Nanotubes Carbon Nanostruct. **23**(5), 392–398 (2015)
360. J. Yang, S. Esconjauregui, A.W. Robertson, Y. Guo, T. Hallam, H. Sugime, G. Zhong, G.S. Duesberg, J. Robertson, Growth of high-density carbon nanotube forests on conductive TiSiN supports. Appl. Phys. Lett. **106**(8), 083108 (2015)
361. M. Mohsin Hossain, H. Shima, B.-C. Ku, J. Ryang Hahn, Nanoforests composed of ZnO/C core–shell hexagonal nanosheets: fabrication and growth in a sealed thermolysis reactor and optical properties. J. Mater. Sci. **50**, 93–103 (2015)
362. N. Matsumoto, A. Oshima, S. Sakurai, T. Yamada, M. Yumura, K. Hata, D.N. Futaba, The application of gas dwell time control for rapid single wall carbon nanotube forest synthesis to acetylene feedstock. Nano **5**, 1200–1210 (2015)
363. J. Huang, Q. Zhang, M. Zhao, F. Wei, Process intensification by CO_2 for high quality carbon nanotube forest growth: double-walled carbon nanotube convexity or single-walled carbon nanotube bowls? Nano Res. **2**, 872–881 (2009)
364. M. Zhang, O. O. I. Okoli, H. Hoang Van, Graphene nanoribbons and methods. US Patent 2015/0013896 A1, 2015
365. S. Santhanagopalan, A. Balram, E. Lucas, F. Marcano, D. Desheng Meng, High voltage electrophoretic deposition of aligned nanoforests for scalable nanomanufacturing of electrochemical energy storage devices. Key Eng. Mater. **507**, 67–72 (2012)
366. D.S. Jensen, S.S. Kanyal, N. Madaan, M.A. Vail, A.E. Dadson, M.H. Engelhard, M.R. Linford, Multiwalled carbon nanotube forest grown via chemical vapor deposition from iron catalyst nanoparticles, by XPS. Surf. Sci. Spectra **20**, 62–67 (2013)
367. G. Chen, Y. Seki, H. Kimura, S. Sakurai, M. Yumura, K. Hata, D.N. Futaba, Diameter control of single-walled carbon nanotube forests from 1.3–3.0 nm by arc plasma deposition. Sci. Rep. **4**, 3804 (2014)
368. M. Vahdani Moghaddam, P. Yaghoobi, G.A. Sawatzky, A. Nojeh, Photon-impenetrable, electron-permeable: the carbon nanotube forest as a medium for multiphoton thermal-photoemission. ACS Nano **9**(4), 4064–4069 (2015)
369. N.J. Ginga, W. Chen, S.K. Sitaraman, Waviness reduces effective modulus of carbon nanotube forests by several orders of magnitude. Carbon **66**, 57–66 (2014)
370. J.-W. Jiang, Strain engineering for thermal conductivity of single-walled carbon nanotube forests, Cornell University Library, arXiv:1406.4559
371. P. Pour Shahid Saeed Abadi, S.B. Hutchens, J.R. Greer, B.A. Cola, S. Graham, Buckling-driven delamination of carbon nanotube forests. Appl. Phys. Lett. **102**, 223103 (2013)
372. G. Chen, D.N. Futaba, H. Kimura, S. Sakurai, M. Yumura, K. Hata, Absence of an ideal single-walled carbon nanotube forest structure for thermal and electrical conductivities. ACS Nano **7**(11), 10218–10224 (2013)
373. P. Joseph, C. Cottin-Bizonne, J.-M. Benoıt, C. Ybert, C. Journet, P. Tabeling, L. Bocquet, Slippage of water past superhydrophobic carbon nanotube forests in microchannels. Phys. Rev. Lett. **97**, 156104 (2006)
374. K.K.S. Lau, J. Bico, K.B.K. Teo, M. Chhowalla, G.A.J. Amaratunga, W.I. Milne, G.H. McKinley, K.K. Gleason, Superhydrophobic carbon nanotube forests. Nano Lett. **3**(12), 1701–1705 (2003)
375. R. Kant, M. Birla Singh, Generalization of the Gouy-Chapman-Stern model of an electric double layer for a morphologically complex electrode: deterministic and stochastic morphologies. Phys. Rev. E **88**, 052303 (2013)
376. A. Ozhan Altun, S. Ki Youn, N. Yazdani, T. Bond, H.G. Park, Metal-dielectric-CNT nanowires for femtomolar chemical detection by surface enhanced Raman spectroscopy. Adv. Mater. **25**(32), 4377–4377 (2013)

377. S. Deng, M. Kurttepeli, D.J. Cott, S. Bals, C. Detavernier, Porous nanostructured metal oxides synthesized through atomic layer deposition on a carbonaceous template followed by calcination. J. Mater. Chem. A **3**(6), 2642–2649 (2015)
378. M.P. Down, A.P. Lewis, L. Jiang, J.W. McBride, A nano-indentation study of the contact resistance and resistivity of a bi-layered Au/multi-walled carbon nanotube composite. Appl. Phys. Lett. **106**(10), 101911 (2015)
379. Y. Yoon, G.S. Lee, K. Yoo, J.-B. Lee, Fabrication of a microneedle/CNT hierarchical micro/nano surface electrochemical sensor and its in-vitro glucose sensing characterization. Sensors **13**, 16672–16681 (2013)
380. E. Gikunoo, A. Abera, E. Woldesenbet, A novel carbon nanofibers grown on glass microballoons immunosensor: a tool for early diagnosis of malaria. Sensors **14**, 14686–14699 (2014)
381. P. Sui, D. Duckworth, G. Weaver, Joints comprising carbon nanoforests. US Patent 2015/0204444 A1, 2015
382. J.H. Taphouse, T.L. Bougher, V. Singh, P.P.S.S. Abadi, S. Graham, B.A. Cola, G.W. Woodruff, Carbon nanotube thermal interfaces enhanced with sprayed on nanoscale polymer coatings. Nanotechnology **24**(10), 105401 (2013)
383. D. Luo, L. Wu, J. Zhi, Fabrication of boron-doped diamond nanorod forest electrodes and their application in nonenzymatic amperometric glucose biosensing. ACS Nano **3**(8), 2121–2128 (2009)
384. D.G. Lee, S.J. Park, Y.O. Park, E.I. Ryu, Synthesis of nanostructures by direct growth of carbon nanotubes on micron-sized metal fiber filter and its filtration performance. Hwahak Konghak **45**(3), 264–268 (2007)
385. S.J. Park, D.G. Lee, Performance improvement of micron-sized fibrous metal filters by direct growth of carbon nanotubes. Carbon **44**(10), 1930–1935 (2006)
386. T. Ohtani, T. Nishikawa, K. Harada, K. Ikeda, N. Takayama, Novel nanocarbons with a mushroom shape found in glassy carbon powder. J. Alloys Compd. **483**(1–2), 491–494 (2009)
387. X. Peng, K. Koczkur, A. Chen, Synthesis of well-aligned bamboo-like carbon nanotube arrays from ethanol and acetone. J. Phys. D. Appl. Phys. **41**(9), 095409/1–095409/6 (2008)
388. B.I. Kharisov, A review for synthesis of nanoflowers. Recent Pat. Nanotechnol. **2**(3), 190–200 (2008)
389. H. Heli, A. Rahi, Synthesis and applications of nanoflowers. Recent Pat. Nanotechnol. **10**(2), 86–115 (2016)
390. C.N.R. Rao, F.L. Deepak, G. Gundiah, A. Govindaraj, Inorganic nanowires. Prog. Solid State Chem. **31**(1), 5–147 (2003)
391. J. Du, Z. Liu, Z. Li, B. Han, et al., Carbon nanoflowers synthesized by a reduction–pyrolysis–catalysis route. Mater. Lett. **59**(4), 456–458 (2005)
392. S. Thongtem, P. Singjai, T.P.S. Thongtem, Growth of carbon nanoflowers on glass slides using sparked iron as a catalyst. Mater. Sci. Eng. A **423**(1), 209–213 (2006)
393. Y. He, H. Zhao, X. Kong, CN 1962431 A 20070516, 2007
394. J. Xua, K. Houa, Z. Jua, et al., Synthesis and electrochemical properties of carbon dots/manganese dioxide (CQDs/MnO_2) nanoflowers for supercapacitor applications. J. Electrochem. Soc. **164**(2), A430–A437 (2017)
395. C. Qian, P. Guo, X. Zhang, et al., Nitrogen-doped mesoporous hollow carbon nanoflowers as high performance anode materials of lithium ion batteries. RSC Adv. **6**, 93519–93524 (2016)
396. J. Wang, C. Luo, T. Gao, A. Langrock, A.C. Mignerey, C. Wang, An advanced MoS_2/carbon anode for high-performance sodium-ion batteries. Small **11**(4), 473–481 (2015)
397. C.H. Pei, K. Shen, Synthesis of the nitrogen-doped carbon nanotube (NCNT) bouquets and their electrochemical properties. Electrochem. Commun. **35**, 80–83 (2013)
398. B. Nanda Sahoo, K. Balasubramanian, Facile synthesis of nano cauliflower and nano broccoli like hierarchical superhydrophobic composite coating using PVDF/carbon soot particles via gelation technique. J. Colloid Interface Sci. **436**, 111–121 (2014)
399. T. Krupenkin, Nanograss, nanobricks, nanonails, and other things useful in your nanolandscaping, in *Abstracts of Papers, 237th ACS National Meeting*, Salt Lake City, UT, United States, 22–26 Mar 2009, POLY-333
400. M. Wei, C. Terashima, M. Lv, A. Fujishima, Z.-Z. Gu, Boron-doped diamond nanograss array for electrochemical sensors. Chem. Commun. (24), 3624–3626 (2009)
401. M. Lv, M. Wei, F. Rong, C. Terashima, A. Fujishima, Z.-Z. Gu, Electrochemical detection of catechol based on as-grown and nanograss array boron-doped diamond electrodes. Electroanalysis **22**(2), 199–203 (2010)
402. K. Kakehi, S. Noda, S. Maruyama, Y. Yamaguchi, Individuals, grasses, and forests of single- and multi-walled carbon nanotubes grown by supported Co catalysts of different nominal thicknesses. Appl. Surf. Sci. **254**(21), 6710–6714 (2008)
403. M. Luling, G. Matthieu, A. Veneruso, Nanograss gamma detector. Eur. Pat. Appl. EP 2007-103888, 2008(13 pp)
404. X. Qi, W. Zhong, Y. Deng, C. Au, Y. Du, Synthesis of helical carbon nanotubes, worm-like carbon nanotubes and nanocoils at 450°C and their magnetic properties. Carbon. Volume Date 2010 **48**(2), 365–376 (2009)
405. L.S. Panchakarla, A. Govindaraj, Carbon nanostructures and graphite-coated metal nanostructures obtained by pyrolysis of ruthenocene and ruthenocene–ferrocene mixtures. Bull. Mater. Sci. **30**(1), 23–29 (2007)
406. S.-C. Wong, E.M. Sutherland, F.M. Uhl, Materials processes of graphite nanostructured composites using ball milling. Mater. Manuf. Process. **21**, 159–166 (2006)
407. J. Gonzalez, J. Herrero, Graphene wormholes: a condensed matter illustration of Dirac fermions in curved space. Nucl. Phys. B **B825**(3), 426–443 (2009)., Volume Date 2010
408. Y. Wang, Encapsulation of palladium crystallites in carbon and the formation of wormlike nanostructures. J. Am. Chem. Soc. **116**(1), 397–398 (1994)
409. B. Hu, Q. Zhang, Y. Wang, Pd/graphite as a superior catalyst for the direct synthesis of hydrogen peroxide from H_2 and O_2. Chem. Lett. **38**(3), 256–257 (2009)
410. L. Sousa Lobo, Intrinsic kinetics in carbon gasification: understanding linearity, “nanoworms” and alloy catalysts. Appl. Catal. B Environ. **148–149**, 136–143 (2014)
411. S.A.C. Carabineiro, L. Sousa Lobo, Understanding the reactions of CO_2, NO, and N_2O with activated carbon catalyzed by binary mixtures. Energy Fuel **30**(9), 6881–6891 (2016)

412. Y. Piao, K. An, J. Kim, T. Yu, T. Hyeon, Sea urchin shaped carbon nanostructured materials: carbon nanotubes immobilized on hollow carbon spheres. J. Mater. Chem. **16**(29), 2984–2989 (2006)
413. Y. Zhu, J. Li, M. Wan, L. Jiang, Electromagnetic functional urchin-like hollow carbon spheres carbonized by polyaniline micro/nanostructures containing $FeCl_3$ as a precursor. Eur. J. Inorg. Chem. **2009**(19), 2860–2864 (2009), https://onlinelibrary.wiley.com/doi/abs/10.1002/ejic.200900040
414. J. Shu, Urchin-structured MWNTs/HCS composite as anode material for high-capacity and high-power lithium-ion batteries. Electrochem. Solid-State Lett. **11**(12), A219–A222 (2008)
415. Z.H. Han, B. Yang, S.H. Kim, M.R. Zachariah, Application of hybrid sphere/carbon nanotube particles in nanofluids. Nanotechnology **18**, 105701, 4 pp (2007)
416. J.M. Romo-Herrera, D.A. Cullen, E. Cruz-Silva, D. Ramirez, B.G. Sumpter, V. Meunier, H. Terrones, D.J. Smith, M. Terrones, The role of sulfur in the synthesis of novel carbon morphologies: from covalent Y-junctions to sea-urchin-like structures. Adv. Funct. Mater. **19**(8), 1193–1199 (2009)
417. J. Chen, F. Cheng, Combination of lightweight elements and nanostructured materials for batteries. Acc. Chem. Res. **42**(6), 713–723 (2009)
418. Y. Wang, G. Xing, Z. Jun Han, Pre-lithiation of onion-like carbon/MoS_2 nano-urchin anodes for high-performance rechargeable lithium ion batteries. Nanoscale **6**, 8884–8890 (2014)
419. Y. Wang, Z. Jun Han, S. Fung Yu, et al., Core-leaf onion-like carbon/MnO_2 hybrid nano-urchins for rechargeable lithium-ion batteries. Carbon **64**, 230–236 (2013)
420. T.-H. Chen, T.-Y. Tsai, K.-C. Hsieh, S.-C. Chang, N.-H. Tai, H.-L. Chen, Two-dimensional metallic nanobowl array transferred onto thermoplastic substrates by microwave heating of carbon nanotubes. Nanotechnology **19**(46), 465303/1–465303/6 (2008)
421. J. Huang, Q. Zhang, M. Zhao, F. Wei, Process intensification by CO_2 for high quality carbon nanotube forest growth: double-walled carbon nanotube convexity or single-walled carbon nanotube bowls? Nano Res. **2**(11), 872–881 (2009)
422. Y. Tang, B.L. Allen, D.R. Kauffman, A. Star, Electrocatalytic activity of nitrogen-doped carbon nanotube cups. J. Am. Chem. Soc. **131**(37), 13200–13201 (2009)
423. H. Chun, M.G. Hahm, Y. Homma, R. Meritz, K. Kuramochi, L. Menon, L. Ci, P.M. Ajayan, Y.J. Jung, Engineering low-aspect ratio carbon nanostructures: nanocups, nanorings, and nanocontainers. ACS Nano **3**(5), 1274–1278 (2009)
424. M. Ohtani, K. Saito, S. Fukuzumi, Synthesis, characterization, redox properties, and photodynamics of donor-acceptor nanohybrids composed of size-controlled cup-shaped nanocarbons and porphyrins. Chem Eur J **15**(36), 9160–9168 (2009)., S9160/1-S9160/3
425. M. Gwan Hahm, A. Leela Mohana Reddy, D.P. Cole, et al., Carbon nanotube–nanocup hybrid structures for high power supercapacitor applications. Nano Lett. **12**(11), 5616–5621 (2012)
426. B. Kumar Gupta, G. Kedawat, P. Kumar, Field emission properties of highly ordered low-aspect ratio carbon nanocup arrays. RSC Adv. **6**, 9932–9939 (2016)
427. A.A. Moosa, F. Kubba, M. Raad, S.A. A. Ramazani, Mechanical and thermal properties of graphene nanoplates and functionalized carbon-nanotubes hybrid epoxy nanocomposites. Am. J. Mater. Sci. **6**(5), 125–134 (2016)
428. Y. Soo Yun, S. Youn Cho, J. Shim, et al., Microporous carbon nanoplates from regenerated silk proteins for supercapacitors. Adv. Mater. **25** (14), 1993–1998 (2013)
429. S. Lee, M. Eui Lee, M. Yeong Song, et al., Morphologies and surface properties of cellulose-based activated carbon nanoplates. Carbon Lett. **20**, 32–38 (2016)
430. J. Cao, C.J. Jafta, J. Gong, et al., Synthesis of dispersible mesoporous nitrogen-doped hollow carbon nanoplates with uniform hexagonal morphologies for supercapacitors. ACS Appl. Mater. Interfaces **8**(43), 29628–29636 (2016)
431. J.R. Roberts, R.R. Mercer, A.B. Stefaniak, et al., Evaluation of pulmonary and systemic toxicity following lung exposure to graphite nanoplates: a member of the graphenebased nanomaterial family. Part. Fibre Toxicol. **13**(34), 22 (2016)
432. D.N. Futaba, K. Miyake, K. Murata, Y. Hayamizu, T. Yamada, S. Sasaki, M. Yumura, K. Hata, Dual porosity single-walled carbon nanotube material. Nano Lett. **9**(9), 3302–3307 (2009)
433. M.N. Ghasemi-Nejhad, A. Cao. Editor(s): M. Laudon; B. Romanowicz. Development of nanodevices, nanostructures, nanocomposites, and hierarchical nanocomposites at Hawaii Nanotechnology Laboratory. in *NSTI Nanotech 2007, Nanotechnology Conference and Trade Show*, Santa Clara, 20–24 May 2007, 4, 538–542
434. S. Chakrabarti, T. Nagasaka, Y. Yoshikawa, L. Pan, Y. Nakayama, Growth of super long aligned brush-like carbon nanotubes. Jpn. J. Appl. Phys. **45**(28), L720–L722 (2006)
435. J. Dinesh, M. Eswaramoorthy, C.N.R. Rao, Use of amorphous carbon nanotube brushes as templates to fabricate GaN nanotube brushes and related materials. J. Phys. Chem. C **111**(2), 510–513 (2007)
436. V. Pushparaj, L. Mahadevan, S. Sreekala, L. Ci, R. Nalamasu, P.M. Ajayan, Deformation and capillary self-repair of carbon nanotube brushes. Carbon **50**, 5618–5630 (2012)
437. W. Marks, S. Yang, G. Dombi, S. Bhatia, Hydrogel composites containing carbon nanobrushes as tissue scaffolds. MRS Proc. **1498**, 53–58 (2013)
438. W. Marks, S. Yang, G. Dombi, S. Bhatia, Carbon nanobrush-containing poloxamer hydrogel. Composites for tissue regeneration. J. Long Term Eff. Med. Implants. **22**(3), 229–236 (2012)
439. Z. Zhu, L. Garcia-Gancedo, A.J. Flewitt, F. Moussy, Y. Li, W.I. Milne, Design of carbon nanotube fiber microelectrode for glucose biosensing. Chem. Techn. Biotechnol. **87**(2), 256–262 (2012)
440. J.-G. Fan, J.-X. Fu, A. Collins, Y.-P. Zhao, The effect of the shape of nanorod arrays on the nanocarpet effect. Nanotechnology **19**(4), 045713/1–045713/8 (2008)
441. Y.-P. Zhao, J.-G. Fan, Clusters of bundled nanorods in nanocarpet effect. Appl. Phys. Lett. **88**(10), 103123/1–103123/3 (2006)
442. J.-G. Fan, D. Dyer, G. Zhang, Y.-P. Zhao, Nanocarpet effect: pattern formation during the wetting of vertically aligned nanorod arrays. Nano Lett. **4**(11), 2133–2138 (2004)
443. M. Castellino, M. Tortello, S. Bianco, S. Musso, M. Giorcelli, M. Pavese, R.S. Gonnelli, A. Tagliaferro, Thermal and electronic properties of macroscopic multi-walled carbon nanotubes blocks. J. Nanosci. Nanotechnol. **10**(6), 3828–3833 (2010)

444. K. Krzysztof, M. Shaffer, A. Windle, Three-dimensional internal order in multiwall carbon nanotubes grown by chemical vapor deposition. Adv. Mater. **17**(6), 760–763 (2005)
445. N. Grobert, M. Mayne, M. Terrones, J. Sloan, R. E. Dunin-Borkowskif, R. Kamalakaran, T. Seeger, H. Terrones, M. Riihle, D.R.M. Walton, H. W. Kroto, H. L. Hutchisonf. Metal and alloy nanowires: iron and invar inside carbon nanotubes. in: CP591, *Electronic Properties of Molecular Nanostructures*, ed by H. Kuzmany, et al. (Ed), (American Institute of Physics, College Park, Mariland, USA, 2001), pp. 287–290
446. S.Y. Chen, H.Y. Miao, J.T. Lue, M.S. Ouyang, Fabrication and field emission property studies of multiwall carbon nanotubes. J. Phys. D. Appl. Phys. **37**, 273–279 (2004)
447. E.B. Sansom, D. Rinderknecht, M. Gharib, Controlled partial embedding of carbon nanotubes within flexible transparent layers. Nanotechnology **19**, 035302, 6 pp (2008)
448. H. Kai-Hsuan, T. Shinn-Shyong, K. Wen-Shyong, W. Bingqing, K. Tse-Hao, Growth of carbon nanofibers on carbon fabric with Ni nanocatalyst prepared using pulse electrodeposition. Nanotechnology **19**, 295602 (2008)
449. F. Seichepine, S. Salomon, M. Collet, et al., A combination of capillary and dielectrophoresis-driven assembly methods for wafer scale integration of carbon-nanotube-based nanocarpets. Nanotechnology **23**(9), 1–7 (2012)
450. J. Zhang, K. Wang, Q. Xu, et al., Beyond yolk–shell nanoparticles: Fe_3O_4@Fe_3C core@shell nanoparticles as yolks and carbon nanospindles as shells for efficient lithium ion storage. ACS Nano **9**(3), 3369–3376 (2015)
451. R. Liping, Z. Hangyu, L. Hanlin, L. Jingping, T. Fushan, S. Ying-Kang, Z. Xiaojun, Designed amphiphilic peptide forms stable nanoweb, slowly releases encapsulated hydrophobic drug, and accelerates animal hemostasis. PNAS **106**(13), 5105–5110 (2009) http://www.pnas.org/content/106/13/5105.full.pdf+html
452. S. Borhani, S.A.H. Ravandi, S.G. Etemad, Evaluation of surface roughness of polyacrylonitrile nanowebs. Iran. J. Polym Sci. Technol. (Persian Edition) **21**(1), 61–69 (2008)
453. G. Chen, H.J.C. Gommeren, L.M. Knorr, Liquid filtration media. U.S. Pat. Appl. US 2009026137, Publ. 2009, 8 pp. Cont.-in-part of U.S. Ser. No. 74,164. A1 20090129 US 2008-284027
454. C.-H. Chi, H.S. Lim, Pleated nanoweb structures for filters. Appl. Publ. 2009, 8 pp. US 2009064648 A1 20090312 US 2007-899803
455. D. C. Jones, W. H. Stone Fuel filter. U.S. Pat. Appl. Publ. 2008, 5 pp. US 2008105626 A1 20080508 US 2006-591733
456. S. Torres-Peiro, A. Diez, J.L. Cruz, M.V. Andres, C.M.B. Cordeiro, C.J. de Matos Fabrication and postprocessing of Ge-doped nanoweb fibers. in *SAIP Conference Proceedings*, 2008, 1055 (1st Workshop on Specialty Optical Fibers and Their Applications, 2008), 50–53
457. K.W. Hutchenson, M.A. Page, A. Raghavanpillai, S. Reinartz, C.M. Stancik, J.J. Van Gorp, Method for production of nanoweb composite material containing short perfluorinated alkyl chains. US Patent Appl. Publ. 2009, 11 pp. US 2009047498 A1 20090219 US 2007-837647
458. K.A. Darling, C.L. Reynolds Jr., D.N. Leonard, G. Duscher, R.O. Scattergood, C.C. Koch, Self-assembled three-dimensional Cu-Ge nanoweb composite. Nanotechnology **19**(13), 135603/1–135603/6 (2008)
459. B.W. Ahn, Y.S. Chi, T.J. Kang, Preparation and characterization of multi-walled carbon nanotube/poly(ethylene terephthalate) nanoweb. J. Appl. Polym. Sci. **110**(6), 4055–4063 (2008)
460. D. Kimmer, P. Slobodian, D. Petras, M. Zatloukal, R. Olejnik, P. Saha, Polyurethane/multiwalled carbon nanotube nanowebs prepared by an electrospinning process. J. Appl. Polym. Sci. **111**(6), 2711–2714 (2009)
461. T.-G. Kim, D. Ragupathy, A.I. Gopalan, K.-P. Lee, Electrospun carbon nanotubes-gold nanoparticles embedded nanowebs: prosperous multifunctional nanomaterials. Nanotechnology **21**(13), 134021 (2010)
462. S.-G. Kang, Y.-H. Bae, S.-L. Quan, I.-J. Chin, Electrospun PMMA/polyhedral oligomeric silsesquioxane (POSS) nanohybrid nanofibers. PMSE Prepr. **101**, 1293–1294 (2009)
463. N. Yahya, B.H. Guan, L.K. Pah, Catalytic effect of formation of a web-like carbon nanostructures. Solid State Sci. Technol. **15**(1), 22–29 (2007)
464. C.K. Chung, S.T. Hung, C.W. Lai, Effect of microstructure on the mechanical properties of carbon nanofilms deposited on the Si(100) at high temperature under ultra high vacuum. Surf. Coat. Technol. **204**(6–7), 1066–1070 (2009)
465. M. Endo, T. Hayashi, Y.A. Kim, M. Terrones, M.S. Dresselhaus, Applications of carbon nanotubes in the twenty-first century. Phil. Trans. R. Soc. Lond. A **362**, 2223–2238 (2004)
466. H.E. Cho, S.J. Seo, M.-S. Khil, H. Kim, Preparation of carbon nanoweb from cellulose nanowhisker. Fibers Polym. **168**(2), 271–275 (2015)
467. H.-D. Lim, Y. SooYun, Y. Ko, et al., Three-dimensionally branched carbon nanowebs as air-cathode for redox-mediated Li-O_2 batteries. Carbon **118**, 114–119 (2017)
468. L. Li, A. Manthiram, O- and N-doped carbon nanowebs as metal-free catalysts for hybrid Li-air batteries. Adv. Energy Mater. **4**(10), 1301795 (2014)
469. Z. Yang, Q. Meng, Z. Guo, et al., Highly reversible lithium storage in uniform $Li_4Ti_5O_{12}$/carbon hybrid nanowebs as anode material for lithium-ion batteries. Energy **55**, 925–932 (2013)
470. Q. Huang, L. Liu, D. Wang, et al., One-step electrospinning of carbon nanowebs on metallic textiles for high-capacitance supercapacitor fabrics. J. Mater. Chem. A **4**, 6802–6808 (2016)
471. S. Liu, L. Li, H.S. Ahn, A. Manthiram, Delineating the roles of Co_3O_4 and N-doped carbon nanoweb (CNW) in bifunctional Co_3O_4/CNW catalysts for oxygen reduction and oxygen evolution reactions. J. Mater. Chem. A **3**, 11615–11623 (2015)
472. G. Benedek, H. Vahedi-Tafreshi, E. Barborini, P. Piseri, P. Milani, C. Ducati, J. Robertson, The structure of negatively curved spongy carbon. Diam. Relat. Mater. **12**(3–7), 768–773 (2003)
473. F.H. Oliveira Carvalho, A. Rodrigues Vaz, S. Moshkalev, R. Valentim Gelamo, Synthesis of carbon nanostructures near room temperature using microwave PECVD. Mater. Res. **18**(4), 860–866 (2015)
474. N.Q. Le, Increasing carbon nanosponge oil absorbency through infusion of boron. AAAS 2015 Annual Meeting, 2015., https://aaas.confex.com/aaas/2015/webprogram/Paper15430.html
475. D.P. Hashim, N.T. Narayanan, J.M. Romo-Herrera, et al., Covalently bonded three-dimensional carbon nanotube solids via boron induced nanojunctions. Sci. Rep. **2**, 363 (2012)
476. F.C.C. Moura, R.M. Lago, Catalytic growth of carbon nanotubes and nanofibers on vermiculite to produce floatable hydrophobic “nanosponges” for oil spill remediation. Appl. Catal. B Environ. **90**(3–4), 436–440 (2009)

477. W. Zhou, R.P. Tiwari, R. Annamalai, R. Sooryakumar, V. Subramaniam, D. Stroud, Sound propagation in light-modulated carbon nanosponge suspensions. Phys. Rev. B **79**, 104204 (2009)
478. A.V. Rode, E.G. Gamaly, A.G. Christy, J.G. Fitz Gerald, S.T. Hyde, R.G. Elliman, B. Luther-Davies, A.I. Veinger, J. Androulakis, J. Giapintzakis, Unconventional magnetism in all-carbon nanofoam. Phys. Rev. B **70**, 054407, 9 pp (2004)
479. N.K. Sidhu, A.C. Rastogi, Bifacial carbon nanofoam-fibrous PEDOT composite supercapacitor in the 3-electrode configuration for electrical energy storage. Synth. Met. **219**, 1–10 (2016)
480. K. Lee, H. Song, K. Hoon Lee, et al., Nickel nanofoam/different phases of ordered mesoporous carbon composite electrodes for superior capacitive energy storage. ACS Appl. Mater. Interfaces **8**(34), 22516–22525 (2016)
481. R. Della Noce, S. Eugénio, M. Boudard, et al., One-step process to form a nickel-based/carbon nanofoam composite supercapacitor electrode using Na_2SO_4 as an eco-friendly electrolyte. RSC Adv. **6**, 15920–15928 (2016)
482. P. Ramakrishnan, S. Shanmugam, J. Hyun Kim, Dual heteroatom-doped carbon nanofoam-wrapped iron monosulfide nanoparticles: an efficient cathode catalyst for Li–O_2 batteries. ChemSusChem **10**(7), 1554–1562 (2017)
483. C.N. Chervin, M.J. Wattendorf, J.W. Long, N.W. Kucko, D.R. Rolison, Carbon nanofoam-based cathodes for Li–O_2 batteries: correlation of pore–solid architecture and electrochemical performance. J. Electrochem. Soc. **160**(9), A1510–A1516 (2013)
484. N. Frese, S. Taylor Mitchell, C. Neumann, A. Bowers, A. Gölzhäuser, K. Sattler, Fundamental properties of high-quality carbon nanofoam: from low to high density. Beilstein J. Nanotechnol. **7**, 2065–2073 (2016)
485. Z. Zhu, D. Tomanek, Formation and stability of cellular carbon foam structures: an ab initio study. Phys. Rev. Lett. **109**, 135501 (2012)
486. Y.-L. Li, W. Luo, X.-J. Chen, Z. Zeng, H.-Q. Lin, R. Ahuja, Formation of Nanofoam carbon and re-emergence of Superconductivity in compressed CaC_6. Sci. Rep. **3**, 3331 (2013)
487. E.G. Gamaly, A.V. Rode, Nanostructures created by lasers, in *Encyclopedia of Nanoscience and Nanotechnology*, ed. by H. S. Nalwa (Ed), vol. 7, (American Scientific Publishers, Valencia, California, 2004), pp. 783–809
488. A. Seral-Ascaso, R. Garriga, M.L. Sanjuán, et al., 'Laser chemistry' synthesis, physicochemical properties, and chemical processing of nanostructured carbon foams. Nanoscale Res. Lett. **8**, 233 (2013)
489. A.V. Rode, E.G. Gamaly, B. Luther-Davies, Formation of cluster-assembled carbon nano-foam by high-repetition-rate laser ablation. *Appl. Phys. A Mater. Sci. Process.* **70**, 135–144 (2000)
490. S. Li, J. Guangbin, L. Liya, Magnetic carbon nanofoams. J. Nanosci. Nanotechnol. **9**, 1133–1136 (2009)
491. D.W.M. Lau, D.G. McCulloch, N.A. Marks, N.R. Madsen, A.V. Rode, High-temperature formation of concentric fullerene-like structures within foam-like carbon: experiment and molecular dynamics simulation. Phys. Rev. B **75**, 233408 (2007)
492. Z. Liu, S.-K. Joung, T. Okazaki, K. Suenaga, Y. Hagiwara, T. Ohsuna, K. Kuroda, S. Iijima, Self-assembled double ladder structure formed inside carbon nanotubes by encapsulation of $H_8Si_8O_{12}$. ACS Nano **3**(5), 1160–1166 (2009)
493. S.P. Sharma, S.C. Lakkad, Morphology study of carbon nanospecies grown on carbon fibers by thermal CVD technique. Surf. Coat. Technol. **203**(10–11), 1329–1335 (2009)
494. C. Ronning, D. Schwen, One dimensional material from semiconductors. Nanowires, nanosaws, nanospirals. Physik in Unserer Zeit **37**(1), 34–40 (2006)
495. V.Y. Prinz, Three-dimensional self-shaping nanostructures based on free stressed heterofilms. Russ. Phys. J. (Translation of Izvestiya Vysshikh Uchebnykh Zavedenii, Fizika) **46**(6), 568–576 (2003)
496. P.G. Mezey, Computational quantum chemistry design of nanospirals and nanoneedles. Lecture Series on Computer and Computational Sciences **6**(Trends and Perspectives in Modern Computational Science), 222–230 (2006)
497. S. Vaudreuil, M. Bousmina, Stretchable carbon nanosprings production by a catalytic growth process. J. Nanosci. Nanotechnol. **9**(8), 4880–4885 (2009)
498. L. Liu, J. Zhao, Toroidal and coiled carbon nanotubes, in *Syntheses and Applications of Carbon Nanotubes and Their Composites*, (InTech, London, UK, 2013), pp. 257–281
499. A. Zettl, C. John, Sharpened nanotubes, nanobearings, and nanosprings, in *CP544, Electronic Properties of Novel Materials—Molecular Nanostructures*, ed. by H. Kuzmany et al. (Eds), (American Institute of Physics, College Park, Maryland, USA, 2000)
500. K. Mukhopadhyay, D. Porwal, K.U.B. Rao, Carbon micro/nano spring structures in the absence of sulphurous promoter by CCVD method. J. Nanosci. Nanotechnol. **7**(6), 1851–1854 (2007)
501. N. Tang, W. Kuo, C. Jeng, L. Wang, K. Lin, Y. Du, Coil-in-coil carbon nanocoils: 11 gram-scale synthesis, single nanocoil electrical properties, and electrical contact improvement. ACS Nano **4**(2), 781–788 (2010)
502. K. Nakamatsu, J. Igaki, M. Nagase, T. Ichihashi, S. Matsui, Mechanical characteristics of tungsten-containing carbon nanosprings grown by FIB-CVD. Microelectron. Eng. **83**(4–9), 808–810 (2006)
503. K. Nakamatsu, T. Ichihashi, K. Kanda, Y. Haruyama, T. Kaito, S. Matsui, Nanostructure analysis of nanosprings fabricated by focused-ion-beam chemical vapor deposition. Jpn. J. Appl. Phys. **48**(10), 105001/1–105001/4 (2009)
504. X. Chen, S. Zhang, D.A. Dikin, W. Ding, R.S. Ruoff, Mechanics of a carbon nanocoil. Nano Lett. **3**(9), 1299–1304 (2003)
505. M. Mahdi Zaeria, S. Ziaei-Rad, Elastic behavior of carbon nanocoils: a molecular dynamics study. AIP Adv. **5**, 117114 (2015)
506. M. Neek-Amal, J. Beheshtian, F. Shayeganfar, S.K. Singh, J.H. Los, F.M. Peeters, Spiral graphone and one-sided fluorographene nanoribbons. Phys. Rev. B **87**, 075448 (2013)
507. J. Liu, Y.-L. Lu, M. Tian, F. Li, J. Shen, Y. Gao, L. Zhang, The interesting influence of nanosprings on the viscoelasticity of elastomeric polymer materials: simulation and experiment. Adv. Funct. Mater. **23**(9), 1156–1163 (2013)
508. J. Zhan. Editor(s): Voler, Nicolas H., Carbon nanotubes as use of nanothermometer. Bando, Yoshio. Materials Integration **17**(6), 34–40 (2004)
509. Y. Bando, World smallest nanothermometer using carbon nanotube. Kagaku **59**(6), 20–24 (2004)
510. Y. Bando, Oxide-nanotubes as use of nanothermometer. Seramikkusu **41**(4), 262–266 (2006)
511. Y. Bando, Nanothermometer using oxide nanotubes. Materials Integration **18**(1), 42–47 (2004). Volume Date 2005
512. Y. Bando, Study of nanomaterials by using state-of-the-art microscopy. Kagaku to Kogyo **57**(6), 595–600 (2004)
513. G. Yihua, B. Yoshio, Carbon nanothermometer containing gallium. Nature **415**(7), 599–600 (2002)

514. A.M. Popova, Y.E. Lozovik, E. Bichoutskaia, G.S. Ivanchenko, N.G. Lebedev, E.K. Krivorotov, An electromechanical nanothermometer based on thermal vibrations of carbon nanotube walls. Phys. Solid State **51**(6), 1306–1314 (2009)
515. R. Ansari, M. Daliri, M. Hosseinzadeh, On the van der Waals interaction of carbon nanotubes as electromechanical nanothermometers. Acta Mech. Sinica **29**(4), 622–632 (2013)
516. Z. Liu, Y. Bando, J. Hu, K. Ratinac, S.P. Ringer, A novel method for practical temperature measurement with carbon nanotube nanothermometers. Nanotechnology **17**(15), 3681–3684 (2006)
517. J. Zhan, Y. Bando, J. Hu, D. Golberg, Nanothermometers: bulk synthesis and calibration, in *Abstracts of Papers,* 232nd ACS National Meeting, San Francisco, 10–14 Sept 2006, INOR-488
518. Y. Gao, Y. Bando, D. Golberg, Melting and expansion behavior of indium in carbon nanotubes. Appl. Phys. Lett. **81**(22), 4133–4135 (2002)
519. A.M. Popov, Y.E. Lozovik, E. Bichoutskaia, G.S. Ivanchenko, N.G. Lebedev, E.K. Krivorotov, An electromechanical nanothermometer based on thermal vibrations of carbon nanotube walls. Phys. Solid State **51**(6), 1306–1314 (2009)
520. A.M. Popov, Y.E. Lozovik, E. Bichoutskaia, G.S. Ivanchenko, N.G. Lebedev, E.K. Krivorotov, Electromechanical nanothermometer based on carbon nanotubes. Fullerenes, Nanotubes, Carbon Nanostruct. **16**(5–6), 352–356 (2008)
521. A. Vyalikh, R. Klingeler, S. Hampel, D. Haase, M. Ritschel, A. Leonhardt, E. Borowiak-Palen, M. Rümmeli, A. Bachmatiuk, R.J. Kalenczuk, H.-J. Grafe, B. Büchner, A nanoscaled contactless thermometer for biological systems. Phys. Status Solidi B **244**(11), 4092–4096 (2007)
522. C. Wang, K. Jiang, Q. Wu, J. Wu, C. Zhang, Green synthesis of red-emitting carbon nanodots as a novel "turn-on" nanothermometer in living cells. Chem. Eur. J. **22**(41), 14475–14479 (2016)
523. X. Liu, X. Tang, Y. Hou, Q. Wu, G. Zhang, Fluorescent nanothermometers based on mixed shell carbon nanodots. RSC Adv. **5**, 81713–81722 (2015)
524. K. Jiang, J. Wu, Q. Wu, X. Wang, C. Wang, Y. Li, Stable fluorescence of green-emitting carbon nanodots as a potential nanothermometer in biological media. Part. Part. Syst. Charact. **4**(2), 1600197 (2017)
525. Y. Yang, W. Kong, H. Li, et al., Fluorescent N-doped carbon dots as in vitro and in vivo nanothermometer. ACS Appl. Mater. Interfaces **7**(49), 27324–27330 (2015)
526. Y. Nakayama, Nanomachine "nanotweezers". Kagaku to Kogyo **56**(6), 663–666 (2003)
527. C. M. Lieber, J. H. Hafner, C. Cheung Li, P. Kim, Direct growth of carbon nanotubes, and their use in nanotweezers, 2002, 46 pp. WO 2002026624
528. J. Chang, B.-K. Min, J. Kim, S.-J. Lee, L. Lin, Electrostatically actuated carbon nanowire nanotweezers. Smart Mater. Struct. **18**(6) (2009). 065017/1-065017/7
529. J. Lee, S. Kim, Manufacture of a nanotweezer using a length controlled CNT arm. Sensors Actuators A Phys. **A120**(1), 193–198 (2005)
530. G. Liu, Y. Miyake, N. Komatsu, Nanocalipers as novel molecular scaffolds for carbon nanotubes. Org. Chem. Front. **4**, 911–919 (2017)
531. J. M. Tour, NanoCars, in *Abstracts*, *65th Southwest Regional Meeting of the American Chemical Society*, El Paso, 4–7 Nov 2009, SWRM-130
532. T. Sasaki, A.J. Osgood, L.B. Alemany, K.F. Kelly, J.M. Tour, Synthesis of a nanocar with an angled chassis. Toward circling movement. Org. Lett. **10**(2), 229–232 (2008)
533. T. Sasaki, J.M. Tour, Synthesis of a dipolar nanocar. Tetrahedron Lett. **48**(33), 5821–5824 (2007)
534. A.V. Akimov, A.V. Nemukhin, A.A. Moskovsky, A.B. Kolomeisky, J.M. Tour, Molecular dynamics of surface-moving thermally driven nanocars. J. Chem. Theory Comput. **4**(4), 652–656 (2008)
535. T. Sasaki, J.M. Guerrero, J.M. Tour, The assembly line: self-assembling nanocars. Tetrahedron **64**(36), 8522–8529 (2008)
536. S. Khatua, J.M. Guerrero, K. Claytor, G. Vives, A.B. Kolomeisky, J.M. Tour, S. Link, Micrometer-scale translation and monitoring of individual nanocars on glass. ACS Nano **3**(2), 351–356 (2009)
537. G.J. Simpson, V. García-López, P. Petermeier, L. Grill, J.M. Tour, How to build and race a fast nanocar. Nat. Nanotechnol. **12**, 604–606 (2017)
538. G. Vives, J.M. Tour, Synthesis of single-molecule nanocars. Acc. Chem. Res. **42**(3), 473–487 (2009)
539. G. Vives, J. M. Tour, Synthesis of a nanocar with organometallic wheels, in *Abstracts of Papers,* 238th ACS National Meeting, Washington, DC, 16–20 Aug 2009, INOR-346
540. G. Vives, J.M. Tour, Synthesis of a nanocar with organometallic wheels. Tetrahedron Lett. **50**(13), 1427–1430 (2009)
541. J.-F. Morin, Y. Shirai, J.M. Tour, En route to a motorized nanocar. Org. Lett. **8**(8), 1713–1716 (2006)
542. Y. Shirai, A.J. Osgood, Y. Zhao, Y. Yao, L. Saudan, H. Yang, Y.-H. Chiu, L.B. Alemany, T. Sasaki, J.-F. Morin, J.M. Guerrero, K.F. Kelly, J.M. Tour, Surface-rolling molecules. J. Am. Chem. Soc. **128**(14), 4854–4864 (2006)
543. Y. Shirai, A.J. Osgood, Y. Zhao, K.F. Kelly, J.M. Tour, Directional control in thermally driven single-molecule nanocars. Nano Lett. **5**(11), 2330–2334 (2005)
544. Z.L. Wang, P. Poncharal, W.A. de Heer, Measuring physical and mechanical properties of individual carbon nanotubes by in situ TEM. J. Phys. Chem. Solids **61**, 1025–1030 (2000)
545. A. Mirmohseni, M. Shojaei, M.A.H. Feizi, F.F. Azhar, M. Rastgouye-Houjaghan, Application of quartz crystal nanobalance and principal component analysis for detection and determination of nickel in solution. J. Environ. Sci. Health, Part A: Tox. Hazard. Subst. Environ. Eng. **45** (9), 1119–1125 (2010)
546. O.A. Williams, V. Mortet, M. Daenen, K. Haenen, The diamond nano-balance. J. Nanosci. Nanotechnol. **9**(6), 3483–3486 (2009)
547. Y. Huang, X. Bai, Y. Zhang, In situ mechanical properties of individual ZnO nanowires and the mass measurement of nanoparticles. J. Phys. Condens. Matter **18**(15), L179–L184 (2006)
548. J. Bai, X. Zhong, S. Jiang, Y. Huang, X. Duan, Graphene nanomesh. Nat. Nanotechnol. **5**(3), 190–194 (2010)
549. B. Jingwei, Z. Xing, J. Shan, H. Yu, D. Xiangfeng, Graphene nanomesh. Nat. Nanotechnol. **5**(3), 190–194 (2010)
550. X. Liang, Y.-S. Jung, S. Wu, A. Ismach, D.L. Olynick, S. Cabrini, J. Bokor, Formation of bandgap and subbands in graphene nanomeshes with sub-10 nm ribbon width fabricated via nanoimprint lithography. Nano Lett. **10**(7), 2454–2460 (2010)
551. O. Akhavan, Graphene nanomesh by ZnO nanorod photocatalysts. ACS Nano **4**(7), 4174–4180 (2010)
552. H.L. Zhang, W. Chen, H. Huang, L. Chen, A.T.S. Wee, Preferential trapping of C_{60} in nanomesh voids. J. Am. Chem. Soc. **130**, 2720–2721 (2008)

553. H. Wang, L. Zhi, K. Liu, et al., Thin-sheet carbon nanomesh with an excellent electrocapacitive performance. Adv. Funct. Mater. **25**(34), 5420–5427 (2015)
554. D.-P. Yang, X. Wang, X. Guo, et al., UV/O_3 generated graphene nanomesh: formation mechanism, properties, and FET studies. J. Phys. Chem. C **118**(1), 725–731 (2014)
555. H.-H. Byeon, W. Chul Lee, W. Kim, et al., Bio-fabrication of nanomesh channels of single-walled carbon nanotubes for locally gated field-effect transistors. Nanotechnology **28**, 025304 (2017)
556. X.-L. Su, M.-Y. Cheng, L. Fu, et al., Superior supercapacitive performance of hollow activated carbon nanomesh with hierarchical structure derived from poplar catkins. J. Power Sources **362**, 27–38 (2017)
557. S.-J. Choi, P. Bennett, D. Lee, J. Bokor, Highly uniform carbon nanotube nanomesh network transistor. Nano Res. (8), 1320 (2015)
558. X.F. Yang, H.L. Wang, Y.S. Chen, et al., Giant spin thermoelectric effects in all-carbon nanojunctions. Phys. Chem. Chem. Phys. **17**, 22815–22822 (2015)
559. Y. Liao, Y. Xie, K. Pan, et al., Fe_3W_3C/WC/graphitic carbon ternary nanojunction hybrids for dye-sensitized solar cells. ChemSusChem **8**(4), 726–733 (2015)
560. I.A. Pshenichnyuk, P.B. Coto, S. Leitherer, M. Thoss, Charge transport in pentacene-graphene nanojunctions. J. Phys. Chem. Lett. **4**(5), 809–814 (2013)
561. M.M. Hassan, A.A. El-Barbary, M.A. Kamel, K.M. Eid, H.O. Taha, Mono-vacancy and B-doped defects in carbon heterojunction nanodevices. Graphene **4**, 84–90 (2015)
562. D. Szczesniak, A. Khater, Z. Bak, R. Szczesniak, M. Abou Ghantous, Quantum conductance of silicon-doped carbon wire nanojunctions. Nanoscale Res. Lett. **7**, 616 (2012)
563. A.G. Krivenko, N.S. Komarova, Electrochemistry of nanostructured carbon. Russ. Chem. Rev. **77**(11), 927–943 (2008)
564. A. Barhoum, P. Samyn, T. Öhlundd, A. Dufresnee, Review of recent research on flexible multifunctional nanopapers. Nanoscale **9**, 15181–15205 (2017)
565. Y. Zhao, E.D. Cabrera, M.C. Jose, L.J. Lee, Chapter 4 - Carbon nanopaper: a platform to high-performance multifunctional composites, in *Nanopapers From Nanochemistry and Nanomanufacturing to Advanced Applications*, Micro and Nano Technologies, (Elsevier Science, New York, 2018), pp. 87–120
566. L. Hu, N. Liu, M. Eskilsson, G. Zheng, J. McDonough, L. Wågberg, Y. Cui, Silicon-conductive nanopaper for Li-ion batteries. Nano Energy **2**, 138–145 (2013)
567. D.P. Wong, R. Suriyaprabha, R. Yuvakumar, V. Rajendran, Y.-T. Chen, B.-J. Hwang, L.-C. Chen, K.-H. Chen, Binder-free rice husk-based silicon–graphene composite as energy efficient Li-ion battery anodes. J. Mater. Chem. A **2**, 13437–13441 (2014)
568. J. Zhuge, J. Gou, R.-H. Chen, et al., Fire retardant evaluation of carbon nanofiber/graphite nanoplatelets nanopaper-based coating under different heat fluxes. Compos. Part B **43**, 3293–3305 (2012)
569. H. Lu, Y. Liu, J. Leng, Carbon nanopaper enabled shape memory polymer composites for electrical actuation and multifunctionalization. Marcomol. Mater. Eng. **297**(12), 1138–1147 (2012)
570. H. Lu, Y. Liu, J. Gou, J. Leng, S. Du, Electrical properties and shape-memory behavior of self-assembled carbon nanofiber nanopaper incorporated with shape-memory polymer. Smart Mater. Struct. **19**(7), 075021/1–075021/7 (2010)
571. H. Lu, Y. Liu, J. Gou, J. Leng, S. Du, Synergistic effect of carbon nanofiber and carbon nanopaper on shape memory polymer composite. Appl. Phys. Lett. **96**(8), 084102/1–084102/3 (2010)
572. H. Lu, P. Bai, W. Yin, F. Liang, J. Gou, Magnetically aligned carbon nanotubes in nanopaper for electro-activated shape-memory nanocomposites. Nanosci. Nanotechnol. Lett. **5**(7), 732–736 (2013)
573. H. Lu, F. Liang, Y. Yao, J. Gou, D. Hui, Self-assembled multi-layered carbon nanofiber nanopaper for significantly improving electrical actuation of shape memory polymer nanocomposite. Compos. Part B **59**, 191–195 (2014)
574. H. Lu, W.M. Huang, J. Leng, Functionally graded and self-assembled carbon nanofiber and boron nitride in nanopaper for electrical actuation of shape memory nanocomposites. Compos. Part B **62**, 1–4 (2014)
575. X. Zhao, J. Gou, G.G. Song, J. Ou, Strain monitoring in glass fiber reinforced composites embedded with carbon nanopaper sheet using Fiber Bragg Grating (FBG) sensors. Compos. Part B Eng. **40B**(2), 134–140 (2009)
576. M.R. Bromberg, A. Patlolla, R. Segal, Y. Feldman, Q. Wang, Z. Iqbal, A.I. Frenkel, Synthesis and characterization of platinum nanoparticles on single-walled carbon nanotube “nanopaper” support. J. Phys. Conf. Ser. **190**, 012155 (2009)
577. J. Gou, R. Blanco, Z. Zhao, A. Khan, A. Appalla, Synthesis of nickel-coated carbon nanopaper sheets by pulse laser deposition. Materials Research Society Symposium Proceedings*,* 2007, 1006E (Transport Behavior in Heterogeneous Polymeric Materials and Composites), No pp. given, Paper #: 1006-R01-09
578. M. Das, C. Bittencourt, J.-J. Pireaux, S.A. Shivashankar, Metallic Li in carbonaceous nanotubes grown by metalorganic chemical vapor deposition from a metalorganic precursor. Appl. Organomet. Chem. **22**(11), 647–658 (2008)
579. D.A. Lowy, A. Patrut, Nanobatteries: decreasing size power sources for growing technologies. Recent Pat. Nanotechnol. **2**(3), 208–219 (2008)
580. Fast-charging nano batteries. Am. Ceram. Soc. Bull. **85**(10), 21–22 (2006) https://bulletin-archive.ceramics.org/uctv2f/
581. J.W. Long, B. Dunn, D.R. Rolison, H.S. White, Three-dimensional battery architectures. Chem. Rev. **104**, 4463–4492 (2004)
582. P. Sehrawat, C. Julien, S.S. Islam, Carbon nanotubes in Li-ion batteries: a review. Mater. Sci. Eng. B **213**, 12–40 (2016)
583. B. Liu, X. Wu, S. Wang, et al., Flexible carbon nanotube modified separator for high-performance lithium-sulfur batteries. Nano **7**, 196 (2017)
584. W.-J. Yu, C. Liu, L. Zhang, et al., Synthesis and electrochemical lithium storage behavior of carbon nanotubes filled with iron sulfide nanoparticles. Adv. Sci. **3**, 1600113 (2016)
585. W.-S. Kim, J. Choi, S.-H. Hong, Meso-porous silicon-coated carbon nanotube as an anode for lithium-ion battery. Nano Res. **9**(7), 2174–2181 (2016)
586. C. Shen, J. Xie, M. Zhang, et al., Carbon nanotube (CNT) foams as sulfur hosts for high performance lithium sulfur battery. ECS Trans. **77**(11), 457–465 (2017)
587. A.-R.O. Raji, R. Villegas Salvatierra, N. Dong Kim, et al., Lithium batteries with nearly maximum metal storage. ACS Nano **11**(6), 6362–6369 (2017)

588. http://www.nanowerk.com/spotlight/spotid=3331.php
589. A.C. Romain, J. Nicolas, Long term stability of metal oxide-based gas sensors for e-nose environmental applications: an overview. Sensors Actuators B Chem. **B146**(2), 502–506 (2010)
590. F. Korel, M.O. Balaban, Electronic nose technology in food analysis, in *Handbook of Food Analysis Instruments*, ed. by S. Otles (Ed), (CRC Press, Boca Raton, FL, USA, 2009), pp. 365–378
591. H. Nanto, Electronic nose (e-NOSE) system. Materials Integration **21**(5, 6), 99–104 (2008)
592. A.D. Wilson, M. Baietto, Applications and advances in electronic-nose technologies. Sensors **9**(7), 5099–5148 (2009)
593. C. Wongchoosuk, A. Wisitsoraat, A. Tuantranont, T. Kerdcharoen, Portable electronic nose based on carbon nanotube-SnO_2 gas sensors and its application for detection of methanol contamination in whiskeys. Sensors Actuators B Chem. **B147**(2), 392–399 (2010)
594. S. Kaur, A. Kumar, J.K. Rajput, P. Arora, H. Singh, SnO_2—glycine functionalized carbon nanotubes based electronic nose for detection of explosive materials. Sens. Lett. **14**(7), 733–739 (2016)
595. P. Lorwongtragool, E. Sowade, N. Watthanawisuth, R.R. Baumann, T. Kerdcharoen, A novel wearable electronic nose for healthcare based on flexible printed chemical sensor array. Sensors **14**, 19700–19712 (2014)
596. B.D. Lampson, A. Khalilian, J.K. Greene, Y.J. Han, D.C. Degenhardt, Development of a portable electronic nose for detection of cotton damaged by Nezara viridula (Hemiptera: Pentatomidae). J. Insects **2014**, 297219, 8 pp (2014)
597. M.L. Rodríguez-Méndez, J.A. De Saja, R. González-Antón, et al., Electronic noses and tongues in wine industry. Front. Bioeng. Biotechnol. **4**, 81 (2016)
598. A.M. Popov, E. Bichoutskaia, Y.E. Lozovik, A.S. Kulish, Nanoelectromechanical systems based on multi-walled nanotubes: nanothermometer, nanorelay, and nanoactuator. Phys. Status Solidi A **204**(6), 1911–1917 (2007)
599. J. Li, X. Wang, L. Zhao, X. Gao, Y. Zhao, R. Zhouc, Rotation motion of designed nano-turbine. Sci. Rep. **4**, 5846 (2014)
600. J. Basu, C. Roy Chaudhuri, Graphene nanogrids FET immunosensor: signal to noise ratio enhancement. Sensors **16**, 1481 (2016)
601. O.E. Glukhova, I.N. Salii, V.P. Meshchanov, Nano-autoclave on the basis of carbon nanopeapod. Nano- i Mikrosistemnaya Tekhnika **10**, 47–52 (2007)
602. A. Mayoral, H. Barron, R. Estrada-Salas, A. Vazquez-Duran, M. Jose-Yacaman, Nanoparticle stability from the nano to the meso interval. Nanoscale **2**, 335–342 (2010)
603. W. Wang, T. Christensen, A.-P. Jauho, K.S. Thygesen, M. Wubs, N.A. Mortensen, Plasmonic eigenmodes in individual and bow-tie graphene nanotriangles. Sci. Rep. (2015). https://doi.org/10.1038/srep09535
604. H.P. Heiskanen, M. Manninen, J. Akola, Electronic structure of triangular, hexagonal and round graphene flakes near the Fermi level. 2008, arXiv:0809.4162v1. https://arxiv.org/pdf/0809.4162
605. D. Gorakh Babar, B. Pakhira, S. Sarkar, DNA–carbon nano onion aggregate: triangle, hexagon, six-petal flower to dead-end network. Appl. Nanosci. **7**(6), 291–297 (2017)
606. V.I. Merkulov, A.V. Melechko, M.A. Guillorn, D.H. Lowndes, M.L. Simpson, Effects of spatial separation on the growth of vertically aligned carbon nanofibers produced by plasma-enhanced chemical vapor deposition. Appl. Phys. Lett. **80**(3), 476–478 (2002)
607. M. Hu, X. Dong, Y. Pan, et al., A metallic carbon consisting of helical carbon triangle chains. J. Phys. Condens. Matter **26**, 235402, 6 pp (2014)
608. Y. Masuda, H. Yoshida, S. Takeda, H. Kohno, In situ transmission electron microscopy of individual carbon nanotetrahedron/nanoribbon structures in Joule heating. Appl. Phys. Lett. **105**, 083107 (2015)
609. H. Kohno, Y. Masuda, *In situ* transmission electron microscopy of individual carbon nanotetrahedron/ribbon structures in bending. Appl. Phys. Lett. **106**, 193103 (2015)
610. H. Kohno, T. Hasegawa, Chains of carbon nanotetrahedra/nanoribbons. Sci. Rep. **5**, 8430 (2015)
611. T. Hasegawa, H. Kohno, Splitting and joining in carbon nanotube/nanoribbon/nanotetrahedron growth. Phys. Chem. Chem. Phys. **17**, 3009–3013 (2015)
612. S. Kumar Sonkar, M. Saxena, M. Saha, S. Sarkar, Carbon nanocubes and nanobricks from pyrolysis of rice. J. Nanosci. Nanotechnol. **10**, 4064–4067 (2010)
613. B. Sun, S. Chen, H. Liu, G. Wang, Mesoporous carbon nanocube architecture for high-performance lithium–oxygen batteries. Adv. Funct. Mater. **25**, 4436–4444 (2015)
614. G. Oza, M. Ravichandran, V.-I. Merupo, et al., Camphor-mediated synthesis of carbon nanoparticles, graphitic shell encapsulated carbon nanocubes and carbon dots for bioimaging. Sci. Rep. **6**, 21286 (2016)
615. Y. Liang, J. Wei, X. Zhang, et al., Synthesis of nitrogen-doped porous carbon nanocubes as a catalyst support for methanol oxidation. ChemCatChem **8**(11), 1901–1904 (2016)
616. F. Gao, F. Zhou, Y. Yao, et al., Ordered assembly of platinum nanoparticles on carbon nanocubes and their application in the non-enzymatic sensing of glucose. J. Electroanal. Chem. **803**, 165–172 (2017)
617. X.-W. Liu, Z.-J. Yao, Y.-F. Wang, X.-W. Wei, Graphene oxide sheet-prussian blue nanocomposites: green synthesis and their extraordinary electrochemical properties. Colloids Surf. B. Biointerfaces **81**(2), 508–512 (2010)
618. J. Xi, Y. Xia, Y. Xu, J. Xiao, S. Wang, (Fe,Co)@nitrogen-doped graphitic carbon nanocubes derived from polydopamine-encapsulated metal–organic frameworks as a highly stable and selective non-precious oxygen reduction electrocatalyst. Chem. Commun. **51**, 10479–10482 (2015)
619. W. Chen, X. Zhang, F. Ai, Graphitic carbon nanocubes derived from ZIF-8 for photothermal therapy. Inorg. Chem. **55**(12), 5750–5752 (2016)
620. X. Fang, L. Jiao, S.-H. Yu, H.-L. Jiang, Metal–organic framework-derived FeCo-N-doped hollow porous carbon nanocubes for electrocatalysis in acidic and alkaline media. ChemSusChem **10**, 3019–3024 (2017)
621. S. Chen, B. Sun, X. Xie, et al., Multi-chambered micro/mesoporous carbon nanocubes as new polysulfides reservoirs for lithium–sulfur batteries with long cycle life. Nano Energy **16**, 268–280 (2015)
622. H.X. Zhang, P.X. Feng, Synthesis of the vertically aligned carbon hexagonal nanoprism arrays and their application for field emission. Appl. Surf. Sci. **255**, 5939–5942 (2009)